รายงานฉบับสมบูรณ์

โครงการ

"สารลดแรงตึงผิวประยุกต์, พลาสมาและปฏิกิริยาเคมี และเชื้อเพลิงชีวภาพ"

โดย

ศาสตราจารย์ ดร. สุเมธ ชวเดช

วิทยาลัยปิโตรเลียมและปิโตรเคมี

จุฬาลงกรณ์มหาวิทยาลัย

เสนอต่อ

สำนักงานกองทุนสนับสนุนการวิจัย

กันยายน2560

รายงานฉบับสมบูรณ์

โครงการ

"สารลดแรงตึงผิวประยุกต์, พลาสมาและปฏิกิริยาเคมี และเชื้อเพลิงชีวภาพ"

โดย

ศาสตราจารย์ ดร. สุเมธ ชวเดช

วิทยาลัยปิโตรเลียมและปิโตรเคมี

จุฬาลงกรณ์มหาวิทยาลัย

(ความเห็นในรายงานนี้เป็นของผู้วิจัยสกว.และจุฬาลงกรณ์มหาวิทยาลัย ไม่จำเป็นต้องเห็นด้วยเสมอไป)

รายงานฉบับสมบูรณ์

ชื่อหัวหน้าโครงการวิจัยผู้รับทุน ศาสตราจารย์ ดร. สุเมธ ชวเดช

รายงานในช่วงตั้งแต่ 1 กันยายน 2557ถึง 31 สิงหาคม2560

1. กิจกรรมที่ได้ดำเนินการ

-ได้ช่วยแก้ไขบทความวิจัยตีพิมพ์ในวารสารนานาชาติของอาจารย์ในกลุ่มวิจัยจำนวน 10เรื่อง

-ได้ตีพิมพ์ผลงานวิจัยในวารสารนานาชาติ

-ได้ให้คำแนะนำงานวิจัยของอาจารย์ในกลุ่มวิจัย

-ผลิตบัณฑิต

-แสวงหาทุนวิจัยทั้งของตัวเองและช่วยอาจารย์ในกลุ่มวิจัย

2. ผลงาน

2.1 ผลงานตีพิมพ์ในวารสารวิชาการนานาชาติ

1. Intanoo, P., Suttikul, T., Leethochawalit, M., Gulari, E. and Chavadej*, S. (2014), Hydrogen Production from Alcohol Wastewater with Added Fermentation Residue by an Anaerobic Sequencing Batch Reactor (ASBR) under Thermophilic Operation, *International Journal of Hydrogen Energy,* 39, 9611-9620 (impact factor = 3.313)

2. Pornmai, K., Arthiwet, N., Rueangjitt, N., Sekiguchi, H. and Chavadej*, S. (2014), Synthesis Gas Production by Combined Reforming of CO_2-Containing Natural Gas with Steam and Partial Oxidation in a Multistage Gliding Arc Discharge System*, Industrial and Engineering Chemistry Research*, 53, 11891-11900 (impact factor = 2.587)

3. Intanoo, P., Rangsanvigit, P., Malakul, P. and Chavadej*, S. (2014), Optimization of Separate Hydrogen and Methane Production from Cassava Wastewater using Two-Stage Upflow Anaerobic

Sludge Blanket Reactor (UASB) System under Thermophilic Operation, *Bioresource Technology*, 173, 256-265 (impact factor = 4.494)

4. Echaroj, S., Santikunaporn*, M. and Chavadej, S. (2015), Micro-Kinetics Modeling of The Catalytic Dehydration of 1-Decanol over Precipitated γ-Al$_2$O$_3$, *Reaction Kinetics, Mechanisms and Catalysis*, 114, 75-91 (impact factor = 1.265)

5. Insorn, P. and Kitiyanan*, B. (2015), Selective Hydrogenation of Mixed C4 Containing High Vinyl Acetylene by Mn-Pd, Ni-Pd and Ag-Pd on Al$_2$O$_3$ Catalysts, *Catalysis Today*, 256, 23-230 (impact factor = 4.321)

6. Itsadanont, S., Thaptat, P., Scamehorn, J.F., Soontravanich, S., Sabatoni, D.A. and Chavadej*, S. (2015), Dissolution of Soap Scum by Surfactants Part III. Effect of Chelant Type on Equilibrium Solubility and Dissolution Rate of Calcium and Magnesium Soap Scums in Various Surfactant Systems, *Journal of Surfactants and Detergents*, 18, 925-932 (impact factor = 1.853)

7. Intanoo, P., Chaimonkol, P. and Chavadej*, S. (2016), Hydrogen and Methane Production from Cassava Wastewater using Two-Stage Upflow Anaerobic Sludge Blanket Reactors (UASB) with an Emphasis on Maximum Hydrogen Production, *International Journal of Hydrogen Energy*, 41, 6107-6114 (impact factor = 3.582)

8. Kanokkan, P., Shiina, T., and Chavadej*, S. (2016), Continuous Multistage Froth Flotation for Motor Oil Removal: Effect of Operational Parameters, *Separation Science and Technology*, 51, 1847-1861 (impact factor = 1.106)

9. Chavadej, S., Dulyalaksananon, W. and Suttikul*, T. (2016), Ethylene Epoxidation in a Low-Temperature Parallel Plate Dielectric Barrier Discharge System with Two Frosted Glass Plates, *Chemical Engineering and Processing: Process Intensification*, 107, 127-137 (impact factor =2.234)

10. Insorn, P. and Kittiyanan*, B., (2016), Selective Hydrogenation of Concentrated Vinyl Acetylene Mixed C4 by Modified Pd Catalysts: Effect of Cu, *Catalysis*, 6, 199-211 (impact factor=6.844)

11. Prukasawan, S., Kitiyanan*, B. and Ziff, R. M. (2016), "Partial Oxidation of Methane on a Nickel Catalyst: Kinetic Monte-Carlo Simulation Study" *Chemical Engineering Science*, **147**, 128-136.(impact factor=2.895)

12. Echaroj, S., Santikunaporn*, M. and Chavadej, S. (2017), Oligomerization of 1-Decene over Sulfated Alumina Catalysts for The Production of Synthetic Fuels and Lubricants: Modelling and Verification, *Reaction Kinetics, Mechanisms and Catalysis*, 121, 629-644(impact factor=1.264 in 2016)

13. Chanwattanakit, J., Scamehorn, J. F., Sabatini, D. A. and Chavadej*, S. (2017), Laundry Detergency of Solid Non Particulate Soil or Waxy Solids: Part I. Relation to Oily Soil Removal Above Melting Point, *Journal of Surfactants and Detergents*, 20, 815-830 (impact factor = 1.45 in 2016)

14. Seneesrisakul, K., Guralp, S. A., Gulari, E. and Chavadej*, S. (2017),Escherichia coli Expressing Endoglucanase Gene from Thai Higher Termite Bacteria for Enzymatic Hydrolysis and Microbial Hydrolysis of Cellulosic Materials, *Electronic Journal of Biotechnology*, 27, 70-79 (impact factor =1.527 in 2016)

15. Tangkathitipong, P., Intanoo, P. and Chavadej*, S.(2017), Separate Production of Hydrogen and Methane from Biodiesel Wastewater with Added Glycerin by Two-Stage Anaerobic Sequencing Batch Reactor (ASBR), *Renewable Energy*,113, 1077-1085 (impact factor = 4.357 in 2016)

16. Kanokkarn, P., Shina, T. and Chavadej*, S.(2017), Equilibrium and Dynamic Surface Tension of Various Surfactant Solutions in Relation to Foaming Properties, *Colloids and Surfaces A: Physiochemical and Engineering Aspects*,24, 135-142 (impact factor = 2.714 in 2016)

17. Echaroj, S., Asavatesanupap, C., Santikunaporn*, M., and Chavadej, S., (2017), Transformation of Bio-derived 1-Decanol to Diesel-like Fuel and Bio-based Oil via Dehydration and Oligomerization Reactions, *Energy and Fuels*, 31, 9465-9476 (impact factor=3.091 in 2016)

18. Chanwattanakit, J., and Chavadej*, S., Laundry Detergency of Solid Non-Particulate Soil Using Microemulsion-Based Formulation, *Journal of Oleo Science* (submitted)

19. Suttikul, T. and Chavadej*, S., Ethylene Epoxidation in a Low-Temperature Parallel Plate Dielectric Barrier Discharge System: Effect of Oxygen Source, *Industrial and Engineering Chemistry Research* (submitted)

20. Pormai, K., Suvachitanont, S. and Chavadej*, S. (2017), Improvement of Reforming CO_2-Containing Natural Gas by Steam Addition in AC Gliding Arc Discharge, *Journal of Chemical Engineering of Japan* (submitted)

21. Chavadej, S., Wangmor, T. and Intanoo*, P. (2017), Separate Production of H_2 and CH_4 from Cassava Wastewater under Thermophilic Temperature: Effect of Added Cassava Residue, *Biomass and Bioenergy* (submitted)

22. Kungsanant*, S., Kittisrisawai, S., Suriya-amrit, P., Kitiyanan, B., Chavadej, S., Osuwan, S. and Scamehorn, J. F. (2017), Study of Nonionic Surfactants on HVOCs Removal from Coacervate Solutions Using Co-Current Vacuum Stripping in a Packed Column, *Separation Science and Technology* (submitted)

23. Jiraprasertwong, A., Seneesrisakul, K., Kanokkarn, P. and Chavadej*, S., Hydrogen and Methane Production from Cassava Wastewater using Three-Stage Upflow Anaerobic Sludge Blanket (UASB) Reactor, *Bioresource Technology* (in preparation)

24. Seneesrisakul, K., Jiraprasertwong, A., Kanokarn, P., Pornmai, K. and Chavadej*, S., Biogas Production from Ethanol Wastewater by an Anaerobic Sequencing Batch Reactor under Mesophilic and Thermophilic Operation: Mass and Energy Balance, *Water Research* (in preparation)

25. Jiraprasertwong, A., Seneesrisakul, K., Kanokkarn, P. and Chavadej*, S., Three-Stage Anaerobic Sequencing Batch Reactors for Biogas Production: Nutrient Uptakes and Micronutrient Transport, *Chemical Engineering Journal* (in preparation)

2.2 <u>ความก้าวหน้าในการสร้างทีมวิจัย</u>

-ได้ช่วยแก้ไขบทความงานวิจัยตีพิมพ์ในวารสารนานาชาติและในการประชุมวิชาการทั้งในประเทศและต่างประเทศให้อาจารย์ที่อยู่ในกลุ่ม จำนวน 8 เรื่องให้กับอาจารย์ในกลุ่ม ได้แก่ ผศ.ดร.มาลี สันติคุณาภรณ์, ผ.ศ.ดร.นงค์นุช เรืองจิตต์, ผ.ศ.ดร.ฐิติพร สุทธิกุล, อ.ดร.พัชรี อินธนู และอ.ดร.สุรัสวดี กังสนันท์

-ได้อนุญาตให้อาจารย์ในกลุ่ม ได้แก่ อ. ดร. ธิฎิพร สุทธิกุล และนักศึกษาของ ผศ. ดร. มาลี สันติคุณาภรณ์ เข้ามาใช้เครื่องมือวิจัยที่ห้องปฏิบัติการทางด้านพลาสมา ที่วิทยาลัยปิโตรเลียมและปิโตรเคมี

-ได้เป็นอาจารย์พี่เลี้ยง (Mentor) ให้ อ. ดร. ธิฎิพร สุทธิกุล ได้รับทุนหลังปริญญาเอกจาก สกว. ชื่อเรื่อง "การศึกษาปฏิกิริยาเอทธิลีนออกไซด์ในระบบประกายไฟฟ้าพลาสมา (Ethylene Epoxidation in a

Low-Temperature AC Dielectric Barrier Discharge System: Effect of Dielectric Surface Roughness, Number of Dielectric Barrier, and Oxygen Source"

-ได้สร้างเครื่องมือวิจัยให้ อ.ดร. พัชรี อิทธนู ซึ่งประกอบด้วยระบบหมักแบบ CSTR และTwo-stage UASB

-ได้ช่วยแก้ไขข้อเสนอโครงการวิจัยของอาจารย์ในกลุ่ม

2.4 <u>ผลงานผลิตบัณฑิต</u>

-ผลิตบัณฑิตปริญญาเอก จำนวน 3 คน

-ผลิตบัณฑิตปริญญาโท 12 คน

ชื่อ นามสกุล	อาจารย์ที่ปรึกษา	ปีที่สำเร็จการศึกษา	ปริญญา	สถาบันที่ศึกษา
น.ส. จตุพร ปานทอง	อ.ดร.สุรัสวดี กังสนันท์	2560	เอก	มหาวิทยาลัยสงขลานครินทร์
นาย ไพศาล อินสร	ร.ศ. ดร.บุนยรัตน์ กิติยานันท์	2558	เอก	จุฬาลงกรณ์มหาวิทยาลัย
น.ส. ปวีนา กนกการ	ศ.ดร.สุเมธ ชวเดช	2560	เอก	จุฬาลงกรณ์มหาวิทยาลัย
นาย สนันตน์เขม อิชโรจน์	ร.ศ.ดร.มาลี สันติคุณาภรณ์	2560	โท	มหาวิทยาลัยธรรมศาสตร์
นาย ณัฐพล ศรีอุบล	ศ.ดร.สุเมธ ชวเดช	2559	โท	จุฬาลงกรณ์มหาวิทยาลัย
น. ส. ไพรินทร์ ตันติวิชยานนท์	ศ.ดร.สุเมธ ชวเดช	2559	โท	จุฬาลงกรณ์มหาวิทยาลัย
นาย อัครินทร์ อังกุรากินันท์	ศ.ดร.สุเมธ ชวเดช	2559	โท	จุฬาลงกรณ์มหาวิทยาลัย
น.ส. อารดา สุขแก้ว	ศ.ดร.สุเมธ ชวเดช	2559	โท	จุฬาลงกรณ์มหาวิทยาลัย
น.ส. ชนกนันท์ พงษ์เรือง	ศ.ดร.สุเมธ ชวเดช	2559	โท	จุฬาลงกรณ์มหาวิทยาลัย
น.ส. กิ่งกาญจน์ ปันเต	ศ.ดร.สุเมธ ชวเดช	2559	โท	จุฬาลงกรณ์มหาวิทยาลัย

นาย โยธิน กันทะวงค์	ผศ.ดร.นงค์นุช เรือง จิตต์	2560	โท	มหาวิทยาลัยเชียงใหม่
น.ส.กิ่งสุดา มะหูนี	ศ.ดร.สุเมธ ชวเดช	2560	โท	จุฬาลงกรณ์มหาวิทยาลัย
นาย กรพงษ์ วิชัย ธนพัฒน์	ศ.ดร.สุเมธ ชวเดช	2560	โท	จุฬาลงกรณ์มหาวิทยาลัย
นาย ทรงพล ใจ้แก้ว	ศ.ดร.สุเมธ ชวเดช	2560	โท	จุฬาลงกรณ์มหาวิทยาลัย
นาย ธีธัช เปลี่ยนวงษ์	ร.ศ. ดร.บุนยรัตน์ กิติ ยานันท์	2560	โท	จุฬาลงกรณ์มหาวิทยาลัย

2.5 ตำแหน่งวิชาการ

ชื่อ นามสกุล	ตำแหน่งวิชาการ	
	ก่อนโครงการฯ	หลังโครงการฯ
ดร.สุเมธ ชวเดช	ศาสตราจารย์	ศาสตราจารย์
ดร.บุนยรัตน์ กิติยานันท์∗	ผู้ช่วยศาสตราจารย์	รองศาสตราจารย์
ดร.มาลี สันติคุณาภรณ์	ผู้ช่วยศาสตราจารย์	รองศาสตราจารย์
ดร.ธรวิภา พวงเพชร	อาจารย์	ผู้ช่วยศาสตราจารย์
ดร.นงนุช เรืองจิตต์	ผู้ช่วยศาสตราจารย์	ผู้ช่วยศาสตราจารย์
ดร.มาลินี ลีโทชวลิต	อาจารย์	อาจารย์
ดร.ฐิติพร สุทธิกุล	อาจารย์	ผู้ช่วยศาสตราจารย์
ดร.พัชรี อินธนู	อาจารย์	อาจารย์

∗อยู่ระหว่างรอผลการขอตำแหน่งศาสตราจารย์

2.6การนำผลงานวิจัยไปใช้ประโยชน์

กำลังนำผลงานวิจัยไปใช้ในการเพิ่มประสิทธิภาพการผลิตก๊าซชีวภาพเป็นสองเท่าที่โรงงาน
อุตสาหกรรมสองแห่ง ได้แก่ โรงงานทรัพย์ทิพย์ และโรงงานในกลุ่มบางจาก

2.7การจดสิทธิบัตร

ได้ยื่นเรื่องการจดสิทธิบัตรไทยจำนวนสามเรื่อง ได้แก่

1. กรรมวิธีเพิ่มประสิทธิภาพการผลิตก๊าซชีวภาพจากน้ำเสียโดยการสารคีแลนท์ในถังหมักผลิตก๊าซ
ชีวภาพ (Improvement of Biogas Production from Wastewaters by Adding Chelant in Biogas
Reactors)

2. กระบวนการเติมอากาศเพื่อเพิ่มประสิทธิภาพการผลิตก๊าซชีวภาพของถังหมักก๊าซชีวภาพจากน้ำเสีย
(Process of Air Addition for Biogas Production Improvement of Biogas Bioreactors Treating
Wastewaters)

3. กรรมวิธีการเพิ่มประสิทธิภาพการผลิตก๊าซชีวภาพจากน้ำเสียโดยการเติมอากาศในปริมาณน้อยใน
ถังหมักผลิตก๊าซชีวภาพ (Improvement Technique of Biogas Production from Wastewaters by
Adding Air with a limited amount of air (Microaeration) in Biogas Reactors)

   โดยชื่อหน่วยงานที่เป็นเจ้าของสิทธิบัตร ได้แก่

   -จุฬาลงกรณ์มหาวิทยาลัย

   -สำนักงานกองทุนสนับสนุนการวิจัย

   -สำนักงานพัฒนาวิทยาศาสตร์และเทคโนโลยีแห่งชาติ

   -กระทรวงพลังงาน

4. **กิจกรรมที่เกี่ยวข้อง**

-ศ. ดร. สุเมธ ชวเดช ได้รับทุนวิจัยเรื่อง "Improvement of Biogas Production Performance by
Micronutrient Control and Development of Three-Stage Anaerobic System for Maximum Production
of Both Hydrogen and Methane"เป็นเงิน 3,600,000 บาท จาก สวทช. ตั้งแต่ 1 กันยายน 2559-สิงหาคม
2561

-ศ.ดร.สุเมธ ชวเดช ได้รับทุนวิจัยเรื่อง "Development of Catalysts for Epoxidation of Ethane"จาก
บริษัท พีทีที โกลบอลเคมีคอล จำกัด เป็นเงิน 835,300 บาท ตั้งแต่ 30 กันยายน 25559-เมษายน 2559

-ศ.ดร.สุเมธ ชวเดช ได้รับทุนวิจัยเรื่อง "โครงการการเพิ่มประสิทธิภาพการผลิตก๊าซชีวภาพโดยการ
ควบคุมสารอาหารที่ต้องการในปริมาณน้อยและการพัฒนาระบบหมักไร้อากาศแบบสามขั้นตอนเพื่อ

ผลิตแยกก๊าซไฮโดรเจนและมีเทน˝ เป็นเงิน 5,685,200 บาท จากกระทรวงพลังงาน ตั้งแต่ พฤศจิกายน 2559- ตุลาคม 2560

-ศ.ดร.สุเมธ ชวเดช ได้รับทุนวิจัยเรื่อง ˝การเพิ่มประสิทธิภาพการผลิตก๊าซชีวภาพโดยการควบคุมสารอาหารที่ต้องการในปริมาณน้อยในระดับอุตสาหกรรม˝ จากสำนักงานกองทุนสนับสนุนการวิจัย (สกว.) เป็นเงิน 2,925,700 บาท ตั้งแต่ 15 กรกฎาคม 2560-14 มกราคม 2562

4. ความเห็นของผู้วิจัย

ในฐานะหัวหน้าโครงการยังพบว่ามีความยากลำบากในการผลักดันให้อาจารย์ที่ร่วมในโครงการผลิตผลงานวิจัย ทั้งนี้เนื่องจากอาจารย์ทุกท่านมีภาระการสอนและอื่นๆ นอกจากนี้งานวิจัยที่ดำเนินการมีค่าใช้จ่ายสูง จึงจำเป็นต้องหาทุนวิจัยเพิ่มเติม

5. เอกสารแนบ

5.1 Reprints and accepted manuscripts

5.2 รายงานการเงิน

ลงนาม

(ศาสตราจารย์ ดร. สุเมธ ชวเดช)
หัวหน้าโครงการวิจัยผู้รับทุน
วันที่ 27 กันยายน2560

Available online at www.sciencedirect.com

ScienceDirect

journal homepage: www.elsevier.com/locate/he

Hydrogen production from alcohol wastewater with added fermentation residue by an anaerobic sequencing batch reactor (ASBR) under thermophilic operation

CrossMark

Patcharee Intanoo [a], Thitiporn Suttikul [a], Malinee Leethochawalit [b], Erdogen Gulari [c], Sumaeth Chavadej [a,d,]*

[a] The Petroleum and Petrochemical College, Chulalongkorn University, Soi Chula 12, Phyathai Road, Pathumwan, Bangkok 10330, Thailand
[b] Innovation Learning Center, Srinakarinwirot University, Bangkok 10110, Thailand
[c] Department of Chemical Engineering, University of Michigan, Ann Arbor, MI, USA
[d] Center of Excellence on Petrochemical and Materials Technology, Chulalongkorn University, Bangkok 10330, Thailand

ARTICLE INFO

ABSTRACT

The objective of this study was to investigate the enhancement of hydrogen production from alcohol wastewater by adding fermentation residue using an anaerobic sequencing batch reactor (ASBR) under thermophillic operation (55 °C) and at a constant pH of 5.5. The digestibility of the added fermentation residue was also evaluated. For a first set of previous experiments, the ASBR system was operated to obtain an optimum COD loading rate of 50.6 kg/m^3 d of alcohol wastewater without added fermentation residue and the produced gas contained 31% H_2 and 69% CO_2. In this experiment, the effect of added fermentation residue (100–1200 mg/l) on hydrogen production performance was investigated under a COD loading rate of 50.6 kg/m^3 d of the alcohol wastewater. At a fermentation residue concentration of 1000 mg/l, the produced gas contained 40% H_2 and 60% CO_2 without methane and the system gave the highest hydrogen yield and specific hydrogen production rate of 128 ml/g COD removed and 2880 ml/l d, respectively. Under thermophilic operation with a high total COD loading rate (51.8 kg/m^3 d) and a short HRT (21 h) at pH 5.5, the ASBR system could only break down cellulose (41.6%) and hemicellulose (21.8%), not decompose lignin.

Introduction

The main energy source presently used worldwide is derived from fossil fuels, oil, coal, natural gas, and shale oil. The consumption of fossil fuels has increased steadily. In addition, when these fossil fuels are used to generate energy, large quantities of greenhouse gases, including carbon dioxide (CO_2), nitrogen oxides (NO_x) and sulfur dioxide (SO_2) are released into atmosphere, consequently resulting in global

warming. Hydrogen, as an energy source, has been increasingly investigated because it does not produce carbon dioxide after combustion. Hydrogen can be produced from different raw materials with the most attractive raw materials being renewable resources, particularly concentrated organic wastewaters via dark fermentation [1]. The process can be operated under atmospheric pressure and ambient temperature. Alcohol wastewater is one of the promising sources for hydrogen production because it has a high organic concentration [2,3]. The use of alcohol wastewater not only provides hydrogen as a clean and renewable fuel but also enhances the sub-sequential step of methanogenesis to produce methane [4].

In the ethanol fermentation industry, one of the serious problems is the large quantity of fermentation residue that has to be removed from the wastewater because it upsets the process performance of the anaerobic units, especially in the upflow anaerobic sludge blanket (UASB) bioreactors. Hence, it has to be separated from the wastewater, leading to a large quantity of the fermentation residue. As a result, it causes environmental problems, bad smell and water pollution. Because of the low degradation rates of cellulosic materials under anaerobic conditions [5], the improvement of digestibility is of great interest. To enhance the digestibility of fermentation residue, several pretreatment methods are available—physical pretreatment (mechanical disturbance including milling, crushing, or grinding), chemical pretreatment (acid/base hydrolysis or solvent extraction), biological pretreatment (using enzymes or fungi) [6], and metal nanoparticle pretreatment (adding silver or nickel nanoparticles) [7,8]. All of these pretreatment methods have the unique purpose of to breaking down the resistance layer of lignin. Lignin is a complex compound with a polymeric structure, resulting in high resistance to biological degradation. Large amounts of lignin have been found to reduce the efficiency of cellulose degradation because lignin serves as a protective barrier to both cellulose and hemicelluloses [10]. One of the most innovative methods used to enhance the digestibility of cellulosic residues is to operate anaerobic bioreactors for methane production under severe conditions (50–60 °C and pH 4–5) [9]. The use of thermophilic operation at a low pH (4–5) was also found to enhance the digestibility of cornstack for hydrogen production [6]. Lynd et al. [10], reported that the anaerobic degradation of cellulose at 60 °C was much higher than that at a low temperature (30–40 °C). Under high temperatures, microorganisms can produce cellulolytic enzymes to hydrolyze cellulose [11]. Pavlostathis et al. [12], studied cellulose destruction at a low temperature (37 °C) and found that the cellulose destruction could be increased by increasing HRT from 0.25 to 2 d, leading to a larger bioreactor volume being required.

Several attempts to utilize biomass residues to produce hydrogen (agricultural residues including rice straw [13], wheat straw [14], cassava starch [15], and grasses [16]) for the co-digestion of wastewaters using pretreated seed sludges have been reported [17]. Lo et al. [13], reported that, in a batch test, hydrogen yields increased from 0.70 mol H_2/mol xylose to 0.76 mol H_2/mol xylose when rice straw was pretreated with NaOH. Fan et al. [14], reported that, in batch fermentation tests, hydrogen yield at a HRT of 126.5 h increased from 13.8 ml H_2/g TVS to 68.1 ml H_2/g TVS when increasing the concentration of the 2.0% HCl solution pretreated wheat straw from 5 to 25 g/l. The wheat straw was pretreated by a 2.0% HCl solution with microwave heating for 8 min. The highest hydrogen yield of 68.1 ml H_2/g TVS from the microwave treated wheat straw was about 136 times more as compared with that from the un-treated wheat straw [14]. Sigurbjornsdottir and Orlygsson [16], found the hydrogen concentration increased from 28.0 ± 0.2 mmol/l to 40.5 ± 2.1 mmol/l when the grass was pretreated with a 0.75 %NaOH solution.

Alcohol wastewater has been investigated for hydrogen production without adding cellulosic residue, as reported in our previous works [18,19]. Poontaweegeratigarn et al. [18], studied hydrogen production from alcohol wastewater by using UASB under mesophilic temperature (37 °C) and at pH 5.5. The maximum hydrogen production rate of 18 l/d and the highest H_2 yield of 125.1 ml H_2/g COD removed were found at a COD loading rate of 46 kg/m^3 d. Intanoo et al. [19], further studied hydrogen production from the same wastewater under thermophilic temperature (55 °C) and pH 5.5 using an ASBR system and the highest hydrogen yield of 130 ml H_2/g COD removed was found at a COD loading rate of 68 kg/m^3 d. They concluded that hydrogen production performance, in terms of hydrogen yield and SHPR at thermophilic temperature, were much higher than those at the mesophilic temperature.

This present work is the second part of a series, of our research group, to investigate the enhancement of hydrogen production performance by adding fermentation residue without pretreatment to alcohol wastewater under thermophilic operation. The ability of thermophiles to degrade the un-treated fermentation residue as an additional biomass substrate under thermophilic temperature (55 °C) and a constant pH of 5.5 by using an anaerobic sequencing batch reactor (ASBR) was also investigated. The ASBR was fed by the alcohol wastewater at an optimum COD loading rate 50.6 kg/m^3 d with a short HRT of 21 h [19]. The fermentation residue was added to the alcohol wastewater at different concentrations of suspended solids (SS; ranging from 100 to 1200 mg/l) in order to determine an optimum loading of the fermentation residue for maximization of hydrogen production performance.

Materials and methods

Seed sludge

A seed sludge sample collected from the UASB biogas plant at Sapthip Lopburi Co., Ltd., Thailand, was first concentrated by sedimentation, and the concentrated sludge was then ground and screened by sieving to remove large particles. In order to eliminate or block the growth of methane-producing bacteria or hydrogen consumers, the seed sludge was boiled at 95 °C for 15 min [1,20–23]. The heat-treated sludge enriching hydrogen-producing bacteria was then added to an ASBR. The microbial concentration in terms of MLVSS (mixed liquid volatile suspended solids) for the start-up in this study was about 12,000 mg/l.

Alcohol wastewater and fermentation residue

The alcohol wastewater used in this study was also obtained from Sapthip Lopburi Co., Ltd., Thailand with cassava chips being used as the raw material for alcohol fermentation. The discharge from the bottom of the distillation columns still contains a large quantity of unfermented cassava chips, which is preliminarily removed by decantation before being pumped to the existing UASB biogas production plant. The collected alcohol wastewater was filtered through a 0.2 mm sieve to remove any large solid particles and kept at 4 °C before use. A sample of the fermentation residue, taken from the decanter, was dried at 105 °C, then crushed and milled to reduce particle size and finally sieved to 40–60 mesh (average diameter of the fermentation residue was about 250 μm).

Anaerobic sequencing batch reactor (ASBR) operation

Two identical units of anaerobic sequencing batch reactors (ASBR) were used independently to produce hydrogen from the alcohol wastewater with added fermentation residue at different fermentation residue concentrations. The possibility of photosynthetic bacteria activity was inhibited by using PVC material in the construction of the bioreactors. Each of the bioreactors had an inner diameter of 13 cm and a height of 30 cm. The bioreactors were operated with a liquid working volume of 4 L. Each ASBR unit was equipped with a magnetic stirrer (450 rpm) to suspend both microbial cells and the added fermentation residue homogeneously. The heat-treated sludge (1000 ml) was added as a seed sludge to each of the ASBR units. Both ASBR units were operated under the optimum COD loading rate of 50.6 kg/m^3 d [19] at a temperature of 55 °C, a constant solution pH of 5.5 [24,25] and at 6 cycles per day with operating time of 15, 90, 120 and 15 min for feeding, reacting, settling and decanting, respectively [19]. To investigate the effect of the added fermentation residue, different concentrations (100–1200 mg/l) of fermentation residue were added to the alcohol wastewater. The system was operated for approximately two weeks to reach a steady state for any fermentation residue concentration before taking the effluent and producing gas samples for analysis and measurement. Steady state conditions were attained when both effluent COD and the gas production rate did not change with time. After the ASBR systems reached steady state, the samples taken during the reacting step were filtered for the analysis of microbial and fermentation residue concentrations and chemical composition of remaining fermentation residue. The effluent samples taken during the decanting step were also filtered and analyzed for the same parameters to indicate the washout of both microbial cells and fermentation residue.

Measurements and analytical methods

The gas production rate was measured by using a wet gas meter (Ritter, TGO5/5). The gas composition of the produced gas was analyzed by a gas chromatograph (GC, Perkin–Elmer, AutoSystem) equipped with a thermal conductivity detector (TCD) and a packed column (HayeSep D 100/120 mesh, Altech) according to previous experiments [19]. The total amount of volatile fatty acids (VFA) in each effluent sample was determined by the distillation and titration method [26]. The VFA composition of each effluent sample after the distillation step was analyzed by a different gas chromatograph (Perichrom, PR2100) equipped with a flame ionization detector and a DB-WAXetr capillary column (J & W Scientific) in the splitless mode with helium as a carrier gas, hydrogen as a combustion gas, and air zero as a combustion-supporting gas. The analysis conditions were described in our previous work [19].

The COD values in the feed and effluent samples were determined by the dichromate oxidation method with an absorbance measurement using a spectrophotometer (HACH, DR 2700). Nitrogen analyses (organic nitrogen measured by the diazotization and cadmium reduction method, and inorganic nitrogen measured by the salicylate method) in the feed and effluent samples were carried out by TNT persulfate digestion. The total phosphorous content in the feed and effluent samples were determined by the molybdovanadate method with acid persulfate digestion (Hach Company) [19].

The mixed liquor suspended solids (MLSS) and the mixed liquor volatile suspended solids (MLVSS) in the samples taken during the reacting step, were used to represent the microbial concentration with the accumulated fermentation residue in the bioreactor and the SS and the volatile suspended solids (VSS) in the effluent samples, taken during the decanting step, and used to represent the microbial washout and the fermentation residue floating out from the system were measured according to standard methods [26].

The dried sample of fermentation residue was analyzed for elemental and chemical compositions. An elemental analyzer (TruSpec-CHN) was used to determine C, H, O, N and S contents in the sample. Combustion and burner temperatures were kept at 950 °C and 850 °C, respectively, with oxygen, helium, and air used as carrier gases. The concentrations of glucose in the dried sample of fermentation residue and the effluent were determined by the enzymatic method with a glucose (HK) assay kit (Sigma–Aldrich, Inc).

For the analyses of both fractions of microbial cells and remaining fermentation residue, the dried samples of the fermentation residue, the MLSS from the ASBR units and the effluent SS were analyzed according to suggested methods of Lin [27]. Firstly, the organic nitrogen of the dried microbial sludge sample was analyzed and converted into a microbial concentration with a known nitrogen content of 11.21% (in the dried weight basis) in the microbial cells which was obtained from the growth of microbes with the studied wastewater without added fermentation residue. The remaining fermentation residue fraction was obtained after substracting the microbial weight fraction. For the chemical composition analysis of the fermentation residue, a dried sample was first extracted by acetone. The weight loss of the acetone extraction step represented oils and phenolic compounds in the sample. Next, the acetone-extracted sample was dissolved in a 0.5 M NaOH solution at 90 °C for 2 h. The weight loss from this step indicated the fraction of hemicellulose and starch. The starch fraction in the NaOH dissolution solution was then determined by the amylase/amyloglucosidase method using a starch assay kit (Sigma–Aldrich, Inc). Next, the remaining residue, after the NaOH dissolution step, was further treated with a 72 wt% H$_2$SO$_4$ solution at 8 °C for 24 h to dissolve the lignin fraction. The weight of the H$_2$SO$_4$ undissolved solids

represented the fractions of cellulose and ash. Finally, the undissolved solids were placed in an oven at 550 °C for 1 h to burn out the cellulose fraction. The weight loss in this step represents the cellulose fraction. The average values of the analysis results (with less than 5% standard deviation) were used to determine the process performance of the studied ASBR system.

Calculations and process performance evaluation

Calculations for process performance evaluation were similar to our previous work [21]. The hydrogen yield was determined from a volume of hydrogen produced per g of COD applied or removed. The specific hydrogen production rates (SHPR) were based on both the bioreactor volume and microbial dried weight, which are important parameters for both design and operation of a hydrogen production unit, and were also determined at different fermentation residue concentrations. The digestibility of the added fermentation residue was determined by performing mass balance under steady state conditions, as expressed below:

$$\text{Digestibility or degradation} = \text{Input} - \text{Output} - \text{Accumulation} \quad (1)$$

Results and discussion

Chemical composition of alcohol wastewater and fermentation residue

As shown in Table 1, the alcohol wastewater has a high chemical oxygen demand (COD) value of 45,000 mg/l with a COD:nitrogen:phosphorous ratio of 100:1.33:1.23, indicating that the wastewater contains sufficient amounts of both nutrients (N and P) for anaerobic degradation (the theoretical ratio of COD:N:P = 100:1:0.2 for anaerobic decomposition with biogas production [19]). Therefore, an addition of nutrients was not required in this study. Most of the nitrogen in the wastewater was in the form of nitrate and organic nitrogen with a significant amount of ammonium nitrogen.

The elemental and chemical composition of the fermentation residue samples are shown in Table 2. The major elements of the fermentation residue are hydrogen, oxygen and

Table 2 – Elemental and chemical composition of the fermentation residue samples.

Elemental composition	wt%, dry basis	mol%
Carbon	39.66	25.93
Hydrogen	6.02	47.22
Nitrogen	1.52	0.85
Oxygen	52.72	25.85
Sulfur	0.08	0.02
Chemical composition	wt%, dry basis	
Starch	39.7	
Hemicellulose	14.5	
Cellulose	21.5	
Lignin	14.9	
Extractives	5.4	
Ash	4.0	

carbon based on molar basis. It should be mentioned here that both protein and sugar were found to be extremely low and they were excluded from the list. Surprisingly, 39.74% starch was found to present in the fermentation residue sample, indicating that a significant amount of starch was embedded in the rigid structure of the lignocellulosic fiber network. Apart from the starch fraction, the order of all fractions in the fermentation residue sample was cellulose > lignin ≈ hemicellulose > ash >> extractive. The high fraction of ash (4.0%) present in the fermentation residue was due to the sand content, which is generally added by middle men to increase the weight of cassava chips before selling to the factory.

Effects of fermentation residue concentration

Organic removal results

The organic removal, in terms of COD removal increased greatly with increasing fermentation residue concentration up to 200 mg/l and only slightly increased with further increasing fermentation residue concentration to 1000 mg/l (Fig. 1a). Beyond the fermentation residue concentration of 1000 mg/l, COD removal decreased slightly with further increasing fermentation residue concentration from 1000 to 1200 mg/l. The results can be explained that an increase in fermentation residue concentration simply increased the organic loading in the system, leading to increased microbial activity. However, a further increase in fermentation residue beyond 1000 mg/l, resulted in an increase in VFA in the system beyond the inhibitory level, affecting microbial activity.

Hydrogen production results

As shown in Fig. 1a, the gas production rate has a similar trend to the COD removal. Fig. 1b shows two main components of hydrogen and carbon dioxide without methane in the produced gas for all studied fermentation residue concentrations. This implies that the methanogenic activity was completely suppressed by the high COD loading rate operation, causing toxicity from the organic acid accumulation to the methanogens in the studied ASBR [28,29]. Both profiles of hydrogen content and hydrogen production rate mirrored that of COD removal while that of carbon dioxide content showed an opposite trend. The maximum content of hydrogen (40%) and

Table 1 – Characteristics of the alcohol wastewater sample.

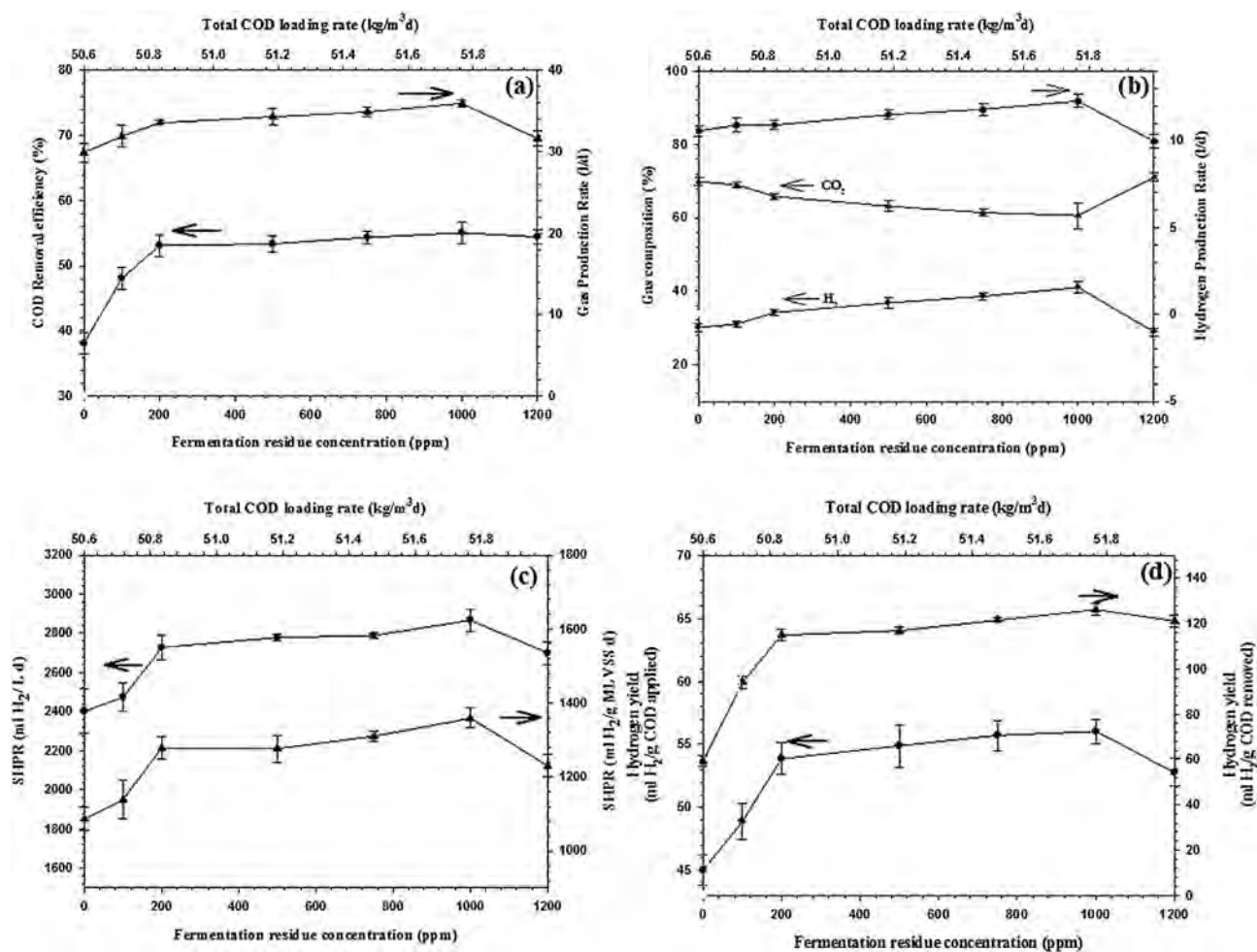| Parameter	Unit	Value
pH	–	4.6
COD	mg/l	45,000
Total VFA	mg/l	4000
Ethanol concentration	mg/l	534
Total solids (TS)	mg/l	12,000
Total phosphorous	mg/l	580
Total nitrogen	mg/l	600
Organic nitrogen (Org-N)	mg/l	208
Ammonium (NH_4^+-N)	mg/l	40
Nitrate (NO_3^--N)	mg/l	350
Nitrite (NO_2^--N)	mg/l	1.6
COD:N:P	–	100:1.33:1.23

Fig. 1 – Effect of fermentation residue concentration on (a) COD removal and gas production rate, (b) gas composition and hydrogen production rate, (c) specific hydrogen production rates and (d) hydrogen yields when the ASBR system was operated with the ethanol wastewater at constant COD loading rate of 50.6 kg/m³ d, pH 5.5, and 55 °C.

maximum hydrogen production rate (12.5 l/d) were found at the fermentation residue concentration of 1000 mg/l. A higher fermentation residue concentration in the alcohol wastewater, which had a higher concentration of all organic compounds, made more organic compound especially starch available for the microbes to digest, causing more hydrogen gas to be produced. However, at a fermentation residue concentration greater than 1000 mg/l, both hydrogen content and hydrogen production rate decreased because of increasing toxicity of VFA accumulation.

The SHPR, based on either microbial concentration in the ASBR unit or reactor volume, increased with increasing fermentation residue concentration and attained a maximum value of 1390 ml H_2/g MLVSS d (or 2880 ml H_2/l d) at a fermentation residue concentration of 1000 mg/l (Fig. 1c). It was being consistent with the maximum hydrogen content and hydrogen production rate, and COD removal, as shown in Fig. 1a and b. When the fermentation residue concentration further increased from 1000 mg/l to 1200 mg/l, both SHPR values abruptly decreased, corresponding to the decreases in

the hydrogen production rate, hydrogen content, and COD removal.

Both the hydrogen yield of 128 ml H_2/g COD removed and 58 ml H_2/g COD applied were also observed at the fermentation residue concentration of 1000 mg/l, as shown in Fig. 1d. With further increasing fermentation residue concentration greater than 1000 mg/l, hydrogen yield decreased significantly.

Volatile fatty acid (VFA) results

Fig. 2 shows that the total VFA concentration increases steadily with increasing fermentation residue concentration and attains the highest value of 12,000 mg/l as acetic acid at the highest fermentation residue concentration of 1200 mg/l. The results reveal that the total VFA concentration directly affects the process performance, in terms of both COD removal and hydrogen production [30]. Since the studied ASBR was operated at a constant pH of 5.5, the optimum pH for acidogenic fermentation, the system could withstand a remarkably high level of total VFA of up to 10,800 mg/l [19]. The addition of NaOH to maintain the system pH of 5.5 could
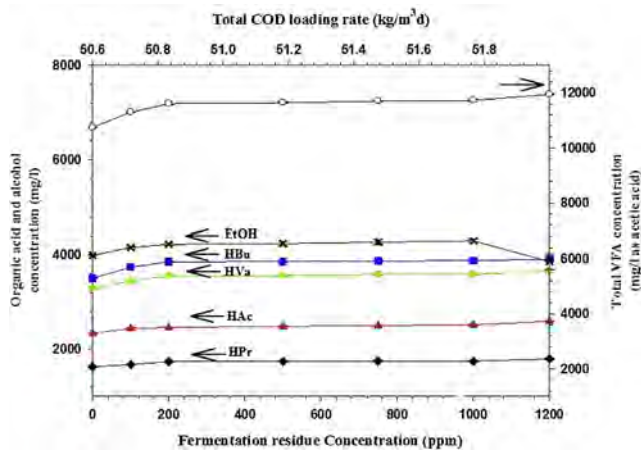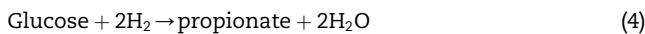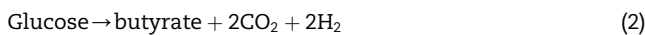
Fig. 2 – Total VFA, VFA composition and ethanol concentration at different fermentation residue concentrations when the ASBR system was operated with the ethanol wastewater at a constant COD loading rate of 50.6 kg/m³ d, 55 °C, and pH 5.5.

reduce the undissociated form of organic acids, leading to lower VFA the toxicity as compared to a higher concentration of undissociated acids at a lower pH [31].

The major components of produced VFA are acetic acid (HAc), propionic acid (HPr), butyric acid (HBu), and valeric acid (HVa) with a high ethanol concentration, as shown in Fig. 2. All organic acids increased significantly with increasing fermentation residue concentration up to 200 mg/l. Beyond the fermentation residue concentration of 200 mg/l, the concentration of each produced organic acid increased slightly with further increasing fermentation residue concentration from 200 mg/l to 1200 mg/l. All organic acids are associated with hydrogen evolution while the formation of propionic acid is derived from the consumption of hydrogen, as shown in the following equations [32,33].

$$Glucose \rightarrow butyrate + 2CO_2 + 2H_2 \tag{2}$$

$$Glucose + 2H_2O \rightarrow 2acetate + 2CO_2 + 4H_2 \tag{3}$$

$$Glucose + 2H_2 \rightarrow propionate + 2H_2O \tag{4}$$

The ethanol concentration increased with increasing fermentation residue concentration and attained the maximum value of 4300 mg/l at a fermentation residue concentration of 1000 mg/l (Fig. 2), which was consistent with the highest hydrogen production performance (Fig. 1). It sharply decreased with further increasing fermentation residue concentration from 1000 mg/l to 1200 mg/l. The ethanol concentration profile mirrored both of COD removal and hydrogen content in the produced gas. The organic substrate can be converted to both hydrogen and ethanol, as shown below [19,34].

$$Glucose \rightarrow H_2 + ethanol \tag{5}$$

It is interesting to point out that in the present work, the alcohol concentration (3800–4200 mg/l) in the effluent was extremely high, which is similar to other works using alcohol

wastewater [34,35]. The high ethanol concentration was a result of the alcohol wastewater being contaminated by yeast cells, which further metabolized the glucose produced by the thermophiles to ethanol.

Microbial concentration and microbial washout results
The microbial concentration, along with the accumulated fermentation residue in the ASBR bioreactor, in terms of MLSS and MLVSS, decreases steadily with increasing fermentation residue concentration up to 1200 mg/l, as shown in Fig. 3a. Both the thermophiles and accumulated fermentation residue also had a similar trend. The microbial washout profile from the bioreactors, in terms of effluent SS or effluent VSS (Fig. 3b) and the fermentation residue washout profile had an opposite trend. The toxicity level of organic acids produced by the hydrogen-producing bacteria at pH 5.5 was found to be around 12,000 mg/l, in agreement with the first set of experiments [19]. When the fermentation residue concentration was increased in the alcohol wastewater, the total VFA increased,
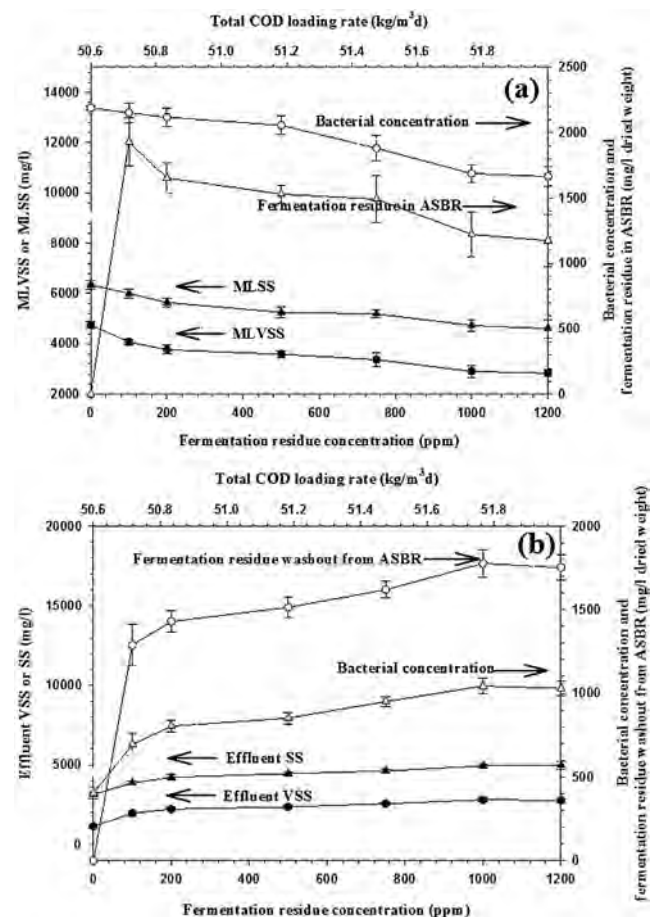

Fig. 3 – Effect of fermentation residue concentration on (a) bacteria concentration in ASBR, fermentation residue in ASBR (mg/l dried weight), MLVSS and MLSS and (b) bacteria concentration washout from ASBR, fermentation residue washout from ASBR (mg/l dried weight), effluent VSS and effluent SS when the ASBR system was operated with the ethanol wastewater at a constant COD loading rate of 50.6 kg/m³ d, 55 °C, and pH 5.5.

suggesting that the degree of VFA toxicity to the microbes increased with increasing fermentation residue content, causing an increase in microbial washout and decrease in microbial concentration in the system. The decrease in microbial concentration eventually caused both the reduction of COD removal and hydrogen production performance as well as an increase in the washout of fermentation residue. When the fermentation residue concentration increased from 100 mg/l to 1000 mg/l, the microbial concentration in the ASBR bioreactor decreased significantly whereas hydrogen production performance increased. Thermophiles have an ability to hydrolyze both cellulose and hemicellulose, resulting in increased hydrogen production performance, as further discussed later. Conversely, the hydrogen production performance decreased at a high fermentation residue concentration of 1200 mg/l due to increasing toxicity from VFA accumulation. Under the optimum COD loading rate of 50.6 kg/m^3 d of the alcohol wastewater with the optimum fermentation residue concentration of 1000 mg/l at 55 °C and pH 5.5, the glucose concentration in the effluent was found to be very low (0.3 mg/l), indicating that most glucose produced

was immediately converted to hydrogen, carbon dioxide and organic acids by the thermophiles, as well as ethanol by the yeast.

Nitrogen and phosphorous results

Both nitrogen and phosphorous are essential nutrients for the growth of microbes [18,19]. Both nitrogen and phosphorous uptakes increased greatly with increasing fermentation residue concentration from 100 mg/l to 1000 mg/l (Fig. 4a). With further increasing fermentation residue concentration from 1000 to 1200 mg/l both nitrogen and phosphorous uptakes remained almost unchanged. Interestingly, the optimum concentration of added fermentation residue to the alcohol wastewater at 1000 mg/l gave the highest nutrient uptakes of both nitrogen and phosphorous, corresponding to the highest hydrogen production performance. The nitrogen sources for microbial growth came from ammonium-nitrogen, nitrate-nitrogen, nitrite-nitrogen, and organic nitrogen [36]. As shown in Fig. 4b, the organic nitrogen concentration in the ASBR decreases markedly with increasing fermentation residue concentration while the nitrate-nitrogen concentration slightly decreases. Both ammonium and nitrite nitrogen concentrations remained almost unchanged with increasing fermentation residue concentration in the studied conditions. The results suggest that most organic nitrogen was preferentially consumed by the hydrogen-producing bacteria for their growth under the studied conditions.

Digestibility results

Fig. 5 shows the digestibility of all chemical components of the fermentation residue and the microbial concentration profile in relation to the fermentation residue concentration. The digestibility of cellulose, starch, or hemicellulose increased steadily with increasing fermentation residue concentration from 100 to 1000 mg/l and was mostly unchanged with further increasing fermentation residue concentration from 1000 to
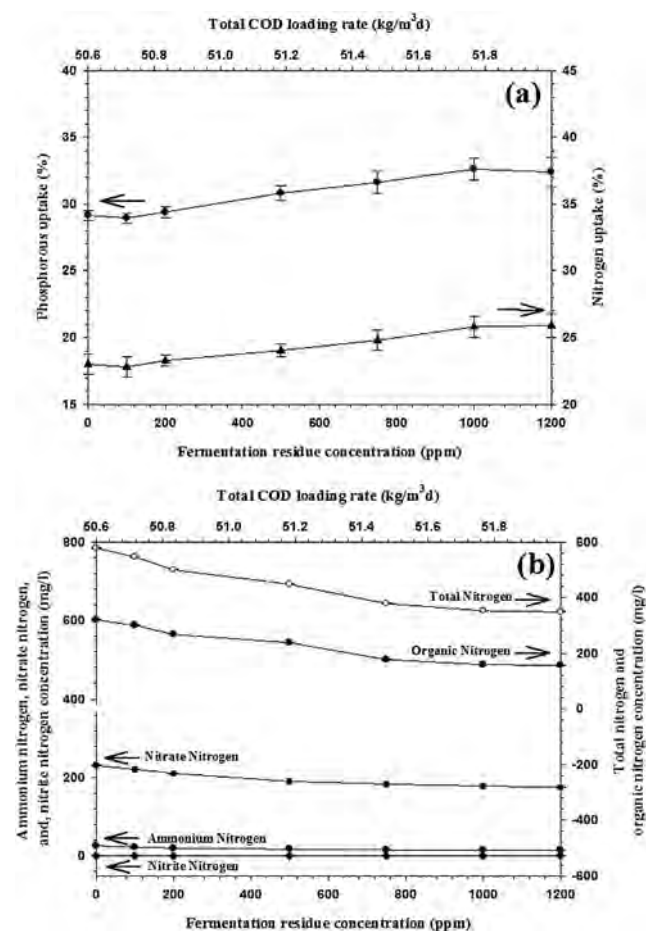

Fig. 4 – Effect of fermentation residue concentration on (a) nitrogen and phosphorous uptakes and (b) total nitrogen, organic nitrogen and inorganic nitrogen concentrations when the ASBR system was operated with the ethanol wastewater at a constant COD loading rate of 50.6 kg/m^3 d, 55 °C, and pH 5.5.
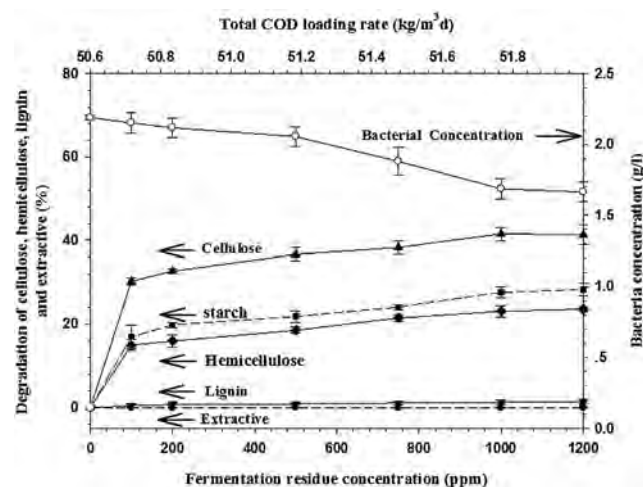

Fig. 5 – Digestibility of fermentation residue and microbial concentration in relation to the fermentation residue concentration when the ASBR system was operated with the ethanol wastewater at a constant COD loading rate of 50.6 kg/m^3 d, 55 °C, and pH 5.5.

Table 3 — Comparison of the digestibility of various lignocellulosic materials under various conditions [40].

Feed stock	Pretreatment	Organic loading rate	System/condition	Temperature (°C)/pH	HRT (h)	Cellulose digestibility (%)	Ref.
Cassava residue	No	51.73 kg/m³d	ASBR	55/5.5	21	41.6	Present study
Cellulose	No	3 g/l	CSTR/anaerobic	37/6.4—6.5	48	71.4	[12]
Avical	No	5 g/l	Batch/anaerobic	30/7.0	240	10	[37]
Avical	No	5 g/l	Batch/aerobic	30/7.0	240	27	[37]
Cornstalk	Lime	5 g/l	Batch/anaerobic	60/7.0	60	58.6	[6]
Cornstalk	No	5 g/l	Batch/anaerobic	60/7.0	84	18.3	[6]
Wheat straw stillage	Hydrothermal	17.1 kg/m³d	UASB	55/6.8	48	25	[38]
Cellulose	No	10 g/l	CSTR/anaerobic	70/5.3—5.7	240	64.9	[39]
Corn stover	Alkali/enzymatic hydrolysis	—	CSTR/anaerobic	35/—	720	45	[40]
Corn stover	Alkali/enzymatic hydrolysis	—	CSTR/anaerobic	35/—	960	60	[40]
Corn stover	Alkali/enzymatic hydrolysis	—	CSTR/anaerobic	35/—	1200	50	[40]
Laminaria japonica	No	3.4 g/l	CSTR/anaerobic	35/5.5	144	0.19 ± 0.02 FPU/ml[a]	[41]
Laminaria japonica	No	3.4 g/l	CSTR/anaerobic	50/5.5	144	0.11 ± 0.03 FPU/ml[a]	[41]
Laminaria japonica	No	3.4 g/l	CSTR/anaerobic	65/5.5	144	0.08 ± 0.02 FPU/ml[a]	[41]

[a] Cellulase activity indicated the hydrolysis efficiency [41].

1200 mg/l, whereas both the lignin and extractive fractions remained almost unchanged. The results suggest that the thermophiles cannot digest lignin or phenolic and oily compounds but they show high ability to degrade both cellulose and hemicellulose. Surprisingly, the digestibility or degradability of both cellulose and hemicellulose were found to be as high as that of starch. The layer of cellulose and hemicellulose with lignin had to be hydrolyzed prior to the hydrolysis of the embedded starch by the extracellular enzymes secreted from the thermophiles. As a result, the digestibility of both cellulose and hemicellulose was as high as that of starch.

As shown in Table 3, the digestibility of various lignocellulosic materials at high temperatures are higher than those at low temperatures [6,37] because under anaerobic condition at high temperatures, facultative and obligatory anaerobic bacteria can produce more effective enzymes to hydrolyze the lignocellulosic materials [11]. Moreover, the digestibility of pretreated lignocellulosic materials with heat, acid solution, or lime solution was also higher than those of the un-treated ones [6]. Pretreatment can remove the barriers and makes cellulose more accessible to microbial hydrolysis [42]. A continuous system seems to provide higher digestibility of cellulose than a batch system. The studied system showed high digestibility for both cellulose (41.6%) and hemicellulose (21.8%), without pretreatment under thermophilic operation.

Conclusions

Hydrogen production from alcohol wastewater containing fermentation residue using an anaerobic sequencing batch reactor under thermophilic temperature, and a controlled pH of 5.5 was investigated. The ASBR system was operated at the optimum COD loading rate of 50.6 kg/m³ d using alcohol wastewater while the fermentation residue was added at

different concentrations in the alcohol wastewater. An optimum fermentation residue concentration of 1000 mg/l gave the highest hydrogen production performance with a maximum specific hydrogen production rate of 1390 ml H_2/g MLVSS d and maximum hydrogen yield of 125 ml H_2/g COD removed. The results confirmed that thermophiles have a high ability to digest both cellulose (41.6%) and hemicellulose (21.8%) under acidogenic fermentation even though the studied ASBR system was operated at an extremely high COD loading rate of 50.6 kg/m³ d of the alcohol wastewater with a very short HRT of 21 h. The lignin fraction could not be broken down anaerobically.

Acknowledgments

REFERENCES

[1] Kapdan IK, Kargi F. Bio-hydrogen production from waste materials. Enzyme Microb Technol 2006;38:569—82.
[2] Luo G, Xie L, Zou Z, Wang W, Zhou Q. Exploring optimal conditions for thermophilic fermentative hydrogen

production from cassava stillage. Int J Hydrogen Energy 2010;35:6161—9.

[3] Zhang Q, He J, Tian M, Mao Z, Tang L, Zhang J, et al. Enhancement of methane production from cassava residues by biological pretreatment using a constructed microbial consortium. Bioresour Technol 2011;102:8899—906.

[4] Luo G, Xie L, Zhou Q, Angelidaki I. Enhancement of bioenergy production from organic wastes by two-stage anaerobic hydrogen and methane production process. Bioresour Technol 2011;18:8700—6.

[5] Mabee WE, McFarlane PN, Saddler JN. Biomass availability for lignocellulosic ethanol production. Biomass Bioenergy 2011;35:4519—29.

[6] Cao GL, Guo WQ, Wang AJ, Zhao L, Xu CJ. Enhanced cellulosic hydrogen production from lime-treated cornstalk wastes using thermophilic anaerobic microflora. Int J Hydrogen Energy 2012;37:13161—6.

[7] Zhao W, Zhang Y, Du B, Wei D, Wei Q, Zhao Y. Enhancement effect of silver nanoparticles on fermentative biohydrogen production using mixed bacteria. Bioresour Technol 2013;142:240—5.

[8] Mullia P, Yogeswari MK, Sridevi K. Optimisation and enhancement of biohydrogen production using nickel nanoparticles — a novel approach. Bioresour Technol 2012;141:212—9.

[9] Kim SK, Lee T. Degradation of lignocellulosic materials under sulfidogenic and methanogenic conditions. Waste Manag 2009;29:224—7.

[10] Lynd LR, Weimer PJ, Zyl WH, Pretorius IS. Microbial cellulose utilization: fundamentals and biotechnology. Microbiol Mol Biol Rev 2002;66:506—77.

[11] Cheng CL, Lo YC, Lee KS, Lee DJ, Lin CY, Chang JS. Biohydrogen production from lignocellulosic feedstock. Bioresour Technol 2012;102:8514—23.

[12] Pavlostathis SG, Miller TL, Wolin MJ. Cellulose fermentation by continuous cultures of *Ruminococcus albus* and *Methanobrevibacter smithii*. Appl Microbiol Biotechnol 1990;33:109—16.

[13] Lo YC, Lu WC, Chen CY, Chang JS. Dark fermentative hydrogen production from enzymatic hydrolysate of xylan and pretreated rice straw by *Clostridium butyricum* CGS5. Bioresour Technol 2010;101:5885—91.

[14] Fan YT, Zhang YH, Zhang SF, Hou HW, Ren BZ. Efficient conversion of wheat straw wastes into biohydrogen gas by cow dung compost. Bioresour Technol 2006;97:500—5.

[15] Su H, Cheng J, Zhou J, Song W, Cen K. Improving hydrogen production from cassava starch by combination of dark and photo fermentation. Int J Hydrogen Energy 2009;34:1780—6.

[16] Sigurbjornsdottir MA, Orlygsson J. Combined hydrogen and ethanol production from sugars and lignocellulosic biomass by thermoanaerobacterium AK54, isolated from hot spring. Appl Energy 2012;97:785—91.

[17] Kim DH, Lee DY, Kim MS. Enhanced biohydrogen production from tofu residue by acid/base pretreatment and sewage sludge addition. Int J Hydrogen Energy 2011;36:13922—7.

[18] Poontaweegeratigarn T, Chavadej S, Rangsunvigit P. Hydrogen production from alcohol wastewater by upflow anaerobic sludge blanket reactors under mesophilic temperature. Int J Chem Biol Eng 2012;6:305—8.

[19] Intanoo P, Rangsunvigit P, Namprohm W, Thamprajamchit B, Chavadej J, Chavadej S. Hydrogen production from alcohol wastewater by an anaerobic sequencing batch reactor under thermophilic operation: nitrogen and phosphorous uptakes and transformation. Int J Hydrogen Energy 2012;37:11104—12.

[20] Argun H, Kargi F, Kapdan IK, Oztekin R. Biohydrogen production by dark fermentation of wheat powder solution: effects of C/N and C/P ratio on hydrogen yield and formation rate. Int J Hydrogen Energy 2008;33:1813—9.

[21] Hawkes FR, Hussy I, Kyazze G, Dinsdale R, Hawkes DL. Continuous dark fermentative hydrogen production by mesophilic microflora: principles and progress. Int J Hydrogen Energy 2007;32:174—84.

[22] Lin CY, Hung WC. Enhancement of fermentative hydrogen/ethanol production from cellulose using mixed anaerobic cultures. Int J Hydrogen Energy 2008;33:3660—7.

[23] Cheng J, Su H, Zhou J, Song W, Cen K. Hydrogen production by mixed bacteria through dark and photo fermentation. Int J Hydrogen Energy 2011;36:450—7.

[24] Lee KS, Hsu YF, Lo YC, Lin PJ, Lin CY, Chang JS. Exploring optimal environmental factors for fermentative hydrogen production from starch using mixed anaerobic microflora. Int J Hydrogen Energy 2008;32:1565—72.

[25] Hwang JH, Choi JA, Shanab RA, Bhatnagar A, Min B, Song H, et al. Effect of pH and sulfate concentration on hydrogen production using anaerobic mixed microflora. Int J Hydrogen Energy 2009;34:9702—19.

[26] Eaton AD, Clesceri LS, Rice EW, Greenberg AE. Standard methods for the examination of water and wastewater. Washington, DC: American Public Health Association, American Water Works Association & Water Environment Federation; 2005.

[27] Lin L, Yan R, Liu Y, Jiang W. In-depth investigation of enzymatic hydrolysis of biomass wastes based on three major components: cellulose, hemicelluloses and lignin. Bioresour Technol 2010;101:8217—23.

[28] Sreethawong T, Niyamapa T, Neramitsuk H, Rangsunvigit P, Leethochawalit M, Chavadej S. Hydrogen production from glucose-containing wastewater using an anaerobic sequencing batch reactor: effects of COD loading rate, nitrogen content. and organic acid composition. Chem Eng J 2010;160:322—32.

[29] Fang HH, Liu H. Effect of pH on hydrogen production from glucose by a mixed culture. Bioresour Technol 2002;82:87—93.

[30] Lee J. Biological conversion of lignocellulosic biomass to ethanol. J Biotechnol 1997;56:1—24.

[31] Appels L, Baeyens J, Degrève J, Dewil R. Principles and potential of the anaerobic digestion of waste-activated sludge. Prog Energy Combust 2008;34:755—81.

[32] Hawkes FR, Dinsdale R, awkes DL, Hussy I. Sustainable fermentative hydrogen production: challenges for process optimization. Int J Hydrogen Energy 2002;27:1339—47.

[33] Han SK, Kim SH, Shin SH. UASB treatment of wastewater with VFA and alcohol generated during hydrogen fermentation of food waste. Process Biochem 2005;40:2897—905.

[34] Guo WQ, Ren NQ, Wang XJ, Xiang WS, Meng ZH, Ding J, et al. Biohydrogen production from ethanol-type fermentation of molasses in an expanded granular sludge bed (EGSB) reactor. Int J Hydrogen Energy 2008;33:4981—8.

[35] Limwattanalert N. Hydrogen production from ethanol wastewater by usong upflow anaerobic sludge blanket reactor [M.S. thesis]. The Petroleum and PetrochemicalCollege, Chulalongkorn University; 2011.

[36] Gao DW, An R, Tao Y, Li J, Li XX, Ren NQ. Simultaneous methane production and wastewater reuse by a membrane-based process: evaluation with raw domestic wastewater. J Hazard Mater 2011;186:383—9.

[37] Song N, Cai HY, Yan ZS, Jiang HL. Cellulose degradation by one mesophilic strain *Caulobacter sp*. FMC1 under both aerobic and anaerobic conditions. Bioresour Technol 2013;131:281—7.

[38] Kaparaju P, Serrano M, Angelidaki I. Optimization of biogas production from wheat straw stillage in UASB reactor. Appl Energy 2010;87:3779—83.

[39] Gadow SI, Jiang H, Hojo T, Li YY. Cellulosic hydrogen production and microbial community characterization in hyper-thermophilic continuous bioreactor. Int J Hydrogen Energy 2013;38:7259–67.

[40] Yue Z, Chen R, Yang F, MacLellan J, Marsh T, Liu Y, et al. Effect of dairy manure and corn stover co-digestion on anaerobic microbes and corresponding digestion performance. Bioresour Technol 2013;128:65–71.

[41] Shi X, Kim DH, Shin HS, Jung KW. Effect of temperature on continuous fermentative hydrogen production from *Laminaria japonica* by anaerobic mixed culture. Bioresour Technol 2013;144:225–31.

[42] Balat M. Production of bioethanol from lignocellulosic materials via the biochemical pathway: a review. Energy Convers Manag 2011;52:858–75.

Synthesis Gas Production by Combined Reforming of CO₂-Containing Natural Gas with Steam and Partial Oxidation in a Multistage Gliding Arc Discharge System

Krittiya Pornmai,[†] Narissara Arthiwet,[†] Nongnuch Rueangjitt,[‡] Hidetoshi Sekiguchi,[§] and Sumaeth Chavadej*[,†,‖]

[†]The Petroleum and Petrochemical College and [‖]Center of Excellence on Petrochemical and Materials Technology, Chulalongkorn University, Soi Chula 12, Phyathai Road, Pathumwan, Bangkok 10330, Thailand

[‡]Department of Industrial Chemistry, Faculty of Science, Chiang Mai University, 239 Huay Kaew Road, Muang District, Chiang Mai 50200, Thailand

[§]Department of Chemical Engineering, Tokyo Institute of Technology, 2-12-1 O-okayama, Meguro-ku, Tokyo 152-8552, Japan

ABSTRACT: In this research, the effect of multistage gliding arc discharge system on the process performance of combined natural gas reforming with steam and partial oxidation has been investigated. The simulated natural gas used in this study contains 70% methane, 5% ethane, 5% propane, and 20% carbon dioxide. An increase in stage number of gliding arc reactors from 1 to 3, at a constant feed flow rate, enhances all reactant conversions and H_2 yield with a substantial reduction of energy consumption. However, at a given residence time, an increase in stage number from 1 to 3 shows no effect on any hydrocarbon reactant conversions or the selectivities for H_2 and CO but has a drastic reduction of energy consumption. For either the constant feed flow rate or the constant residence time, 3 stages are found to be an optimum stage number of gliding arc reactors for synthesis gas production from the reforming of CO_2-containing natural gas with steam and partial oxidation, in terms of the lowest specific energy consumptions, and highest CO_2 conversion with reasonably high yields for both H_2 and CO.

1. INTRODUCTION

Synthesis gas (a mixture of hydrogen and carbon monoxide, which is produced commercially by catalytic reforming of natural gas) is an important starting chemical for the synthesis of various products such as ammonia, methanol, acetic acid, and dimethyl ether.[1] Technically, a vast variety of raw materials: coal, petroleum, natural gas, naphtha, liquefied petroleum gas, liquefied natural gas, and biomass can be used to produce synthesis gas. The most economical synthesis gas production process seems to be through catalytic reforming reactions of methane with steam and/or partial oxidation since they provide the highest H/C atomic ratio (up to 4) with the lowest production cost.[2,3] All methane reforming processes require metal catalysts, such as nickel, platinum, or rhodium to improve efficiency and lower energy consumption.[4] The catalytic process still requires relatively high operation temperatures (>600 °C), causing catalyst deactivation resulting from catalyst agglomeration and coke deposition.

With the above-mentioned drawback of conventional catalysis, plasma reforming technology is considered an alternative to initiate several high-temperature chemical reactions including natural gas reforming at a lower bulk gas temperature. Thermal plasma has been demonstrated to offer high conversion efficiency with low energy conversion efficiency as a result of high operational temperature.[5] In addition, the extremely high temperature of thermal plasma also causes the erosion and evaporation of the electrodes.[6] In contrast, nonthermal plasma (low-temperature plasma) offers high chemical conversion with relatively low energy consumption since it can produce highly energetic electrons to activate chemical reactions under low bulk gas temperature conditions. There are several types of nonthermal plasma reactors used for various chemical reactions including microwave discharge,[7−10] pulsed corona discharge,[11,12] pulsed spark discharge,[13] dielectric barrier discharge,[14,15] and gliding arc discharge.[16−22] Gliding arc discharge is considered an ideal technique for conversion of hydrocarbons because it provides a high energy density discharge with a relatively low bulk gas temperature.[23]

In our previous work,[2,23−25] the challenge concept of direct reforming of raw natural gas with a high CO_2 content was explored by using an AC gliding arc discharge system. The effect of each gas component in a simulated natural gas, operational parameters, and steam addition in feed were investigated. The results showed that the addition of a small amount of steam effectively minimized carbon deposits on the electrode surface and reactor wall and also enhanced the performance of CO_2-containing natural gas reforming in terms of high reactant conversions, desired product selectivities, and desired product yields, with relatively low specific energy consumptions.[23] In this present work, the combined reforming of CO_2-containing natural gas with steam and partial oxidation using multistage gliding arc reactors was, for the first time, employed for the enhancement of synthesis gas production. The effects of stage number of the gliding arc reactors for either
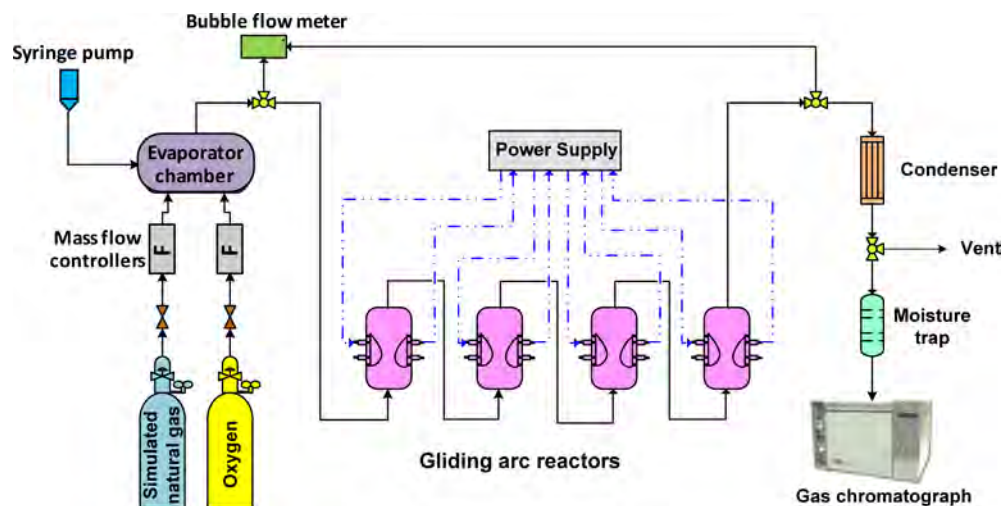
Figure 1. Schematic of gliding arc discharge system.

fixed residence time or fixed total feed flow rate were investigated. The simulated natural gas having a molar ratio of $CH_4:C_2H_6:C_3H_8:CO_2$ of 70:5:5:20 was used in this study because it was representative of high CO_2 content natural gas found in Southeast Asia region.

2. EXPERIMENTAL SECTION

2.1. Reactant Gases. The simulated natural gas used in this work consisted of CH_4, C_2H_6, C_3H_8, and CO_2, with a $CH_4:C_2H_6:C_3H_8:CO_2$ molar ratio of 70:5:5:20, and pure oxygen (O_2) were specially manufactured by Thai Industry Gas (Public) Co., Ltd.

2.2. AC Gliding Arc Discharge System. The schematic of a low-temperature gliding arc system used in this work is depicted in Figure 1. Each of the four gliding arc plasma reactors, connected in a series, was made of a glass tube with an outer diameter of 9 cm and an inner diameter of 8.5 cm and had two diverging knife-shaped electrodes, which were made of 1.2 cm wide stainless steel sheets. The gap distance between the pair of electrodes was fixed at 6 mm. A quantity of steam was regulated by a syringe pump to control a desired water flow rate. The steam fed into the system was generated by passing water through an evaporator chamber, controlled at a constant temperature of 120 °C, wrapped in electric heating tape. The flow rates of the simulated natural gas and O_2 were controlled by using mass flow controllers with transducers. A 7-μm stainless steel filter was placed upstream of each mass flow controller in order to trap any solid particles in the reactant gases. A check valve was also placed downstream of each mass flow controller to prevent any back flow. The mixture of the simulated natural gas, oxygen, and steam was directly fed upward into the first gliding arc reactor. The studied system was operated at atmospheric pressure and ambient temperature. To prevent water condensation in the feed line, the outlet line, and the gas lines between the gliding arc reactors, all stainless steel tubes were heated to ~120 °C by using heating tape. The compositions of the feed gas mixtures and the outlet gas were quantitatively analyzed by an online gas chromatograph (GC;HP, 5890) equipped with two separate columns, a Carboxen 1000 packed column, and a PLOT Al_2O_3 "s" capillary column, which were capable of analyzing all hydrocarbons, CO, CO_2, and H_2.

A power supply unit was used to generate plasma. The process consisted of three sequential steps. For the first step, a domestic AC input of 220 V and 50 Hz was converted to a DC output of 70 V by a DC power supply converter. For the second step, a 500 W power amplifier with a function generator was used to transform the DC into AC current with a sinusoidal waveform and different frequencies. For the third step, the outlet voltage of the second step was stepped up by using a high voltage transformer. The output voltage and frequency were controlled by the function generator. The voltage and current at the low voltage side were measured, instead of those at the high voltage side, by using a power analyzer because the plasma generated is nonequilibrium in nature. The high side voltage and current were thereby calculated by multiplying and dividing each by a factor of 130.[2,23−25]

The feed gas mixture was first introduced into the gliding arc reactors without turning on the power supply unit for any studied conditions. After the composition of outlet gas became invariant, the power supply unit was turned on. The flow rate of the outlet gas was also measured by using a bubble flow meter. The composition of outlet gas was analyzed every 30 min by the online GC. After the multistage gliding arc discharge system reached a steady state with an invariant outlet gas composition, a sample of the outlet gas was then taken for analysis at least a few times every hour. The averaged data, with less than 0.05% error, were used to assess the process performance of the multistage gliding arc discharge system.

2.3. Reaction Performance Calculation. The plasma system performance was evaluated by reactant conversions, product selectivities, H_2, CO, and C_2 yields, and specific energy consumption. The reactant conversion is defined as

$$\% \text{ Reactant conversion} = \frac{(\text{Moles of reactant in} - \text{Moles of reactant out}) \times (100)}{(\text{Moles of reactant in})} \quad (1)$$

The selectivity of any C-containing product is defined by eq 2. The percentage of coke formed is calculated from the difference between the total reactant conversions and total C-containing products, as given in eq 3

$$\% \text{ Product selectivity} = \frac{\text{moles of product produced} \times 100}{\text{moles of total products produced}} \quad (2)$$

$$\% \text{ Coke} = \left[\frac{\sum [R_i]C_{Ri} - \sum [P_i]C_{Pi}}{\sum [P_i]C_{Pi}} \right] \times (100) \tag{3}$$

where $[P_i]$ = moles of each product in the outlet gas stream, $[R_i]$ = moles of each reactant in the feed stream to be converted, C_{Pi} = number of carbon atoms in each product molecule, and C_{Ri} = number of carbon atoms in each reactant molecule.

The different yields of various products are calculated using the following equations:

% C_2 hydrocarbon yield

$$= [[\Sigma(\%CH_4, \%C_2H_6, \%C_3H_8, \text{ and } \%CO_2 \text{ conversions})]$$
$$\times [\Sigma(\%C_2H_2, \%C_2H_4 \text{ selectivities})]]/(100) \tag{4}$$

% H_2 yield

$$= [[\Sigma(\%CH_4, \%C_2H_6, \text{ and } \%C_3H_8 \text{ conversions})]$$
$$\times [\%H_2 \text{ selectivity}]]/(100) \tag{5}$$

% CO yield

$$= [[\Sigma(\%CH_4, \%C_2H_6, \%C_3H_8, \text{ and } \%CO_2 \text{ conversions})]$$
$$\times [\%CO \text{ selectivity}]]/(100) \tag{6}$$

The specific energy consumption is calculated in a unit of eV per C-containing reactant molecule converted and Ws per H_2 molecule produced using the following equation

$$\text{Specific energy consumption} = \frac{(P) \times (60)}{(N) \times (M) \times (F)} \tag{7}$$

where P = power measured at the low voltage side of the power supply unit (W), N = Avogadro's number (6.02×10^{23} molecule g mol^{-1}), M = rate of converted carbon or the rate of produced H_2 molecules (g mole min^{-1}), and F = conversion factor (1 eV = 1.602176×10^{-19} Ws).

The residence time was calculated based on the reaction volume of the gilding arc reactor divided by the feed flow rate. The reaction volume was calculated from the plasma area multiplied by the electrode width, whereas the plasma area was estimated from visual observation (Figure 2).

3. RESULTS AND DISCUSSION

In general, for any given input voltage and frequency, the probability of collisions between reactant molecules and highly energetic electrons in the plasma zone is governed by both
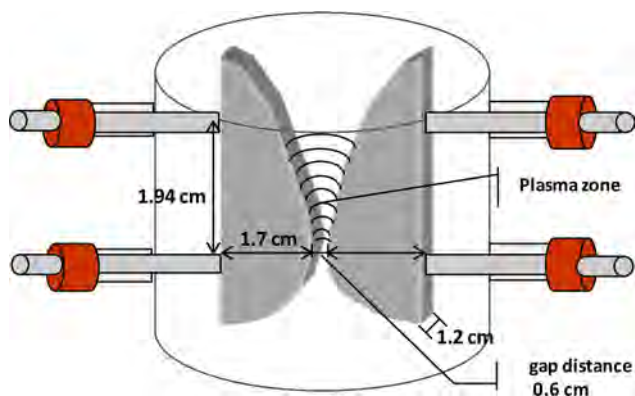

Figure 2. Schematic of plasma area.

residence time and stage number of gliding arc reactors.[2] In order to determine the effect of stage number, two sets of experiments were conducted. First, the effects of the stage number of gliding arc reactors on the process performance at a constant total feed flow rate of 100 cm^3/min were studied by varying the number of gliding arc reactors, while other operating parameters were controlled at the base condition (a feed ratio of CH_4:C_2H_6:C_3H_8:CO_2:O_2:H_2O = 42:3:3:12:30:10, an input voltage of 14.5 kV, an input frequency of 300 Hz, and an electrode gap distance of 6 mm).[23] Hence, the residence times of the single stage, 2, 3, and 4 stage reactors were 1.37, 2.71, 4.11, and 5.48 s, respectively. Second, the effects of the stage number at a constant residence time of 4.11 s were investigated by varying the total feed flow rate of 33.3, 66.6, 100, and 133.3 cm^3/min for the single stage, 2, 3, and 4 stages, respectively, and the other operational parameters were also controlled at the base condition, as mentioned above.

In a plasma environment, the highly energetic electrons generated by gliding arc discharge collide with various hydrocarbons and CO_2 gaseous molecules, creating a variety of chemically active radicals. All of the possible chemical pathways occurring under the studied conditions are expressed below to provide a better understanding of the plasma reforming reactions of the multistage gliding arc system.[23−25] The free radicals of the oxygen active species and hydroxyl active species, as well as hydrogen, are produced during the water dissociation reactions by collisions with electrons (eqs 8 and 9).
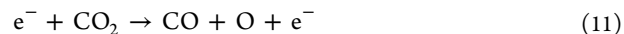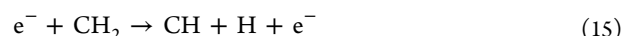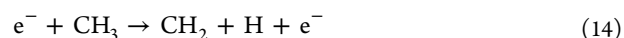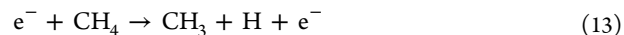
Electron-water collisions:

$$e^- + H_2O \rightarrow O^- + H_2 \tag{8}$$

$$e^- + H_2O \rightarrow OH^- + H \tag{9}$$

Additionally, the free radicals of the oxygen active species can be produced during the collisions of electrons with CO_2, as shown in eqs 10 and 11. Moreover, the produced CO can be further dissociated from the collisions with electrons to form coke and oxygen active species (eq 12). The simultaneous collisions between electrons and all hydrocarbons present in the feed, to produce hydrogen and various hydrocarbon species for subsequent reactions, are described by eqs 13−25.

Electron-carbon dioxide collisions:
Dissociation reactions of carbon dioxide:

$$e^- + CO_2 \rightarrow CO + O^- \tag{10}$$

$$e^- + CO_2 \rightarrow CO + O + e^- \tag{11}$$

$$e^- + CO \rightarrow C + O + e^- \tag{12}$$

Electron-methane collisions:

$$e^- + CH_4 \rightarrow CH_3 + H + e^- \tag{13}$$

$$e^- + CH_3 \rightarrow CH_2 + H + e^- \tag{14}$$

$$e^- + CH_2 \rightarrow CH + H + e^- \tag{15}$$

$$e^- + CH \rightarrow C + H + e^- \tag{16}$$

$$H + H \rightarrow H_2 \tag{17}$$

Electron-ethane collisions:

$$e^- + C_2H_6 \rightarrow C_2H_5 + H + e^- \tag{18}$$

$$e^- + C_2H_5 \rightarrow C_2H_4 + H + e^- \tag{19}$$

$$e^- + C_2H_4 \rightarrow C_2H_3 + H + e^- \qquad (20)$$

$$e^- + C_2H_3 \rightarrow C_2H_2 + H + e^- \qquad (21)$$

$$e^- + C_2H_6 \rightarrow CH_3 + CH_3 + e^- \qquad (22)$$
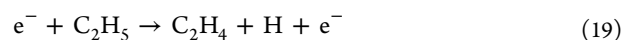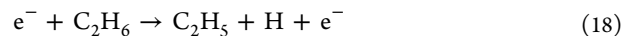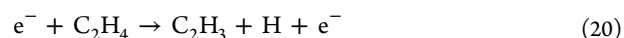
Electron-propane collisions:

$$e^- + C_3H_8 \rightarrow C_3H_7 + H + e^- \qquad (23)$$

$$e^- + C_3H_7 \rightarrow C_3H_6 + H + e^- \qquad (24)$$

$$e^- + C_3H_8 \rightarrow C_2H_5 + CH_3 + e^- \qquad (25)$$
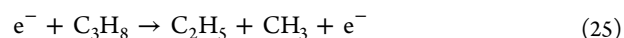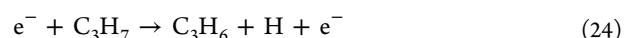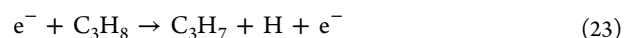
Under the presence of oxygen, several chemical reactions can be initiated in the plasma environment to produce oxygen active species.

Dissociative attachment:

$$e^- + O_2 \rightarrow 2O + e^- \rightarrow O^- + O \qquad (26)$$

Attachment:

$$e^- + O_2 \rightarrow O_2^- \qquad (27)$$
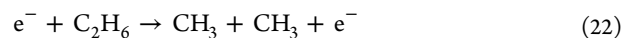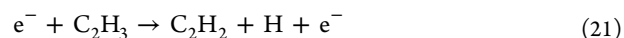
Dissociation:

$$e^- + O_2 \rightarrow 2O + e^- \qquad (28)$$

The oxygen active species derived from the CO_2 dissociation reaction and O_2 dissociative attachment can further extract hydrogen atoms from the molecules of hydrocarbon gases via oxidative dehydrogenation reactions (eqs 29−42), consequently producing several chemically active radicals and water.
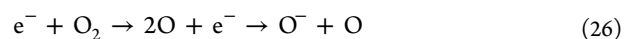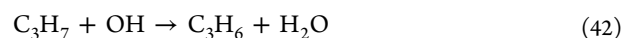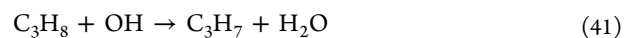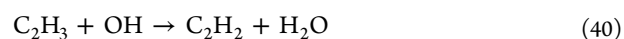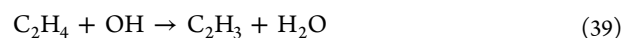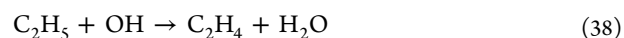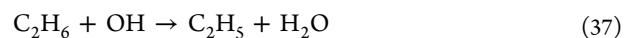
Oxidative dehydrogenation reactions:

$$CH_4 + O \rightarrow CH_3 + OH \qquad (29)$$

$$C_2H_6 + O \rightarrow C_2H_5 + OH \qquad (30)$$

$$C_2H_5 + O \rightarrow C_2H_4 + OH \qquad (31)$$

$$C_2H_4 + O \rightarrow C_2H_3 + OH \qquad (32)$$

$$C_2H_3 + O \rightarrow C_2H_2 + OH \qquad (33)$$

$$C_3H_8 + O \rightarrow C_3H_7 + OH \qquad (34)$$

$$C_3H_7 + O \rightarrow C_3H_6 + OH \qquad (35)$$

$$CH_4 + OH \rightarrow CH_3 + H_2O \qquad (36)$$

$$C_2H_6 + OH \rightarrow C_2H_5 + H_2O \qquad (37)$$

$$C_2H_5 + OH \rightarrow C_2H_4 + H_2O \qquad (38)$$

$$C_2H_4 + OH \rightarrow C_2H_3 + H_2O \qquad (39)$$

$$C_2H_3 + OH \rightarrow C_2H_2 + H_2O \qquad (40)$$

$$C_3H_8 + OH \rightarrow C_3H_7 + H_2O \qquad (41)$$

$$C_3H_7 + OH \rightarrow C_3H_6 + H_2O \qquad (42)$$

The C_2H_5, C_2H_3, and C_3H_7 radicals can be further converted to form ethylene, acetylene, and propane either by electron collisions (eqs 19−21 and 24) or by the oxidative dehydrogenation reactions (eqs 31−33, 35−38, 40, and 42). The extracted hydrogen atoms immediately form hydrogen gas (eq 17). However, no propene was detected in the outlet gas stream.[13] It is, therefore, believed that the propene species is unstable and may possibly undergo further reactions (eqs 43 and 44).
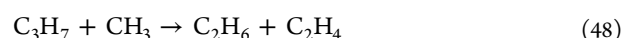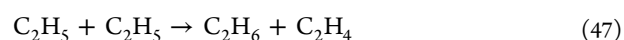
Propene hydrogenation and cracking reactions:

$$C_3H_6 + H_2 \rightarrow C_3H_8 \qquad (43)$$

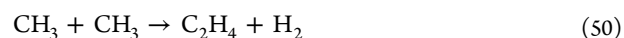$$C_3H_6 \rightarrow C_2H_2 + CH_4 \qquad (44)$$
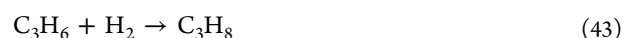
In addition, the free radicals of the hydrocarbons and hydrogen derived from the earlier reactions further react with themselves and the other free radicals to form ethane, ethylene, acetylene, propane, and butane, as shown in eqs 45−60. In addition, ethane can be further dehydrogenated to form ethylene, while ethylene can also be dehydrogenated to form acetylene by either electron collision or oxidative dehydrogenation (eqs 18, 19, 30, 31, 37, and 38 for ethylene formation and eqs 20, 21, 32, 33, 39, and 40 for acetylene formation).

Coupling reactions of active species:

Ethane formation reactions:

$$CH_3 + CH_3 \rightarrow C_2H_6 \qquad (45)$$

$$C_2H_5 + H \rightarrow C_2H_6 \qquad (46)$$

$$C_2H_5 + C_2H_5 \rightarrow C_2H_6 + C_2H_4 \qquad (47)$$

$$C_3H_7 + CH_3 \rightarrow C_2H_6 + C_2H_4 \qquad (48)$$

Ethylene formation reactions:

$$CH_2 + CH_2 \rightarrow C_2H_4 \qquad (49)$$

$$CH_3 + CH_3 \rightarrow C_2H_4 + H_2 \qquad (50)$$

$$C_2H_5 + H \rightarrow C_2H_4 + H_2 \qquad (51)$$

$$C_3H_7 + H \rightarrow C_2H_4 + CH_4 \qquad (52)$$

Acetylene formation reactions:

$$CH + CH \rightarrow C_2H_2 \qquad (53)$$

$$CH_2 + CH_2 \rightarrow C_2H_2 + H_2 \qquad (54)$$

$$CH_3 + CH \rightarrow C_2H_2 + H_2 \qquad (55)$$

$$C_2H_5 + H \rightarrow C_2H_2 + H_2 + H_2 \qquad (56)$$

$$C_3H_7 + H \rightarrow C_2H_2 + CH_4 + H_2 \qquad (57)$$
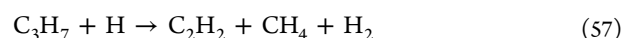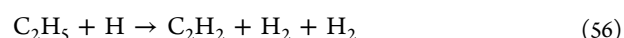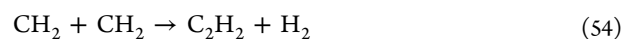
Propane formation reactions:

$$C_2H_5 + CH_3 \rightarrow C_3H_8 \qquad (58)$$

Butane formation reactions:

$$C_2H_5 + C_2H_5 \rightarrow C_4H_{10} \qquad (59)$$

$$C_3H_7 + CH_3 \rightarrow C_4H_{10} \qquad (60)$$

Moreover, CO can be produced under the studied conditions, particularly in the feed with high oxygen content. CO may be mainly formed via the CO_2 dissociation reaction (eqs 10 and 11). Equations 61−65 show the partial oxidative pathways of methane to form CO and H_2 as end products. The partial oxidation reactions of the hydrocarbons can occur under lean oxygen conditions, as shown in eqs 66−68. Even though the experiments were carried out under oxygen lean conditions, a deep oxidation reaction of hydrocarbons can partially occur, as shown in eqs 69−71. The formation of water is believed to occur via the oxidative hydrogenation reactions (eqs 36−42). In addition, water can be formed by the reactions between hydrogen or hydrogen active radicals and oxygen active radicals, as shown in eqs 72−74.

Carbon monoxide formation reactions:
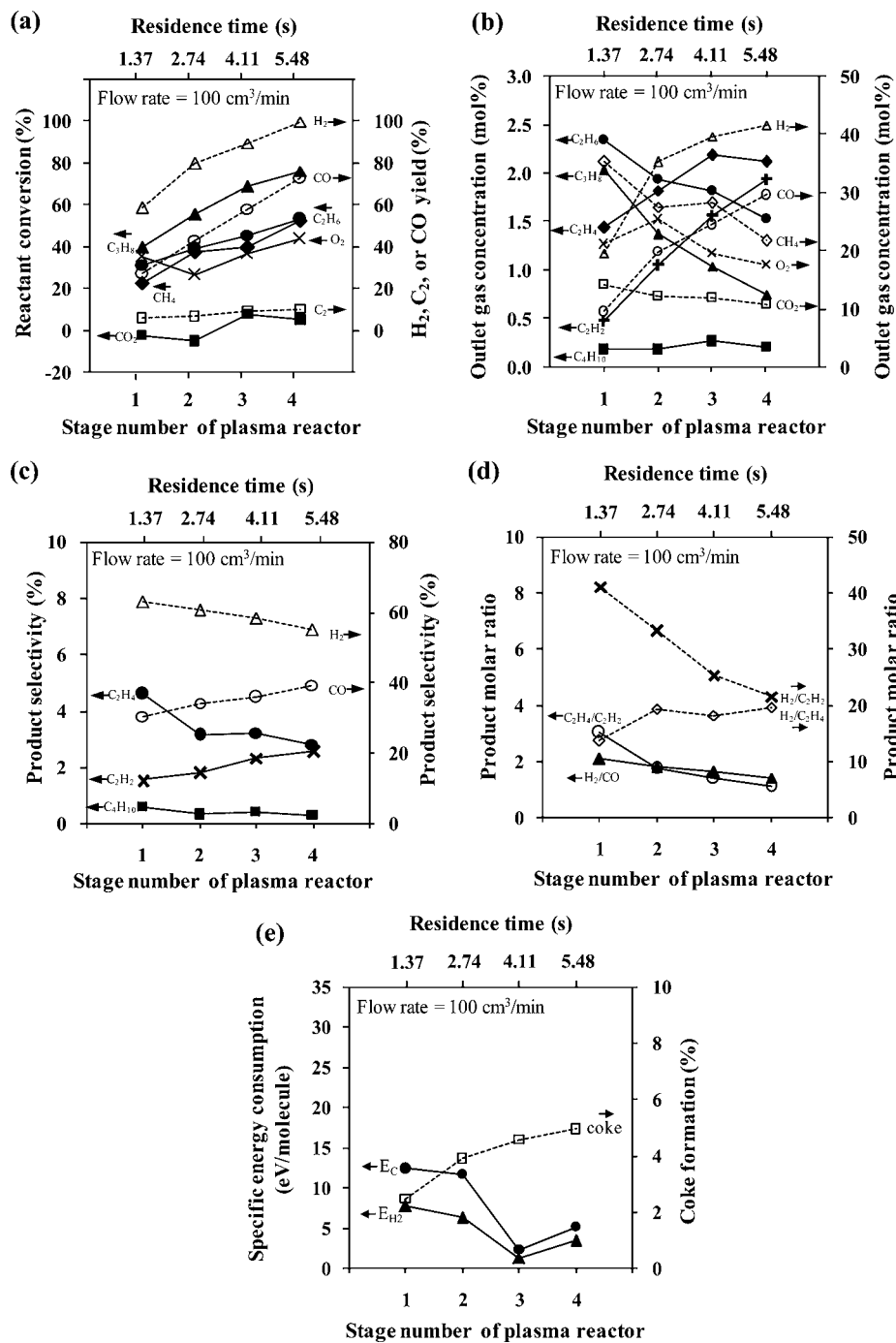
Figure 3. Effect of stage of plasma reactors at constant total feed flow rate of 100 cm^3/min on (a) reactant conversions and product yields, (b) outlet gas concentration, (c) product selectivity, (d) product molar ratios, and (e) specific energy consumptions and coke formation under studied conditions: CH$_4$:C$_2$H$_6$:C$_3$H$_8$:CO$_2$:O$_2$:H$_2$O = 42:3:3:12:30:10; input voltage, 14.5 kV; input frequency, 300 Hz; and electrode gap distance, 6 mm (E_c: power per reactant molecule converted; E_{H2}: power per H$_2$ molecule produced).

$$CH_3 + O \rightarrow HCHO \quad (61)$$

$$HCHO + O \rightarrow OH + CHO \quad (62)$$

$$CHO + O \rightarrow OH + CO \quad (63)$$

$$CHO + OH \rightarrow CO + H_2O \quad (64)$$

$$CHO + H \rightarrow H_2 + CO \quad (65)$$

Partial oxidation reactions of hydrocarbons

$$CH_4 + O_2 \rightarrow CO + H_2O \quad (66)$$

$$C_2H_6 + O_2 \rightarrow CO + H_2O \quad (67)$$

$$C_3H_8 + O_2 \rightarrow CO + H_2O \quad (68)$$

$$CH_4 + \frac{3}{2}O_2 \rightarrow CO_2 + H_2O \quad (69)$$

$$C_2H_6 + \frac{7}{2}O_2 \rightarrow 2CO_2 + 3H_2O \quad (70)$$

$$C_3H_8 + 5O_2 \rightarrow 3CO_2 + 4H_2O \quad (71)$$
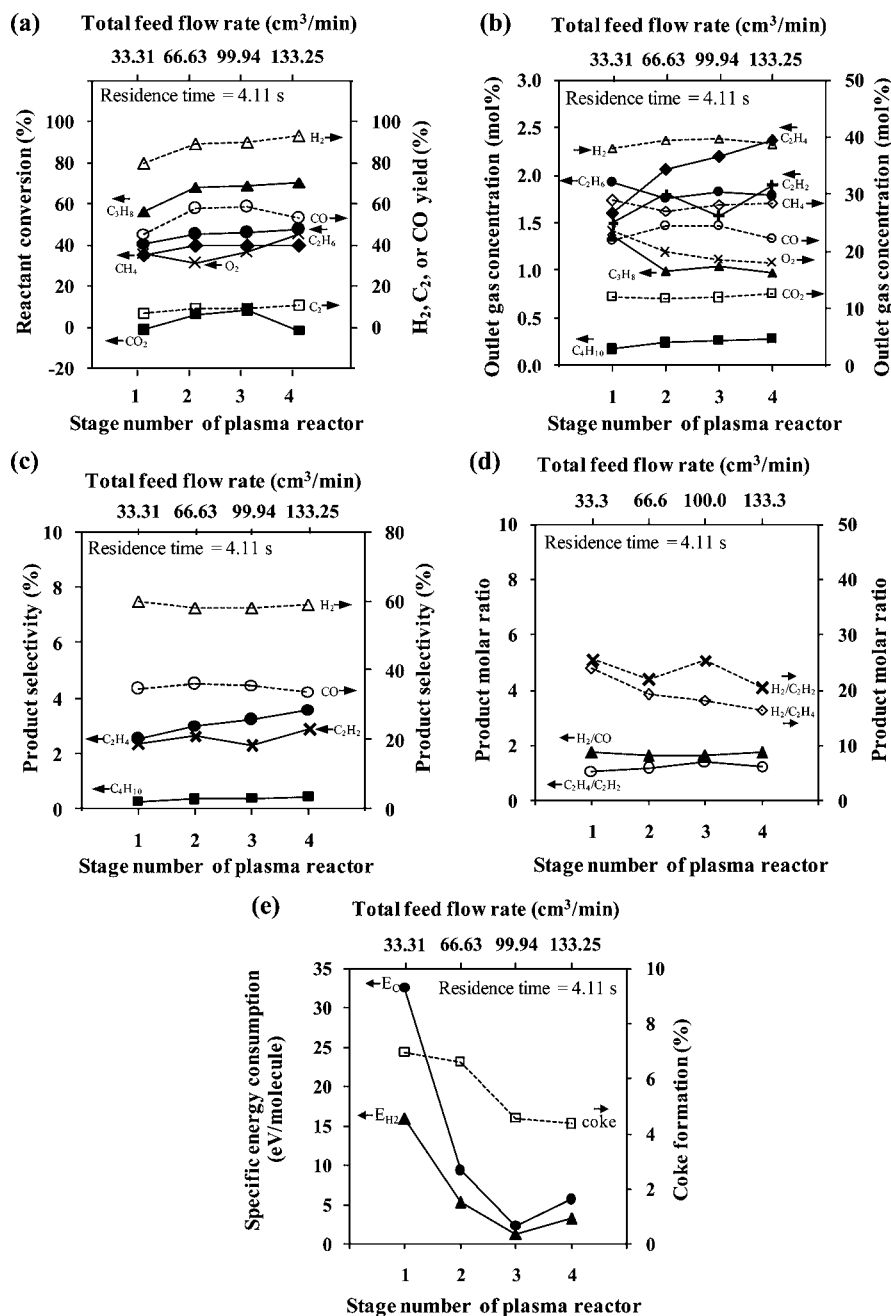
Figure 4. Effect of stage of plasma reactors at constant residence time of 4.11 s on (a) reactant conversions and product yields, (b) outlet gas concentration, (c) product selectivity, (d) product molar ratios, and (e) specific energy consumptions and coke formation under studied conditions: $CH_4:C_2H_6:C_3H_8:CO_2:O_2:H_2O = 42:3:3:12:30:10$; input voltage, 14.5 kV; input frequency, 300 Hz; and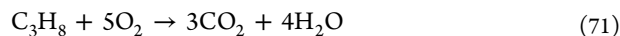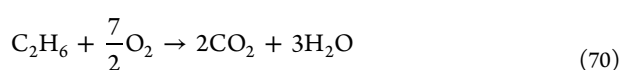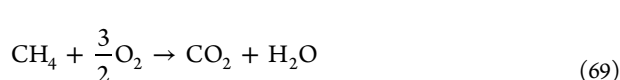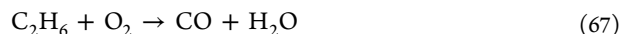 electrode gap distance, 6 mm (E_c: power per reactant molecule converted; E_{H2}: power per H_2 molecule produced).

Water formation reactions:

$$2H + O \rightarrow H_2O \tag{72}$$

$$H_2 + O \rightarrow H_2O \tag{73}$$

$$H_2 + \frac{1}{2}O_2 \rightarrow H_2O \tag{74}$$

Additionally, hydrocarbon molecules may crack to form carbon and hydrogen via cracking reactions (eqs 75−77).

$$CH_4 \rightarrow C + 2H_2 \tag{75}$$

$$C_2H_6 \rightarrow 2C + 3H_2 \tag{76}$$

$$C_3H_8 \rightarrow 3C + 4H_2 \tag{77}$$

Effect of Stage Number of Gliding Arc Reactors at Constant Total Feed Flow Rate. Figure 3a illustrates the influence of the stage number on reactant conversions and product yields at a constant total feed flow rate of 100 cm³/min. The results showed that all hydrocarbon reactant conversions tended to significantly increase with increasing stage number, especially the C_3H_8 conversion. For the fixed total feed flow rate, the increase in stage number directly increased the residence time or reaction time in the system. The higher the residence time, the higher the opportunity for all reactants to collide with highly energetic electrons in the

plasma reaction zones, leading to an increase in all hydrocarbon reactant conversions. The highest C_3H_8 conversion, as compared with the other reactants, results from its lowest dissociation energy. (The bond dissociation energy values of C_3H_8, C_2H_6, CH_4, O_2, and CO_2 are 395, 410, 431, 497, and 532 kJ/mol, respectively.[26])

The CO_2 conversion was found to only reach to a positive value when the system was operated at the 3 or 4 stages, which was different from our previous work of the combined reforming and partial oxidation of CO_2-containing natural gas using an AC multistage gliding arc system.[2] An explanation of the results will be discussed later.

Both H_2 and CO yields dramatically increase with increasing stage number from 1 to 4, whereas the C_2 yield only slightly increases, as shown in Figure 3a. The results suggest that under the studied conditions, an increase in the stage number at a fixed total feed flow rate or an increase in residence time, by increasing stage number, affects the oxidative dehydrogenation reactions of the hydrocarbon reactants (eqs 29−42) to generate OH for CO formation (eq 64), the electron-water collision to produce H_2 (eqs 8 and 9), and the partial oxidation of all hydrocarbon reactants to produce CO (eqs 61−68).

As shown in Figure 3b, the CH_4, C_2H_6, and C_3H_8 concentrations in the outlet gas remarkably decrease with increasing stage number, whereas the concentrations of CO and H_2 rapidly increase. These results correspond well to the increases in the CH_4, C_2H_6, and C_3H_8 conversions, as well as the increases in H_2 and CO yields. Interestingly, with increasing the stage number of gliding arc reactors from 1 to 2 stages, the O_2 concentration in the outlet stream drastically increased, while the CO_2 concentration slightly decreased. The opposite trends of the CO_2 and O_2 concentration profiles can be used to explain the negative values of the CO_2 conversion at both the single stage and 2 stages, owing to a higher formation rate of CO_2 by the complete hydrocarbon oxidation than the CO_2 reduction rate by the reforming reactions (eqs 10−12).

A further increase in stage number from 2 to 4 decreased the oxygen concentration in the outlet gas; however, the CO_2 concentration slightly decreased. The results indicate that the rate of CO_2 formation was still lower than that of CO_2 reduction when the system was operated at a high stage number (3 or 4 stages). Hence, a multistage gliding arc discharge system can be used for the reforming of CO_2-containing natural gas to achieve a reduction of CO_2.

The effects of stage number on product selectivities at a constant total feed flow rate of 100 cm³/min are shown in Figure 3c. The selectivities for C_2H_2 and CO increased with increasing stage number of gliding arc reactors from 1 to 4, which were well related to the increases in the CO and C_2H_2 concentrations (Figure 3b). Conversely, the H_2, C_2H_4, and C_4H_{10} selectivities decreased with increasing stage number of gliding arc reactors, while the H_2, C_2H_4, and C_4H_{10} concentrations increased. The formation rates of CO and C_2H_2 were much higher than the formation rates of the H_2, C_2H_4, and C_4H_{10} when the stage number increased. Therefore, the decreases in H_2, C_2H_4, and C_4H_{10} occurred even though the H_2, C_2H_4, and C_4H_{10} concentrations increased. These results are well relevant to the significant decreases in both H_2/C_2H_2 and C_2H_4/C_2H_2 molar ratios with increasing stage number (Figure 3d). In addition, the apparent increase in H_2/C_2H_4 with increasing stage number implies that the H_2 production rate was higher than the C_2H_4 production rate. With increasing stage number, the H_2/CO molar ratio slightly decreased,

corresponding to the decrease in H_2 selectivity and increase in CO selectivity.

Figure 3e shows a sharp decrease in the specific energy consumption per mole of all hydrocarbon reactants converted or per mole of hydrogen produced with increasing stage number from 1 to 3, but it adversely increased with further increasing stage number from 3 to 4. Interestingly, the coke formation increased markedly with increasing stage number of gliding arc reactors from 1 to 4. As mentioned earlier, an increase in stage number directly increased the residence time under the lean oxygen condition, leading to increases in all subsequential reactions including the cracking reactions, to yield more coke in the system. The minimum specific energy consumption was 2.18 eV per mole of hydrocarbon reactants converted and 1.28 eV per mole of hydrogen produced at 3 stages.

Effects of Stage Number of Gliding Arc Reactors at Constant Residence Time. The reactant conversions and product yields as a function of stage number at a constant residence time of 4.11 s are depicted in Figure 4a. The results reveal that the CH_4 and C_2H_6 conversions and the C_2 yield slightly increased with increasing stage number, while the C_3H_8 greatly increased with increasing stage number of gliding arc reactors from 1 to 2 and then slightly increased with further increasing stage number from 2 to 4. These reactant conversion results were consistent with the decreases in the CH_4, C_2H_6, and C_3H_8 concentrations in the effluent gas with increasing stage number (Figure 4b). The similar trends of both the effects of stage number for the constant total feed flow rate and the constant residence time on C_2 yield, suggest that both residence time and stage number have a slightly effect on C_2 yield. Besides, CO_2 conversion tended to increase with increasing stage number from 1 to 3 and then declined to a negative value with further increasing stage number from 3 to 4. The CO yield showed a similar trend to CO_2 conversion. It was apparent that O_2 conversion decreased with increasing stage number from 1 to 2 and then increased beyond the 2 stages, which was similar to the O_2 conversion results in the case of fixed total feed flow rate. The results suggest that CO formation mainly results from CO_2 reduction, which can be confirmed by the increase in CO_2 reforming with increasing stage number. However, an increase in stage number from 3 to 4 resulted in a decrease in CO_2 conversion and CO yield, suggesting that CO was further oxidized to CO_2. A similar trend of H_2 yield to all hydrocarbon conversions suggests that hydrogen production mainly came from the dehydrogenation reactions, of all hydrocarbon reactants, apart from the reforming reaction of added steam.

The effect of stage number on product selectivities at a constant residence time of 4.11 s is depicted in Figure 4c. With increasing stage number from 1 to 4, the selectivities for C_2H_2, C_2H_4, and C_4H_{10} tended to slightly increase, whereas the selectivities for H_2 and CO remained almost unchanged. These results correspond well to the increases in the C_2H_2, C_2H_4, and C_4H_{10} concentrations in the outlet gas (Figure 4b). The different results of H_2 selectivity in the constant total feed flow rate and the constant residence time suggest that the increase in stage number with constant residence time has an insignificant effect on H_2 formation, while for the constant total feed flow rate, a very long residence time by increasing stage number of gliding arc reactors can decrease H_2 formation because the produced H_2 is further oxidized or used for the hydrogenation reactions.

Figure 5. Comparisons of (a) CH_4 and CO_2 conversions, (b) H_2 and CO yields for the reforming of CO_2-containing natural gas under various conditions, (c) product selectivity, and (d) specific energy consumptions (E_c: power per reactant molecule converted; E_{H2}: power per H_2 molecule produced).

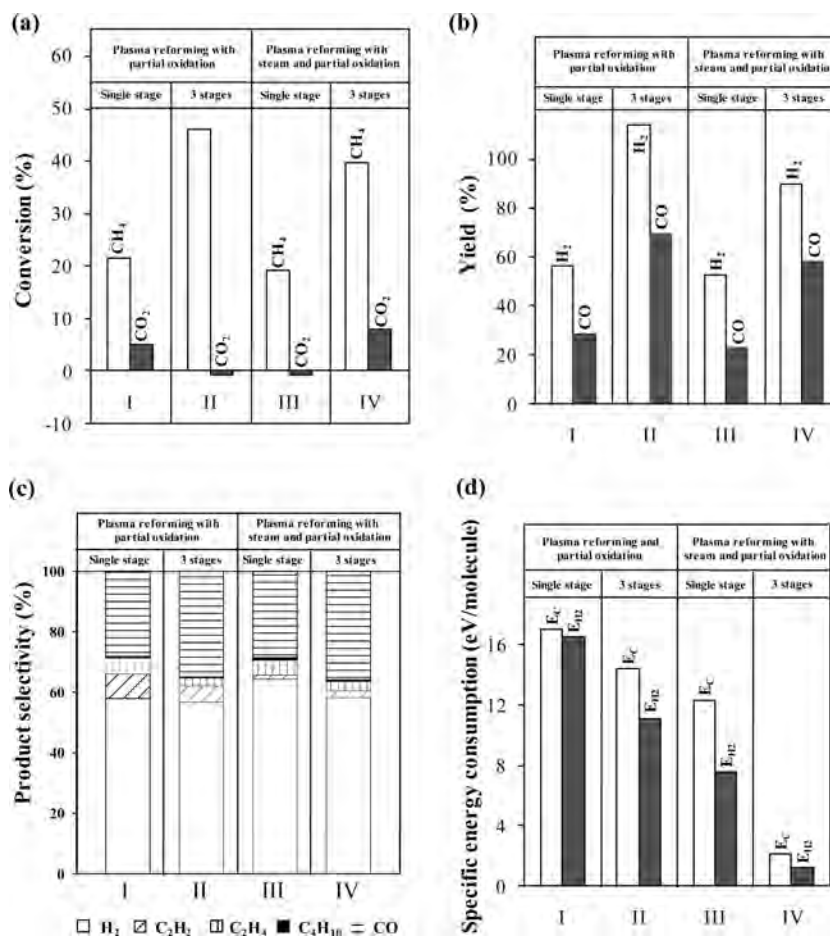The ratios of H_2/C_2H_2 and H_2/C_2H_4 tended to decrease with increasing stage number of the gliding arc reactors for a constant residence time, whereas the ratio of H_2/CO and C_2H_4/C_2H_2 seemed to remain almost unchanged (Figure 4d).

Figure 4e shows the effect of stage number of gliding arc reactors on specific energy consumption and coke deposition at a constant residence time of 4.11 s. The specific energy consumption per mole of all hydrocarbon reactants converted or hydrogen produced tended to dramatically decrease with increasing stage from 1 to 3 stages, and beyond the 3 stages, and they increased with further increasing stage number of gliding arc reactors from 3 to 4 stages. In comparisons of both cases of the constant total feed flow rate and the constant residence time, the effects of stage number of gliding arc reactors at the constant residence time showed more prominently than that at the constant total feed flow rate on the specific energy consumption. The minimum specific energy consumption was found at the same stage number of 3. The coke formation was found to decrease with increasing stage number of gliding arc reactors at a constant residence time of 4.11 s. The coke formation results for both cases of constant total feed flow rate and constant residence time were opposite. The optimum conditions of a total feed flow rate of 100 cm^3/min, a steam content of 10 mol %, a HCs-to-O_2 feed molar ratio of 2/1, 3 stages number, an electrode gap distance of 6 mm, input voltage of 14.5 kV, and an input frequency of 300

Hz provided the lowest specific energy consumption with reasonably high yields for both H_2 and CO.

From the present results, for either the constant total feed flow rate or the constant residence time, 3 stages was found to be an optimum number of gliding arc reactor in which is in a good agreement with our previous work.[29]

Comparison of CO_2−Containing Natural Gas Reforming Performance with Different Plasma Reforming Systems. Figure 5a illustrates the comparisons of CH_4 and CO_2 conversions with different plasma reforming systems under optimum conditions. Table 1 shows the optimum operational conditions of the four plasma systems for reforming the simulated natural gas. The combined plasma reforming with steam and partial oxidation using both single stage (Case III) and multistage (Case IV) produced lower CH_4 conversions, as compared to the combined plasma reforming with partial oxidation processes with single stage (Case I) and multistage (Case II), respectively. It should be noted that there are competitive collision reactions of electrons with both hydrocarbons and steam, leading to lower possibilities of electro-hydrocarbon collisions.[27] It can be clearly seen that both multistage systems gave higher CH_4 conversions than both single stage systems. The multistage gliding arc system used in this study provided a greater opportunity of electron collision with all reactants including CH_4 as compared with the single stage gliding arc system. Interestingly, the negative values of CO_2 conversion were observed in both the plasma reforming

Table 1. Optimum Operational Conditions of the Four Plasma Systems for Reforming of CO_2-Containing Natural Gas at a 2/1 HCs/O_2 Molar Ratio, Input Frequency of 300 Hz, and Electrode Gap Distance of 6 mm

	steam content (mol %)	total feed flow rate (cm³/min)	input voltage (kV)	stage number of plasma reactor (stage)	residence time (s)
Case I[a]		125	17.5	1	1.09
Case II[b]		125	17.5	3	4.38
Case III[c]	10	100	14.5	1	1.37
Case IV[d]	10	100	14.5	3	4.11

[a]Plasma reforming with partial oxidation using single stage plasma reactor.[7] [b]Plasma reforming with partial oxidation using multistage plasma reactors.[10] [c]Plasma reforming with steam and partial oxidation using single plasma reactor.[24] [d]Plasma reforming with steam and partial oxidation using multistage plasma reactors (present work).

with steam and partial oxidation in the single stage gliding arc system (Case III) and the plasma reforming with partial oxidation in the multistage gliding arc system (Case II). As mentioned earlier, a significant enhancement of CO_2 conversion was found to reach a maximum value (7.78%) when the system was operated with the plasma reforming with steam and partial oxidation in the multistage gliding arc system at 3 stages. The results imply that the multistage gliding arc system plays an important role in the improvement of CO_2 conversion even though it is operated with steam and partial oxidation.

Figure 5b shows the comparison of H_2 and CO yields with different plasma reforming systems. The results reveal that the use of both multistage gliding arc systems can enhance both H_2 and CO yields, when compared to both single stage gliding arc systems (Figure 5b). Again, the higher the residence time, the greater the opportunity for collisions between both the reactant gases and highly energetic electrons, leading to higher H_2 and CO yields. For the single stage gliding arc system, both the plasma reforming with partial oxidation and the plasma reforming with steam and partial oxidation showed insignificant differences in both H_2 and CO yields. Generally, the presence of steam in the plasma reforming of hydrocarbons is expected to increase both H_2 and CO yields, whereby the highest H_2 and CO yields were found in the plasma reforming with partial oxidation in the multistage gliding arc system. The results can be explained by the fact that both H_2 and CO yields were calculated by including all reactant conversions and all product selectivities (eqs 5 and 6). As mentioned earlier, the addition of steam in the plasma reforming provided competitive collision reactions of highly energetic electrons with both hydrocarbons and steam, resulting in lower hydrocarbon conversions. As a result, the H_2 and CO yields were lower.

As shown in Figure 5c, for all studied plasma reforming systems, the product selectivities are in the following order: H_2 > CO > C_2H_2 ≈ C_2H_4 > C_4H_{10}. In the comparison between the plasma reforming with partial oxidation and the plasma reforming with steam and partial oxidation, the addition of steam in the plasma reforming of CO_2-containing natural gas could provide higher H_2 production for both the single and multistage gliding arc system because the added steam could generate more hydroxyl radicals (OH^-) and hydrogen radicals (H^-) to facilitate all subsequential reactions.

As shown in Figure 5c, the addition of steam does not have a significant effect on CO selectivity for either the single stage or the multistage gliding arc system. It can be explained by the fact

that the CO formation is mostly derived from the partial oxidation of all hydrocarbons in the simulated natural gas. These results agree well with a previous work.[28] The use of a multistage gliding arc system with or without steam could improve CO selectivity, as compared to the single stage gliding arc system. These results imply that CO formation favorably occurs at a high residence time. A significant decrease in C_2H_2 selectivity was observed with the addition of steam. The opposite trends of C_2H_2 and H_2 selectivities, in the presence of steam, are hypothesized to provide a greater opportunity for dehydrogenation reactions of hydrocarbon species (C_2H_2 and C_2H_4) to produce H_2.

Figure 5d shows the comparisons of the specific energy consumptions of the different plasma reforming systems. For either the single stage or multistage gliding arc system, the addition of steam in the plasma reforming of the CO_2-containing natural gas with partial oxidation could reduce significantly both the specific energy consumptions per H_2 product molecule produced and per reactant molecule converted. The lowest specific energy consumptions both per reactant molecule converted (2.18 eV/molecule) and per H_2 molecule produced (1.28 eV/molecule) were obtained from plasma reforming with steam and partial oxidation using a multistage gliding arc system.

4. CONCLUSIONS

The combined steam reforming and partial oxidation of CO_2-containing natural gas using a multistage gliding arc system was investigated under either a constant feed flow rate or a constant residence time to determine the effects of the stage numbers of the gliding arc reactors. The major products were hydrogen and carbon monoxide. An increase in the stage number of the gliding arc reactors under the constant residence time of 4.11 s showed more dominant effects on all hydrocarbon reactant conversions, H_2 and CO yields, and most product selectivities than that under a constant total feed flow rate of 100 cm³/min. The addition of steam provided higher selectivities for H_2 and CO with lower H_2 and CO yields. Moreover, 3 stage of the multistage gliding arc system was considered to be an optimum stage number because it provided much lower specific energy consumption per either mole of hydrogen produced or mole of hydrocarbons converted for the reforming of CO_2-containing natural gas with steam and partial oxidation as compared with that without steam.

■ AUTHOR INFORMATION

Corresponding Author

*Phone: +66-2-218-4139. Fax: +66-2-218-4139. E-mail: sumaeth.c@chula.ac.th.

Notes

The authors declare no competing financial interest.

11899

dx.doi.org/10.1021/ie500516m | *Ind. Eng. Chem. Res.* 2014, 53, 11891−11900

■ REFERENCES

(1) Aasberg-Petersen, K.; Dybkjaer, I.; Ovensen, C. V.; Schjodt, N. C.; Sehested, J.; Thomsen, S. G. Natural gas to synthesis gas-catalysts and catalytic processes. *J. Nat. Gas Sci. Eng.* **2001**, *3*, 423.

(2) Rueangjitt, N.; Jittiang, W.; Pornmai, K.; Chamnanmanoontham, J.; Sreethawong, T.; Chavadej, S. Combined reforming and partial oxidation of CO_2-containing natural gas using an AC multistage gliding arc system: Effect of number of plasma reactors. *Plasma Chem. Plasma Process.* **2009**, *29*, 433.

(3) Rueangjitt, N.; Sreethawong, T.; Chavadej, S.; Sekiguchi, H. Plasma-catalytic reforming of methane in AC microsized gliding arc discharge: Effect of input power, reactor thickness, and catalyst existence. *Chem. Eng. J.* **2009**, *155*, 874.

(4) Wang, S.; Lu, G. Q. (M.); Graeme, J. M. Carbon dioxide reforming of methane to produce synthesis gas over metal-supported catalyst: State of the art. *Energy Fuels* **1996**, *10*, 896.

(5) Hu, Y. P.; Gesheng, L.; Yingduo, Y.; Xiaohong, G.; Zhihong, L. Hydrogen generation from hydro-ethanol reforming by DBD-plasma. *Int. J. Hydrogen Energy* **2012**, *37*, 1044.

(6) Changming, D.; Hongxia, L.; Lu, Z.; Jing, W.; Dongwei, H.; Mudan, X.; Jiawen, C.; Yabin, C.; Hanlu, Y.; Ya, X.; Yi, X. Hydrogen production by steam-oxidative reforming of bio-ethanol assisted by Laval nozzle arc discharge. *Int. J. Hydrogen Energy* **2012**, *37*, 8318.

(7) Jivotov, V. K.; Potapkin, B. V.; Rusanov, V. D. Low temperature plasma chemistry. In *Encyclopedia of Low Temperature Plasma*; Lebedev, Y. A., Plate, N. A., Fortov, V. E., Eds.; Pleiades: Moscow, 2005.

(8) Rusanov, V. D.; Babaritskii, A. I.; Baranov, I. E.; Bibikov, M. B.; Deminskii, M. A.; Demkin, S. A.; et al. Nonequilibrium effect of atmospheric-pressure microwave-discharge plasma on methane and kerosene conversion into synthesis gas. *Doklady Chem.* **2004**, *395* (2), 82.

(9) Benilov, M. S.; Naidis, G. V. Modeling of hydrogen-rich gas production by plasma reforming of hydrocarbon fuels. *Int. J. Hydrogen Energy* **2006**, *31*, 769.

(10) Deminsky, M.; Jivotov, C.; Potapkin, B.; Rusanov, V. Plasma-assisted production of hydrogen from hydrocarbons. *Pure Appl. Chem.* **2002**, *74* (3), 413.

(11) Okumoto, M.; Kim, H. H.; Takashima, K.; Katsura, S.; Mizuno, A. Reactivity of methane in nonthermal plasma in the presence of oxygen and inert gases at atmospheric pressure. *IEEE Trans Ind. Appl.* **2001**, *37* (6), 1618.

(12) Supat, K.; Chavadej, S.; Lobban, L. L.; Mallinson, R. G. Combined steam reforming and partial oxidation of methane to synthesis gas under electrical discharge. *Ind. Eng. Chem. Res.* **2003**, *42*, 16.

(13) Sekine, Y.; Urasaki, K.; Kado, S.; Matsukata, M.; Kikuchi, E. Nonequilibrium pulsed discharge: A novel method for steam reforming of hydrocarbons or alcohols. *Energy Fuels* **2004**, *18*, 455.

(14) Kogelschatz, U.; Zhou, L. M.; Xue, B.; Eliasson, B. In *Greenhouse Gas Control Technologies*; Eliasson, B., Riemer, P. W. F., Wokaun, A., Eds.; Pergamon (Elsevier): Oxford, 1999.

(15) Larkin, D. W.; Caldwell, T. A.; Lobban, L. L.; Mallinson, R. G. Oxygen pathways and carbon dioxide utilization in methane partial oxidation in ambient temperature electric discharges. *Energy Fuels* **1998**, *12*, 740.

(16) Bromberg, L.; Cohn, D. R.; Rabinovich, A.; Alexeev, N. Plasma catalytic reforming of methane. *Int. J. Hydrogen Energy* **1999**, *24*, 1131.

(17) Czernichowski, A.; Czernichowski, M.; Czernichowski, P.; Cooley, T. Reforming of methane into syngas in a plasma assisted reactor. *Fuel Chem. Div. Prepr.* **2002**, *47* (1), 280.

(18) Kalra, C. S.; Gutsol, A. F.; Fridman, A. A. Gliding arc discharges as a source of intermediate plasma for methane partial oxidation. *IEEE Trans. Plasma Sci.* **2005**, *33* (1), 32.

(19) Mutaf-Yardimci, O.; Saveliev, A. V.; Fridman, A. A.; Kennedy, L. A. Employing plasma as a catalyst in hydrogen production. *Int. J. Hydrogen Energy* **1998**, *23* (12), 1109.

(20) Indarto, A. Kinetic of CO_2 reduction by gliding arc plasma. *Asian J. Water Environ. Pollut.* **2006**, *4* (1), 191.

(21) Lesueur, H.; Czernichowski, A.; Chapelle, J. Electrically assisted partial oxidation of methane. *Int. J. Hydrogen Energy* **1994**, *19*, 139.

(22) Indarto, A.; Yang, D. R.; Choi, J. W.; Lee, H.; Song, H. K. Gliding arc plasma processing of CO_2 conversion. *J. Hazardous Mater.* **2006**, *146* (1/2), 309.

(23) Pornmai, K.; Jindanin, A.; Sekiguchi, H.; Chavadej, S. Synthesis gas production from CO_2-containing natural gas by combined steam reforming and partial oxidation in an AC gliding arc discharge. *Plasma Chem. Plasma Process.* **2012**, *32*, 723.

(24) Rueangjitt, N.; Akarawitoo, C.; Sreethawong, T.; Chavadej, S. Reforming of CO_2-containing natural gas using an AC gliding arc system: Effect of gas component in natural gas. *Plasma Chem. Plasma Process.* **2007**, *27*, 559.

(25) Rueangjitt, N.; Sreethawong, T.; Chavadej, S. Reforming of CO_2-containing natural gas using an AC gliding arc system: effects of operational parameters and oxygen addition in feed. *Plasma Chem. Plasma Process.* **2008**, *28*, 49.

(26) Dean, J. A. *Lange's Handbook of Chemistry*; McGraw-Hill: New York, 1999.

(27) Sugasawa, M.; Terasawa, T.; Futamura, S. Effects of initial water content on steam reforming of aliphatic hydrocarbons with non-thermal plasma. *J. Electrostat.* **2010**, *68*, 212.

(28) Pornmai, K. *Synthesis gas production from CO_2-containing natural gas by combined steam reforming and partial oxidation in multi-stage gliding arc discharge system*. Ph.D. Thesis, Chulalongkorn University, Thailand, 2013.

(29) Rueangjitt, N.; Jittiang, W.; Pornmai, K.; Chamnanmanoontham, J.; Sreethawong, T.; Chavadej, S. Combined reforming and partial oxidation of CO_2-containing natural gas using an AC multistage gliding arc discharge system: Effect of stage number of plasma reactors. *Plasma Chem. Plasma Process.* **2009**, *29*, 433.

CrossMark

Optimization of separate hydrogen and methane production from cassava wastewater using two-stage upflow anaerobic sludge blanket reactor (UASB) system under thermophilic operation

Patcharee Intanoo [a], Pramoch Rangsanvigit [a,b], Pomthong Malakul [a,b], Sumaeth Chavadej [a,b,*]

[a] The Petroleum and Petrochemical College, Chulalongkorn University, Bangkok, Thailand
[b] Center of Excellence on Petrochemical and Materials Technology, Chulalongkorn University, Bangkok 10330, Thailand

HIGHLIGHTS

- Recycling operation can help eliminate a use of NaOH for pH control in a H_2 unit.
- The VFA inhibition level for hydrogen-producing bacteria is around 8800 mg/l.
- The VFA inhibition level for methane-producing bacteria is around 350 mg/l.
- Optimum loading rate of the two-stage UASB provides maximum H_2 and CH_4 productions.
- Two-stage UASB produces mixed gas with higher heating value than single-stage.

ARTICLE INFO

ABSTRACT

The objective of this study was to investigate the separate hydrogen and methane productions from cassava wastewater by using a two-stage upflow anaerobic sludge blanket (UASB) system under thermophilic operation. Recycle ratio of the effluent from methane bioreactor-to-feed flow rate was fixed at 1:1 and pH of hydrogen UASB unit was maintained at 5.5. At optimum COD loading rate of 90 kg/m^3 d based on the feed COD load and hydrogen UASB volume, the produced gas from the hydrogen UASB unit mainly contained H_2 and CO_2 which provided the maximum hydrogen yield (54.22 ml H_2/g COD applied) and specific hydrogen production rate (197.17 ml/g MLVSS d). At the same optimum COD loading rate, the produced gas from the methane UASB unit mainly contained CH_4 and CO_2 without H_2 which were also consistent with the maximum methane yield (164.87 ml CH_4/g COD applied) and specific methane production rate (356.31 ml CH_4/g MLVSS d). The recycling operation minimized the use of NaOH for pH control in hydrogen UASB unit.

1. Introduction

Biogas technology is currently being widely applied to several industrial wastewaters and animal wastes (Sirirote et al., 2010). It not only produces combustible biogas, which is widely used to substitute fuel oil for steam generation in industry, but also reduces treatment cost. Several types of industrial wastewaters such as food wastewater (Zhu et al., 2011), cassava wastewater (Wang et al., 2012), and cornstalk waste (Cheng et al., 2012) can be used to produce biogas. Apart from producing the combustible

biogas, anaerobic digestion offers several benefits; for example, it can be operated at a high organic loading rate under ambient conditions, which reduces the overall treatment cost, decreases the emission of greenhouse gases, and eliminates odorous problems (Biofuels, Waste Energy, 2008). However, the anaerobic processes require a rather large size of bioreactor because of slow rates. One of innovative techniques for the improvement of biogas production from wastewaters is a use of two-stage processes (Wikimedia Foundation, 2014).

The two-stage anaerobic process consists of two sequential steps of hydrogen and methane production units (Zhu et al., 2008). In the first unit, organic compounds in wastewater are hydrolyzed and converted anaerobically to hydrogen, carbon dioxide, and volatile fatty acids (VFA) by acidogenic bacteria. Next, the effluent liquid from the first unit is continuously fed to the second

unit to further produce methane by methanogenic bacteria. The two-stage anaerobic processes can produce a higher methane production rate and yield due to a better balance between the rates of VFA production and consumption as compared to a single process (Xia et al., 2011). Sarada and Joseph (1996) reported that a two-stage anaerobic system operated at a temperature of 30 °C, a hydraulic retention time (HRT) of 24 d and an organic loading rate of 4.5 kg/m^3 d gave 50% increase in the gas production rate and 40% increase in the methane yield when being compared with a single-stage anaerobic process. Liu et al. (2006) reported that the methane production efficiency of a two-stage hydrogen–methane process treating household solid waste increased about 21% when compared with one-stage process. Sarada and Joseph (1996) reported that a toxic level of VFA to methanogens was found to be about 400 mg/l in a two-stage system treating tomato processing wastewater.

Temperature is another of important factor, affecting the process performance of anaerobic fermentation. A two-stage process operated under thermophilic temperature (55 °C) gave a higher biogas production rate than that operated at a low temperature (35–37 °C) because under the high temperature, the reaction rate is higher (Xia et al., 2011). Luo et al. (2010) reported that the hydrogen and methane yields in a two-stage thermophilic continuous stirred tank reactor (CSTR) of cassava stillage were 55 ml H$_2$/g VS and 94 ml CH$_4$/g VS, respectively which were higher than those of two-stage mesophilic fermentation process of food waste (Nathao et al., 2013).

In this research, spontaneous hydrogen and methane productions from cassava wastewater were investigated by using a two-stage UASB process at a constant high temperature of 55 °C. The first hydrogen UASB unit was controlled at a constant pH 5.5. The effluent from the hydrogen bioreactor was further fed to the methane UASB bioreactor to produce methane without pH control. The two-stage UASB unit was operated at different COD loading rates. The recycle ratio of the effluent flow rate from the methane UASB bioreactor to the feed flow rate was fixed at 1:1 in order to minimize the use of NaOH for pH adjustment in the hydrogen UASB unit. It was hypothesized that both hydrogen and methane production efficiency could be maximized by the combination of two-stage process, the pH control at 5.5 for the hydrogen UASB unit, and the effluent recycle operation, under thermophilic operation for both UASB units.

2. Methods

2.1. Feed preparation

Cassava wastewater used in this study was obtained from Ubon Bioethanol Co., Ltd., Ubon Ratchathani, Thailand. It was sieved to remove any large solid particles and kept at 4 °C before use. The cassava wastewater used in the present work had a chemical oxygen demand (COD) value of 14,500 mg/l and a ratio of COD:nitrogen:phosphorous of 100:2.98:2.03, indicating that the studied cassava wastewater had sufficient amounts of both nutrients for anaerobic degradation (the theoretical ratio of COD:nitrogen:phosphorous is 100:1:0.4 for anaerobic decomposition for biogas production (Intanoo et al., 2012; Sreethawong et al., 2010)).

2.2. Seed sludge

A granular sludge sample taken from the full-scale UASB unit treating cassava wastewater of the same factory was used as seeds for starting up of both studied UASB bioreactors. The seed sludge only for the hydrogen UASB was heated at 95 °C for 15 min in order to enrich hydrogen-producing bacteria and to eliminate methane-

producing bacteria (hydrogen-consuming bacteria) (Intanoo et al., 2012; Sreethawong et al., 2010; Poontaweegeratigarn, 2012). The initial microbial concentration in terms of MLVSS (mixed liquor volatile suspended solids) of each UASB bioreactor was about 12,000 mg/l.

2.3. UASB operation

The UASB reactors used in the study were constructed from borosilicate glass with 4 and 24 l working volumes for the hydrogen and methane UASB bioreactors, respectively. The temperatures inside both bioreactors were controlled constant at 55 °C by a water jacket surrounding each bioreactor and a circulating/heating bath. The cassava wastewater was fed continuously to the bottom of the hydrogen UASB bioreactor (in an upward direction) at any desired flow rate by using a peristaltic pump to obtain different COD loading rates (30, 60, 90, 120, and 150 kg/m^3 d based on the feed COD load and hydrogen UASB working volume or 5, 10, 15, 20 and 25 kg/m^3 d based on the feed COD load and methane UASB working volume). The pH of the hydrogen UASB unit was maintained at 5.5 by using a pH controller. The effluent from the hydrogen UASB unit was directly pumped into the methane UASB unit by a peristaltic pump with a level control probe. The pH of the methane UASB unit was not controlled. In order to minimize the consumption of NaOH for the pH adjustment in the hydrogen UASB unit, a recycle ratio of the methane UASB effluent flow rate to the feed flow rate of 1:1 was used in this study. The schematic of the two-stage UASB unit is shown in Fig. 1. At any given COD loading rate, the two-stage UASB system was operated to reach steady state before taking effluent and produced gas samples for analysis and measurement. For each studied COD loading rate, the two-stage UASB system was operated approximately 4 weeks to reach steady state condition. The steady state was justified when both of the gas production rates and the effluent COD values of both hydrogen and methane UASB units did not change with time.

2.4. Measurements and analytical methods

The volumes of produced gases from both UASB bioreactors were recorded daily by wet gas meters (Ritter, TGO5/5). The compositions of both produced gas samples were determined by a gas chromatograph (GC; Auto System GC, Perkin–Elmer) equipped with a thermal conductivity detector (TCD) and a packed column (stainless-steel 10′ × 1/8′ × .085″ HayeSep D 100/120 mesh, Altech) and the analysis conditions were given in our previous study (Intanoo et al., 2012). The COD in the feed and effluent samples were quantified by the dichromate method using a COD reactor and a spectrophotometer (HACH, DR 2700). The mixed liquor volatile suspended solid (MLVSS) representing the microbial concentration in each UASB unit was measured by taking all the sludge in each bioreactor at the end of each studied COD loading rate. The effluent volatile suspended solid (effluent VSS), representing the microbial washout from each UASB unit, was measured according to the standard methods (Eaton et al., 2005). The total amount of volatile fatty acids in each bioreactor at any given COD loading rate was determined by the distillation-titration method (Eaton et al., 2005). The samples obtained from the steam distillation step were additionally taken for the determination of organic acid compositions by using another gas chromatograph (GC; PR 2100, Perichrom) equipped with a flame ionization detector (FID) and the analysis conditions were given in our previous study (Intanoo et al., 2012). Nitrogen analyses (in terms of organic nitrogen measured by the diazotization, cadmium reduction method, and inorganic nitrogen measured by the salicylate method) in the feed and effluent samples were carried out with the TNT persulfate digestion. The total phosphorous contents in
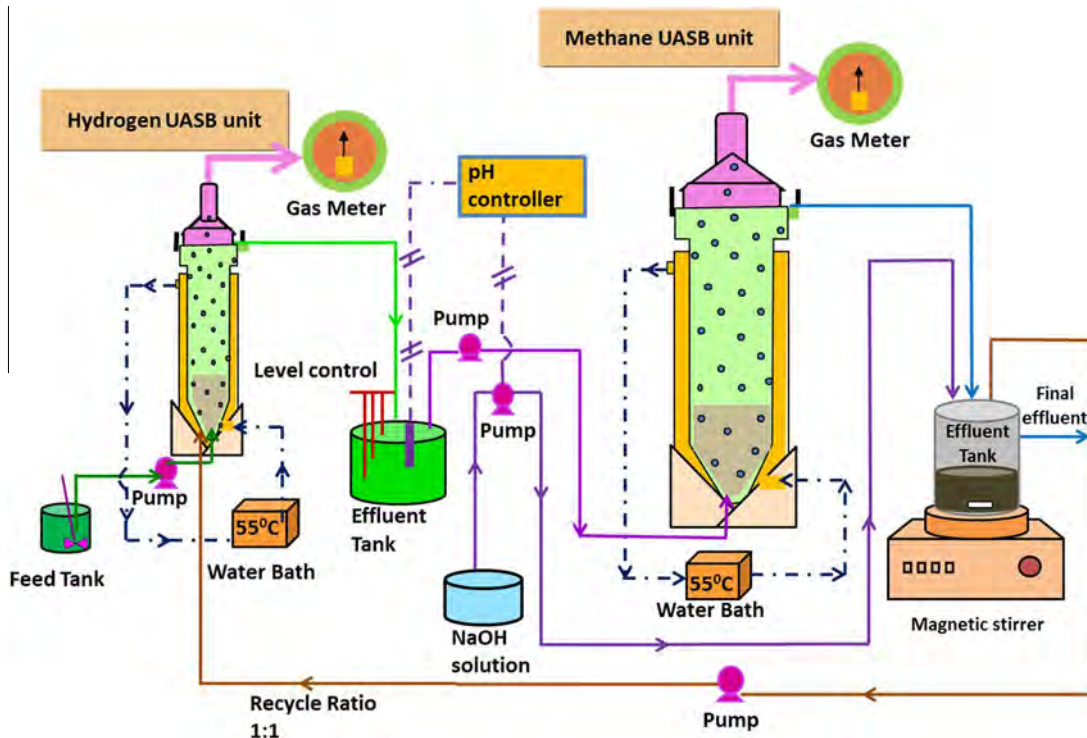
Fig. 1. The schematic of the two-stage upflow anaerobic sludge blanket (UASB) unit.

the feed and effluent samples were determined by the molybdo-vanadate method with acid persulfate digestion (Hach Company) (Intanoo et al., 2012). The effluent samples of both the hydrogen and methane bioreactors were measured for pH and alkalinity. The sodium concentrations in the effluents of both the hydrogen and methane UASB units were measured using an atomic absorption spectrophotometer (AAS; SpectrAA 300, Varian). The average values of all analysis and measurements (<5% SD) were used to access the process performance of the two-stage UASB system.

3. Results and discussion

3.1. Hydrogen production performance results

3.1.1. COD removal and gas production rate

Fig. 2a shows the effects of COD loading rate on COD removal and gas production rate of the hydrogen UASB unit operated at 55 °C and pH 5.5. Since the constant recycle ratio of 1:1 was used to operate the two-stage UASB system, the actual COD loading rate calculated from the COD values of both feed and recycle effluent was also presented for comparison. The COD removal increased with increasing COD loading rate and attained a maximum value of 35% at a COD loading rate of 90 kg/m³ d. Beyond the COD loading rate of 90 kg/m³ d, the COD removal decreased with further increasing COD loading rate. The gas production rate also shows a similar trend to the COD removal. The maximum gas production rate (5.5 l/d) was found at the same COD loading rate of 90 kg/m³ d. The cassava wastewater contains a high organic content in terms of a COD value of 14,500 mg/l. Hence a higher COD loading rate provided a greater organic compound amount available for microbial activity, leading to increase in both COD removal and gas production rate. However, with further increasing COD loading rate from 90 to 150 kg/m³ d, the decreases in both COD removal and gas production rate resulted from the increasing toxicity from organic acid accumulation which will be discussed latter.

3.1.2. Hydrogen production efficiency

The gas composition and hydrogen production rate of the hydrogen UASB unit are shown in Fig. 2b. The produced gas of the hydrogen UASB bioreactor mainly contained hydrogen and carbon dioxide with a small amount of methane. The methane content decreased steadily with increasing COD loading rate, corresponding to a reduction of hydraulic retention time (HRT) from 12 h at a COD loading rate of 30 kg/m³ d to 2.4 h at a COD loading rate of 150 kg/m³ d (Solera et al., 2002). The hydrogen content increased with increasing COD loading rate from 30 to 90 kg/m³ d and then decreased with further increasing COD loading rate from 90 to 150 kg/m³ d. The maximum values of both hydrogen content and hydrogen production rate were 40% and 2.2 l/d, respectively, at the same COD loading rate of 90 kg/m³ d. The first increase in hydrogen production rate with increasing COD loading rate resulted from the increase in organic load available for the microbial activity. However, both decreases in hydrogen production rate and content with further increasing COD loading rate from 90 to 150 kg/m³ d resulted from the increasing toxicity of increasing VFA in the system (Luo et al., 2010). The CO_2 concentration in the produced gas showed an opposite trend to the H_2 concentration.

The specific hydrogen production rate (SHPR) is used to indicate the ability of microbes to produce hydrogen from organics of any particular wastewater per unit volume of reactor or per unit dried weight of microbes, which is very useful for scaling up a bioreactor. Both SHPR values increased with increasing COD loading rate from 30 to 90 kg/m³ d, then decreased with further increasing COD loading rate from 90 to 150 kg/m³ d (Fig. 2c). Both maximum SHPR values found at the same COD loading rate of 90 kg/m³ d were 197.17 ml H_2/g MLVSS d and 530 ml H_2/l d which were consistent with the maximum values of hydrogen production rate, hydrogen content, and COD removal.

In addition, hydrogen yield, used to indicate the efficiency of conversion of organic compounds to hydrogen by microbes in
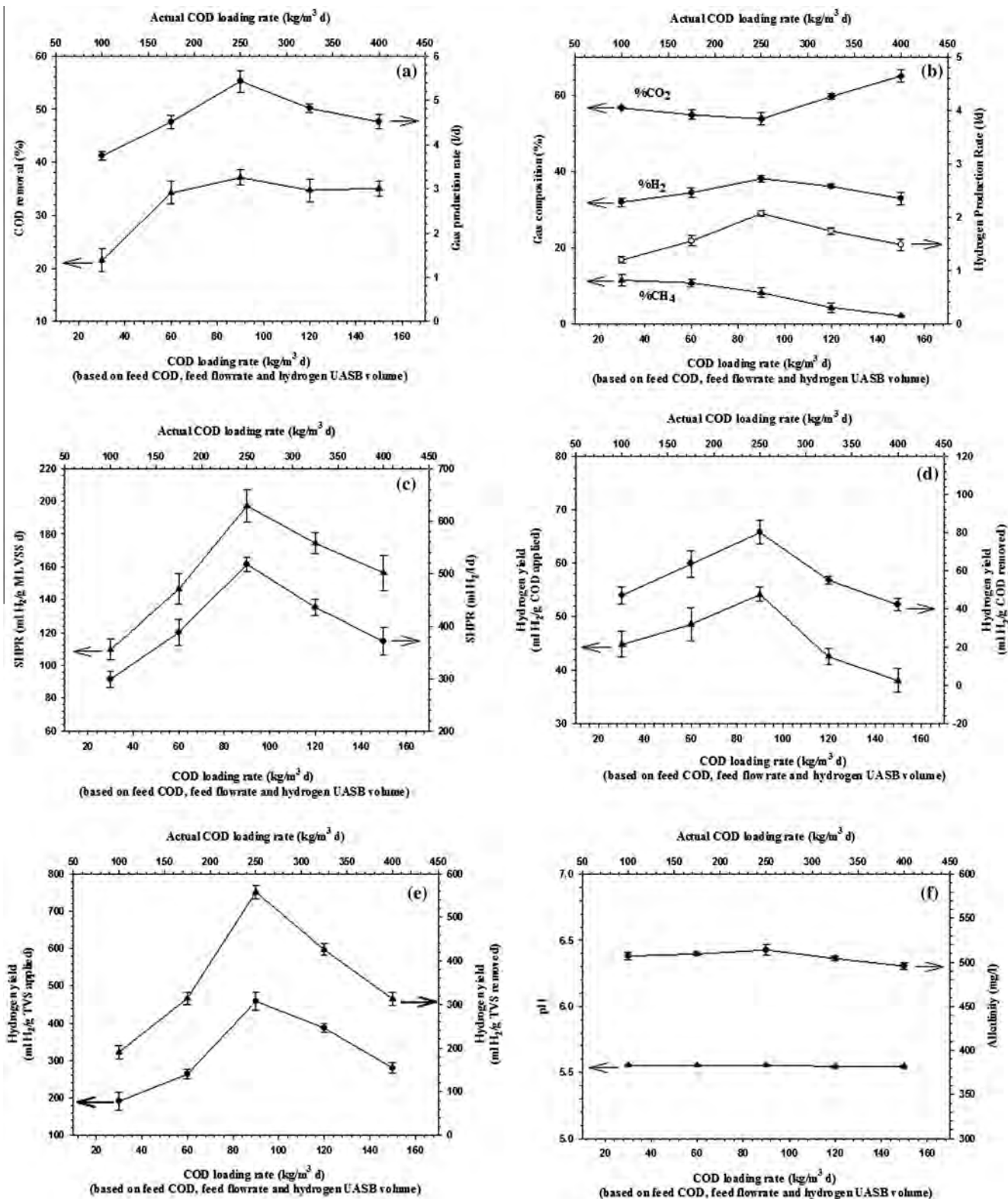
Fig. 2. Effects of COD loading rate on (a) COD removal and gas production rate, (b) gas composition and hydrogen production rate, (c) specific hydrogen production rates, (d) hydrogen yields in the hydrogen UASB unit, (e) hydrogen yields in terms of ml H_2/g TVS applied and (f) pH and alkalinity.

terms of ml H_2/g COD applied or ml H_2/g COD removed was also determined in this study. They showed a similar trend to the SHPR values (Fig. 2c and d). The maximum hydrogen yield of 80.25 ml H_2/g COD removed (or 54.22 ml H_2/g COD applied) was found at the same COD loading rate of 90 kg/m³ d, which corresponded to the highest SHPR and hydrogen production

performance. The higher hydrogen production efficiency resulted from the greater organic load in the system to provide more food for the microorganisms to produce more hydrogen. Again, the SHPR and hydrogen yield sharply decreased when the COD loading rate increased beyond 90 kg/m³ d due to toxicity from the VFA accumulation. In our previous work, using anaerobic sequencing

batch reactor to produce hydrogen from alcohol wastewater under a constant pH of 5.5 at 55 °C without effluent recycle (Intanoo et al., 2012), the maximum hydrogen yield of 130 ml H_2/g COD removed (or 30 ml H_2/g COD applied) was found at a COD loading rate of 68 kg/m³ d. The hydrogen yield values obtained from the present work are comparable to those of the previous work. The hydrogen yield from cassava wastewater under the two-stage thermophilic UASB process of the present study is about 50% higher than that under the two-stage mesophilic UASB process (12.82 ml H_2/g COD removed) (Chaimongkol, 2009).

As shown in Fig. 2f, the alkalinity of the hydrogen UASB unit slightly increases with increasing COD loading rate and reaches a maximum level at a COD loading rate of 90 kg/m³ d. With further increasing COD loading rate from 90 to 150 kg/m³ d, the system alkalinity slightly decreased. The decrease in alkalinity resulted from the increase in VFA in the system. It should be mentioned that the alkalinity range in the hydrogen UASB unit was considerably low because of the low system pH of 5.5.

3.1.3. Volatile fatty acid (VFA) and VFA composition

The effects of COD loading rate on total VFA and VFA composition in the hydrogen UASB unit are shown in Fig. 3. The total VFA

increased markedly with increasing COD loading rate from 30 to 120 kg/m³ d, but it slightly increased with further increasing COD loading rate beyond 120 kg/m³ d. The maximum total VFA concentration (13000 mg/l as acetic acid) was at the highest COD loading rate of 150 kg/m³ d. The high VFA result suggests that the cassava wastewater was easily converted to VFA since it contains mostly starch. As compared the results shown in Figs. 2 and 3, it can be concluded that the toxic level of VFA to hydrogen-producing bacteria was around 8800 mg/l as acetic acid under the studied conditions, which is consistent to our previous work (Intanoo et al., 2012; Poontaweegeratigarn, 2012; Sreethawong et al., 2010; Chaimongkol, 2009; Thungmanee, 2011).

As shown in Fig. 3, the main components of produced VFA are butyric acid (HBu), valeric acid (HVa), acetic acid (HAc), and propionic acid (HPr). All produced organic acids had a similar trend to that of the total VFA concentration except the HPr concentration slightly increased with increasing COD loading rate. In this study, the HBu concentration was the highest while HPr concentration was the lowest, which contributed to the system having high hydrogen production performance (Wang et al., 2009a,b; Hawkes et al., 2002). According to the microbial metabolic pathway, all organic acids are produced in conjunction with the production of
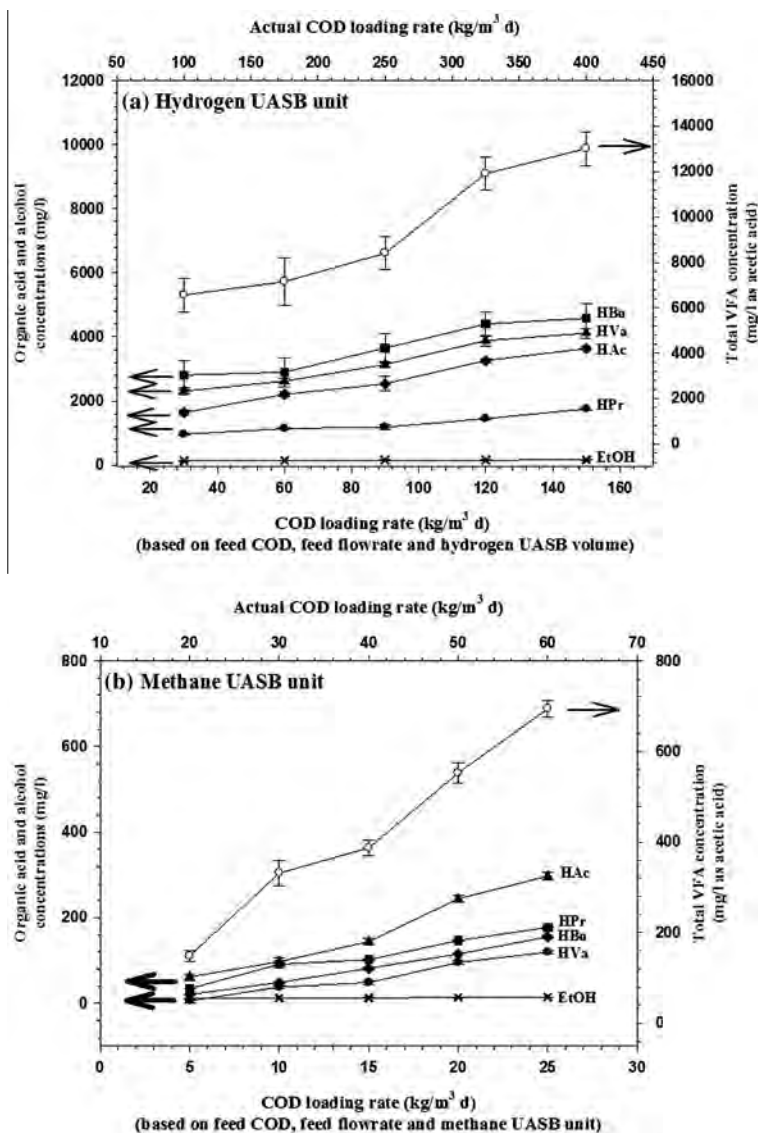

Fig. 3. (a) Total VFA and VFA composition in hydrogen UASB unit and (b) Total VFA and VFA composition in methane UASB unit.

hydrogen while the consumption of hydrogen results in the formation of HPr (Antonopoulou et al., 2011), as shown in the following equation.

$$CH_3COOH + H_2 \rightarrow CH_3CH_2OH + H_2O \qquad (1)$$

Another component that also shows a negative effect to the efficiency of hydrogen production is the formation of ethanol. One mole of ethanol is produced by consuming one mole of hydrogen under anaerobic condition (Thungmanee, 2011). However, in this study, there was a very small amount of ethanol produced and the ethanol concentration remained almost unchanged throughout the COD loading rate range of 30–150 kg/m^3 d. Therefore, the effect of produced ethanol can be negligible for this study.

3.2. Methane production performance results

3.2.1. COD removal and gas production rate

As described before, the liquid effluent from the hydrogen UASB unit was directly fed to the methane UASB unit for further production methane. The methane bioreactor was also operated under thermophilic temperature (55 °C) without pH control. Fig. 4a shows the COD removal at different COD loading rates (based on either the feed COD load and methane UASB volume or the actual incoming COD load and methane UASB volume). The COD removal increased with increasing COD loading rate and reached a maximum value of 72% at a COD loading rate of 15 kg/m^3 d (based on the feed COD load and methane UASB volume). Beyond the optimum COD loading rate of 15 kg/m^{3}d, the COD removal slightly decreased with further increasing COD loading rate. The gas production rate showed a similar trend to the COD removal. Interestingly, the gas production rate of the methane UASB unit was about 4 times higher than that of hydrogen UASB unit, corresponding to the size ratio of both bioreactors.

3.2.2. Methane production efficiency

The produced gas from the methane UASB unit mainly contained methane and carbon dioxide with a very small amount of hydrogen (less than 0.5%) (Fig. 4b). Both methane content and methane production rate increased with increasing COD loading rate from 5 to 15 kg/m^3 d, but decreased with further increasing COD loading rate from 15 to 25 kg/m^3 d (Fig. 4b). In contrast, the CO$_2$ content in the produced gas showed an opposite trend. The maximum methane content and methane production rate of 68% and 16 l/d, respectively, were found at a COD loading rate of 15 kg/m^3 d, corresponding to the optimum COD loading rate of 90 kg/m^3 d (based on the feed COD load and hydrogen UASB volume) for maximum hydrogen production performance.
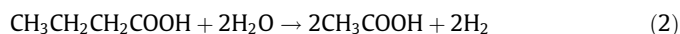
Fig. 4c and d show the specific methane production rates (SMPR) and methane yields, which increased with increasing COD loading rate from 5 to 15 kg/m^3 d, and then decreased with further increasing COD loading rate from 15 to 25 kg/m^3 d. The maximum values of SMPRs (650 ml CH$_4$/l d or 356.31 ml CH$_4$/g MLVSS d) and methane yields (183.31 ml CH$_4$/g COD removed or 98.87 ml CH$_4$/g COD applied) were at a COD loading rate of 15 kg/m^3 d. Hence, the COD loading rate of 15 kg/m^3 d was considered to be an optimum organic loading rate for both production of hydrogen and methane by the two-stage thermophilic UASB system. The maximum methane yield of 840 CH$_4$/g TVS applied found in this study (Fig. 4e) was about 100% higher than that from household solid waste using one-stage process at 37 °C (413 ml CH$_4$/g TVS applied) (Liu et al., 2006; Poontaweegeratigarn, 2012).

The pH and alkalinity of the methane UASB unit increased with increasing COD loading rate and reached a maximum level at a COD loading rate of 15 kg/m^3 d (Fig. 4f). With further increasing COD loading rate from 15 to 25 kg/m^3 d, the system pH and alkalinity sharply decreased. The sharp decreases in pH and alkalinity

resulted from the increase in VFA in the system. The decrease in pH from 6.65 to 6.04 in the methane UASB unit affected the activity of methane-forming bacteria, causing a decrease in methane production performance because of the toxicity from the VFA accumulation (Kvesitadze et al., 2012; Chandra et al., 2012), as indicated latter.

3.2.3. Volatile fatty acid (VFA) and VFA composition

Fig. 3b shows the effect of COD loading rate on total VFA and VFA composition in the methane UASB unit. The total VFA increased steadily with an increase in COD loading rate. The maximum total VFA of 780 mg/l as acetic acid was at the highest COD loading rate of 25 kg/m^3 d. Based on the results of COD removal, gas production rate and total VFA, the toxic level of VFA to the methane-producing bacteria is around 350 mg/l under the studied conditions which is in good agreement with previous work (Sarada and Joseph, 1996). Similar to the organic acids produced in the hydrogen UASB unit, the methane UASB unit also only generated HAc, HPr, HBu and HVa and all produced organic acids also increased gradually when the COD loading rate increased. At any given COD loading rate, the concentration of HAc was the highest followed by HPr, HBu, and HVa, respectively. The highest HAc concentration resulted from the further degradation of both HPr and HBu, according to Eqs. (2) and (3) (Abbasi et al., 2012). The production of methane mainly resulted from the two basic bioconversion reactions of hydrogenotrophic and acetotrophic pathways, as shown in Eqs. (4) and (5) (Abbasi et al., 2012; FAO Corporate, 1997).

$$CH_3CH_2CH_2COOH + 2H_2O \rightarrow 2CH_3COOH + 2H_2 \qquad (2)$$

$$CH_3CH_2COOH + 2H_2O \rightarrow CH_3COOH + CO_2 + 3H_2 \qquad (3)$$

$$CO_2 + 4H_2 \rightarrow CH_4 + 2H_2O \qquad (4)$$

$$CH_3COOH \rightarrow CH_4 + CO_2 \qquad (5)$$

3.2.4. Microbial concentration and microbial washout

As shown in Fig. 5, the MLVSS (representing the microbial concentration) in each UASB bioreactor decreases with increasing COD loading rate, whereas the microbial washout (effluent VSS) from each UASB unit shows an opposite trend. The results of both steady increases in hydrogen and methane production efficiency, with decreasing microbial concentration in the studied COD loading rate range of 5–15 kg/m^3 d (based on the feed COD load and methane UASB volume), suggest that an increase in COD loading rate increases the organic load available for microbial activities to produce more both gases. There was an increase in microbial washout from both UASB bioreactors with increasing COD loading rate. This probably indicates that the only inactive microbes were washed out. However, the results showing the decreases in both production performance of hydrogen and methane with further increasing COD loading rate from 90 to 150 kg/m^3 d based on the feed COD load and hydrogen UASB volume or 15 to 25 kg/m^3 d based on the feed COD load and methane UASB volume can be explained by the fact that the increasing organic acid concentration greater than 8800 and 350 mg/l increased the toxicity to the microbes in the hydrogen UASB unit and the methane UASB unit, respectively, causing increasing washout of active microbes from both UASB bioreactors. As a consequence, microbial activities in both hydrogen and methane productions of both UASB units decreased with further increasing COD loading rate.

In this study, sodium hydroxide (NaOH) used to adjust pH in the hydrogen UASB unit could affect the microbial activity in both UASB bioreactors, depending on its concentration (Rinzema et al., 1988). A low concentration of sodium (230–350 mg/l) serves as
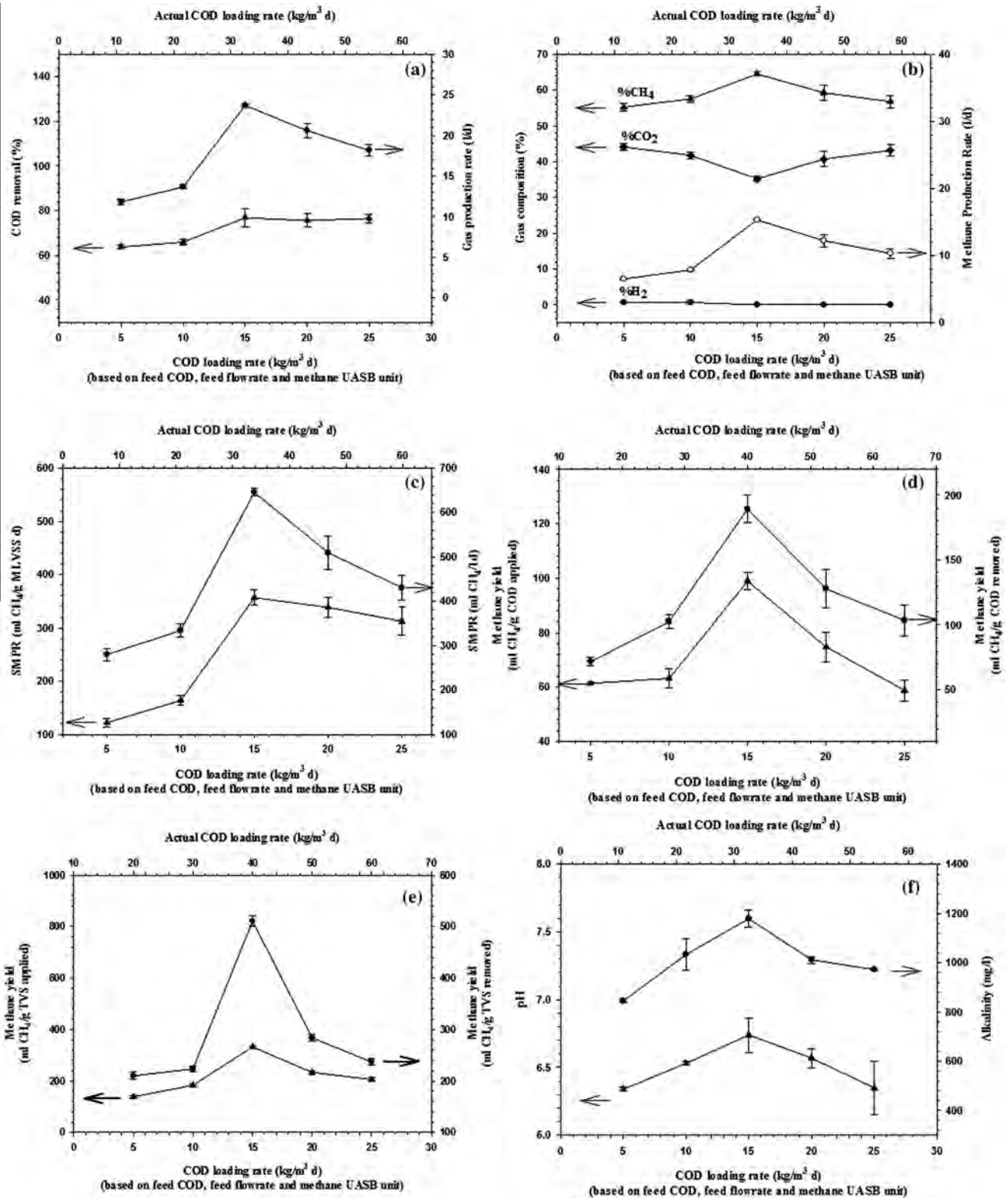
Fig. 4. Effects of COD loading rate on (a) COD removal and gas production rate, (b) gas composition and methane production rate, (c) specific methane production rates, (d) methane yields in the methane UASB unit, (e) methane yields in terms of ml CH_4/g TVS applied and (f) pH and alkalinity.

an essential element to stimulate the activity of methanogenic bacteria (Rinzema et al., 1988). However, a high content of sodium greater than 16,000 mg/l, exhibits toxicity to anaerobic microbes (Chen et al., 2003). In this study, the sodium content in both UASB units was in the 150–220 mg/l range, which is much lower than

the sodium toxic level to the anaerobic microbes. This low sodium level in the two-stage UASB system resulted from the effluent recycle operation.

The sodium concentrations of feed (138 mg/l) and the final effluent (150–220 mg/l) were not significantly different, indicating
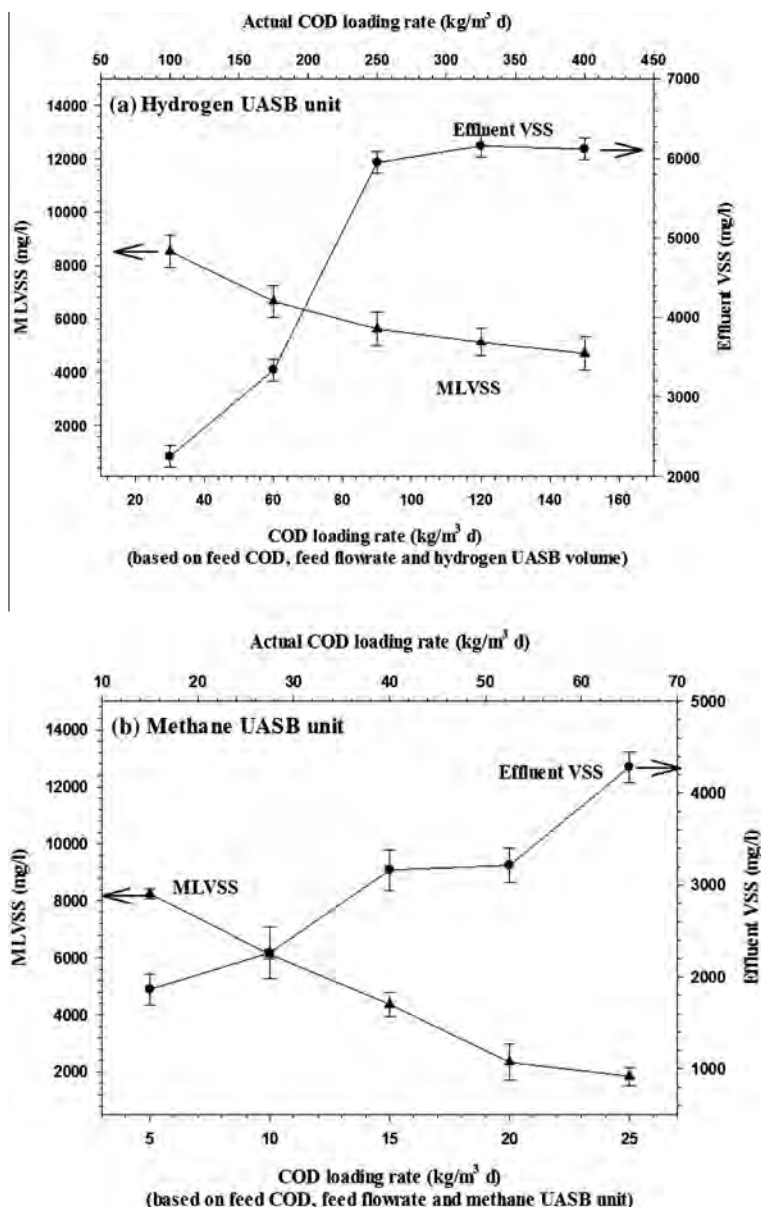
Fig. 5. MLVSS and effluent VSS (a) of the hydrogen UASB unit, (b) of the methane UASB unit.

that effluent recycling could reduce the NaOH consumption for pH adjustment in the hydrogen UASB unit.

3.2.5. Nitrogen and phosphorous uptakes and transformation

Fig. 6 shows the nitrogen and phosphorous uptakes and nitrogen compound transformation in both steps of acidogenesis and methanogenesis. Both of nitrogen and phosphorous uptakes for the acidogenic and methanogenic steps increased with increasing COD loading rate. The higher the COD loading rate, the higher the nutrient uptakes. For any given COD loading rate, both N and P uptakes in the hydrogen UASB unit were significantly higher than those in the methane UASB unit. The utilization of nitrogen by microbes can come from different nitrogen sources: ammonium-nitrogen, nitrate-nitrogen, nitrite-nitrogen, and organic-nitrogen (Hendriks and Zeeman, 2009). The concentrations of ammonium-nitrogen, and nitrate-nitrogen from both steps decreased slightly with increasing COD loading rate, whereas the organic-nitrogen concentration decreased drastically, suggesting that the nitrogen uptakes of both steps mostly came from organic-nitrogen

compounds (Luo et al., 2010). At the optimum COD loading rate for both UASB units, the ratio of COD removal:N uptake:P uptake in the methane UASB unit was found to be 100:2.59:1.96, which is slightly higher than that in hydrogen UASB unit (100:2.20:1.31). Both N and P uptakes were much higher than the theoretical nutrient requirement for anaerobic decomposition for methane production in mesophilic temperature (COD:N:P = 100:1.0:0.2). This is because the system was operated under thermophilic temperature, which requires higher nutrients (Intanoo et al., 2012; Sreethawong et al., 2010).

3.2.6. Overall performance

Table 1 compares the process performance in terms of hydrogen and methane production of the present study with some previous results. This two-stage UASB process operated at the optimum COD loading rate of 12 kg/m³ d (based on the total volume of both UASB units and feed COD load) provided the hydrogen yield in terms of 130 ml H_2/g TVS applied and the methane yields of 988 ml CH_4/g TVS applied (Table 1), which were significantly higher than those
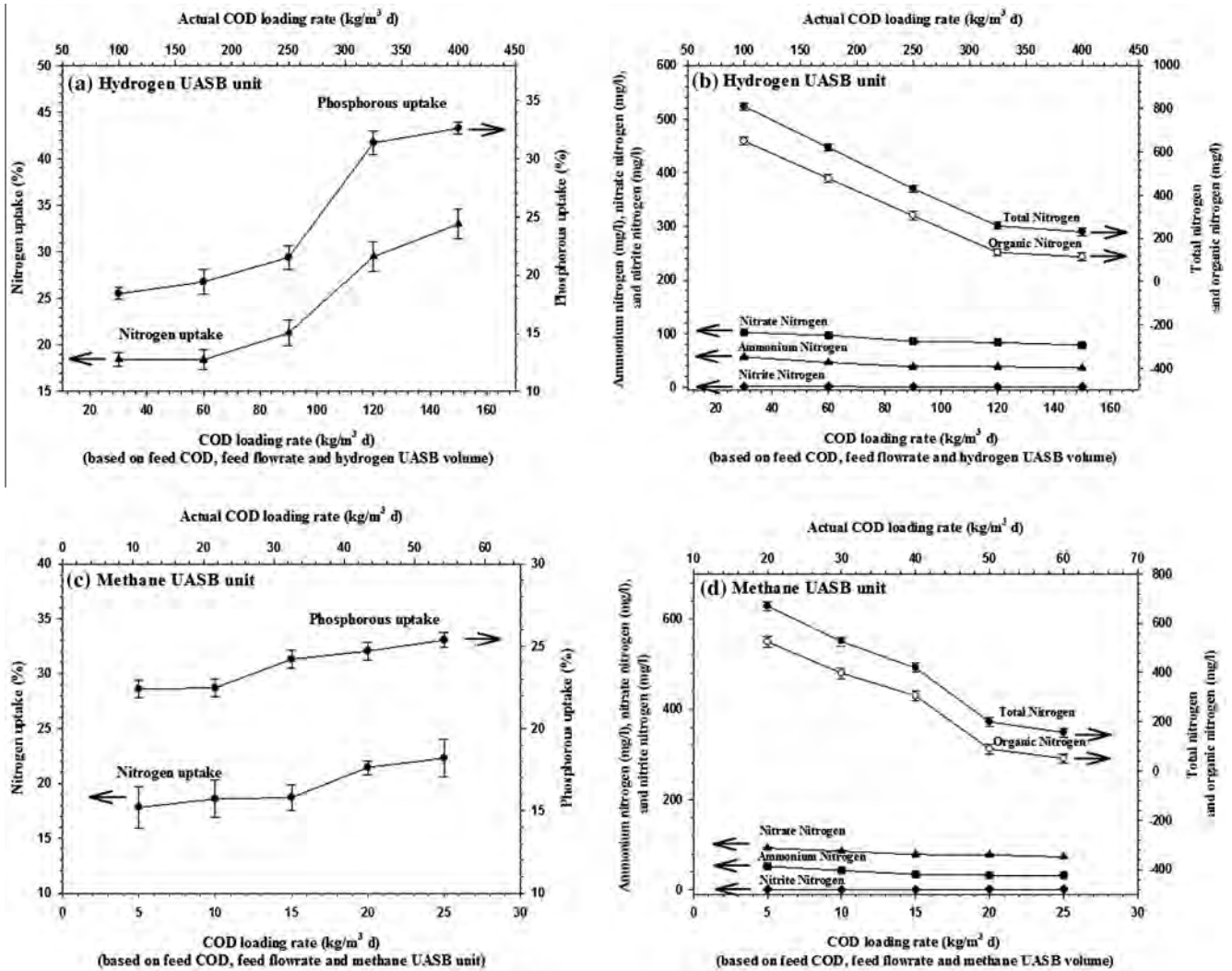
Fig. 6. Effects of COD loading rate on (a) nitrogen and phosphorous uptakes of the hydrogen UASB unit, (b) total nitrogen, organic nitrogen and inorganic nitrogen concentrations in the hydrogen UASB unit, (c) nitrogen and phosphorous uptakes of the methane UASB unit and (d) total nitrogen, organic nitrogen, and inorganic nitrogen concentrations in the methane UASB unit.

Table 1
Comparison of overall performance of the two-stage used in this study to some other studies.

	Two-stage UASB process, present study	Two-stage CSTR process Luo et al. (2010)	CSTR process Wang et al. (2012)	Two-stage CSTR process Zhu et al. (2008)
Type of wastewater	Cassava wastewater	Cassava stillage	Cassava ethanol wastewater	Potato waste
Temperature (°C)	55	55	60	35
Optimum COD loading rate (kg/m^3 d)	12	10	30	41
COD removal (%)	86.4	58	62.2	64
Specific hydrogen production rate (l/l d)	0.078	–	–	0.092
Specific methane production rate (l/l d)	0.56	–	–	0.56
Hydrogen yields				
ml H$_2$/g COD removed	169			
ml H$_2$/g TVS removed	169	56.6	–	–
ml H$_2$/g TVS applied	130	–	37.1	–
Methane yields				
ml CH$_4$/g COD removed	921	–	–	–
ml CH$_4$/g TVS removed	1,280	249	–	183
ml CH$_4$/g TVS applied	988	–	365	–
H$_2$/CH$_4$ ratio	1:7.6	1:4.4	1:9.8	1:6.1

of two-phase thermophilic CSTR process at an organic loading rate of 10 g VS/l d (hydrogen yield of 56.6 ml H$_2$/g VS applied and methane yield of 249 ml H$_2$/g VS applied) (Luo et al., 2010). The H$_2$/CH$_4$ ratio (1:7.6) of the mixed gas produced from this study was lower

than that of the two-phase thermophilic CSTR process (1:4.4) (Luo et al., 2010); because the continuously stirred tank reactor (CSTR) was operated at much lower rate, leading to the dominance of methanogenesis (Abbasi et al., 2012; Kim et al., 2013). The mixed

gas produced from both UASB units used in this study, known as hythane, contained 7.11% H_2, 54.13% CH_4 and 38.75% CO_2 at the optimum COD loading rate. The calculated values of higher heating value (HHV) and the lower heating value (LHV) of the mixed gas (hythane) are 23.62 and 21.14 MJ/m^3, respectively (Green and Perry, 2008). The biogas produced from a single-stage UASB unit typically contains 70% CH_4 and 30% CO_2 without H_2. The HHV and LHV of the biogas are 22.70 and 20.43 MJ/m^3, respectively. Hence, it can be concluded that the use of two-stage anaerobic process provide a higher heating value of produced mixed gas as compared to that obtained from a single-stage anaerobic process.

4. Conclusions

In this study, separate production of hydrogen and methane from cassava wastewater using a two-stage upflow anaerobic sludge blanket reactor (UASB) process under thermophilic temperature (55 °C) was optimized by recycling the methane UASB effluent to the hydrogen UASB unit at a constant recycle ratio of 1:1 and by controlling the hydrogen UASB unit at pH 5.5. The highest hydrogen production performance in terms of the highest hydrogen content (40%), yield (54.22 ml H_2/g COD applied) and SHPR (197.17 ml H_2/g MLVSS d) and COD removal (35%) was achieved at a COD loading rate of 90 kg/m^3 d (based on the feed COD load and hydrogen UASB volume) corresponding to the optimum COD loading rate of 15 kg/m^3 d (based on the feed COD load and methane UASB volume) which also provided maximum process performance of the methane UASB (in terms of the highest methane content of 68%, methane yield of 164.87 ml CH_4/g COD applied, and SMPR of 356.31 ml CH_4/g MLVSS d, and COD removal of 72%.

Acknowledgements

References

Abbasi, T., Tauseef, S.M., Abbasi, S.A., 2012. Anaerobic digestion for global warming control and energy generation—an overview. Renew. Sust. Energy Rev. 16, 3228–3242.

Antonopoulou, G., Gavala, H.N., Skiadas, I.V., Lyberatos, G., 2011. Effect of substrate concentration on fermentative hydrogen production from sweet sorghum extract. Int. J. Hydrogen Energy 36, 4843–4851.

Biofuels, Waste Energy, Anaerobic Digestion of Biomass. URL <http://www.alternative-energy-news.info/anaerobic-digestion-biomass/>, 2008.

Chaimongkol, P., 2009. Two-stage anaerobic fermentation for hydrogen and methane production from cassava wastewater using upflow anaerobic sludge blanket reactors (M.S. thesis). The Petroleum and Petrochemical College, Chulalongkorn University.

Chandra, R., Takeuch, I.H., Hasegawa, T., 2012. Methane production from lignocellulosic agricultural crop waste: a review in content to second generation of biofuel production. Renew. Sust. Energy Rev. 16, 1462–1476.

Chen, W.H., Han, S.K., Sung, S., 2003. Sodium inhibition of thermophilic methanogens. J. Environ. Eng. 129, 506–512.

Cheng, X.Y., Li, Q., Liu, C.Z., 2012. Coproduction of hydrogen and methane via anaerobic fermentation of cornstalk waste in continuous stirred tank reactor integrated with up-flow anaerobic sludge bed. Bioresour. Technol. 114, 327–333.

Eaton, A.D., Clesceri, L.S., Rice, E.W, Greenberg, A.E., 2005. Standard Methods for the Examination of Water and Wastewater, American Public Health Association (APHA), American Water Works Association (AWWA) & Water Environment Federation (WEF), Washington, DC.

Food and Agriculture Organization of the United Nation (FAO Corporate), Renewable biological systems for alternative sustainable energy production, URL: <http://www.fao.org/docrep/w7241e/w7241e0f.htm#4.1.2 acetogenesis and Dehydrogenation>, 1997.

Green, D.W., Perry, R.H., 2008. Perry Chemical Engineers' Handbook, 8th ed. The McGraw-Hill Companies, The United States.

Hawkes, F.R., Dinsdale, R., Hawkes, D.L., Hussy, I., 2002. Sustainable fermentative hydrogen production: challenges for process optimization. Int. J. Hydrogen Energy 27, 1339–1347.

Hendriks, A.T.W.M., Zeeman, G., 2009. Pretreatments to enhance the digestibility of lignocellulosic biomass. Bioresour. Technol. 100, 10–18.

Intanoo, P., Rangsunvigit, P., Namprohm, W., Thamprajamchit, B., Chavadej, J., Chavadej, S., 2012. Hydrogen production from alcohol wastewater by an anaerobic sequencing batch reactor under thermophilic operation: nitrogen and phosphorous uptakes and transformation. Int. J. Hydrogen Energy 37, 11104–11112.

Kim, M.S., Cha, J., Kim, D.H., 2013. Fermentative Biohydrogen Production from Solid Wastes, Clean Fuel Center, Korea Institute of Energy Research, Daejeon 305–343, Republic of Korea.

Kvesitadze, G., Sadunishvili, T., Dudauri, T., Zakariashvili, N., Partskhaladze, G., Ugrekhelidze, V., Tsiklauri, G., Metreveli, B., Jobava, M., 2012. Two-stage anaerobic process for bio-hydrogen and bio-methane combined production from biodegradable solid wastes. Energy 37, 94–102.

Liu, D., Liu, D., Zeng, R.J., Angelidaki, I., 2006. Hydrogen and methane production from household solid waste in the two-stage fermentation process. Water Res. 40, 2230–2236.

Luo, G., Xie, L., Zou, Z., Wang, W., Zhou, Q., Shim, H., 2010. Anaerobic treatment of cassava stillage for hydrogen and methane production in continuously stirred tank reactor (CSTR) under high organic loading rate (OLR). Int. J. Hydrogen Energy 35, 11733–11737.

Nathao, C., Sirisukpok, A.U., Pisutpaisal, N., 2013. Production of hydrogen and methane by one and two stage fermentation of food waste. Int. J. Hydrogen Energy 38, 15764–15769.

Poontaweegeratigarn, T., 2012. Hydrogen and methane production from alcohol wastewater by upflow anaerobic sludge blanket reactors (M.S. thesis). The Petroleum and Petrochemical College, Chulalongkorn University.

Rinzema, A., Lier, J., Lettinga, G., 1988. Sodium inhibition of acetoclastic methanogens in granular sludge from a UASB reactor. Enzyme Microb. Technol. 10, 24–32.

Sarada, R., Joseph, R., 1996. A comparative study of single and two stage processes for methane production from tomato processing waste. Process Biochem. 31, 337–340.

Sirirote, P., Thanaboripat, D., Klinkroon, N., Tripak, S., 2010. The production of biogas from cassava tubers. KMITL Sci. Tech. J. 10, 30–36.

Solera, R., Romero, L.I., Sales, D., 2002. The evolution of biomass in a two-phase anaerobic treatment process during start-up. Chem. Biochem. Eng. Q. 16, 25–29.

Sreethawong, T., Chatsiriwatana, S., Rangsunvigit, P., Chavadej, S., 2010. Hydrogen production from cassava wastewater using an anaerobic sequencing batch reactor: effects of operational parameters, COD:N ratio, and organic acid composition. Int. J. Hydrogen Energy 35, 4092–4102.

Thungmanee, A., 2011. Hydrogen production from alcohol distillery wastewater using a anaerobic sequencing batch reactor under thermophilic condition (M.S. thesis). The Petroleum and Petrochemical College, Chulalongkorn University.

Wang, W., Xie, L., Luo, G., Zhou, Q., Lu, Q., 2012. Optimization of biohydrogen and methane recovery within a cassava ethanol wastewater/waste integrated management system. Bioresour. Technol. 120, 165–172.

Wang, Y., Zhang, Y., Meng, L., Wang, J., Zhang, W., 2009a. Hydrogen–methane production from swine manure: effect of pretreatment and VFAs accumulation on gas yield. Biomass Bioenergy 33, 1131–1138.

Wang, Y., Zhang, Y., Wang, J., Meng, L., 2009b. Effects of volatile fatty acid concentrations on methane yield and methanogenic bacteria. Biomass Bioenergy 33, 848–853.

Wikimedia Foundation, Anaerobic Digestion. URL: <http://en.wikipedia.org/wiki/Anaerobic_digestion>, 2014.

Xia, Y., Zhang, T., Fang, H.H.P., 2011. Thermophilic anaerobic degradation of microcrystalline cellulose using mixed culture enriched from anaerobic digestion sludge. Procedia Environ. Sci. 12, 3–8.

Zhu, H., Stadnyk, A., Beland, M., Seto, P., 2008. Co-production of hydrogen and methane from potato waste using a two-stage anaerobic digestion process. Bioresour. Technol. 99, 5078–5084.

Zhu, H., Parker, W., Conidi, D., Basnar, R., Seto, P., 2011. Eliminating methanogenic activity in hydrogen reactor to improve biogas production in a two-stage anaerobic digestion process co-digesting municipal food waste and sewage sludge. Bioresour. Technol. 201, 7086–7092.

Micro-kinetic modeling of the catalytic dehydration of 1-decanol over precipitated γ-Al₂O₃

Snunkheam Echaroj, Malee Santikunaporn & Sumaeth Chavadej

Springer

Springer

Micro-kinetic modeling of the catalytic dehydration of 1-decanol over precipitated γ-Al$_2$O$_3$

Snunkheam Echaroj · Malee Santikunaporn · Sumaeth Chavadej

Abstract The mechanisms of the dehydration reaction of 1-decanol to 1-decene over precipitated gamma-alumina (γ-Al$_2$O$_3$) by means of the micro-kinetic modeling approach were investigated. Experimental data were collected in the reaction temperature range of 533–608 K, while the retention time was varied from 0.029 to 0.15 h. The γ-Al$_2$O$_3$ catalyst was synthesized using a traditional precipitation method. The yield of both internal olefins and 1-decene increased with increasing reaction temperature. Conversely, the yield of di-*n*-decyl ether decreased with increasing temperature. An increase in retention time increased the yield of 1-decene and internal olefins. These experimental data correlated well with the rate equation that assumes the formation of 1-decene to be reversible and a dual-site reaction. It is reasonable to state that internal isomerization is reversible with a single-site reaction. The apparent activation energy for the dehydration reaction of 1-decanol to 1-decene, obtained from the Arrhenius plot data, was 102 ± 2 kJ/mol.

Keywords Dehydration · 1-Decanol · 1-Decene · Internal isomerization · Precipitation · Gamma-alumina

List of symbols

K_{DeOH}	Equilibrium constant for the adsorption of 1- decanol
K_{D_1}	Equilibrium constant for the adsorption of 1-decene
K_{D_2}	Equilibrium constant for the adsorption of internal olefins
K_{DDE}	Equilibrium constant for the adsorption of di-*n*-decyl ether

S. Echaroj · M. Santikunaporn (✉)
Department of Chemical Engineering, Faculty of Engineering, Thammasat University, Pathumthani 12120, Thailand
e-mail: smalee@engr.tu.ac.th

S. Chavadej
Petrochemical College, Chulalongkorn University, Bangkok 10330, Thailand

P_i	Partial pressure of species i
θ_V	Fractional coverage of vacant sites
θ_i	Fractional coverage of species i
S	Vacant sites
W	Water molecule (H_2O)
k_{s,D_1}^+	Rate constant for the forward dehydration reaction to 1-decene
k_{s,D_1}^-	Rate constant for the backward dehydration reaction to 1-decanol
k_{s,D_2}^+	Rate constant for the forward isomerization reaction to internal olefins
k_{s,D_2}^-	Rate constant for the backward isomerization reaction to 1-decene

Introduction

Catalytic dehydration of alcohol, used especially to produce olefins, has been studied intensively due to the demand for olefins in the petrochemical industry. At present, naphtha distilled from crude oil is converted to olefins through the steam thermal cracking reaction, which is operated at approximately 1,073 K [1] and consumes approximately 20 MJ/kg of ethylene produced [2]. Compared to the conventional steam thermal cracking process, the dehydration reaction is operated at a lower temperature, leading to a lower production cost of olefins. Moreover, both short- and long-chain alcohols can be obtained from renewable resources such as sugar cane [3] and palm oil [4]. These alcohols are promising renewable feedstocks that can be used for olefin production through the dehydration reaction. Therefore, it is anticipated that short-chain alcohols can be converted to olefins, thus serving as building blocks for the plastics industry [5]. Long-chain alcohols can be converted to 1-decene, which is an important starting material for the production of premium grade synthetic lubricant oils [6].

The dehydration of alcohol is an elimination reaction (E1). It is initiated by the protonation of the hydroxyl group and the loss of water molecules, as shown in Fig. 1, which cause the formation of a carbonium ion intermediate.

Several studies have reported the effects of operating conditions and catalyst type on the dehydration reaction of short-chain alcohols, such as methanol, ethanol, and butanol. These studies have indicated that at high temperatures, the dehydration reaction yields mostly olefins, whereas at low temperatures ether is dominantly formed [7–10]. Apart from observing the effects of operating conditions, various solid acidic catalysts such as silica-alumina [11], NaY [12] and H-ZSM5 [13], as well as gamma-alumina (γ-Al_2O_3) based catalysts, have been intensively studied for the dehydration reaction. For the dehydration of short-chain alcohols, these catalysts have given both reasonably high conversion of alcohol and selectivity for alkene. Chen et al. [14] have reported that γ-Al_2O_3 doped with TiO_2 has the potential to become an industrial catalyst used for the production of ethylene from bioethanol.

Analysis of the dehydration reaction mechanism, through kinetic modeling, is a necessary step used to simulate the production of olefins on an industrial scale.
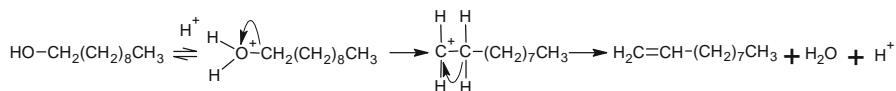
Fig. 1 The mechanism of 1-decanol dehydration to form 1-decene by elimination of the hydroxyl group over heterogeneous acid catalyst [7]

There are two major types of kinetic modeling. The first type is usually referred to as the lumped model, and the second type is called the micro-kinetic model [15]. The micro-kinetic model is usually more accurate because it includes the three main phenomenon of adsorption, surface reaction, and desorption, which are included in the formulation of modeling [16]. On the contrary, the lumped model considers the surface reaction only. Kaymanova et al. [17] simulated the dehydration of bioethanol using the lumped model—for approximately 60,000 t of ethylene produced per year—using an industrial fixed bed reactor operated in the temperature range of 643–723 K. Dumesic et al. [11] used the micro-kinetic model to confirm that the amount of vacant sites on the catalyst increased with an increase in the inert gas flow rate for the gaseous dehydration of 1-butanol.

Most of the earlier studies on the dehydration reaction were performed on short-chain alcohols using only equilibrium constants while the internal isomerization reaction was neglected. Therefore, these models cannot be employed for predicting the behaviors of the dehydration of long-chain alcohols. Arno de Klerk et al. attempted to study the dehydration of long-chain alcohols. However, this work does not report the formation of internal olefins and the kinetics of alkene formation on heterogeneous catalyst. Most importantly, their result on 1-decanol was anomalous [18]. Katritzky et al. [19] reported that the internal isomerization of olefins became more favorable as temperature increased. According to the reaction pathway, as illustrated in Fig. 2, the dehydration of 1-decanol (DeOH) gives 1-decene (D_1) and di-n-decyl ether (DDE). The internal isomerization takes place simultaneously to convert 1-decene (D_1) to internal olefins (D_2).

The main purpose of this research was to acquire more insight into the dehydration of long-chain 1-decanol over synthesized γ-Al$_2$O$_3$. Alumina was chosen because it belongs to a group of mesoporous catalysts with large pore size to allow an efficient internal diffusion of 1-decanol. Additionally, alumina is inexpensive, easy to prepare and thermally stable, and qualified as an industrial catalyst [20]. A series of dehydration experiments was systematically carried out and micro-kinetic models were formulated based on both dehydration and internal isomerization reactions. The γ-Al$_2$O$_3$ used was synthesized by a precipitation method using an aluminum precursor. The kinetic constants obtained from this research will be very useful to simulate the production of 1-decene on an industrial level.

Kinetic model formulation

In this study, the Langmuir–Hinshelwood (L–H) approach was initially used to establish the rate equations. The surface reaction was assumed to be the rate
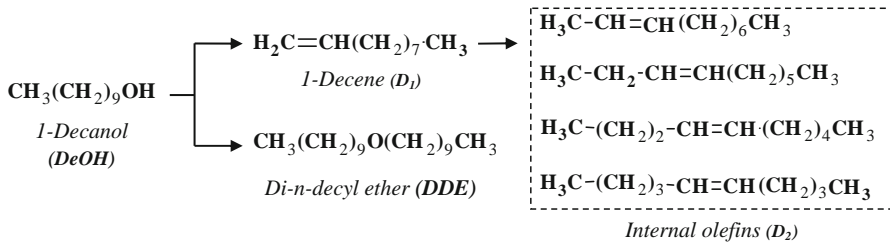
$CH_3(CH_2)_9OH$

1-Decanol
(DeOH)

→ $H_2C=CH(CH_2)_7\cdot CH_3$ →

1-Decene (D_1)

→ $CH_3(CH_2)_9O(CH_2)_9CH_3$

Di-n-decyl ether (DDE)

$H_3C\text{-}CH=CH(CH_2)_6CH_3$

$H_3C\text{-}CH_2\text{-}CH=CH(CH_2)_5CH_3$

$H_3C\text{-}(CH_2)_2\text{-}CH=CH\cdot(CH_2)_4CH_3$

$H_3C\text{-}(CH_2)_3\text{-}CH=CH(CH_2)_3CH_3$

Internal olefins (D_2)

Fig. 2 Reaction network for the dehydration of 1-decanol and internal isomerization of 1-decene

determining step (RDS) [21]. To construct an accurate micro-kinetic model, the first step was to make all reasonable assumptions for the proposed reactions. A series of rate equations were then formulated based on those underlying assumptions. Then, all unknown kinetic and equilibrium constants were determined by fitting the rate of the reactions calculated from the derived rate equations with the experimental data using a computer regression program. There were usually several possible mechanisms considered to find out which alternative was most likely to occur within the catalytic system.

Marchi et al. [22] used the mentioned steps above for the model formulation and concluded that the formation of olefin proceeded through dual-site surface reactions, where adsorbed reactant interacted with the neighboring vacant sites to form an olefin product and water. Meanwhile, ether was formed through the Eley–Rideal mechanism, which is when the adsorbed reactant interacts with the reactant in the gaseous phase. For the micro-kinetic modeling performed in this paper, it was assumed that 1-decene is formed through the dual-site mechanism, while DDE was formed through the Eley–Rideal mechanism. Internal isomerization proceeded through the reversible single site surface reaction. There were two alternative assumptions for the formation of 1-decene. The first assumption, as shown in Eq. 2, anticipated that the reaction was irreversible. The second assumption, Eq. 3, anticipated that the reaction was reversible. These two equations were also the RDS for the reaction sequence. The objective of this research was to find out which assumptions could produce the most suitable model for the dehydration of 1-decenol reaction. The L–H reaction sequence is depicted by Eqs. 1–7.

$$DeOH + S \rightleftharpoons DeOH \cdot S, \quad \theta_{DeOH} = K_{DeOH}P_{D_1}\theta_V \tag{1}$$

$$DeOH \cdot S + S \xrightarrow{k^+_{s,D_1}} D_1 \cdot S + S + W, \quad r_{s,D_1} = k^+_{s,D_1}\theta_{DeOH}\theta_V \tag{2}$$

$$DeOH \cdot S + S \underset{k^-_{s,D_1}}{\overset{k^+_{s,D_1}}{\rightleftharpoons}} D_1 \cdot S + S + W, \quad r_{s,D_1} = k^+_{s,D_1}\theta_{DeOH}\theta_V - k^-_{s,D_1}\theta_{D_2}\theta_V \tag{3}$$

$$D_1 \cdot S \underset{k^-_{s,D_2}}{\overset{k^+_{s,D_2}}{\rightleftharpoons}} D_2 \cdot S, \quad \theta_{D_2} = \frac{k^+_{s,D_2}\theta_{D_1}}{k^-_{s,D_2}} \tag{4}$$

$$DDE \cdot S \rightleftharpoons DDE + S, \quad \theta_{DDE} = K_{DDE}P_{DDE}\theta_V \tag{5}$$

Table 1 L–H kinetic models tested with experimental data obtained from the research

Model	
I	$r_{s,D_1} = \dfrac{k_{S,D_1} P_{DeOH}}{K_1(1+K_{EQ})^2}$
II	$r_{s,D_1} = k^+_{s,D_1}\left(\dfrac{P_{DeOH}}{K_1(1+K_{EQ})^2} - \dfrac{P_{D_1}}{K_2 K_{D_1}(1+K_{EQ})^2}\right)$
IIA	$r_{s,D_1} = k^+_{s,D_1}\left(\dfrac{P_{DeOH}}{K_1(1+K_{DeOH}P_{DeOH}+K_{D_1}P_{D_1}(K_3+1))^2} - \dfrac{P_{D_1}}{K_2 K_{D_1}(1+K_{DeOH}P_{DeOH}+K_{D_1}P_{D_1}(K_3+1))^2}\right)$
IIB	$r_{s,D_1} = k^+_{s,D_1}\left(\dfrac{P_{DeOH}}{K_1(1+K_{DeOH}P_{DeOH}+K_{D_1}P_{D_1})^2} - \dfrac{P_{D_1}}{K_2 K_{D_1}(1+K_{DeOH}P_{DeOH}+K_{D_1}P_{D_1})^2}\right)$

$$D_1 \cdot S \rightleftharpoons D_1 + S, \quad \theta_{D_1} = K_{D_1} P_{D_1} \theta_V \tag{6}$$

$$D_2 \cdot S \rightleftharpoons D_2 + S, \quad \theta_{D_2} = K_{D_2} P_{D_2} \theta_V \tag{7}$$

When the fractional coverage of all species on the catalyst were added together, they were equated to one, as shown in Eq. 8. The equation for the vacant site was derived and then it was plugged into the rate expression (Eqs. 2 and 3), the resulting formation of 1-decene rate equation for models 1 and 2, and is shown on Table 1. The first model was derived from the notion that the formation of 1-decene was irreversible, while the second model was based on the idea that the reaction is reversible. Simplification of the rate equation was completed by using K_2 as the ratio between the forward and reverse rate of the 1-decene formation reaction and K_3 as the ratio between the forward and reverse rate of internal olefins formation.

$$1 = \theta_v + \theta_{DeOH} + \theta_{D_1} + \theta_{D_2} + \theta_{DDE} \tag{8}$$

$$\theta_v = \frac{1}{1 + K_{DeOH}P_{DeOH} + K_{D_1}P_{D_1}(K_3+1) + K_{DDE}P_{DDE}} = \frac{1}{1+K_{EQ}} \tag{9}$$

$$K_{EQ} = K_{DeOH}P_{DeOH} + K_{D_1}P_{D_1}(K_3+1) + K_{DDE}P_{DDE} \tag{9.1}$$

$$K_1 = \frac{1}{K_{DeOH}}, \quad K_2 = \frac{k^+_{s,D_1}}{k^-_{s,D_1}}, \quad K_3 = \frac{k^+_{s,D_2}}{k^-_{s,D_2}} \tag{9.2}$$

Experimental

Synthesis of γ-Al$_2$O$_3$

The catalyst, γ-Al$_2$O$_3$, used in this study was synthesized via a precipitation method using aluminum nitrate (QReC) as a precursor and ammonium carbonate (QReC) as a precipitating agent. Ammonium carbonate (0.6 M, 400 mL) was added slowly to the aluminum nitrate solution (0.6 M, 200 mL) under vigorous stirring at 343 K for 6 h to obtain an opaque white solution. A hydrothermal method was applied by

heating the solution at 363 K for 19 h. The solution was then filtered and the filtered precipitate was washed twice with warm water and dried in an oven at 350 K for 7 h to obtain the γ-Al$_2$O$_3$ catalyst. To activate the catalyst, the alumina gel was removed from the oven and was placed in a quartz tube and calcined at 823 K under the presence of oxygen gas with a flow rate of 60 mL/min for 3 h. The temperature of the furnace was raised at a rate of 1 K/min from room temperature to 823 K.

Catalyst characterization techniques

The nitrogen sorption isotherm of the synthesized catalyst was measured at 77 K on a Quantachrome Autosorb®-1-C analyzer. Prior to measurement, the sample was degassed under vacuum at 573 K for 6 h. The Brumauer-Emmett-Teller (BET) technique was employed to calculate the specific surface area, using adsorption data in a relative pressure range from 0.04 to 0.30. The Barrett-Joyner-Halenda (BJH) model was utilized to calculate pore volumes and pore size distributions.

The X-ray diffraction (XRD) patterns of the synthesized catalyst between 2θ range of 10° to 80° were obtained by a PANalytical (X'Pert pro) XRD system using Cu K$_\alpha$ radiation (40 kV, 40 mA) at a scanning speed of 2°/min. The synthesized γ-Al$_2$O$_3$ was analyzed and compared with the synthesized γ-Al$_2$O$_3$ (obtained from Sasol Germany).

The acid concentration of γ-Al$_2$O$_3$ was determined by the temperature programmed desorption of ammonia (NH$_3$-TPD). Before adsorption and desorption of NH$_3$, the catalyst sample of 0.1 g was treated at 773 K for 2 h under helium atmosphere (30 mL/min). After cooling down to room temperature, 10 % NH$_3$ in He gas was adsorbed onto the sample in excess. After the adsorption step, the sample was heated at 373 K under He gas (30 mL/min) to eliminate excess NH$_3$. A NH$_3$-TPD curve was obtained by increasing temperature from 373 to 973 K and the desorbed NH$_3$ was detected using a TCD (Sri Instrument).

Catalytic dehydration

To evaluate the effect of internal mass transfer, the dehydration experiments were conducted using different particle size catalysts; 0.1 to 0.4 mm and at different temperatures ranging from 533 to 608 K. The results showed the catalyst particle size within 0.1 to 0.4 mm had insignificant effect on the 1-decanol conversion, suggesting that the internal mass transfer effect was negligible. Next, the external mass transfer limitation was tested by varying the flow rate of 1-decanol at different temperatures and a constant W/F ratio of 0.15 h. The results showed that the conversion of 1-decanol increased with increasing 1-decanol flow rate when the reaction temperature was greater than 558 K except at a temperature of 533 K, the 1-decanol conversion remained almost unchanged, indicating that the dehydration reaction of 1-decanol to 1-decene was limited by external mass transfer except at the lowest reaction temperature of 533 K. It can be concluded that at the lowest reaction temperature of 533 K, the effects of internal and external mass transfer limitation can be neglected.

From the previous study to investigate the mass transfer effect on the dehydration reaction of 1-decanol over γ-Al$_2$O$_3$, 0.15 g of the γ-Al$_2$O$_3$ catalyst with different particle sizes (0.1–0.3 mm) secured with quartz wool plugs was located in a cylindrical stainless steel reactor with an inner diameter of 10 mm and inserted in a temperature-controlled furnace. Ceramic balls were packed at the bottom and at the top of the catalyst bed to facilitate heat transfer to the reactant. Prior to each run, the reactor was purged by inert nitrogen gas at flow rate of 50 mL/min for 2 h, and then pure 1-decanol was fed into the reactor by an Eldex ReciPro pump at a flow rate between 0.02 and 0.1 mL/min. A heating coil was wrapped around the pipeline to preheat 1-decanol before 1-decanol enters the reactor. All runs were performed under atmospheric pressure. The constituents of the collected outlet samples were analyzed by a gas chromatograph (HP 6890 series) equipped with a FID detector and a DB-1 (15 m $\times$ 0.530 mm $\times$ 0.15 μm) column. Each experiment was conducted three times in order to obtain a standard error for each data point.

Results and discussion

Catalyst characterization results

The nitrogen sorption isotherms of the synthesized γ-Al$_2$O$_3$, as illustrated in Fig. 3, shows an IUPAC type IV isotherm with a H3 hysteresis loop. The presence of a H3 type hysteresis indicates that this catalyst is mesoporous with narrow-slit shape pores. The surface area was 184 m^2/g and pore volume was 0.47 cm^3/g. The pore size distribution (inset of Fig. 3), obtained from the adsorption curve of the
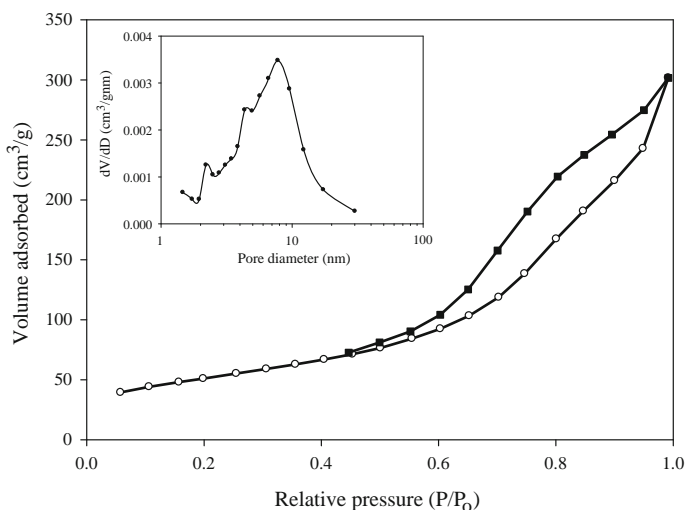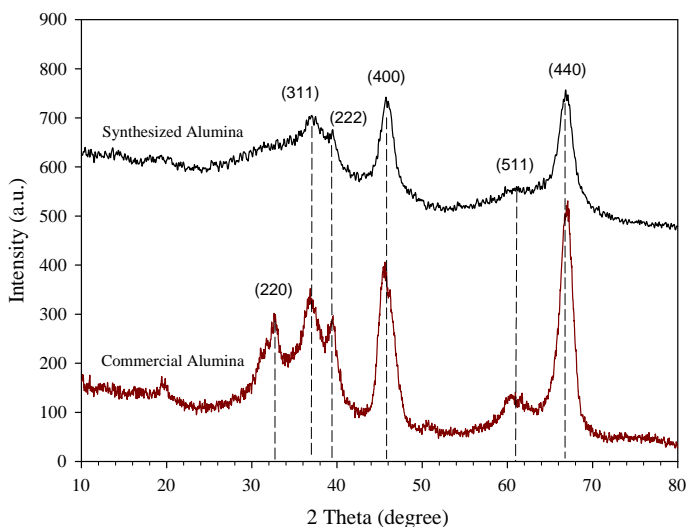

Fig. 3 Isotherms and pore size distributions (*inset*) of synthesized γ-Al$_2$O$_3$ after calcination at 823 K

Table 2 Summary of textural properties and amount of acid sites of γ-Al$_2$O$_3$

Catalyst	Textural Properties			Amount of acid sites (mmol/g)		
	Surface Area (m^2/g)	Pore Volume (cm^3/g)	Pore size (nm)	Weak acid site	Strong acid sites	Total
γ-Al$_2$O$_3$	183	0.48	7.9	0.441	0.389	0.828

Fig. 4 XRD patterns of synthesis γ-Al$_2$O$_3$ compared with commercial γ-Al$_2$O$_3$

isotherms by using BJH model is centered at 7.8 nm. The textural properties of synthesized γ-Al$_2$O$_3$ are summarized in Table 2.

The XRD pattern of the synthesized γ-Al$_2$O$_3$ catalyst is compared with the commercial γ-Al$_2$O$_3$ catalyst in Fig. 4. The peaks at 2θ = 36.5°, 39.8°, 46.0°, 61.0° and 66.5° are characteristics of γ-Al$_2$O$_3$ catalyst (JCPDS Card No. 46-1131). The reflections in terms of Miller indeces of the synthesized γ-Al$_2$O$_3$ are almost identical to those of a commercial γ-Al$_2$O$_3$ catalyst. However, the XRD peak at 220 of the synthesized γ-Al$_2$O$_3$ was missing, which is in a good agreement with Fang et al. and Zhang et al. [21, 23].

The NH$_3$-TPD results of the γ-Al$_2$O$_3$ suggest that the catalyst contained both weak and strong acidic sites. The amounts of weak and strong acid sites are summarized in Table 2. The concentration of weak acid sites is 0.441 mmol/g, while the concentration of strong acid sites is 0.389 mmol/g. A larger amount of the weak acid sites compared to the strong acid sites is a typical characteristic of a γ-Al$_2$O$_3$ catalyst [24].
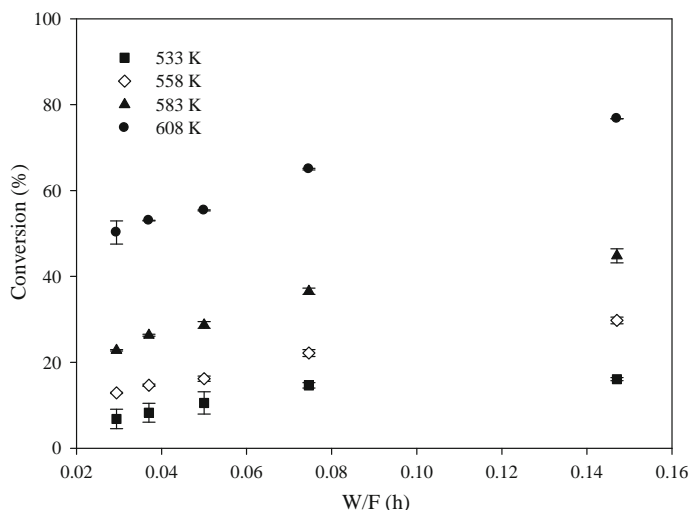
Fig. 5 Influence of retention time and operating temperature on the conversion of 1-decanol over γ-Al$_2$O$_3$. Reaction condition: Total pressure = 101.3 kPa; Temperature = 533–608 K; 1-decanol flow rate = 0.02–0.1 mL/min; N$_2$ flow rate = 50 mL/min; Catalyst weight (W) = 0.15 g

## Influence of retention time and temperature

As the amount of time the reactant spends inside the catalytic system increases (increase in retention time), the conversion of 1-decanol also increases, as shown in Fig. 5. This is because the reactant has more time to interact with the acid site located in the catalyst pores. Similarly, an increase in temperature causes the curve to shift upward, indicating an increase in conversion for all retention times. As expected, the obtained data agree with the fact that the reaction of dehydration to 1-decene is endothermic.

The influence of retention time and temperature on the amount of 1-decene, internal olefin and DDE are shown in Fig. 6a–c. The amount of 1-decene and internal olefins were extremely dependent on both the retention time and temperature of the system. As shown in Fig. 6a, b, both amounts increased with increasing temperature and retention time. In contrast, Fig. 6c suggests that the amount of DDE decreased with increasing temperature, but it still increased with increasing retention time only at a temperature higher than 558 K. Therefore, in order to obtain the highest yield of 1-decene, the temperature and retention time have to be increased. However, if the temperature was too high and retention time was too long, there is a possibility that 1-decene will transform into internal olefins. Moreover, internal olefins are not detected when the temperature is below 558 K.

Activation energy results

Data from the Arrhenius plot, derived from Eq. 10 and shown in Fig. 7 shows that the apparent activation energy is approximately 102 ± 2 kJ/mol. For comparison,

Fig. 6 a Influence of temperature and retention time on the amount of 1-decene over γ-Al$_2$O$_3$. Reaction conditions: Total pressure = 101.3 kPa; Temperature = 533–608 K; 1-decanol flow rate = 0.02–0.1 mL/min; N$_2$ flow rate = 50 mL/min; Catalyst weight (W) = 0.15 g. **b** Influence of temperature and retention time on the amount of internal olefins over γ-Al$_2$O$_3$. Reaction conditions: Total pressure = 101.3 kPa; Temperature = 533–608 K; 1-decanol flow rate = 0.02–0.1 mL/min; N$_2$ flow rate = 50 mL/min; Catalyst weight (W) = 0.15 g. **c** Influence of temperature and retention time on the amount of DDE over γ-Al$_2$O$_3$. Reaction conditions: Total pressure = 101.3 kPa; Temperature = 533–608 K; 1-decanol flow rate = 0.02–0.1 mL/min; N$_2$ flow rate = 50 mL/min; Catalyst weight (W) = 0.15 g
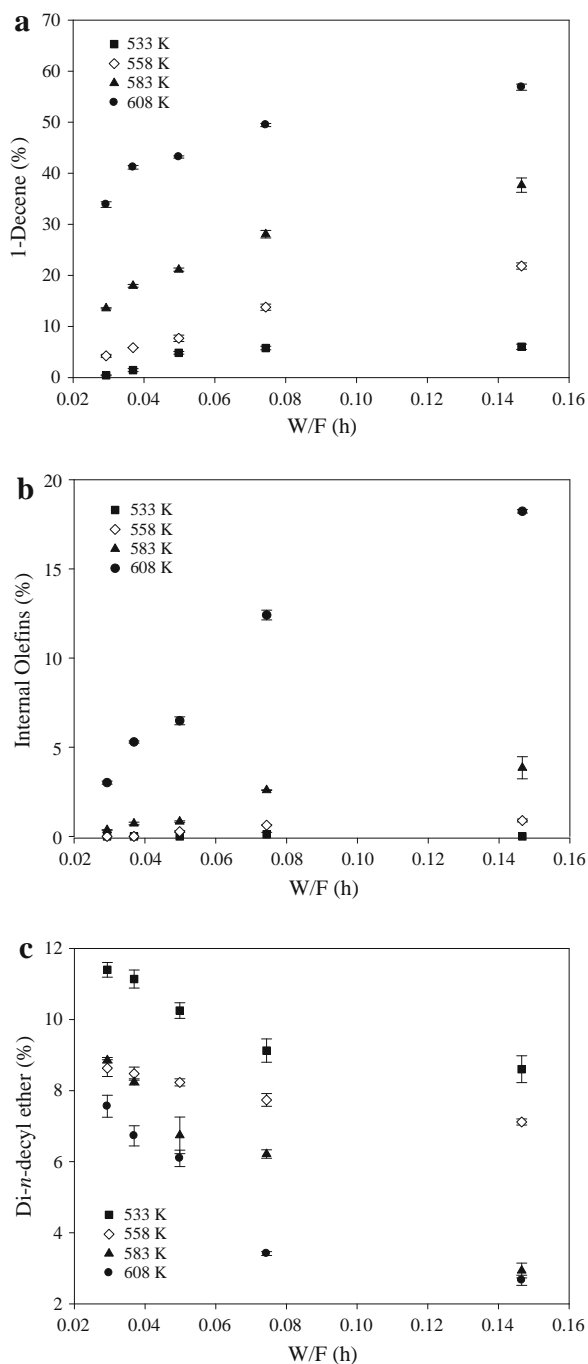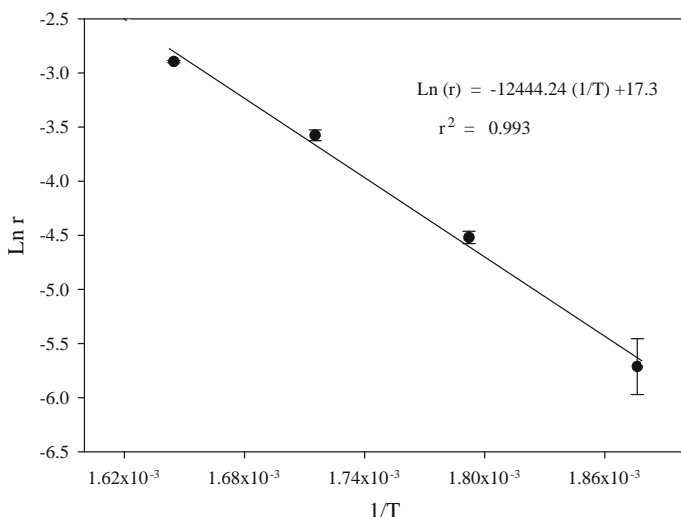
Fig. 7 Arrhenius plot to calculate activation energy for the formation of 1-decene over γ-Al_2O_3

the apparent activation energy for the dehydration of ethanol in the temperature range of 423–523 K over heteropoly acid is 43 kJ/mol [25] and the activation energy for 2-butanol dehydration at 348–423 K over Al_2O_3–ZrO_2/SO_4^{2-} is 46 kJ/mol [26]. Another kinetic model analysis conducted by Marchi et al. [22] reported the activation energy of 95 kJ/mol for styrene formation from 1-phenylethanol at temperature between 353 and 373 K. Consequently, we can conclude that a higher molecular weight of alcohol has greater apparent activation energy for the dehydration reaction.

$$\ln r = A_o - \frac{E_a}{R}\left(\frac{1}{T}\right) \qquad (10)$$

Kinetic modeling results

The unknown equilibrium and rate constant of any reaction can be obtained by fitting the experimental data using the Polymath program. The partial pressure data of each species (1-decanol, 1-decene, internal olefin and DDE) were plugged into the program. The value of the partial pressure of each species was calculated using Eq. 11.

$$P_i = \left(\frac{N_i}{N_{Total}}\right)P_{Total} \qquad (11)$$

Here i refers to any species involved.

The experimental rate of dehydration toward 1-decene has been calculated by using the product composition obtained from GC analysis. Once the production rate of 1-decene per hour is known, it is divided by the amount of catalyst used as shown

in Eq. 12. This equation assumes that the rate is constant at all point along the reactor, which is valid if the catalyst bed is either shallow or the conversion is extremely small. For this experiment, the assumption is valid because the catalyst bed is shallow.

$$r_{\exp} = \frac{\dot{n}_p}{m_{cat}} \tag{12}$$

This Polymath nonlinear regression was developed using the Levenberg–Marquardt (LM) algorithm. Similarly to other types of regression algorithms, the main function of the LM algorithm is to minimize the sum of square errors (r^2) created by the difference between the experimental rates (r_{iexp}) and the calculated rates (r_{icalc}). There are three main criteria used to assess the quality of the fit. The first obvious one is the valve of r^2, as shown in Eq. 13. An optimized model would give the value of r^2 close to 1. The second criterion is the variance, s, which is used to compare different models. The variance should be as small as possible. For the fitting to be valid, the confidence level must also be smaller than the value of any parameter, the smaller the better. Furthermore, the standard error (SE) is calculated by dividing the standard deviation (σ) by the square root of the number of experiment trails (N) as shown in Eq. 14.

$$r^2 = 1 - \frac{\sum\limits_{i=1}^{n} \left(r_{i_{\exp}} - r_{i_{cal}}\right)^2}{\sum\limits_{i=1}^{n} \left(r_{i_{\exp}} - \bar{r}\right)^2} \tag{13}$$

$$SE = \frac{\sigma}{\sqrt{N}} \tag{14}$$

The results of the regression analysis using the polymath program are shown in Table 3. Model I showed very poor correlation to the experimental data, which was referred as "*non*" under the r^2 column. Therefore, the first model was discarded. A better correlation was accomplished when the formation of 1-decene was assumed to be reversible. However, the values of some equilibrium constants were negative, which is not possible. Therefore, it was further assumed that DDE did not attach to the surface of the catalyst, suggesting that the adsorption equilibrium constant for di-*n*-decyl ether (K_{DDE}) was zero. The modified rate equation was named model IIA. After modification, it seemed that the new model (IIA) still showed negative constants. Next, model IIB was formulated for assumption that both K_{DDE} and K_3 were zero. Unlike other models, model IIB gave reasonable results and the value of the equilibrium constant was valid. However, it can be observed that the rate constant (k_{s,D_1}^+) increased linearly at a lower temperature between 533 and 583 K, but increased almost three-fold when the temperature rose to 608 K. The results imply that mass transfer limitation is pronounce at a high reaction temperature but it can be neglected at a low reaction temperature. This finding is similar to that of Marchi et al. work, that the rate constant increased tremendously at a high

Table 3 Results from regression analysis of the experimental and calculated rate of each reaction

T (K)	Model	K_1	K_{D1}	K_{DDE}	$K_{s,D}^+$
533	I	$1.85 \times 10^{-1} \pm 8.69 \times 10^{-2}$	$1.53 \times 10^{-3} \pm 4.20 \times 10^{-1}$	-1.72 ± 7.56	$1.01 \times 10^{-1} \pm 1.14 \times 10^{-2}$
	II	$3.76 \times 10^{2} \pm 3.72 \times 10^{2}$	$2.49 \times 10^{2} \pm 3.95 \times 10$	$1.23 \times 10^{1} \pm 1.21 \times 10^{1}$	$8.29 \times 10^{-2} \pm 4.30 \times 10^{-2}$
	IIA	6.25 ± 1.56	$3.96 \pm 5.79 \times 10^{-1}$	–	$9.61 \times 10^{-2} \pm 6.02 \times 10^{-2}$
	IIB	$6.00 \times 10^{-1} \pm 8.96 \times 10^{-2}$	$9.06 \times 10^{-1} \pm 4.00 \times 10^{-2}$	–	$1.09 \pm 6.61 \times 10^{-2}$
558	I	$1.86 \times 10^{-1} \pm 5.25 \times 10^{-2}$	1.01 ± 1.01	$-1.55 \times 10^{1} \pm 8.55$	$2.98 \times 10^{-1} \pm 9.75 \times 10^{-2}$
	II	$4.09 \times 10^{1} \pm 4.26 \times 10^{1}$	$7.28 \times 10^{1} \pm 2.23 \times 10^{1}$	$-1.23 \times 10^{-1} \pm 5.82 \times 10^{-2}$	$2.89 \times 10^{-2} \pm 9.16 \times 10^{-3}$
	IIA	$1.62 \times 10^{1} \pm 1.62 \times 10^{1}$	$3.32 \times 10^{1} \pm 3.28 \times 10^{1}$	–	$9.32 \times 10^{-1} \pm 8.63 \times 10^{-1}$
	IIB	$6.08 \times 10^{-1} \pm 1.18 \times 10^{-1}$	$1.99 \times 10^{-1} \pm 7.84 \times 10^{-3}$	–	$1.15 \pm 4.23 \times 10^{-2}$
583	I	$2.71 \times 10^{-1} \pm 1.74 \times 10^{-2}$	$8.82 \times 10^{1} \pm 5.16 \times 10^{1}$	$-7.29 \pm 4.28 \times 10^{1}$	$1.10 \pm 1.27 \times 10^{-1}$
	II	1.51 ± 3.45	-3.96 ± 5.27	$3.35 \times 10^{-1} \pm 7.44 \times 10^{-2}$	$3.89 \times 10^{-2} \pm 2.52 \times 10^{-2}$
	IIA	$-3.82 \pm 5.71 \times 10^{-1}$	$3.06 \times 10^{-1} \pm 4.85 \times 10^{-2}$	–	$7.32 \times 10^{-2} \pm 2.20 \times 10^{-2}$
	IIB	$9.11 \times 10^{-1} \pm 1.86 \times 10^{-1}$	$1.31 \times 10^{-1} \pm 3.16 \times 10^{-2}$	–	$1.44 \pm 2.24 \times 10^{-1}$
608	I	$2.11 \times 10^{-1} \pm 5.65 \times 10^{-2}$	$-1.79 \times 10^{-5} \pm 4.91 \times 10^{-6}$	$-2.76 \times 10^{-1} \pm 1.73 \times 10^{1}$	3.32 ± 1.97
	II	-1.09 ± 1.05	$3.18 \times 10^{1} \pm 3.51 \times 10^{1}$	$6.63 \times 10^{-1} \pm 2.41 \times 10^{-2}$	$3.45 \times 10^{-2} \pm 7.11 \times 10^{-2}$
	IIA	$-3.36 \pm 8.60 \times 10^{-1}$	$3.35 \pm 4.15 \times 10^{-2}$	–	$1.18 \times 10^{-1} \pm 4.22 \times 10^{-2}$
	IIB	$2.11 \pm 1.09 \times 10^{-1}$	$6.64 \times 10^{-2} \pm 1.29 \times 10^{-3}$	–	$3.44 \pm 2.42 \times 10^{-1}$

T (K)	Model	K_2	K_3	R^2
533	I	–	$-9.97 \times 10^{-1} \pm 8.40 \times 10^{-4}$	non
	II	$3.40 \times 10^{1} \pm 3.40 \times 10^{1}$	–	non
	IIA	$-9.97 \times 10^{1} \pm 9.54 \times 10^{-2}$	$2.76 \times 10^{1} \pm 9.72$	non
	IIB	$1.02 \times 10^{2} \pm 7.45 \times 10^{-4}$	–	0.922

Table 3 continued

T (K)	Model	K_2	K_3	R^2
558	I	–	$-1.00 \pm 5.47 \times 10^{-4}$	non
	II	$-8.39 \times 10^{-1} \pm 1.06$	–	non
	IIA	$2.92 \times 10^{-1} \pm 1.27 \times 10^{-1}$	-7.37 ± 7.38	non
	IIB	$9.14 \times 10^{1} \pm 1.06 \times 10^{1}$	–	0.999
583	I	–	$7.14 \times 10^{-1} \pm 1.03$	0.978
	II	$1.09 \times 10^{-1} \pm 5.70 \times 10^{-2}$	–	0.999
	IIA	$2.61 \times 10^{-1} \pm 4.98 \times 10^{-2}$	$-4.22 \pm 5.78 \times 10^{-1}$	0.999
	IIB	$9.11 \times 10^{1} \pm 1.09 \times 10^{1}$	–	0.999
608	I	–	1.07 ± 2.07	0.985
	II	$3.07 \times 10^{-1} \pm 1.60 \times 10^{-1}$	–	0.999
	IIA	$3.84 \times 10^{-1} \pm 9.08 \times 10^{-2}$	$-3.07 \pm 1.59 \times 10^{-1}$	0.999
	IIB	$1.02 \times 10^{1} \pm 1.35 \times 10^{1}$	–	0.999

Fig. 8 **a** Experimental value (*symbols*) and regression line of product composition (*solid line*) at 533 K. Reaction conditions: Total pressure = 101.3 kPa; 1-decanol flow rate = 0.02–0.1 mL/min; N₂ flow rate = 50 mL/min; Catalyst weight (W) = 0.15 g. **b** Experimental value (*symbols*) and regression line of product composition (*solid line*) at 558 K. Reaction conditions: Total pressure = 101.3 kPa; 1-decanol flow rate = 0.02–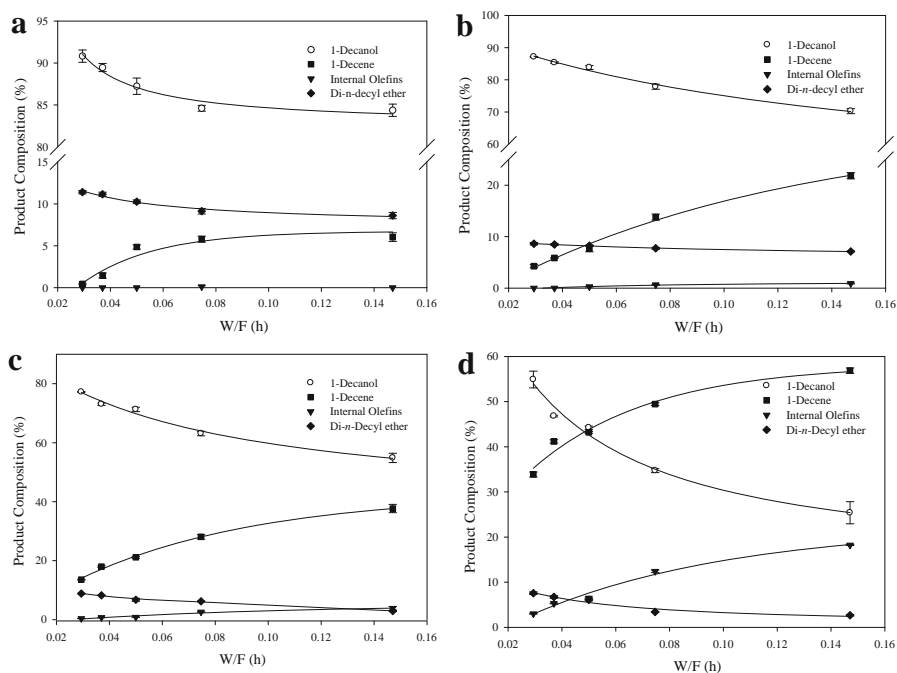0.1 mL/min; N₂ flow rate = 50 mL/min; Catalyst weight (W) = 0.15 g. **c** Experimental value (*symbols*) and regression line of product composition (*solid line*) at 583 K. Reaction conditions: Total pressure = 101.3 kPa; 1-decanol flow rate = 0.02–0.1 mL/min; N₂ flow rate = 50 mL/min; Catalyst weight (W) = 0.15 g. **d** Experimental value (*symbols*) and regression line of product composition (*solid line*) at 608 K. Reaction conditions: Total pressure = 101.3 kPa; 1-decanol flow rate = 0.02–0.1 mL/min; N₂ flow rate = 50 mL/min; Catalyst weight (W) = 0.15 g

temperature reaction compared to the increase in rate constant at a lower temperature [22].

The theoretical rates of 1-decene production for all reaction temperatures were determined by using the best-fit model (IIB) shown in Table 1. In order to obtain the partial pressure of each species the product composition of each run was fitted as shown in Fig. 8a–d and then applying Eq. 11. The theoretical rate of 1-decene production was then calculated and plotted with the experimental rate as shown in Fig. 9. The values obtained from the experimental data and from the model (IIB) are reasonably close together, as indicated by the r^2 value of close to unity. This kinetic model (IIB) can be used to estimate the rate of production of 1-decene over other catalysts, provided that the type of surface reactions and the type of adsorption are the same as these used to formulate this model. Fang et al. pointed out that the rate equations of methanol dehydration on different catalysts were similar to each other and that it reflects the dissociative natural of adsorption on the catalyst [23].
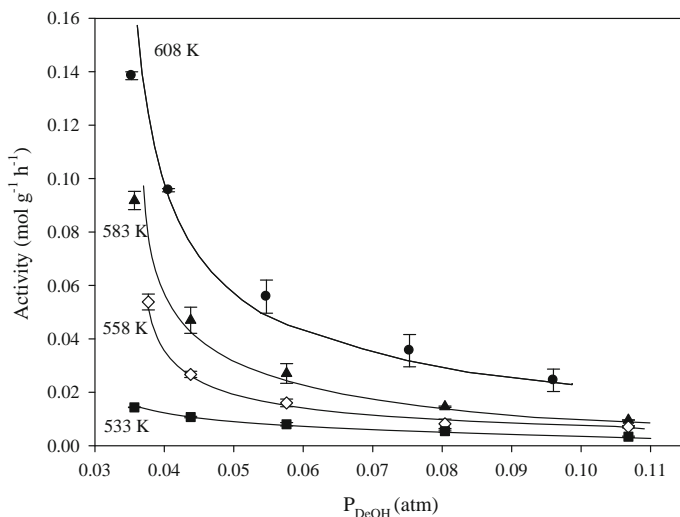
Fig. 9 Experimental rate (*symbols*) fitted with theoretical calculated rate (*solid line*) by using model IIB

Conclusions

The conversion of 1-decanol and yield of each product species in the product were strongly affected by retention time and reaction temperature. Increases in conversion and yield of 1-decene and internal olefins were observed with increasing temperature. The activation energy for the formation of 1-decene over γ-Al$_2$O$_3$ was 102 ± 2 kJ/mol, which is higher than the apparent activation energy values of ethanol and 2-butanol given by other researchers. The results indicate that model II, without the equilibrium constant K_{DDE} and K_3, is a reasonable model. The model verifies that the formation of 1-decene is reversible. The values of the equilibrium constants obtained from this reaction model can be used to simulate the production of 1-decene on an industrial scale.

References

1. Haghighi SS, Rahimpour M, Raeissi S, Dehghani O (2013) Chem Eng J 228:1158–1167
2. Lee B, Yoo S, Kang C, Lee H, Ahn SM, Nath R (2004) Honeywell User Group 2004, Phoenix, Arizona
3. Brethauer S, Wyman CE (2010) Bioresour Technol 101:4862–4874
4. Mudge SM (2005) Soap Deterg Assoc 3:11–17
5. Shenga Q, Linga K, Li Z, Zhao L (2013) Fuel Process Technol 110:73–78
6. Mortier RM, Fox MF, Orszulik ST (2010) Chemistry and technology of lubricants. Springer Science, New York

7. Tanabe K, Tsutomu T (1974) Bull Chem Soc Jpn 47:424–429
8. Ptaszek A, Grzesik M (2010) Chem Process Eng 31:43–51
9. Arenamnarta S, Trakarnpruk W (2006) Int J Appl Sci Eng 4:21–32
10. Baertsch CD, Komala KT, Chua YH, Iglesia E (2002) J Catal 205:44–57
11. West RM, Braden DJ, Dumesic JA (2009) J Catal 262:134–143
12. Park C, Keane MA (2001) J Mol Catal A 166:303–322
13. Ivanova S, Vanhaecke E, Dreibine L, Louis B, Pham-Huu C (2009) Appl Catal A359:151–157
14. Chen G, Li S, Jiao F, Yuan Q (2007) Catalytic dehydration of bioethanol to ethylene over TiO_2/γ-Al_2O_3 catalysts in microchannel reactors. Catal Today. doi:10.1016/j.cattod.2007.01.071
15. Najafabadi AT, Fatemi S, Sohrabi M, Salmasi M (2012) J Ind Eng Chem 18:29–37
16. Fatourehchia N, Sohrabia M, Royaeea SJ, Mirarefina SM (2011) Chem Eng Res Des 89:811–816
17. Kagyrmanova A, Chumachenko V, Korotkikh V, Kashkin V, Noskov A (2011) Chem Eng J 176:188–194
18. Nel RJJ, Klerk A (2009) Ind Eng Chem Res 48:5230–5238
19. Katritzky AR, Nichols D, Siskin M, Murugan R, Balasubramanian M (2001) Chem Rev 101(4):837–892
20. Wu Q, Zhang F, Yang J, Li Q, Tu B, Zhao D (2011) Microporous Mesoporous Mater 143:406–412
21. Zhang L, Zhang HT, Ying WY, Fang DY (2011) World Acad Sci 59:1538–1543
22. Bertero NM, Apesteguía CR, Marchi AJ (2009) Catal Commun 10:1339–1344
23. Wu Q, Zhang F, Yang J, Li Q, Tu B, Zhao D (2011) Microporous Mesoporous Mater 143:406–412
24. Weingarten R, Tempsett G, Conner WC, Hyber GW (2011) J Catal 279:174–182
25. Bokad VV, Yadav GD (2011) Appl Clay Sci 53:263–271
26. Skrdla PJ, Lindemann C (2003) Appl Catal A 246:227–235

Selective hydrogenation of mixed C4 containing high vinyl acetylene by Mn-Pd, Ni-Pd and Ag-Pd on Al_2O_3 catalysts

Paisan Insorn, Boonyarach Kitiyanan *

The Petroleum and Petrochemical College, Chulalongkorn University, Soi Chula 12, Phyathai Road, Pathumwan, Bangkok 10330, Thailand

ABSTRACT

The waste stream containing high vinyl acetylene concentration from a commercial mixed C4 process was tested for the hydrogenation reaction by Pd, Mn-Pd, Ni-Pd, and Ag-Pd supported on alumina catalysts in a recirculating reactor. Mn-promoted Pd/Al_2O_3 catalyst with Pd/Mn molar ratio 1:2 not only increases the activity, but also significantly increases the selectivity and yield toward 1,3-butadiene. Adding Ni to Pd/Al_2O_3 catalysts improves only the activity, but not the selectivity, while adding Ag improves neither the activity nor the selectivity toward 1,3-butadiene.

1. Introduction

Mixed C4 is a product from cracking units and is composed mainly of four-carbon-atom compounds [1] which can be separated to yield several C4 products including 1,3-butadiene, methyl-*tert*-butyl-ether (MTBE), and 1-butene [2]. However, Mixed C4 also contains about 0.5-3 wt% of acetylenic compounds [1,3–8], which are considered impurities in C4 products that must be removed by the butadiene extraction process [1,5,7,8]. A separate acetylenic stream can contain up to 30 wt% vinyl acetylene. Currently, this concentrated vinyl acetylene stream is combusted due to safety concerns [7,9]. Therefore, to minimize waste and to recover additional C4 products, selective hydrogenation of vinyl acetylene into more valuable compounds such as 1,3-butadiene and 1-butene has been suggested [10–16].

Supported Pd catalysts have been widely studied in both gas and liquid phases for the selective hydrogenation of alkyne [12,17–20]. Furthermore, unpromoted and promoted Pd/Al_2O_3 catalysts are being used commercially in many hydrogenation applications [4,21–23]. In addition, several transition metals have been added to Pd/Al_2O_3 to promote the catalytic performances for selective alkyne hydrogenation. Lamberov et al. [11] reported testing cobalt promoted Pd/Al_2O_3 catalysts prepared by a sequential penetration method. The Pd:Co molar ratio on the catalysts was varied from 1:2 to 3:1. The reaction was conducted with industrial grade

C4 containing up to 6 wt% acetylene hydrocarbons in a pilot-scale seven-liter adiabatic flow reactor. Their results show that the unpromoted $0.5\%Pd/\delta$-Al_2O_3 catalyst can completely convert the vinyl acetylene, though the selectivity for 1,3-butadiene decreases significantly. For the Co-promoted Pd/δ-Al_2O_3 catalyst, the selectivity for 1,3-butadiene is lower than for the unpromoted catalyst, and vinyl acetylene conversion decreases with increasing Co loading. They report that the catalyst with a 1:1 Pd:Co molar ratio provides 100% vinyl acetylene conversion and 61.5% 1,3-butadiene selectivity.

Huang et al. [24] studied the selective hydrogenation of acetylene mixed with ethylene using Pd, Ni, Ag, Pd-Ni, and Pd-Ag supported Al_2O_3 and β-zeolite catalysts. They found that among the studied catalysts, the Pd-Ag/Al_2O_3 catalyst has the highest selectivity for acetylene hydrogenation to ethylene. Pd-Ni/Al_2O_3 and Pd/Al_2O_3 catalysts exhibit similar performance in selectivity toward ethylene, while the Ni-promoted Pd/Na+-β-zeolite shows higher selectivity than unpromoted Pd/Na+-β-zeolite. The use of alumina as the catalyst support provides higher hydrogenation activity than using silica, though using silica generally offers better performance in selective hydrogenation. Kim et al. [25] investigated the addition of Cu and Ag to Pd/Al_2O_3 by using a surface redox and impregnation techniques and found that adding Cu and Ag to Pd/Al_2O_3 enhances ethylene selectivity but decreases the activity for the reaction.

Moyes et al. [26] studied the hydrogenation of gas phase 1,3-butadiene by the injection of 50 Torr 1,3-butadiene and 100 Torr hydrogen into a vessel containing one of the following metal films, V, Co, Ni, Pd or Mn. Their results show that V, Co, Ni, and Pd

metals provided high activity, with conversions greater than 50%. Mn achieved 22% butadiene conversion which is 1.8, 7, 20 times higher than Cu, Ag, and Au, respectively Among all tested transition metals, Mn shows the highest 1-butene selectivity but with the lowest butane yield. Manganese is reported to improve the catalytic hydrogenation of CO and aromatic compounds. Gong-Xin et al. [27] reported the hydrogenation of CO using Cu/Al_2O_3 catalyst with the addition of Mn at Mn/Cu molar ratios of 1:1 and 3:2. The CO hydrogenation activity is increased significantly and the Cu dispersion is also high at these Mn/Cu molar ratios. Their temperature programmed reduction (TPR) results suggest that an interaction between Mn and Cu is the likely reason for enhanced Cu dispersion.

Herranz et al. [28] studied the carbon monoxide hydrogenation using Fe-Mn catalyst prepared by microemulsion method. Fe-Mn catalyst improves the conversion of CO hydrogenation compared to Fe-alone catalyst. Hongmei et al. [29] studied the promoted Rh/SiO_2 catalyst for CO hydrogenation. Adding 1 wt% Mn to a Rh/SiO_2 catalyst, the CO conversion increases more than three-fold compared to the unpromoted Rh/SiO_2 catalyst. For hydrogenation of aromatic compounds, Han et al. [30] studied the liquid phase hydrogenation of *p*-chloronitrobenzene by using transition metal (e.g., Mn, Fe, Co, Ni, and Cu) promoted Pt/CNTs catalyst. The catalysts contained metal promoters and active Pt at 0.1 and 0.3 wt%, respectively. They found that the addition of metal promoters, with the exception of Cu, enhances the rates of hydrogenation reaction. The addition of Mn increases the reaction rate up to 77%. Han et al. [31] also reported using transition metal promoted Pt/TiO_2 catalyst for the hydrogenation of *p*-chloronitrobenzene. Mn and Co promoters increased reaction rates by approximately 39%, performing better than the Cr and Cu promoters. Xiaoli et al. [32] investigated the hydrogenation of benzene to cyclohexene on Ru catalysts promoted with Mn and Zn, synthesized by the co-precipitation method. The Mn-Ru catalyst provides the highest benzene conversion compared to Zn-Ru and Mn-Zn-Ru catalysts, however the Mn-Zn-Ru catalyst provides the highest selectivity. Cheng et al. [33] studied the effect of Mn addition on CeO_2-Al_2O_3 catalyst for benzoic acid hydrogenation. The catalysts were prepared at 5, 10, and 20 wt% Mn by the co-precipitation method. They found that both the conversion of benzoic acid and the selectivity of the reaction toward benzaldehyde increased with increasing Mn levels. TPR and XRD results suggest that the addition of Mn enhances the reducibility of catalyst and thus improves the catalyst activity.

In this work, Mn, Ni, and Ag are examined as metal promoters on a Pd catalyst for the selective hydrogenation of vinyl acetylene. The Pd, Mn-Pd, Ni-Pd and Ag-Pd on alumina catalysts are prepared by a conventional incipient wetness impregnation method. The catalysts are tested for their activity and selectivity in a circulated flow reactor system containing concentrated vinyl acetylene-mixed C4 diluted in liquid hexane.

2. Experimental

2.1. Materials

The concentrated vinyl acetylene-mixed C4 was obtained from Bangkok Synthetics Co., Ltd. This mixture is composed of various C4s (e.g., vinyl acetylene, 1,3-butadiene and butenes). Prior to testing, the concentrated vinyl acetylene-mixed C4 was analyzed by a gas chromatograph to obtain the initial component concentrations. Analytical reagent grade (AR grade) hexane was purchased from Fisher Scientific. Alumina pellets, palladium (II) nitrate dihydrate, manganese (II) acetate tetrahydrate, silver nitrate, and Nickel (II) chloride were purchased from Sigma–Aldrich. High purity (HP, 99.95%) hydrogen and nitrogen gases were purchased from Thai Industrial Gas.

2.2. Catalyst preparation

The monometallic Pd/Al_2O_3 catalyst was prepared by the incipient wetness impregnation technique, with the bimetallic catalysts prepared using the same technique sequentially for the second metal. Alumina (Al_2O_3), 2–4 mm spherical form, was first treated at 1000 °C for 2 h. The support was impregnated with the palladium (II) nitrate dihydrate aqueous solution to obtain 0.3 wt% Pd loading. The catalyst was then dried at 110 °C for 8 h and, then calcined at 500 °C for 3 h. The bimetallic catalysts, Mn-Pd, Ni-Pd, and Ag-Pd, were prepared using the following procedure. First, the support was impregnated with palladium (II) nitrate dihydrate precursor, then dried at 110 °C for 8 h and calcined at 500 °C for 1 h. Subsequently, the calcined Pd/Al_2O_3 was further impregnated with an aqueous solution of one of the metal promoter precursors, manganese (II) acetate tetrahydrate, silver nitrate, or Nickel (II) chloride. The bimetallic catalysts were prepared by varying Pd:Metal atomic ratios from 1:4 to 2:1. After impregnation, the catalysts were dried at room temperature overnight and then in an oven at 110 °C for 8 h. Finally, the catalysts were calcined under atmospheric air at 500 °C for 3 h. All calcined catalysts were first reduced in flowing hydrogen gas at 300 °C for 1 h prior to testing.

2.3. Reaction test

The reaction test was performed by recirculating a liquid phase through an external fixed-bed reactor as shown in Fig. 1 [34,35]. An amount of catalyst (0.5 g) was packed in a tubular stainless steel reactor. The packed catalyst was *in-situ*-treated by 150 °C hydrogen gas for 8 h. The piping, reactor and vessel were then purged by nitrogen gas in order to remove residual oxygen before the test. The reservoir was then filled with 650 ml hexane and the system again purged by nitrogen gas. Concentrated vinyl acetylene – mixed C4 in the stainless steel container was then introduced into the sample reservoir by open the valve connecting between the container and the reservoir. Hydrogen gas was applied to the reservoir at the 5.5 bar. The liquid mixture in the sample reservoir was continuously stirred by magnetic stirrer and circulated through the fixed-bed reactor at a flow rate of 500 ml/min using a diaphragm pump. In order to follow the reaction, samples were drawn every 30 min and analyzed by gas chromatography (HP, 5890 II Plus), equipped with flame ionization detector (FID) and a GS-alumina capillary column. The reaction temperature was controlled at 35 °C for both the fixed-bed reactor and sample reservoir. The catalytic activity and selectivity were obtained from the analysis of C4 compositions.

2.4. Catalyst characterization

Temperature programmed reduction (TPR) profiles of calcined catalysts were recorded using a TPDRO 1100 equipped with thermal conductivity detector (TCD). The TPR was performed using a 5% hydrogen in nitrogen gas mixture at a flow rate of 20 ml/min. The catalyst samples were heated from 30 to 800 °C at an increase of 10 °C/min.

Temperature programmed oxidation (TPO) was utilized to quantify the amount of deposited carbon and its oxidation temperature. The spent catalysts were packed in a quartz tube and 5% oxygen in helium gas was flowed through the catalyst-containing sample tube. The catalysts were heated from 30 to 900 °C at an increase of 10 °C/min. The combustion gases (CO_2 and/or CO) were flowed through a methanator where the CO/CO_2 were converted into methane gas which was quantified by flame ionized detection (FID).
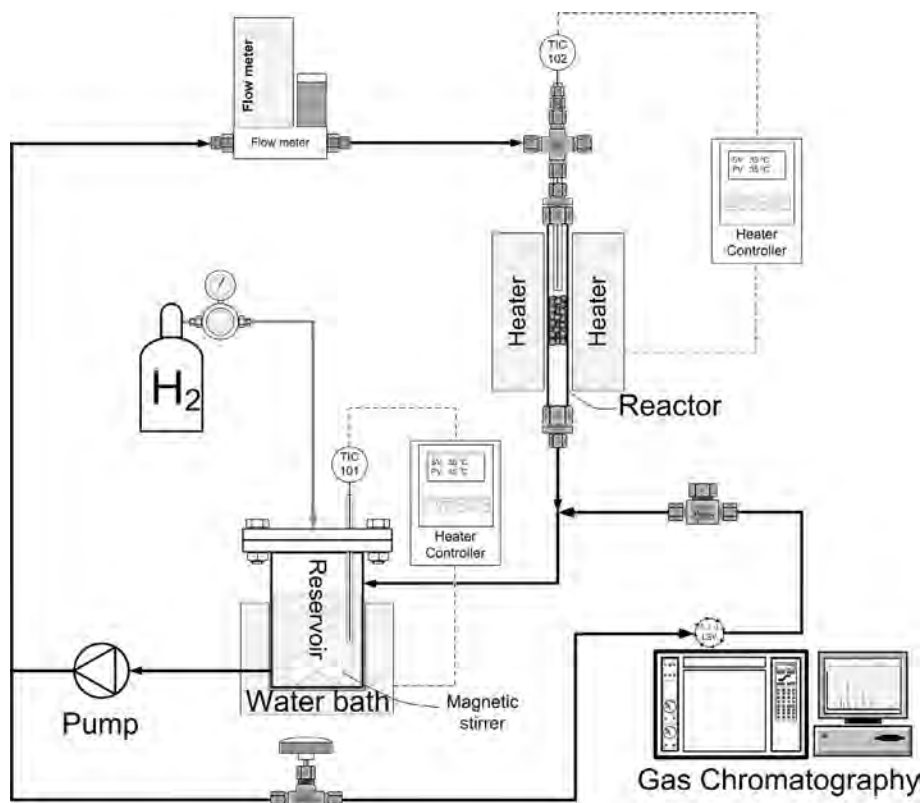
Fig. 1. Schematic flow diagram for the experimental set-up for selective hydrogenation of vinyl acetylene.

3. Results and discussion

3.1. Reaction of vinyl acetylene by Pd/Al₂O₃ catalyst

The concentration in mole% of each compound in the mixed C4 as a function of reaction time is shown in Fig. 2. From 0 to 3.5 h, the vinyl acetylene concentration decreases while the 1,3-butadiene concentration increases. The concentration of butenes, including 1-butene, *trans*-2-butene and *cis*-2-butene, slightly increased during this period. From 3.5 to 5.0 h, the vinyl acetylene concentration slightly decreases while the 1,3-butadiene concentration rapidly drops. The concentration of butenes dramatically increases, indicating that the hydrogenation of 1,3-butadiene to butenes is taking place. Reaction times longer than 5.0 h result in a decrease in the concentration of butenes and an increase in the *n*-butane concentration. As expected, the concentrations of isobutylene and *i*-butane are constant during the reaction.

The results clearly show that during the first 3.5 h the alkyne group in vinyl acetylene is hydrogenated to 1,3-butadiene and a mixture of butenes [13]. The main product of vinyl acetylene hydrogenation is likely to be 1,3-butadiene, indicating that the alkyne group is preferentially hydrogenated over the alkene group (*i.e.* no 1-butyne is detected). Subsequently, 1,3-butadiene reacts to form butenes, especially 1-butene [13,35,36]. For reaction times longer than 5 h, butenes are hydrogenated to *n*-butane. The products from each hydrogenation step can be written as shown in Fig. 3.

The selectivity and yield of 1,3-butadiene are defined as the following equations;

%1, 3 − Butadiene selectivity

$$= \frac{\text{Final mole of 1, 3} - \text{butadiene} - \text{Intial mole of 1, 3} - \text{butadiene}}{\text{Initial mole of viny acetylene} - \text{Final mole of vinyl acetylene}}$$
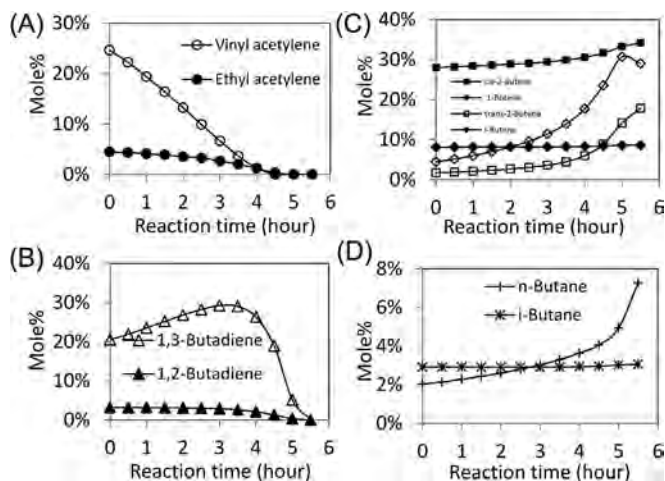
$$\times 100$$

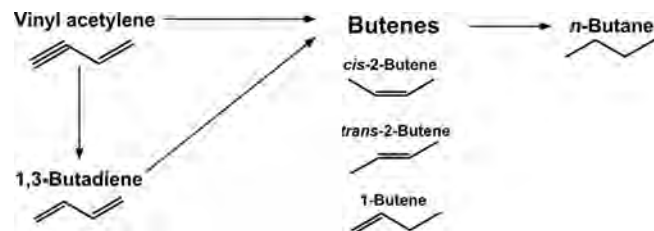**Fig. 2.** Concentration of C4 compounds during reaction over Pd/Al₂O₃ catalyst.

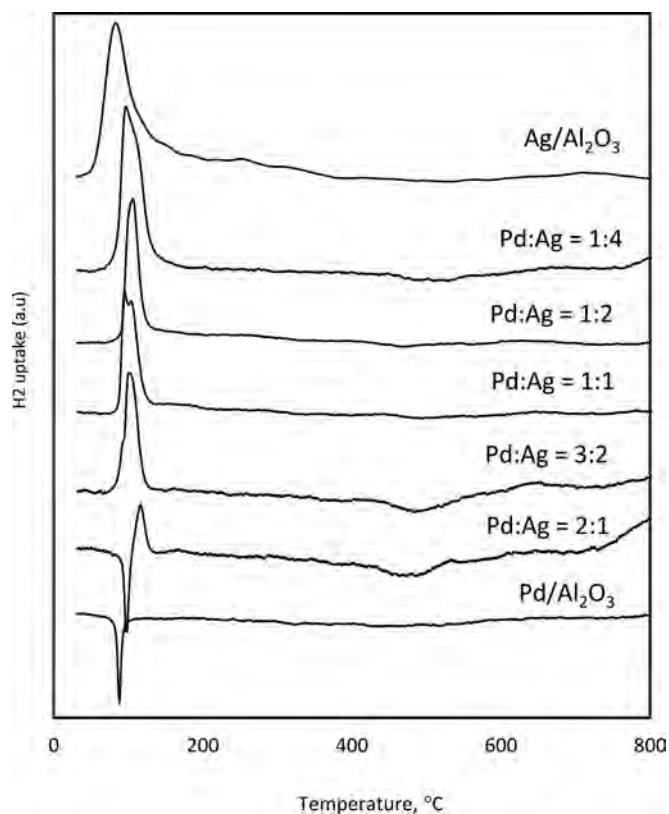**Fig. 3.** The possible products of vinyl acetylene hydrogenation.
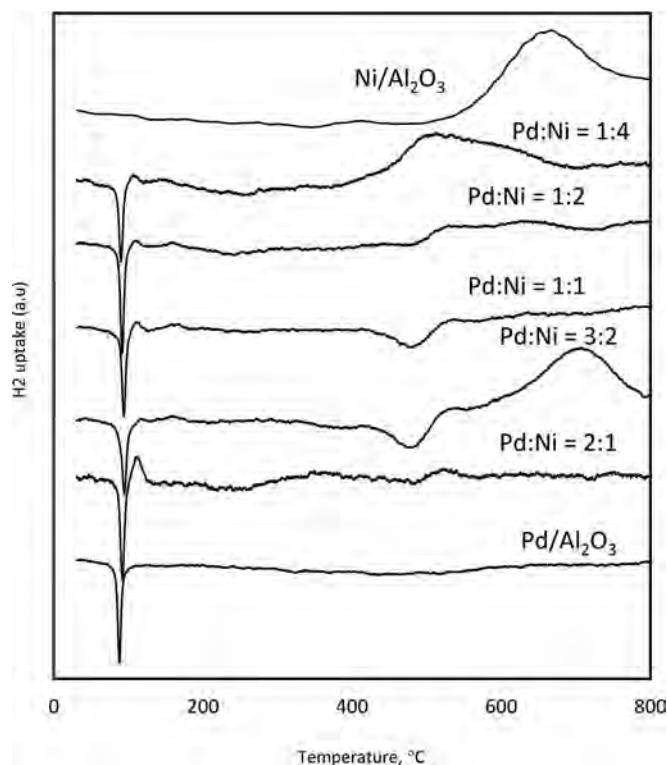
Fig. 4. TPR profiles of Ag-Pd/Al$_2$O$_3$ catalysts.

Fig. 5. TPR profiles of Ni-Pd/Al$_2$O$_3$ catalysts.

%1, 3 − Butadiene yield = %viny acetylene conversion

×%1, 3 − butadiene selectivity

3.2. Effect of promoted metal to Pd/Al$_2$O$_3$ on vinyl acetylene hydrogenation

3.2.1. Temperature programmed reduction (TPR) of metal promoted Pd/Al$_2$O$_3$

Results of TPR of single metal on alumina (Ag, Ni, Mn and Pd/Al$_2$O$_3$) and Ag-, Ni-, and Mn-Pd/Al$_2$O$_3$ are shown in Figs. 4–6. The monometallic Pd on alumina shows a negative peak at about 87 °C possibly due to the decomposition of palladium hydride (PdH$_x$), which can form at room temperatures in hydrogen containing atmosphere. Ag, Ni, and Mn/Al$_2$O$_3$ exhibit their significant peaks at 79, 652, and 500 °C, respectively. This reflects to the reduction temperatures of those metals, which suggests that, among Ag, Ni and Mn, Ag is the easiest to be reduced. As observed in Fig. 4, the addition of Ag into Pd/Al$_2$O$_3$ leads to an appearance of an additional positive peak at about 100 °C. Furthermore, adding more Ag causes a disappearance of a negative peak of PdH$_x$, while the positive peak is increased. This suggests that Ag interferes with PdH$_x$ formation, thus an interaction between Pd and Ag more likely happens. For Ni-promoted Pd/Al$_2$O$_3$ catalysts, a negative of PdH$_x$ is still observed at all Ni contents. Considering the reduction peak of nickel oxide at high temperature, it is observed that the reduction peak of nickel oxide shifts to lower temperatures in the present of Pd, especially at Pd:Ni molar ratio of 1:4. This implies that reduced Pd (possibly Pd^0 form) facilitates nickel oxide reduction via H$_2$ dissociation and spillover. For Mn-promoted Pd/Al$_2$O$_3$ catalyst, at Pd/Mn molar ratios of 3:2 and 2:1, the negative PdH$_x$ peak can still be
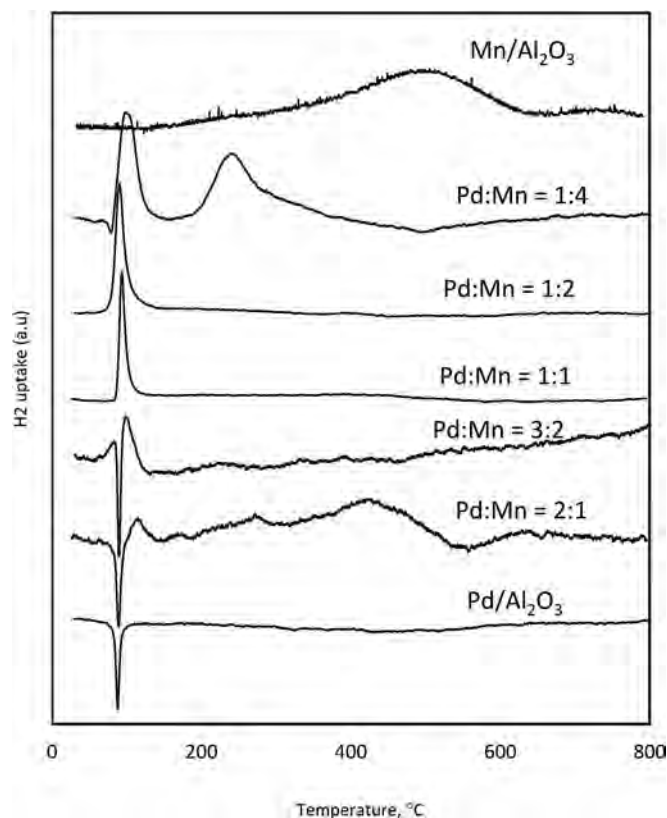

Fig. 6. TPR profiles of Mn-Pd/Al$_2$O$_3$ catalysts.

seen. Moreover, a positive peak appears at around 100 °C. When more Mn is added to obtain Pd:Mn molar ratios of 1:1 and 2:1, only one hydrogen consumption peak occurs at around 100 °C and no reduction peak of manganese oxides. However, at high Mn content (Pd:Mn ratio of 1:4), the catalyst exhibits two broad peaks, which appear at around 110 °C and 220 °C. The first peak is the reduction of palladium oxide, while the second peak is likely due to reduction of manganese oxide. This suggest that appropriate amounts of Mn strongly interact with Pd and prevent the formation of PdH_x. However, when the Mn content gets too high, some of Mn interacts with the Pd while the excess Mn appears to agglomerate by itself, as evidenced by the presence of the second TPR peak at higher temperature.

3.2.2. Vinyl acetylene hydrogenation reaction by prepared catalysts

Fig. 7 shows the rate of vinyl acetylene hydrogenation versus vinyl acetylene conversion with 5% error bars. The rate of hydrogenation by each catalyst is relatively constant for vinyl acetylene conversions less than 70%, and, as expected, the rate of reaction dramatically drops for the conversion approximately greater than 70%, due to low vinyl acetylene concentration at high conversion. For metal-promoted Pd/Al$_2$O$_3$ catalysts, it can be observed that the additions of Mn and Ni enhance the reaction rate compared to unpromoted Pd/Al$_2$O$_3$ catalyst, while adding Ag lowers the activity. Furthermore, adding more Ag to Pd/Al$_2$O$_3$ catalyst results in less catalytic activity. The activity does not significantly change as the Ni content increases in the Ni-Pd/Al$_2$O$_3$ catalyst. Interestingly, Mn-promoted Pd/Al$_2$O$_3$ catalysts containing Pd/Mn molar ratios of 3:2 and 2:1 are the most active catalysts, with the catalyst with a Pd/Mn ratio of 2:1 providing the highest reaction rate as shown in Table 2. Thus, the activity of the catalysts can be ordered as following: Mn-Pd/Al$_2$O$_3$ > Ni-Pd/Al$_2$O$_3$ > Pd/Al$_2$O$_3$ > Ag-Pd/Al$_2$O$_3$.

Table 1
Amount of deposited carbon on spent catalyst.

Catalyst	Deposited Carbon[a] wt%
Pd/Al$_2$O$_3$	1:16
Pd:Ag 1:4	2.10
Pd:Ag 1:2	2.60
Pd:Ag 1:1	2.55
Pd:Ag 3:2	2:19
Pd:Ag 2:1	2.62
Pd:Ni 1:4	1.14
Pd:Ni 1:2	1.11
Pd:Ni 1:1	1.34
Pd:Ni 3:2	1.82
Pd:Ni 2:1	3:22
Pd:Mn 1:4	1.21
Pd:Mn 1:2	3:23
Pd:Mn 1:1	1.96
Pd:Mn 3:2	3:22
Pd:Mn 2:1	1.49

[a] TPO of catalysts after reaction test.

The selectivity and yield of 1,3-butadiene can be enhanced if an appropriate amount of Mn is added as illustrated in Figs. 8 and 9. Addition of Ag inhibits the selectivity, especially at high Ag loadings, as summarized in Table 2. Unlike Ag, Ni improves 1,3-butadiene selectivity at higher Ni loadings. For Mn-promoted Pd/Al$_2$O$_3$ catalysts, low Mn content catalysts (Pd/Mn molar ratios of 3:2 and 2:1) show relatively high selectivity toward 1,3-butadiene. However, increasing the Mn content from Pd/Mn molar ratios of 1:4 to 1:1 does not improve the selectivity for 1,3-butadiene (Fig. 8).

The yield of 1,3-butadiene, which is calculated from conversion and selectivity (Fig. 9), is high when the vinyl acetylene conversion is less than 60%. The yield is then relatively constant for a vinyl acetylene conversion of 60-80%. However, when the conversion is higher than 80%, the yield of 1,3-butadiene drops sharply. In this work, the yield of 1,3-butdiene is highest when the conversion of
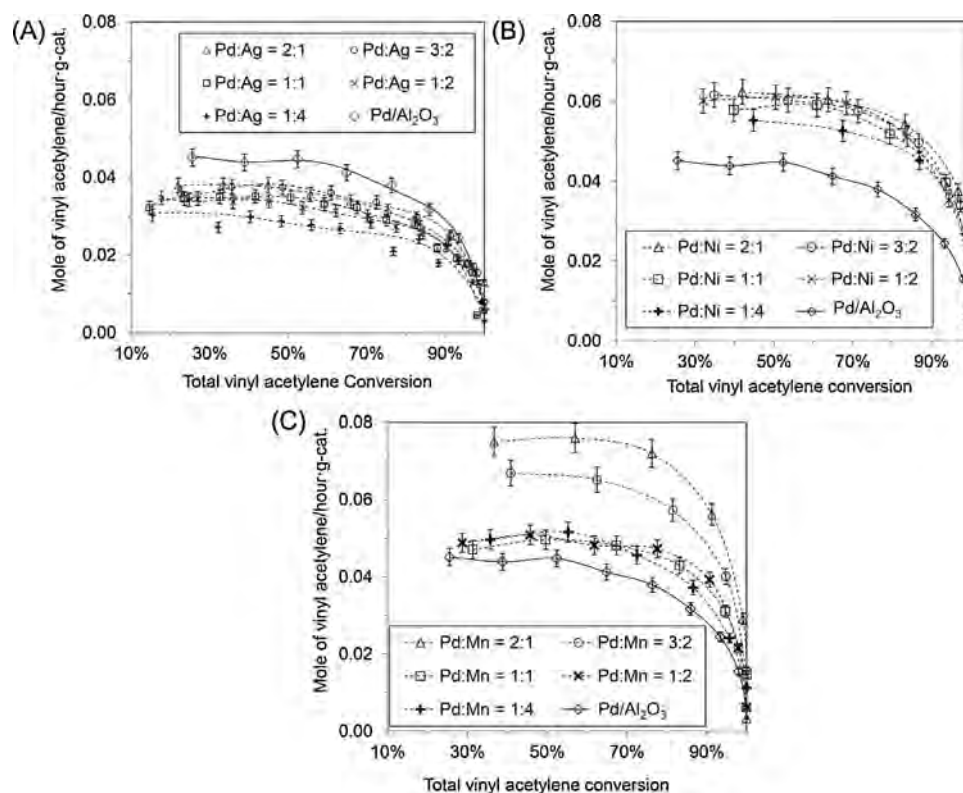
Fig. 7. The rate of vinyl acetylene hydrogenation as a function of vinyl acetylene conversion using Ag-Pd/Al$_2$O$_3$ (A), Ni-Pd/Al$_2$O$_3$ (B) and Mn-Pd/Al$_2$O$_3$ (C) catalysts compared to Pd/Al$_2$O$_3$ catalyst.
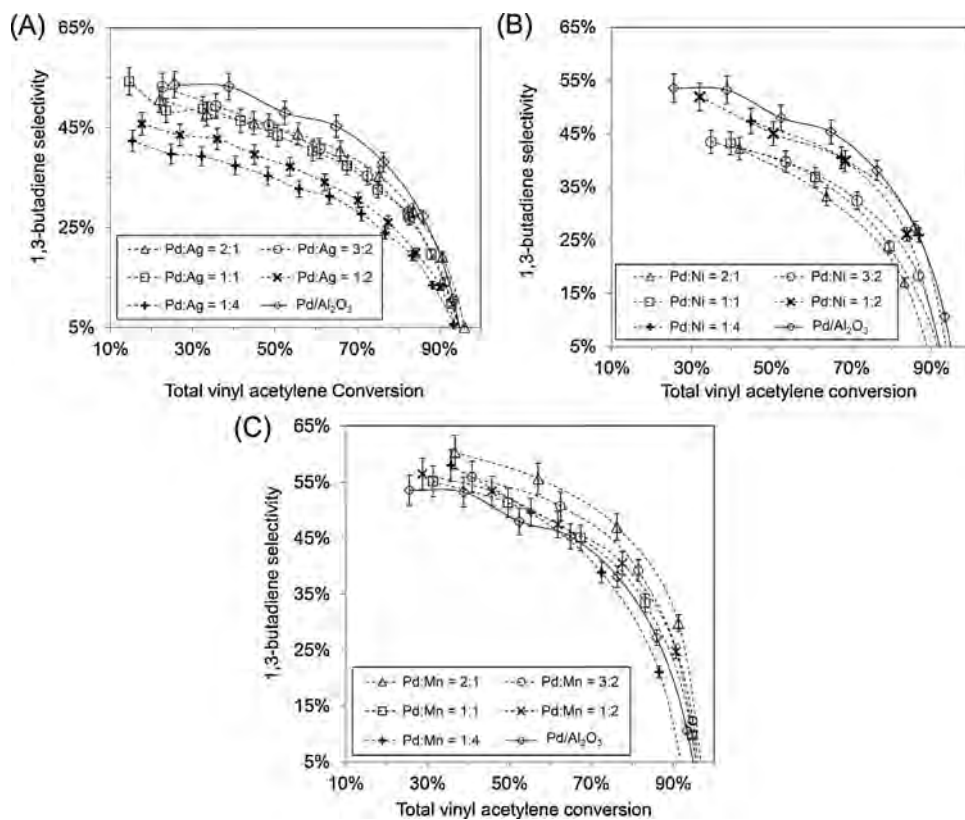
Fig. 8. The selectivity of 1,3-butadiene as a function of vinyl acetylene conversion using Ag-Pd/Al$_2$O$_3$ (A), Ni-Pd/Al$_2$O$_3$ (B) and Mn-Pd/Al$_2$O$_3$ (C) catalysts compared to Pd/Al$_2$O$_3$ catalyst.

Fig. 9. The yield of 1,3-butadiene as a function of vinyl acetylene conversion using Ag-Pd/Al$_2$O$_3$ (A), Ni-Pd/Al$_2$O$_3$ (B) and Mn-Pd/Al$_2$O$_3$ (C) catalysts compared to Pd/Al$_2$O$_3$ catalyst.
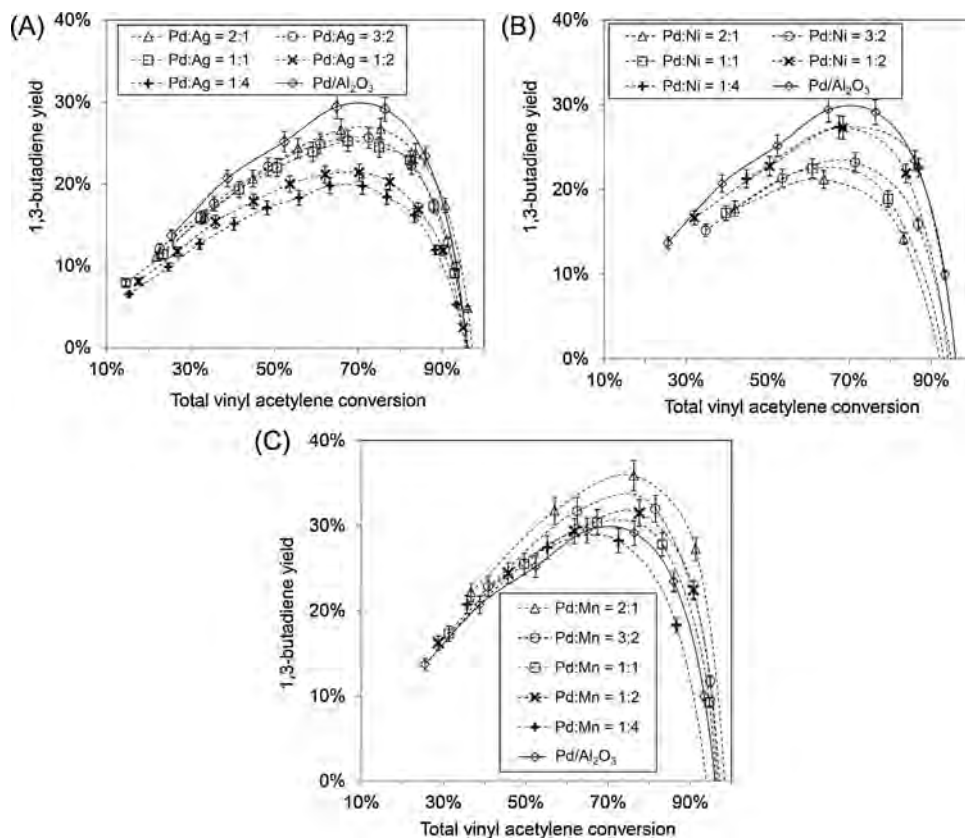
Table 2
Reaction rate of vinyl acetylene and 1,3-butadiene selectivity and yield at 70% vinyl acetylene conversion of unpromoted and promoted Pd/Al_2O_3 catalysts.

Catalyst	Reaction rate mole VA:h·g-catalyst	%1,3-butadiene selectivity	%1,3-butadiene yield
Pd/Al_2O_3	0.0406	46.6	29.9
Pd:Ag 1:4	0.0266	28.3	19.8
Pd:Ag 1:2	0.0302	30.6	21.4
Pd:Ag 1:1	0.0309	35.9	25.2
Pd:Ag 3:2	0.0342	36.8	25.8
Pd:Ag 2:1	0.0330	38.5	26.9
Pd:Ni 1:4	0.0520	39.4	27.5
Pd:Ni 1:2	0.0590	38.9	27.2
Pd:Ni 1:1	0.0566	31.9	22.4
Pd:Ni 3:2	0.0579	33.4	23.4
Pd:Ni 2:1	0.0592	29.4	20.6
Pd:Mn 1:4	0.0471	40.6	28.7
Pd:Mn 1:2	0.0463	44.0	31.3
Pd:Mn 1:1	0.0472	43.8	30.5
Pd:Mn 3:2	0.0625	48.1	33.3
Pd:Mn 2:1	0.0735	50.8	35.6

vinyl acetylene is around 70%. Catalytic performance at the highest yields (70% vinyl acetylene conversion) were compared by calculating the reaction rate, 1,3-butadiene selectivity, and 1,3-butadiene yield, which are listed in Table 2. In summary, the catalysts can be ranked according to the 1,3-butadiene selectivity and yield as following: Mn-Pd/Al$_2$O$_3$ > Pd/Al$_2$O$_3$ > Ni-Pd/Al$_2$O$_3$ > Ag-Pd/Al$_2$O$_3$. The best catalyst, which provides highest 1,3-butadiene yield is Mn-Pd/Al$_2$O$_3$ at a Pd:Mn molar ratio of 2:1. It should be noted that the proper amount of Mn addition to Pd/Al$_2$O$_3$ catalyst enhances both activity and product selectivity for the vinyl acetylene hydrogenation. Adding Ni can accelerate the rate of hydrogenation but lowers selectivity, while adding Ag leads to both lower both reaction rates and product selectivity for this particular reaction.

3.2.3. Temperature programmed oxidation (TPO) of spent catalysts

TPO characterization of the spent catalysts is summarized in Figs. 10–12 and in Table 1 which shows the amount of carbon
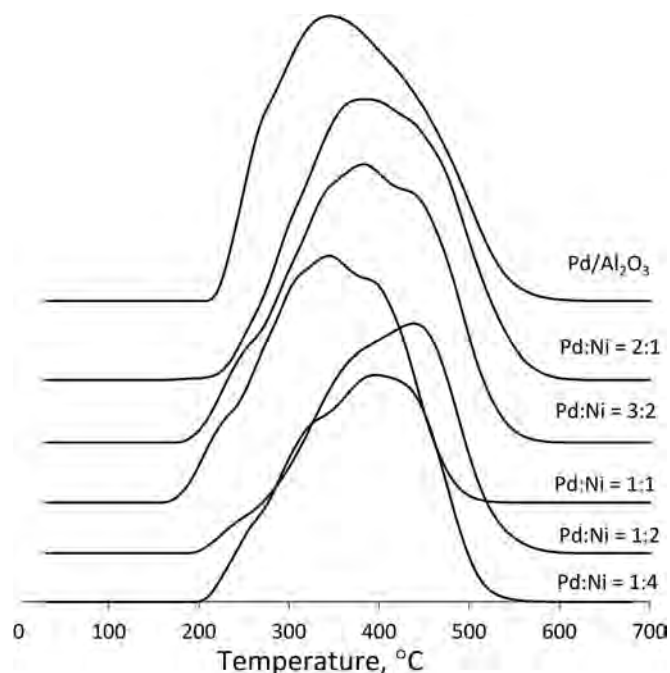
Fig. 11. TPO profiles of spent Ni-Pd/Al$_2$O$_3$ catalysts.

deposited on each catalyst during the testing. The unpromoted Pd/Al$_2$O$_3$ catalyst exhibits lowest deposited carbon content, 1.06%, while Ag-Pd/Al$_2$O$_3$, Ni-Pd/Al$_2$O$_3$ and Mn-Pd/Al$_2$O$_3$ catalysts show the amount of carbon at 2.1–2.6%, 1.1–1.8%, and 1.2–1.9% respectively. However, from the TPO profile, the oxidation temperature of spent Mn-Pd/Al$_2$O$_3$ catalysts is lower than that for the unpromoted Pd/Al$_2$O$_3$ catalyst as shown in Fig. 12. Moreover, this lower oxidation temperature is more pronounced if the catalyst contains a higher amount of Mn (that is, at lower Pd:Mn ratios).

Fig. 10. TPO profiles of spent Ag-Pd/Al$_2$O$_3$ catalysts.

Fig. 12. TPO profiles of spent Mn-Pd/Al$_2$O$_3$ catalysts.

4. Conclusions

Unpromoted and promoted Pd/Al$_2$O$_3$ catalysts have been tested in a liquid phase hydrogenation of concentrated vinyl acetylene-mixed C4 by recirculating reactor. The r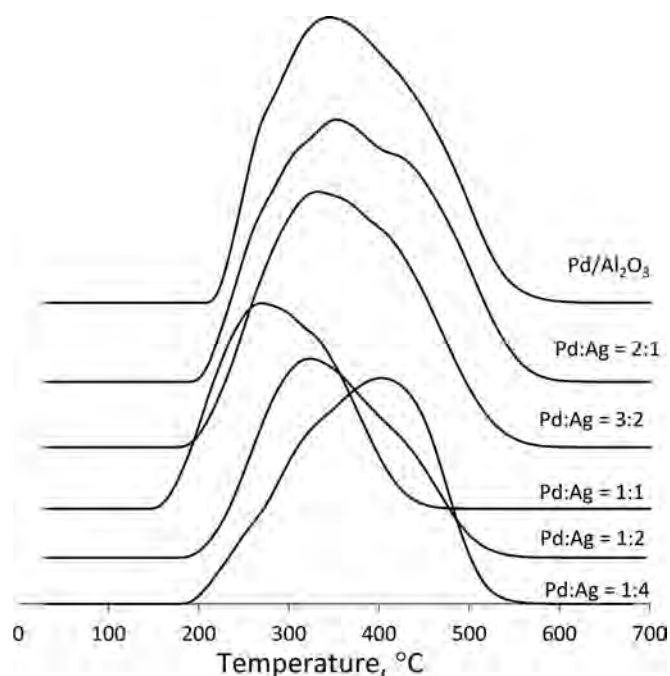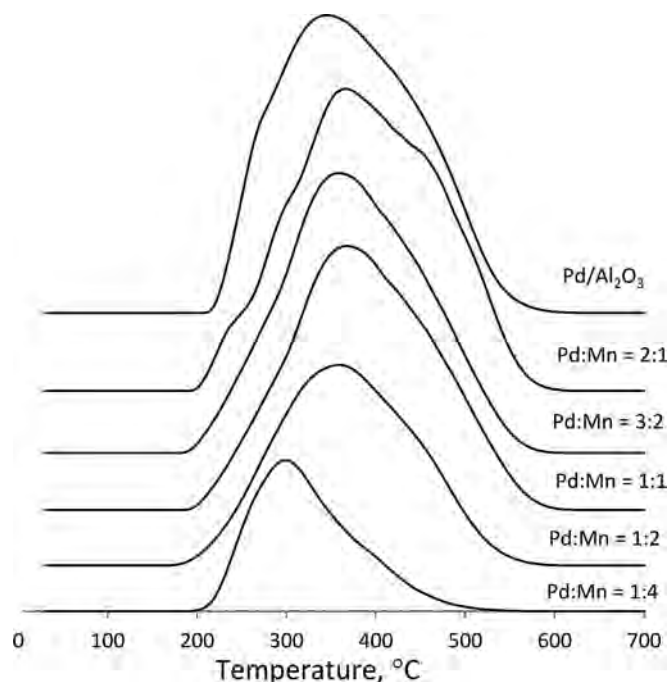esults showed that a Mn-promoted Pd/Al$_2$O$_3$ catalyst at a 2:1 Pd/Mn molar ratio significantly increases the activity and moderately increases the yield and selectivity for 1,3-butadiene. Adding Ni to Pd/Al$_2$O$_3$ catalysts improves only the activity but adding Ag even inhibits the activity. The TPR results suggest the interaction between Pd and the added metals. Furthermore the TPR profile of Pd:Mn 2:1 catalyst indicates interactions between Pd and Mn with no remaining manganese oxide. In addition, TPO results shows that promoted catalysts tend to increase carbon deposition on the catalyst. The amount of deposited carbon on the Mn-promoted catalyst is lower than that of Ag and Ni promoted catalyst.

Acknowledgements

References

[1] W.C. White, Chem. Biol. Interact. 166 (2007) 10.
[2] UOP C4 Processing, vol. 2013, UOP A Honeywell Company, 2013.
[3] T. Adrian, G. Bohner, T. Hill, G. Kaibel, K. Kindler, G. Meyer, M. Pahl, K. Pickenaecker, Method and device for treating a C4 fraction, in: B. Aktiengesellschaft (Ed.), Vol. US20030181772 A1, USA, 2003.
[4] W. Büchele, H. Roos, H. Wanjek, H.J. Müller, Catal. Today 30 (1996) 33.
[5] Butadiene Product Stewardship Guidance Manual, American Chemistry Council Olefins Panel, American Chemistry Council, 2001.
[6] UOP (Ed.), BASF-UOP Butadiene Process, UOP, 2000.
[7] Boosting Butadiene Extraction by Converting Acetylene, in: SK-KBR (Ed.), C4AC Maximizing Butadiene Production.
[8] Butadiene Extraction BASF NMP Process, in: L. GmbH (Ed.).
[9] T. Ikegami, Phys. Chem. Soc. Jpn. 32 (1/2) (1963) 13.
[10] R.A. Koeppel, J.T. Wehrli, M.S. Wainwright, D.L. Trimma, N.W. Cant, Appl. Catal. A: Gen. 120 (1994) 163.
[11] A.A. Lamberov, I.R. Il'yasov, S.R. Egorova, M.V. Nazarov, V.M. Shatilov, Catal. Ind. 1 (2009) 229.
[12] Y.A. Ryndin, M.V. Stenin, A.I. Boronin, V.I. Bukhtiyarov, V.I. Zaikovskii, Appl. Catal. 54 (1989) 277.
[13] Y.A. Ryndin, L.V. Nosova, A.I. Boronin, A.L. Chuvilin, Appl. Catal. 42 (1988) 131.
[14] I. Setiawan, K.J. Cavell, Appl. Catal. A: Gen. 131 (1995) 225.
[15] Y.J. Ryu, J.R. Adams, W.A. Groten, Selective Hydrogenation of Acetylenes, C07C7/167, Catalytic Distillation Technologies, USA, 2008.
[16] Y.J. Ryu, Process for the selective hydrogenation of alkynes, C07C7/167, Catalytic Distillation Technologies, 2004.
[17] A.M. Venezia, L.F. Liotta, G. Deganello, Z. Schay, L. Guczi, J. Catal. 182 (1999) 449.
[18] M. Crespo-Quesada, R.R. Dykeman, G. Laurenczy, P.J. Dyson, L. Kiwi-Minsker, J. Catal. 279 (2011) 66.
[19] D.R. Kennedy, G. Webb, S.D. Jackson, D. Lennon, Appl. Catal. A: Gen. 259 (2004) 109.
[20] D. Teschner, E. Vass, M. Hävecker, S. Zafeiratos, P. Schnörch, H. Sauer, A. Knop-Gericke, R. Schlögl, M. Chamam, A. Wootsch, A.S. Canning, J.J. Gamman, S.D. Jackson, J. McGregor, L.F. Gladden, J. Catal. 242 (2006) 26.
[21] Axens-Headquarters, Axens catalysts and adsorbents, in: Axens (Ed.), Product Listing, 2011.
[22] Süd-Chemie, General catalogue Süd-Chemie catalysts, in: Süd-Chemie (Ed.), Catalyst Index and Contact Details, 2007.
[23] J. Krauter, Continuous Process Catalysts, Accelerating Your Chemistry®, Evonik Industries AG, 2009.
[24] W. Huang, J.R. McCormick, R.F. Lobo, J.G. Chen, J. Catal. 246 (2007) 40.
[25] S.K. Kim, J.H. Lee, I.Y. Ahn, W.-J. Kim, S.H. Moon, Appl. Catal. A: Gen. 401 (2011) 12.
[26] R.B. Moyes, P.B. Wells, J. Grant, N.Y. Salman, Appl. Catal. A: Gen. 229 (2002) 251.
[27] G.-X. Qi, X.-M. Zheng, J.-H. Fei, Z.-Y. Hou, J. Mol. Catal. A: Chem. 176 (2001) 195.
[28] T. Herranz, S. Rojas, F.J. Pérez-Alonso, M. Ojeda, P. Terreros, J.L.G. Fierro, Appl. Catal. A: Gen. 311 (2006) 66.
[29] H. Yin, Y. Ding, H. Luo, H. Zhu, D. He, J. Xiong, L. Lin, Appl. Catal. A: Gen. 243 (2003) 155.
[30] X.X. Han, Q. Chen, R.X. Zhou, J. Mol. Catal. A: Chem. 277 (2007) 210.
[31] X. Han, R. Zhou, G. Lai, B. Yue, X. Zheng, J. Mol. Catal. A: Chem. 209 (2004) 83.
[32] X. Zhou, H. Sun, W. Guo, Z. Liu, S. Liu, J. Nat. Gas Chem. 20 (2011) 53.
[33] D. Cheng, C. Hou, F. Chen, X. Zhan, J. Rare Earths 27 (2009) 723.
[34] J.A. Alves, S.P. Bressa, O.M. Martínez, G.F. Barreto, Chem. Eng. J. 125 (2007) 131.
[35] N.O. Ardiaca, S.P. Bressa, J.A. Alves, O.M. Martínez, G.F. Barreto, Stud. Surf. Sci. Catal. 133 (2001) 527.
[36] J.A. Alves, S.P. Bressa, O.M. Martínez, G.F. Barreto, J. Ind. Eng. Chem. 18 (2012) 1353.

Dissolution of Soap Scum by Surfactants. Part III. Effect of Chelant Type on Equilibrium Solubility and Dissolution Rate of Calcium and Magnesium Soap Scums in Various Surfactant Systems

Sawwalak Itsadanont, Prariyada Theptat, John F. Scamehorn, Sukhwan Soontravanich, David A. Sabatini & Sumaeth Chavadej

JOURNAL OF SURFACTANTS AND DETERGENTS
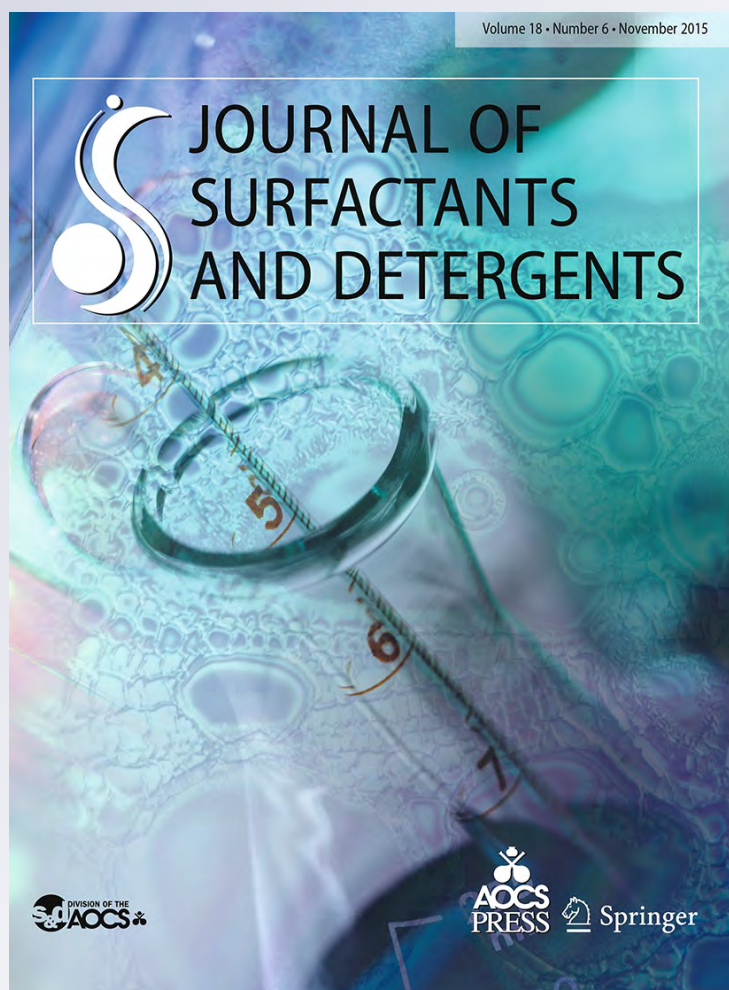
Springer

Springer

CrossMark

ORIGINAL ARTICLE

Dissolution of Soap Scum by Surfactants. Part III. Effect of Chelant Type on Equilibrium Solubility and Dissolution Rate of Calcium and Magnesium Soap Scums in Various Surfactant Systems

Sawwalak Itsadanont[1] · Prariyada Theptat[1] · John F. Scamehorn[2] ·
Sukhwan Soontravanich[2] · David A. Sabatini[2] · Sumaeth Chavadej[1,3]

Abstract Soap scum can be effectively removed by using an appropriate surfactant with a chelating agent at a high solution pH. The equilibrium solubilities and dissolution rates of two model soap scums [calcium stearate and magnesium stearate: $Ca(C_{18})_2$ and $Mg(C_{18})_2$] were investigated in aqueous solutions containing three different types of surfactants [methyl ester sulfonate (MES) as an anionic surfactant; alcohol ethoxylate (EO9) as a nonionic surfactant; and dimethyldodecylamine oxide (DDAO) as an amphoteric surfactant] in the presence of different biodegradable chelants: trisodium ethylenediamine disuccinic acid (Na_3EDDS) and tetrasodium glutamate diacetic acid (Na_4GLDA) compared with disodium ethylenediamine tetraacetate (Na_2EDTA), a chelant with poor biodegradability. The highest equilibrium solubility and dissolution rate of either soap scum were observed at high pH in the DDAO system with Na_4GLDA. In addition, the calcium soap scum had a similar to higher equilibrium solubility and a higher dissolution rate constant as compared with the magnesium soap scum.

Keywords Soap scum · Anionic surfactant · Nonionic surfactant · Amphoteric surfactant · Biodegradable chelating agents

✉ Sumaeth Chavadej
sumaeth.c@chula.ac.th

1 The Petroleum and Petrochemical College, Chulalongkorn University, 254 Soi Chulalongkorn12, Phayathai Rd., Wangmai, Patumwan, Bangkok 10330, Thailand

2 Institute for Applied Surfactant Research, University of Oklahoma, Norman, OK, USA

3 Center of Excellence on Petrochemical and Materials Technology, Chulalongkorn University, Bangkok, Thailand

Introduction

The dissolution rates of two model soap scums [calcium stearate or $Ca(C_{18})_2$, and magnesium stearate or $Mg(C_{18})_2$] have been found to be significantly enhanced by the dissociation of calcium or magnesium ions (hardness cations) by added chelant and the simultaneous formation of mixed micelles using an amphoteric surfactant at high solution pH [1]. In general, calcium (or magnesium) removal from soap scum is aided by either exchange of hardness cations in soap scum by hydrogen ions in an acidic condition or the abstraction of these hardness cations through complexation with ethylenediamine tetraacetate (EDTA).

While acidic formulations for soap scum removal have the disadvantages of corrosion and environmental concerns, they have the advantage of scale (e.g., calcium carbonate) removal. In this study, only soap scum dissolution is addressed.

Mixed micelle formation of the dissociated soap scum and added surfactant requires charge and structural compatibility between the fatty acid and added surfactant in order to significantly enhance soap scum dissolution [2]. The effects of surfactant type, solution pH, and the presence of disodium ethylenediaminetetraacetate (Na_2EDTA) chelant on the equilibrium solubility and dissolution rate of two model soap scums were investigated in our previous papers [1, 3]. The use of amphoteric surfactant dimethyldodecylamine oxide (DDAO) at the highest pH studied (11) was found to give the highest equilibrium solubility and dissolution rate of either calcium or magnesium soap scum. However, the chelant EDTA is coming under increasing scrutiny because of its low biodegradation [4]. At high concentrations, it is toxic to bacteria and mammals since it chelates metal ions in the outer cell membrane affecting cell membrane permeability [5]. Hence, in many

Springer AOCS

developed countries, especially in Western Europe, EDTA's use as a chelant is restricted [6], making identification of alternative chelants with favorable biodegradation profiles of great interest.

An attractive chelant with more favorable biodegradability is ethylenediamine disuccinic acid (EDDS). However, only the (S,S) isomer has biodegradability of more than 60 % [6], while other stereo-isomers of EDDS (RR-, RS-, SR-) are only partly or non-biodegradable [7]. The tetrasodium salt of N,N-bis(carboxymethyl)-L-glutamate (Na$_4$GLDA), marketed as Dissolvine GL-47-S, is another attractive alternative to EDTA [8]. GLDA is classified as a readily biodegradable chelant according to the internationally recognized OECD 301D test [9]. Moreover, according to the Swedish Society for Nature Conservation, GLDA is 86 % based on renewable resources [9] because it is produced from a flavor enhancer of monosodium glutamate (MSG). However, only the L-form of GLDA, whose biodegradability is greater than 83 % [6], is a practical alternative chelant, while the D-form is not biodegradable. In the present study, the equilibrium solubilities and dissolution rates of calcium and magnesium soap scums using these biodegradable chelants and different types of surfactants were investigated.

Experimental

Materials

The (S,S)-ethylenediamine-N,N'-disuccinic acid trisodium salt solution (Na$_3$EDDS) was purchased from Sigma-Aldrich (St. Louis, MO, USA). The tetrasodium salt of N,N-bis(carboxymethyl)-L-glutamate or tetrasodium glutamate diacetic acid (Na$_4$GLDA) was kindly provided by Akzo Nobel Functional Chemicals (Chicago, IL, USA). All other chemicals used in this study were described in Part I of this series [1].

Methods

Synthesis Procedure of Soap Scums

The synthesis methods of both calcium and magnesium soap scums were described in Part I of this series [1].

Soap Scum Equilibrium Solubility

An excess of the synthesized calcium or magnesium soap scum was added to a solution containing different surfactants at a concentration of 0.1 M with varying chelating agents (0.1 M of chelant concentration) at a range of

equilibrium pH values. All solutions were prepared at pH values in the range of 4–11 using HCl and NaOH solutions and heated to around 70 °C in a water bath for 3 h. Next, the solutions were equilibrated at 25 °C in a temperature-controlled water bath for at least 1 week with routine shaking. After that, the solutions were filtered using a 0.2-μm nylon filter membrane to remove the remaining undissolved soap scum. Finally, concentrations of dissolved calcium or magnesium ions in the clear solutions were analyzed by an atomic absorption spectrophotometer (AAS) (SpectrAA-300; Varian). The average results were obtained from at least three replicate measurements with less than 1 % variance.

Kinetic Experiments

Figure 1 shows the experimental set-up of the flow cell apparatus used in this study to determine the dissolution rates of calcium and magnesium soap scums under different conditions. A quantity of 0.95 g of the synthesized soap scum (calcium or magnesium soap scum) was placed in between two 0.22-μm nylon membranes of a filter cartridge (Whatman, 1980-002). A 0.1-M DDAO solution with 0.1 M of different chelating agent types (Na$_2$EDTA, Na$_3$EDDS, or Na$_4$GLDA) was fed continuously to dissolve the calcium or magnesium soap scum sample placed in the filter cartridge at a constant flow rate of 1 mL/min and a pH of 11. The kinetic method was described in Part II of this series [3].

Results and Discussion

Solubilities of Soap Scums with Chelating Agents in Surfactant-free Solutions

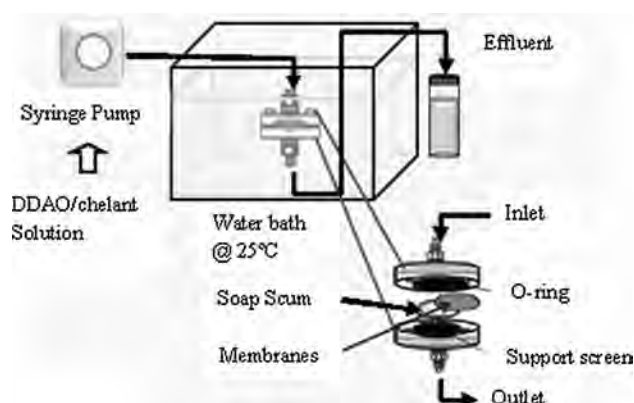Figure 2 shows the equilibrium solubilities of both soap scums [Ca(C$_{18}$)$_2$ and Mg(C$_{18}$)$_2$] in different chelant

Fig. 1 Flow cell apparatus used in this study

Fig. 2 Equilibrium solubilities of $Ca(C_{18})_2$ and $Mg(C_{18})_2$ in different chelant systems as a function of pH and at a constant temperature of 25 °C
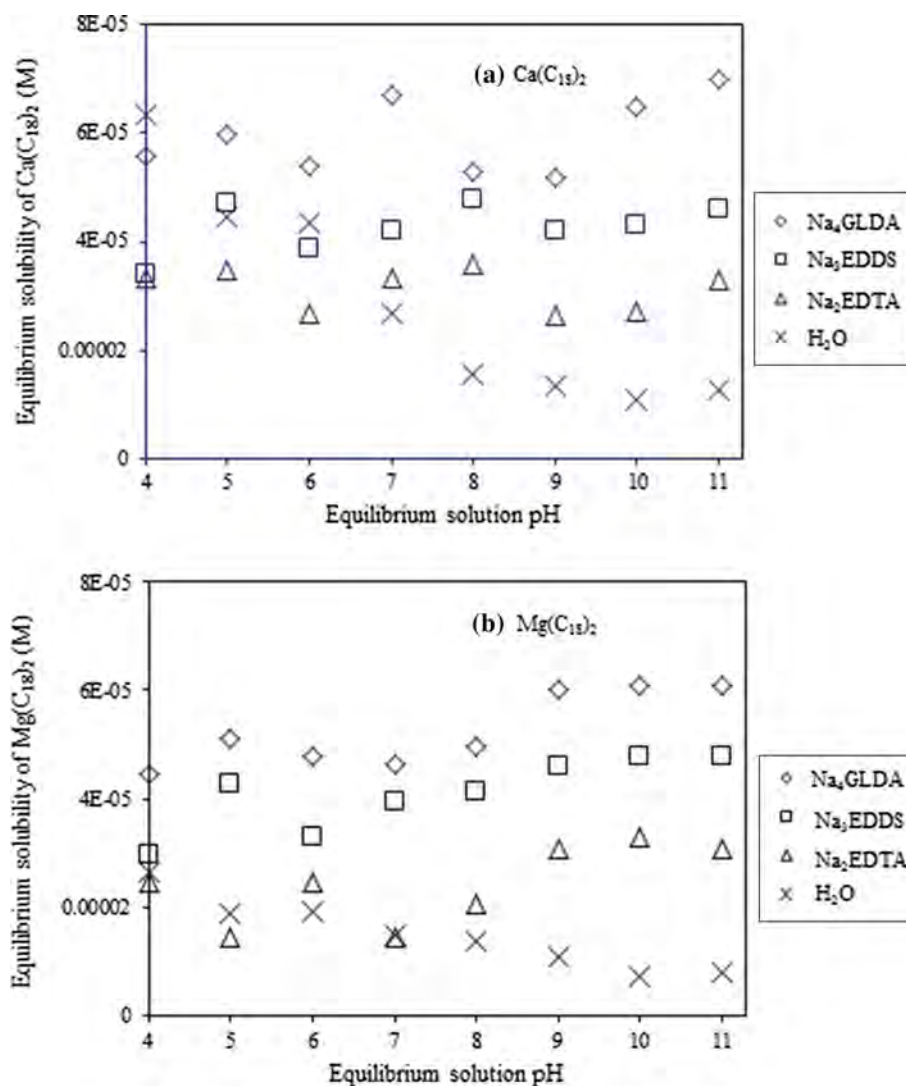
solutions as a function of equilibrium solution pH. The use of chelant (Na₄GLDA, Na₃EDDS or Na₂EDTA) alone has little effect on soap scum solubility and gives a very low solubility at any given solution pH. The effectiveness of chelating agents for soap scum dissolution is in the following order: Na₄GLDA > Na₃EDDS > Na₂EDTA. However, the equilibrium solubility of each studied soap scum in an aqueous solution containing any studied chelant is significantly higher than that of pure water, especially at high solution pH values. The results can be explained by the fact that, at low solution pH, soap scum can be protonated to form nonionic stearic acid. In addition, the chelants are also protonated, resulting in less effective chelation of hardness cations. Although the most effective chelant form appears at a high solution pH, the dissolution of soap scum was found to be very low because the stearate anion has a very low solubility (as quantified by a small solubility product or Ksp) at high pH.

From Fig. 2, Na₄GLDA had the highest equilibrium solubility for both calcium and magnesium soap scums. The chelant form depends on solution pH (H_4Y, H_3Y^-, H_2Y^{2-}, HY^{3-}, and Y^{4-}) [2]. The most effective chelant forms to bind with hardness cations are HY^{3-} and Y^{4-} which exist at very high solution pH, with Y^{4-} being the most effective form. At high solution pH, the Na₄GLDA dissociates in water to yield the most effective form of Y^{4-}, while Na₃EDDS and Na₂EDTA exist in the less effective form as HY^{3-} and H_2Y^{2-}, respectively. However, the solubilities of both soap scums in chelant-only systems are still very low because at high solution pH, soap scum is dissociated to the stearate anion which has very low water solubility. The solubility is less than the CMC for the $Ca(C_{18})_2$ and $Mg(C_{18})_2$, so no micelles form in the absence of a co-surfactant.

Comparing the two model soap scums, in pure water or chelant systems, the solubility of calcium soap scum is

higher than that of magnesium soap scum at all pH levels, consistent with solubility product values from the literature [10]. As discussed in Part I of this series [1], calcium has a higher stability constant than magnesium [11] with Na_2EDTA, so calcium soap scum has a higher equilibrium solubility than magnesium soap scum for the Na_2EDTA system. However, for the Na_4GLDA or Na_3EDDS systems, the stability constant of magnesium was found to be slightly higher than that of calcium [11]. The higher solubility of $Ca(C_{18})_2$ compared to $Mg(C_{18})_2$ for Na_4GLDA and Na_3EDDS suggests that the effect of water solubility of $Ca(C_{18})_2$ and $Mg(C_{18})_2$ on soap scum dissolution is greater than the effect of stability constant between hardness cations and chelants.

Solubilities of Soap Scum with Surfactant

The equilibrium solubility of the two model soap scums [$Ca(C_{18})_2$ and $Mg(C_{18})_2$] in different surfactant solutions with different chelating agents at various solution pHs is presented in Fig. 3. All three surfactants studied significantly increase soap scum solubilities in either the presence or absence of each chelant (Na_4GLDA or Na_3EDDS or Na_2EDTA), as compared to the pure water and chelant-only systems. The improvement of the equilibrium solubility of soap scum depends on chelant complexation with hardness cations and on mixed micelle formation between added surfactants and fatty acids as described in Parts I and II of this series [1, 3].

With the anionic MES surfactant (Fig. 3a, b), the equilibrium solubility of either calcium or magnesium soap scum decreases with increasing solution pH for all three chelants. As discussed in detail in Part I of this series [1], as pH increases, a lower fraction of the fatty acid is protonated, so it is more anionic. At low pH, the protonated fatty acid has greater synergism in mixed micelle formation with the anionic MES than at high pH with anionic fatty acid and anionic MES. As discussed in the previous section of this paper, the chelation ability of all chelants increases as pH increases. Thus, the micelle synergism effect overcomes the chelant complexation effectiveness and soap scum solubility increases with decreasing pH for the anionic co-surfactant.

In the MES system, the effectiveness of chelating agents for soap scum dissolution is in the following order: $Na_4GLDA > Na_3EDDS > Na_2EDTA$ at a pH of 4 and $Na_4GLDA \approx Na_3EDDS > Na_2EDTA$ at pH values in the range of 5–11. From the previous section, the order of effectiveness in the absence of any surfactant is $Na_4GLDA > Na_3EDDS > Na_2EDTA$, so this same order is observed with the anionic co-surfactant. The calcium soap has a modestly higher solubility than the magnesium soap, consistent with surfactant-free system results. So,

solubility enhancement of the fatty acid molecule by mixed micellization still dictates the order of solubility over stability constants for different hardness ions and all ligands in complexation with MES. Further, the choice of chelant significantly improves solubility for the calcium soap scum, from an average of 101 % for Na_4GLDA to 62 % for Na_3EDDS, and to 22 % for Na_2EDTA, and for the magnesium soap scum, from an average of 190 % for Na_4GLDA to 190 % for Na_3EDDS, and to 69 % for Na_2EDTA at pH 4.

The data in Fig. 3 show that, for the EO9 surfactant system, the equilibrium solubilities of both calcium and magnesium soap change little with pH in the absence of chelant, but increase with pH in the presence of each chelant. This chelant effect is opposite to the trend in the MES system. The low equilibrium solubility at low pH can be explained by the fact that the synergism of nonionic stearic acid/nonionic EO9 surfactants to form mixed micelles is low, leading to low equilibrium solubilities of soap scum. Conversely, at a high solution pH, formation of anionic stearate/nonionic EO9 mixed micelles is synergistic, such as the increased complexation constants of hardness cations with ligands. However, in the absence of chelant, the greater synergism of the anionic/nonionic mixed micelles at high pH is probably offset by the decreasing water solubility of the soap scum.

For the EO9 system, the equilibrium solubility of soap scum is in the following order: $Na_4GLDA \approx Na_3EDDS > Na_2EDTA$. The chelant addition in the EO9 system substantially improves the solubility for the calcium soap scum, from an average of 352 % for Na_4GLDA to 300 % for Na_3EDDS, and to 111 % for Na_2EDTA, and for the magnesium soap scum, from an average of 64 % for Na_4GLDA to 64 % for Na_3EDDS, and to 15 % for Na_2EDTA at pH 11. The equilibrium solubility of calcium soap scum is significantly higher than that of magnesium soap scum for any added chelant at all studied pH values. As with the MES surfactant, this is because the Ksp of calcium soap scum is greater than that of magnesium soap scum [10].

The highest equilibrium solubilities of both soap scums were found in the DDAO system (Fig. 3), and are much higher than those in the MES and EO9 systems due to the greater mixed micelle synergism of nonionic stearic acid/cationic DDAO at a low solution pH and stearate anion/zwitterionic DDAO at a high solution pH. As pH increases, the greater mixed micelle synergism as well as the fact that all chelants complex hardness cations more effectively at higher pH cause higher equilibrium solubility for all chelant systems. The effectiveness in equilibrium soap scum dissolution is in the order of $Na_4GLDA > Na_3EDDS > Na_2EDTA$ for the calcium soap scum and $Na_4GLDA \approx Na_3EDDS \approx Na_2EDTA$ for the
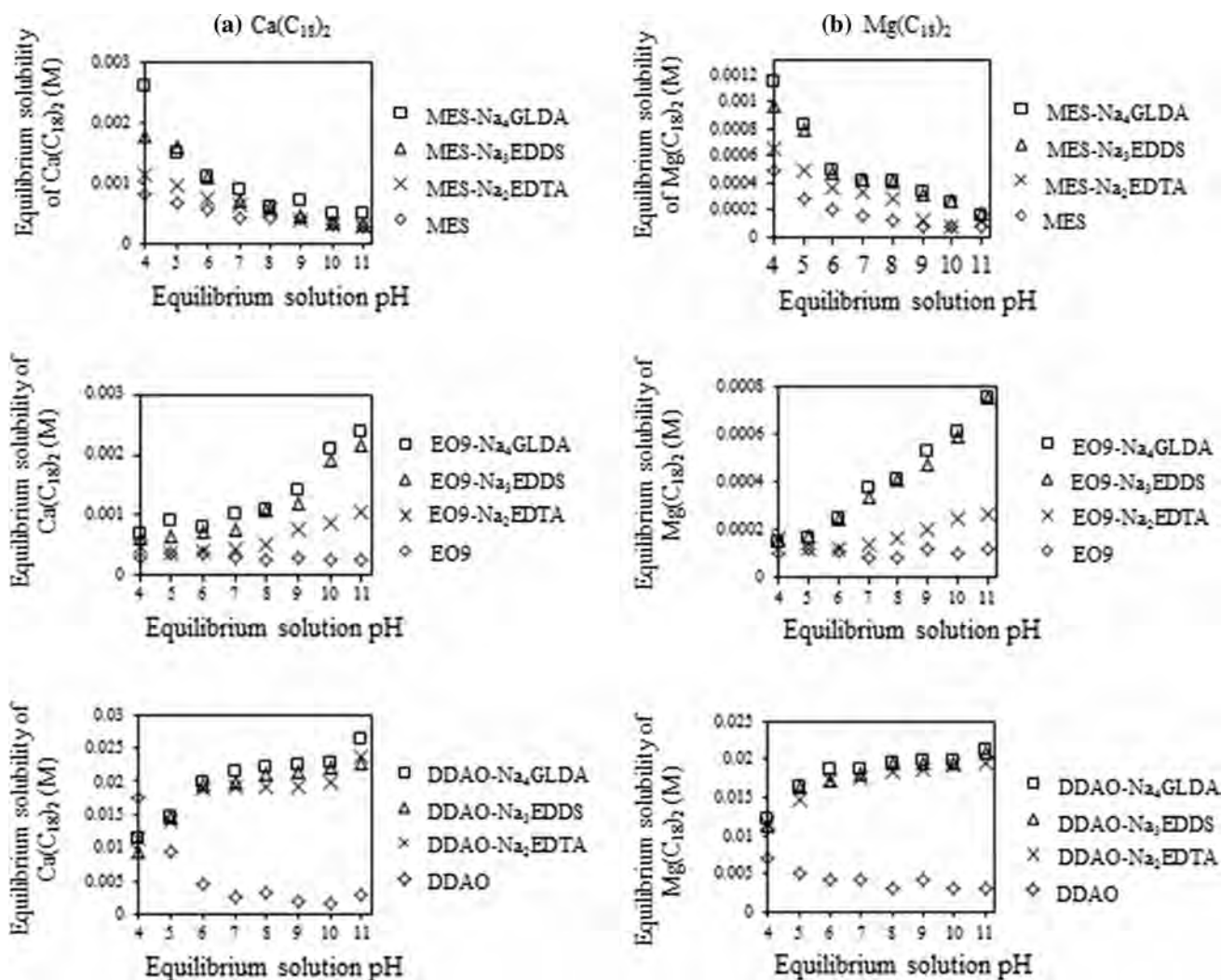
Fig. 3 Equilibrium solubility of $Ca(C_{18})_2$ and $Mg(C_{18})_2$ in different surfactant solutions, as a function of pH at a constant temperature of 25 °C

magnesium soap scum. The calcium soap scum has similar solubility to the magnesium soap scum. The presence of chelant in the DDAO system greatly improves equilibrium solubility, especially at a high pH [11], for calcium soap scum, from an average of 595 % for Na_4GLDA to 551 % for Na_3EDDS, and to 512 % for Na_2EDTA, and for magnesium soap scum, from an average of 379 % for Na_4GLDA to 369 % for Na_3EDDS, and to 349 % for Na_2EDTA.

For all studied surfactant systems, the presence of the chelant significantly increases soap scum solubility (from 15 to 595 %). The improvement resulting from the presence of the chelant increases as the mixed micelle synergism between the soap and the added surfactant increases. The highest solubility is for the amphoteric surfactant (DDAO) at high pH levels. The order of effectiveness of the three chelants studied was the same for all surfactants as for the chelants alone: $Na_4GLDA > Na_3EDDS > Na_2EDTA$.

Dissolution Rates of Soap Scums

The dissolution rates of the two model soap scums in the DDAO solutions with Na_2EDTA were found to follow first-order kinetics in our previous study (Part II of this series) [3]. To quantify the rate, the initial rate constant (k_i) was used in the previous study because the soap scum dissolution often reached 100 % dissolved early which is not the case here. In the present study, the overall rate constant (k) is more appropriate to fit the set of data and describes the overall data better than the initial rate constant (k_i). The overall rate constant (k) was the best fit to data over the 30 min of soap scum dissolution experiments. This was calculated from the slope of the plot between $[-\ln[M/M_0]]$ versus time. The values of R^2 of all rate constants for all experiments were in the range of 0.96–1.00, confirming that the soap scum dissolution rates follow first-order kinetics.

Figure 4 compares experimental dissolution data as a function of time to the theoretical first-order dissolution kinetics as shown by the solid lines generated by using the best fit k values for each system. Shown are $Ca(C_{18})_2$ and $Mg(C_{18})_2$ in DDAO solutions with different chelants. From Fig. 4, the highest rate constant of any soap scum was observed in the DDAO/Na_4GLDA system. Table 1 shows the equilibrium solubility and k-value of all systems at pH 11. From the table, the rate constants and equilibrium solubilities of three calcium and three magnesium systems did not exhibit substantial variation between different ligand types. For the calcium systems, the solubility only varied by 16 % and rate constants by 41 % between the different ligands. For the magnesium systems, the solubility only varied by 9 % and rate constants by 21 %

between the different ligands. From the results, rate constants increase with solubilities for calcium systems, but the variables do not correlate for magnesium. But the solubility varies so little between ligand systems that the lack of correlation is not significant. Previous studies of variables such as surfactant type have shown a clear correlation between increasing soap scum solubility and increasing rate of dissolution, but large effects of variable were seen there. So, these results of ligand type effects neither support nor contradict those previous correlations. The DDAO/Na_4GLDA system provides the highest equilibrium solubility and dissolution rate for both model soap scums. The calcium soap scum was found to give higher equilibrium solubility and dissolution rate than the magnesium soap scum for all three chelants.
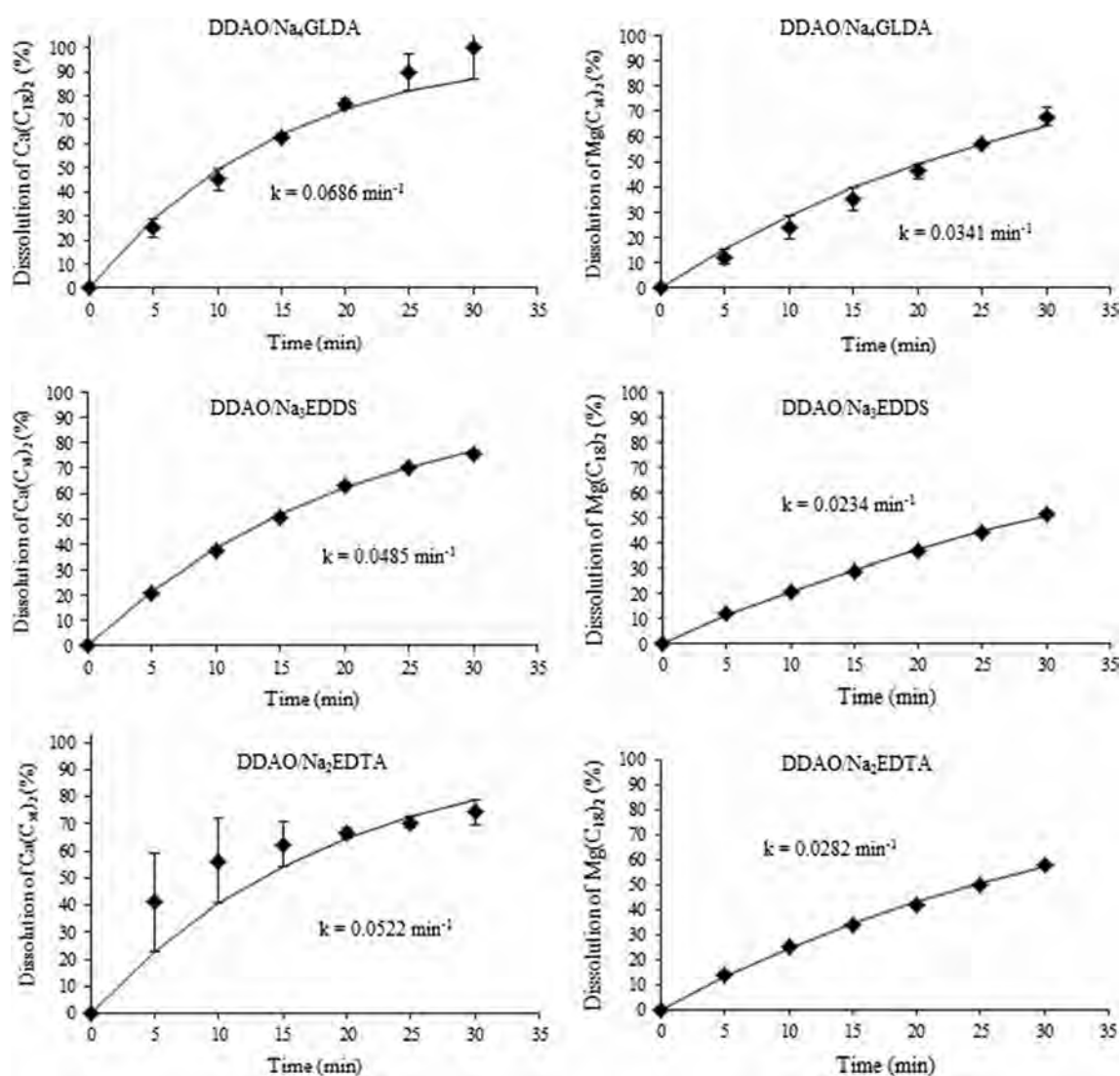

Fig. 4 Dissolution of $Ca(C_{18})_2$ and $Mg(C_{18})_2$ as a function of time in 0.1 M DDAO with different chelant solutions at a temperature of 25 °C and a pH of 11 (flow rate: 1 mL/min, initial soap scum 0.95 g)

Table 1 Equilibrium solubility and rate constant or k-value of all systems at pH 11

System	$Ca(C_{18})_2$		$Mg(C_{18})_2$	
	Equilibrium solubility (M)	k overall (min^{-1})	Equilibrium solubility (M)	k overall (min^{-1})
DDAO/Na$_4$GLDA	0.02625	0.0686	0.02123	0.0341
DDAO/Na$_3$EDDS	0.02260	0.0485	0.02095	0.0234
DDAO/Na$_2$EDTA	0.02358	0.0522	0.01942	0.0282

References

1. Itsadanont S, Scamehorn JF, Soontravanich S, Sabatini DA, Chavadej S (2013) Dissolution of soap scum by surfactant. Part I. Effects of chelant and type of soap scum. J Surfact Deterg 17:849–857

2. Soontravanich S, Lopez HE, Scamehorn JF, Sabatini DA, Scheuing DR (2010) Dissolution study of salt of long chain fatty acids (soap scum) in surfactant solutions. Part I. Equilibrium dissolution. J Surfact Deterg 13:367–372

3. Itsadanont S, Ratanalert D, Soontravanich S, Scamehorn JF, Sabatini DA, Chavadej S (2013) Dissolution of soap scum by surfactant. Part II. Effects of NaCl and added chelant on equilibrium solubility and dissolution rate of calcium soap scum in amphoteric surfactant solutions. J Surfact Deterg 17:859–864

4. Leštan D, Luo C, Li X (2008) The use of chelating agents in the remediation of metal-contaminated soils: a review. J Environ Pollut 153:3–13

5. Handcock REW (1984) Alterations in outer membrane permeability. Ann Rev Microbiol 38:237–264

6. Kołodyńska D (2011) Cu(II), Zn(II), Co(II) and Pb(II) removal in the presence of the complexing agent of a new generation. J Desalin 267:175–183

7. Schowanek D, Feijtel TCJ, Perkins CM, Hartman FA, Federle TW, Larson RJ (1997) Biodegradation of [S, S], [R, R] and mixed stereoisomers of ethylene diamine disuccinic acid (EDDS), a transition metal chelator. J Chemosp 34:2375–2391

8. Azko Nobel introduces a new biodegradable chelating agent. http://www.chemserv.com/pdf/Dissolvine%20GL%20Article.pdf. Accessed Aug 2013

9. Azko Nobel functional chemicals chelates: Dissolvine® GL Technical Brochure. http://www.akzonobel.com/dissolvinegl/system/images/AkzoNobel_Gl_Technical_brochure_tcm80-42056.pdf. Accessed Aug 2013

10. Callander J, Barford JP (2004) Precipitation, chelation, and the availability of metals as nutrients in anaerobic digestion. I. Methodoloty. Biotechnol Bioeng. doi:10.1002/bit.260250805

11. Kołodyńska D (2011) Chelating agents of a new generation as an alternative to conventional chelators for heavy metal ions removal from different waste waters. Expanding Issues in Desalination. Maria Curie-Skłodowska University, Poland, pp 339–370

Sawwalak Itsadanont received her B.Eng. (2007) in Petrochemicals and Polymeric Materials from Faculty of Engineering and Industrial Technology, Silpakorn University, and her Ph.D. in the Petrochemical Technology Program at The Petroleum and Petrochemical College, Chulalongkorn University, Thailand. Currently, she holds a post-doctoral fellowship at Chulalongkorn University.

Prariyada Theptat received a B.Sc. in Chemical Engineering and a M.Sc. in Petrochemical Technology from Chulalongkorn University in Bangkok, Thailand. She is a process safety analyst at Chevron, Thailand.

John F. Scamehorn is Emeritus Director of the Institute for Applied Surfactant Research at the University of Oklahoma where he is Asahi Glass Chair Emeritus in Chemical Engineering. He received his B.Sc. and M.Sc. at the University of Nebraska and his Ph.D. at the University of Texas, all in chemical engineering. Dr. Scamehorn has worked for Shell, Conoco, and DuPont and has been on a number of editorial boards for journals in the area of surfactants and of separation science. He has coedited five books and coauthored over 200 technical papers. His research interests include surfactant properties important in consumer product formulation and thermodynamics of surfactant aggregation processes.

Sukhwan Soontravanich received a B.Sc. in Chemical Engineering and M.Sc. in Petroleum Engineering from Chulalongkorn University in Bangkok, Thailand, and a Ph.D. in Chemical Engineering from the University of Oklahoma in the USA. Currently, she is a lead chemist at Ecolab.

David A. Sabatini is David Ross Boyd Professor and Sun Oil Company Endowed Chair of Civil Engineering and Environmental Science, Associate Director of the Institute for Applied Surfactant Research and Director of the WaTER Center at the University of Oklahoma. He received his B.Sc. from the University of Illinois (1981), his M.Sc. from Memphis State University (1985), and his Ph.D. from Iowa State University (1989). His research focuses on surfactant-based environmental technologies, advanced microemulsion systems for vegetable oil extraction, biofuel production and cleaning systems, and sustainable technologies for drinking water treatment in developing countries.

Sumaeth Chavadej is a professor at The Petroleum and Petrochemical College, Chulalongkorn University. He received his B.Sc. in chemical engineering from Chulalongkorn University (1971), his

M.Sc. in public health engineering from The University of Newcastle upon Tyne (1978), and his Ph.D. in chemical engineering from Monash University, Australia (1985). He has published more than 140 articles in international journals. His research focuses on the areas of applied surfactants, low-temperature plasma for chemical conversion and air pollution control, biohydrogen and biomethane, and photocatalysis.

Hydrogen and methane production from cassava wastewater using two-stage upflow anaerobic sludge blanket reactors (UASB) with an emphasis on maximum hydrogen production

CrossMark

Patcharee Intanoo [a], Patcharaporn Chaimongkol [b], Sumaeth Chavadej [b,c,*]

[a] Department of Industrial Chemistry and Textile Technology, Faculty of Science, Maejo University, Chiang Mai 50290, Thailand
[b] The Petroleum and Petrochemical College, Chulalongkorn University, Soi Chula 12, Phyathai Road, Pathumwan, Bangkok 10330, Thailand
[c] Center of Excellence on Petrochemical and Materials Technology, Chulalongkorn University, Bangkok 10330, Thailand

ABSTRACT

The objective of this study was to produce hydrogen and methane from cassava wastewater using two steps of upflow anaerobic sludge blanket reactors (UASB), emphasizing maximum hydrogen production. For the first hydrogen production stage, the UASB system was operated at 37 °C and pH 5.5 at different COD loading rates. A maximum specific H_2 production rate of 0.39 l H_2/l d and a maximum H_2 yield of 39.83 l H_2/kg COD removed were found at a COD loading rate of 25 kg/m^3d and the gas produced contained 36.4% H_2, and 63.6% CO_2 without methane. For the second methane production stage, the UASB was fed by the effluent produced from the hydrogen production step operated at the optimum COD loading rate. A maximum specific CH_4 production rate of 0.91 l CH_4/l d and a maximum CH_4 yield of 115.23 l CH_4/kg COD removed were found at a COD loading rate of 8 kg/m^3d. The inhibition levels of organic acids to acidogens and methanogens were found to be 10,000 and 400 mg/l as acetic acid, respectively.

Copyright © 2015, Hydrogen Energy Publications, LLC. Published by Elsevier Ltd. All rights reserved.

Introduction

Anaerobic digestion is a biological degradation process to convert organic compounds such as carbohydrates, proteins, and fats, into methane and carbon dioxide, known as biogas, in the absence of dissolved oxygen. It is widely used to stabilize the excess sludge from aerobic treatment systems and is currently applied for treating high strength wastewaters to produce biogas, as well as to reduce post-treatment costs [1]. One industrial wastewater, Cassava wastewater, is considered to be feasible economically for biogas production. In Thailand,

* Corresponding author. The Petroleum and Petrochemical College, Soi Chulalongkorn 12, Phayathai Road, Pathumwan, Bangkok 10330, Thailand. Tel./fax: +66 2 218 4139.
E-mail address: sumaeth.c@chula.ac.th (S. Chavadej).

several cassava factories have already been employed mostly covering anaerobic ponds to produce biogas economically.

The anaerobic digestion process consists of four sequential steps of hydrolysis, acidogenesis, acetogenesis and methanogenesis [2]. Firstly, complex organic compounds are hydrolyzed by external enzymes secreted by hydrolytic bacteria to form water soluble simple organic compounds. For the acidogenic step, soluble simple organic compounds are converted into organic acids, carbon dioxide, hydrogen and alcohols by acidogenic bacteria (acidogens). For the third step of acetogenesis, the organic acids produced are further broken down to acetic acid, carbon dioxide and hydrogen. Both hydrogen and acetic acid are finally converted into methane and carbon hydroxide in the final step of methanogenesis [3]. To gain more profit and higher energy conversion efficiency, the hydrogen produced in both steps of acidogenesis and acetogenesis has to be separated immediately once it is produced. This can be done by using a two-stage anaerobic system. A first bioreactor is used to produce hydrogen, which is taken out from the system while the effluent containing mostly organic acids is directly pumped to a second bioreactor to convert the produced organic acids into methane and carbon dioxide. The hydrogen produced in this bioreactor is also converted to methane [3].

Cassava wastewater has been investigated for hydrogen and methane production, as reported in our previous works [4–6]. Intanoo et al. [4] studied hydrogen and methane production from cassava wastewater by using a two-stage UASB under the thermophilic temperature (55 °C). The maximum hydrogen production rate of 2.2 L/d and the highest H_2 yield of 80.25 ml H_2/g COD removed were found at a COD loading rate of 90 kg/m^{3}d, whereas the highest CH_4 yield of 183.31 ml CH_4/g COD removed was found at the same optimum COD loading rate. Wangmor [5] also studied hydrogen and methane production from cassava wastewater with added cassava residue under a thermophilic two-stage UASB process. The maximum H_2 and CH_4 yields of 15 ml H_2/g COD removed and 259 ml CH_4/g COD removed, respectively were found at an optimum cassava residue concentration of 1200 mg/l. Limwattanalert [6] studied hydrogen production from ethanol wastewater by using an upflow anaerobic sludge blanket (UASB) reactor under the mesophilic temperature (37 °C). At an optimum COD loading rate of 30 kg/m^{3}d based on H_2 UASB volume, the system provided the highest hydrogen production performance in terms of the maximum H_2 yield (114.5 ml H_2/g COD removed) and the maximum SHPR (46.1 ml H_2/g MLVSS d) corresponding to the maximum COD removal efficiency.

The main objective of this study was to investigate the use of the effluent from a hydrogen UASB treating cassava wastewater for the further production of methane. For the first step of hydrogen production, the UASB was operated at 37 °C and pH 5.5 in order to maximize the hydrogen production efficiency. The effluent from the first bioreactor operated at the optimum COD loading rate was further fed to the second methane bioreactor to produce methane without pH control. The results of this investigation can be used as the base performance for both production of hydrogen and methane from starch-rich cassava wastewater with the emphasis on maximum hydrogen production.

Materials and methods

Seed sludge preparation

A bacterial sludge sample, collected from the bottom of a first anaerobic pond treating a cassava wastewater of Sahamitr Tapioca factory at Chonburi, Thailand, was used as a seed sludge for both bioreactors in this study. The pH and total suspended solids (TSS) of the seed sludge sample were 4.5 and 54 g/L, respectively. Before being introduced into the bioreactors, the sludge was screened by sieving to eliminate large particulates and inorganic materials. The screened sludge was boiled at 95 °C for 15 min in order to eliminate methane-producing bacteria and to enrich hydrogen-producing bacteria before being added to the bioreactors for the first hydrogen production stage [7,8]. For the second methane production stage, the screened sludge was not boiled. For each start-up, an initial microbial concentration was about 20,000 mg/l in terms of MLSS (Mixed Liquors Suspended Solids).

Studied wastewater

The cassava wastewater was also obtained from the same factory. It was screened by sieving to remove large solid particles and kept at 4 °C before use. The cassava wastewater had chemical oxygen demand (COD) values in the range of 19000–22000 mg/l and a ratio of COD: nitrogen: phosphorous of 100:0.7:2.3, indicating that the studied wastewater contained insufficient nitrogen for anaerobic degradation but the phosphorus content was sufficient for bacterial growth (the theoretical ratio of COD:N:P = 100:1:0.4 for anaerobic decomposition for biogas production [4,7,8]). Therefore, NH_4HCO_3 was only added to the cassava wastewater to obtain a COD:N ratio of about 100:1. The cassava wastewater with the nitrogen supplement was fed to both bioreactors for the hydrogen production rate.

UASB operation

For the first step of hydrogen production, two identical units of UASB reactors were constructed from borosilicate glass with a 24 L working volume with a water jacket. The temperature inside both bioreactors was controlled to be constant at 37 °C by circulating water through the water jacket by a circulating/heating bath. The cassava wastewater was fed continuously to the bottom of each UASB at different flow rates by using a peristaltic pump in order to obtain different COD loading rates (10, 20, 25, and 30 kg/m^{3}d). The effluent pH was maintained at pH 5.5 using a pH controller and a recycle ratio of the effluent flow rate to feed flow rate was fixed at 1:1. At any given COD loading rate, the hydrogen UASB system was operated to reach a steady state before samples of effluents and produced gas were taken for measurement and analysis. The steady state was justified when both the gas production rate and the effluent COD value were invariant with time. For each COD loading, it took about 10 d to reach a steady state. The experimental data, under steady state conditions, were averaged and this data were used to access the process performance.

For the second methane production step, the effluent from the hydrogen UASB operated at an optimum COD loading rate was used as a feed to both methane UASB units at different COD loading rates under 37 °C without pH control. To minimize the degradation rate of effluent from the hydrogen UASB units, the effluent sample was kept refrigerated at 4 °C until use. The same two UASB units were started with the seed sludge without heat treatment. At any given COD loading rate (2, 4, 6, 8, and 10 kg/m^{3}d), the studied UASB system was operated to reach a steady state before effluent and produced gas samples were taken for measurement and analysis. Steady state conditions were attained when both effluent COD and gas production rate were invariant with time. For each COD loading rate, the system was found to take about 4 weeks to reach steady state. Similar to the hydrogen production step, the average data were used to evaluate the process performance of the methane production step.

Measurements and analytical methods

The organic contents in the cassava wastewater and the effluent samples of both UASB units were quantified by using the chemical oxygen demand method (COD). The microbial concentration in each UASB bioreactor was measured by taking the whole sludge in the bioreactor at the end of operation for each COD loading rate. The sludge sample was filtered and the filtered solids were burnt at 550 °C to obtain MLVSS (mixed liquor volatile suspended solids) to represent the microbial concentration in the system. The analytical methods of COD and effluent VSS followed standard methods [9]. The total volatile fatty acids (VFA) of the effluent samples were measured by the steam distillation and titration method [9]. The samples obtained from the steam distillation were also taken for the determination of organic acid compositions by using a gas chromatograph (Perichrom, PR2100) equipped with a flame ionization detector (FID) and a capillary column (50 m × 0.32 ID, 0.25 μm film thickness DB-WAXetr, J &W scientific) in splitless mode with helium as a carrier gas, hydrogen as a combustion gas, and air zero as a combustion-supporting gas. The column temperature program was kept at 60 °C, heated to 125 °C at a ramping rate of 10 °C/min, held for 2 min, then heated to 180 °C at a ramping rate of 15 °C/min, and held for 15 min. The temperatures of both injector and conductor were kept constant at 250 °C. The gas production rate was measured by using the water replacement method. The gas composition was analyzed with a gas chromatograph (Perkin–Elmer, AutoSystem GC) equipped with a thermal conductivity detector (TCD) and a packed column (stainless-steel 10′ × 1/8′ × 0.085″ HayeSep D 100/120 mesh, Altech). Injector, column, and detector temperatures were kept at 60, 35, and 150 °C, respectively. Argon was used as a carrier gas.

Results and discussion

Hydrogen production results

The effects of COD loading rate on COD removal efficiency and gas production rate of the hydrogen UASB units is shown in Fig. 1a. The COD removal efficiency increased with increasing COD loading rate from 10 to 25 kg/m^{3}d and then decreased with further increasing COD loading rate from 25 to 30 kg/m^{3}d. The maximum COD removal was 43.8% at a COD loading rate of 25 kg/m^{3}d. The increase in COD loading rate resulted from an increase in organic compounds available for microbial degradation, leading to increasing COD removal. However, at a very high COD loading rate greater than 25 kg/m^{3}d, the concentration of produced volatile fatty acids exceeded their inhibitory level to the hydrogen-producing bacteria, causing the reduction of both COD removal and the microbial concentration – this will be discussed further later. The gas production rate rapidly increased with increasing COD loading rate from 10 to 25 kg/m^{3}d. However, the gas production rate slowly increased when the COD loading rate further increased from 25 to 30 kg/m^{3}d. The results can be explained in that an increase in COD loading rate provided higher substrates available for microbes to produce higher quantities of gaseous products. An increase in COD loading rate from 25 to 30 kg/m^{3}d resulted in lowering the increasing rate of gas production because of the toxicity from VFA accumulation, which will be further explained later.

Fig. 1b shows the composition of the produced gas and hydrogen production rate at different COD loading rates for the hydrogen production step. Both of the hydrogen production rate and hydrogen content in the produced gas showed similar trends to that of the COD removal of the hydrogen UASB unit whereas the CO_2 content had an opposite trend.

The same explanation for the effect of COD loading rate on both COD removal and gas production rate can be used for the results of hydrogen production rate and the composition of the produced gas. Interestingly, the methane content decreased from 10% to zero when the COD loading rate increased from 10 to 25 kg/m^{3}d. The results of the reduction of methanogenic activity with increasing COD loading rate can be explained by the fact that the growth of methanogens require organic acids and hydrogen produced from both steps of acidogenesis and acetogenesis and the inhibitory level by the accumulated organic acids to methanogens is about 400 mg/l as acetic acid, which is much lower than that (10,000 mg/l as acetic acid) to hydrogen producing bacteria [7]. Hence, the increase in COD loading rate beyond 25 kg/m^{3}d could completely washout all methanogens from the system.

A specific hydrogen production rate (SHPR) is defined as the hydrogen production rate per unit weight of the microbial cells in the system or per unit liquid volume of the system. Fig. 1c shows that the specific hydrogen production rates increase from 1.96 l H_2/kg MLVSS d (0.03 l H_2/l d) at a COD loading rate of 10 kg/m^{3}d to 10.92 l H_2/kg MLVSS d (0.39 l H_2/l d) at a COD loading rate of 25 kg/m^{3}d. After that, it significantly declined to 8.67 l H_2/kg MLVSS d (0.27 l H_2/l d) with further increasing COD loading rate from 25 to 30 kg/m^{3}d. The profiles of SHPR showed a similar trend to those of COD removal, hydrogen production rate and hydrogen content in the produced gas. The results will be further discussed later.

The yield of hydrogen production is defined as a ratio of the amount of produced hydrogen to the amount of organic substrates (in terms of COD applied or COD removed). Fig. 1d shows that the yields of hydrogen production increased from 15.82 l H_2/kg COD removed (or 3.15 l H_2/kg COD applied) at a COD loading rate of 10 kg/m^{3}d to 39.83 l H_2/kg COD removed

Fig. 1 − Effects of COD loading rate on (a) COD removal and gas production rate, (b) gas composition and hydrogen production rate, (c) Specific hydrogen production rates and (d) hydrogen yields at pH 5.5 and 37 °C in biohydrogen reactor.

(or 15.84 l H_2/kg COD applied) at a COD loading rate of 25 kg/m^3d, which was the highest yields of hydrogen production obtained in this study. However, when the COD loading rate increased from 25 to 30 kg/m^3d, the yields of hydrogen production adversely decreased to 36.38 l H_2/kg, COD removed (or 8.91 l H_2/kg COD applied). From the results, the optimum COD loading rate of 25 kg/m^3d was selected to operate the two identical UASB units to produce effluent, which was further used to produce methane from the two UASB units at different COD loading rates, as discussed in the next section.

Fig. 2 shows the total VFA (mg/l as acetic acid) and its composition in the effluent of the hydrogen UASB units as a function of COD loading rate. The total VFA concentration increased with increasing COD loading rate and attained a

highest value of 13,800 mg/l as acetic acid at the highest COD loading rate of 30 kg/m^3d. However, at the highest COD loading rate of 30 kg/m^3d, hydrogen production performance decreased due to the toxicity of VFA accumulation [10]. It can be concluded that the maximum VFA tolerance level of the hydrogen producing bacteria under the mesophilic temperature (37 °C) is around 10,000 mg/l as acetic acid, which is in good agreement with our previous study [7].

We can conclude that the VFA tolerance levels of both mesophiles and thermopliles are more or less the same. The major components of VFA in the liquid effluent were acetic acid (HAc), propionic acid (HPr), butyric acid (HBu), and valeric acid (HVa). Under the optimum COD loading rate of 25 kg/m^3d, the concentrations of all organic acids produced were 48% HBu, 34% HAc, 12% HVa, and 6% HPr. Moreover, the highest HBu-to-HAc ratio of 1.41:1 was obtained at this optimum condition causing the maximum hydrogen production. In general, the production of HAc and HBu is favorable for hydrogen production, according to Equations (1) and (2) [11].

Acetic acid production:

$$C_6H_{12}O_6 + H_2O \rightarrow 2CH_3COOH + 2CO_2 + 4H_2 \tag{1}$$

Butyric acid production:

$$C_6H_{12}O_6 \rightarrow CH_3(CH_2)_2COOH + 2CO_2 + 2H_2 \tag{2}$$
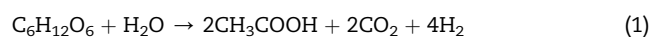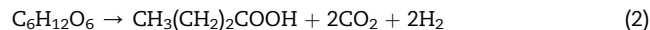
In addition, the production of HVa and HPr was also important in affecting the consumption of hydrogen initially produced, according to Equations (3)−(6) [11,12].

Fig. 2 − Total VFA, and VFA composition versus COD loading rate at 37 °C and pH 5.5 in biohydrogen reactor.

Propionic acid production:

$$C_6H_{12}O_6 + 2H_2 \rightarrow 2CH_3CH_2COOH + 2H_2O \tag{3}$$

Valeric acid production:

$$CH_3CH_2COOH + CH_3(CH_2)_2COOH \rightarrow CH_3(CH_2)_3COOH + CH_3COOH \tag{4}$$

$$CH_3CH_2COOH + CH_3COOH + H_2 \rightarrow CH_3(CH_2)_3COOH + 2H_2O \tag{5}$$

$$CH_3CH_2COOH + 2CO_2 + 6H_2 \rightarrow CH_3(CH_2)_3COOH + 4H_2O \tag{6}$$

Methane production results

The liquid effluent from both hydrogen UASB units operated at the optimum COD loading rate of 25 kg/m³d was further fed into the same UASB units, which had been started up with new seed sludge without heat pretreatment. Both of the methane UASB units were operated without pH control at the same mesophilic temperature (37 °C). The effect of COD loading rate on COD removal efficiency and gas production rate is shown in Fig. 3a. Both COD removal and gas production rate increased remarkably with an increasing COD loading rate from 2 to 8 kg/m³d. However, with further increasing COD loading rate from 8 to 10 kg/m³d, the COD removal slightly decreased, whereas the gas production rate drastically decreased. The maximum COD removal was found at the optimum COD loading rate of 8 kg/m³d. At a very high COD loading rate, especially 10 kg/m³d, the system had both a very high organic load and a very short hydraulic retention time (HRT). This caused an imbalance between increasing organic acids' load as the input and lower organic acids consumption (in the methanogenesis), indicating the increasing profile of total VFA concentration with increasing COD loading rate. This will be discussed later. Interestingly, the COD removal of the methane UASB units was much higher than that of hydrogen UASB units, suggesting most of the liquid effluent produced from the hydrogen UASB units contained mostly soluble organic acids, which is easily degraded and further converted to methane and carbon dioxide [13].

The composition of the produced gas and methane production rate as a function of COD loading rate are shown in Fig. 3b. Under the studied conditions, the produced gas contained mainly methane (greater than 80%) and carbon dioxide without hydrogen. The methane production rate had a similar trend to the COD removal. The methane content increased slightly with an increasing COD loading rate and reached a maximum of 83% at a COD loading rate of 8 kg/m³d. With further increasing COD loading rate greater than 8 kg/m³d, the methane content decreased slightly.

The results obtained from this study suggest that the two-stage anaerobic process can produce biogas with very high methane content (greater than 80%) from a second methane bioreactor, as compared to that (50–75% methane content) of

biogas production by a single stage anaerobic system. The carbon dioxide content had an opposite trend to that of the methane content. An increase in COD loading rate up to 8 kg/m³d simply increased the amount of produced organic acids available for methanogens to produce more methane. In addition, both steps of acidogenesis and acetogenesis went on to produce more hydrogen in the methane UASB units, which could be easily converted to methane via the hydrogenotrophic methanogenesis pathway [3] as in the following biochemical reaction Equation (7) [14]:

$$CO_2 + 4H_2 \rightarrow CH_4 + 2H_2O \tag{7}$$

Both SMPR values and methane yields also showed similar trends to both methane content and methane production rate (Fig. 3c–d). The decreases in SMPR values and methane yields with increasing COD loading rate from 8 to 10 kg/m³d resulted from the increasing toxicity of VFA accumulation [15–18].

The effects of COD loading rate on the total VFA concentration (mg/l as acetic acid) and VFA composition in the methane UASB unit are shown in Fig. 4. The total VFA concentration increased as the COD loading rate increased. The profile of acetic acid concentration shows a similar trend to that of the total VFA concentration whereas the profiles of all organic acids (HPr, HBu, and HVa) slightly increased with increasing COD loading rate. As compared to all produced organic acids between the hydrogen and methane UASB units, the acidogenic step mostly occurred in the hydrogen UASB unit, while the acetogenic step mostly happened in the methane UASB unit [19].

It can be concluded that under the studied conditions, the main production of methane resulted from the utilization of acetic acid via the acetotrophic metabolic pathway; according to Equation (8) [3,18,20]. Methane content higher than 80% in the produced gas from the methane UASB unit suggests that a significant portion of methane production was derived from the hydrogenotrophic methanogenic pathway in which hydrogen and carbon dioxide are utilized to form methane [21]. It is estimated that the hydrogen production from both steps of acidogenesis and acetogenesis in the methane UASB unit was about 150% of methane produced [22–24].

$$CH_3COOH \rightarrow CH_4 + CO_2 \tag{8}$$

In a comparison between the process performance, especially in terms of COD removal and methane production efficiency (Fig. 3), and the total VFA concentration (Fig. 4), the toxicity level of VFA to methanogens was found to be about 400 mg/l as acetic acid. This is in good agreement with our previous study [4].

Microbial concentration results

Mixed liquid volatile suspended solids (MLVSS) were used to represent the microbial concentrations in both of the UASB units and the volatile suspended solids (VSS) of the effluent samples were used to represent the microbial wash-out from the system. Fig. 5 shows the effects of COD loading rate on
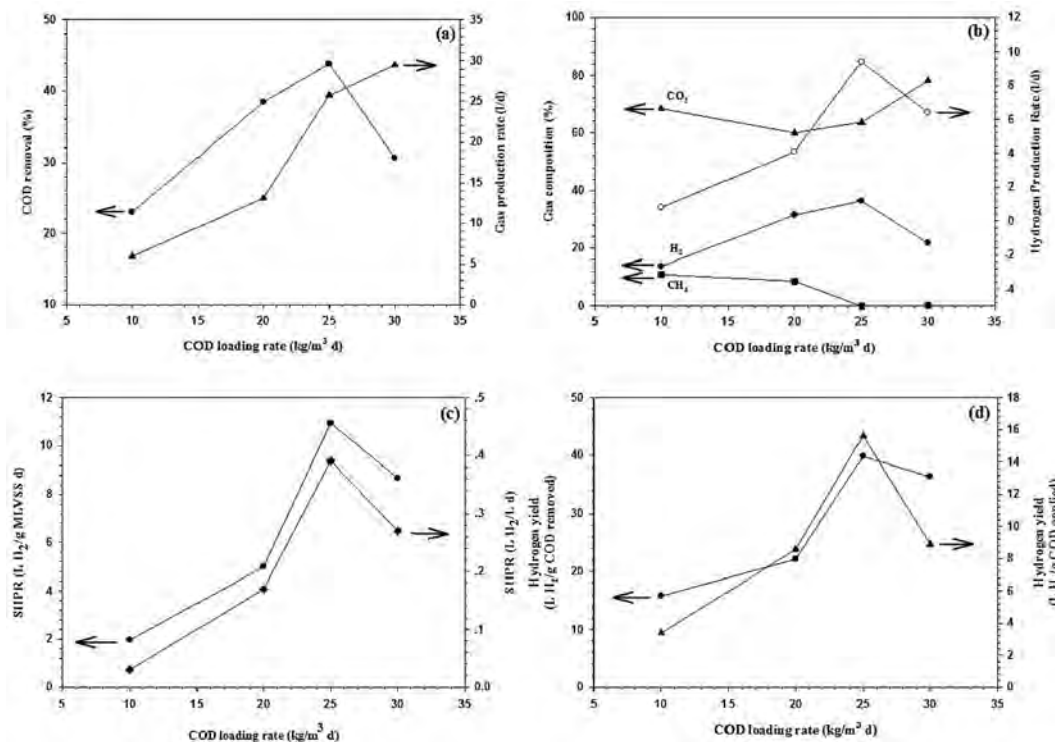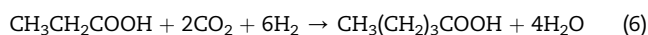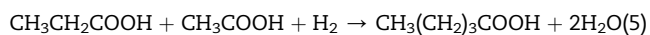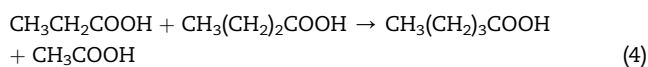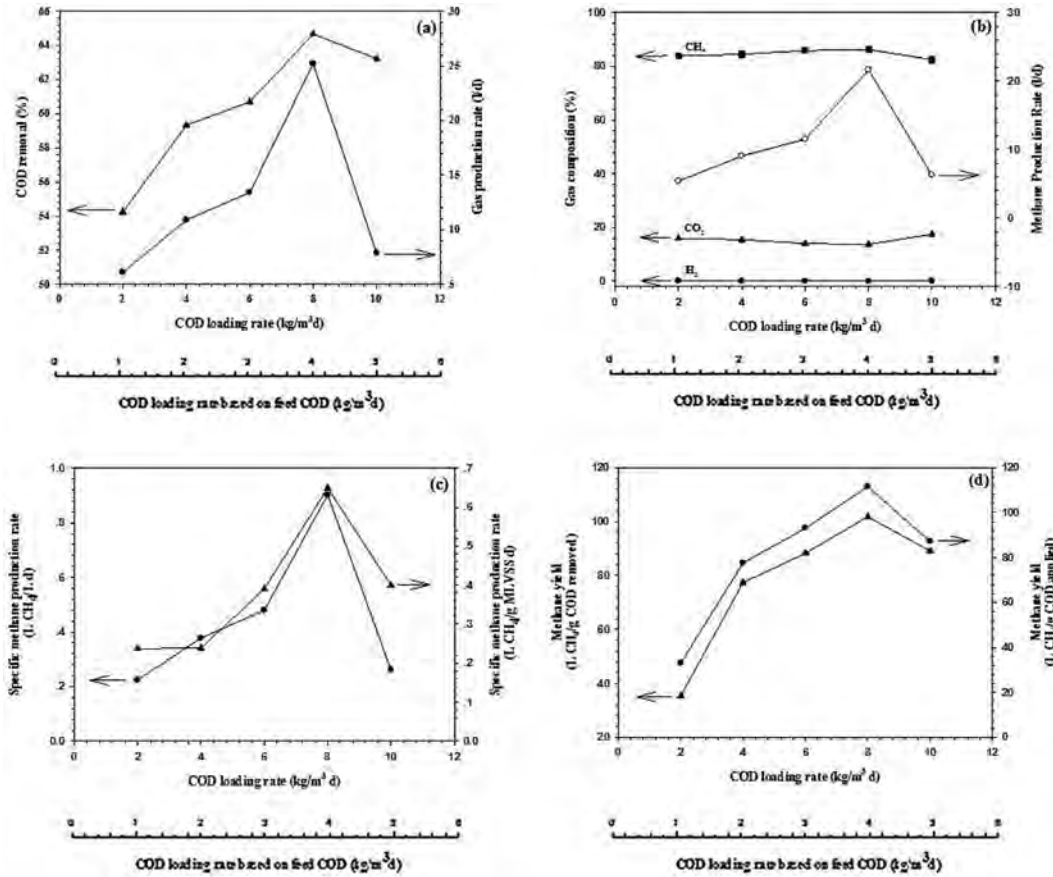
Fig. 3 – Effects of COD loading rate on (a) COD removal and gas production rate, (b) gas composition and methane production rate, (c) Specific methane production rates and (d) methane yields at 37 °C without pH control in biomethane reactor.

both MLVSS and the effluent VSS. The results showed that with increasing COD loading rate from 10 to 25 kg/m³d based on hydrogen UASB units (or 2–8 kg/m³d based on methane production process), the MLVSS increased to reach a maximum, but the effluent VSS decreased to reach a minimum. Subsequently, the increase in COD loading rate higher than 25 kg/m³d based on hydrogen UASB units (or 8 kg/m³d based on methane UASB units) resulted in the decrease in the MLVSS and the increase in the effluent VSS.

The results point out that at the optimum COD loading rate, the microbial growth in both UASB units was the highest, accompanying the least loss of the microbes from both UASB units corresponding to the maximum COD removal and the maximum of both hydrogen and methane production. Another parameter that significantly affects much to the growth of anaerobic bacteria is pH. The acceptable pH for the growth of acidogens and methanogens is around 5.5 and in the range of 7.0–7.2 [25].
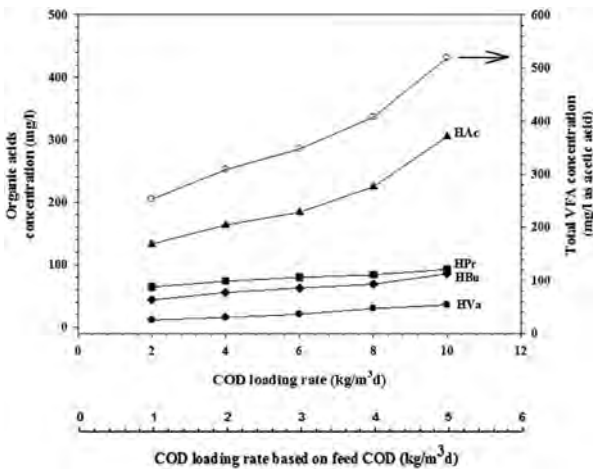
Fig. 4 – Total VFA, and VFA composition versus COD loading rate at 37 °C without pH control in biomethane reactor.

Conclusions

This research focused on the production of both hydrogen and methane from cassava wastewater using two upflow anaerobic sludge blanket reactors (UASB). For the hydrogen production stage, maximum hydrogen production was achieved at a COD loading rate of 25 kg/m³d under a controlled pH of 5.5 at the mesophilic temperature (37 °C) and the produced gas contained 36.4% hydrogen and 63.6% carbon dioxide without methane. Under this optimum COD loading
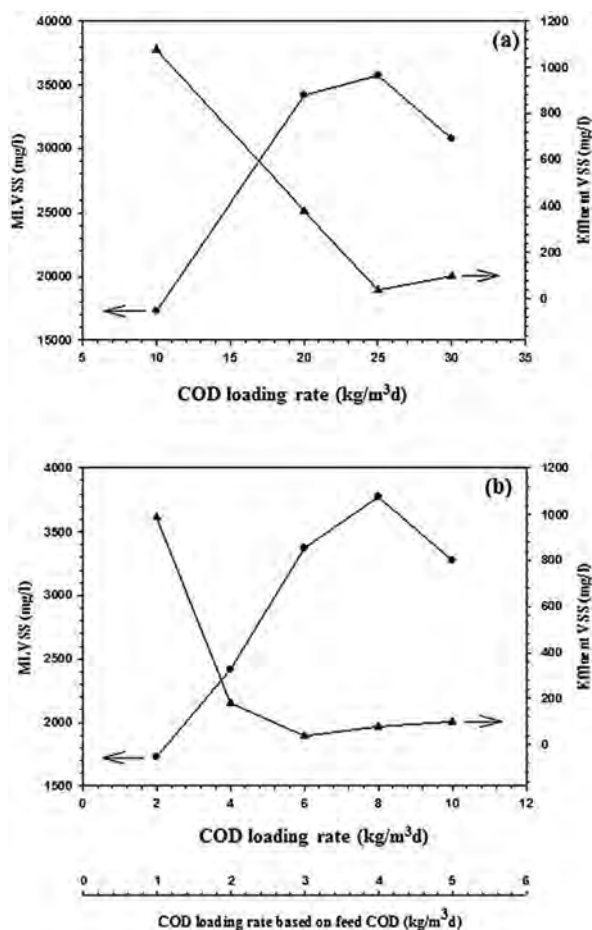
Fig. 5 – Effect of COD loading rate on MLVSS and effluent VSS under mesophilic temperature (37 °C) of (a) biohydrogen reactor at pH 5.5 and (b) biomethane reactor without control pH.

rate, the highest hydrogen yield (39.8 l/kg COD removed), the highest specific hydrogen production rate (10.92 l H$_2$/kg MLVSS d), the highest COD removal (43.8%), the highest butyric acid concentration (25%), and the lowest propionic acid concentration (10%) were obtained. For the methane production stage, the UASB was fed with effluent from the hydrogen production step at a constant temperature of 37 °C, without pH control. The maximum methane production was found at an optimum COD loading rate of 8 kg/m^{3}d to provide the highest COD removal (93.2%), the highest methane yield (100 l/kg COD removed), and the highest specific methane production rate (0.65 l CH$_4$/kg MLVSS d).

Acknowledgments

REFERENCES

[1] Das D, Veziroglu TN. Hydrogen production by biological processes: a survey of literature. Int J Energy 2001;26:13–28.

[2] Yu HQ, Fang HHP. Acidification of mid- and high-strength dairy wastewaters. Water Res 2001;35:3697–705.

[3] Abbasi SA, Nipaney PC, Panholzer MB. Biogas production from the aquatic weed pistia (*Pistia stratiotes*). Bioresour Technol 1991;37:211–4.

[4] Intanoo P, Rangsanvigit P, Malakul P, Chavadej S. Optimization of separate hydrogen and methane production from cassava wastewater using two-stage upflow anaerobic sludge blanket reactor (UASB) system under thermophilic operation. Bioresour Technol 2014;173:256–65.

[5] Wangmor T. Effect of added cassava residue on hydrogen and methane production from cassava wastewater using a two stage UASB system [M.S. thesis]. The Petroleum and Petrochemical College, Chulalongkorn University; 2014.

[6] Limwattanalert N. Hydrogen production from ethanol wastewater by using upflow anaerobic sludge blanket reactor [M.S. thesis]. The Petroleum and Petrochemical College, Chulalongkorn University; 2011.

[7] Intanoo P, Rangsunvigit P, Namprohm W, Thamprajamchit B, Chavadej J, Chavadej S. Hydrogen production from alcohol wastewater by an anaerobic sequencing batch reactor under thermophilic operation: nitrogen and phosphorous uptakes and transformation. Int J Hydrogen Energy 2012;37:11104–12.

[8] Sreethawong T, Chatsiriwatana S, Rangsunvigit P, Chavadej S. Hydrogen production from cassava wastewater using an anaerobic sequencing batch reactor: effects of operational parameters, COD: N ratio, and organic acid composition. Int J Hydrogen Energy 2010;35:4092–102.

[9] Eaton AN, Clesceri LS, Rice EW, Greenberg AE. Edition standard methods for the examination of water & wastewater. Washington, DC: American Public Health Association; 2005.

[10] Poontaweegeratigarn T, Chavadej S, Rangsunvigit P. Hydrogen production from alcohol wastewater by upflow anaerobic sludge blanket reactors under mesophilic temperature. Int J Chem Biol Eng 2012;6:305–8.

[11] Mohan SV, Mohanakrishna G, Sarma PN. Integration of acidogenic and methanogenic processes for simultaneous production of biohydrogen and methane from wastewater treatment. Int J Hydrogen Energy 2008;33:2156–66.

[12] Zhao QB, Yu HQ. Fermentative H$_2$ production in an upflow anaerobic sludge blanket reactor at various pH values. Bioresour Technol 2008;99:1353–8.

[13] Gavalla HN, Skiadas IV, Ahring BK. Biological hydrogen production in suspended and attached growth anaerobic reactor system. Int J Hydrogen Energy 2006;31:1164–75.

[14] Cooney M, Maynard N, Cannizzaro C, Benemann J. Two-phase anaerobic digestion for production of hydrogen–methane mixtures. Bioresour Technol 2007;98:2641–51.

[15] Kvesitadze G, Sadunishvili T, Dudauri T, Zakariashvili N, Partskhaladze G, Ugrekhelidze V, et al. Two-stage anaerobic process for bio-hydrogen and bio-methane combined

production from biodegradable solid wastes. Energy 2012;37:94—102.

[16] Wang Y, Zhang Y, Wang J, Meng L. Effects of volatile fatty acid concentrations on methane yield and methanogenic bacteria. Biomass Bioenergy 2009;33:848—53.

[17] Stafford DA. The effects of mixing and volatile fatty acid concentrations on anaerobic digester performance. Biomass 1982;2:43—55.

[18] Wang Y, Zhang Y, Meng L, Wang J, Zhang W. Hydrogen—methane production from swine manure: effect of pretreatment and VFAs accumulation on gas yield. Biomass Bioenergy 2009;33:1131—8.

[19] Ting CH, Lee DJ. Production of hydrogen and methane from wastewater sludge using anaerobic fermentation. Int J Hydrogen Energy 2007;32:677—82.

[20] Luo G, Xie L, Zhou Q, Angelidaki I. Enhancement of bioenergy production from organic wastes by two-stage anaerobic hydrogen and methane production process. Bioresour Technol 2011;102:8700—6.

[21] Xie BF, Cheng J, Zhou JH, Song WL, Liu JZ, Cen KF. Production ofhydrogen and methane from potatoes by two-phase anaerobic fermentation. Bioresour Technol 2008;99:5942—6.

[22] Chuang YS, Lay CH, Sen B, Chen CC, Gopalakrishnan K, Wud JH, et al. Biohydrogen and biomethane from water hyacinth (*Eichhornia crassipes*) fermentation: effects of substrate concentration and incubation temperature. Int J Hydrogen Energy 2011;36:14195—203.

[23] Wang Q, Kuninobu M, Ogawa HI, Kato Y. Degradation of volatile fatty acids in highly efficient anaerobic digestion. Biomass Bioenerg 1999;16:407—16.

[24] Zhao R, Zhang Z, Zhang R, Li M, Lei Z, Utsumi M, et al. Methane production from rice straw pretreated by a mixture of acetic—propionic acid. Bioresour Technol 2010;101:990—4.

[25] Mawson AJ, Earle RL, Larsen VF. Degradation of acetic and propionic acids in the methane fermentation. War Res 1991;25:1549—54.

Removal of motor oil by continuous multistage froth flotation: Effect of operational parameters

P. Kanokkarn, T. Shiina, T. Suttikul & S. Chavadej

Taylor & Francis
Taylor & Francis Group

Removal of motor oil by continuous multistage froth flotation: Effect of operational parameters

P. Kanokkarn[a], T. Shiina[b,c], T. Suttikul[d], and S. Chavadej[a,e]

[a]The Petroleum and Petrochemical College, Chulalongkorn University, Bangkok, Thailand; [b]Faculty of Horticulture, Graduate School of Horticulture, Chiba University, Chiba, Japan; [c]National Food Research Institute, National Agriculture and Food Research Organization, Ibaraki, Japan; [d]Division of Chemical Process Engineering Technology, Faculty of Engineering and Technology, King Mongkut's University of Technology North Bangkok (Rayong Campus), Rayong, Thailand; [e]Center of Excellence on Petrochemical and Materials Technology, Chulalongkorn University, Bangkok, Thailand

ABSTRACT

A continuous multistage froth flotation column was employed to remove motor oil from water at a low concentration (500 mg/L) using an extended surfactant – branched alcohol propoxylate sulphate sodium salt (C_{14-15}–8PO–SO_4–Na) – as a frother. The highest separation efficiency (97% motor oil removal with the enrichment ratio of 16 for motor oil) was obtained at a foam height of 60 cm, an air flow rate of 40 L/min, a feed flow rate of 60 mL/min, a surfactant concentration of 0.3% (w/v), and an NaCl concentration of 1.5% (w/v). The process performance increased with increasing tray number but beyond 4 trays, the system could only offer lower concentrations of motor oil and surfactant in the effluent.

Introduction

Motor oil is a lubricant for the moving parts of internal combustion engines. However, it undergoes thermal as well as mechanical degradation and needs to be periodically replaced, resulting in used motor oil often being found in wastewater. In order to comply with environment regulations, a proper treatment system for motor oil contaminated wastewater has to be employed prior to discharging it to the environment. A variety of treatment techniques have been developed and applied for the removal of oil from wastewater, including coagulation/flocculation,[1,2] biological treatment,[3,4] membrane-separation process,[5,6] and ultrafiltration.[7–9] However, these traditional treatment techniques are not economically feasible for applying to wastewater containing a low concentration of oil. Adsorptive bubble separation, typically a froth flotation technique, is one of the most promising oily wastewater treatment processes due to its several advantages, such as low space and energy requirement; simplicity in design, operation, and scale-up; low operating cost, and no solvent or heat requirement.[10,11] The froth flotation technique has been successfully employed for the removal of various oil types in our research group, such as ortho-dichlorobenzene,[12,13] ethylbenzene,[14,15] diesel oil,[16,17] motor oil,[18] and cutting oil.[19] Based on the above research, it can be concluded that froth flotation is considered one of the most effective treatment processes for concentrating, as well as for separating, both suspended solids and oils, especially at low concentrations.

In a froth flotation operation, air is introduced at the bottom of a froth flotation column to generate rising air bubbles. Both the added surfactant and target material can adsorb preferentially at the air/water interface of the rising air bubbles and then they emerge from the solution surface to form foam (foamate),which flows out from the column or is scraped out from a flotation tank. The process performance of the froth flotation is governed by two mechanisms of the adsorptive transport and the bulk liquid transport. The former is an upward stream of the adsorbed materials on the foam surface while the latter is an upward stream of lamella liquid with unadsorbed molecules, known as the entrained liquid. The bulk liquid transport not only contributes to the removal but also causes the reduction of the enrichment ratio and separation factors of any target material due to the dilution of the entrained liquid. On the other hand, the adsorptive transport is responsible for the increase in the enrichment ratios and separation factors, apart from the removal of both surfactant and target material.[20]

Froth flotation has been mostly applied in single-stage systems in either a batch or continuous mode.

Continuous multistage froth flotation has seldom received attention although much higher separation efficiency can be achieved.[21,22] In the present work, a continuous multistage froth flotation unit was employed, for the first time, for motor oil removal from water using an extended surfactant (Alfoterra© C145–8PO) as a frother. Several factors affecting the separation efficiency including foam height, air flow rate, feed flow rate, and surfactant and salt concentrations were systematically investigated. The separation efficiency was determined based on the following evaluating parameters: removal percentage, enrichment ratios, residual factors, and separation factors of both surfactant and motor oil. The process performance was also correlated to surfactant adsorption and dynamic surface tension in order to gain a better understanding of how oil can be removed by generating foam .

Experiment

Materials and chemicals

Branched alcohol propoxylate sulphate; sodium salt (C_{14-15} $(PO)_8SO_4Na$) or Alfoterra© C145–8PO; an anionic extended surfactant having 14–15 carbon atoms and eight groups of propylene oxide (PO) with sulphate as a hydrophilic group (molecular weight of 783 with of 28.7% in liquid form) was kindly supplied by Sasol North America Inc. (USA). Motor oil (Performa Synthetic grade, SAE 5W–40, API SM/CF, commercially available for gasoline engines in Thailand), model contaminant oil, produced by PTT Public Co., Ltd (Thailand) was used. It consists of 85% v/v of a complex mixture of lubricating oils (petroleum), C_{20-50} hydrotreated neutral oil–base, and 10–15% v/v lubricant additive package. NaCl (analytical grade, 99% purity) was obtained from Labscan Asia Co., Ltd. (Thailand). All chemicals were used as received without further purification; distilled water was used throughout the experiment.

CMC and surface tension isotherm determination

The surface tension of test solutions containing different concentrations of surfactant and NaCl was measured by using a tensiometer (Krüss, K100, Germany) with a Wilhelmy plate at $25°$C. An abrupt change in the slope of the plot between surface tension and log of surfactant concentration was used to identify the critical micelle concentration (CMC). The surface excess concentration or adsorption density of the surfactant ions at the air/water interface (Γ) in mol/cm^2 was calculated from the following Gibbs adsorption isotherm equation[23]:

$$\Gamma = -\frac{1}{nRT} \cdot \frac{d\gamma}{dlnC}$$

where γ is the equilibrium surface tension (mN/m), C is the bulk surfactant concentration (µM), n can be either 1 or 2—the former for an ionic surfactant with a swarming concentration of added electrolyte or for a nonionic surfactant and the latter for an ionic surfactant in the absence of electrolyte, R is the gas constant (8.31 J/mol K), and T is the absolute temperature (K).

Dynamic surface tension measurement

Dynamic surface tension was measured using a bubble pressure tensiometer (Krüss, BP2, Germany) at 25°C. A gas bubble was generated by introducing air zero through a capillary tube. The pressure inside the air bubble generated at the tip of the capillary tube was monitored and recorded with time until the air bubble burst. The final pressure and the diameter of the capillary tube were used to calculate a value of dynamic surface tension at different bubble ages.

Multistage froth flotation experiments

Figure 1 illustrates the configuration of the multistage froth flotation column and the bubble caps in each tray. The multistage froth flotation column used in this experiment had four stainless steel trays connected in series. Each tray had an inner diameter of 20 cm with a tray spacing of 15 cm. Each tray had 16 bubble caps with a weir height of 5 cm, a cap diameter of 2.5 cm, and a sample port for taking liquid samples. The top tray was connected to a stainless steel foam column having the same inner diameter (20 cm) with different foam outlet heights of 30, 60, and 90 cm.[21,24] To achieve high process separation performance; (i) the generated foam must pass through the bubble caps (not passing through the downcomer) and (ii) the liquid flows only through the downcomer (not passing through the bubble caps).[22] A well-mixed solution containing a constant motor oil concentration of 500 mg/L at two different surfactant concentrations, 0.3% and 0.5% (w/v), was fed continuously to the top of the column at different feed flow rates in the range of 40–100 mL/min controlled by a peristaltic pump (Masterflex®, L/S® Digital Drives). The motor oil concentration of 500 mg/L was selected in this study because it represented a low oil concentration that is not possible both technically and economically to use a conventional oil-trap chamber for oil separation. The water solubility of motor oil was around 10 mg/L in pure water at room temperature while it increased to 40 mg/L in the 0.3% (w/v) surfactant solution. Hence, the added
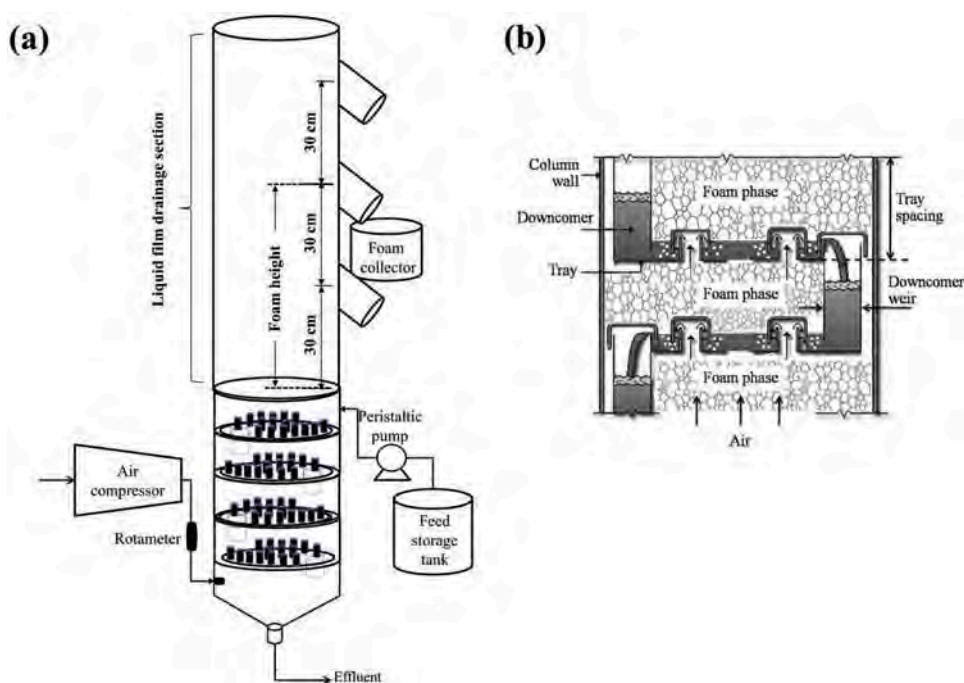
Figure 1. Schematic drawing of (a) multistage froth flotation column and (b) foam phase in equilibrium with aqueous phase for froth flotation system.

motor oil in the feed was mostly present in free oil (92%) with a very low portion of 8% solubilized in micelles. The reason why these two surfactant concentrations (0.3% and 0.5%) were used in this study will be explained later. Filtered air was introduced at the bottom of the column and the air flow rate was regulated in the range of 20–80 L/min using a rotameter. The generated foam rose up through the multistage froth flotation column and was collected at the top of the column with different foam heights—30, 60, and 90 cm. The experiments were carried out at room temperature (25–30°C). Each run was operated to reach a steady state, at which both concentrations of surfactant and motor oil in the foamate and effluent samples were invariant with time. The experimental data taken from the steady state condition (at least three replicate) were averaged and these data were then used to determine the process performance. The concentrations of surfactant and the total concentration of both surfactant and motor oil were determined by an UV-visible spectrophotometer (Perkin-Elmer, Lambda 10, USA) at a wavelength of 210 nm and a total organic carbon analyser (Shimadzu, TOC-VCSH, Japan), respectively. The concentration of motor oil was calculated by subtracting the surfactant concentration in terms of total organic carbon (TOC) from the total TOC concentration. The material balance was used to calculate the error of experimental data. Less than 10% error of surfactant mass balance was acceptable for this experiment.[21,22]

Foamability and foam stability measurements

Foamability and foam stability measurements were independently conducted using a glass column, having an internal diameter of 5 cm and a column height of 120 cm. One hundred mL of a well-mixed solution, containing a constant motor oil concentration of 500 mg/L and a constant surfactant concentration of 0.3% (w/v) at various NaCl concentrations, was added to the column. Compressed air was introduced at the bottom of the column at a rate of 0.1 L/min, which was regulated by a mass flow controller (Aalborg, GFC171S), to generate fine air bubbles by passing through a sintered glass disk with pore size diameters in the range of 16–40 μm.[18] The time required to reach a maximum height of 120 cm was used to indicate foamability. The time required for the foam to collapse from 120 cm to 60 cm without introducing air was used to indicate foam stability.[21] The froth characteristic experiments were carried out at room temperature (25-30°C).

Calculation of process performance

The separation efficiency performance of the multistage froth flotation column was determined in terms of the enrichment ratios, removals, residual, and separation factors of surfactant and motor oil.[22,25] All these evaluating parameters are described below:

$$\text{Enrichment ratio} = C_f/C_i \qquad (1)$$

$$\text{Residual factor} = C_e/C_i \qquad (2)$$

$$\text{Separation factor} = C_f/C_e \qquad (3)$$

$$\text{Removal percentage} = (V_iC_i - V_eC_e) \times 100/(V_iC_i) \qquad (4)$$

$$\text{Foamate volumetric ratio} = V_f/V_i \qquad (5)$$

where C_e is the concentration of motor oil or surfactant in the effluent sample, C_f is the concentration of motor oil or surfactant in the foamate (collapsed foam), C_i is the initial concentration of motor oil or surfactant in feed solution, V_e is the volumetric flow rate of effluent, V_f is the volumetric flow rate of foamate, and V_i is the volumetric flow rate of inlet (or feed) solution.

Results and discussion

Fundamental properties of surfactant

The use of extended surfactant has been reported to provide potential benefits for treating aqueous systems containing immiscible hydrocarbon oils. This is because the unique molecular structure of extended surfactant provides a smoother transition between hydrophilic and hydrophobic regions of the interface between aqueous and hydrocarbon phases to create a more suitable environment for solubilization of both water and oil.[17,26] The presence of propoxylate (PO) group in the alkyl chain length of surfactant can lower the critical microemulsion concentration (CμC) and increase oil solubilization, resulting in an increase in oil removal in a single stage froth flotation system.[27,28] In our previous studies, it was revealed that the maximum oil removal well corresponded to the minimum interfacial tension (IFT) of the system.[13–17,29] Later, both process parameters of foamability (how easy to form foam) and foam stability (how long the generated foam to exist) are very crucial to the oil separation efficiency. Hence, the extended surfactant (Alfoterra© C145–8PO), as anionic surfactant, was chosen for this study, which can provide high oil solubilization with a high water solubility, low IFT, and high foamability and foam stability. It was hypothesized to be a good frother to remove motor oil from water.

The plots of surface tension versus log of the initial surfactant concentration with and without 1.5% (w/v) NaCl for determining the CMC and the calculated values of surfactant adsorption density are shown in Figs. 2 and 3, respectively. The reason for investigating only the addition of 1.5% (w/v) NaCl will be described later. Table 1 summarizes the CMC, the surface tension

at CMC (γ_{CMC}), the negative logarithm of surfactant concentration in the bulk phase required to reduce the surface tension by 20 mN/m (pC_{20}), and the effectiveness of adsorption (Γ_m) of the surfactant with and without NaCl. The surface tension isotherm shifted toward lower surfactant concentration and the surface tension above the CMC decreased greatly with the addition of 1.5% (w/v) NaCl. The values of CMC of the 0.3% (w/v) surfactant solution and the 0.3% (w/v) surfactant solution with 1.5% (w/v) NaCl were 12.75 and 8.75 μM or 9.98 and 6.96 mg/L, respectively. Hence, the added surfactant was in the form of micelles. A larger value of pC_{20} indicates a higher surfactant adsorption efficiency at the air/water interface and a higher ability for the reduction of surface tension.[23] The pC_{20} value of the surfactant with 1.5% (w/v) NaCl was observed to be higher than that without NaCl, suggesting that the addition of NaCl can enhance the surfactant adsorption density. The effectiveness of surfactant adsorption onto the air/water interface is an important factor affecting several properties of the surfactant, including foaming, which directly governs the process performance of froth flotation. By using the Gibbs close-pack monolayer equation,[23,25,30] the surfactant adsorption density was reviewed to be greatly enhanced (approximately four times) by adding NaCl (see Fig. 3). The increase in surfactant adsorption at the air/water interface by adding NaCl results from the counterion effect (Na^+) to reduce the repulsion force between the negatively charged head group of the surfactant.[31] The higher the surfactant adsorption onto the air/water interface, the higher the foamability and foam stability.

In this study, the lowest surfactant concentration of 0.3% (w/v) was found to be capable to produce stable foam to reach a highest foam height of 90 cm. Beyond a surfactant concentration of 0.5% (w/v), the separation efficiency was very low because the system had a very high foamate fraction (high bulk liquid transport). Thus, only two surfactant concentrations, 0.3% and 0.5% (w/v), to represent dry and wet foam, respectively, were selected to study the froth flotation performance.

Dynamic surface tension

Froth flotation is a process fundamentally governed by foam formation (foamability) and foam stability, which are related to the surfactant adsorption density at the air bubble interface between a dispersed gas phase and a bulk liquid phase.[24] A sufficient air flow rate is basically needed to generate air bubbles through the retaining solution in each tray to produce foam rising up through the bubble caps of an upper tray. The
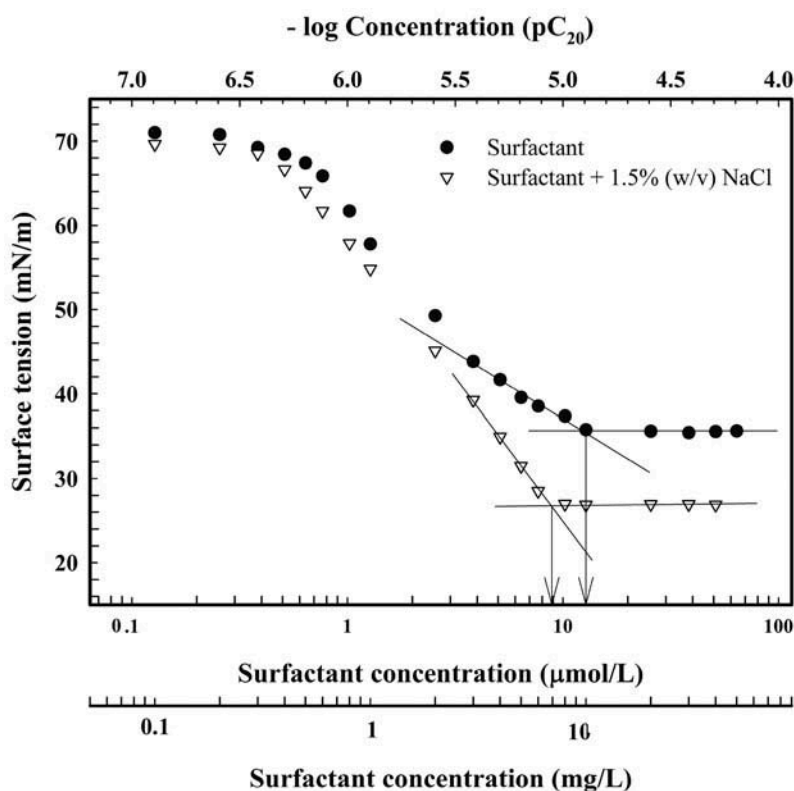
Figure 2. Surface tension isotherms of surfactant with and without NaCl addition at 25℃.
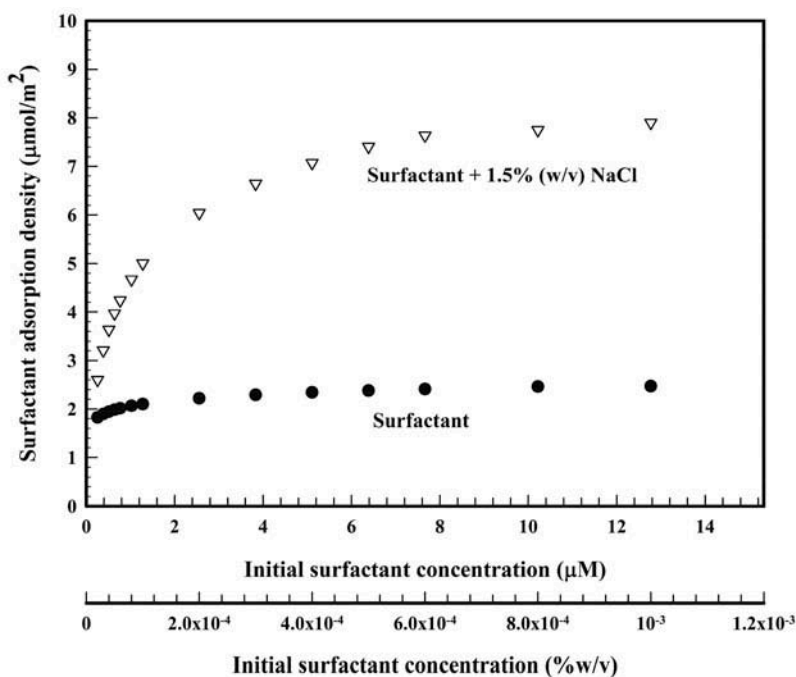
Figure 3. Adsorption density of surfactant with and without 1.5% (w/v) NaCl addition at air–liquid interface at 25℃.

superficial velocity of air was used to correlate how fast air bubbles pass through the solution in each tray. Dynamic surface tension can be used to indicate how fast an added surfactant adsorbs on the interface of generated air bubbles, which can directly affect the process performance of the froth flotation.[32] Figure 4 shows the dynamic surface tension profiles of the 0.3% (w/v) surfactant solution with and without added NaCl. The

Table 1. Calculated values of CMC, γ_{cmc}, pC_{20}, and saturated surface concentrations (Γ_m) of surfactant with and without NaCl addition.

Solution	CMC (µM)	γ_{CMC} (mN/m)	pC_{20}	Γ_m (mmol/m²)
Surfactant	12.75	35.5	5.38	2.39
Surfactant + 1.5 %wt/v NaCl	8.87	27	5.74	7.83

presence of NaCl lowered the dynamic surface tension, indicating that the addition of NaCl can shorten the time for surfactant adsorption on the air/water interface.[18] Under the studied conditions, the superficial air velocity was in the range of 1.06–4.24 cm/s and so the required time for air bubbles to pass through the solution in each tray was greater than 1 s. Based on the minimum contact time of rising air bubbles of 1 s, the surface tension reduction is about 72% for the pure surfactant solution or 62% for the surfactant solution with 1.5% (w/v) NaCl, suggesting that both foamability and foam stability in each tray could reach at least more than 50% of their maximum values. The results suggest that an increase in the liquid depth in each tray can improve the process performance of the studied multistage froth flotation unit.

Operating limits

The principles of the multistage froth flotation system with bubble caps are quite similar to those of a distillation unit. Vapour–liquid phase equilibrium is applied for the distillation unit while foam–liquid phase equilibrium is applied for the froth flotation unit. The efficiency of the multistage froth flotation depends on column configuration, operational

conditions, and the types and concentrations of surfactants and electrolytes.[22,25,33] Hence, the multistage froth flotation has to be appropriately operated to achieve the expected functions. Foam rises only through the bubble caps (not passing through the downcomer) and the liquid flows down only through the downcomer (not passing through the bubble caps) for all trays.[25] Figure 5 shows the operational region (dash line) of the studied multistage froth flotation column operated at a feed solution having 0.3% or 0.5% (w/v) surfactant concentration and 500 mg/L motor oil. As shown in Fig. 5, there are three unstable regions: (i) no foaming region, (ii) dumping region, and (iii) flooding region.[34] The first region occurred when the system was operated
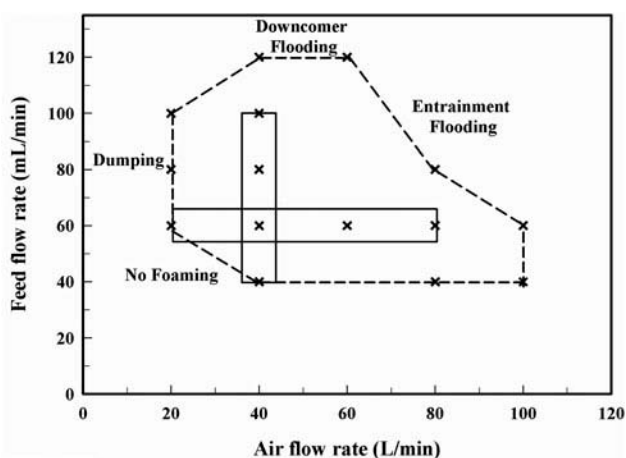
Figure 5. Boundaries of operational zone of flotation column. [Conditions: Surfactant concentrations of 0.3% and 0.5% (w/v) and motor oil concentration of 500 mg/L.]
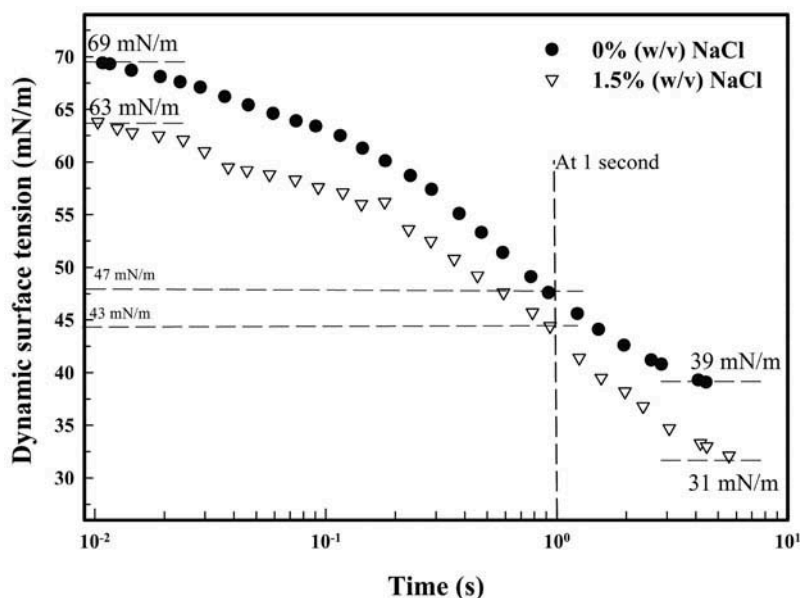
Figure 4. Dynamic surface tension of 0.3% (w/v) surfactant solution with and without 1.5% (w/v) NaCl addition.

at both very low air and feed flow rates. The generated foam could not reach the foam outlet, causing no separation of both surfactant and motor oil. The second region only took place at a very low air flow rate. Since the pressure of the air was not high enough to hold up the liquid in each tray, a substantial portion of liquid could flow down through bubble caps and finally dump through to the base of the column; therefore, performance separation significantly could decrease.[25] The last region was the flooding, which can be classified into two sub-regions: (i) downcomer flooding and (ii) entrainment flooding. The downcomer flooding occurred when the liquid level in each tray was higher than the overflow weir of the downcomer when the system was operated under a very high air flow rate with a moderate feed flow rate. At a very high throughput of feed with a moderate air flow rate, a significant quantity of liquid could pass through the upper tray though the downcomer, resulting in entrainment flooding.[34]

To conduct all experiments, both air and liquid flow rates selected were located in the operational zone. The air flow rate was investigated in the range of 20–80 L/min, while the feed flow rate varied in the range of 40–100 mL/min.

Effects of foam height

Figure 6 shows the effect of the foam height on the process performance of the multistage froth flotation unit operated at an air flow rate of 40 L/min, a feed flow rate of 60 mL/min, and two different surfactant concentrations of 0.3% and 0.5% (w/v). For any surfactant concentration in the feed solution, both motor oil removal and surfactant recovery decrease with the increase in foam height, whereas the enrichment ratios, separation factors, residual factors, and effluent concentrations of both motor oil and surfactant increase, as shown in Fig. 6a–e, respectively. The present results are in good agreement with several previous studies.[17,20,21,24,35,36] The results can be explained by the fact that an increase in foam height basically increases the residence time of generated foam, allowing more liquid to drain out from the foam lamellae, resulting in drier foam,
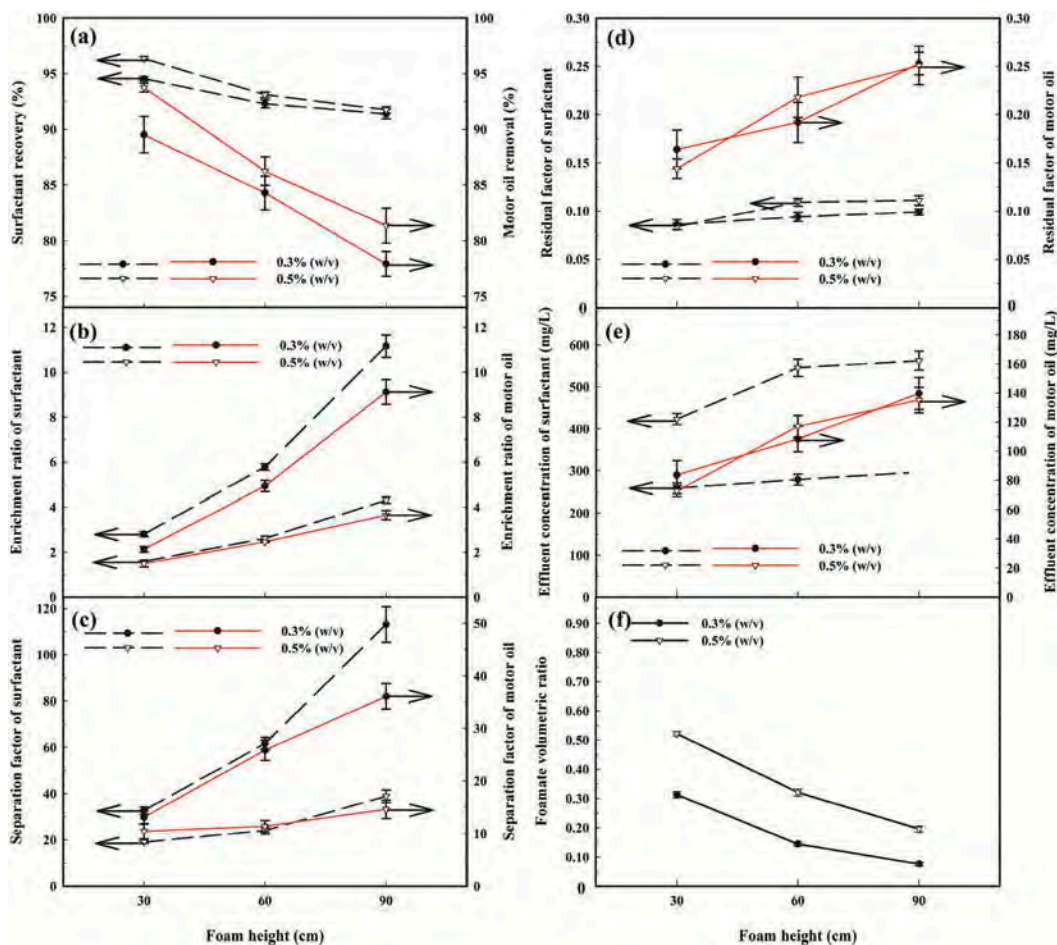
Figure 6. Effect of foam height on (a) enrichment ratio, (b) residual factor, (c) separation factor, (d) surfactant recovery and motor oil removal, (e) effluent concentration, and (f) foamate volumetric ratio under two different surfactant concentrations [0.3% and 0.5% (w/v)]. [Conditions: air flow rate of 40 L/min, feed flow rate of 60 mL/min, and motor oil concentration of 500 mg/L].

as evidenced experimentally by the reduction of the foa-mate volumetric ratio, as shown in Fig. 6f. Hence, an increase in foam height simply reduces the bulk liquid transport, causing increases in the enrichment ratios and separation factors of both surfactant and motor oil, except the motor oil removal and surfactant recovery, which rely on both adsorptive and bulk liquid transports. However, surfactant recovery was found to be moderately decreased with increasing foam height as compared with the drastic decrease in motor oil removal. It is due to most of the surfactant molecules adsorbing at the air/water interface of generated foam, leading to a small fraction of surfactant in the liquid drainage.[22,23]

It is very interesting to point out that by visual observation, the structures of generated foam changed along the foam height. The generated foam at the bottom of the foam column, known as fresh foam, had a spherical shape with thick liquid films while the foam, especially at the highest foam height, looked polyhedral with thinner liquid films.[33,37] This observa-tion confirms that the drainage of excess liquid from the foam lamellae increased as foam height increased.

In a comparison of the two surfactant concentra-tions, the low surfactant concentration of 0.3% (w/v), which was found to be the lowest surfactant concentra-tion capable of producing stable foam to reach the highest foam height of 90 cm, provided better separa-tion efficiency than the high surfactant concentration of 0.5% (w/v). From the foamate volumetric ratio results (Fig. 6f), it can be concluded that a lower surfactant concentration can reduce the bulk liquid transport. The results are in good agreement with previous studies.[20,24,35]

The present results suggest that an optimum foam height has to trade off between the bulk liquid transport and the adsorptive transport in order to achieve both high removal and high enrichment ratio of motor oil. Hence, a foam height of 60 cm was selected for further investigation of the effects of other operational parameters.

Effect of air flow rate

Figure 7 shows the effects of the air flow rate on the separation performance of the studied multistage froth flotation unit by varying the air flow rate stepwise from 20 to 80 L/min at a foam height of 60 cm, a feed flow rate of 60 mL/min and two different feed surfactant concentrations, 0.3 and 0.5% (w/v), with 500 mg/L motor oil. As the air flow rate increased, both motor oil removal and surfactant recovery increased for both surfactant concentrations (Fig. 7a). Conversely, the enrichment ratios, separation factors, residual factors,

and effluent concentrations of both motor oil and sur-factant decreased markedly with increasing air flow rate, as shown in Fig. 7b–e, respectively. These observa-tions are in good agreement with those of other studies.[19,21,24,38–40] The results of the increase in foa-mate volumetric ratio with increasing air flow rate (see Fig. 7f), suggest that the bulk liquid transport increases with the increase in air flow rate. It can be explained by the fact that an increase in air flow rate (increasing superficial velocity from 1.06 to 4.24 cm/s) increases both foam production rate and foam rising velocity, leading to a lowering of the residence time of generated foam. The higher the air flow rate, the higher the amount of water entrained by the bubbles (wetter foam) or the higher the bulk liquid transport.[35] It can be used to explain why the motor oil removal and surfactant recovery increased while the enrichment ratios and separation factors decreased with the increase in the air-flow rate.[14,25]

An increase in surfactant concentration from 0.3% to 0.5% (w/v) caused significant reduction of the enrichment ratios and separation factors but had an insignificant effect on both motor oil removal and surfactant recovery; this is consistent with some pre-vious works.[10,24,39,41] An increase in surfactant con-centration basically increases both foam production rate and water content in produced foam as indicated experimentally by the increase in foamate volumetric ratio, causing a large increase in the bulk liquid trans-port with a small increase in the adsorptive transport.

The results presented earlier suggest that a multi-stage froth flotation column has to be operated at a proper air flow rate (not too low and not too high) to trade off between the two removal mechanisms of adsorptive transport and bulk liquid transport in order to achieve both high removal and enrichment ratio of oil. Hence, the optimum air flow rate of 40 L/min was chosen for further investigation of other effects in order to maximize the process performance of the studied multistage froth flotation unit.

Effect of feed flow rate

An increase in the feed flow rate results in the decreases in motor oil removal, surfactant recovery, enrichment ratios and separation factors of both surfactant and motor oil, as shown in Fig. 8a–c, respectively. In con-trast, Fig. 8d and e show the residual factors and efflu-ent concentrations of both surfactant and motor oil increase substantially with the increase in feed flow rate, especially at high feed flow rates (beyond 80 mL/min). The results can be explained by the fact that an increased feed flow rate expands the quantity of

Figure 7. Effect of air-flow rate on (a) enrichment ratio, (b) residual factor, (c) separation factor, (d) surfactant recovery and motor oil removal, (e) effluent concentration, and (f) foamate volumetric ratio under two different surfactant concentrations [0.3% and 0.5% (w/v)]. [Conditions: foam height of 60 cm, feed flow rate of 60 mL/min, and motor oil concentration of 500 mg/L].

surfactant to promote a foam production rate, leading to higher bulk liquid transport as confirmed experimentally in Fig. 8f (an escalation in foamate volumetric ratio with increasing feed flow rate). However, at a very high feed flow rate, the separation performance in terms of motor oil removal, surfactant recovery, enrichment ratios, and separation factors of both surfactant and motor oil decreased sharply with the increase in feed flow rate. At a very high feed flow rate (greater than 80 mL/min), an increase in feed flow rate directly increased the quantities of both surfactant and motor oil in the system, leading to lowering the separation efficiency. The results are consistent with previous studies.[20,22]

In a comparison between the two surfactant concentrations in the feed solution, the motor oil removal and surfactant recovery did not depend on the surfactant concentration but the enrichment ratios and separation factors of both motor oil and surfactant decreased significantly with increasing surfactant concentration from 0.3% to 0.5% (w/v). As can be seen in Fig. 8f,

the foamate volumetric ratio escalates with increasing surfactant concentration from 0.3% to 0.5% (w/v), indicating that the increasing surfactant concentration from 0.3% to 0.5% (w/v) simply increased the bulk liquid transport, leading to lowering both enrichment and separation factors but it did not affect the motor oil removal and surfactant recovery.[41,42]

Effects of salt concentration

The presence of salt is one of the key factors affecting the froth flotation performance when an ionic surfactant is used as a frother. Most of real wastewaters contain a significant concentration of salts and so studies of salt effects are directly beneficial to the application of forth flotation to wastewater treatment. Several studies reported that the addition of salt in an anionic surfactant system could enhance oil removal efficiency.[16–18] Hence, the effect of NaCl concentration on the froth flotation performance was observed in this study under the base operational conditions (a foam height of 60 cm, an air
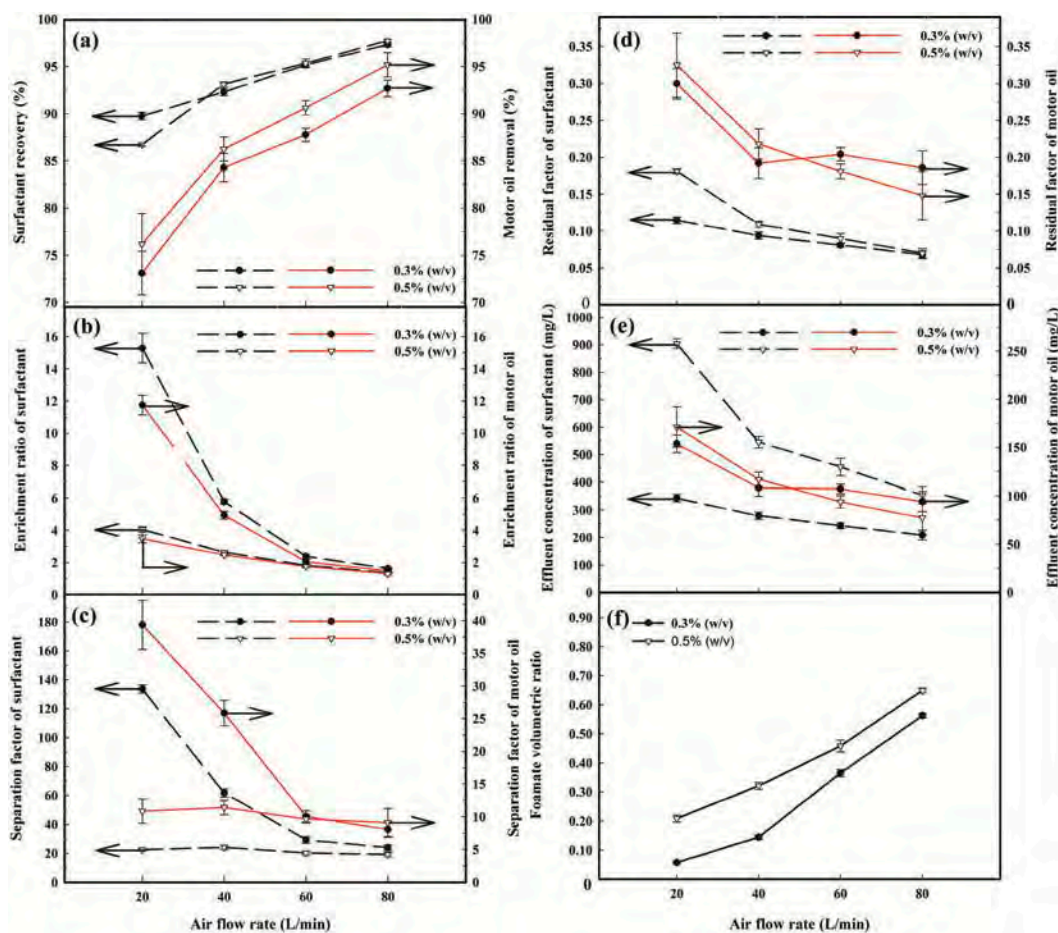
Figure 8. Effect of feed-flow rate on (a) enrichment ratio, (b) residual factor, (c) separation factor, (d) surfactant recovery and motor oil removal, (e) effluent concentration, and (f) foamate volumetric ratio under two different surfactant concentrations [0.3% and 0.5% (w/v)]. [Conditions: foam height of 60 cm, air flow rate of 40 L/min, and motor oil concentration of 500 mg/L].

flow rate of 40 L/min, a feed flow rate of 60 mL/min, and a surfactant concentration of 0.3% wt/v with 500 mg/L motor oil). Figure 9 shows the effect of added NaCl on the separation process performance of the studied multistage froth flotation column. As shown in Fig. 9a–c, both motor oil removal and surfactant recovery slightly rise and the enrichment ratios and separation factors remarkably increase with the increase in NaCl concentration up to 1.5% (w/v) and they reached maximum levels at a NaCl concentration of 1.5% (w/v). However, with a further rise in the NaCl concentration from 1.5% (the optimum NaCl concentration) to 2.0% (w/v), they decreased drastically. In contrast, both residual factors and effluent concentrations of surfactant and motor oil showed opposite trends (see Fig. 9d and e). The foamate volumetric ratio was found to significantly decrease with the increase in NaCl concentration up to 1.5% (w/v). Beyond the optimum NaCl concentration of 1.5% (w/v), the foamate volumetric ratio slightly decreased with further increase in NaCl concentration (see Fig. 9f). An addition of NaCl in any ionic surfactant system can affect both foamability and

foam stability, leading to significant effects on the separation process performance of the studied multistage froth flotation unit. The foam characteristics as a function of NaCl concentration will be discussed later.

From the results, the best process performance for motor oil removal as well as surfactant recovery by the studied multistage froth flotation system can be achieved at a foam height of 60 cm, an air flow rate of 40 L/min, a feed flow rate of 60 mL/min, and a NaCl concentration of 1.5% (w/v).

Foam characteristics

For a better understanding of the separation mechanisms of the multistage froth flotation column, foam characteristic experiments were carried out to determine both foamability and foam stability of the generated foam in order to correlate to the separation process performance. The longer the time to reach the maximum foam height (120 cm), the lower the ability to produce foam (foamability), whereas the longer the time required for the
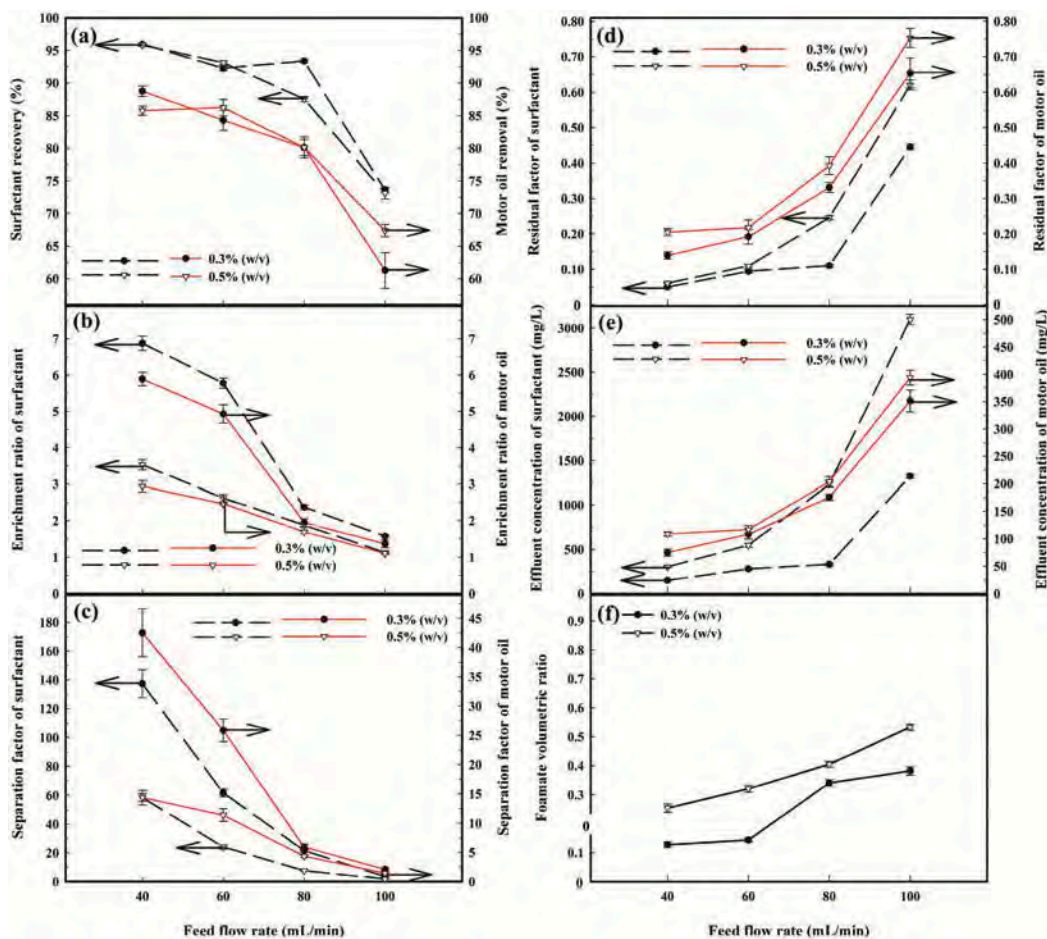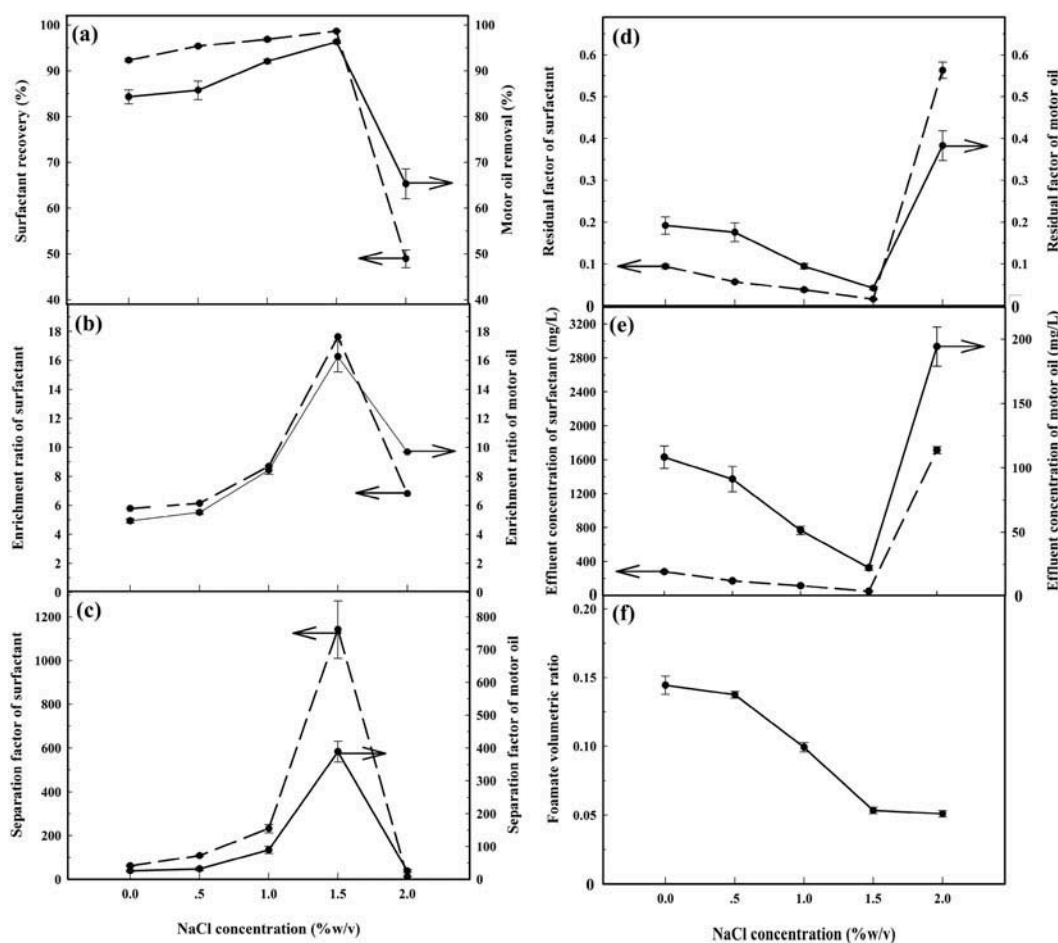
Figure 9. Effect of salt concentration on (a) enrichment ratio, (b) residual factor, (c) separation factor, (d) surfactant recovery and motor oil removal, (e) effluent concentration, and (f) foamate volumetric ratio under 0.3% (w/v) surfactant. [Conditions: foam height of 60 cm, air flow rate of 40 L/min, feed flow rate of 60 mL/min, and motor oil concentration of 500 mg/L].

generated foam to collapse from 120 to 60 cm, the higher the foam stability. The effects of NaCl concentration on foamability and foam stability are shown in Fig. 10. An increase in NaCl concentration up to 0.5% (w/v) slightly increased foamability but beyond the optimum salinity of 0.5% (w/v), both foamability and foam stability decreased remarkably with further increase in NaCl concentration.

An addition of NaCl can provide the co-adsorption of counterions of Na$^+$ ions to reduce the repulsion force between negatively charged head groups of the surfactant, resulting in increasing surfactant adsorption on the foam lamella surfaces. As a result, both foamability and foam stability increased when NaCl was added up to 0.5% (w/v). However, when NaCl was further added beyond the optimum NaCl concentration of 0.5% (w/v), both foamability and foam stability decreased remarkably with further increase in NaCl concentration. When too much NaCl is added, it simply reduces the repulsion forces between the two surfaces of foam lamellae by adding Na$^+$ ions to neutralize the negatively charged head group of

surfactant adsorbing on the foam lamellae surfaces, causing a reduction of both foamability and foam stability. This explanation can be used for the effects of added NaCl on the separation process performance of the continuous multistage froth flotation system, as described earlier. Interestingly, the optimum NaCl concentration, as shown in Figs. 9 and 10, was much different. The great difference in the optimum NaCl concentrations in these two experiments resulted from the different operational conditions. The multistage froth flotation column was operated in a continuous mode while the foam characteristic experiment was operated in a batch mode.

Concentration profiles of surfactant and motor oil

Figure 11 shows the concentration profiles of surfactant and motor oil in the solution in each tray, as compared to those in the feed solution and effluent under the optimum operational conditions. The lowest concentrations of both surfactant and motor oil were observed at
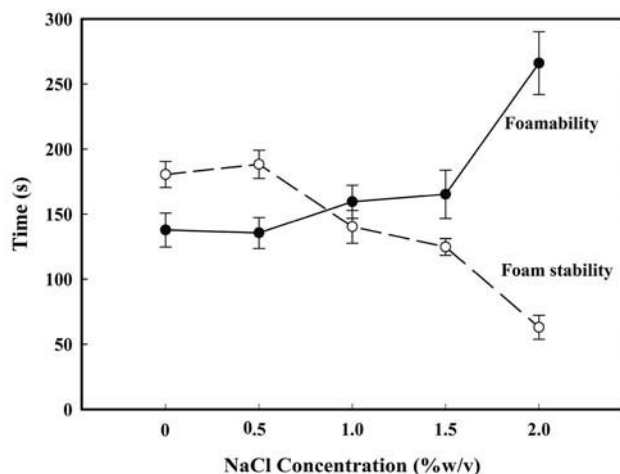
Figure 10. Foam characteristics in terms of foamability and foam stability as a function of NaCl concentration [0.3% (w/v) surfactant and 500 mg/L motor oil].

the bottom tray while the highest concentration could be found at the topmost tray. In each tray, surfactant and motor oil adsorbing on the air bubble surface and then were carried together with the rising air bubbles and emerged from the solution to form foam. After that, the rising foam was collapsed when passing through the caps on the upper tray of the column, causing the enrichments of both surfactant and motor oil in the solution of the upper tray. As a result, the transport direction of both surfactant and motor oil is upward. From the results, it can be concluded that the higher the tray number, the higher the removal efficiencies of both surfactant and motor oil. However, in a comparison of the concentrations of both surfactant and motor oil in the solution in each tray to those in a lower tray, they decreased greatly for the first two top trays (tray 4 and tray 3). The removal efficiency by the last tray (tray 1) was relatively low. Hence, an increase

in tray number greater than 4 is not recommended for a design and operation of a multistage froth flotation column.

Comparisons of separation process performance

Table 2 shows a comparison of the separation performance of the studied multistage with previous batch and single-stage froth flotation units. It can be clearly observed that the main problem of batch and continuous mode of all single-stage froth flotation could provide almost complete removal of any studied oil (>99%) with a very low enrichment ratio of oil (~2), while this studied multistage froth flotation column gave more or less high oil removal with extremely high enrichment ratios of both motor oil and surfactant (16.3 and 17.6, respectively). Similar to a distillation column, both motor oil and surfactant can be enriched in the upward direction for a multistage froth flotation column. Both high enrichment ratios of motor oil and surfactant can lead to a possibility of both economic recovery of the motor oil and surfactant.

Conclusions

In the present work, a continuous multistage froth flotation system was found to be a promising technique for motor oil removal. When it was operated under the optimum operational conditions, the highest motor oil removal performance (97.9%) could be achieved with the highest values of enrichment ratios of 16.3 and 17.6 for motor oil and surfactant, respectively, which are much higher than those of previous batch and continuous single-stage systems. To optimize the process performance of a continuous multistage froth flotation
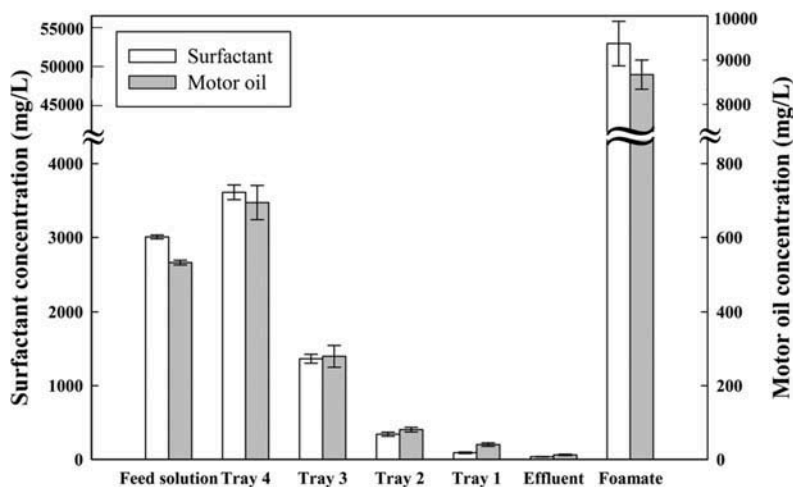
Figure 11. Concentration profiles of surfactant and motor oil under 0.3% (w/v) surfactant and 1.5% (w/v) NaCl. [Conditions: foam height of 60 cm, air flow rate of 40 L/min, feed flow rate of 60 mL/min, and motor oil concentration of 500 mg/L].

Table 2. Comparison of the process performance of different froth flotation units.

Type of oil	Surfactant	NaCl (% wt/v)	Oil concentration	Process	HRT (min)	% Removal		Enrichment ratio		Ref
						Oil	Surfactant	Oil	Surfactant	
ODCB	SDS (3.5% w/v) CPC (3.5% w/v) DADS (3.5% w/v)	1.25 1.75 7	Oil/water = 1/100	Batch, Single stage	-	~ 40 ~55 ~50	~20 ~35 ~25	- - -	- - -	(12)
ODCB	Total surf conc. (5% w/v) (SDS/NP(EO)10 = 4/1)	-	Oil/water = 1/100	Batch, Single stage	-	Almost 100%	100 % for NP(EO)10 80 % for SDS	-	-	(13)
Ethylbenzene	AMA (0.3% w/v)	3	Oil/water = 1/1	Batch, Single stage	-	Almost 100%	~80	1.75	-	(14, 15)
Diesel Oil	Alfoterra 145-4PO (0.1% w/v)	3	Oil/water = 1/1	Batch, Single stage	-	91.54	98.3	1.53	-	(16)
Diesel Oil	Alfoterra 145-4PO (0.1% w/v) and SDS (0.5% w/v)	4	Oil/water = 1/19	Continuous, Single stage	60	~75	~96	~2	~1.8	(17)
Motor oil	Alfoterra 145-5PO (0.5% w/v)	5	Oil 500 mg/L	Continuous, Single stage	30	~60	~50	~1.7	~2	(18)
Cutting oil	SDS (0.1% w/v)	6	Oil 500 mg/L	Continuous, Single stage with packing volume of 50%	60	98.1	84.9	2.3	7.8	(19)
Motor oil	Alfoterra 145-8PO (0.3% w/v)	1.5	Oil 500 mg/L	Continuous, Multi stage	94*	97.9	98.9	16.3	17.6	This study

Note: ODCB is ortho-dichlorobenzene, SDS is sodium dodecyl sulfate, DADS is mono and di-hexadecyl diphenyloxide disulphonate sodium salt, NP(EO)10 is nonylphenol ethoxylate, AMA is di-1, 3-dimethylbutyl sulfosuccinate and Alfoterra 145-4PO/Alfoterra 145-5PO/Alfoterra 145-8PO is Branched alcohol propoxylate sulfate sodium salt with 14 to 15 carbons in the alkyl chain, and an average of 4, 5 and 8 propylene oxides, respectively.

*Hydraulic retention time (HRT) calculated from the liquid volume in the column divided by the feed flow rate.

system in terms of high removal and high enrichment ratio of oil, it has to be operated to obtain high adsorptive transport with low bulk liquid transport. An addition of NaCl, at a proper concentration, can enhance the separation performance of a continuous multistage froth flotation column when an ionic surfactant is used as a frother. The higher the stage number, the higher the separation process performance. However, it has a maximum stage number for operating a multistage froth flotation column because at a very low surfactant concentration in any tray, the generated foam cannot reach an upper tray.

Acknowledgments

Funding

References

[1] Zeng, Y.; Yang, C.; Zhang, J.; Pu, W. (2007) Feasibility investigation of oily wastewater treatment by combination of zinc and PAM in coagulation/flocculation. *Journal of Hazardous Materials*, 147: 991–996.

[2] Shi-Qian, L.; Pei-Jiang, Z.; Ling, D.; Kai, F. (2011) Treatment of oily wastewater using composite flocculant of polysilicate ferro–aluminum sulfate–rectorite. *Journal of Water Resource and Protection*, 3: 253–261.

[3] Nadarajah, N.; Singh, A.; Ward, O.P. (2002) De-emulsification of petroleum oil emulsion by a mixed bacterial culture. *Process Biochemistry*, 37: 1135–1141.

[4] Perez, M.; Rodriguez-Cano, R.; Romero, L.I.; Sales, D. (2007) Performance of anaerobic thermophilic fluidized bed in the treatment of cutting-oil wastewater. *Bioresource Technology*, 8: 3456–3463.

[5] Gryta, M.; Karakulski, K.; Morawski, A.W. (2001) Purification of oily wastewater by hybrid UF/MD. *Water Research*, 35: 3665–3669.

[6] Masuelli, M.; Marchese, J.; Ochoa, N.A. (2009) SPC/PVDF membranes for emulsified oily wastewater treatment. *Journal of Membrane Science*, 326: 688–693.

[7] Li, Y.S.; Yan, L.; Xiang, C.B.; Hong, L.J. (2006) Treatment of oily wastewater by organic–inorganic composite tubular ultrafiltration (UF) membranes. *Desalination and Water Treatment*, 196: 76–83.

[8] Hua, F.L.; Tsang, Y.F.; Wang, Y.J.; Chan, S.Y.; Chua, H.; Sin, S.N. (2007) Performance study of ceramic microfiltration membrane for oily wastewater treatment. *Chemical Engineering Journal*, 128: 169–175.

[9] Yan, L.; Hong, S.; Li, M.L.; Li, Y.S. (2009) Application of the Al_2O_3–PVDF nanocomposite tubular ultrafiltration (UF) membrane for oily wastewater treatment and its antifouling research. *Separation and Purification Technology*, 66: 347–352.

[10] Wong, C.; Hossain, M.; Davies, C. (2001) Performance of a continuous foam separation column as a function of process variables. *Bioprocess and Biosystems Engineering*, 24: 73–81.

[11] Burghoff, B. (2012) Foam fractionation applications. *Journal of Biotechnology* 161: 126–137.

[12] Pondstabodee, S.; Scamehorn, J.F.; Chavedej, S.; Harwell, J.H. (1998) Cleanup of oily wastewater by froth flotation: Effect of microemulsion formation. *Separation Science and Technology*, 33: 591–609.

[13] Chavadej, S.; Ratanarojanatam, P.; Phoochinda, W.; Yanatatsaneejit, U.; Scamehorn, J.F. (2004) Clean–up of oily wastewater by froth flotation: Effect of microemulsion formation II: Use of anionic/nonionic surfactant mixtures. *Separation Science and Technology*, 39: 3079–3096.

[14] Yanatatsaneejit, U.; Chavadej, S.; Rangsunvigit, P.; Scamehorn, J.F. (2005) Ethylbenzene removal by froth flotation under conditions of middle-phase microemulsion formation II: Effects of air flow rate, oil-to-water ratio, and equilibration time. *Separation Science and Technology*, 40: 1609–1620.

[15] Yanatatsaneejit, U.; Witthayapanyanon, A.; Rangsunvigit, P.; Acosta, E.J.; Sabatini, D.A.; Scamehorn, J.F.; Chavadej, S. (2005) Ethylbenzene removal by froth flotation under conditions of middle-phase microemulsion formation I: Interfacial tension, foamability, and foam stability. *Separation Science and Technology*, 40: 1537–1553.

[16] Watcharasing, S.; Angkathunyakul, P.; Chavadej, S. (2008) Diesel oil removal from water by froth flotation under low interfacial tension and colloidal gas aphron conditions. *Separation and Purification Technology*, 62: 118–127.

[17] Yanatatsaneejit, U.; Chavadej, S.; Scamehorn, J.F. (2008) Diesel oil removal by froth flotation under low interfacial tension conditions I: Foam characteristics, and equilibration time. *Separation Science and Technology*, 43: 1520–1534.

[18] Watcharasing, S.; Kongkowit, W.; Chavadej, S. (2009) Motor oil removal from water by continuous froth flotation using extended surfactant: Effects of air bubble parameters and surfactant concentration. *Separation and Purification Technology*, 70: 179–189.

[19] Bunturngpratoomrat, A.; Pornsunthorntawee, O.; Nitivattananon, S.; Chavadej, J.; Chavadej, S. (2013) Cutting oil removal by continuous froth flotation with packing media under low interfacial tension conditions. *Separation and Purification Technology*, 107: 118–128.

[20] Rujirawanich, V.; Chavadej, S.; O'Haver, J.H.; Rujiravanit, R. (2011) Removal of trace Cd^{2+} using continuous multistage ion foam fractionation: Part II—the effects of operational parameters. *Separation Science and Technology*, 46: 1673–1683.

[21] Boonyasuwat, S.; Chavadej, S.; Malakul, P.; Scamehorn, J.F. (2005) Surfactant Recovery from water using a multistage foam fractionator: Part I effects of air flow rate, foam height, feed flow rate and number of stages. *Separation Science and Technology*, 40: 1835–1853.

[22] Rujirawanich, V.; Chuyingsakultip, N.; Triroj, M.; Malakul, P.; Chavadej, S. (2012) Recovery of surfactant from an aqueous solution using continuous multistage foam fractionation: Influence of design parameters. *Chemical Engineering and Processing: Process Intensification*, 52: 41–46.

[23] Rosen, M.J. (2004) Surfactants and Interfacial Phenomena. John Wiley & Sons, Inc., p. 34–104. <Please provide missing location for the Ref. [23].>

[24] Boonyasuwat, S.; Chavadej, S.; Malakul, P.; Scamehorn, J.F. (2003) Anionic and cationic surfactant recovery from water using a multistage foam fractionator. *Chemical Engineering Journal*, 93: 241–252.

[25] Rujirawanich, V.; Chavadej, S.; O'Haver, J.H.; Rujiravanit, R. (2010) Removal of trace Cd^{2+} using continuous multistage ion foam fractionation: Part I—The effect of feed SDS/Cd molar ratio. *Journal of Hazardous Materials*, 182: 812–819.

[26] Tamura, T.; Kaneko, Y.; Ohyama, M. (1995) Dynamic surface tension and foaming properties of aqueous polyoxyethylene n-dodecyl ether solutions. *Journal of Colloid and Interface Science*, 173: 493–499.

[27] Childs, J.D.; Acosta, E.; Scamehorn, J.F.; Sabatini, D.A. (2000) Dynamic surface tension and adsorption mechanisms of surfactants at the air–water interface. *Advances in Colloid and Interface Science*, 85: 103–144.

[28] Childs, J.D.; Acosta, E.; Scamehorn, J.F.; Sabatini, D.A. (2004) Surfactant-enhanced treatment of oil-based drill cuttings. *Journal of Energy Resources Technology*, 127 153–162.

[29] Witthayapanyanon, A.; Phan, T.; Heitmann, T.; Harwell, J.; Sabatini, D. (2010) Interfacial properties of extended surfactant based microemulsions and related macroemulsions. *Journal of Surfactants and Detergents*, 13: 127–134.

[30] Witthayapanyanon, A.; Acosta, E.J.; Harwell, J.H.; Sabatini, D.A. (2006) Formulation of ultralow interfacial tension systems using extended surfactants. *Journal of Surfactants and Detergents*, 9: 331–339.

[31] Wang, L.; Yoon, R.H. (2004) Hydrophobic forces in the foam films stabilized by sodium dodecyl sulfate: Effect of electrolyte. *Langmuir*, 20: 11457–11464.

[32] Comley, B.A.; Harris, P.J.; Bradshaw, D.J.; Harris, M.C. (2002) Frother characterisation using dynamic surface tension measurements. *International Journal of Mineral Processing*, 64: 81–100.

[33] Chuang, K.T.; Nandakumar, K. (2000) Tray columns: Design. *Encyclopedia of Separation Science*, 1135–1140.

[34] Bennett, D.L.; Douglas, L. (2000) Optimize distillation columns. *Chemical Engineering Progress*, 96(5): 19–34.

[35] Tadakamalla, K.; Marathe, K.V. (2011) Hydrodynamic study and optimization strategy for the surfactant recovery from aqueous solutions. *Desalination and Water Treatment*, 266: 98–107.

[36] Tharapiwattananon, N.; Scamehorn, J.F.; Osuwan, S.; Harwell, J.H.; Haller, K.J. (1996) Surfactant recovery from water using foam fractionation. *Separation Science and Technology*, 31: 1233–1258.

[37] Pugh, R.J. (2005) Experimental techniques for studying the structure of foams and froths. *Advances in Colloid and Interface Science*, 114–115:239–251.

[38] Chungchamroenkit, P.; Chavadej, S.; Scamehorn, J.F.; Yanatatsaneejit, U.; Kitiyanan, B. (2009) Separation of carbon black from silica by froth flotation part 1: Effect of operational parameters. *Separation Science and Technology*, 44: 203–226.

[39] Zhang, J.; Jing, Y.; Wu, Z.; Li, Q. (2009) Removal of trace Cu^{2+} from aqueous solution by foam fractionation. *Desalination and Water Treatment*, 249: 503–506.

[40] Yang, Q.W.; Wu, Z.L.; Zhao, Y.L.; Wang, Y.; Li, R. (2011) Enhancing foam drainage using foam fractionation column with spiral internal for separation of sodium dodecyl sulfate. *Journal of Hazardous Materials*, 192: 1900–1904.

[41] Gerken, B.M.; Nicolai, A.; Linke, D.; Zorn, H.; Berger, R.G.; Parlar, H. (2006) Effective enrichment and recovery of laccase C using continuous foam fractionation. *Separation Science and Technology*, 49: 291–294.

[42] Qu, Y.H.; Zeng, G.M.; Huang, J.H.; Xu, K.; Fang, Y.Y.; Li, X.; Liu, H.L. (2008) Recovery of surfactant SDS and Cd^{2+} from permeate in MEUF using a continuous foam fractionator. *Journal of Hazardous Materials*, 155: 32–38.

[43] Persson, C.M.; Jonsson, A.P.; Bergström, M.; Eriksson, J. C. (2003) Testing the Gouy–Chapman theory by means of surface tension measurements for SDS–NaCl–H$_2$O mixtures. *Journal of Colloid and Interface Science*, 267: 151–154.

Ethylene epoxidation in a low-temperature parallel plate dielectric barrier discharge system with two frosted glass plates

Sumaeth Chavadej[a,b], Weerayut Dulyalaksananon[a], Thitiporn Suttikul[c,*]

[a] The Petroleum and Petrochemical College, Chulalongkorn University Soi Chula 12, Phyathai Road, Pathumwan, Bangkok 10330, Thailand
[b] Center of Excellence on Petrochemical and Materials Technology, Chulalongkorn University, Bangkok 10330, Thailand
[c] Division of Chemical Process Engineering Technology, Faculty of Engineering and Technology, King Mongkut's University of Technology North Bangkok, Rayong Campus, Rayong 201180, Thailand

ABSTRACT

The objective of this work was to investigate ethylene oxide (EO) performance in a low-temperature parallel plate dielectric barrier discharge (DBD) system with two frosted glass plates as the dielectric barrier material under ambient temperature and atmospheric pressure. A separate feed technique was used to reduce all undesirable reactions in order to maximize ethylene oxide production. The effects of applied voltage, input frequency, and O_2/C_2H_4 feed molar ratio, as well as ethylene feed position, on ethylene epoxidation activity were examined. The DBD system with two frosted glass plates was found to provide the highest EO selectivity of 68.15% and the highest EO yield of 10.88% at 23 kV, 500 Hz, an O_2/C_2H_4 feed molar ratio of 1:5, and an ethylene feed position fraction of 0.5, which gave double the EO yield of both DBD systems with single or two smooth dielectric glass plates.

© 2016 Published by Elsevier B.V.

1. Introduction

EO is commercially produced from the gas-phase partial oxidation of ethylene or ethylene epoxidation over Ag/low surface area (LSA) α-Al_2O_3 catalysts with an addition of promoters [1–6]. This commercial process can give a higher EO selectivity under a moderate temperature operation but the process performance declines with time resulting from the catalyst deactivation by coke deposits. Therefore, a search for a new method with lower energy consumption, a lower reaction temperature and without the use of a catalyst is of great interest. Non-thermal plasma has been reported to be an alternative technique for several reactions including ethylene epoxidation [7,8], natural gas reforming (H_2 production) [9–13], chemical vapor deposition [14–21], and desulfurization [22,23].

The most important advantage of non-thermal plasma over thermal plasma is to have highly energetic generated electrons (approximately 10^4–10^5 K) with a low bulk gas temperature (close to ambient temperature) [19,24]. This makes it possible to activate several chemical reactions under ambient temperature and atmospheric pressure, leading to a lowering of energy consumption.

Dielectric Barrier Discharge (DBD) is one type of non-thermal plasma and has been commonly used in various applications because of its fairly uniform plasma distribution [19]. For discharge generation, electrons receive sufficient energy from the applied voltage to overwhelm the potential barrier between the two electrode surfaces and then the generated electrons directly collide with the gaseous molecules present in the plasma zone to generate new ions and neutral species. Subsequently, the dissociated species or generated excited species, having higher reactivity than neutral species at the ground state, can initiate several reactions that normally occur at high reaction temperatures. The examples of chemical synthesis using non-thermal plasma include O_3 generation [25,26], synthesis of acetylene (C_2H_2) [27], synthesis of methanol [28], and synthesis of ammonia [29].

A DBD reactor generally consists of one or two dielectric layers between two electrodes. The configuration of electrodes was found to influence the efficiency of EO production in that a cylindrical DBD provided superior ethylene epoxidation performance as compared to a parallel plate DBD [7]. The input power, voltage, and electrode gap distance significantly affected the performance of methane reforming [11,12,30–32], corresponding to the study that the dielectric material and thickness changed the plasma behavior [33].

Our research group has investigated ethylene epoxidation reaction in several types of low-temperature plasma reactors: a corona discharge [4,34,35], a parallel DBD [8], a cylindrical DBD

[7,36], a DBD jet [37], a parallel DBD with supported Ag catalysts [38] and a single clear glass plate [39]. In this work, a low-temperature parallel plate dielectric barrier (DBD) with two frosted glass plates was investigated for ethylene epoxidation reaction. The effects of various operating parameters, including feed O_2/C_2H_4 molar ratio, applied voltage, input frequency, and ethylene feed position on the ethylene epoxidation activity were examined.

2. Experiment

2.1. Chemicals and gases for reaction experiment

Two sand blasted frosted glass Plates 2 mm thick were used for dielectric barrier sheets on the surface of both electrodes of a DBD reactor. Both frosted glass plates were cleaned with distilled water and acetone before being used. The 99.995% helium (high purity grade), 40% ethylene in helium ($\pm$ 1% uncertainty), and 97% oxygen
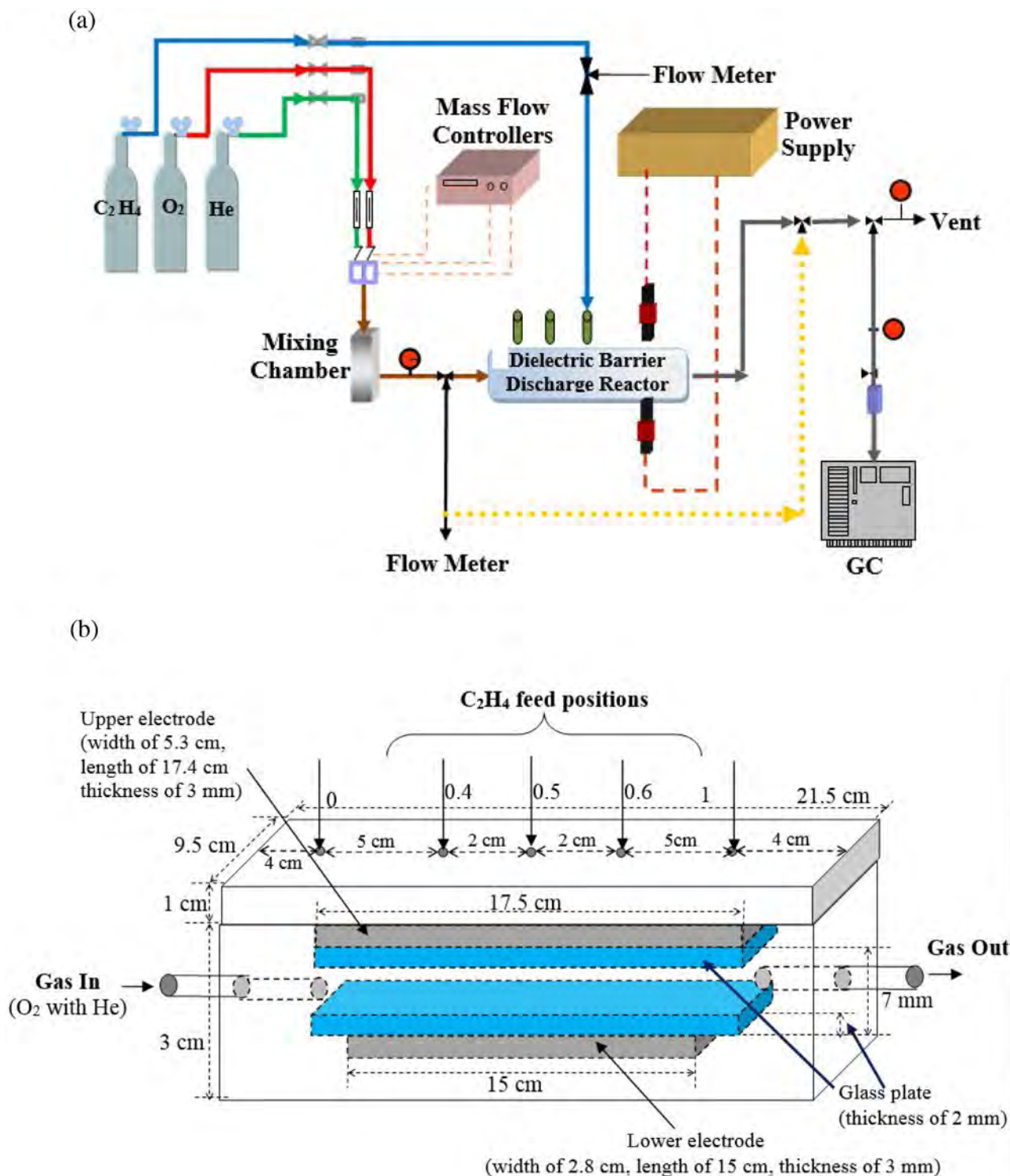

Fig. 1. (a) Schematic of the experimental setup of the DBD plasma system for the ethylene epoxidation reaction and (b) the configuration of the parallel plate DBD reactor.

in helium ($\pm 1\%$ uncertainty) were specially blended by the Thai Industrial Gas Co., Ltd. In addition, a 30% ethylene oxide in helium ($\pm 1\%$ uncertainty) was used as a standard gas to obtain the calibration curve of gas chromatography (GC) for EO analysis (supplied by the same company).

2.2. Frosted glass plate dielectric barrier characterization

X-ray fluorescence (XRF) was used to measure the elemental composition of the frosted glass plates used as a dielectric barrier material by using PANalytical analysis instruments with AXIOS & SUPERQ version 4.0 systems with the IQ+ program. A filed emission scanning electron microscope (FE-SEM, JEOL 5200-2AE) operated at 1–20 kV was used to observe the surface morphology of the glass plate samples. The samples were coated with platinum (Pt) prior to being loaded into an atomic force microscope (AFM) to observe the surface roughness. The AFM (XE-100 Series Park Systems SPM Controller) was operated with non-contact mode, a scan of 20 μm, and a scan rate of 0.1 Hz.

2.3. Setup and reaction activity experiments

The schematic of the setup for ethylene epoxidation reaction using the DBD system is shown in Fig. 1a. The acrylic-made reactor sizes were 1.5 cm height x 5.5 cm width $\times$ 17.5 cm length for inner dimensions and 4 cm height x 9.5 cm width x 21.5 cm length for outer dimensions, as shown in Fig. 1b. The DBD reactor consisted of two stainless steel electrodes. The bottom electrode size was 2.8 cm width $\times$ 15 cm length with 0.3 cm thickness, while the top electrode size – a larger electrode – was 5.3 cm width $\times$ 17.4 cm length with 0.3 cm thickness. The differences in the dimensions of both electrodes were made to eliminate the intense electron emission at the boundary of electrodes when two identical electrodes are used, which can damage the reactor. The gap between the two electrodes was fixed at 7 mm and the thickness of each glass plate was 2 mm.

In this study, a concept of a separate feed of ethylene was applied in order to minimize all undesirable reactions including cracking, coupling, dehydrogenation and EO oxidation [36]. The ethylene feed position was varied along the electrode length while the oxygen was fed throughout the electrode length. The micro discharge plasma was generated by using an alternating current (AC, 200 V and 50 Hz) power. Three steps were required to convert the domestic AC power to a high-voltage AC, as described in our previous work [36]. A power analyzer (Extech Instruments Corporation, True RMS Single Phase Power Analyzer, 380801) was used to measure the input power of the DBD system while the output voltage and current were measured by a digital multimeter (U1273A) with a high voltage prove (CT2700).

The reactant gases (ethylene and oxygen, balanced with helium) fed through the DBD reactor were controlled by a set of electronic mass flow controllers. All reactant lines had 7 μm in-line filters before the mass flow controllers in order to trap any foreign particles. The reactor pressure was controlled via a needle valve. The outlet of the reactor was either vented to the atmosphere via a rubber tube exhaust or connected to an on-line gas chromatograph (PerkinElmer, AutoSystem GC) to analyze the gas product composition. The moisture in the effluent gas was removed by a water trap and a water adsorption column before entering the on-line GC. The GC was equipped with both a thermal conductivity detector (TCD) and a flame ionization detector (FID). For the TCD channel, a packed column (Carboxen 1000) was used for separating the gases produced, including hydrogen (H_2), oxygen (O_2), carbon monoxide (CO), and carbon dioxide (CO_2). For the FID channel, a capillary column (OV-Plot U) was employed for the analysis of ethylene oxide (EO) and other by-product gases, i.e. methane (CH_4), acetylene (C_2H_2), ethane (C_2H_6), and propane (C_3H_8). Power was turned on to generate a discharge after the feed composition had remained unchanged with time. When the system reached a steady state, the composition of the product gas stream was analyzed by the GC every 20 min (at least three times).

The experimental data with less than 5% error were averaged and then used to evaluate the DBD system performance in terms of the C_2H_4 and O_2 conversions, the product selectivities, including H_2, CO, CO_2, EO, CH_4, C_2H_6, C_2H_2, and traces of C_3, and the EO yield, which were calculated using the following equations:

$$\%\text{Reactant conversion} = \frac{(\text{moles of reactant in} - \text{moles of reactant out}) \times 100}{\text{moles of reactant in}} \quad (1)$$

$$\%\text{Product selectivity} = \frac{[(\text{number of carbon or hydrogen atom in product})(\text{moles of product produced})] \times 100}{[(\text{number of carbon or hydrogen atom in C2H4})(\text{moles of C2H4 converted})]} \quad (2)$$

$$\%\text{EO yield} = \frac{(\%\text{C2H4 conversion}) \times (\%\text{EO selectivity})}{100} \quad (3)$$

In addition, power consumption was calculated in a unit of Ws per C_2H_4 molecule converted or per EO molecule produced using the following equation:

$$\text{Power consumption} = \frac{P \times 60}{N \times M} \quad (4)$$

where P = Power (W), N = Avogadro's number = 6.02×10^{23} molecules/mol and M = Rate of converted C_2H_4 molecules in feed or rate of produced EO molecules (mol/min).

3. Results and discussion

3.1. Surface characterization results

The chemical compositions of the clear and frosted glass plates are shown in Table 1. The compositions of both glass plates were almost the same with a major content of silica oxide (SiO_2) of more than 70%. As shown in Fig. 2, the roughness of the frosted glass plate used in this study is in the range of 0.18-1.22 μm, as measured by AFM. In addition, the AFM and SEM results indicate that the

Table 1
Chemical compositions of clear and frosted glass plates analyzed by XPF.

Chemical compositions	Clear glass plate (wt.%)	Frosted glass plate (wt.%)
SiO_2	71.1	74.3
Na_2O	13.5	9.5
CaO	10.9	11.9
MgO	2.9	2.7
Al_2O_3	1.0	1.1
Other	0.6	0.5

(a)

(b)

(c)
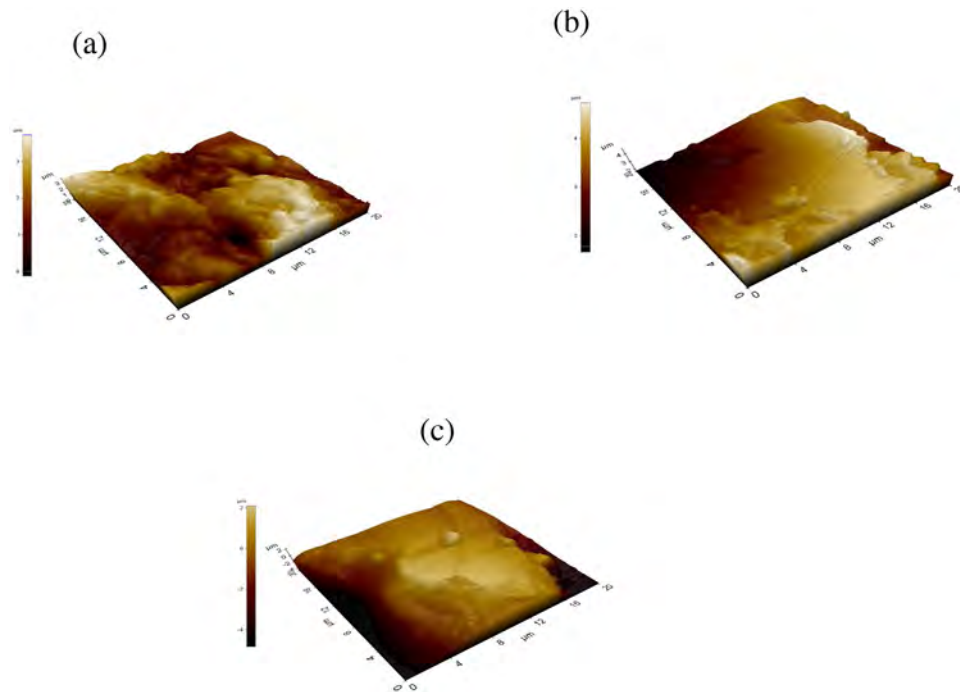
Fig. 2. Surface images of the rough-surfaced glass plate by AFM. (a) Left-edge side, (b) middle-edge side, and (c) right-edge side.

(a)

(b)

(c)
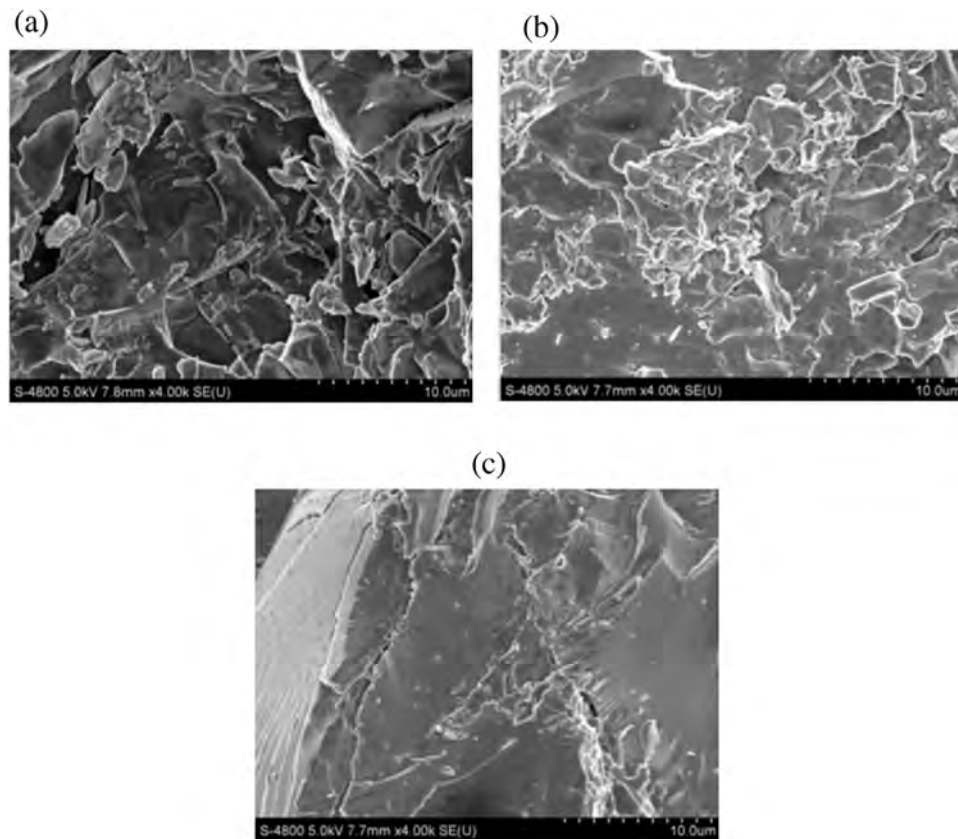
Fig. 3. SEM images of the rough surfaced glass plate (Accelerating voltage of 5 kV, emission current of 9000 nA and Magnification of 4k (a) left-edge side, (b) middle-edge side, and (c) right-edge side).

surface morphology of the frosted glass plate were heterogeneous (see Figs. 2 and 3).

3.2. Possible chemical reactions

The most likely chemical pathways that may appear in the DBD system used in this study are proposed as in the following equations [35,36,39].

Active oxygen formation:

$$O_2 + 2e^- \rightarrow 2O + 2e^- \tag{5}$$

Ethylene epoxidation:

$$C_2H_4 + O \rightarrow C_2H_4O \tag{6}$$

$$C_2H_4 + 1/2O_2 \rightarrow C_2H_4O \tag{7}$$

Partial and complete oxidations:

$$C_2H_4 + 2O \rightarrow 2H_2 + 2CO \tag{8}$$

$$C_2H_4 + 4O \rightarrow 2H_2 + 2CO_2 \tag{9}$$

$$C_2H_4 + 6O \rightarrow 2H_2O + 2CO_2 \tag{10}$$

$$C_2H_4 + 2O_2 \rightarrow 2H_2O + 2CO \tag{11}$$

$$C_2H_4 + 2O_2 \rightarrow 2H_2 + 2CO_2 \tag{12}$$

$$C_2H_4 + 3O_2 \rightarrow 2H_2O + 2CO_2 \tag{13}$$

$$C_2H_4O + O \rightarrow 2H_2 + 2CO \tag{14}$$

$$C_2H_4O + 3O \rightarrow 2H_2O + 2CO \tag{15}$$

Fig. 4. Ethylene epoxidation performance in terms of, (a) C_2H_4 and O_2 conversions, (b) EO selectivity and yield, (c) other product selectivities, and, (d) power consumption as function of applied voltage (an O_2/C_2H_4 feed molar ratio of 0.2, an input frequency of 500 Hz, and a total feed flow rate of 50 cm³/min).

$$C_2H_4O + 5O \rightarrow 2H_2O + 2CO_2 \tag{16}$$

$$C_2H_4O + O_2 \rightarrow 2H_2O + CO \tag{17}$$

Dehydrogenation

$$H_2O + 2e \rightarrow H + OH + 2e \tag{18}$$

$$H_2O + 2e \rightarrow 2H + O + 2e \tag{19}$$

$$H_2O + 2e \rightarrow H_2 + O + 2e \tag{20}$$

$$H_2 + 2e \rightarrow 2H + 2e \tag{21}$$

$$C_2H_4 + O \rightarrow OH + C_2H_3 \tag{22}$$

$$C_2H_3 + 2O \rightarrow CO + 3H \tag{23}$$

Cracking:

$$C_2H_4 + 4e \rightarrow 2C + 4H + 4e \tag{24}$$

$$C_2H_4 + e \rightarrow 2CH_2 + e \tag{25}$$

$$CH_2 + e \rightarrow CH + H + e \tag{26}$$

$$CH + e \rightarrow C + H + e \tag{27}$$

Coupling:

$$CH_2 + 2H \rightarrow CH_4 \tag{28}$$

$$3CH_2 + 2H \rightarrow C_3H_8 \tag{29}$$

$$C_2H_4 + CH_2 + 2H \rightarrow C_3H_8 \tag{30}$$

Fig. 5. Ethylene epoxidation performance in terms of, (a) C_2H_4 and O_2 conversions, (b) EO selectivity and yield, (c) other product selectivities, and (d) power consumption as function of input frequency (an O_2/C_2H_4 feed molar ratio of 0.2, an applied voltage of 23 kV, C_2H_4 feed position fraction of 0.5, and a total feed flow rate of 50 cm³/min).

$$CH + CH_2 + 3H \rightarrow C_2H_6 \tag{31}$$

3.3. Reaction activity performance

3.3.1. Effect of applied voltage

Fig. 4 shows the effects of applied voltage on the ethylene epoxidation performance, other product selectivities, and power consumption of the studied DBD system with double frosted glass plates operated at an input frequency of 500 Hz, a feed molar ratio of O_2/C_2H_4 of 0.2:1, an ethylene feed position fraction of 0.5, and a total feed flow rate of 50 cm^3/min, according to our previous study [39]. The studied DBD system was only operated in the voltage range of 13–25 kV because an applied voltage below 13 kV could not generate plasma and the O_2 conversion approached 100% at an applied voltage of 25 kV. As shown in Fig. 4a, the C_2H_4 conversion rises with increasing applied voltage, whereas the O_2 conversion increases and reaches 100% at an applied voltage of 25 kV. The C_2H_4 conversion was much lower than the O_2 conversion since the feed molar ratio of O_2/C_2H_4 of 0.2:1 was under an oxygen lean condition (a theoretical malar ratio of $O_2/C_2H_4 = 3:1$ for complete oxidation).

As shown in Fig. 4b, the EO yield increases remarkably from 0.8 to 10.9% with increasing applied voltage from 13 to 23 kV, and then it adversely decreases to 9.3% with further increasing applied

voltage from 23 to 25 kV. The EO selectivity exhibited the same trend as the EO yield. The maximum EO selectivity of 68.2% was found at the same applied voltage of 23 kV which also provided the maximum EO yield of 10.9%. Interestingly, the maximum EO selectivity of 68.2% of the present work was almost the same as compared to that of our previous work [39], in which an Ag catalyst was loaded on a single glass plate of a DBD system.

Fig. 4c shows all other product selectivities as a function of applied voltage. Both CO and CO_2 selectivities varied sinuously with applied voltage. The maximums of both selectivities of 0.61 and 0.54 for CO and CO_2, respectively, were found at an applied voltage of 21 kV. The maximums of H_2 and C_2H_6 selectivities were 29.0% and 15.1%, respectively, at the lowest applied voltage of 13 kV and then they tended to decrease with a further increase in the applied voltage over 13 kV. In contrast, the C_3H_8 selectivity steadily increased to reach the highest value of 19.3% at 23 kV. However, the C_3H_8 selectivity decreased when the applied voltage further increased to 25 kV, whereas the CH_4 selectivity was constant in the entire applied voltage range of 13–25 kV. The results can be explained by the fact that the DBD system provided a higher amount of generated energetic electrons with increasing applied voltage from 13 to 25 kV, leading to more opportunities of collisions between C_2H_4 and dissociated O_2 molecules to form

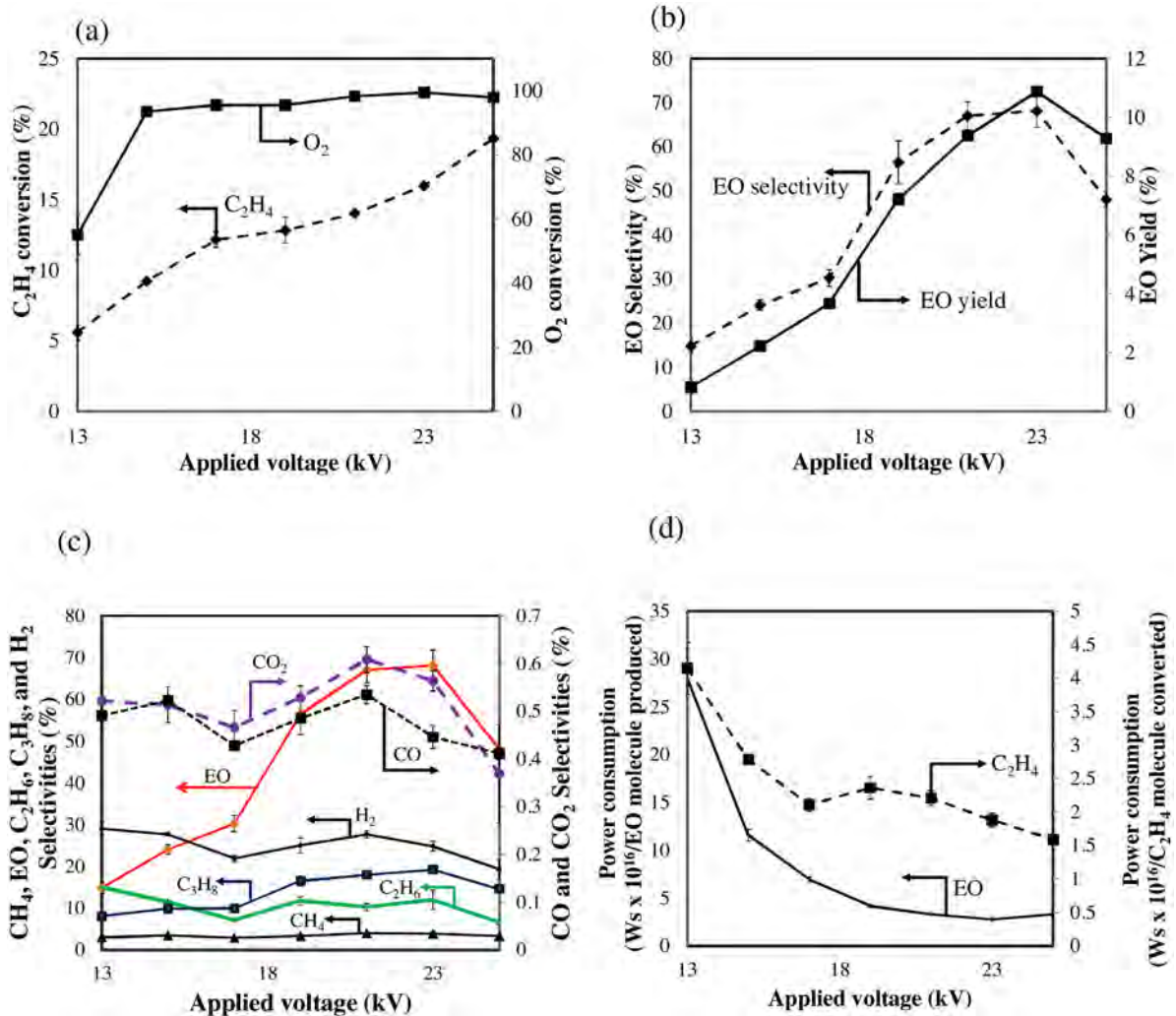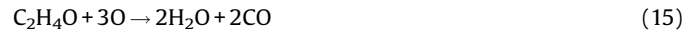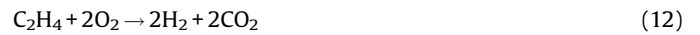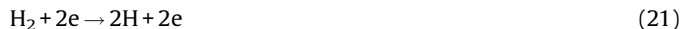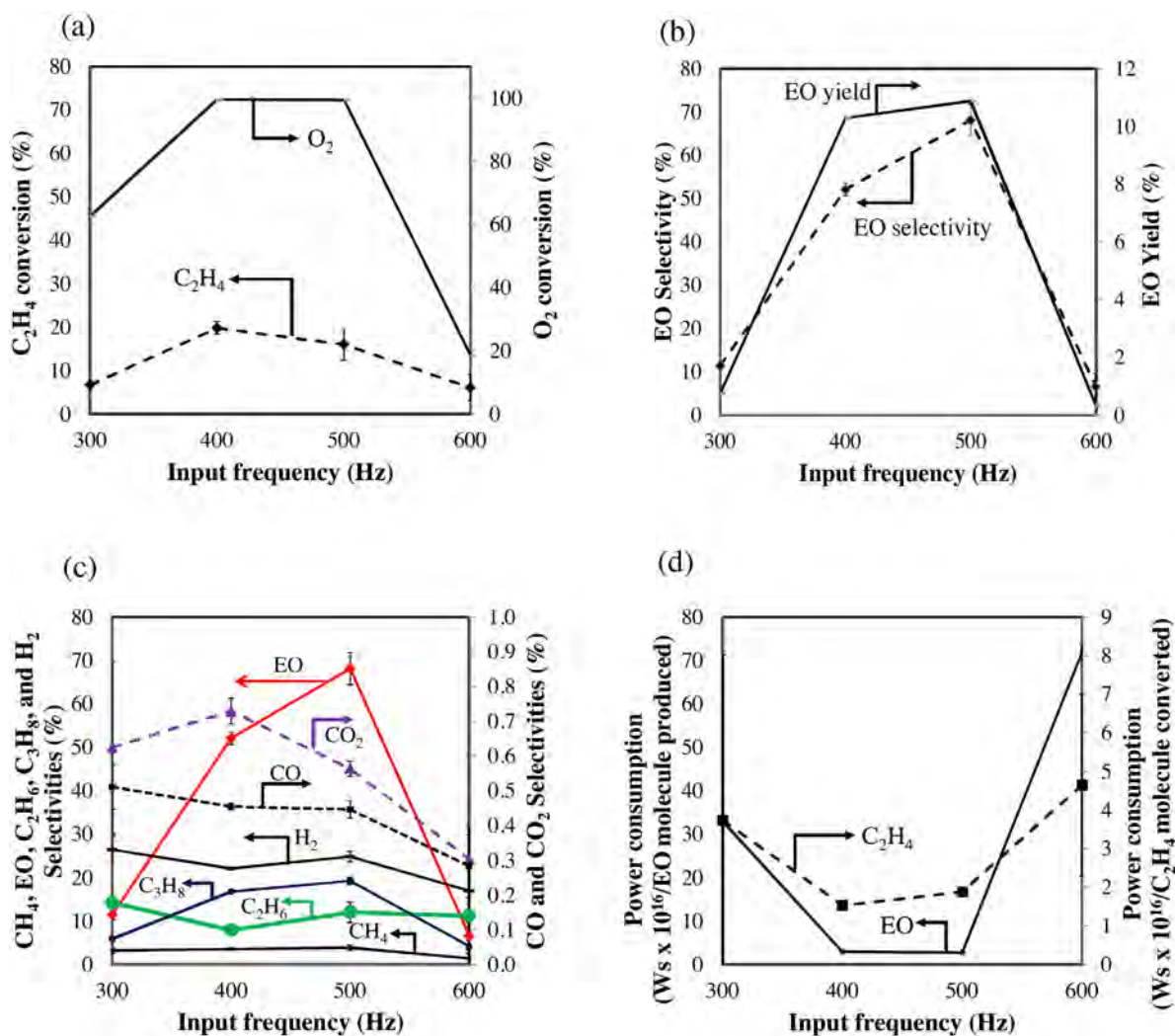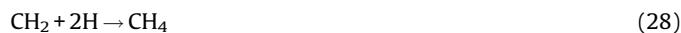**Fig. 6.** Ethylene epoxidation performance in terms of, (a) C_2H_4 and O_2 conversions, (b) EO selectivity and yield, (c) other product selectivities, and (d) power consumption as function of O_2/C_2H_4 feed malar ratio (an applied voltage of 23 kV, an input frequency of 500 Hz, C_2H_4 feed position fraction of 0.5, and a total feed flow rate of 50 cm^3/min).

EO (Eqs. (6)–(7)). All other reactions of oxidations, (Eqs. (8)–(17)), the dehydrogenation (Eqs. (18)–(23)), cracking reactions (Eqs. (24)–(27)), and coupling reactions (Eqs. (29)–(30)) varied insignificantly with applied voltage because the separate feed of C_2H_4 could lower the opportunity of C_2H_4 to be collided by generated electrons. Both EO selectivity and yield as well as all other product selectivities decreased when the applied voltage was increased from 23 to 25 kV. This was a result of coke deposition on the glass surface, leading to the reduction of all chemical reaction activities as well as ethylene epoxidation. By performing the carbon balance, the carbon deposit increased from 2-3% in the applied voltage range of 13–23 kV to 6% at the applied voltage of 25 kV. The selectivities for C_2H_4O, CH_4 and other products including C_2H_6, C_3H_8, H_2, CO, and CO_2 decreased at the highest applied voltage of 25 kV, suggesting that a very high applied voltage simply promoted the cracking reactions (Eqs. (24)–(27)).

The power consumptions per C_2H_4 molecule converted and per EO molecule produced as a function of applied voltage are shown in Fig. 4d. Both power consumptions had an opposite trend with C_2H_4 conversion and EO selectivity (Fig. 4a and b) that increased with increasing applied voltage in the entire range of 13–25 kV. The minimum of the power consumption per EO molecule produced was found at an applied voltage of 23 kV. Therefore, the applied voltage of 23 kV was considered to be an optimum and was

selected for the following experiments because it provided the highest ethylene oxide selectivity and yield with the lowest power consumption per EO molecule produced.

3.3.2. Effect of input frequency

The effect of input frequency on the ethylene epoxidation performance was investigated by varying input frequency from 300 to 600 Hz in which the other operational parameters were fixed at an applied voltage of 23 kV, an O_2/C_2H_4 feed molar ratio of 0.2:1, an C_2H_4 feed position fraction of 0.5, and a total feed flow rate of 50 cm^3/min. At an input frequency lower than 300 Hz, the generated current was very high, causing a very high temperature to damage the plasma reactor while an input frequency higher than 600 Hz gave unstable plasma. As shown in Fig. 5a, the O_2 conversion increased to 99.5% with increasing input frequency to 400 Hz. The O_2 conversion was nearly unchanged with further increasing of the input frequency from 400 to 500 Hz. Afterwards, it rapidly decreased when input frequency increased over 500 Hz. The effect of input frequency on the C_2H_4 conversion was almost the same as on the O_2 conversion, which increased to reach a maximum at an input frequency of 400 Hz, and then decreased markedly with further increasing input frequency over 400 Hz.

Both EO selectivity and yield rose with increasing input frequency and reached maximum levels at the same input
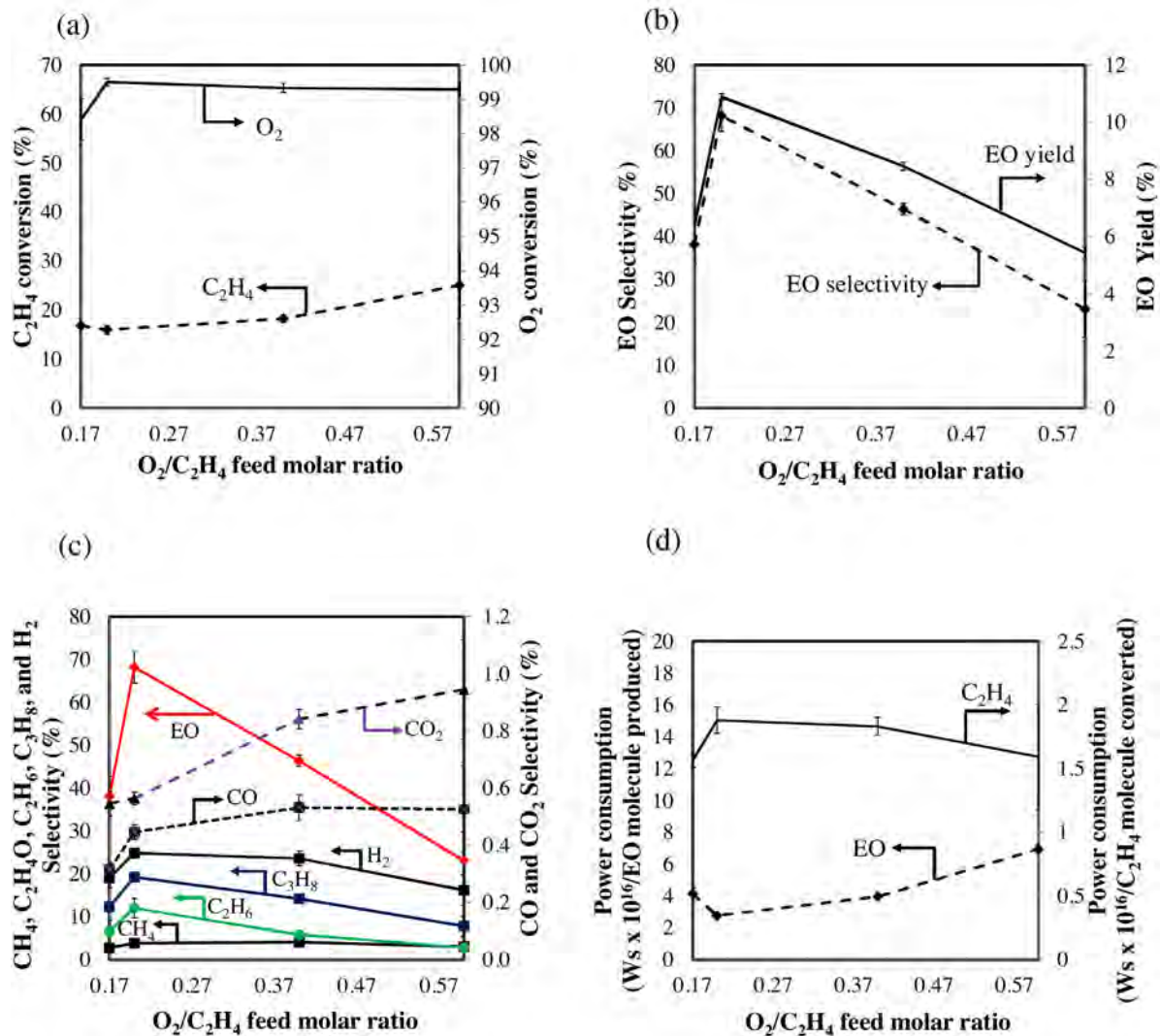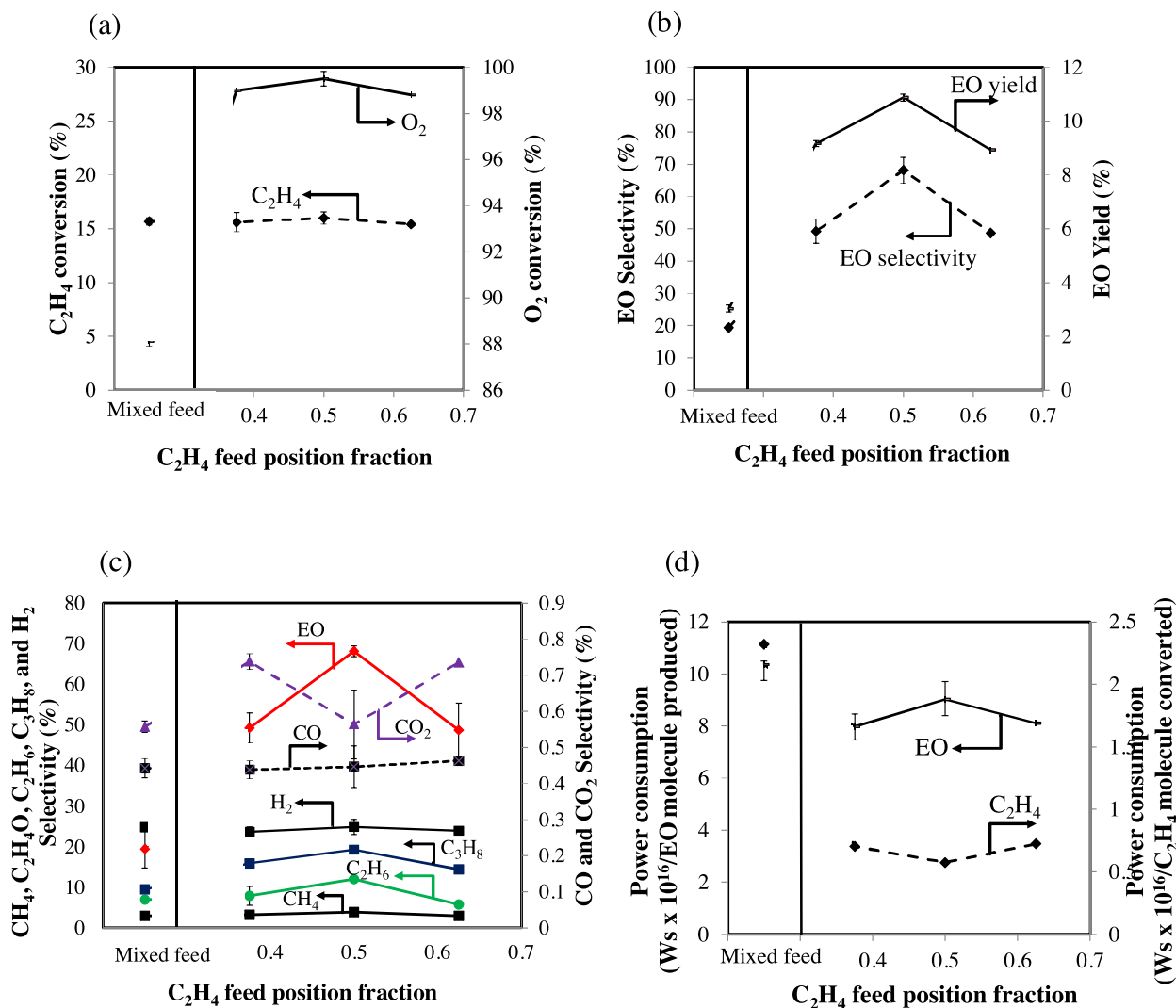

Fig. 7. Ethylene epoxidation performance in terms of, (a) C_2H_4 and O_2 conversions, (b) EO selectivity and yield, (c) other product selectivities, and (d) power consumption as function of C_2H_4 feed position fraction (an O_2/C_2H_4 feed molar ratio of 0.2, an applied voltage of 23 kV, an input frequency of 500 Hz, and a total feed flow rate of 50 cm^3/min).

frequency of 500 Hz, as shown in Fig. 5b. Beyond the input frequency of 500 Hz, they sharply dropped with further increasing input frequency from 500 to 600 Hz. The selectivities for other products including CO, CO_2, CH_4, C_2H_6, C_3H_8, and H_2 as a function of input frequency are shown in Fig. 5c. The selectivities for CO, CO_2, and H_2 tended to decrease when input frequency increased whereas the CH_4 and C_2H_6 selectivities slightly changed with input frequency. Interestingly, the C_3H_8 selectivity exhibited a similar profile as those of C_2H_4 conversion, EO selectivity and EO yield.

Under the optimum input frequency of 500 Hz, the product selectivities were in the following order: EO >> H_2> C_3H_8> C_2H_6> CH_4 >> CO_2> CO. The results can be explained by the fact that a decrease in input frequency increased the current (data not shown) to yield a higher number of electrons to be generated, leading to the EO produced to be further oxidized to CO and CO_2 (Eqs. (15)-(17)), as confirmed experimentally. In contrast, an increase in input frequency from 500 to 600 Hz caused a significant reduction of the current (data not shown), resulting in the lowering of all chemical reactions. As a result, the selectivities of all products decreased greatly when the input frequency increased from 500 to 600 Hz.

The power consumptions required to convert C_2H_4 and to produce EO as a function of input frequency are shown in Fig. 5d. Both the power consumptions per EO molecule produced and C_2H_4 molecule converted decreased with increasing input frequency to 400 Hz, then remained almost unchanged in the input frequency range of 400–500 Hz, and finally adversely increased when further increasing input frequency from 500 to 600 Hz. The minimum power consumption per EO molecule produced was found at the input frequency of 500 Hz.

From the results, the input frequency of 500 Hz was considered to be optimum for the maximum ethylene epoxidation performance in the DBD system with two frosted glasses and selected for the subsequent experiments.

3.3.3. Effect of O_2/C_2H_4 feed molar ratio

Fig. 6 shows the effect of O_2/C_2H_4 feed molar ratio on the process performance of the studied DBD. The C_2H_4 conversion tended to slightly rise with an increasing O_2/C_2H_4 feed molar ratio. The O_2 conversion rose with an increasing O_2/C_2H_4 feed molar ratio from 0.17 to 0.2 and remained unchanged with a further increasing O_2/C_2H_4 feed molar ratio beyond 0.2. The low C_2H_4 conversion (18–26%) and the high O_2 conversion (> 99%) resulted from the system being operated under oxygen lean conditions.

As shown in Fig. 6b, the EO selectivity and yield increased and reach maximum values at the same O_2/C_2H_4 feed molar ratio of 0.2. Beyond the optimum O_2/C_2H_4 feed molar ratio of 0.2, they decreased markedly with an increasing O_2/C_2H_4 feed molar ratio. Interestingly, the selectivities for CH_4, C_2H_6, C_3H_8, and H_2 showed to reach maximum levels at the same O_2/C_2H_4 feed molar ratio of 0.2, except the selectivities for CO and CO_2 rose with an increasing O_2/C_2H_4 feed molar ratio. The studied DBD was operated under oxygen lean conditions in order to minimize all undesirable reactions including partial and complete oxidation (Eqs. (8)–(17)) and cracking reactions (Eqs. (24)–(27)). When the feed oxygen content was too low (O_2/C_2H_4 feed molar ratio < 0.2), all reactions, including ethylene epoxidation, were found to be very low, indicated by low selectivities for all products including EO. This is because the lower the oxygen content, the lower the active oxygen species to initiate all plasma reactions. When the O_2/C_2H_4 feed molar ratio was greater than 0.2, the selectivities for CO and CO_2 rose with an increasing O_2/C_2H_4 feed molar ratio because of the higher oxygen content available for both partial and complete oxidation reactions (Eq. (8)–(17)). As a consequence, all other reactions including cracking, coupling, and dehydrogenation as well as decreased from sequent oxidations with an increasing O_2/C_2H_4 feed molar ratio beyond the optimum ratio. The results reveal an oxygen lean condition is one of important process parameters to minimize all unwanted products for the ethylene epoxidation reaction.

As shown in Fig. 6d, the power consumption per C_2H_4 molecule converted mirrors the O_2 conversion whereas the power consumption per EO molecule produced had the opposite tendency. The optimum O_2/C_2H_4 feed molar ratio of 0.2 was selected for further experiments because this ratio provided the highest EO selectivity and yield with reasonably low CO and CO_2 selectivities and lowest power consumption per EO molecule produced.

3.3.4. Effect of C_2H_4 feed position fraction

As shown in our previous studies [36], a technique of C_2H_4 separate feed can enhance ethylene epoxidation with significant reduction of undesired reactions (Eqs. (8)–(31). Fig. 7 shows the process performance of the studied DBD as a function of C_2H_4 feed position fraction. The C_2H_4 feed position fraction was defined according to the flow direction along the electrode length. The O_2 conversion rose with increasing C_2H_4 feed position fraction from 0.4 to 0.5, and after that it decreased with further increasing C_2H_4 feed position fraction. A lower C_2H_4 feed position fraction of 0.5

Table 2
Comparison of the plasma systems on the ethylene epoxidation performance.

Plasma System (conditions)	Conversion (%)		EO selectivity (%)	EO yield (%)	Power consumption (Ws/molecule)	
	C_2H_4	O_2			C_2H_4 converted	EO produced
Parallel DBD using a clear glass plate [8] (Mixed feed, O_2/C_2H_4 molar ratio of 1/1, a gap distance of 1 cm, an applied voltage of 19 kV, an input frequency of 500 Hz, and a total feed flow rate of 50 cm³/min)	91.0	93.7	6.2	5.6	0.4×10^{-16}	6.1×10^{-16}
Parallel DBD/10 wt.% Ag/glass plate [39] (Separate feed [C_2H_4 feed position of 0.5], O_2/C_2H_4 molar ratio of 0.2/1, a gap distance of 0.7 cm, an applied voltage of 19 kV, an input frequency of 500 Hz, and a total feed flow rate of 50 cm³/min)	1.6	83.0	72.1	1.3	23.0×10^{-16}	16.6×10^{-16}
Parallel DBD using two clear glass plates (This work) (Separate feed [C_2H_4 feed position of 0.5], O_2/C_2H_4 molar ratio of 0.2/1, a gap distance of 0.7 cm, an applied voltage of 19 kV, an input frequency of 500 Hz, and a total feed flow rate of 50 cm³/min)	12.7	89.8	41.3	5.2	2.1×10^{-16}	5.0×10^{-16}
Parallel DBD using two frosted glass plates (This work) (Separate feed [C_2H_4 feed position of 0.5], O_2/C_2H_4 molar ratio of 0.2/1, a gap distance of 0.7 cm, an applied voltage of 23 kV, an input frequency of 500 Hz, and a total feed flow rate of 50 cm³/min)	19.8	99.5	68.1	10.9	1.9×10^{-16}	2.8×10^{-16}

resulted in more residence time of ethylene in the DBD reactor, leading to a higher opportunity for ethylene cracking. Moreover, at a C_2H_4 feed position fraction higher than 0.5, the ethylene had a short residence time for epoxidation reaction.

3.3.5. Performance comparisons of different DBD systems

Table 2 shows a comparison of four DBD systems with a single clear glass plate, 10 wt.% Ag/clear glass plate, two clear glass plates, and two frosted glass plates operated under their own optimum conditions. The DBD system with a single glass plate provided the poorest ethylene epoxidation performance in terms of the lowest EO selectivity with a relatively low EO yield. The use of Ag loaded on a single clear glass plate was found to give the highest EO selectivity of 72.1% with a very low EO yield (1.3%) and C_2H_4 conversion (1.6%). The DBD system with two clear glass plates could only marginally improve EO selectivity (41.3%) with more or less the same EO yield, as compared to that with a single glass plate. Interestingly, the DBD system with two frosted glass plates showed the best process performance in terms of the highest EO yield (10.9%) and the lowest power consumption (2.8×10^{-16} Ws/ EO molecule produced) with a reasonably high EO selectivity. The high surface roughness of two frosted glass plates was found to provide more uniform micro discharge, leading to the generated electrodes having lower energy than those with either single or two clear glass plates. As known, electrons can emit preferentially from any sharp points or edges than smooth or flat surface. The frosted glass plates provided much more sharp points than a clear glass plate, leading to more uniform plasma with better energy density distribution to be generated. As a result, the use of two frosted glass plates in a DBD system can reduce undesirable reactions especially partial and complete oxidation reactions to form CO and CO_2 which, in turn, enhances the ethylene epoxidation reaction.

4. Conclusion

The optimum conditions for the highest EO product of the DBD system with two frosted glass plates were an applied voltage of 23 kV, an input frequency of 500 Hz, an O_2/C_2H_4 feed molar ratio of 0.2:1, and an C_2H_4 feed position fraction of 0.5. Interestingly, the DBD system using two frosted glass plates provided a reasonably high EO selectivity and much higher EO yield as compared to the DBD with Ag catalyst loaded on single glass plate. A combination of two frosted glass plates and an Ag catalyst in a DBD system will be investigated in a future study.

Acknowledgements

References

[1] W. Diao, C.D. DiGiulio, M.T. Schaal, S. Ma, J.R. Monnier, An investigation on the role of Re as a promoter in AgCsRe/α-Al2O3 high-selectivity, ethylene epoxidation catalysts, J. Catal. 322 (0) (2015) 14–23, doi:http://dx.doi.org/10.1016/j.jcat.2014.11.007.

[2] J.C. Dellamorte, J. Lauterbach, M.A. Barteau, Palladium–silver bimetallic catalysts with improved activity and selectivity for ethylene epoxidation, Appl. Catal. A 391 (1–2) (2011) 281–288, doi:http://dx.doi.org/10.1016/j.apcata.2010.06.023.

[3] J.T. Jankowiak, M.A. Barteau, Ethylene epoxidation over silver and copper-silver bimetallic catalysts: II. Cs and Cl promotion, J. Catal. 236 (2) (2005) 379–386, doi:http://dx.doi.org/10.1016/j.jcat.2005.10.017.

[4] T. Sreethawong, T. Suwannabart, S. Chavadej, Ethylene epoxidation in low-temperature AC corona discharge over Ag catalyst: effect of promoter, Chem. Eng. J. 155 (1–2) (2009) 396–403, doi:http://dx.doi.org/10.1016/j.cej.2009.07.056.

[5] A. Chongterdtoonskul, J.W. Schwank, S. Chavadej, Comparative study on the influence of second metals on Ag-loaded mesoporous SrTiO3 catalysts for ethylene oxide evolution, J. Mol. Catal. A: Chem. 372 (0) (2013) 175–182, doi: http://dx.doi.org/10.1016/j.molcata.2013.02.016.

[6] J.C. Dellamorte, J. Lauterbach, M.A. Barteau, Rhenium promotion of Ag and Cu-Ag bimetallic catalysts for ethylene epoxidation, Catal. Today 120 (2) (2007) 182–185, doi:http://dx.doi.org/10.1016/j.cattod.2006.07.051.

[7] T. Sreethawong, N. Permsin, T. Suttikul, S. Chavadej, Ethylene epoxidation in low-temperature AC dielectric barrier discharge: effect of electrode geometry, Plasma Chem. Plasma Process. 30 (4) (2010) 503–524.

[8] T. Sreethawong, T. Suwannabart, S. Chavadej, Ethylene epoxidation in low-temperature AC dielectric barrier discharge: effects of oxygen-to-ethylene feed molar ratio and operating parameters, Plasma Chem. Plasma Process. 28 (5) (2008) 629–642.

[9] N. Rueangjitt, W. Jittiang, K. Pornmai, J. Chamnanmanoontham, T. Sreethawong, S. Chavadej, Combined reforming and partial oxidation of CO 2-containing natural gas using an AC multistage gliding arc discharge system: effect of stage number of plasma reactors, Plasma Chem. Plasma Process. 29 (6) (2009) 433–453.

[10] N. Rueangjitt, C. Akarawitoo, T. Sreethawong, S. Chavadej, Reforming of CO 2-containing natural gas using an AC gliding arc system: effect of gas components in natural gas, Plasma Chem. Plasma Process. 27 (5) (2007) 559–576.

[11] N. Rueangjitt, T. Sreethawong, S. Chavadej, Reforming of CO 2-containing natural gas using an AC gliding Arc system: effects of operational parameters and oxygen addition in feed, Plasma Chem. Plasma Process. 28 (1) (2008) 49–67.

[12] P.W.E. Blom, G.W. Basson, Non-catalytic plasma-arc reforming of natural gas with carbon dioxide as the oxidizing agent for the production of synthesis gas or hydrogen, Int. J. Hydrogen Energy 38 (14) (2013) 5684–5692, doi:http://dx.doi.org/10.1016/j.ijhydene.2013.03.042.

[13] B. Spasova, D. Tiemann, M. O'Connell, A. Ziogas, G. Kolb, V. Hessel, Synthesis gas production from methane and propane in a miniaturized GlidArc® reformer, Int. J. Hydrogen Energy 39 (24) (2014) 12657–12666, doi:http://dx.doi.org/10.1016/j.ijhydene.2014.06.065.

[14] A.M. Harling, D.J. Glover, J.C. Whitehead, K. Zhang, The role of ozone in the plasma-catalytic destruction of environmental pollutants, Appl. Catal. B: Environ. 90 (1–2) (2009) 157–161, doi:http://dx.doi.org/10.1016/j.apcatb.2009.03.005.

[15] A.M. Harling, V. Demidyuk, S.J. Fischer, J.C. Whitehead, Plasma-catalysis destruction of aromatics for environmental clean-up: effect of temperature and configuration, Appl. Catal. B: Environ. 82 (3-4) (2008) 180–189, doi:http://dx.doi.org/10.1016/j.apcatb.2008.01.017.

[16] X. Fan, T.L. Zhu, M.Y. Wang, X.M. Li, Removal of low-concentration BTX in air using a combined plasma catalysis system, Chemosphere 75 (10) (2009) 1301–1306, doi:http://dx.doi.org/10.1016/j.chemosphere.2009.03.029.

[17] A.M. Vandenbroucke, M.T. Nguyen Dinh, N. Nuns, J.M. Giraudon, N. De Geyter, C. Leys, J.F. Lamonier, R. Morent, Combination of non-thermal plasma and Pd/LaMnO3 for dilute trichloroethylene abatement, Chem. Eng. J. 283 (2016) 668–675, doi:http://dx.doi.org/10.1016/j.cej.2015.07.089.

[18] R. Zhu, Y. Mao, L. Jiang, J. Chen, Performance of chlorobenzene removal in a nonthermal plasma catalysis reactor and evaluation of its byproducts, Chem. Eng. J. 279 (2015) 463–471, doi:http://dx.doi.org/10.1016/j.cej.2015.05.043.

[19] A.M. Vandenbroucke, R. Morent, N. De Geyter, C. Leys, Non-thermal plasmas for non-catalytic and catalytic VOC abatement, J. Hazard. Mater. 195 (2011) 30–54, doi:http://dx.doi.org/10.1016/j.jhazmat.2011.08.060.

[20] K.P. Francke, H. Miessner, R. Rudolph, Cleaning of air streams from organic pollutants by plasma–catalytic oxidation, Plasma Chem. Plasma Process. 20 (3) (2000) 393–403, doi:http://dx.doi.org/10.1023/A:1007048428975.

[21] S. Chavadej, W. Kiatubolpaiboon, P. Rangsunvigit, T. Sreethawong, A combined multistage corona discharge and catalytic system for gaseous benzene removal, J. Mol. Catal. A: Chem. 263 (1–2) (2007) 128–136, doi:http://dx.doi.org/10.1016/j.molcata.2006.08.061.

[22] H. Yi, S. Zhao, X. Tang, C. Song, F. Gao, B. Zhang, Z. Wang, Y. Zuo, Low-temperature hydrolysis of carbon disulfide using the FeCu/AC catalyst modified by non-thermal plasma, Fuel 128 (2014) 268–273, doi:http://dx.doi.org/10.1016/j.fuel.2014.03.021.

[23] L. Ban, P. Liu, C. Ma, B. Dai, Deep oxidative/adsorptive desulfurization of model diesel oil by DBD/FeCl3–SiO2, Catal. Today 211 (2013) 78–83, doi:http://dx.doi.org/10.1016/j.cattod.2013.04.007.

[24] A. Fridman, A. Gutsol, Y.I. Cho, Non-thermal atmospheric pressure plasma, Advances in Heat Transfer 40 (2007), doi:http://dx.doi.org/10.1016/S0065-2717(07)40001-6.

[25] U. Kogelschatz, B. Eliasson, W. Egli, From ozone generators to flat television screens: history and future potential of dielectric-barrier discharges, Pure Appl. Chem. 71 (10) (1999) 1819–1828, doi:http://dx.doi.org/10.1351/pac199971101819.

[26] H.L. Chen, H.M. Lee, S.H. Chen, Review of packed-Bed plasma reactor for ozone generation and air pollution control, Ind. Eng. Chem. Res. 47 (7) (2008) 2122–2130, doi:http://dx.doi.org/10.1021/ie071411s.

[27] B. Eliasson, U. Kogelschatz, Nonequilibrium volume plasma chemical processing, Plasma Science, IEEE Transactions 19 (6) (1991) 1063–1077, doi:http://dx.doi.org/10.1109/27.125031.

[28] B. Rajanikanth, M. Okumoto, S. Katsura, A. Mizuno, Nonthermal plasma approach in direct methanol synthesis from CH4. In: Industry Applications Conference, 1996. Thirty-First IAS Annual Meeting, IAS '96., Conference Record

of the 1996 IEEE, 6–10 October 1996. pp. 1813–1817 vol.1813. 10.1109/IAS.1996.559314

[29] R. Ruan, S. Deng, Z. Le, P. Chen, 2009. Non-thermal plasma synthesis of ammonia. Google Patents.

[30] M.M. Moshrefi, F. Rashidi, Hydrogen production from methane by DC spark discharge: effect of current and voltage, J. Nat. Gas Sci. Eng. 16 (0) (2014) 85–89, doi:http://dx.doi.org/10.1016/j.jngse.2013.12.001.

[31] N. Rueangjitt, T. Sreethawong, S. Chavadej, H. Sekiguchi, Non-oxidative reforming of methane in a mini-gliding arc discharge reactor: effects of feed methane concentration, feed flow rate, electrode gap distance, residence time, and catalyst distance, Plasma Chem. Plasma Process. 31 (4) (2011) 517–534.

[32] N. Rueangjitt, T. Sreethawong, S. Chavadej, H. Sekiguchi, Plasma-catalytic reforming of methane in AC microsized gliding arc discharge: effects of input power, reactor thickness, and catalyst existence, Chem. Eng. J. 155 (3) (2009) 874–880, doi:http://dx.doi.org/10.1016/j.cej.2009.10.009.

[33] F.O. Thomas, T.C. Corke, M. Iqbal, A. Kozlov, D. Schatzman, Optimization of dielectric barrier discharge plasma actuators for active aerodynamic flow control, AIAA Journal 47 (9) (2009) 2169–2178, doi:http://dx.doi.org/10.2514/1.41588.

[34] S. Chavadej, A. Tansuwan, T. Sreethawong, Ethylene epoxidation over alumina-supported silver catalysts in low-temperature AC corona discharge, Plasma

Chem. Plasma Process. 28 (5) (2008) 643–662, doi:http://dx.doi.org/10.1007/s11090-008-9150-2.

[35] T. Suttikul, S. Yaowapong-aree, H. Sekiguchi, S. Chavadej, J. Chavadej, Improvement of ethylene epoxidation in low-temperature corona discharge by separate ethylene/oxygen feed, Chem. Eng. Process. Process Intensif. 70 (2013) 222–232.

[36] T. Suttikul, C. Tongurai, H. Sekiguchi, S. Chavadej, Ethylene epoxidation in cylindrical dielectric barrier discharge: effects of separate ethylene/oxygen feed, Plasma Chem. Plasma Process. 32 (6) (2012) 1169–1188.

[37] T. Suttikul, S. Kodama, H. Sekiguchi, S. Chavadej, Ethylene epoxidation in an AC dielectric barrier discharge jet system, Plasma Chem. Plasma Process. 34 (1) (2014) 187–205.

[38] T. Suttikul, T. Sreethawong, H. Sekiguchi, S. Chavadej, Ethylene epoxidation over alumina- and silica-supported silver catalysts in low-temperature AC dielectric barrier discharge, Plasma Chem. Plasma Process. 31 (2) (2011) 273–290, doi:http://dx.doi.org/10.1007/s11090-010-9280-1.

[39] T. Suttikul, B. Paosombat, M. Santikunaporn, M. Leethochawalit, S. Chavadej, Improvement of ethylene epoxidation in a parallel plate dielectric barrier discharge system by ethylene/oxygen separate feed and Ag catalyst, Ind. Eng. Chem. Res. 53 (10) (2014) 3778–3786.

Selective Hydrogenation of Concentrated Vinyl Acetylene Mixed C4 by Modified Pd Catalysts: Effect of Cu

Paisan Insorn [1] and Boonyarach Kitiyanan [1,2,*]

[1] The Petroleum and Petrochemical College, Chulalongkorn University, Soi Chula 12, Phyathai Road, Pathumwan, Bangkok 10330, Thailand; paisan_i@yahoo.com

[2] Center of Excellence on Petrochemical and Materials Technology, Chulalongkorn University, Bangkok 10330, Thailand

* Correspondence: boonyarach.k@chula.ac.th; Tel.: +66-2-218-4144

Abstract: The Pd and Pd-Cu on alumina catalysts were tested for hydrogenation of vinyl acetylene in mixed C4 in a circulating tubular reactor. The results showed that adding proper amounts of Cu improved the reaction activity, but inhibited 1,3-butadiene selectivity. Moreover, the presence of Cu retarded the carbon deposition on catalysts during the reaction. Temperature programmed oxidation (TPO), Temperature programmed reduction (TPR), H_2 chemisorption, and X-ray photoelectron spectroscopy (XPS) were utilized to characterize the catalysts. The characterization suggested both geometric and electronic modifications.

1. Introduction

Concentrated vinyl acetylene mixed C4, containing vinyl acetylene up to 30 wt %, generated from the butadiene extraction process is continuously flared due to safety reason [1,2]. Therefore, converting vinyl acetylene in this stream by selective hydrogenation to 1,3-butadiene is not only a benefit to environmental concerns, but also to the economics of the entire C4 processes. However, the available catalysts for selective hydrogenation of a large portion of vinyl acetylene are still very limited [1,3]. Therefore, we attempted to test the catalysts for hydrogenation of vinyl acetylene in mixed C4 from a commercial butadiene extraction process. In this study we show the results from using alumina-supporting Pd-Cu catalysts and compare them to monometallic Pd catalyst.

Supporting Pd catalysts have been studied in selective hydrogenation of alkyne in both gas and liquid phases [4–8]. In particular, Pd supported on alumina (Pd/Al_2O_3) is utilized as a catalyst in several commercial hydrogenation processes [9–11]. Furthermore, Pd/Al_2O_3 can be promoted or doped by other transition metals (e.g., Cu, Ag, Pb) to improve the catalytic performance. Pachulski et al. [12] investigated Ag-promoted Pd/Al_2O_3 catalysts prepared by the incipient wetness impregnation technique on gas phase acetylene hydrogenation and observed that, by adding Ag to Pd/Al_2O_3, the catalytic activity was slightly reduced, but ethylene selectivity and catalytic stability are significantly improved. Kim et al. [13] studied the effect of adding Cu and Ag to Pd/Al_2O_3 by using a surface redox and impregnation on selective hydrogenation of acetylene. They reported that, if the catalysts are prepared by the surface redox method, Cu-promoting catalysts provided the highest ethylene selectivity while Ag promoting catalysts showed the highest ethylene selectivity if the catalysts are prepared by impregnation method. Nevertheless, catalyst promoted by either Cu and Ag showed significantly drop in their activity. Lederhos et al. [14] also reported that the Pd-W

and W-Pd bimetallic catalysts can greatly improve both selectivity and conversion in the liquid phase hydrogenation of 1-heptyne.

Cu was selected to promote the Pd catalyst for vinyl acetylene hydrogenation because Cu was reported to be active and selective in the hydrogenation of alkyne hydrogenation. For example, Koeppel et al. [15] investigated the hydrogenation of unsaturated C4 including vinyl acetylene, 1-butyne and 1,3-butadiene by Cu on silica catalysts. Their results showed that the catalysts can hydrogenate only alkynes but not alkenes. Setiawan et al. [16] also reported the removal of alkynes contaminants from industrial C4 stream by using Cu on silica catalysts. Wehrli et al. [17,18] studied the hydrogenation of propyne by supported Cu catalysts and they found that the supported Cu catalysts have the high selectivity of propyne hydrogenation toward propene. Friedrich et al. [19] studied partial acetylene hydrogenation by 60:40 atomic ratio of Cu:Pd catalyst. They reported that the $Cu_{60}Pd_{40}$ catalysts provide higher ethylene selectivity with less deactivation than the Pd catalyst. Furthermore, Cai et al. [20] studied the denitrification reaction of nitrate by Pd-Cu alloy nanocatalysts on alumina under a hydrogen atmosphere. It was found that adding Cu increases nitrate conversion compared to Pd monocatalyst and the Pd:Cu 50:50 provides the highest nitrate conversion.

In this work, the Pd and Pd-Cu catalysts are prepared by conventional incipient wetness impregnation method and tested for catalytic hydrogenation of vinyl acetylene in the mixed C4. The reaction conditions, including temperature and pressure of hydrogen, are set in the safety region and the reaction is conducted in liquid hexane. The catalytic performances including rate of vinyl acetylene conversion and 1,3-butadiene selectivity are then obtained. Furthermore, the catalysts are also characterized by several techniques, including X-ray photoelectron spectroscopy (XPS), temperature programed reduction (TPR), temperature programed oxidation (TPO), and H_2-chemisorption.

2. Results and Discussion

Figure 1 shows the rate of vinyl acetylene, 1,3-butadiene selectivity and yield of Pd-Cu catalysts compared to those of the Pd catalyst. As shown in Figure 1A, Pd-Cu catalysts have a relative constant rate of vinyl acetylene conversion until vinyl acetylene conversion is around 80%, beyond 80% conversion, the rate is significantly decreased similar to the case of using Pd/Al_2O_3 catalyst. Comparing to Pd, Pd:Cu 1:1 and 3:2 catalysts exhibited the higher rate of hydrogenation while Pd:Cu 1:4, 1:2, and 2:1 exhibited the lower rate. To observe the catalysts' performance, we compare the rate of vinyl acetylene conversion of each prepared catalyst at the 70% conversion where the yield of 1,3-butadiene is the maximum (Figure 1C). The rate of vinyl acetylene conversion for Pd:Cu 1:4, 1:2, 1:1, 3:2, 2:1, and Pd catalysts are 0.032, 0.039, 0.048, 0.052, 0.040, and 0.047 (mole vinyl acetylene per gram catalyst per hour), respectively, as illustrated in Figure 1D. Obviously, a proper amount of added Cu to Pd/Al_2O_3 catalyst improves the rate of vinyl acetylene conversion. It is interesting to note that the Pd:Cu ratio of 3:2 shows the highest reaction rate which corresponds to the highest hydrogen adsorption per Pd as obtained from hydrogen chemisorption experiments. For comparison purposes, the Cu/Al_2O_3 catalyst was also tested and the hydrogenation did not take place.

The turn-over frequency (TOF) number of vinyl acetylene on Pd is calculated based on the exposed Pd obtained from chemisorption. As shown in Figure 2, 1:4, 1:2, and 1:1 Pd:Cu catalysts exhibit TOF around 4 s^{-1} which is higher than TOF number of Pd:Cu at ratios 3:2, 2:1, and Pd catalysts (TOF around 2.5 s^{-1}). This suggests that Pd with more neighboring Cu is more active, possibly due to the electronic modification as hinted by the results from XPS.

In Figure 1B, the selectivity of 1,3-butadiene is gradually decreased with increasing vinyl acetylene conversion, however, the 1,3-butadiene selectivity is significantly dropped when the vinyl acetylene conversion is greater than 80%, due to further hydrogenation of 1,3-butadiene to butenes as shown in Figure S1 and S2. Interestingly, the amount of added copper does not have significant effect on 1,3-butadiene selectivity, as shown in Figure 1E.

As illustrated in Figure 1C, the yield of 1,3-butadiene for each catalyst is increased with an increase of the conversion and reached the maximum at around 70%–80% conversion. The yield is

dramatically dropped when the conversion is beyond 80%. Figure 1F shows the yield of 1,3-butadiene at 70% conversion of vinyl acetylene for different Pd:Cu atomic ratio catalysts. It can be observed that adding Cu has no effect on 1,3-butadiene yield for the tested catalyst.

Adding Cu to Pd/Al_2O_3 catalyst can cause both positive and negative effects on the rate of vinyl acetylene hydrogenation. For the Pd:Cu ratio of 1:4 and 1:2, adding Cu to the Pd/Al_2O_3 catalyst significantly reduces the rate of vinyl acetylene hydrogenation per gram of catalyst, but the selectivity toward 1,3-butadiene is still comparable to the Pd/Al_2O_3 catalyst at 70% conversion. However, as the ratio of Pd to Cu increases, until the Pd:Cu ratio of 1:1 and 3:2, the rate of vinyl acetylene hydrogenation is higher than that of monometallic Pd catalyst. However, if the Pd:Cu ratio is increased to 2:1, the rate of vinyl acetylene hydrogenation is significantly dropped, as shown in Figure 1D.
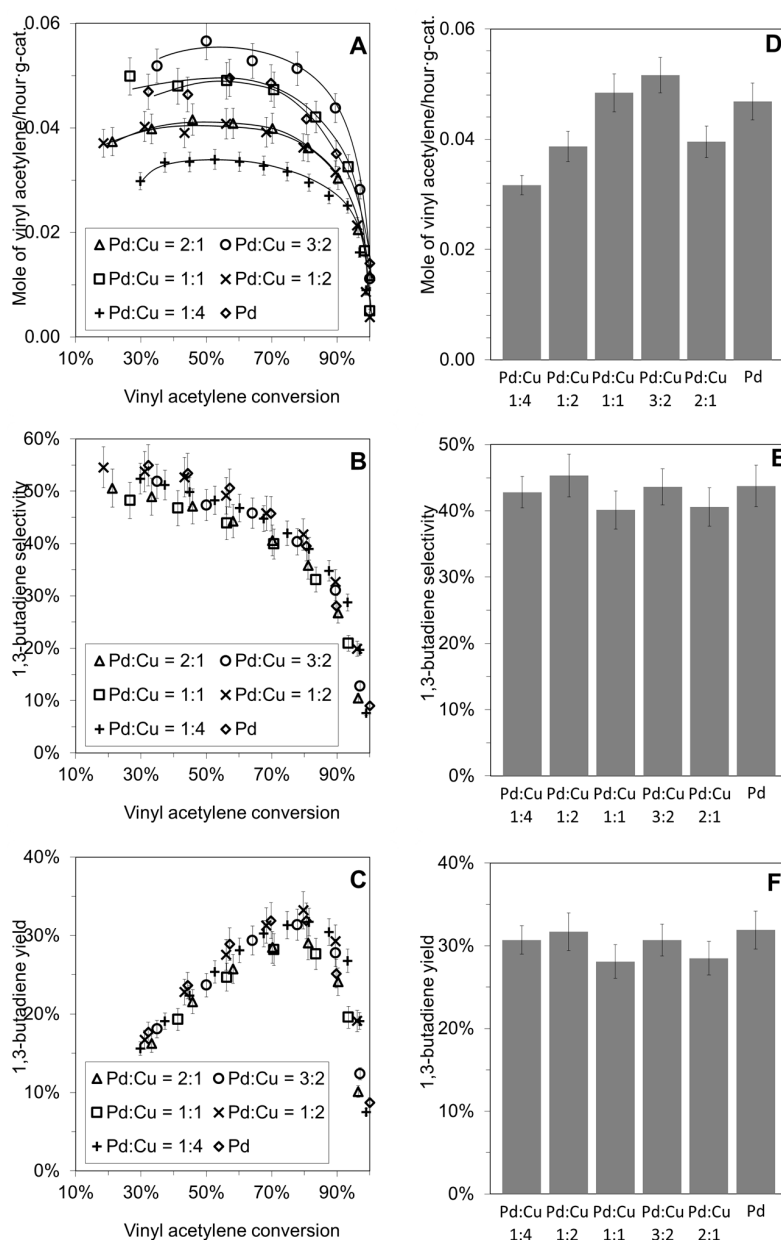
Figure 1. Catalytic performances: (**A**) reaction rate; (**B**) 1,3-butadiene selectivity; and (**C**) 1,3-butadiene yield as the function of vinyl acetylene conversion; (**D**) rate of vinyl acetylene at 70% vinyl acetylene conversion; (**E**) 1,3-butadiene selectivity at 70% vinyl acetylene conversion; and (**F**) 1,3-butadiene yield at 70% vinyl acetylene conversion against Pd:Cu atomic ratios.
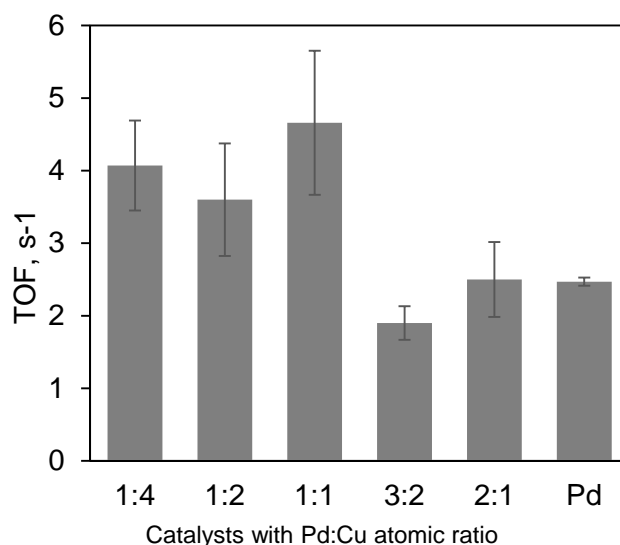
Figure 2. Turn-over frequency of Pd and Pd-Cu catalysts.

The Pd dispersion based on the results of hydrogen chemisorption on the studied catalysts are summarized in Table 1. The Pd/Al_2O_3 catalyst has 19% dispersion while the $Pd-Cu/Al_2O_3$ catalysts with Pd to Cu ratio less than 1 show significantly lower Pd dispersion. However, for $Pd-Cu/Al_2O_3$ catalysts with the Pd:Cu ratio higher than 1, the catalyst shows the metal dispersion at the similar level of the Pd/Al_2O_3 catalyst. Moreover, only Pd:Cu 3:2 catalyst provides about 27% dispersion which is higher than the monometallic Pd catalyst.

Table 1. Measured Pd and Cu contents and Pd dispersion of catalysts.

Properties	Pd	Pd:Cu Catalyst				
		1:4	1:2	1:1	3:2	2:1
Pd wt % [1]	0.352 ± 0.012	0.273 ± 0.010	0.328 ± 0.012	0.270 ± 0.009	0.288 ± 0.010	0.287 ± 0.010
Cu wt % [1]	-	0.612 ± 0.022	0.358 ± 0.013	0.179 ± 0.006	0.119 ± 0.004	0.096 ± 0.003
Pd Dispersion [2], %	19.35 ± 0.44	7.83 ± 0.76	10.63 ± 1.53	16.35 ± 4.77	27.11 ± 1.61	15.70 ± 2.12
Actual Pd/Cu	-	0.266 ± 0.019	0.548 ± 0.039	0.902 ± 0.063	1.446 ± 0.101	1.783 ± 0.124

[1] by AAS; [2] by hydrogen chemisorption.

The results of temperature program reduction (TPR) of calcined catalysts are illustrated in Figure 3. For the calcined copper on alumina (calcined Cu/Al_2O_3), a broad positive peak which is maximum at 261 °C indicates the reduction of CuO by hydrogen. Interestingly, the TPR of calcined Pd/Al_2O_3 has a negative peak at 88 °C possibly due to hydrogen generating from palladium hydride decomposition [21,22]. For the $Pd-Cu/Al_2O_3$ catalyst with a high Pd:Cu ratio (Pd:Cu 2:1, 3:2, and 1:1), TPR of these catalysts shows both negative and positive peaks of Pd at around 90 °C, while the lower Pd:Cu ratio catalysts (Pd:Cu 1:2 and 1:4) show only positive TPR peaks. It is interesting to note that the negative peak at low temperature is smaller as the amount of Cu is increased in the prepared catalysts suggesting that less Pd hydride is formed. Moreover, the TPR peaks of PdO in calcined $Pd-Cu/Al_2O_3$ are shifted to a higher temperature as the amount of Cu is increased. Furthermore, the reduction peaks of copper in the calcined $Pd-Cu/Al_2O_3$ are at a lower temperature than the reduction peak in the calcined Cu/Al_2O_3. These indicate the possibility of Pd-Cu interaction in the calcined $Pd-Cu/Al_2O_3$ catalysts as suggested in the work done by Molenbroek et al. [23].
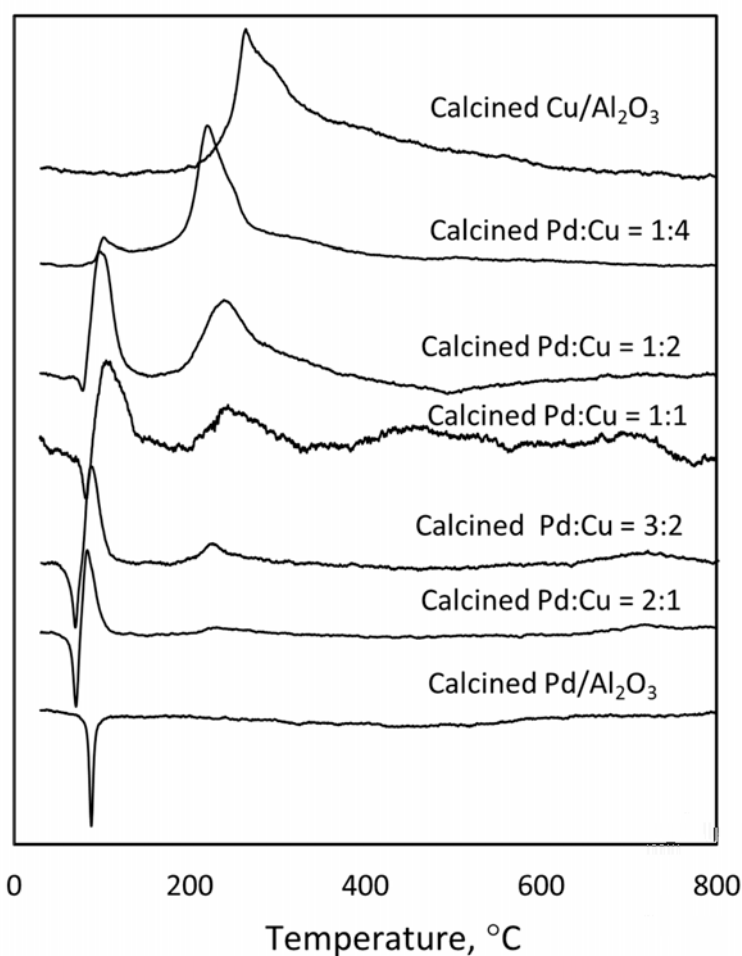
Figure 3. TPR profile of calcined Pd-Cu/Al_2O_3 catalysts compared to calcined Pd/Al_2O_3 and calcined Cu/Al_2O_3.

From the TPR results, Pd on all catalysts should be completely reduced by hydrogen at 300 °C, however, at this condition, copper may not be completely reduced to metallic Cu, particularly copper in the copper-rich catalysts (1:4, 1:2, and 1:1 Pd:Cu) may not be completely reduced. The XPS results, as shown in Figures 4 and 5, and summarized in Table 2, also suggest a similar observation. In Figure 4, the Pd 3d binding energy of reduced Pd/Al_2O_3 catalyst is observed at 334.2 eV with the full width at half maximum (FWHM) of 1.97, while the calcined catalyst (PdO/Al_2O_3) spectra shows at 336.4 eV with 1.23 FWHM. This confirmed that Pd from reduced Pd/Al_2O_3 and from PdO/Al_2O_3 are Pd(0) and Pd(II), respectively. The reduced Pd-Cu/Al_2O_3 catalysts show the Pd 3d spectra around 334.5–334.6 eV which is 0.3–0.4 eV higher than the reduced Pd/Al_2O_3 catalyst. This suggests that Pd may be electronically modified when Cu is added. In addition, Pd-Cu catalysts may contain some Pd+ species as suggested by the broader Pd 3d FWHM of Pd-Cu catalysts which is around 1.98–2.43 eV. The Pd may be oxidized possibly due to the brief exposure to air during sample transfer to XPS. As shown in Figure 5, the Cu $2p_{3/2}$ is observed around 932.7 eV for the all the prepared catalysts containing copper. In addition, weak Cu $2p_{3/2}$ satellite peak are also observed at around 10 eV higher (B.E. about 940–945 eV) for the CuO/Al_2O_3, and copper-rich sample (1:4, 1:2, and 1:1 Pd:Cu on alumina catalyst) suggesting the presence of Cu^{2+} [24]. Moreover, the satellite peak is also observed in reduced Cu/Al_2O_3 indicating that the sample is not completely reduced, possibly due to the reduction condition and the oxidation by air when transferring the samples to XPS. For the sample with low copper loading (3:2 and 2:1 Pd:Cu on alumina catalyst), the satellite peak is not clearly observed probably due to the low copper

loading. In addition, the Pd/Cu intensity ratios of bimetallic catalysts were 10.04, 6.90, 5.15, 3.20, and 1.80 for Pd:Cu 2:1, 3:2, 1:1, 1:2, and 1:4, respectively, caused by the dilution of Pd by Cu.
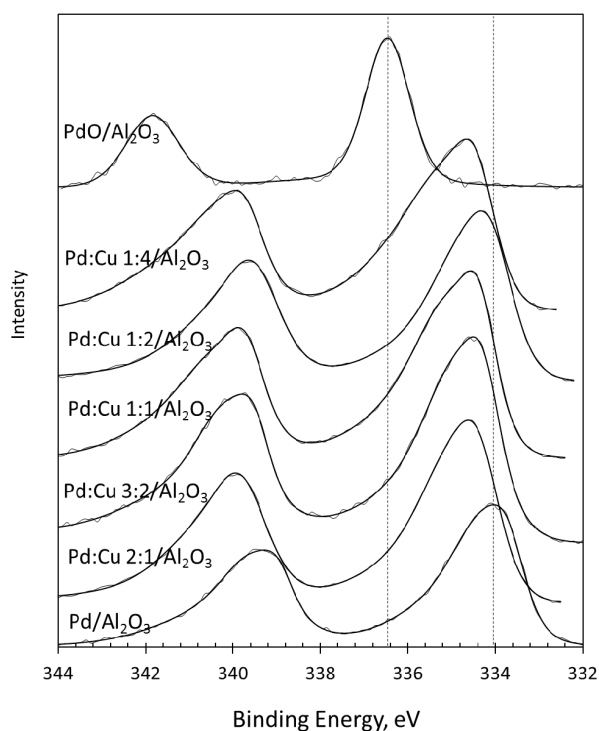
Figure 4. X-ray photoelectron spectra of the Pd 3d of each catalyst.
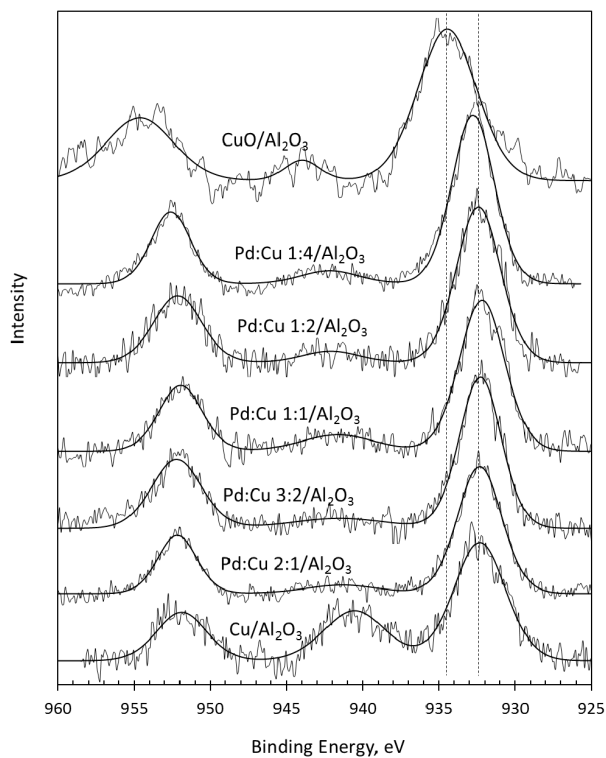
Figure 5. X-ray photoelectron spectra of the Cu 2p of each catalyst.

Table 2. The measured binding energy (eV), full width at half maximum (FWHM), and intensity ratios of Pd, Cu, and Pd-Cu on Al_2O_3.

Catalysts	Pd $3d_{5/2}$		Cu $2p_{3/2}$		Pd/Al	Cu/Al	Pd/Cu
	Position	FWHM	Position	FWHM			
PdO/Al_2O_3	336.4	1.23	-	-	0.07	-	-
Pd/Al_2O_3	334.2	1.97	-	-	0.09	-	-
Pd:Cu 2:1/Al_2O_3	334.6	1.98	932.4	3.50	0.16	0.016	10.04
Pd:Cu 3:2/Al_2O_3	334.6	2.04	932.3	3.21	0.02	0.003	6.90
Pd:Cu 1:1/Al_2O_3	334.6	2.11	932.2	3.10	0.13	0.025	5.15
Pd:Cu 1:2/Al_2O_3	334.5	2.43	932.3	3.43	0.09	0.028	3.20
Pd:Cu 1:4/Al_2O_3	334.6	2.24	932.8	3.28	0.07	0.039	1.80
Cu/Al_2O_3	-	-	932.3	3.75	-	0.003	-
CuO/Al_2O_3	-	-	934.4	4.57	-	0.016	-

The addition of Cu to Pd/Al_2O_3 catalyst leads to both electronic and geometric modifications [25,26]. For geometric effect, Cu may induce Pd to be more exposed at the metal surface, particularly at Pd:Cu 3:2, which also has the highest Pd dispersion.

The Pd:Cu 3:2 catalyst was selected to study the effect of prolonged reaction time by refilling the system with concentrated vinyl acetylene mixed C4 without catalyst replacement for six cycles. Each reaction cycle proceeded until vinyl acetylene was completely used up, which takes about 5–7 h. The reaction rate and 1,3-butadiene selectivity as the function of reaction cycles are illustrated in Figures 6 and 7, respectively. As observed in Figure 6, the rate of reaction in case of using Pd:Cu 3:2 catalyst is decreased until four cycles, and then it is relative stable. On the other hand, Pd/Al_2O_3 catalyst indicates the continuously decreasing reaction rate along six cycles. Interestingly, catalyst Pd/Al_2O_3 provides higher 1,3-butadiene selectivity than Pd:Cu 3:2 catalyst as shown in Figure 7 (except cycle 6). The Pd:Cu 3:2 catalyst has potential to improve the catalyst stability for the hydrogenation of vinyl acetylene.
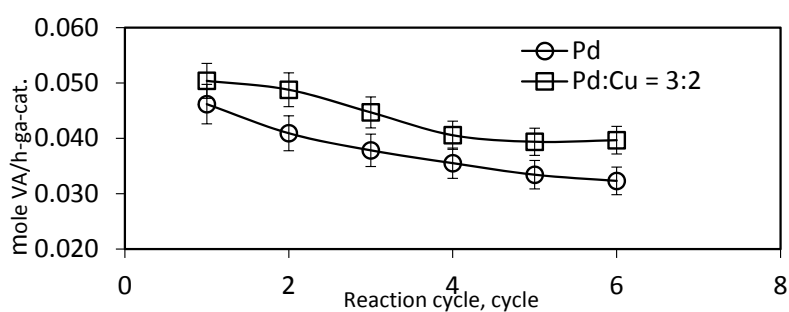
Figure 6. The vinyl acetylene reaction rate of Pd/Al_2O_3 and Pd:Cu 3:2 on Al_2O_3 catalysts as the function of reaction cycles.
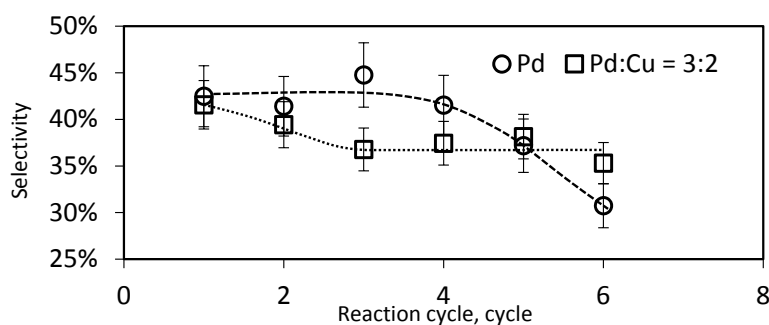
Figure 7. The 1,3-butadiene selectivity of Pd/Al_2O_3 and Pd:Cu 3:2 on Al_2O_3 catalysts as a function of the reaction cycles.

The TPO was used to characterize the deposited carbon on spent catalysts. The TPO profiles of spent catalysts are shown in Figure 8. The used Pd catalyst shows a broad TPO peak around 200 to 600 °C while the used Pd-Cu catalyst containing highest Cu (at Pd:Cu = 1:4) shows between 120 and 470 °C. The order of peak boarding are Pd/Al$_2$O$_3$ > Pd:Cu 2:1 > Pd:Cu 3:2 > Pd:Cu 1:1 > Pd:Cu 1:2. It can be inferred that a higher Cu content reflects a lower TPO temperature.

Carbon content of spent catalysts is calculated and shown in Table 3. Among one reaction cycle, the carbon content of Pd-Cu/Al$_2$O$_3$ catalysts is not significantly lower than of Pd/Al$_2$O$_3$ catalyst. The Pd/Al$_2$O$_3$ catalyst has carbon content 2.12 wt % while Pd-Cu/Al$_2$O$_3$ catalysts have carbon content in the same magnitude, 1.79–2.62 wt %. On the other hand, among spent catalyst with six reaction cycles, Pd:Cu 3:2 catalyst produces carbon to 3.19 wt % while Pd/Al$_2$O$_3$ catalyst shows carbon content 5.96 wt %. Therefore Pd-Cu/Al$_2$O$_3$ catalyst can inhibit the polymerization of polyolefins in this system and should promote the longer catalyst life.

Table 3. Deposited carbon on spent catalysts performed reaction tests of one and six cycles.

Catalysts	Deposited Carbon, wt %
1 Cycle	
Pd	2.12 ± 0.08
Pd:Cu 2:1	2.43 ± 0.10
Pd:Cu 3:2	2.62 ± 0.11
Pd:Cu 1:1	2.13 ± 0.09
Pd:Cu 1:2	1.79 ± 0.07
Pd:Cu 1:4	2.45 ± 0.10
6 Cycles	
Pd	5.96 ± 0.24
Pd:Cu 3:2	3.19±0.13

Figure 8. Temperature programmed oxidation (TPO) profiles of spent Pd-Cu/Al$_2$O$_3$ catalysts.
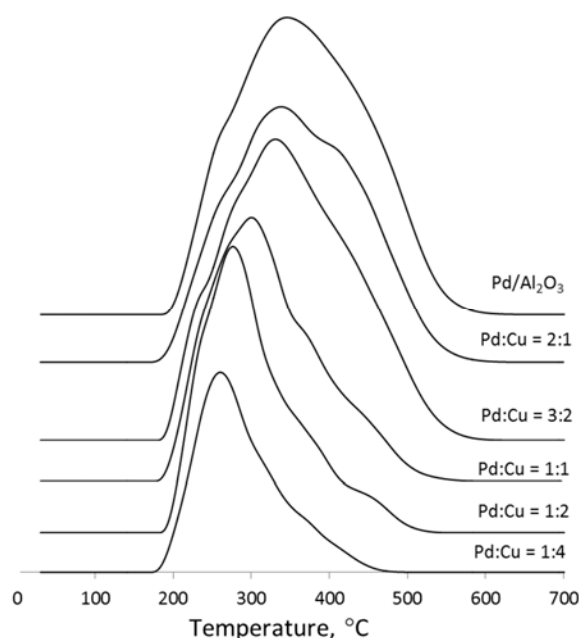
3. Materials and Methods

The concentrated vinyl acetylene mixed C4 was obtained from Bangkok Synthetics Co., Ltd (Rayong, Thailand). Analytical reagent grade (AR grade) hexane was purchased from Fisher Scientific Company LLC. (Pittsburgh, PA, USA). The pelletized aluminium oxide, palladium (II) nitrate dihydrate,

and copper (II) nitrate trihydrate were purchased from Sigma-Aldrich Co. LLC. (St. Louis, MO, USA). The high purity (HP, 99.95%) hydrogen and nitrogen gases were purchased from Linde (Thailand) Public Company Limited (Bangkok, Thailand).

Prior to experiment, γ-Al$_2$O$_3$ was pretreated at 1000 °C in a furnace for 2 h to obtain the mixed phases of alumina [27]. We also found that Pd supported on alumina, pretreated at 1000 °C, provided much less carbon deposition (three times less) than untreated γ-Al$_2$O$_3$, while the 1,3-butadiene yield is also increased, but not significant (about 2%). Subsequently, the pretreated Al$_2$O$_3$ were impregnated by palladium (II) nitrate dihydrate aqueous solution to obtain 0.3 wt % Pd loading on the alumina. The Pd-Cu/Al$_2$O$_3$ catalysts were prepared by sequential impregnation; the support was first impregnated by palladium (II) nitrate dihydrate precursor, then dried at 110 °C and calcined at 500 °C for 1 h. Subsequently, the calcined Pd/Al$_2$O$_3$ was further impregnated by the aqueous solution of copper (II) nitrate trihydrate. The Pd-Cu/Al$_2$O$_3$ catalysts were prepared by varying Pd/Cu atomic ratios from 1:4 to 2:1. The impregnated catalysts were then dried at 110 °C for 8 h and calcined in a furnace at 500 °C for 3 h. The calcined catalysts were reduced by hydrogen at 300 °C for 1 h prior to use.

The reaction was conducted in a recirculating liquid phase through an external fixed-bed reactor (Swagelok Company, Solon, OH, USA) as described in previous work [28]. The known amount of reduced catalyst (0.5 g) was packed in 1/2 inch stainless steel tube fixed-bed reactor. Prior to reaction, the system was sufficiently purged by nitrogen to remove residue oxygen, and the catalyst was reduced in situ by flowing hydrogen at 150 °C for 8 h in order to treat Pd oxide possibly formed during the sample transfer. Subsequently, 650 mL of hexane was filled into the sample reservoir and the system was again purged by nitrogen. Then, the concentrated vinyl acetylene mixed C4 was introduced into the sample reservoir. After that, hydrogen was applied to the reservoir at 5.5 bar. The liquid mixture in the sample reservoir was continuously stirred by a magnetic stirrer and recirculated by a diaphragm pump through the fixed-bed reactor at a flow rate 700 mL/min since we have checked by varying the flow rate and found that at least 400 mL/min is required to avoid external diffusion limitation. The temperature of the fixed-bed reactor and sample reservoir was controlled by a temperature controller (OMRON Electronics Co., Ltd, Bangkok, Thailand). To quantitatively analyze for compositions, a sample was sent every 30 min for gas chromatography (HP, 5890 II Plus) (Agilent Technologies, Inc., Santa Clara, CA, USA) which was equipped with flame ionization detector (FID) and GS-alumina capillary column. The reaction rate and product selectivity were then obtained from the analysis of C4 compositions.

The reaction rate, vinyl acetylene conversion, 1,3-butadiene selectivity, and 1,3-butadiene yield were calculated as described below:

$$\text{Reaction rate } = \frac{VA_\text{i} - VA_\text{f}}{t \times W_\text{cat}} \tag{1}$$

$$\%\text{Vinyl acetylene conversion } = \frac{VA_\text{i} - VA_\text{f}}{VA_\text{i}} \times 100 \tag{2}$$

$$\%1,3\text{-Butadiene selectivity } = \frac{BD_\text{f} - BD_\text{i}}{VA_\text{i} - VA_\text{f}} \times 100 \tag{3}$$

$$\%1,3\text{-butadiene yield} = \%\text{Vinyl acetylene conversion} \times \%1,3\text{-Butadiene selectivity} \tag{4}$$

where:

　　VA_i = initial mole of vinyl acetylene
　　VA_f = final mole of vinyl acetylene
　　t = reaction time in hour
　　W_cat = catalyst weight in gram
　　BD_i = initial mole of 1,3-butadiene
　　BD_f = final mole of 1,3-butadiene

The amount of palladium extracted from the prepared catalysts was determined by a Varian SpectrAA 300 atomic absorption spectroscopy. The reduced catalysts (0.05–0.2 g) were digested in 3 mL of 48% hydrofluoric acid at 50 °C for 6 h. Then 1 mL of aqua regia was added and the solution was kept at 50 °C overnight. After that, it was filtered by syringe filter and diluted by deionized water.

Dispersion of palladium was determined by hydrogen chemisorption. The exposed Pd atom on the surface was calculated from the dissociative chemisorbed hydrogen. First, the reduced catalysts were packed in a quartz tube reactor and heated up to 120 °C with a ramping rate 10 °C/min, and was then kept for 30 min under a hydrogen gas flow. Subsequently, helium was flowed over the catalyst at 120 °C for 30 min. Then, the known amount of hydrogen was pulsed to the reactor containing the catalyst at the previous temperature. The surface of Pd was considered to be saturated when the pulsed hydrogen coming out with the same area of the thermal conductivity detector (TCD) signal for at least three consecutive pulses.

Temperature program reduction, TPR, was performed by heating the calcined catalysts at the rate 10 °C/min from 30–800 °C in a 10 mL/min flow rate of 5% hydrogen in argon gas. The signal of hydrogen were detected by TCD.

For temperature program oxidation, TPO, 5% oxygen in helium gas was flowed over the spent catalysts which packed in quartz tube reactor. The sample of spent catalysts was heated up from 30–900 °C with 10 °C/min ramping rate. The effluent gases (CO_2 and/or CO) generated from oxidation of deposited carbon compounds on the spent catalysts was passed through a methanator which converts CO/CO_2 to methane. The methane was detected by using a flame-ionized detector (FID). Quantification of methane was calibrated by pure methane with 100 μL pulse. Therefore, the carbon content of the spent catalysts was then determined.

The reduced catalysts were also characterized by X-ray photoelectron spectroscopy (XPS, Kratos Model Axis Ultra DLD, Manchester, UK) analyzing area 700 μm × 300 μm, using a monochromator Al K alpha X-ray source and operating at 10 mA anode HT 15 kV. The Pd 3d and Cu 2p spectra were reported with respect to the C 1s spectra (284.6 eV).

4. Conclusions

The Pd/Al_2O_3 and Pd-Cu/Al_2O_3 catalysts were prepared by incipient wetness impregnation and tested for the hydrogenation of vinyl acetylene in the waste stream from the butadiene extraction process. The results show that the adding Cu to Pd/Al_2O_3 catalysts can increase the rate of reaction, while decreasing the amount of carbon deposited on spent catalyst. However, the 1,3-butadiene selectivity is not significantly changed. In addition, among the prepared Pd and Pd-Cu/Al_2O_3 catalysts, Pd:Cu 3:2 catalyst provides the highest reaction rate possibly due to highest Pd dispersion. On the other hand, catalysts with low Pd:Cu ratios, 1:4, 1:2, and 1:1, provide higher TOF number. The stability test found that, compared to Pd catalysts, Pd:Cu 3:2 catalyst has the potential to improve the activity and selectivity for long-term application.

Author Contributions: P.I. and B.K. designed and conducted the experiments; analyzed the data; and wrote the article.

**Conflicts of Interest:** The authors declare no conflict of interest.

References

1. SK-KBR Boosting Butadiene Extraction by Converting Acetylene. Available online: http://www.sk-kbr.com/Technologies-and-Services/License-Technologies/C4AC/C4AC.pdf (accessed on 22 September 2015).
2. Ikegami, T. Studies on explosion reaction of monovinyl acetylene gas: I. Explosion limits of monovinyl acetylene and monovinyl acetylene-air mixture. *Rev. Phys. Chem. Jpn.* **1963**, *32*, 13–29.
3. Johnson-Matthey-Process-Technologies C4 Acetylene Hydrogenation. Available online: http://www.jmprotech.com/olefins-C4-acetylene-hydrogenation-johnson-matthey (accessed on 31 October 2016).
4. Venezia, A.M.; Liotta, L.F.; Deganello, G.; Schay, Z.; Guczi, L. Characterization of Pumice-Supported Ag–Pd and Cu–Pd Bimetallic Catalysts by X-ray Photoelectron Spectroscopy and X-ray Diffraction. *J. Catal.* **1999**, *182*, 449–455. [CrossRef]
5. Crespo-Quesada, M.; Dykeman, R.R.; Laurenczy, G.; Dyson, P.J.; Kiwi-Minsker, L. Supported nitrogen-modified Pd nanoparticles for the selective hydrogenation of 1-hexyne. *J. Catal.* **2011**, *279*, 66–74. [CrossRef]
6. Kennedy, D.R.; Webb, G.; Jackson, S.D.; Lennon, D. Propyne hydrogenation over alumina-supported palladium and platinum catalysts. *Appl. Catal. A Gen.* **2004**, *259*, 109–120. [CrossRef]
7. Ryndin, Y.A.; Stenin, M.V.; Boronin, A.I.; Bukhtiyarov, V.I.; Zaikovskii, V.I. Effect of Pd/C dispersion on its catalytic properties in acetylene and vinylacetylene hydrogenation. *Appl. Catal.* **1989**, *54*, 277–288. [CrossRef]
8. Teschner, D.; Vass, E.; Hävecker, M.; Zafeiratos, S.; Schnörch, P.; Sauer, H.; Knop-Gericke, A.; Schlögl, R.; Chamam, M.; Wootsch, A.; et al. Alkyne hydrogenation over Pd catalysts: A new paradigm. *J. Catal.* **2006**, *242*, 26–37. [CrossRef]
9. Axens-Headquarters (Ed.) Axens catalysts and adsorbents. In *Product Listing*; Axens-Headquarters: Malmaison, France, 2011.
10. Süd-Chemie (Ed.) General catalogue Süd-Chemie catalysts. In *Catalyst Index and Contact Details*; Süd-Chemie: Munich, Germany, 2007.
11. Büchele, W.; Roos, H.; Wanjek, H.; Müller, H.J. Catalyst research—One of the cornerstones of modern chemical production. *Catal. Today* **1996**, *30*, 33–39. [CrossRef]
12. Pachulski, A.; Schödel, R.; Claus, P. Performance and regeneration studies of Pd–Ag/Al$_2$O$_3$ catalysts for the selective hydrogenation of acetylene. *Appl. Catal. A Gen.* **2011**, *400*, 14–24. [CrossRef]
13. Kim, S.K.; Lee, J.H.; Ahn, I.Y.; Kim, W.-J.; Moon, S.H. Performance of Cu-promoted Pd catalysts prepared by adding Cu using a surface redox method in acetylene hydrogenation. *Appl. Catal. A Gen.* **2011**, *401*, 12–19. [CrossRef]
14. Lederhos, C.R.; Maccarrone, M.J.; Badano, J.M.; Torres, G.; Coloma-Pascual, F.; Yori, J.C.; Quiroga, M.E. Hept-1-yne partial hydrogenation reaction over supported Pd and W catalysts. *Appl. Catal. A Gen.* **2011**, *396*, 170–176. [CrossRef]
15. Koeppel, R.A.; Wehrli, J.T.; Wainwright, M.S.; Trimma, D.L.; Cant, N.W. Selective hydrogenation of C4-alkynes over a copper on silica catalyst. *Appl. Catal. A Gen.* **1994**, *120*, 163–177. [CrossRef]
16. Setiawan, I.; Cavell, K.J. Removal of unstaturated contaminants from an industrial C4-stream using Cu/SiO$_2$ catalysts: Subsequent testing of the purified stream with an alkyne sensitive catalyst system. *Appl. Catal. A Gen.* **1995**, *131*, 225–241. [CrossRef]
17. Wehrli, J.T.; Thomas, D.J.; Wainwright, M.S.; Trimm, D.L.; Cant, N.W. Selective hydrogenation of propyne over an ion-exchanged copper on silica catalyst. *Appl. Catal.* **1990**, *66*, 199–208. [CrossRef]
18. Wehrli, J.T.; Thomas, D.J.; Wainwright, M.S.; Trimm, D.L.; Cant, N.W. Selective hydrogenation of propyne over supported copper catalysts: Influence of support. *Appl. Catal.* **1991**, *70*, 253–262. [CrossRef]
19. Friedrich, M.; Villaseca, S.; Szentmiklósi, L.; Teschner, D.; Armbrüster, M. Order-Induced Selectivity Increase of Cu$_{60}$Pd$_{40}$ in the Semi-Hydrogenation of Acetylene. *Materials* **2013**, *6*, 2958–2977. [CrossRef]
20. Cai, F.; Yang, L.; Shan, S.; Mott, D.; Chen, B.; Luo, J.; Zhong, C.-J. Preparation of PdCu Alloy Nanocatalysts for Nitrate Hydrogenation and Carbon Monoxide Oxidation. *Catalysts* **2016**, *6*, 96. [CrossRef]
21. Zhang, Q.; Li, J.; Liu, X.; Zhu, Q. Synergetic effect of Pd and Ag dispersed on Al$_2$O$_3$ in the selective hydrogenation of acetylene. *Appl. Catal. A Gen.* **2000**, *197*, 221–228. [CrossRef]
22. Groppo, E.; Agostini, G.; Piovano, A.; Muddada, N.B.; Leofanti, G.; Pellegrini, R.; Portale, G.; Longo, A.; Lamberti, C. Effect of reduction in liquid phase on the properties and the catalytic activity of Pd/Al$_2$O$_3$ catalysts. *J. Catal.* **2012**, *287*, 44–54. [CrossRef]

23. Molenbroek, A.M.; Haukka, S.; Clausen, B.S. Alloying in Cu/Pd Nanoparticle Catalysts. *J. Phys. Chem. B* **1998**, *102*, 10680–10689. [CrossRef]

24. Figueiredo, R.T.; Andrade, H.M.C.; Fierro, J.L.G. The Role of the Coprecipitation Sequence of Salt Precursors on the Genesis of Cu-ZnO-Al$_2$O$_3$ Catalysts: Synthesis, Characterization and Activity for Low Temperature Shift Reaction. *Braz. J. Chem. Eng.* **1998**, *15*. [CrossRef]

25. Guczi, L.; Schay, Z.; Stefler, G.; Liotta, L.F.; Deganello, G.; Venezia, A.M. Pumice-Supported Cu–Pd Catalysts: Influence of Copper on the Activity and Selectivity of Palladium in the Hydrogenation of Phenylacetylene and But-1-ene. *J. Catal.* **1999**, *182*, 456–462. [CrossRef]

26. Kim, W.-J.; Moon, S.H. Modified Pd catalysts for the selective hydrogenation of acetylene. *Catal. Today* **2012**, *185*, 2–16. [CrossRef]

27. Komeili, S.; Ravanchi, M.T.; Taeb, A. The influence of alumina phases on the performance of the Pd–Ag/Al$_2$O$_3$ catalyst in tail-end selective hydrogenation of acetylene. *Appl. Catal. A Gen.* **2015**, *502*, 287–296. [CrossRef]

28. Insorn, P.; Kitiyanan, B. Selective hydrogenation of mixed C4 containing high vinyl acetylene by Mn–Pd, Ni–Pd and Ag–Pd on Al$_2$O$_3$ catalysts. *Catal. Today* **2015**, *256*, 223–230. [CrossRef]
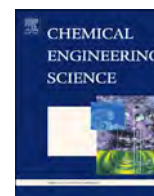
Partial oxidation of methane on a nickel catalyst: Kinetic Monte-Carlo simulation study

Sirawit Pruksawan [a], Boonyarach Kitiyanan [a,*], Robert M. Ziff [b]

[a] The Petroleum and Petrochemical College, Chulalongkorn University, Bangkok 10330, Thailand
[b] Department of Chemical Engineering, University of Michigan, Ann Arbor, MI 48109, USA

HIGHLIGHTS

- Partial oxidation of methane on a nickel surface is modeled by Monte-Carlo method.
- The controlling step for CO production changes when the temperature changes.
- If diagonal actions are allowed, the discontinuous transition becomes continuous.
- The selectivity of H_2 significantly lowers when the diffusion of O^* is allowed.
- The results on the feed and temperature effects agree with previous experiments.

GRAPHICAL ABSTRACT
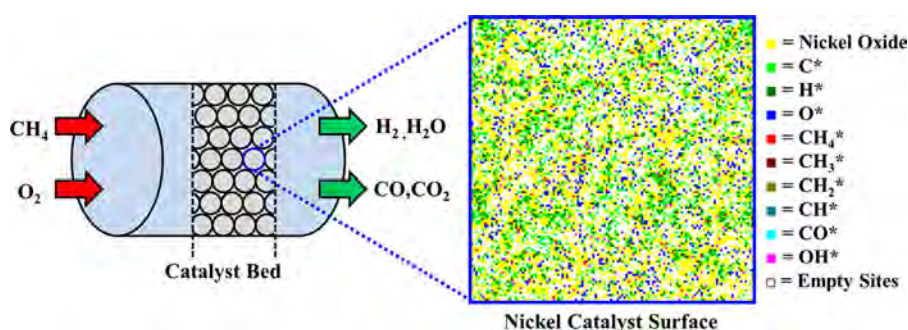
ABSTRACT

Kinetic Monte-Carlo simulation is applied to study the partial oxidation of methane over a nickel catalyst. Based on the Langmuir–Hinshelwood mechanism, the kinetic behavior of this reaction is analyzed and the results are compared with previous experiments. This system exhibits kinetic phase transitions between reactive regions with sustained reaction and poisoned regions without reaction. The fractional coverages of the adsorbed species and the production rates of H_2, CO, H_2O, and CO_2 are evaluated at steady state as functions of feed concentration of the methane and oxygen, and reaction temperature. The influence of lattice coordination number, diffusion, and impurities on the surface is also investigated. The simulation results are in good agreement with the experimental studies where such results are available. It is observed that when the lattice coordination number is increased to eight, the width of the reactive region increases significantly. Moreover, the phase transition becomes continuous. The diffusion of adsorbed O and H on the surface plays a measurable role in the reaction, increasing the maximum production rates as the diffusion rate increases. In systems with impurities, the production rates are greatly reduced and the phase transition is also changed from being abrupt to continuous.

© 2016 Elsevier Ltd. All rights reserved.

1. Introduction

The catalytic conversion of methane is one of the most attractive areas of research in both academia and industry. Steam reforming has been used in industry to produce hydrogen or syngas from methane. Nevertheless, steam reforming is an energy-intensive process. The catalytic partial oxidation (CPOx) process is an attractive alternative because it avoids the need of large amounts of energy and requires smaller reactors due to the faster oxidation reaction. Another advantage of the CPOx process is that the H_2-to-CO ratio in syngas products is 2:1, which allows a

* Corresponding author.
  E-mail address: boonyarach.k@chula.ac.th (B. Kitiyanan).

straightforward syngas utilization for methanol or Fischer–Tropsch synthesis. The CPOx of methane has been extensively studied by various researchers (Hu and Ruckenstein, 1996; Tsipouriari and Verykios, 1998; Smith and Shekhawat, 2011; Al-Sayari, 2013). Even though several catalytic systems have been reported in the literature to be active for this reaction, nickel catalysts are generally believed to be the most promising candidate owing to their moderate cost and good catalytic performance compared to that of noble metals (Al-Sayari, 2013). In spite of the large quantity of experimental studies devoted to the partial oxidation of methane on nickel catalysts, the mechanisms and kinetic studies in this system are still unclear. Theoretical studies have not clarified this issue. Moreover, the published experimental results are contradictory (Smith and Shekhawat, 2011). Therefore, further studies on the kinetic behavior are expected to provide a better understanding to the reaction mechanism.

Kinetic Monte-Carlo (KMC) is an effective tool for investigating surface reaction mechanisms and predicting complex kinetic behaviors. KMC simulation can be viewed as a numerical method to solve the Master Equation that describes the evolution of the catalyst's surface and the adsorbates. The rate constants in this equation are obtained from kinetic studies carried out on the selected catalyst. KMC simulation allows one to visualize the state of surface. One of the simplest kinetic models for the oxidation reaction of CO on a catalytic surface, introduced by Ziff, Gulari and Barshad (ZGB) (Ziff et al., 1986), has provided a source of continual investigation for studies of complex phenomena (Fichthorn et al., 1989; Fichthorn and Weinberg, 1991; Evans, 1993; Tomé and Dickman, 1993; Loscar and Albano, 2003; Machado et al., 2005). Other lattice models have been introduced to simulate different catalytic surface reaction, including CPOx of methane. The CPOx of methane was extensively studied for the oscillatory behavior of the dynamics by a model (Lashina et al., 2012; Ren et al., 2008; Ren and Guoa, 2008). The present work provides information on the kinetic behavior in which the reaction is conducted under steady-state conditions.

The purpose of this work is to develop the KMC simulation for the partial oxidation of methane on a nickel catalyst based on the Langmuir–Hinshelwood (LH) mechanism combined with the formation and removal of nickel oxide under isothermal conditions. The kinetic behavior at steady state is analyzed in different operating conditions and the results are compared with previous experiments. The effects of diffusion of adsorbed species, lattice coordination number and inactive impurities on the surface are also evaluated.

2. Model and simulation procedure

2.1. Model

Our kinetic model was developed for the CPOx on a nickel catalyst based on the reaction mechanism of Lashina et al. (2012). According to these authors, the mechanism of CPOx can be described by an 18-step elementary reaction (Table 1). The steps 1–14 describe the CPOx of methane on the surface of nickel metal (denoted by *) with the formation of CO, H_2, CO_2 and H_2O. The formation of nickel oxide (Ox) in step 15 leads directly or indirectly to the formation of CO, CO_2 and H_2O with the participation of the oxidized form of nickel in steps 16–18 (Shen et al., 1998).

The estimation of the kinetic parameters of elementary reactions was obtained from the literature as summarized in Table 1. Here, steps 3, 4, 5, 6, 11 and 14 are assumed to be instantaneous (probability of an event = 1) since the experiments suggested that they are not kinetically significant (Hei et al., 1998; Chen et al., 2001a, 2001b). The diffusion of adsorbed species is also considered. However, only the diffusion of adsorbed CH_4, O, CO and H is included because of their relatively rapid diffusion rates (Ren et al., 2008; Chen et al., 2001b).

The adsorption constants (k_i) for methane and oxygen in steps 1 and 7 depend on the reactant pressures in the gas phase estimated by Eq. (1), where $k_i°$ is adsorption coefficient and y_i is the feed concentration and P is the pressure of the reactants.

$$k_i = k_i^0 y_i P \tag{1}$$

The reaction constant (k_i) in steps 2, 8, 9, 10, 12, 13, 15, 16, 17 and 18 can be calculated by the Arrhenius equation (Eq. (2)), where A_i is the pre-exponential factor, Ea_i is the activation energy, R is the gas constant and T is the absolute temperature.

$$k_i = A_i \exp(-Ea_i/RT) \tag{2}$$

The diffusion constant (k_{diff}) of adsorbed CH_4, O, CO and H can be calculated by Eq. (3), where D_{0i} is the pre-exponential factor for the diffusion process, a is the cell parameter of the nickel surface with a value of 2.48×10^{-8} cm (Ren and Guoa, 2008) and Q_i is the

Table 1
Elementary reactions and corresponding kinetic parameters used in this work.

Steps (i)	Elementary reactions	A_i or $k_i°$ (s^{-1} or s^{-1} Pa^{-1})	Ea_i (kcal/mol)	References
1	$CH_4(g)+[*] \rightarrow [CH_4*]$	0.0045 (k_1^0)	0	Ren et al. (2008)
2	$[CH_4*] \rightarrow CH_4(g)+[*]$	1.0×10^4	7.9	Ren et al. (2008)
3[a]	$[CH_4*] + [*] \rightarrow [CH_3*] + [H*]$	1.3×10^8	13.8	Hei et al. (1998)
4[a]	$[CH_3*] + [*] \rightarrow [CH_2*] + [H*]$	1.0×10^{13}	27.6	Chen et al. (2001a)
5[a]	$[CH_2*] + [*] \rightarrow [CH*] + [H*]$	1.0×10^{13}	23.2	Chen et al. (2001a)
6[a]	$[CH*] + [*] \rightarrow [C*] + [H*]$	1.0×10^{13}	4.5	Chen et al. (2001b)
7	$O_2(g)+2[*] \rightarrow 2[O*]$	0.011 (k_i^0)	0	Ren et al. (2008)
8	$2[O*] \rightarrow O_2(g)+2[*]$	1.0×10^{11}	44.6	Ren et al. (2008)
9	$[C*] + [O*] \rightarrow [CO*] + [*]$	1.0×10^{12}	35	Ren et al. (2008)
10	$[CO*] \rightarrow CO(g)+[*]$	1.0×10^{10}	27.85	Ren et al. (2008)
11[a]	$2[H*] \rightarrow H_2(g)+2[*]$	3.1×10^{12}	23.3	Chen et al. (2001b)
12	$[CO*] + [O*] \rightarrow CO_2(g)+2[*]$	5.0×10^6	15.2	Ren et al. (2008)
13	$[H*] + [O*] \rightarrow [OH*] + [*]$	1.0×10^7	19.6	Li and Xiang (2000)
14[a]	$[H*] + [OH*] \rightarrow H_2O(g)+2[*]$	3.1×10^{11}	7.7	Chen et al. (2001a)
15	$[O*] \rightarrow [Ox]$	1.0×10^5	15.7	Ren et al. (2008)
16	$[C*] + [Ox] \rightarrow [CO*] + [*]$	1.0×10^7	26.24	Ren et al. (2008)
17	$[CO*] + [Ox] \rightarrow CO_2(g)+2[*]$	1.0×10^5	17	Ren et al. (2008)
18	$[H*] + [Ox] \rightarrow [OH*] + [*]$	5.2×10^3	11	Ren et al. (2008)

Note : [X*] = adsorbed X species.

[a] Assumed instantaneous.

activation energy for the diffusion process. Because the kinetic parameters for the diffusion of adsorbed CH_4, CO and H are not precisely known, we use the kinetic parameters of adsorbed O for all diffusion species; $D_{0i} = 5.45 \times 10^{-3}$ cm^2 s^{-1}, $Q_i = 37.9$ kcal/mol (Nam et al., 2013; Barlow and Grundy, 1969). The effect of diffusion on the overall reaction is small, so knowing the precise diffusion rate is not crucial.

$$k_{diff} = \frac{D_{0i}}{a^2}\exp(-Q_i/RT)$$
(3)

The diffusion number (D_N) is defined to represent the relative rate of diffusion and reaction (Eq. 4). This indicates that adsorbed species diffuse D_N times faster than the reaction of the LH step (step 9) (Ren and Guoa, 2008).

$$D_N = \frac{k_{diff}}{k_{LH}}$$
(4)

2.2. Simulation procedure

The KMC algorithm developed in this work is similar to that of Cortés et al. (2006, 2014). In the simulation, the surface of nickel metal is represented by a two-dimensional square lattice of LxL sites. Periodic boundary conditions are applied to avoid edge effects. The surface is in contact with an infinite reservoir of methane and oxygen gas molecules with fixed feed concentrations y_{CH4} and y_{O2}. Computing time is measured in MC cycles, defined as L^2 attempts of the reaction events listed in (c) below. Our KMC algorithm consists of the following steps:

(a) Choose one site from the surface randomly.

(b) Perform the instantaneous event (steps 3, 4, 5, 6, 11 and 14) if possible. On the site selected in step (a), we check neighboring sites for instantaneous event, whether there is a possible event or not. If the event is possible, the corresponding step is carried out and the surface is changed according to the event. This procedure is repeated if there is further possible event on that site. In the case of more than one possible instantaneous event, such as steps 11 and 14, one of them is chosen randomly and carried out. In the case of chain reaction in neighboring sites, all instantaneous events should be carried out immediately. However, to simplify the program we did not consider the chain reaction in neighboring sites in this study. Because these chain reactions are relatively rare, this assumption should not have too great an effect on the behavior.

(c) Choose a reaction event i from the mechanism steps ($i=1, 2, 7, 8, 9, 10, 12, 13, 15, 16, 17$ and 18; excluding the instantaneous steps) according to the probability of an event i (p_i) defined by Eq. (5). This procedure is known in different sources variously as the n-fold way or Bortz–Kalos–Lebowitz (BKL) or Gillespie algorithm (Bortz et al., 1975; Gillespie, 1976).

$$p_i = \frac{k_i}{\sum k_i}$$
(5)

(d) Perform the reaction event i selected in step (c) according to the following processes:

(d-1) Adsorption

• If the adsorption of CH_4 (step 1) is selected and the site selected in step (a) is empty, the event is successful, the adsorption of CH_4 is carried out and a particle of CH_4^* is placed in the site. If the site is occupied, the attempt is terminated.

• If the dissociative adsorption of O_2 (step 7) is selected and the site selected in step (a) is empty, a neighboring site is then chosen randomly next to the first site. If the latter site is empty, the event is successful, the adsorption of O_2 is carried out and a particle of O^* is placed in each of the two previous sites. If either site is occupied, the attempt is terminated.

(d-2) Desorption

• If the desorption of CH_4 (step 2) is selected and the site selected in step (a) is occupied by a CH_4^* particle, the event is successful, the desorption of CH_4 is carried out, the site is empty and a molecule of CH_4 leaves the surface. If the site is not occupied by a CH_4^* particle, the attempt is terminated.

• If the desorption of CO (step 10) is selected, the procedure is completely analogous to the desorption of CH_4 (step 2).

• If the associative desorption of O_2 (step 8) is selected and the site selected in step (a) is occupied by an O^* particle, a neighboring site is then chosen randomly next to the first site. If the latter site is occupied by the O^* particle, the event is successful, the desorption of O_2 is carried out, the two sites are empty and a molecule of O_2 leaves the surface. If either site is not occupied by an O^* particle, the attempt is terminated.

(d-3) Surface reaction

• If a surface reaction event (steps 9, 13, 16 or 18) is selected and the site selected in step (a) is occupied by a particle corresponding to one of the reactants, a neighboring site is then chosen randomly next to the first site. If the latter site is occupied by the other species of the same reaction, the event is successful, the corresponding reaction is carried out, one particle is replaced by a product particle and the other site is empty. If both sites are not occupied by the appropriate reactants, the attempt is terminated.

(d-4) Surface reaction and desorption

• If the surface reaction and desorption event (steps 12 or 17) is selected, the procedure is analogous to a surface reaction event (step 9, 13, 16, 18) but a molecule of product leaves the surface and the site becomes empty.

(d-5) Formation of nickel oxide

• If the formation of nickel oxide (step 15) is selected and the site selected in step (a) is occupied by an O^* particle, the event is successful, the formation of nickel oxide is carried out and the site is replaced by Ox. If the site is not occupied by the O^* particle, the attempt is terminated.

(e) Perform the diffusion event in proportional to diffusion number (D_N). One site from the surface is randomly chosen. If the site is occupied by a diffusion particle (CH_4^*, O^*, CO^* or H^*) and a randomly chosen neighboring site is empty, the diffusion is successful, the diffusion particle moves to the chosen site. This procedure is repeated an average of D_N times.

(f) Update time from t to $t+\Delta t$ using Eq. (6), where r is a uniformly distributed random number between 0 and 1, L is lattice length and $\sum k_i$ is the sum of all reaction constants (excluding the instantaneous events).

$$\Delta t = \frac{-\ln r}{L^2 \sum k_i}$$
(6)

(g) If the stop condition is fulfilled, then the simulation is stopped. If not, repeat the algorithm.

In this simulation, runs up to 50,000 MC cycles were carried out. In order to get the average value, the initial 10,000 MC cycles were neglected to avoid non-equilibrium behavior, and the production rate (R_i), fractional coverage (θ_i) and selectivity (S_i) were computed by taking averages over the subsequent 40,000 MC cycles. The production rates of produced H_2, CO, CO_2, H_2O are determined by the numbers of product molecules per lattice site in a unit time. The selectivities of H_2 and CO are calculated by Eq. (7) and Eq. (8), respectively.

$$S_{H_2} = \frac{R_{H_2}}{R_{H_2} + R_{H_2O}}$$
(7)

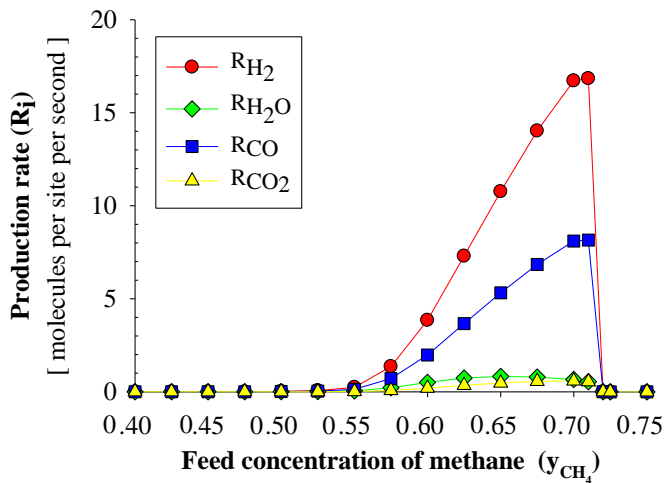$$S_{CO} = \frac{R_{CO}}{R_{CO} + R_{CO_2}}$$
(8)

Fig. 1. Production rates as functions of y_{CH4}; $T=873$ K, $P_{CH4+O2}=6$ kPa, $Z=4$, $D_N=4.02$, $I=0$.

The simulations were started with a 100% metallic nickel surface (empty surface) consisting of 128×128 sites, the feed concentration of methane and oxygen selected as 0.667 and 0.333, respectively, the pressure of the reactants was chosen as 6 kPa, and the temperature chosen as 873 K, corresponding to the experiment condition in (Tsipouriari and Verykios, 1998). The number of neighboring sites corresponding to lattice coordination number was set to four and the surface was considered free of impurities. Then, the lattice size, initial state configuration, temperature, feed concentration, lattice coordination number, diffusion number, and fraction of impurity were adjusted and the results of the different systems were evaluated.

3. Results and discussion

It is important to check the effect of the lattice size. Increasing of the lattice size from 32×32 to 256×256 sites causes only a slight difference in the production rates and fractional coverages, and the overall qualitative nature is not affected. To save the computing time, a lattice size of 128×128 sites was used in our simulations. At this size, there is less than 2% difference in critical values compared to 256×256 sites.

Simulations were performed with different initial configurations of the catalyst's surface, from 100% metallic (reduced) nickel
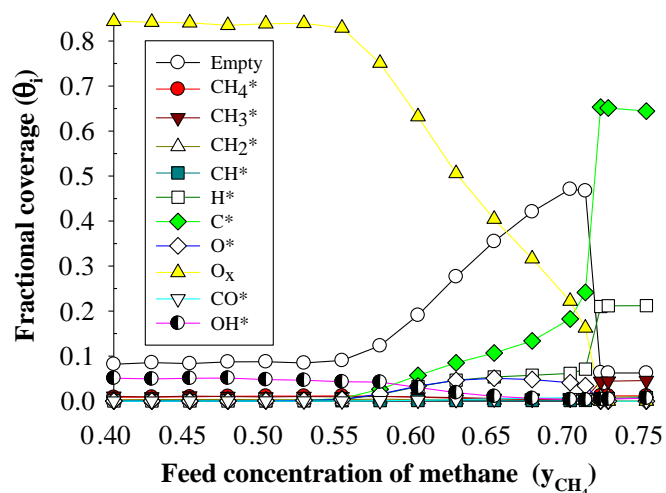

Fig. 2. Fractional coverages as functions of y_{CH4}; $T=873$ K, $P_{CH4+O2}=6$ kPa, $Z=4$, $D_N=4.02$, $I=0$.

surface to the oxidized nickel surface covered with 95% Ox. In all cases, the same results were obtained at steady state with nearly the same production rates and fractional coverages. However, for the oxidized nickel surface, it was observed that the simulation takes a longer time to reach steady state, especially when the surface is covered with a large amount of Ox. This is because the reaction with Ox (steps 16–18) exhibits much lower activity than most other reactions.

3.1. Effect of feed concentration

Fig. 1 presents the production rates as a function of the feed concentration of methane (y_{CH4}) in the gas phase at 873 K. It can be observed that the reaction occurs only for $y_1 < y_{CH4} < y_2$, where $y_1 = 0.47 \pm 0.01$ and $y_2 = 0.71 \pm 0.01$. Outside of this range, the surface is saturated (poisoned) with various species and the reaction cannot take place. The relation of fractional coverages and y_{CH4} is also shown in Fig. 2. According to the result, Ox, C, H* and O* are found in a high portion on the surface while the other species are present at a much lower amount.

As can be seen in Figs. 1 and 2, when y_{CH4} is increased toward 0.71, the production rates of H_2 and CO continuously increase. However, when 0.71 is reached, C* suddenly grows and covers much of the lattice. The surface becomes saturated mainly with C*, H* and CH_3*, and the reaction stops. It can be said that the catalyst is deactivated due to carbon accumulation (poisoning by C*) on a nickel catalyst, as observed in experiments by Qiangu et al. (2000). This deactivation occurs abruptly, with discontinuities of the production rates and fractional coverages, implying that this is a first-order kinetic phase transition (Ziff et al., 1986). Similarly, when y_{CH4} is lowered to 0.47, the surface becomes saturated mainly with Ox and OH*. It corresponds to the non-reactive state in which the surface is oxidized (Lashina et al., 2012). However, this transition is continuous; therefore, it is second-order. In an experiment, the poisoning by Ox may be considered as a reversible process because the possibility of the adsorption of reactants on the Ox surface (Eley–Rideal mechanism) can occur, and when the atmosphere is returned to a condition that allows steady-state operation, the reactive state returns.

For combustion products, the production rate of CO_2 has a similar trend as that of H_2 and CO but the production rate of H_2O has a different trend. It increases up to a maximum value at $y_{CH4}=0.65$ and then decreases for increasing y_{CH4} (Fig. 1). This is because the concentration of OH* decreases and the O* preferentially reacts with the C* to make CO. Note that while the production rates of H_2 and CO drop precipitously at y_2, the production rate of H_2O goes continuously to zero.

Furthermore, it is noted that the maximum H_2 and CO production rates (Fig. 1) and the intersection of the C* and Ox fractional coverages (Fig. 2) are at the same y_{CH4}. This suggests that the reaction between C* and Ox (step 16) is the rate-controlling step at this condition, and therefore, the maximum production rates are achieved when the coverages of C* and Ox are equal.

Fig. 3A illustrates a snapshot of the non-reactive state in which the surface is poisoned with Ox. Fig. 3B shows a snapshot of the steady reactive state at $y_{CH4}=0.67$. At this condition, most of the surface is seen to be covered by C*, Ox and O*. This shows the progress of CO* formation (steps 9 and 16) in the surface when C* reacts with a neighboring Ox or O* to form CO* and then the CO* is desorbed, leaving one empty site. These empty sites subsequently allow the new incoming reactants to adsorb resulting in the reaction to proceed. The snapshot corresponding to the carbon accumulation at $y_{CH4}=0.75$ is shown in Fig. 3C.

The H_2 and CO selectivities and H_2/CO molar ratio are plotted as a function of y_{CH4} in Fig. 4. The simulation result shows that the H_2 and CO selectivities at temperature 873 K and CH_4/O_2 ratio of two
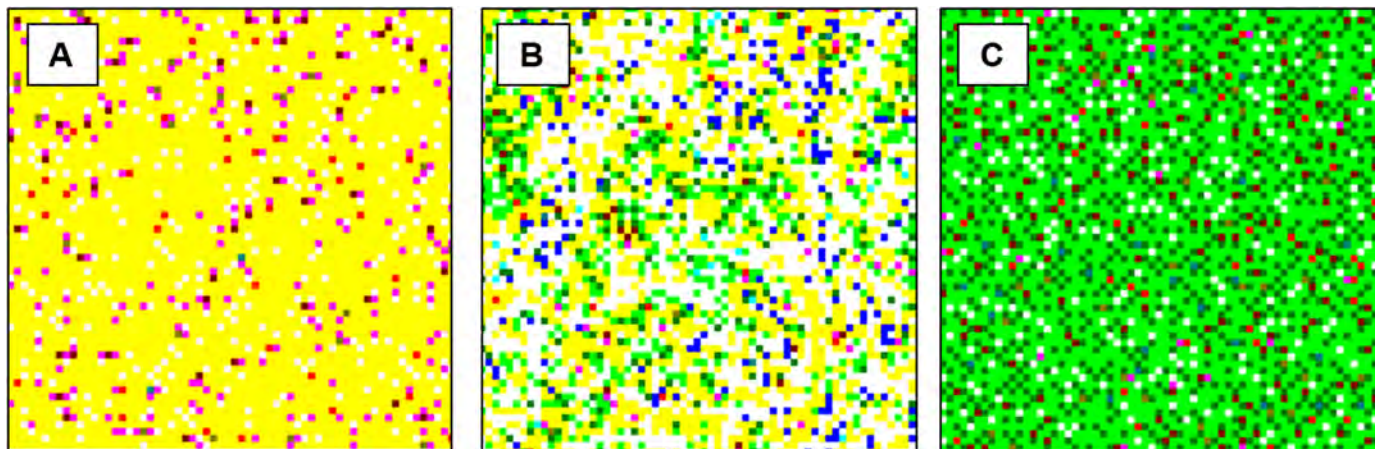
Fig. 3. Snapshots of 1/4 of the surface at (A) $y_{CH4}=0.40$, (B) $y_{CH4}=0.67$, (C) $y_{CH4}=0.75$; $T=873$ K, $P_{CH4+O2}=6$ kPa, $Z=4$, $D_N=4.02$, $I=0$. (▨$=Ox$, ▢$=Empty$, ▨$=H^*$, ▨$=C^*$, ▨$=O^*$, ▨$=CH_4^*$, ▨$=CH_3^*$, ▨$=CH_2^*$, ▨$=CH^*$, ▨$=CO^*$, ▨$=OH^*$).
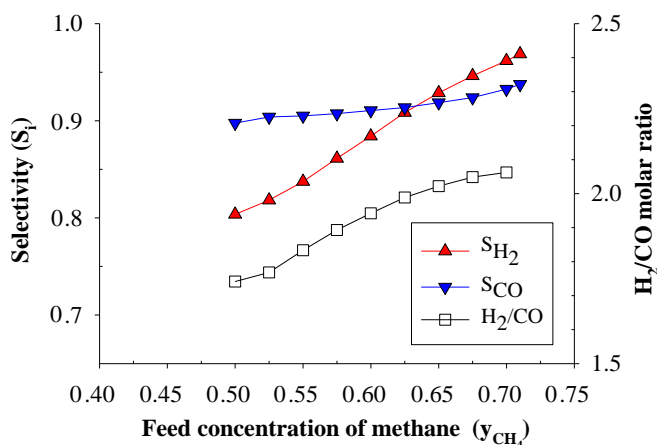
Fig. 4. Selectivities and H_2/CO molar ratio as functions of y_{CH4}; $T=873$ K, $P_{CH4+O2}=6$ kPa, $Z=4$, $D_N=4.02$, $I=0$.

Fig. 6. Fractional coverages as functions of T; $y_{CH4}=0.67$, $P_{CH4+O2}=6$ kPa, $Z=4$, $D_N=4.02$, $I=0$.

Fig. 5. Production rates as functions of T; $y_{CH4}=0.67$, $P_{CH4+O2}=6$ kPa, $Z=4$, $D_N=4.02$, $I=0$.
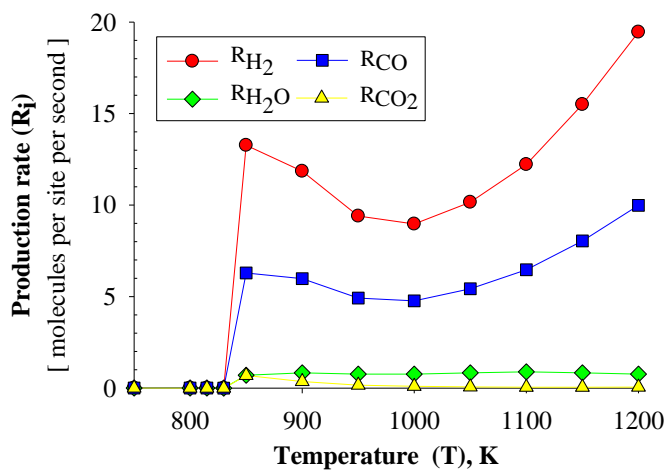
Fig. 7. Selectivities and H_2/CO molar ratio as functions of T; $y_{CH4}=0.67$, $P_{CH4+O2}=6$ kPa, $Z=4$, $D_N=4.02$, $I=0$.

are 0.94 and 0.92, respectively, which are higher than those reported in the experiment by Coleman et al. (2009) on nickel metallic foam. They reported both the H_2 and CO selectivities are at 0.85. The difference between our results and the experimental results might be due to the nature of the catalyst surface and some degree of uncertainty in the experimental kinetic data. Furthermore, increasing methane in the feed results in the increase of H_2

and CO selectivities, as observed in the experiment (Wang et al., 2009). The reason is that this reaction follows the direct mechanism whereby methane directly converts to H_2 and CO, and H_2O and CO_2 are formed by subsequent oxidation of H_2 and CO. Therefore, the decrease of the oxygen in the feed leads to less oxidation of H_2 and CO to H_2O and CO_2 (Eriksson et al., 2007).

Additionally, the H_2/CO molar ratio in the products is around two for the entire range of feed concentrations, as expected from the stoichiometry (Smith and Shekhawat, 2011). It is also noted that the H_2/CO molar ratio increases with increasing y_{CH4}, which suggests that the increase of the methane in the feed gives more H_2 than CO.

3.2. Effect of reaction temperature

The production rates, fractional coverages, selectivities and H_2/CO molar ratio as a function of the reaction temperature are respectively shown in Figs. 5–7, when $y_{CH4}=0.67$. At temperatures below 850 K, the catalyst is deactivated as a result of carbon accumulation on the nickel surface. The fractional coverages as depicted in Fig. 6 show that the coverage of C^* decreases with increasing temperature, thus suppressing the carbon accumulation, and a steady reactive state is reached at temperatures higher than 850 K.

For the reactive regions, the production rates of H_2 and CO decrease with increasing temperature and reach minimum values at a temperature around 1000 K (Fig. 5). Above 1000 K, the rate increases continuously as the temperature increases. This behavior is closely related to the fractional coverages as shown in Fig. 6.

When the temperature is below 1000 K, the reaction between C^* and O_x (step 16) is the controlling step. Since the high fractional coverages of C^* and O_x are dominant, the formation of CO is mainly due to the reaction between C^* and O_x. The O_x formation increases with increasing temperature, causing a lower number of empty sites. As a result, the production rates of H_2 and CO are suppressed.

However, when the temperature is over 1000 K, the reaction between C^* and O^* (step 9) becomes the controlling step, because the fractional coverage of C^* is lower than that of O^* and the C^* prefers to react with O^* rather than O_x. Furthermore, past 1000 K, the O_x coverage decreases substantially. Therefore, the formation of CO is mainly due to the reaction between C^* and O^*. Because the reaction rate increases more rapidly than the O_x formation rate when temperature increases, the O_x coverage decreases with increasing temperature, causing a higher number of empty sites. As a result, the production rates of H_2 and CO increase as the temperature increases.

Notice in Figs. 5 and 6, the H_2 and CO production rates have a similar trend as the fraction of empty sites. The result indicates that the surface state of the catalyst plays a very important role in the kinetic behavior. The O_x, which is the oxidized surface of nickel, is much less reactive than the reduced or empty surface (Li et al., 2000). Apart from the main product, the production rate of H_2O remains unchanged when the temperature goes up. The production rate of CO_2 falls rapidly with increasing temperature, and the selectivity of CO over CO_2 increases up to 0.99 at temperatures above 1075 K.

As shown in Fig. 7, the CO selectivity increases significantly with an increase in temperature, due to the preference to undergo total oxidation at lower temperatures resulting in CO_2 as the product (steps 12 and 17) (Larimi and Alavi, 2012). The H_2 selectivity also increases at temperatures higher than 1000 K, which appears to be related to the change in the production rate curves at 1000 K (Fig. 5). The H_2 and CO selectivities increase from 0.92 to 0.96 and 0.97 to 0.99, respectively, for temperatures spanning 1000–1200 K. This trend is similar to the experimental result of Coleman et al. (2009), in which the H_2 and CO selectivities can increase up to 0.95 and 0.98, respectively, at the highest temperature of 1123 K. Fig. 7 also presents the H_2/CO molar ratio as a function of temperature. It suggests that the increase of temperature leads to more CO than H_2 product.
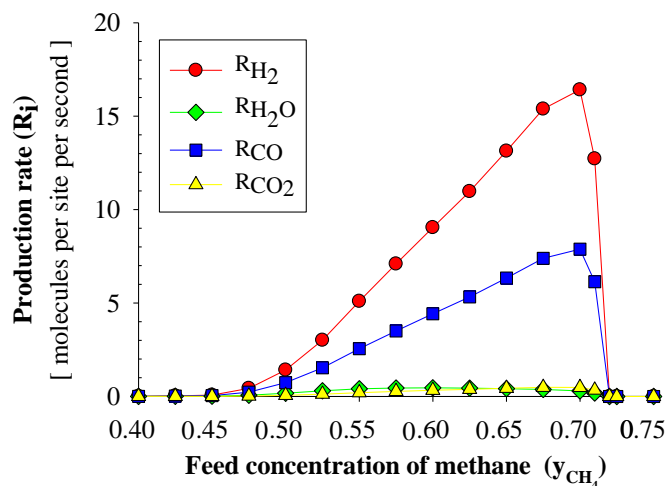
Fig. 8. The same as Fig. 1, but for $Z=8$.
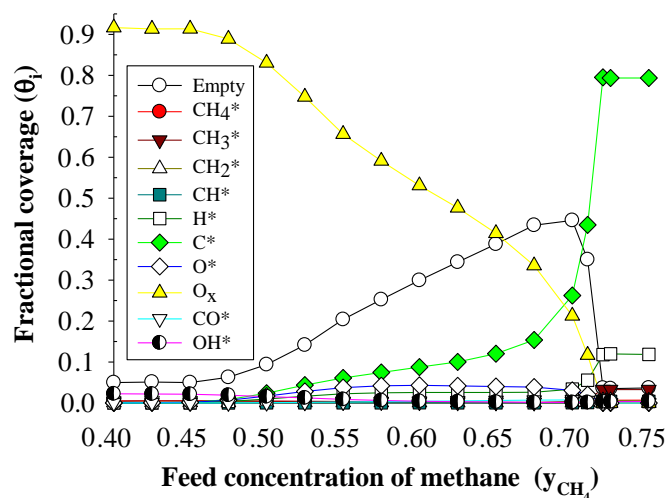
Fig. 9. The same as Fig. 2, but for $Z=8$.

3.3. Effect of lattice coordination number

In this section, the effect of the lattice coordination number is studied. One way of changing the lattice coordination is to allow diagonal interactions on a square lattice. In addition to the four nearest neighbors (nn) sites, the diagonal sites or next nearest neighbours (nnn) sites are also included, increasing the coordination number (Z) of the site from four to eight. It is assumed that the nn and nnn sites are equivalent. This effect has been reported for the oxidation of CO and the reduction reaction of NO by CO and it seems to be a realistic way of modeling the surface (Cortés and Valencia, 1998; Cortés, 1999; Valencia, 2000).

In the case of eight-site coordination, the steady reactive state appears when $0.42 \pm 0.01 < y_{CH4} < 0.71 \pm 0.01$, as shown in Figs. 8 and 9. The width of the steady reactive state is larger than in the four-site coordination case, where $0.47 \pm 0.01 < y_{CH4} < 0.71 \pm 0.01$. This is consistent with the results of Cortés and Valencia (1998) who observe an enlargement of the steady reactive state when they allow diagonal interactions. It is found that y_2, the transition at high concentration of methane, remains constant at 0.71. However, it is seen that y_1, the transition at low concentration of methane, decreases from 0.47 to 0.42 when increasing the coordination number. The reason might be that an increase in the possibility of O^* reactions in diagonal interactions (step 9, 12 and 13) suppresses the possibility of O_x formation from O^* (step 15), requiring a greater feed concentration of oxygen to poison the surface

Fig. 10. Production rate of H_2 as functions of y_{CH4} for different values of D_N; $T=873$ K, $P_{CH4+O2}=6$ kPa, $Z=4$, $I=0$.

Fig. 11. Production rate of CO as functions of y_{CH4} for different values of D_N; $T=873$ K, $P_{CH4+O2}=6$ kPa, $Z=4$, $I=0$.

Table 2
The transition points and the widths of steady reactive states for different value of D_N; $T=873$ K, $P_{CH4+O2}=6$ kPa, $Z=4$, $I=0$.

D_N	y_1	y_2	Widths (y_1–y_2)
0	0.48	0.69	0.21
0.1	0.48	0.69	0.21
1	0.49	0.70	0.21
4.02	0.49	0.71	0.22
10	0.50	0.72	0.22

with Ox. Figs. 8 and 9 also shows the character of the phase transition in the eight-site coordination case, which appears to be continuous at y_2, in contrast to the discontinuous behavior in the four-site coordination case (Figs. 1 and 2). This is also in contrast to the ZGB model, which adding diagonal interactions do not produce a continuous transition (Cortés, 1999). The value of the maximum production rates of products is not much different in both cases. However, if the eight-site coordination is considered, the Ox coverage in the Ox-poisoned region increases slightly and C* coverage in C*-poisoned regions increases significantly.

3.4. Effect of diffusion of adsorbed species

To understand the effects of diffusion, the production rates of H_2 and CO as a function of y_{CH4} are presented at different diffusion
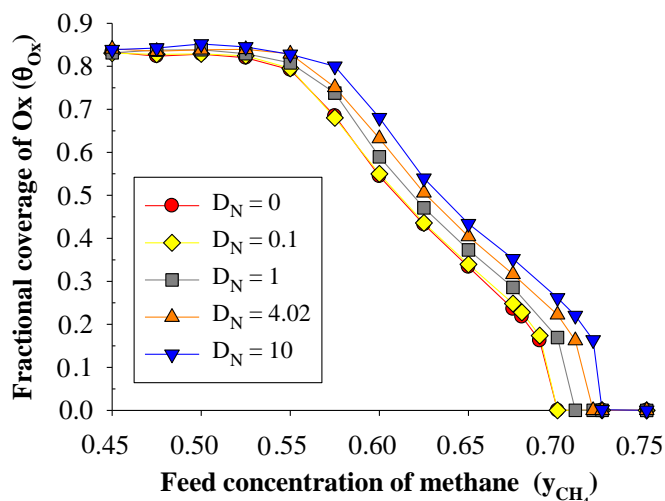
Fig. 12. Fractional coverage of Ox as functions of y_{CH4} for different values of D_N; $T=873$ K, $P_{CH4+O2}=6$ kPa, $Z=4$, $I=0$.

numbers: $D_N=0$, 0.1, 1, 4.02 (the number used in the other simulations) and 10. From Figs. 10 and 11, two important observations can be made. First, the maximum production rates of H_2 and CO increase moderately with the increase of D_N. It is generally expected that diffusion increases the production rates, since the mobility of the adsorbed species facilitates the number of encounters between the reactants. Second, it is found that, with the increase of diffusion rate, the transition points (y_1 and y_2) increase and the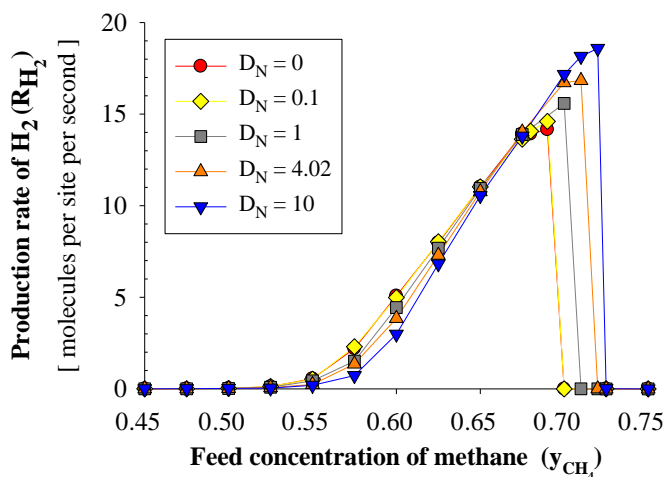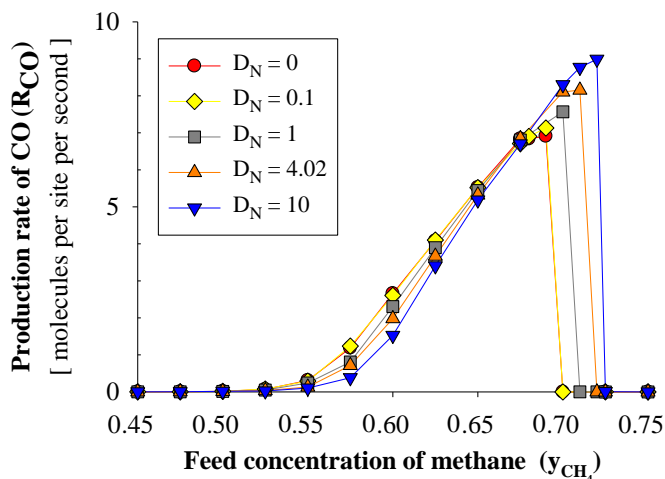 width of the steady reactive state increases slightly. Table 2 summarizes the transition points and the widths of steady reactive states for different values of D_N. It can be seen that the result is almost the same in the case of $D_N=0$ and $D_N=0.1$ and the increasing of D_N from 0 to 10 causes only a slight difference in the transition points and the widths of steady reactive states. This result indicates that the diffusion rate plays a little role in this reaction system. The reason is that only adsorbed CH_4, O, H and CO are allowed to diffuse and these adsorbed species have low fractional coverages on the surface ($\theta_i < 0.1$). The fractional coverages of each species are similar to that obtained in the absence of diffusion. The only notable difference is in Ox coverage, which increases as D_N grows, as shown in Fig. 12. When Ox coverage increases, it requires a greater feed concentration of methane to poison the surface with C* and requires a lesser feed concentration of oxygen to poison the surface with Ox. This makes the transition points moved towards higher values of y_{CH4} with the increase of D_N.

The effect of changing which species are allowed to diffuse was also studied and it is observed that diffusion of CH_4* and CO* has little effect on the reaction due to their extremely low fractional coverages ($\theta_i < 0.01$). In addition, the diffusion of O* has more impact on the production rates than H*. Inclusion of the diffusion of O* produces the largest increase in the production rates and width of the steady reactive state. However, the selectivity of H_2 decreases significantly when the diffusion of O* is introduced, which promotes H_2O formation.

3.5. Effect of inactive impurities on a surface

In experimental systems, the surface can be contaminated with impurities such as sulfur. The impurities can adsorb on the surface, where they do not react with the other adsorbed species. These impurities play an important role in the reaction process. Bitsch-Larsen et al. (2008) experimentally investigated the effect of sulfur in CPOx and found that the presence of small amounts of sulfur

Fig. 13. Production rate of H_2 as functions of y_{CH4} for different values of I; $T=873$ K, $P_{CH4+O2}=6$ kPa, $Z=4$, $D_N=4.02$.

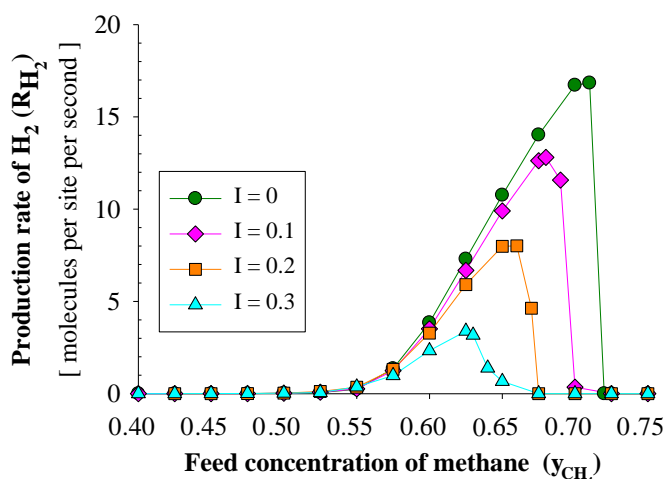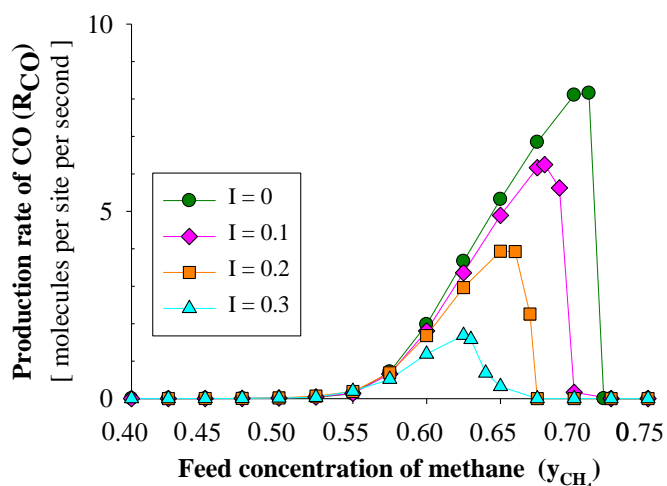**Fig. 14.** Production rate of CO as functions of y_{CH4} for different values of I; $T=873$ K, $P_{CH4+O2}=6$ kPa, $Z=4$, $D_N=4.02$.

Table 3
The transition points and the widths of steady reactive states for different value of I; $T=873$ K, $P_{CH4+O2}=6$ kPa, $Z=4$, $D_N=4.02$.

I	y_1	y_2	Widths (y_1–y_2)
0	0.49	0.71	0.22
0.1	0.49	0.69	0.20
0.2	0.47	0.67	0.20
0.3	0.47	0.66	0.19

have a negative impact on the reaction significantly, decreasing the CH_4 conversion and H_2 selectivity. In this work, the impurity fraction (I) is defined as the fraction of inactive impurities which are on the surface, and these impurities are randomly distributed on the surface. The sites adsorbed by these impurities cannot take part in reaction or diffusion processes.

The behavior of a system with impurities is shown in Figs. 13 and 14, where we plot the production rates of H_2 and CO versus y_{CH4} for different value of impurities fraction: $I=0$, 0.1, 0.2 and 0.3. It is observed that with the increase of impurities, the production rates of H_2 and CO significantly decrease. Furthermore, the transition points move toward a lower value of y_{CH4} with the increase of impurities, as shown in Table 3. The reason is that when impurities increase, the number of neighboring free sites decreases.
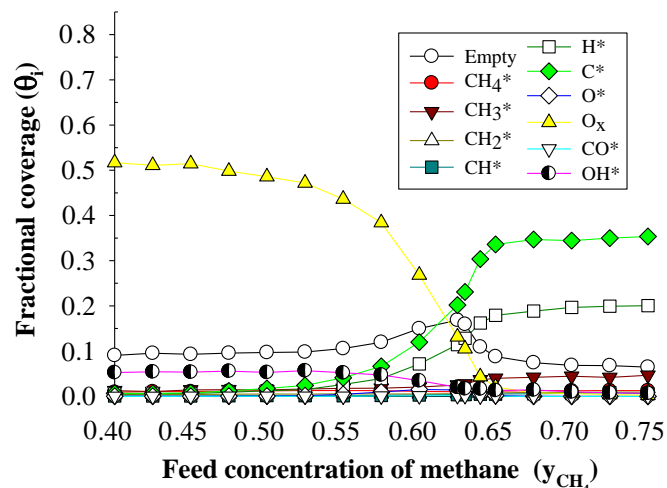
Fig. 15. Fractional coverages as functions of y_{CH4} at $I=0.3$; $T=873$ K, $P_{CH4+O2}=6$ kPa, $Z=4$, $D_N=4.02$.

Therefore, oxygen, which requires two adjacent sites to adsorb, has a lower possibility of adsorbing on the surface. Methane prefers to adsorb rather than oxygen and the transition points shift to lower values of y_{CH4}. However, the widths of the steady reactive state shrink with an increase in impurity fraction, as shown in Table 3, and the reaction stops when the impurity fraction exceeds 0.53. The interesting observation in this system is the conversion of the first-order discontinuous phase transition into a second-order continuous phase transition when impurities are added. As seen in Figs. 13 and 14, the discontinuous transition is softened with the addition of impurities and further converts into a continuous transition. This phenomenon has also been observed previously by Hoenicke and Figueiredo (2000) and Lorenz et al. (2002) in the CO–O_2 reaction and Ahmad and Kaleem (2007) in the NO–CO reaction. It should be noted that the effect of impurities in CPOx has not been studied before. This conversion of a discontinuous phase transition to a continuous one is important because in the discontinuous phase transition, the fluctuations in operating conditions may lead the system into the C^* poisoning region and the system cannot come back to the reactive region. However, for continuous phase transitions, the reaction is sustained and the system can re-enter into the steady reactive state if the atmosphere is returned (Ahmad and Kaleem, 2007). Fig. 15 shows the fractional coverages as a function of y_{CH4} at $I=0.3$. Comparing with the case of no impurities (Fig. 2), it can be seen that, in reactive region, the coverages of O^* and Ox decrease while the coverages of C^* and H^* increase. This implies that methane prefers to adsorb rather than oxygen if there are impurities on the surface.

4. Conclusions

The partial oxidation of methane over a nickel catalyst is simulated by KMC method. According to the simulation results, the reaction occurs only in a certain range of methane feed concentration and reaction temperature. Outside of this range, the surface is poisoned mainly with nickel oxide or carbon. It is shown that both first- and second-order phase transitions occur. This behavior is similar to the ZGB model for the oxidation reaction of CO because both these models essentially deal with the monomer–dimer reaction. It is observed that with the increase of reaction temperature, the controlling step can be changed from the reduction of Ox by adsorbed C (step 16) to the reaction between

adsorbed C and O (step 9). Our results agree with experiments concerning the feed concentration and temperature effects on the selectivities and H_2/CO molar ratio. However, experiments showing the fractional coverages to compare with do not seem to be available. The influence of lattice coordination number is investigated and the result suggests that the width of the steady reactive state is significantly larger if diagonal interactions are allowed. We also find that the first-order phase transition smooths out with eight-site coordination. An increase of the diffusion rate slightly increases the maximum production rates and width of the steady reactive state. Among all adsorbed species, O and H play the most important roles in the diffusion process although the effect is small. When the surface is contaminated with impurities, the production rates are greatly reduced and the reaction stops at a certain point. Furthermore, the discontinuous phase transition transforms into a continuous phase transition in the presence of impurities. Future work on this reaction model would be to find out why diagonal interactions (eight-site coordination) lead to a continuous transition, and to study the behavior on supported catalysts.

Acknowledgments

References

Ahmad, W., Kaleem, M., 2007. The effect of inactive impurities on a surface in NO–CO reaction: a Monte Carlo simulation. Appl. Surf. Sci. 253, 8447–8452. http://dx.doi.org/10.1016/j.apsusc.2007.04.031.

Al-Sayari, S.A., 2013. Recent developments in the partial oxidation of methane to syngas. Open. Catal. J. 6, 17–28. http://dx.doi.org/10.2174/1876214X20130729001.

Barlow, R., Grundy, P.J., 1969. The determination of the diffusion constants of oxygen in nickel and α-iron by an internal oxidation method. J. Mater. Sci. 4, 797–801. http://dx.doi.org/10.1007/BF00551075.

Bitsch-Larsen, A., Degenstein, N.J., Schmidt, L.D., 2008. Effect of sulfur in catalytic partial oxidation of methane over Rh–Ce coated foam monoliths. Appl. Catal. B: Environ. 78, 364–370. http://dx.doi.org/10.1016/j.apcatb.2007.09.006.

Bortz, A.B., Kalos, M.H., Lebowitz, J.L., 1975. A new algorithm for Monte Carlo simulation of Ising spin systems. J. Comput. Phys. 17, 10–18. http://dx.doi.org/10.1016/0021-9991(75)90060-1.

Chen, D., Lodeng, R., Anundskas, A., Olsvik, O., Holmen, A., 2001a. Deactivation during carbon dioxide reforming of methane over Ni catalyst: Microkinetic analysis. Chem. Eng. Sci. 56, 1371–1379. http://dx.doi.org/10.1016/S0009-2509(00)00360-2.

Chen, D., Lodeng, R., Omdahl, K., Anundskas, A., Olsvik, O., Holmen, A., 2001b. A model for reforming on Ni catalyst with carbon formation and deactivation. Stud. Surf. Sci. Catal. 139, 93–100. http://dx.doi.org/10.1016/S0167-2991(01)80185-3.

Coleman, L.J.I., Croiset, E., Epling, W., Fowler, M., Hudgins, R.R., 2009. Evaluation of foam nickel for the catalytic partial oxidation of methane. Catal. Lett. 128, 144–153. http://dx.doi.org/10.1007/s10562-008-9707-y.

Cortés, J., 1999. Monte Carlo and mean field theory studies of the effect of the next nearest neighbour sites of a square lattice on the monomer-dimer surface reaction. Phys. Chem. Chem. Phys. 1, 1577–1581. http://dx.doi.org/10.1039/A808011I.

Cortés, J., Valencia, E., 1998. Next nearest neighbors sites and the reactivity of the CO–NO surface reaction. Chem. Phys. 229, 265–273. http://dx.doi.org/10.1016/S0301-0104(98)00014-7.

Cortés, J., Valencia, E., Araya, P., 2006. Monte Carlo simulation studies of the catalytic combustion of methane. Catal. Lett. 112, 121–128. http://dx.doi.org/10.1007/s10562-006-0174-z.

Cortés, J., Valencia, E., Araya, P., 2014. Monte Carlo simulations in the preferential oxidation of carbon monoxide on a copper–ceria catalyst. Chem. Phys. Lett. 612, 97–100. http://dx.doi.org/10.1016/j.cplett.2014.07.076.

Eriksson, S., Rojas, S., Boutonnet, M., Fierro, J.L.G., 2007. Effect of Ce-doping on Rh/ZrO2 catalysts for partial oxidation of methane. Appl. Catal. A: General. 326, 8–16. http://dx.doi.org/10.1016/j.apcata.2007.03.019.

Evans, J.W., 1993. ZGB surface reaction model with high diffusion rates. J. Chem. Phys. 98, 2463–2465. http://dx.doi.org/10.1063/1.464174.

Fichthorn, K., Gulari, E., Ziff, R.M., 1989. Self-sustained oscillations in a heterogeneous catalytic reaction: a Monte Carlo simulation. Chem. Eng. Sci. 44, 1403–1411. http://dx.doi.org/10.1016/0009-2509(89)85013-4.

Fichthorn, K.A., Weinberg, W.H., 1991. Theoretical foundations of dynamical Monte Carlo simulations. J. Chem. Phys. 95, 1090–1096. http://dx.doi.org/10.1063/1.461138.

Gillespie, D.T., 1976. A general method for numerically simulating the stochastic time evolution of coupled chemical reactions. J. Comput. Phys. 22, 403–434. http://dx.doi.org/10.1016/0021-9991(76)90041-3.

Hei, M., Chen, H., Yi, J., Lin, Y., Lin, Y., Wei, G., Liao, D., 1998. CO2-reforming of methane on transition metal surfaces. Surf. Sci. 417, 82–96. http://dx.doi.org/10.1016/S0039-6028(98)00663-3.

Hoenicke, G.L., Figueiredo, W., 2000. ZGB model with random distribution of inert sites. Phys. Rev. E 62, 6213–6223. http://dx.doi.org/10.1103/PhysRevE.62.621.

Hu, Y.H., Ruckenstein, E., 1996. Transient kinetic studies of partial oxidation of CH4. J. Catal. 158, 260–266. http://dx.doi.org/10.1006/jcat.1996.0025.

Larimi, A.S., Alavi, S.M., 2012. Partial oxidation of methane over Ni/CeZrO2 mixed oxide solid solution catalysts. Int. J. Chem. Eng. Appl. 3, 6–9.

Lashina, E.A., Kaichev, V.V., Chumakova, N.A., Ustyugov, V.V., Chumakov, G.A., Bukhtiyarov, V.I., 2012. Mathematical simulation of self-oscillations in methane oxidation on nickel: an isothermal model. Kinet. Catal. 53, 374–383. http://dx.doi.org/10.1134/S0023158412030081.

Li, C., Yu, C., Shen, S., 2000. Role of the surface state of Ni/Al2O3 in partial oxidation of CH4. Catal. Lett. 67, 139–145. http://dx.doi.org/10.1023/A:1019025807455.

Li, Y., Xiang, S., 2000. Micro-kinetic analysis and Monte Carlo simulation in methane partial oxidation into synthesis gas. Catal. Today 61, 237–242. http://dx.doi.org/10.1016/S0920-5861(00)00368-0.

Lorenz, C.D., Haghgooie, R., Kennebrew, C., Ziff, R.M., 2002. The effects of surface defects in a catalysis model. Surf. Sci. 517, 75–86. http://dx.doi.org/10.1016/S0039-6028(02)01957-X.

Loscar, E.S., Albano, E.V., 2003. Critical Behaviour of Irreversible Reaction Systems. Rep. Prog. Phys. 66, 1343–1382. http://dx.doi.org/10.1088/0034-4885/66/8/203.

Machado, E., Buendía, G.M., Rikvold, P.A., Ziff, R.M., 2005. Response of a catalytic reaction to periodic variation of the CO pressure: increased CO2 production and dynamic phase transition. Phys. Rev. E 71, 016120. http://dx.doi.org/10.1103/PhysRevE.71.016120.

Nam, H.O., Hwang, I.S., Lee, K.H., Kim, J.H., 2013. A first-principles study of the diffusion of atomic oxygen in nickel. Corros. Sci. 75, 248–255. http://dx.doi.org/10.1016/j.corsci.2013.06.006.

Qiangu, Y., Tinghua, W., Jitao, L., Chunrong, L., Weizeng, W., Lefu, Y., Huilin, W., 2000. Mechanism study of carbon deposition on a Ni/Ai2O3 catalyst during partial oxidation of methane to syngas. J. Nat. Gas. Chem. 9, 89–92.

Ren, X., Guoa, X., 2008. Monte Carlo simulation of the oscillatory behavior in partial oxidation of methane on nickel catalyst under nonisothermal conditions. Surf. Sci. 603, 606–610. http://dx.doi.org/10.1016/j.susc.2008.12.018.

Ren, X., Lia, H., Guoa, X., 2008. Monte Carlo simulation of the oscillatory behavior in partial oxidation of methane on nickel catalyst. Surf. Sci. 602, 300–306. http://dx.doi.org/10.1016/j.susc.2007.10.016.

Shen, S., Li, C., Yu, C., 1998. Mechanistic study of partial oxidation of methane to syngas over a Ni/Al2O3 catalyst. Stud. Surf. Sci. Catal. 119, 765–770. http://dx.doi.org/10.1016/S0167-2991(98)80524-7.

Smith, M.W., Shekhawat, D., 2011. Catalytic Partial Oxidation, Fuel Cells: Technologies for Fuel Processing. Elsevier http://dx.doi.org/10.1016/B978-0-444-53563-4.10005-7.

Tomé, T., Dickman, R., 1993. Ziff–Gulari–Barshad model with CO desorption: an Ising-like nonequilibrium critical point. Phys. Rev. E 47, 948–952. http://dx.doi.org/10.1103/PhysRevE.47.948.

Tsipouriari, V.A., Verykios, X.E., 1998. Kinetic study of the catalytic partial oxidation of methane to synthesis gas over Ni/La2O3 catalyst, Studies in Surface Science and Catalysis. Elsevier Masson SAS. http://dx.doi.org/10.1016/S0167-2991(98)80529-6.

Valencia, E., 2000. Effect of the coordination of the superficial site in the monomer–dimer reaction on a disordered substrate. Surf. Sci. 470, 109–115. http://dx.doi.org/10.1016/S0039-6028(00)00859-1.

Wang, Y., Wang, W., Hong, X., Li, B., 2009. Zirconia promoted metallic nickel catalysts for the partial oxidation of methane to synthesis gas. Catal. Commun. 10, 940–944. http://dx.doi.org/10.1016/j.catcom.2008.12.034.

Ziff, R.M., Gulari, E., Barshad, Y., 1986. Kinetic phase transitions in an irreversible surface-reaction model. Phys. Rev. Lett. 56, 2553–2556. http://dx.doi.org/10.1103/PhysRevLett.56.2553.

Oligomerization of 1-decene over sulfated alumina catalysts for the production of synthetic fuels and lubricants: modelling and verification

Snunkheam Echaroj[1] · Malee Santikunaporn[1] ·
Sumaeth Chavadej[2]

Abstract The three-factor Box-Behnken design and the response surface methodology (RSM) were used to optimize the production of C_{20} (transportation fuel) and C_{30}^+ (lubricant oil) hydrocarbons obtained from 15 different oligomerization reactions of 1-decene over sulfated alumina catalysts in batch operation mode. The physiochemical properties of the sulfated alumina catalysts were characterized by N_2 sorption, XRD and NH_3-TPD. The formulated quadratic models as a function of three independent variables of reaction temperature (448–473 K), sulfuric acid concentration (2.5–4.5 M) and catalyst amount (5–15 wt%) were verified by the experimental results (1-decene conversion and product composition) with a coefficient of determination higher than 0.97 for all dependent variables (conversion, amount of C_{20} and C_{30}^+). The optimal amount of C_{20} (65.4 wt%) was achieved at 473 K, using 3.5 M sulfated alumina and 8.8 wt% of catalyst. Similarly, the optimization of C_{30}^+ (47.7 wt%) was revealed at 473 K, using 3.5 M sulfated alumina and 15 wt% of catalyst. It was concluded that oligomerization over sulfated alumina was successfully optimized using Box-Behnken design.

Keywords Oligomerization · Box-Behnken design · Sulfated alumina · Transportation fuel and lubricant oil

✉ Malee Santikunaporn
smalee@engr.tu.ac.th

[1]   Department of Chemical Engineering, Faculty of Engineering, Thammasat University, Pathumthani 12120, Thailand

[2]   Petrochemical College, Chulalongkorn University, Bangkok 10330, Thailand

⌂ Springer

List of symbols

$X_{exp.}$	Conversion of 1-decene (%) from experiment
$C_{20,exp.}$	Amount of dimer from experiment
$C_{30}^{+}{}_{,exp.}$	Amount of trimer and higher from experiment
$X_{pre.}$	Conversion of 1-decene (%) from prediction (model equation)
$C_{20,pre.}$	Amount of dimer from prediction (model equation)
$C_{30}^{+}{}_{,pre.}$	Amount of trimer and higher from prediction (model equation)
β_i	Coefficient from parameter i
A	Reaction temperature (K)
B	H_2SO_4 concentration (M)
C	Amount of catalyst (wt%)

Introduction

Biofuel production from renewable and sustainable sources has become interesting worldwide. This has resulted in the development of transesterification processes for biodiesel production [1–4] and deoxygenation for bio-hydrogenated diesel (BHD) production [5–8] from triglyceride. Unfortunately, due to its poor cold-flow property, biodiesel is usually blended with diesel oil to meet the specification of a transportation fuel. Meanwhile, the deoxygenation reaction is not attractive economically because of the high cost of metal catalysts such as palladium and the requirement of high temperature reaction under a hydrogen atmosphere. In this research, the production of synthetic fuel and lubricant oil from the oligomerization of olefins obtained from dehydration of primary alcohol was investigated. This process is sustainable because alcohol can be obtained from fermentation of lignocellulosic biomass [9–11].

Oligomerization over heterogeneous acid catalysts is initiated when olefin molecules are transformed to carbenium ions on Brønsted acid sites and further combine with olefin molecules in the bulk solution to form larger molecules [12, 13]. The oligomerization reaction has been employed to convert lower olefins, by-products generated from a fluid catalytic cracking unit, to diesel fuel. According to substantial research results, medium pore zeolite catalysts with one-dimensional pores such as TON (ZSM-22), MTT, and EUO are most suitable for the production of linear structure hydrocarbons. However, when a feedstock with large molecules is used, these zeolite catalysts are found to deactivate rapidly due to the formation of coke [14–16]. Apart from the deactivation by coke formation, the oligomerization reaction also suffers from internal diffusion limitation. There are two effective approaches to reduce the internal diffusion limitation inside the pores of one-dimensional catalysts. The first approach is to create a hierarchical zeolite by expanding the size of catalyst pores, leading to an increase in the accessibility of active sites. The second approach is to prepare zeolites with nanosized crystals [17–19]. These two approaches are very effective but they are costly. An alternative is to use alumina-based catalysts with mesoporous structure to replace zeolite

catalysts with microporous structure [20]. The mesostructured alumina is favorable for the internal diffusion of both reactant and product molecules [21].

Alumina-based catalysts in the gamma form (γ-Al_2O_3) have been used intensively because they contain a large portion of Lewis acid sites with high thermal stability [22–24]. However, plain γ-Al_2O_3 material does not possess the Brønsted acid sites necessary for oligomerization reaction to take place. Therefore, in order to obtain Brønsted acid sites, the γ-Al_2O_3 material needs to be modified in an acidic solution. The formation of Brønsted acid sites is in the form of sulfate group anchored in the lattice of γ-Al_2O_3 material after being modified in a sulfuric acid solution [25–27]. An increase in the concentration of the solution during the modification step can increase the acidity. In addition, the temperature also has a significant impact on the strength of Brønsted acid sites [28]. Until now, most research has evaluated the catalytic performance of sulfated alumina through either isomerization or alkylation reaction. It is, therefore, interesting to investigate how a sulfated alumina catalyst performs in the oligomerization reaction.

Based on a three-level factorial design, the Box-Behnken method can provide an effective framework for the response surface methodology (RSM), which is an effective method for investigating the independent variables that influence the responses of a process. Ultimately, this procedure will lead to the optimization of the process responses. Various processes such as the preparation of polysaccharide polymers [29], production of biodiesel [30, 31], and synthesis of nickel oxide nanoparticles [32] have been optimized through the guidelines designed using the Box-Behnken technique. Furthermore, an integration of statistical principles can lead to a better understanding of the interaction between different parameters. Although the Box-Behnken design framework has been widely employed as a reliable method for the optimization of various processes, no research has ever specifically used this framework to model the oligomerization of 1-decene over sulfated alumina catalysts. To understand the role of the operating conditions on oligomerization over sulfated alumina catalysts is the key to developing an industrialized production process for synthetic fuel and lubricant oil.

This research aimed to investigate the oligomerization of 1-decene over sulfated alumina catalysts at atmospheric pressure. Among other available olefin reagents, 1-decene is the most attractive feedstock for the production of liquid fuel and lubricant oil, because the molecular size of 1-decene is relatively large, it is inexpensive and 1-decene can be derived from vegetable oils, which is a sustainable source of feedstock [21, 33]. The reaction was conducted in a glass reactor at various temperatures and different amounts of catalysts treated with sulfuric acid at different concentrations. The response surface analysis with the Box-Behnken design approach was employed to optimize the oligomerization reaction. The mixture of the reaction products consisted of dimers (C_{20}), trimers (C_{30}) and heavier oligomers which contain hydrocarbons with more than 30 carbon atoms. In this work, trimers and heavier oligomers are grouped together and referred to as C_{30}^+. The C_{20} obtained could be used as transportation fuel and C_{30}^+ can be used as automotive lubricant oil.

Experimental

Chemicals

The support γ-Al$_2$O$_3$ was obtained from Sasol Company (catalyst size = 1 mm and surface area = 160 m^2/g). Sulfuric acid (98% pure) was purchased from Ajax Finechem Pty. Feedstock used for oligomerization, 1-decene (95% pure), was purchased from Acros Organics. The chemicals were used as received without any further purification.

Catalyst preparation

Sulfated alumina was prepared by using the wet impregnation technique [34]. 10 g of γ-Al$_2$O$_3$ was immersed in 100 mL of a sulfuric acid solution having different concentrations (2.5, 3.5 and 4.5 M) under vigorous stirring at 333 K for 20 min. After separation, the treated γ-Al$_2$O$_3$ samples were dried in an oven for 12 h at 383 K, grinded and screened by a 0.1–0.3 mm sieve. The dried catalysts were calcined under 270 mL/min air flow for 5 h at 773 K. The sulfated alumina samples were referred to as xM-SA, where x is the concentration of the sulfuric solution used to treat γ-Al$_2$O$_3$.

Catalyst characterization techniques

N$_2$ sorption analysis was performed by a surface area analyzer (Quantachrome, Autosorb-1C) at 77 K using liquid nitrogen and 0.1 to 0.3 g of catalyst samples. Both adsorption and desorption isotherms of N$_2$ were obtained at 77 K. Before analysis, each sample was degassed for at least 4 h at 473 K in the presence of He gas. The Brumauer-Emmett-Teller (BET) technique with adsorption data in the relative pressure (P/P$_o$) range of 0.04 to 0.2 was used to calculate the specific surface areas of the samples. The total pore volumes were found from the amount of N$_2$ adsorbed at the relative pressure of 0.995. The pore size distributions of all samples were obtained by using the Barrett-Joyner-Halenda (BJH) model. The results of the N$_2$ sorption isotherms of the catalysts used are shown in Table 1.

X-ray diffraction (XRD) analysis of all catalyst samples was carried out on a PANalytical (X'Pert pro) XRD system using Cu K$_\alpha$ radiation (40 kV, and 40 mA) at a scanning speed of 2°/min in the ranges of 10° to 80°.

The surface acidity of all catalyst samples was determined using the NH$_3$ temperature-programmed desorption with a thermal conductivity detector (Sri Instruments, model 110). An approximate amount of 0.1 mg of each catalyst sample was placed on quartz wool in a quartz tube. The catalyst was secured by another layer of quartz wool on the outlet side in order to fix the test catalyst sample throughout the analysis. The catalyst sample was first degassed at 773 K for 1 h under a 45 mL/min flow of He gas. After that, it was allowed to cool to 373 K under N$_2$ flow. Next, the NH$_3$ adsorption step was carried out by 10%NH$_3$/He flow of 45 mL/min for at least 15 min to ensure the saturation of NH$_3$ adsorption. After that, the sample was heated

Table 1 Summary of textural properties and amount of acid sites of plain alumina and sulfated alumina catalysts (SA) treated with different H_2SO_4 concentration

Catalyst	Textural properties			Amount of acid sites		
	Surface area (m^2/g)	Pore volume (cm^3/g)	Pore diameter (nm)	Weak acid sites (mmol/g)	Strong acid sites (mmol/g)	Total acid sites (mmol/g)
Al_2O_3	210	0.58	10.6	0.311	–	0.311
2.5 M-SA	236	0.71	12.8	0.615	0.181	0.796
3.5 M-SA	241	0.82	14.0	0.721	0.241	0.962
4.5 M-SA	245	1.01	14.0	0.716	0.247	0.963

to 373 K for 2 h under N_2 flow to remove the physisorbed NH_3 molecules. Next, the temperature was increased from 373 to 1023 K at a heating rate of 10 K/min under the N_2 flow and held at 1023 K for 30 min. The desorption of NH_3 was monitored using a TCD (Sri Instruments, model 110).

Thermal gravimetric analysis (Mettler Toledo; TGA/DSC 2) was employed to measure the amount of coke deposition on used catalysts after the oligomerization reaction. Under the constant flow rate of oxygen (32 mL/min), 50 mg of the sample was heated from room temperature to 973 K at a rate of 10 K/min.

Catalytic activity test

Catalytic activity tests for the oligomerization reaction were carried out in a 500 mL three-necked glass batch reactor. A thermocouple equipped with a data logger (Lutron, TM-947SD) was inserted into one of the necks to control the temperature inside the reactor. An upright condenser was placed on the reactor to prevent the evaporation loss. The third neck was used for feeding. 100 mL 1-decene were put into the reactor and different amounts (5–15 wt%) of catalyst were added for each test. The reaction experiments were performed at different temperatures (423–473 K) with a constant agitation speed of 400 rpm under the atmospheric pressure. It was found from the preliminary results that an agitation speed above 300 rpm did not exhibit external diffusion limitation. Additionally, the internal diffusion resistance was found to be negligible when the particle size of the catalyst was smaller than 0.5 mm and so all test catalysts were prepared to have particle sizes in the range of 0.1 to 0.3 mm. The liquid sample after the oligomerization reaction was analyzed by a GC equipped with a DB-1 column and a FID detector. The conversions of 1-decene ($X_{exp.}$) and product compositions ($C_{20,exp.}$ and $C_{30,exp.}^+$) were calculated by the following equations:

$$X_{exp.}(\text{wt \%}) = \frac{C_{10,in} - C_{10,out}}{C_{10,in}} \times 100 \tag{1}$$

$$C_{20,exp.}(\text{wt \%}) = \frac{C_{20}}{C_{10,out} + C_{20} + C_{30}^+} \times 100 \qquad (2)$$

$$C_{30}^+{}_{,exp.}(\text{wt \%}) = \frac{C_{30}^+}{C_{10,out} + C_{20} + C_{30}^+} \times 100 \qquad (3)$$

Box-Behnken design experiments

Three process parameters of concentration of sulfuric solution (2.5–4.5 M), reaction temperature (423 to 473 K), and amount of catalyst (5–15 wt%), were observed for their influence on the conversion of 1-decene and the composition of products. According to the Box-Behnken design (BBD), three levels of each parameter needed to be investigated. The three levels were coded as -1 (low), 0 (central point) and 1 (high). Table 2 shows the three levels of each parameter for the Box-Behnken design in an uncoded design matrix. The results from the fifteen runs of the experiments as shown in Table 2, were obtained using the Minitab® 17.0 software. As shown in Eq. 4, the system response can be formulated as a quadratic polynomial equation with three independent variables (A, B and C).

Table 2 Experimental design matrix using 3-level Box–Behnken design with three independent variables in terms of uncoded units and experimental responses obtained

Run	Operation conditions			Experimental results		
	A: temperature (K)	B: concentration (M)	C: catalyst amount (wt%)	Conversion (%)	C_{20} (wt%)	C_{30}^+ (wt%)
1	423	2.5	10	49.1	44.2	7.5
2	473	2.5	10	78.3	56.8	22.6
3	423	4.5	10	58.5	49.9	10.6
4	473	4.5	10	72.7	42.1	32.0
5	423	3.5	5	51.0	50.5	2.9
6	473	3.5	5	67.8	58.5	10.9
7	423	3.5	15	61.9	48.8	15.0
8	473	3.5	15	91.7	43.7	48.4
9	448	2.5	5	48.3	33.8	17.1
10	448	4.5	5	40.5	29.8	13.6
11	448	2.5	15	57.5	23.3	36.3
12	448	4.5	15	64.7	31.9	34.6
13	448	3.5	10	83.7	58.2	26.3
14	448	3.5	10	82.7	58.8	24.8
15	448	3.5	10	83.2	56.5	27.6

Reaction conditions: total pressure = 101.3 kPa and agitation speed = 400 rpm

$$Y = \beta_O + \beta_1 A + \beta_2 B + \beta_3 C + \beta_1 \beta_1 A^2 + \beta_2 \beta_2 B^2 + \beta_3 \beta_3 C^2 + \beta_1 \beta_2 AB + \beta_1 \beta_3 AC$$
$$+ \beta_2 \beta_3 BC \tag{4}$$

Here Y is the response and β_O is the intercept. $\beta_1, \beta_2, \beta_3$ are the linear coefficients, $\beta_1 \beta_1, \beta_2 \beta_2, \beta_3 \beta_3$ are the quadratic coefficients and $\beta_1 \beta_2, \beta_1 \beta_3, \beta_2 \beta_3$ are the interactive coefficients. These coefficients were calculated using the Minitab 17.0 software. A is the uncoded independent variable regarding reaction temperature, B is the concentration of sulfuric acid solution used for the catalyst pretreatment and C is the amount of catalyst in terms of weight percentage based on the feedstock weight.

Results and discussion

Characterization

Both the physical and chemical characteristics of solid catalysts have a great impact on the outcome of all reactions in terms of yield and selectivity for any specific product [35–37]. This research investigated and reported the catalyst characterization results obtained from X-ray diffraction, N_2 sorption and NH_3-TPD, in order to correlate to the oligomerization reaction of 1-decene over sulfated alumina.

All sulfated alumina catalysts treated at different H_2SO_4 concentrations possessed type IV adsorption isotherm with type H1 hysteresis loop indicating the mesoporous structure with cylindrical shape, which is in good agreement with other literature [38–40]. As shown in Table 1, there is a significant change in the surface area, pore volume and pore diameter of plain alumina after the treatment with 2.5 M H_2SO_4 solution. These physical characteristics continued to increase by 2% for the specific surface area, 15% for the pore volume and 9% for the pore diameter as the H_2SO_4 concentration increased to 3.5 M. However, an increase in the H_2SO_4 concentration further to 4.5 M showed insignificant effects on both specific surface area and pore diameter, but affected the pore volume by almost 19%.

The XRD patterns of all sulfated alumina catalysts are shown in Fig. 1. All catalyst samples showed the typical five reflection peaks of the (220), (311), (222), (400), (511) and (440) planes of gamma-alumina materials corresponding to the JCPDS database (10-0425) [20, 22]. The XRD results suggest that the modification with sulfuric acid did not have an effect on the crystallinity of the alumina. Interestingly, at a very high sulfuric acid concentration of 4.5 M, the peaks of $Al_2(SO_4)_3$ appeared, which was also reported in other researches [27, 34, 41].

The NH_3-TPD results of all sulfated alumina catalysts are shown in Table 1. The weak acid sites are defined as the integrated areas below 523 K and the strong acids are the areas measured higher than 523 K [23]. The untreated alumina was found to exhibit only weak acid sites. An increase in the concentration of sulfuric acid from 2.5 to 3.5 M resulted in significant increases in both the amounts of weak acid sites and strong acid sites. However, an increase in the H_2SO_4 concentration from 3.5 to 4.5 M did not have a significant effect on the amounts of weak and strong acid sites.
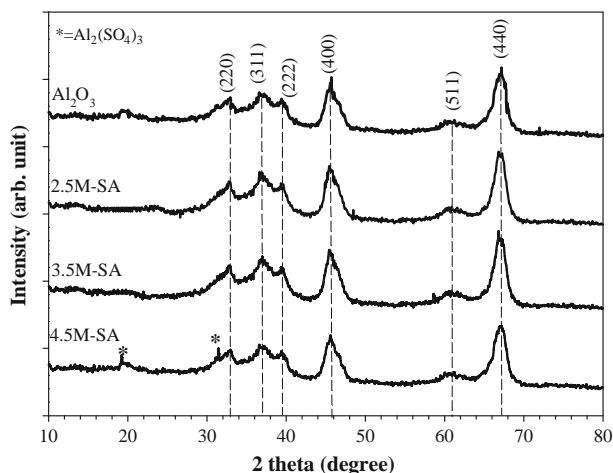
Fig. 1 XRD pattern of plain alumina and sulfated alumina catalyst (SA) treated with different H_2SO_4 concentrations

Validation of regression model and statistical analysis

All 15 experiments were carried out to optimize the three process parameters of temperature (K), concentration of sulfuric acid (M) and amount of catalyst (wt%). The results were analyzed using the quadratic model, as described in Eqs. 5–7. Table 2 shows the results of the oligomerization experiments in terms of conversion and amounts of C_{20}, and C_{30}^+ in the oligomer products at different values of the three variables. The BBD results were found to be fit well with a second order polynomial quadratic equation. The polynomial regression equations for the determination of predicted values of the responses ($X_{pre.}$, $C_{20,pre.}$ and $C_{30}^+{}_{pre.}$) are given below:

$$X_{pre.}\% = -1007 + 3.019A + 178.35B - 1.73C - 0.002574A^2 - 16.954B^2 \\ - 0.5412C^2 - 0.1491A*B + 0.02597A*C + 0.7497B \tag{5}$$

$$C_{20,pre.}(wt\%) = 1178 - 6.94A + 190.5B + 19.28C + 0.00888A^2 - 15.13B^2 \\ - 0.5202C^2 - 0.2041A*B - 0.0261A*C \tag{6}$$

$$C_{30}^+{}_{,pre.}(wt\%) = -2129 + 9.81A - 21.1B - 20.92C - 0.01132A^2 - 0.98B^2 \\ + 0.00612C^2 + 0.0625A*B + 0.0508A*C + 0.085B \tag{7}$$

Here $X_{pre.}$ is the predicted conversion of 1-decene (%), $C_{20,pre.}$ is the predicted amount of dimers in the products, and $C_{30}^+{}_{,pre.}$ is the predicted amount of trimer and higher than C_{30}. A is the reaction temperature (K), B is the concentration of sulfuric acid (M) and C is the amount of catalyst (wt%). The negative sign in front of each parameter term suggests the antagonistic effect while the positive sign simply indicates the synergistic effect on the oligomerization reaction.

The model equations were validated based on the F-value obtained from ANOVA and closeness of the calculated results to the experimental data. The F-values of the models for predicting the conversion of 1-decene, amount of C_{20} and C_{30}^+ were 422, 29.32 and 20.53, indicating that the quadratic regression models presented in this work could be used to accurately predict the outcome of the reaction. The P values of these models were found in the range of 0.001 to 0.002, which suggested that the large F-values did not occur because of noise. Furthermore, the R^2 values of the three responses were found to be greater than 0.97 indicating again that the polynomial models were excellent to predict the conversion of 1-decene and the formation of C_{20} and C_{30}^+, as confirmed by the plots between the data obtained from the experimental and the predicted values calculated by Eqs. 5–7 in Fig. 2a–2c.

The significance of each variable can be justified by using the t-values and probability value (P value). As shown in Table 3, a P value less than 0.050 suggests
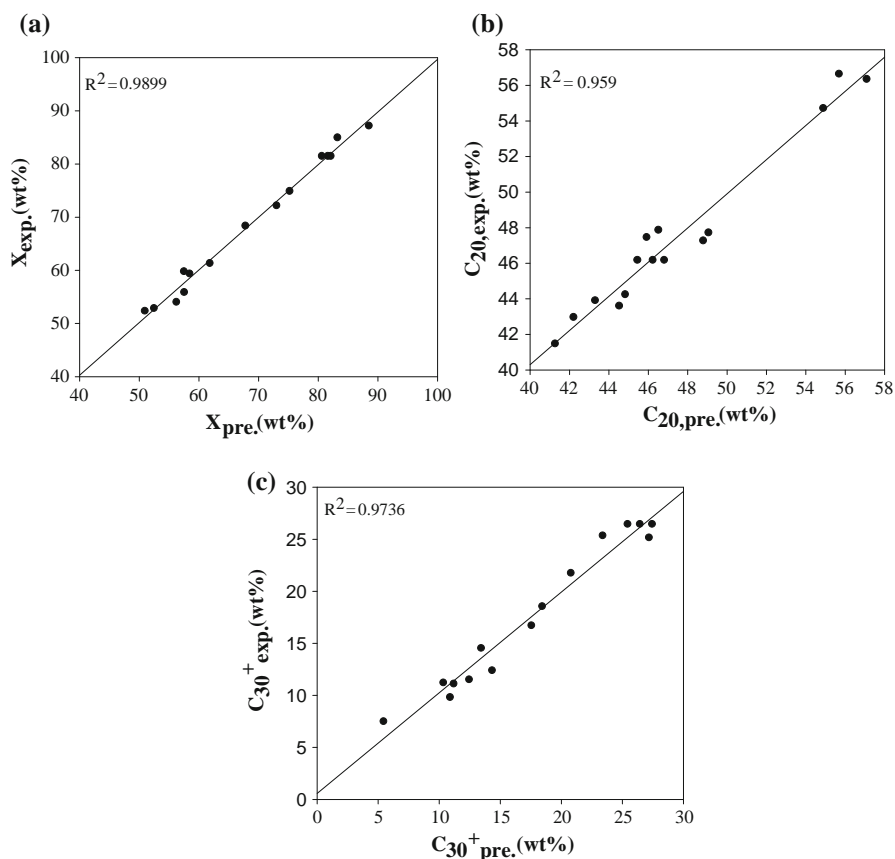
Fig. 2 Linear correlation plots between predicted and experimental data for **a** conversion of 1-decene, **b** the amount of C_{20} and **c** the amount of C_{30}^+. Reaction conditions: total pressure = 101.3 kPa, agitation speed = 400 rpm, temperature = 448–473 K, H_2SO_4 concentration = 2.5–4.5 M and catalyst amount = 5–15 wt%

Table 3 Analysis of variances for response models [Conversion, amount of C_{20} and C_{30}^+ in oligomerization product using second order equation; A = Temperature (K), B = Concentration (M) and C = amount of catalyst (wt%)]

	Conversation			C_{20}			C_{30}^+		
	F-value	P value	Remark	F-value	P value	Remark	F-value	P value	Remark
Model	422	0.000	Sign.	29.32	0.001	Sign.	20.53	0.002	Sign.
Linear	18.76	0.007	Sign.	15.92	0.010	Sign.	18.08	0.008	Sign.
Square	63.51	0.001	Sign.	14.40	0.013	Sign.	0.75	0.425	Insign.
Interaction	27.27	0.003	Sign.	5.03	0.075	Insign.	9.76	0.026	Sign.
Lack of fit	5.23	0.165	Insign.	7.08	0.126	Insign.	9.22	0.099	Insign.
R^2	0.9900			0.9814			0.9736		

	Conversation			C_{20}			C_{30}^+		
	t-Stat	P value	Remark	t-Stat	P value	Remark	t-Stat	P value	Remark
A:	4.33	0.007	Sign.	−3.99	0.010	H.Sign.	4.25	0.008	H.Sign.
B:	7.97	0.001	H.Sign.	3.81	0.013	Sign.	−0.87	0.425	Insign.
C:	−5.22	0.003	Sign.	2.24	0.075	Insign.	−3.00	0.026	Sign.
A^2	−3.28	0.022	Sign.	4.02	0.010	Sign.	−4.00	0.010	Sign.
B^2	−34.58	0.000	Sign.	−10.97	0.000	Sign.	−0.55	0.603	Insign.
C^2	−27.60	0.000	Sign.	−9.43	0.000	Sign.	0.09	0.935	Insign.
A*B	−7.91	0.001	Sign.	−3.85	0.012	Sign.	0.92	0.400	Insign.
A*C	6.89	0.001	Sign.	−2.46	0.057	Insign.	3.74	0.013	Sign.
B*C	7.96	0.001	Sign.	2.37	0.064	Insign.	0.25	0.811	Insign.

Reaction condition: total pressure = 101.3 kPa and agitation speed = 400 rpm

that the terms of A, B, C, A^2, B^2, C^2, AB, AC and BC have significant effects on the conversion of 1-decene. However, it was found that parameter C, the amount of catalyst, did not have a significant impact on the formation of C_{20} hydrocarbons as the P value was higher than 0.050. Furthermore, the amount of C_{30}^+ hydrocarbons was not significantly affected by the concentration of the sulfuric acid used. The large difference between the t-value and P value indicates that the parameter is more significant in comparison with the other parameters with smaller differences between the t-value and P value. Therefore, for the conversion of 1-decene, the parameter B (the H_2SO_4 concentration) with the highest t-value and lowest P value should have the largest influence on the conversion, as compared to the other parameters. According to this concept, the reaction temperature is the most significant parameter affecting the production of dimers and trimers.

Interaction between parameters and optimization

The 3D response surface plots with 2D contours are shown in Figs. 3, 4 and 5. The effect of operating parameters on each response is illustrated in these 2D contours and 3D plots; three 2D contours and 3D plots were obtained for each response. The

Fig. 3 The contour and 3D mesh plots demonstrating the influence of **a** H_2SO_4 concentration and reaction temperature at 10 wt% catalyst and 101.3 kPa on conversion of 1-decene, **b** amount of catalyst and H_2SO_4 concentration at 448 K and 101.3 kPa on conversion of 1-decene, and **c** amount of catalyst and reaction temperature at 3.5 M and 101.3 kPa on the conversion of 1-decene

illustrated representation of the equations in the form of a response surface is used to describe the single and interactive effect of the experimental parameters on the responses. The combined effect of sulfuric acid concentration and temperature on the 1-decene conversion at a constant catalyst amount of 10 wt% is shown in Fig. 3a. The conversion of 1-decene increased significantly with an increase in reaction temperature. It also increased with increasing sulfuric acid concentration up to 3.6 M but it decreased with further increase in the concentration of sulfuric acid beyond 3.6 M. The decrease in 1-decene conversion may be caused by the presence of $Al_2(SO_4)_3$ on the surface of the catalyst. The layer of $Al_2(SO_4)_3$ is not only inactive for the oligomerization reaction but also interferes with the internal diffusion of the products obtained. Additionally, according to the NH_3-TPD analysis, as shown in Table 1, an increase in sulfuric acid concentration up to 4.5 M only increases the weak acid sites of the catalyst. The weak acid sites have been reported not to participate in the oligomerization reaction [26]. Fig. 3b shows the interactive effect of the amount of catalyst (wt%) and sulfuric acid concentration on the 1-decene conversion at a constant temperature of 448 K. Clearly, the conversion in the experimental range was affected by both parameters. The conversion of
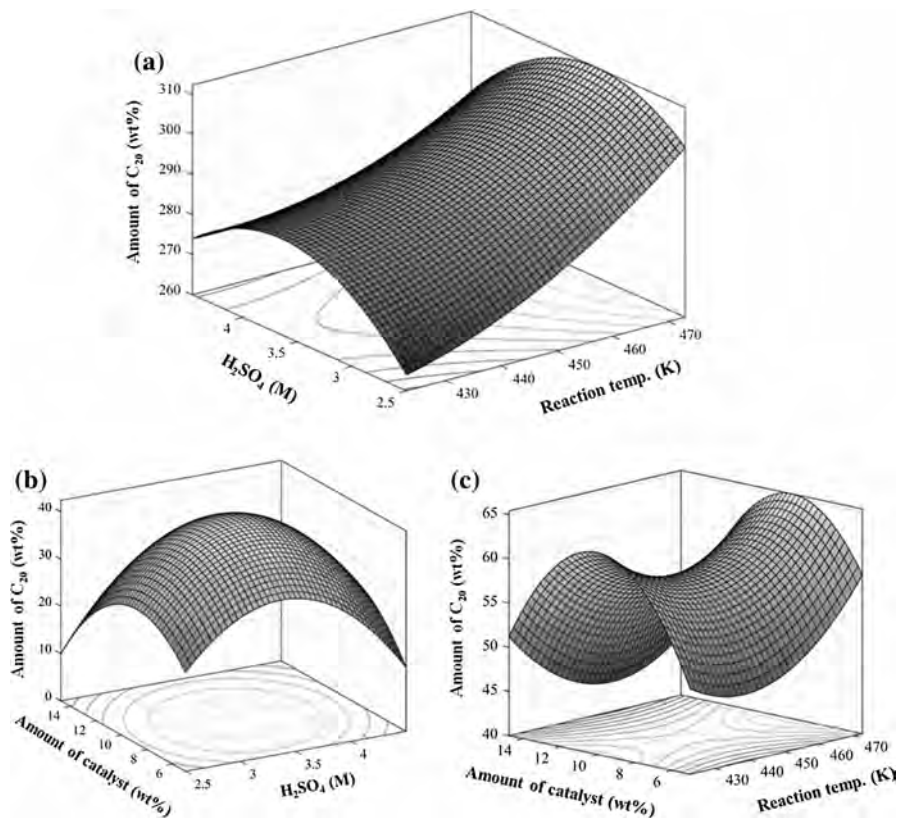
Fig. 4 The contour and 3D mesh plots demonstrating the influence of **a** H_2SO_4 concentration and reaction temperature at 10 wt% catalyst and 101.3 kPa on the amount of C_{20}, **b** amount of catalyst and H_2SO_4 concentration at 448 K and 101.3 kPa on the amount of C_{20}, and **c** amount of catalyst and reaction temperature at 3.5 M and 101.3 kPa on the amount of C_{20}

1-decene increased initially with an increase in either the amount of catalyst or sulfuric acid concentration. An increase in either amount of catalyst or concentration beyond 10 wt% or 3.5 M caused the 1-decene conversion to decrease significantly. This might be because with increasing amount of catalyst, the total external surface area available for the initiation of the isomerization reaction increased, causing more branched molecules to be formed [12]. Since the diffusion coefficients of branched molecules is at least ten times higher than those of linear molecules, branched molecules will create a blockage in the pore of the catalyst which eventually lead to rapid catalyst deactivation [42]. The deposition of coke in catalyst pores is one of major causes of catalyst deactivation [43, 44]. This explanation was confirmed by the TGA results of spent sulfated alumina catalyst. After the reaction experiments, the coke formation increased from 6.2 to 8.3% with increasing catalyst load from 10 to 15%.

As shown in Fig. 3c, an increase in the reaction temperature up to 473 K with 5 wt% catalyst caused the 1-decene conversion to increase from 51 to 67.5%.
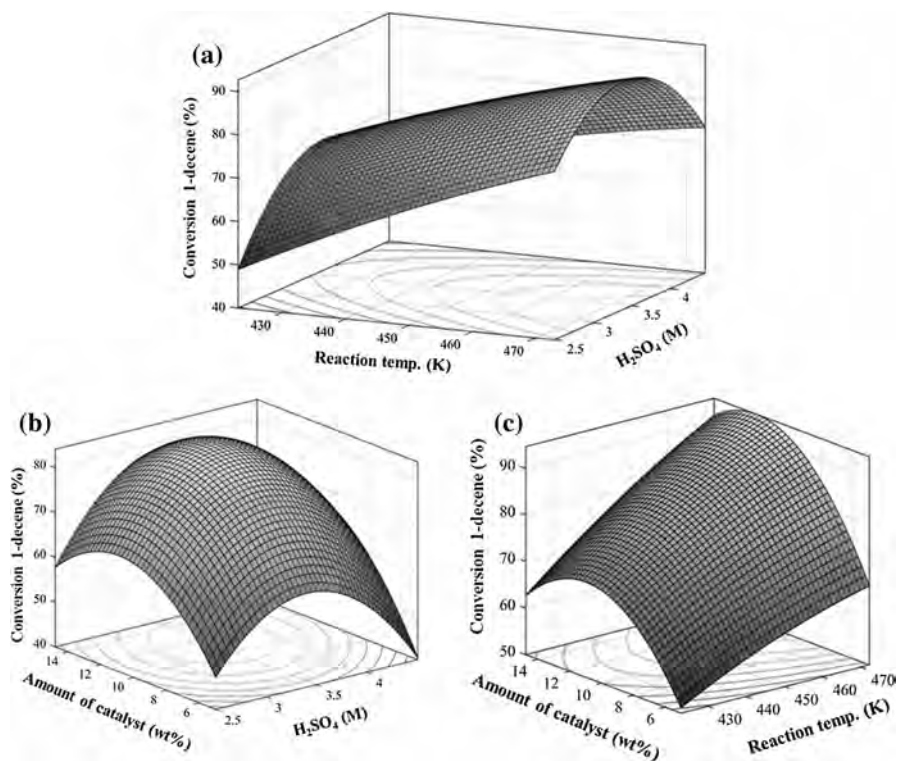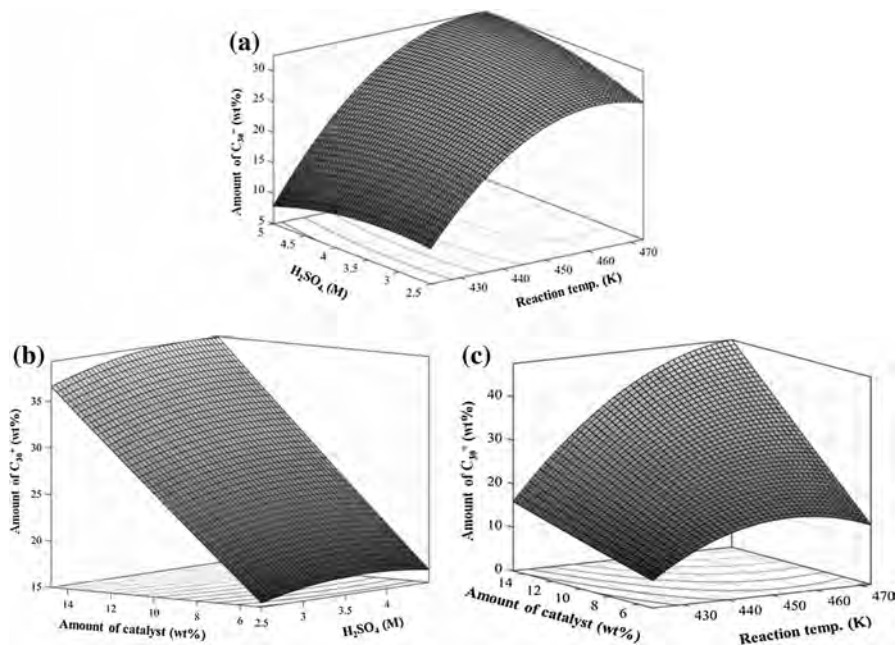
Fig. 5 The contour and 3D mesh plots demonstrating the influence of **a** H_2SO_4 concentration and reaction temperature at 10 wt% catalyst and 101.3 kPa on the amount of C_{30}^+, **b** amount of catalyst and H_2SO_4 concentration at 448 K and 101.3 kPa on the amount of C_{30}^+, and **c** amount of catalyst and reaction temperature at 3.5 M and 101.3 kPa on the amount of C_{30}^+

Furthermore, when the reaction temperature was fixed at 473 K, an increase in the amount of catalyst from 5 to 10 wt% caused the 1-decene conversion to increase to more than 90%.

Fig. 4a depicts the combined effect of sulfuric acid concentration and reaction temperature on the amount of C_{20} hydrocarbon produced at a constant catalyst amount of 10 wt%. Obviously, the reaction temperature was found to have a strong positive impact on the formation of dimers. The present results agree well with other studies [45–47]. The amount of dimer increased initially as the sulfuric acid concentration increased from 2.5 to 3.5 M. An increase in sulfuric acid concentration beyond 3.5 M caused the amount of dimers to reduce significantly. It was also reported that the conversion of olefin to oligomers reached a maximum at a specific catalyst acid strength and then decreased with a further increase in the acid strength due to the decomposition of oligomer molecules [48]. Fig. 4b demonstrates the interactive effect of the amount of catalyst and sulfuric acid concentration on the amount of C_{20} hydrocarbon produced at a reaction temperature of 448 K. The amount of dimer initially increased with an increase in either the amount of catalyst or sulfuric acid concentration but it decreased with further increase in the amount of catalyst greater than 10 wt% or sulfuric acid concentration higher than 3.5 M. Fig. 4c shows the effect of the concentration of H_2SO_4 and reaction temperature on the amount of C_{20} formed during oligomerization reaction. The apparent activation

energy required to form C20 is significantly lower than that for the formation of a heavier molecule. The product collected at a lower temperature was found to have a very small amount of C30. As the reaction temperature increases, a heavier molecule, such as trimers, can be formed easier. The formation of the trimer was found to occur through the combination of 1-decene with C20. Therefore, a reduction in the amount of C20 was found with the formation of trimers [49]. However, as the reaction temperature further increased, the active sites began to deactivate, causing the composition of C20 remaining high.

Fig. 5a shows the combined effect of the sulfuric acid concentration and reaction temperature on the formation of C_{30}^+ keeping the amount of catalyst constant at 10 wt%. Clearly, the reaction temperature had a stronger effect on the content of C_{30}^+ compared to sulfuric acid concentration. An increase in reaction temperature revealed an increase in C_{30}^+. However, the rate of increase in C_{30}^+ was observed to be higher at a lower reaction temperature. Fig. 5b illustrates the interactive effect of the amount of catalyst and sulfuric acid concentration on the amount of C_{30}^+ produced at a constant reaction temperature of 448 K. Evidently, an increase in the amount of catalyst caused a continuous increase in the amount of C_{30}^+ formed. Fig. 5c shows an increase in the amount of C_{30}^+ with the amount of catalyst and reaction temperature. At higher temperature, an increase in the formation of C_{30}^+ due to an increase in the amount of catalyst was larger than that for the system operated at lower temperature. According to mass balances of the reaction experiments, an increase in catalyst also caused product weight loss due to cracking reaction. The weight loss increased slightly from 11.6 to 16.0 wt% as the amount of catalyst increased from 5 to 15 wt%. However, an increase in the amount of catalyst further to 20 wt% caused the weight loss to increase to as high as 23 wt%. Therefore, for economical reason, the amount of catalyst should not be higher than 15 wt%.

The production of C_{20} reached its peak (65 wt%) when the reaction was conducted over the 3.5 M sulfated alumina catalyst with 8.8 wt% catalyst loading at 473 K (Table 4). For the optimization of C_{30}^+, the amount of catalyst used has to be as high as possible but should not be more than 15 wt% in order to avoid large product loss of 17 to 24 wt% due to the cracking reaction. The predicted response

Table 4 Optimization of the amounts of C_{20} and C_{30}^+ in the products obtained from oligomerization reaction at specific conditions

Conversion/ product (%)	Optimum conditions			Predicted value (wt%)	Experimented value (wt%)
	Temperature (K)	H$_2$SO$_4$ Concentration (M)	Catalyst amount (wt%)		
1-decene conversion	473	3.5	12.1	94.7	89.4
C_{20}	473	3.5	8.8	65.4	68.8
C_{30}^+	473	3.5	15.0	47.7	43.7

Reaction condition: total pressure $= 101.3$ kPa and agitation speed $= 400$ rpm

for the optimum point correlated well with the results obtained when using the optimized conditions to conduct the experiment. Successful derivation of the model equations with accurate coefficients for the oligomerization of olefins can be applied to simulate industrial-scale production of C_{20} and C_{30}^{+} hydrocarbons. The products can then be used as diesel fuel and engine lubricant oil, respectively.

Conclusion

In this work, hydrocarbons in the range of diesel (C_{20}) and lubricant oil (C_{30}^{+}) were successfully synthesized through the oligomerization of 1-decene over sulfated alumina. The application of Box-Behnken design for response surface methodology proposed the accurate quadratic models for the optimization of C_{20} and C_{30}^{+} formation by evaluating the interactive effects of the three process variables of reaction temperature, sulfuric acid concentration and catalyst amount for the oligomerization reaction of 1-decene and reduced the number of experiments required. The optimum conditions for C_{20} production were 473 K, 3.5 M, and 8.8 wt% for reaction temperature, concentration of sulfuric acid and catalyst amount. Under the optimum conditions, the predicted C_{20} concentration was 65.4 wt% which was very close to the value obtained from the experiment (68.8 wt%). Similarly, the amount of C_{30}^{+} predicted using the model equation with the optimized process conditions (reaction temperature 473 K, 3.5 M sulfuric concentration and 15 wt% of catalyst) was 47.7 wt%, which was also close to the experimental results (43.7 wt%). In conclusion, the application of Box-Behnken model along with response surface methodology was found to be an effective and cost-saving technique for predicting outcomes of the oligomerization reaction.

References

1. Choedkiatsakul I, Ngaosuwan K, Assabumrungrat S, Mantegna S, Cravotto G (2015) Renew Energy 83:25–29
2. Konwar LJ, Boro J, Deka D (2014) Renew Sust Energy Rev 29:546–564
3. Li X, Yu D, Zhang W, Li Z, Zhang X (2013) Appl Catal A 455:1–7
4. Noiroj K, Intarapong P, Luengnaruemitchai A, Jai-In S (2009) Renew Energy 34:1145–1150
5. Hermida L, Abdullah AZ, Mohamed AR (2015) Renew Sust Energy Rev 42:1223–1233
6. Kordulis C, Bourikas K, Gousi M, Kordouli E, Lycourghiotis A (2016) Appl Catal B Environ 181:156–196
7. Mäki-Arvela P, Kubickova I, Snåre M, Eränen K, Murzin DY (2007) Energy Fuels 21:30–41
8. Snare M, Kova IK, Maki-Arvela P, Chichova D, Eranen K, Murzin DY (2008) Fuel 87:933–945
9. Ajay Kumar Singh SR, Kumar Y, Masih H, Peter JK, Benjamin JC, Singh PK, Singh P (2014) Int J Cur Microbio Appl Sci 3:84–96
10. Su H, Liu G, He M, Tan F (2015) Bioresour Technol 187:149–160
11. Brethauer S, Wyman CE (2010) Bioresour Technol 101:4862–4874

12. Chen CSH, Bridger RF (1996) J Catal 161:687–693
13. Ghosh R, Bandyopadhyay AR, Jasra R, Gagjibhai MM (2014) Ind Eng Chem Res 53:7622–7628
14. Ivanov DP, Sobolev VI, Panov GI (2003) Appl Catal A 241:113–121
15. Guisnet M, Magnoux P (1997) Catal Today 36:477–483
16. Elordi G, Olazar M, Lopez G, Castaño P, Bilbao J (2011) Appl Catal B Environ 102:224–231
17. Muraza O (2015) Ind Eng Chem Res 54:781–789
18. Popov AG, Pavlov VS, Ivanova II (2016) J Catal 335:155–164
19. Kim J, Han J, Kwon TS, Park Y-K, Jeon J-K (2014) Catal Today 232:69–74
20. Wu Q, Zhang F, Yang J, Li Q, Tu B, Zhao D (2011) Microporous Mesoporous Mater 143:406–412
21. Echaroj S, Santikunaporn M, Chavadej S (2015) React Kinet Mech Cat 114:75–91
22. Xiu T, Wang J, Liu Q (2011) Microporous Mesoporous Mater 143:362–367
23. Sung DM, Kim YH, Park ED, Yie JE (2012) Catal Commun 20:63–67
24. Liu Y, He H-X (2013) Microporous Mesoporous Mater 165:27–31
25. Smirnova MY, Urguntsev GA, Ayupov AB, Vedyagin AA, Echevsky GV (2008) Appl Catal A 344:107–113
26. MaL Ferreira (2002) Rueda EH. J Mol Catal A 178:147–160
27. Pan H, Wang J, Chen L, Su G, Cui J, Meng D, Wu X (2013) Catal Commun 35:27–31
28. Guzmán-Castillo ML, López-Salinas E, Fripiat JJ, Sánchez-Valente J, Hernández-Beltrán F, Rodríguez-Hernández A, Navarrete-Bolaños J (2003) J Catal 220:317–325
29. Ding Y, Zheng J, Xia X, Ren T, Kan J (2016) LWT Food Sci Technol 67:206–213
30. Dwivedi G, Sharma MP (2015) Fuel 145:256–262
31. Liu W, Yin P, Liu X, Qu R (2014) Bioresour Technol 173:266–271
32. Ba-Abbad MM, Chai PV, Takriff MS, Benamor A, Mohammad AW (2015) Mater Design 86:948–956
33. Nel RJJ, de Klerk A (2009) Ind Eng Chem Res 48:5230–5238
34. T-s Yang, T-h Chang, C-t Yeh (1997) J Mol Catal A 115:339–346
35. Corma A, Martínez C, Doskocil E (2013) J Catal 300:183–196
36. Christensen CH, Johannsen K, Törnqvist E, Schmidt I, Topsøe H, Christensen CH (2007) Catal Today 128:117–122
37. Busca G (2014) Heterogeneous Catalytic Materials, 1st edn. Elsevier, Amsterdam
38. Huang F, Zheng Y, Cai G, Zheng Y, Xiao Y, Wei K (2010) Scripta Mater 63:339–342
39. Zhang K, Fu Z, Nakayama T, Niihara K (2012) Microporous Mesoporous Mater 153:41–46
40. Aguado J, Escola JM, Castro MC, Paredes B (2005) Microporous Mesoporous Mater 83:181–192
41. T-s Yang, T-h Chang, C-t Yeh (1997) J Mol Catal A 123:163–169
42. Furtado EA, Chaer Nascimento MA (2001) In: Lipscomb WN, Prigogine I, Maruani J, Wilson S, Ågren H, Avnir D et al (eds) Theoretical Aspects of Heterogeneous Catalysis. Springer, Dordrecht
43. Hu H, Ying W, Fang D (2010) J Nat Gas Chem 19:409–416
44. Albers P, Pietsch J, Parker SF (2001) J Mol Catal A 173:275–286
45. Coelho A, Caeiro G, Lemos MA, Lemos F, Ribeiro FR (2013) Fuel 111:449–460
46. Deimund MA, Labinger J, Davis ME (2014) ACS Catal 4:4189–4195
47. Kim YT, Chada JP, Xu Z, Pagan-Torres YJ, Rosenfeld DC, Winniford WL, Schmidt E, Huber GW (2015) J Catal 323:33–44
48. Marczewski M, Popielarska D, Marczewska H (2016) React Kinet Mech Catal 118:267–280
49. Granollers M, Izquierdo JF, Fité C, Cunill F (2013) Chemi Eng J 234:266–275

CrossMark

ORIGINAL ARTICLE

Laundry Detergency of Solid Non-particulate Soil or Waxy Solids: Part I. Relation to Oily Soil Removal Above the Melting Point

Jarussri Chanwattanakit[1] · John F. Scamehorn[2] · David A. Sabatini[2] ·
Sumaeth Chavadej[1,3]

Abstract In this work, methyl palmitate or palmitic acid methyl ester, a monoglyceride, was used as both a model solid fat below the melting point and as an oily soil above the melting point. An anionic extended surfactant [branched alcohol propoxylate sulfate sodium salt (C_{123}-(PO)$_4$-SO$_4$Na)] was used to remove methyl palmitate from cotton and from polyester. Above the melting point ($\sim 30\ ^\circ$C) of methyl palmitate, the maximum oily soil removal was found to correspond to the lowest dynamic interfacial tension, as is common with liquid soils. Below the melting point, the lower the contact angle of the wash solution against the soil (indicating higher wettability), the higher the solid fat soil detergency. The removed methyl palmitate was found to be mostly in unsolubilized droplets or particles with a small fraction of micellar solubilization for both solid and liquid forms. The presence of surfactant can prevent the agglomeration of detached methyl palmitate particles in both liquid and solid forms, reducing redeposition and enhancing detergency. Below the melting point, the surfactant aids the solution wetting the surfaces, then penetrating the waxy solid, causing detachment as small particles, and dispersion of these particles. Unlike particulate soil detergency, electrostatic forces are not the dominant factor in fatty soil detergency.

✉ Sumaeth Chavadej
  sumaeth.c@chula.ac.th

1 The Petroleum and Petrochemical College, Chulalongkorn University, Phayathai Rd., Pathumwan, Bangkok 10330, Thailand

2 Institute for Applied Surfactant Research, University of Oklahoma, Norman, OK, USA

3 Center of Excellence on Petrochemical and Materials Technology, Bangkok, Thailand

Introduction

In laundry detergency, several factors affect the performance such as the nature of soils, the properties of surfactant, nature of solid surface, mechanical action applied during washing, water hardness, washing temperature, electrolyte level, and additives (e.g., builder, enzyme, and anti-redeposition agent) [1–5]. The previous work on oily soil detergency using different liquid oils demonstrated good correlation between detergency efficiency and interfacial tension (IFT) between the oil and the aqueous solution [6–13]. Recently, our research group has published studies of the mechanisms of particulate soil detergency using carbon black as a model hydrophobic soil and kaolinite and ferric oxide as model hydrophilic soils. It was found that electrostatic forces dominate soil removal, even for nonionic surfactants and hydrophobic fabric [14, 15].

Solid non-particulate soil or solid fat soil is a separate class of contaminants which has properties of liquid and/or solid, depending on temperature. Practical examples of such soils are butter, sebum from human skin, or solidified hamburger or bacon grease. These soils are particularly challenging to remove in low temperature laundry detergency, which is a current topic of great interest due to energy savings and fabric damage at high temperatures. Often, soils are mixtures between liquid and solid fat soils in which the liquid oil is entrapped in the crystal structure of solid oil under a moderate temperature, causing it to be hard to remove. Despite the importance of this soil removal in practical detergency, there are few literature studies of

Springer AOCS

solid fat soil detergency. Scheuing [16] studied the detergency mechanism of tristearin (model solid fat soil) using Fourier transform infrared spectroscopy (FT-IR) and reported that the removal of solid triglycerides from a fabric surface was more complex than solid hydrocarbon soils because of the polymorphism in the crystal structure of tristearin. Powe [17] studied detergency of different hydrocarbon soils, and found that the maximum removal of each solid fat soil was somewhere near its melting point. Kawase *et al.* [18, 19] studied the removal mechanism of solid fatty acid soil by using nonionic and anionic surfactants and they reported that solubilization was the dominant mechanism at low temperatures.

An extended surfactant has a group of intermediate polarity, such as polypropylene oxide (PO) or polypropylene–polyethylene oxide (PO–EO) group, inserted between the hydrophilic head and hydrocarbon tail group. As a result of this unique structure, extended surfactants can further extend into both the oil and aqueous phases, resulting in a smoother transition between the hydrophobic and hydrophilic regions at the interface. The presence of a polypropylene oxide group in the hydrocarbon tail of the surfactant molecule helps extend the tail to an oil phase, while still maintaining good interaction with the water phase. Hence, use of an extended surfactant can facilitate the formation of a middle-phase microemulsion, which provides both high solubilization and ultralow interfacial tension (IFT), leading to various applications such as extraction, separation, and textile cleaning [20–23]. Phan *et al.* [24] examined the use of a single extended surfactant in detergency of vegetable oils. High canola oil detergency (>80%) was achieved using a single extended surfactant ($C_{14,15}$-8PO-SO$_4$Na) at concentrations as low as 125 ppm and a temperature of 25 °C. Tanthakit *et al.* [8] studied palm oil removal from fabric using microemulsion-based formulations of a mixture of an extended surfactant ($C_{14,15}$-3PO-SO$_4$Na) and a nonionic secondary alcohol ethoxylated surfactant [$C_{12,14}$-O(EO)$_5$] at a 25:75 weight ratio. The oil removal for this surfactant blend exceeded 90%, which was greater than those of any single surfactant alone and of a commercial liquid laundry detergent. Do *et al.* [25] reported that the mixture of a linear extended surfactant (C_{10}-18PO-2EO-SO$_4$Na) and a hydrophobic twin-tailed sodium dioctylsulfosuccinate surfactant showed synergism in a Winsor Type III microemulsion formulation, leading to high detergency of vegetable oils and semi-solid fats at low salinity and a low washing temperature.

In this paper, methyl palmitate or palmitic acid methyl ester, a monoglyceride, with a melting point around 30 °C, was used as a model single component solid fat or oily soil being removed from either hydrophilic surface (cotton fabric) or hydrophobic surface (polyester fabric) by using a single anionic extended surfactant at temperatures both higher and lower than the soil's melting point. Other fundamental physical properties of the system were studied to better understand the forces involved in soil removal and help guide future development of cold water detergent formulations.

Experimental Procedures

Materials

Methyl palmitate or palmitic acid methyl ester (99.8% purity) and Oil red O (solvent Red 27, No. 26125) were supplied by Sigma-Aldrich (BKK, Thailand). Cotton and polyester were purchased from Test fabrics, Inc. (Middlesex, NJ, USA). The surfactant used in this study was an extended surfactant which is a branched alcohol propoxylate sulfate sodium salt with 12–13 carbon numbers with approximately four propylene oxide (PO) units ($C_{12,13}$-4PO-SO$_4$Na) with an active content of 30 wt%, as provided by Sasol North America (Lake Charles, LA). Sodium chloride (NaCl), dichloromethane, and isopropanol, all analytical grade, were purchased from LabScan Asia Co., Ltd. De-ionized (DI) water was used to prepare all solutions.

Fabric Pretreatment and Soiling Procedure

Pre-washing of the test fabrics was done using de-ionized (DI) water to eliminate all residues of mill-finishing agents. The pre-washing method followed the ASTM standard guide D4265-98 [26]. After pre-washing, the fabric was cut into 3 × 4 inch swatches in a warp and weft direction. Approximately 0.1 g of the oil-soluble dye was added to 100 mL of the oil above its melting point. The colored oil was filtered until clear. Next, 10 mL of the clear dyed oil was diluted with dichloromethane to 100 mL [27]. The swatches were folded and completely submerged in the diluted dyed oil solution for 5 min. The soiled fabrics were then unfolded and laid on a flat glass plate in a ventilated hood at room temperature (25 °C) overnight in order to dry the soiled swatches. All swatches were freshly prepared for each batch of laundry experiments. By this soiling method, the average weight ratios of oil-to-fabric were approximately 0.20 ± 0.01:1 for the cotton and 0.15 ± 0.01:1 for the polyester.

Laundry Experiments

The laundry experiments were conducted using a terg-o-tometer (Copley, DIS 8000), which simulates a home washing-machine action in a bench scale unit. The experimental procedure consisted of a wash step for 20 min with

1000 mL of a surfactant washing solution and two rinse steps for 2 and 3 min with 1000 mL of DI water. An agitation speed for each step was fixed at 120 rpm. Three soiled swatches and one unsoiled swatch for anti-redeposition testing were washed in each bucket for one cycle for replication.

Oil Removal Measurement

Oil removal was quantified based on residual oil on the swatches after washing. The residual oil was extracted by submerging a swatch in isopropanol for 24 h at room temperature, and then the extracted solution was analyzed by an ultraviolet/visible spectrophotometer (Hewlett-Packard, 8452A) [9, 27]. The oil removal was calculated by subtracting the remaining oil residue after washing from the original oil content in each swatch.

Surface Tension Measurements

The surface tension of a surfactant solution with varying surfactant and NaCl concentrations was measured by a Wilhelmy plate tensiometer (Krüss, K100) at two different temperatures (25 and 35 °C). The inflection point of the plot of surface tension versus the log of initial surfactant concentration was used to determine the critical micelle concentration (CMC) [28].

Particle Size Measurement

The particle size distribution of methyl palmitate particles suspended in the washing solution after the wash step at 20 °C was measured by a particle size analyzer (Malvern, Mastersizer X).

Contact Angle Measurement

A 2-μL drop of a surfactant solution with different NaCl concentrations and two surfactant concentrations of 0.1 and 0.3 wt% was placed on the methyl palmitate surface by using a micro-syringe and the contact angle was measured after 30 s by a contact angle measuring instrument (Krüss, DSA 10 Mk2) using the sessile drop technique. During the measurement, the sample chamber was kept at 25 °C in order to prevent melting of the sample (methyl palmitate).

Oil Solubilization Measurement

An excess amount of methyl palmitate was added to a surfactant solution having a surfactant concentration of 1000 mg/L (10 times CMC) with 5 wt% NaCl or a surfactant concentration of 3000 mg/L (30 times CMC) with 1

or 5 wt% NaCl at different temperatures. The solution was stirred at 120 rpm for 20 min. The surfactant solution phase of the mixture was filtered and the filtrate was measured for total carbon concentration of the dissolved methyl palmitate plus the surfactant by a total organic carbon analyzer (TOC) (Shimadzu, TOC 5000). The TOC concentration of dissolved methyl palmitate was obtained by subtracting the total TOC value with the TOC value of surfactant. The solubility of methyl palmitate obtained was then subtracted from the oil removal to determine the portion of unsolubilized (dispersed or emulsified) methyl palmitate. The measurement time of 20 min was selected to be the same as the wash step time used in the washing experiments. In addition, the oil solubilization measurement was also carried out with varying time until each system reached a maximum or equilibrium solubilization level which was found at around 24 h for all studied systems.

Interfacial Tension Measurement

The measurement of dynamic interfacial tension (IFT) between the aqueous phase (the surfactant solution) and the oil phase (methyl palmitate) for varying surfactant concentrations and temperatures (higher than the melting point of methyl palmitate) was conducted using a spinning drop tensiometer (University of Texas, Model 500). A volume of 1–3 μL of methyl palmitate (above the melting point) was injected into a 300-μL capillary tube filled up with a surfactant solution having different NaCl concentrations and two surfactant concentrations of 0.1 and 0.3 wt%. The diameter of the oil drop was recorded 20 min after injection, which corresponded to the time used for the wash step in detergency experiments.

Dispersion Stability Measurement

The dispersion stability of methyl palmitate solid particles having average diameters of 100 μm suspending in DI water or an aqueous solution containing 0.1 or 0.3 wt% surfactant with different NaCl concentrations at 25 °C (below the melting point) was determined by measuring absorbance as a function of time using a UV–visible spectrophotometer (Hewlett-Packard, 8452A). The solution was prepared by adding the methyl palmitate particles in the surfactant solution, after being well mixed; the prepared solution was transferred to a spectrophotometer cuvette. The reading of absorbance at a wavelength of 550 nm was recorded every 10 s for 2 h. The absorbance values in the range of 2000–5000 s were averaged to represent the dispersion stability. The higher the absorbance, the higher the dispersion stability.

PZC Measurement

A powder sample of methyl palmitate or cotton or polyester fabric was added to distilled water at different solution pH values using a 0.1 M HCl or 0.1 M NaOH solution for pH adjustment. After that, the solution with any added powder sample was kept at 20 °C for 24 h. The initial pH value of this solution, prior to adding the powder sample, and the final pH after 24 h were measured by a pH meter (Ultra basic DENVER Instrument). The point of the intersection of the initial and the final pH lines was used to indicate the point of zero charge (PZC) of each material.

Zeta Potential Measurement

About 3.5 mg of methyl palmitate powder was added into a solution having 0.1 wt% surfactant and different NaCl concentrations. The mixture was stirred and kept at 20 °C for 24 h. Subsequently, the solution was transferred to an electrophoretic cell of a zeta meter (Zeta-Meter 3.0+) equipped with a microscope module. After applying a suitable voltage, the charged particles moved towards the electrode having opposite charge until attaining a steady state (the particles moved with a constant velocity). The velocities were measured and averaged and referred to as electrophoretic mobility which was calculated by the zeta meter instrument automatically [29].

Results and Discussion

Detergency Performance: Optimum Concentrations of Surfactant and NaCl

As shown in Table 1, added surfactant or NaCl has a negligible effect on the melting point of methyl palmitate (we use 30 °C throughout this paper). Figure 1 shows the oil removal and oil redeposition as a function of surfactant concentration and salinity for cotton and polyester at 35 and 25 °C in which methyl palmitate is in

Table 1 Melting point of methyl palmitate in various washing solutions

Solution	Melting point (°C)
De-ionized water	29.5–30.4
0.1 wt% $C_{12,13}(PO)_4SO_4Na$	28.5–30.1
0.1 wt% $C_{12,13}(PO)_4SO_4Na$/1 wt% NaCl	28.2–30.3
0.1 wt% $C_{12,13}(PO)_4SO_4Na$/3 wt% NaCl	29.5–30.3
0.1 wt% $C_{12,13}(PO)_4SO_4Na$/5 wt% NaCl	28.0–30.4
0.1 wt% $C_{12,13}(PO)_4SO_4Na$/7 wt% NaCl	29.5–30.2

a liquid form and solid form, respectively. At 35 °C, for any given NaCl concentration, with increasing surfactant concentration, the oil removal increased and leveled off for both test fabrics. For any given surfactant concentration, the oil removal reaches a maximum at 5 wt% NaCl as shown in Fig. 1a-1, b-1. At 25 °C, the oil removal gradually increases with increasing surfactant concentration and the oil removal reaches a maximum at 1 wt% NaCl as shown in Fig. 1c-1, d-1. In this work, the ability of low extended surfactant concentration to achieve good detergency is consistent with results of previous studies [23, 24].

Figure 1 also shows the effects of salinity and surfactant concentration on the oil redeposition on cotton and polyester at 35 and 25 °C. The amount of oil redepositing on both fabrics decreased with increasing surfactant concentration and leveled off at a high surfactant concentration, depending on the concentration of added NaCl. For any fixed surfactant concentration, the oil redeposition reached a minimum value at 5 and 1 wt% NaCl at 35 and 25 °C, respectively. The maximum oil removal with the lowest oil redeposition was found at the same surfactant concentration and salinity for both fabrics types and for both washing temperatures.

CMC Results

The CMC values of the extended surfactant with different NaCl concentrations at 25 and 35 °C are shown in Fig. 2a. Increasing electrolyte NaCl concentration causes the CMC to decrease due to decrease of the absolute value of the electrical potential at the micelle surface and lower electrostatic repulsion between surfactant head groups at the micelle surface [20, 23]. Moreover, the CMC values were relatively independent of temperature (those at 25 °C were slightly higher than those at 35 °C for all NaCl concentrations), consistent with low temperature dependence of CMC on temperature for anionic surfactants [30]. The CMC data from Fig. 2a are plotted as the logarithm of critical micelle concentration versus logarithm of total concentration of counterion in the solution at the CMC (from added NaCl and surfactant) as shown in Fig. 2b. This log–log plot is linear and known as the Corrin–Harkins plot [31]. The absolute value of the slope from these plots is the fractional counterion binding to micelles and at 25 °C is 0.29 and at 35 °C is 0.30. These values are only about half of those measured for other ionic surfactants [32, 33], so extended surfactants show unusual electrostatic properties, probably having to do with the packing of the head groups at the micelle surface. In common with other ionic surfactants, fractional counterion binding on micelles has only slight temperature dependence.
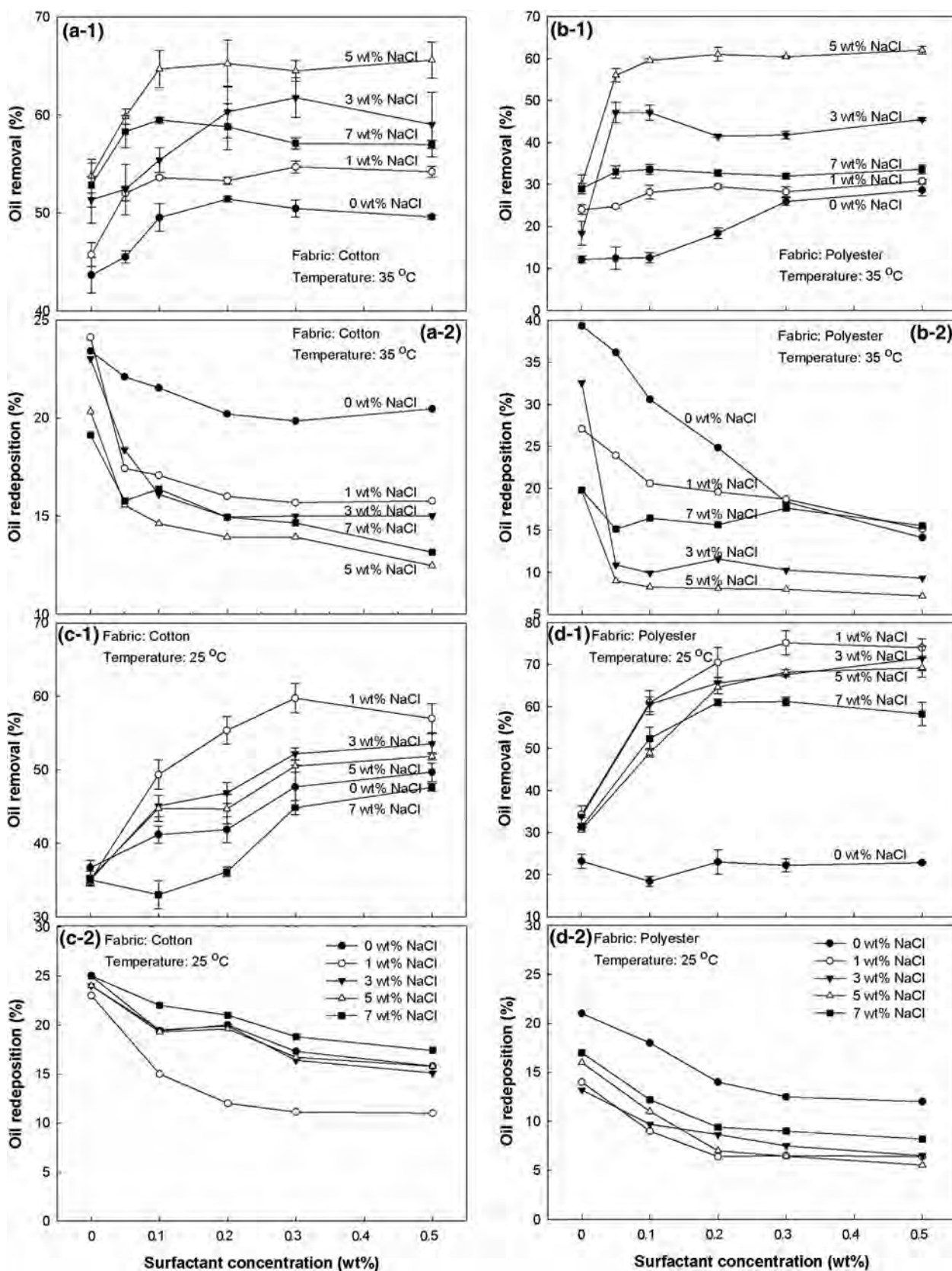
Fig. 1 Oil removal and redeposition of methyl palmitate as a function of surfactant concentration and salinity on both test fabrics **a-1**, **a-2** for cotton at 35 °C, **b-1**, **b-2** for polyester at 35 °C, **c-1**, **c-2** for cotton at 25 °C, **d-1**, **d-2** for polyester at 25 °C
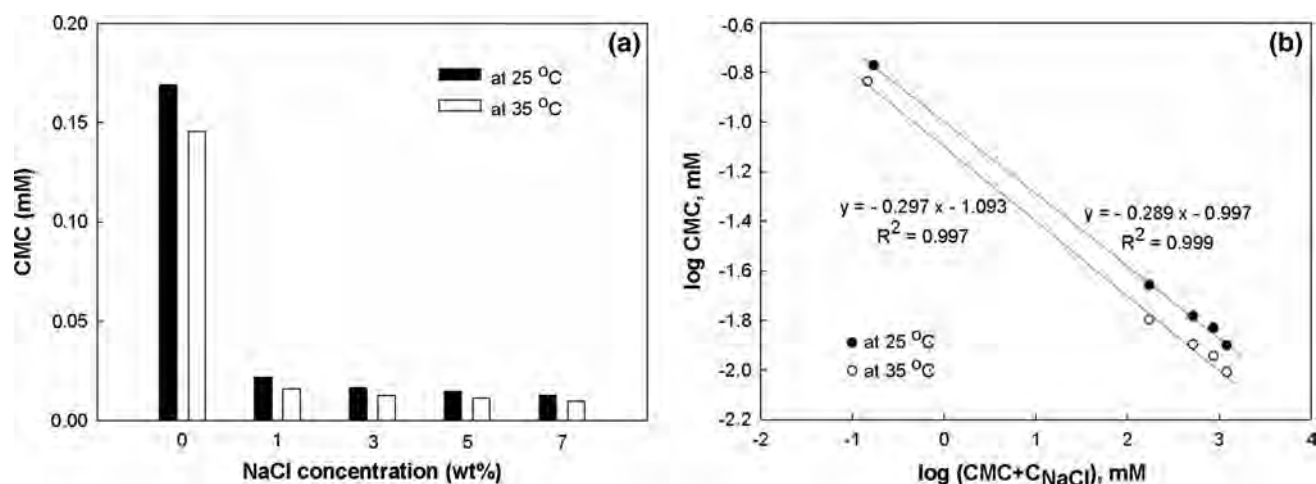
Fig. 2 **a** Critical micelle concentration (CMC) of $C_{12,13}(PO)_4SO_4Na$ at 25 and 35 °C and **b** Corrin and Harkins plot of $C_{12,13}(PO)_4SO_4Na$ from CMC data at 25 and 35 °C

Interfacial Tension (IFT) Results

Figure 3 shows the IFT at the interface of the liquid methyl palmitate and surfactant solution as a function of salinity for two surfactant concentrations of 0.1 and 0.3 wt% at 35°C. The IFT values of the surfactant solution and the liquid oil were measured at 20 min, which is long enough for equilibration [34] and corresponds to the wash step time used in the washing experiments. For both studied surfactant concentrations, all of the surfactant solution–oil IFT values measured (0.0172–0.2773 mN/m) are considered to be in the low and ultralow ranges, except at 0 wt% NaCl (2.39 mN/m) which agree well with the measured IFT values between an extended surfactant and canola oil [24, 34, 35]. All of the measured IFT values were much lower than the deionized water–oil IFT value (7.86 mN/m) and the 5 wt% NaCl deionized water–oil IFT value (7.29 mN/m).

Contact Angle Results

The contact angle is a physical parameter indicative of how well an applied solution wets a surface. The wetting is a first step of the complex process of detergency. Figure 4 shows the contact angles of both 0.1 and 0.3 wt% surfactant solutions on the solid surface of methyl palmitate as a function of NaCl concentration at 25 °C. The contact angle decreases with increasing NaCl concentration and reaches a minimum value (indicating maximum wettability) at a NaCl concentration of 5 and 1 wt% for 0.1 and 0.3 wt% surfactant concentrations, respectively. An increase in surfactant concentration from 0.1 to 0.3 wt% could reduce the optimum NaCl concentration studied for detergency performance from 5 to 1 wt%. This surfactant concentration increase to 0.3 wt% also resulted in a decreased contact angle from 38° to 33° at 5 and 1 wt% NaCl,

Fig. 3 The correlation of equilibrium IFT using 0.1 and 0.3 wt% $C_{12,13}(PO)_4SO_4Na$ as a function of salinity at 35 °C

Fig. 4 Contact angle of 0.1 and 0.3 wt% surfactant solution on methyl palmitate surface at 25 °C as a function of salinity

respectively. So, wettability may be a factor in detergency and the simple contact angle measurement may be predictive of cleaning efficiency which would be helpful in formulation development.

Effects of Fabric Type and Washing Temperature on Detergency Performance

Figure 5 shows the effect of washing temperature on oil removal and oil redeposition for polyester and cotton fabrics in surfactant solutions of 0.3 wt% $C_{12,13}(PO)_4SO_4Na$ with 1 and 5 wt% NaCl concentrations and of 0.1 wt% $C_{12,13}(PO)_4SO_4Na$ with 5 wt% NaCl concentration. The washing temperature range of 15–50 °C was studied in order to cover both solid and liquid states of methyl palmitate (melting point of 30 °C). The oil removal increased with increasing wash temperature for both studied fabrics using the washing solution containing 0.3 and 0.1 wt% surfactant with 5 wt% NaCl concentrations. The deterge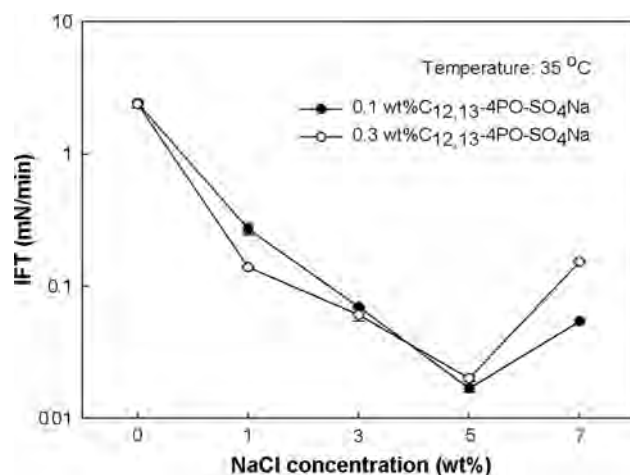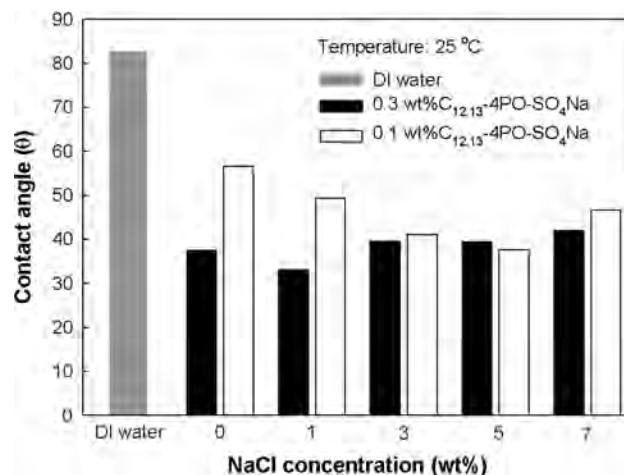ncy performance on the cotton was slightly higher than that on the polyester fabric for any wash temperature. For the washing solution having 0.3 wt% surfactant and 1 wt% NaCl, the detergency performance on the cotton fabric reached a maximum level around the soil melting point (30 °C), but did not change substantially with temperature above the melting point. For polyester fabric with the washing solution of 0.3 wt% surfactant and 1 wt% NaCl, the oil removal increased with increasing washing temperature from 15 to 25 °C. However, detergency decreased dramatically as temperature increased further from 25 to 30 °C. After reaching this minimum oil removal at the melting point, detergency slightly increased as temperature increased further beyond the melting point. This somewhat surprising minimum in detergency is confirmed by photographs of washed polyester at different washing temperatures as shown in Fig. 6.

For all surfactant systems on cotton and two of the three systems on polyester, oil removal generally increases with increasing temperature which is generally true in detergency of different soils. However, this temperature inversion effect has been previously observed on hydrophobic fabric. Morris and Prato [3] found that the best removal of particulate and oily soil from cotton fabric was at high temperatures, whereas the nonpolar fraction of oily soil removed from polyester was better at low wash temperature. Illman et al. [36] and Gordon et al. [37] found that nonpolar sebum was more easily removed from Dacron or Nylon in cold water than hot water. This was attributed to the diffusion of liquid oil into the interior of polyester at high temperatures, causing the oil to have poor contact with the surfactant solution [38].

In our study, the soil was dissolved in a volatile solvent, the fabric immersed in the solvent/soil mixture, then the solvent evaporated at 25 °C, below the oil melting point. So, when the soil was deposited on the fabric upon evaporation of the solvent, it was a solid. It was suspected that this solid did not incorporate itself into the fabric fibers as a liquid soil would. So, in separate experiments, after the soiling procedure, each fabric was heated up to 40 °C so the soil became liquefied and could diffuse/imbibe into the fabric weave, then cooled to the temperature of the detergency experiment. As shown in Table 2, below the melting point, the oil removal was lower than with normal soiling procedures but at a high wash temperature, detergency was increased around 10%. We conclude that if the soil is a liquid without solvent and allowed to contact the hydrophobic fabric before the system is cooled, as would be the case with sebum and warm hamburger/bacon grease, below the melting point, it is much more difficult to remove the soil than if the soil only contacts the fabric as a solid below the melting point. That this effect is only observed on hydrophobic polyester fabric and not on cotton indicates that the hydrophobic monoglyceride soil has a much stronger attractive interaction with the hydrophobic fabric than a hydrophilic fabric. A broader range of soil polarities would need to be studied to determine the generality of this effect and if monoglycerides/triglycerides are peculiar in their interaction with polyester compared to say hydrocarbon soils. And the temperature inversion effect is not observed for every surfactant system (one out of three here). So, it is recommended that a systematic soiling procedure be used for studies of waxy solids when temperature ranges below the melting point are included.

In a comparison of the two NaCl concentrations in the 0.3 wt% surfactant solution (Fig. 5), for any studied fabric, the detergency performance at 5 wt% NaCl was higher than that at 1 wt% NaCl at a washing temperature above the melting point due to the low IFT values of 0.009–0.09 mN/m at 5 wt% NaCl as compared to those of around 0.1 mN/m at 1 wt% NaCl (Fig. 3). In contrast, for any washing temperature below the melting point of 30 °C, the oil removal at 5 wt% NaCl was lower than that at 1 wt% NaCl, especially on the polyester fabric. The oil removal on the cotton fabric was higher than that on the polyester fabric under studied conditions except at washing temperatures below the melting point with the NaCl concentration of 1 wt%. There is apparently a high affinity of the liquid methyl palmitate and hydrophobic polyester as compared to that on the hydrophilic cotton fabric. However, at a temperature lower than the melting point, the oil removal for the polyester fabric was much higher than that on the cotton fabric, suggesting that the contact of the solid methyl palmitate with the fabric is less than for liquid methyl palmitate. This supports the same conclusion reached from different soiling procedures about solid soil not interacting well with polyester.
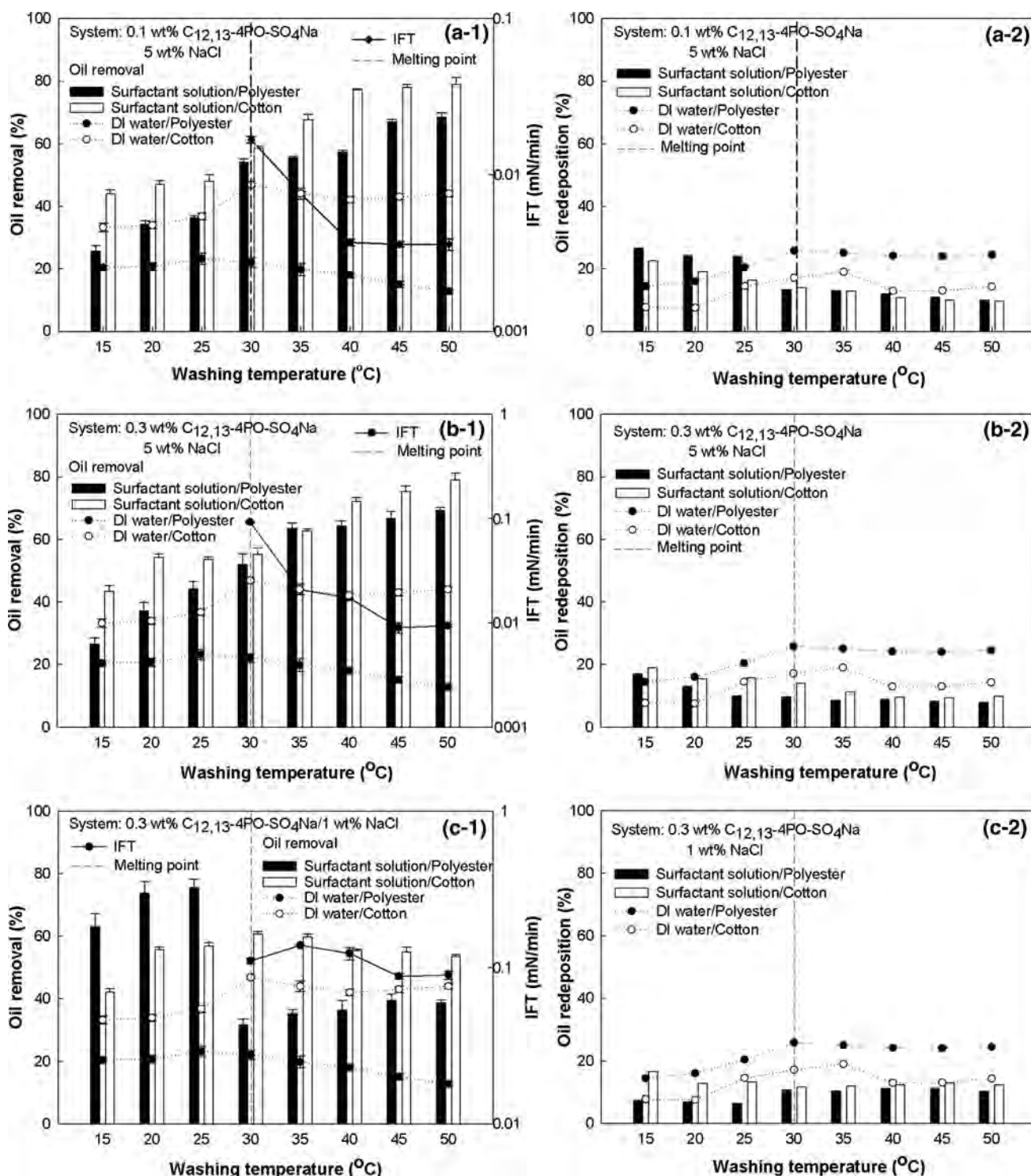
Fig. 5 Oil removal and redeposition as a function of washing temperature in relation to equilibrium IFT at **a** 0.1 wt% $C_{12,13}(PO)_4SO_4Na$ with 5 wt% NaCl, **b** 0.3 wt% $C_{12,13}(PO)_4SO_4Na$ with 5 wt% NaCl, and **c** 0.3 wt% $C_{12,13}(PO)_4SO_4Na$ with 1 wt% NaCl on both test fabrics of cotton and polyester

The use of surfactant showed a much higher oil removal at any washing temperature as compared to DI water. For DI water systems, the oil removal slightly increased and reached a maximum level at about the melting point for both test fabrics. Beyond the melting point (30 °C), the oil removal on polyester fabric slightly decreased with further increasing washing temperature. Therefore, the best conditions found at any temperature below the melting point
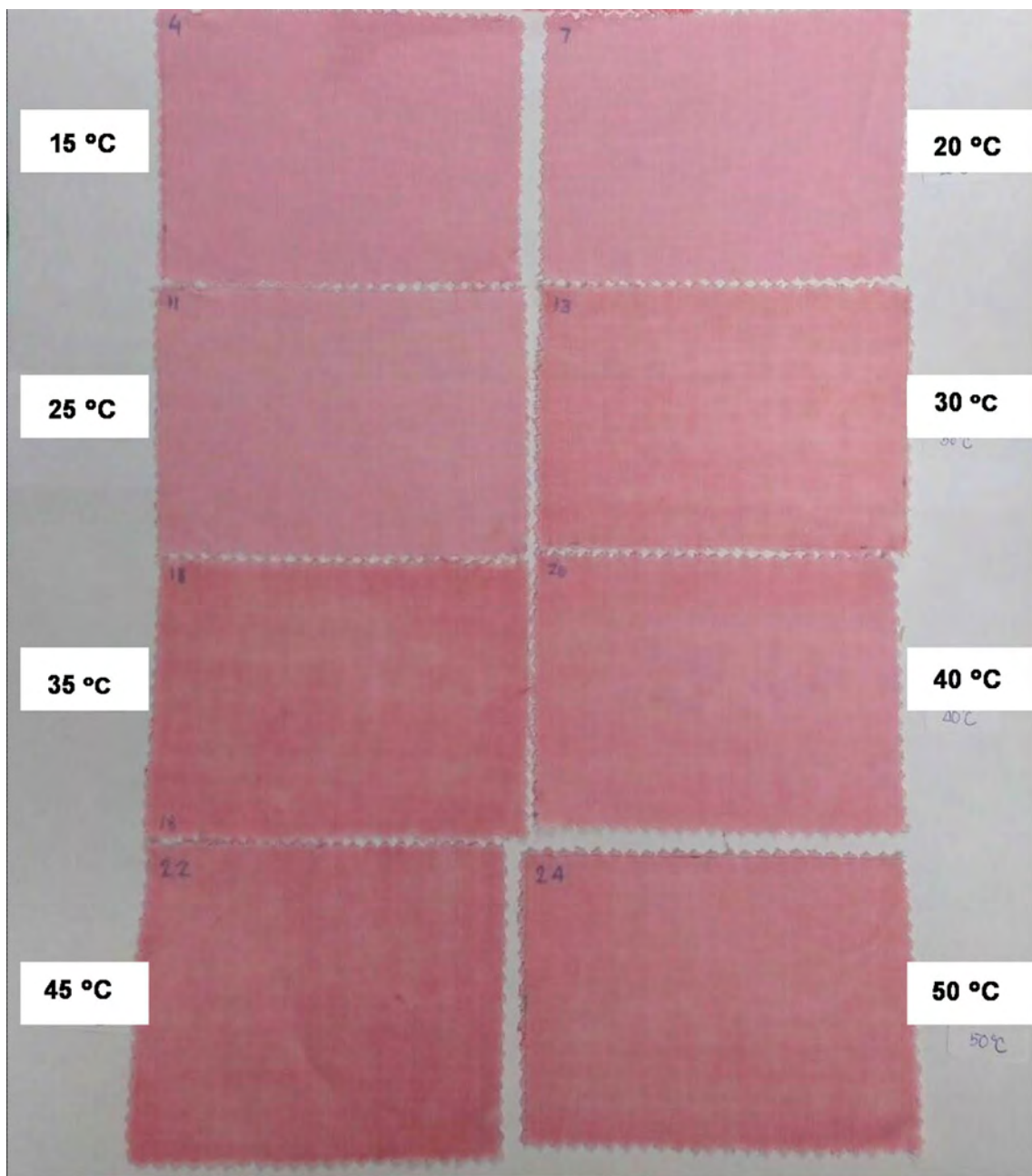
Fig. 6 Picture of washed fabrics at different washing temperatures of 0.3 wt% $C_{12,13}$-4PO-SO$_3$Na with 1 wt% NaCl

Table 2 The effect of soiling procedure on detergency performance for polyester

Washing temperature (°C)	Oil removal (%)	
	Not heated soiling (25°)	Heated soiling (40°)
15	63.3 ± 4.12	30.96 ± 2.84
20	73.79 ± 3.69	35.23 ± 1.91
25	75.50 ± 2.80	30.05 ± 3.88
30	31.63 ± 1.84	40.90 ± 3.91
35	35.32 ± 1.24	50.95 ± 1.73
40	36.40 ± 3.02	46.74 ± 2.08
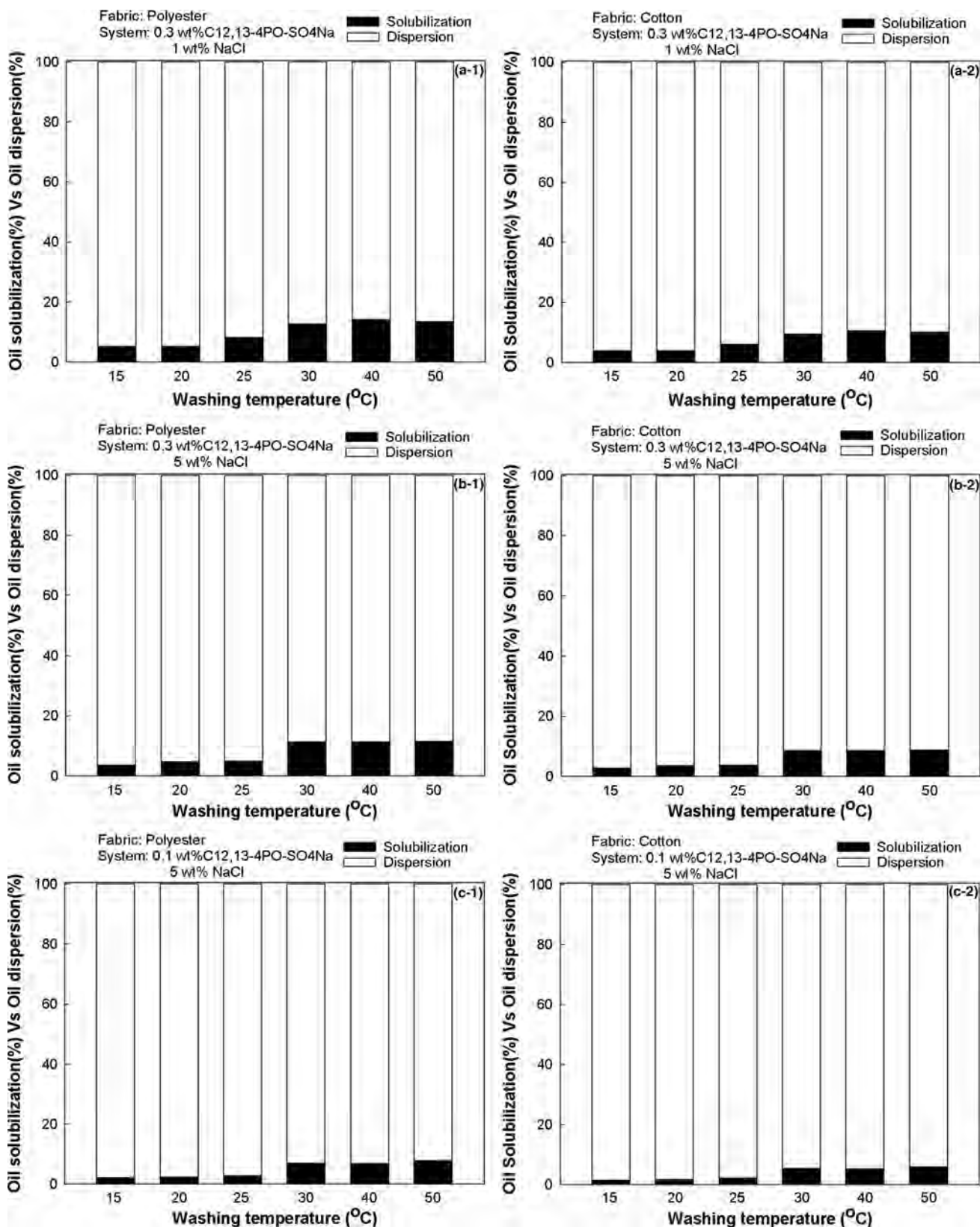
Fig. 7 Solubilized portions and unsolubilized portions of removed oil at 20 min; **a** 0.3 wt% $C_{12,13}(PO)_4SO_4Na$ with 1 wt% NaCl, **b** 0.3 wt% $C_{12,13}(PO)_4SO_4Na$ with 5 wt% NaCl, and **c** 0.1 wt% $C_{12,13}(PO)_4SO_4Na$ with 5 wt% NaCl on both test fabrics of cotton and polyester

Table 3 The ratio of oil solubilization at 20 min to equilibrium oil solubilization with different surfactant systems

Temperature (°C)	Oil solubilization (g/L)		Ratio
	At 20 min	At equilibrium	(At 20 min/at equilibrium)
0.3 wt% C$_{12,13}$-4PO-SO$_4$Na/1 wt% NaCl			
20	0.0235 ± 0.0035	0.190 ± 0.020	0.1236
25	0.0365 ± 0.0034	0.342 ± 0.012	0.1069
30	0.0570 ± 0.0014	0.226 ± 0.016	0.2519
40	0.0635 ± 0.0233	0.662 ± 0.030	0.0959
50	0.0605 ± 0.0149	0.634 ± 0.033	0.0955
0.3 wt% C$_{12,13}$-4PO-SO$_4$Na/5 wt% NaCl			
20	0.0210 ± 0.0014	0.304 ± 0.023	0.0691
25	0.0220 ± 0.0056	0.262 ± 0.005	0.0841
30	0.0510 ± 0.0010	0.272 ± 0.004	0.1872
40	0.0520 ± 0.0014	0.506 ± 0.006	0.1028
50	0.0500 ± 0.0028	0.532 ± 0.038	0.0940
0.1 wt% C$_{12,13}$-4PO-SO$_4$Na/5 wt% NaCl			
20	0.0105 ± 0.0021	0.109 ± 0.008	0.0959
25	0.0125 ± 0.0035	0.104 ± 0.026	0.1202
30	0.0318 ± 0.0017	0.123 ± 0.008	0.2585
40	0.0312 ± 0.0024	0.160 ± 0.009	0.1950
50	0.0350 ± 0.0036	0.233 ± 0.012	0.1502
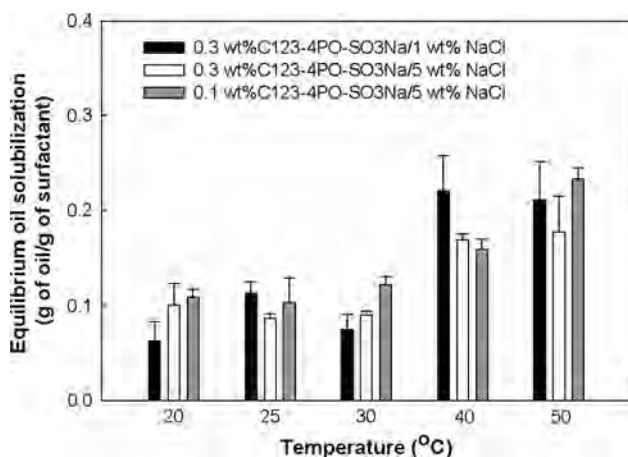
Fig. 8 Equilibrium oil solubilization in different surfactant systems as a function of temperature

were a 0.3 wt% surfactant concentration with a 1 wt% NaCl concentration whereas the same surfactant concentration of 0.3 and 5 wt% NaCl were found to be better for a washing temperature above the melting point. Generally, it is known that an increase in temperature results in increasing hydrophilicity of anionic surfactants but nonionic surfactants have the opposite trend. The studied extended surfactant has the polypropylene oxide groups inserted between the hydrophobic tail and hydrophilic head group, making it less sensitive to temperature than conventional anionic surfactants [39]. This may suggest that the studied extended surfactant has mixed properties

between anionic and nonionic surfactants, explaining good oily detergency over a wide range of washing temperatures.

Figure 5c-2 shows the oil redeposition as a function of washing temperature for both DI water solution and 0.3 wt% surfactant with 1 wt% NaCl concentrations for both polyester and cotton fabrics. For DI water, the oil redeposition reached the maximum at about the melting point for both studied fabrics. For the surfactant solution, the oil redeposition on the cotton fabric reached a slight minimum at the melting point whereas the oil redeposition on the polyester fabric showed a sharp decrease with increasing temperature at the melting point, similar to the decrease in oil removal at the melting point. For cotton, this anomalous behavior is not seen. As shown in Fig. 5a-2, b-2, 0.3 wt% surfactant with 1 wt% NaCl concentration and 0.1 wt% surfactant and 5 wt% NaCl concentration, the oil redeposition generally decreased with increasing temperature just as oil removal generally increased with temperature. So the surprising temperature inversion observed at the melting point, observed only for polyester, is evidenced in both oil removal and oil redeposition.

Solubilization Results

Figure 7 shows both solubilized and unsolubilized portions of removed oil in different washing solutions at different washing temperatures for both test fabrics at 20 min. For any washing temperature, most of removed oil was found to be in a separate dispersed phase (either emulsified liquid

droplets or dispersed solid particles) with a very small portion solubilizing in micelles. The solubilized portion slightly increased with increasing washing temperature. An increase in surfactant concentration from 0.1 to 0.3 wt% increased the solubilization portion of removed oil. This is because an increase in surfactant concentration simply increases the concentration of micelles, leading to an increase in oil solubilization. The results of most removed oil being in free oil particles suggest that the dispersion stability of detached oil particles plays an important role in the overall detergency performance. The differences between the oil solubilization at 20 min and the equilibrium oil solubilization at different temperatures are shown in Table 3. For all studied systems, equilibrium oil solubilization was attained at a very long time (about 24 h). Most of the oil solubilization values at 20 min were around 10% of the equilibrium oil solubilization values, suggesting that the washing time used in the washing experiment as well as in actual application is too short for effective solubilization so most detached oil is in unsolubilized form. Comparing the three surfactant systems in term of g of oil/g of surfactant in Fig. 8 shows that at any temperature below the melting point ($\sim$30 °C) for all studied surfactant systems, the equilibrium oil solubilization values were almost unchanged with temperature and significantly lower than those at any temperature higher than the melting point. With increasing washing temperature above the melting point, the equilibrium oil solubilization value considerably increased and tended to level off at a temperature around 40–50 °C.

Particle Size Distribution of Detached Oil Particles after Wash Step

Table 4 shows the particle size distribution of methyl palmitate particles suspended in the washing solution after the 20 min wash step for both fabrics using either surfactant or DI water at 25 °C. At 25 °C, the solid nature of the particles of methyl palmitate made it possible to measure the particle size distribution. For any wash system, the particle size distribution of the methyl palmitate solid particles detached from any fabric consisted of a trimodal distribution or three ranges of particle sizes (1–5, 5–100, 100–600 μm). Compared to the surfactant formulation, when DI water was used in the wash step, the detached particles of methyl palmitate had larger sizes in the ranges of 5–100 and 100–600 μm with mean sizes of about 100 and 120 μm for the cotton and polyester fabrics, respectively. Interestingly, the use of surfactant resulted in particle sizes of the detached methyl palmitate solid particles being about one third to one fourth of those of the DI water system. The results suggest that surfactant solution penetrates the methyl palmitate by wetting, the soil is then

Table 4 Particle size distribution and averaged sizes of methyl palmitate after washing step with DI water and surfactant solution with various salinities at 25 °C

Washing solution	Cotton							Polyester						
	1–5 μm		5–100 μm		100–600 μm		Mean size (μm)	1–5 μm		5–100 μm		100–600 μm		Mean size (μm)
	Size (μm)	Vol. (%)	Size (μm)	Vol. (%)	Size (μm)	Vol. (%)		Size (μm)	Vol. (%)	Size (μm)	Vol. (%)	Size (μm)	Vol. (%)	
De-ionized water	2.32 ± 0.02	9.45	23.2 ± 1.11	58.4	282 ± 5.28	32.2	101 ± 3.88	2.76 ± 0.48	6.50	30.0 ± 0.11	57.1	280 ± 26.8	36.4	120 ± 17.8
C$_{12,13}$(PO)$_4$SO$_4$Na	2.46 ± 0.01	31	10.6 ± 0.13	60.8	309 ± 1.84	8.19	36.2 ± 1.78	2.51 ± 0.01	24.1	11.8 ± 0.06	64.1	313 ± 12.2	11.7	45.8 ± 1.41
C$_{12,13}$(PO)$_4$SO$_4$Na/1wt %NaCl	2.39 ± 0.05	21.5	15.6 ± 0.51	70.5	276 ± 9.31	8.02	29.4 ± 2.47	2.37 ± 0.01	28.1	13.3 ± 0.35	62.1	313 ± 8.07	9.79	40.0 ± 0.55
C$_{12,13}$(PO)$_4$SO$_4$Na/3wt %NaCl	2.43 ± 0.11	21.3	14.3 ± 0.77	74.2	223 ± 3.48	4.48	21.0 ± 0.67	2.39 ± 0.01	26.4	13.1 ± 0.17	63.6	344 ± 4.67	10.0	44.4 ± 1.73
C$_{12,13}$(PO)$_4$SO$_4$Na/5wt %NaCl	2.40 ± 0.04	32.7	12.6 ± 1.98	61.8	289 ± 10.2	5.53	24.1 ± 3.46	2.37 ± 0.01	23.9	14.3 ± 0.51	66.7	335 ± 3.25	8.81	38.7 ± 1.81
C$_{12,13}$(PO)$_4$SO$_4$Na/7wt %NaCl	2.37 ± 0.01	34.8	13.6 ± 0.04	59.9	348 ± 2.66	5.34	24.7 ± 2.62	2.38 ± 0.11	20.2	15.8 ± 3.51	71.3	289 ± 25.9	8.50	37.2 ± 6.68

Table 5 Point of zero charge (PZC) and zeta potential of methyl palmitate, cotton, and polyester in various solutions at 25 °C

Properties	Cotton	Polyester	Methyl palmitate
Point of zero charge (PZC)	2.90[a]	2.40[a]	2.20
Zeta potential (mV) in:			
DI water	−20.3 ± 5.0	−50.0 ± 5.0	−46.2 ± 2.7
0.1 wt% $C_{12,13}$-4PO-SO$_4$Na	−73.5 ± 6.7	−139 ± 7.6	−157 ± 5.5
0.1 wt% $C_{12,13}$-4PO-SO$_4$Na/1 wt% NaCl	−54.9 ± 3.4	−60.9 ± 7.2	−57.0 ± 4.3
0.1 wt% $C_{12,13}$-4PO-SO$_4$Na/3 wt% NaCl	−48.0 ± 4.8	−54.4 ± 4.6	−53.7 ± 2.0
0.1 wt% $C_{12,13}$-4PO-SO$_4$Na/5 wt% NaCl	−33.3 ± 1.0	−33.1 ± 2.8	−34.1 ± 2.3
0.1 wt% $C_{12,13}$-4PO-SO$_4$Na/7 wt% NaCl	−30.8 ± 2.7	−28.7 ± 2.5	−29.9 ± 1.2

[a] Data from previous work [14]
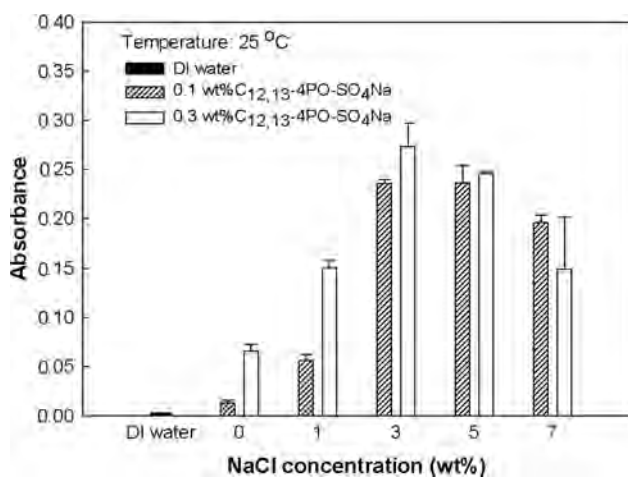
Fig. 9 Dispersion stability (absorbance) of methyl palmitate particles in surfactant solutions as a function of salinity as compared to DI water at 25 °C

dislodged as small particles or droplets, so the small particle size correlates with good wettability leading to high detergency efficiency.

Point of Zero Charge and Zeta Potential Results

Table 5 shows the point of zero charge (PZC) and zeta potential values of methyl palmitate, cotton, and polyester particles in various solution systems at 25 °C (pH 4–6). The PZC values of methyl palmitate, cotton, and polyester were 2.20, 2.90, and 2.40, respectively, indicating that the net surface charges of these three materials are always negative in detergency experiments because of the much higher pH values of both DI water and the studied extended surfactant solutions. The magnitude of the zeta potential of methyl palmitate is high despite it being fairly hydrophobic (contact angle with water of 82°) because of the ester functional group in methyl palmitate which is hydrolyzed into carboxyl and hydroxyl groups to provide negative charges [14, 15, 40, 41]. When DI water was replaced by the 0.1 wt% surfactant solution, the zeta potential of

methyl palmitate became more negative from −46.2 to −157 mV because of the anionic surfactant adsorption. The zeta potential values of both cotton, and polyester in the studied extended surfactant solution became more negative as compared to those in DI water and they also increased when the surfactant concentration increased [42]. This is probably due to higher surfactant adsorption on the solid with higher surfactant concentration, although higher adsorption doesn't necessarily occur since concentrations are well above the CMC. In contrast, with increasing NaCl concentration for any fixed extended surfactant concentration, the zeta potential of methyl palmitate, cotton, and polyester became less negative, due to compression of the double layer or reduction of Debye length next to the surface with increasing ionic strength [43, 44]. A high absolute zeta potential indicates that electrostatic repulsion could be an important factor in dispersion stability [45, 46].

Dispersion Stability

Figure 9 shows the dispersion stability (absorbance) of methyl palmitate solid particles (in terms of average absorbance values) as a function of salinity in the two surfactant systems (0.1 and 0.3 wt%) at 25 °C. The higher the absorbance, the greater the concentration of particles dispersed in the aqueous phase and thus the higher the dispersion stability. The presence of extended surfactant without added NaCl only marginally improved the dispersion stability of methyl palmitate solid particles as compared to DI water despite the fact that the zeta potential is much more negative in the presence of surfactant. Increasing NaCl concentration can greatly improve the dispersion stability; the maximum dispersion stability was found in the salinity range of 3–5 wt% which also produced the best detergency performance. So, dispersion stability is an important component of detergency since the dominant mechanism of solid removal is as particles, not through solubilization. However, the zeta potential decreases in magnitude with increasing NaCl concentration. Comparing effects of surfactant and NaCl

concentrations on zeta potentials and dispersion stability lead to the important conclusion that electrostatic stabilization of the dispersed particles is not the dominant factor in dispersion stability. Dispersion stability is not highest when the zeta potential is at maximum value. Parfitt and Wharton [47] studied the dispersion of solid particles in a surfactant solution and found that the dispersion followed a three-stage process. First, the wettability of solid particle surface occurred, as reflected by the corresponding contact angle. The surfactant solution is better able to penetrate into inter-particle clusters and crevices due to the reduction of the contact angle. Second, the solid particles are suspended in the solution by wetting, and thus dispersion stability occurs. Therefore, deaggregation of the solid

particle is required to achieve a good dispersion by repulsive force between charged particles. After the solid particles have been dispersed in the solution, the danger is that they will coagulate (aggregate) and redeposit. Therefore, the wettability (contact angle), particle size distribution, and dispersion stability of the particles are important to detergency efficiency.

Visual Observations

Figure 10 shows pictures of the washing solutions after the wash step using DI water (Fig. 10a) and two surfactant solutions (0.1 wt% surfactant with 5 wt% NaCl and 0.3 wt% surfactant with 1 wt% NaCl) at temperatures
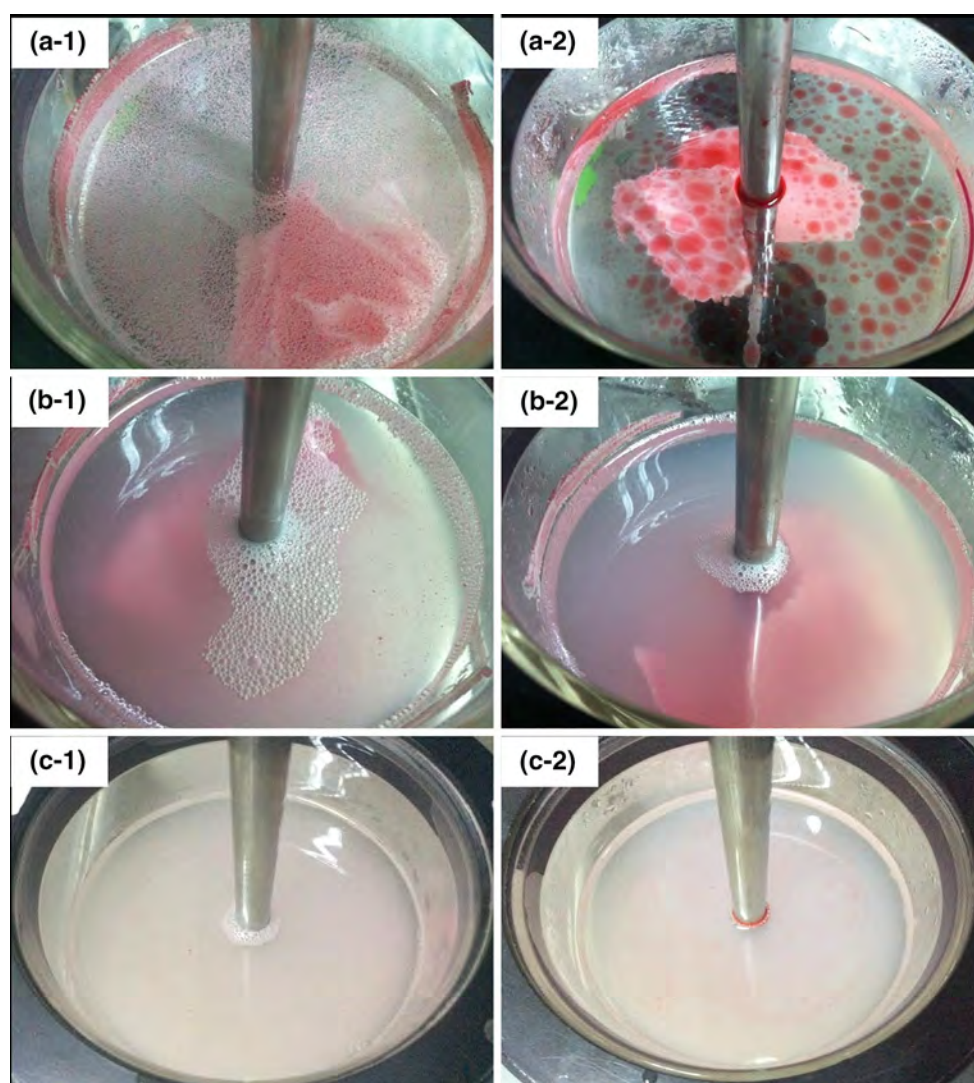
Fig. 10 Photographs of washing solutions after the wash step: **a-1** at below the melting point (25 °C) in DI water, **a-2** above the melting point (35 °C) in DI water, **b-1** below the melting point (25 °C) in 0.1 wt% $C_{12,13}(PO)_4SO_4Na$ and 5 wt% NaCl, **b-2** above the melting point (35 °C) in 0.1 wt% $C_{12,13}(PO)_4SO_4Na$ and 5 wt% NaCl, **c-1** below the melting point (25 °C) in 0.3 wt% $C_{12,13}(PO)_4SO_4Na$ and 1 wt% NaCl, **c-2** above the melting point (35 °C) in 0.3 wt% $C_{12,13}(PO)_4SO_4Na$ and 1 wt% NaCl

below and above the oil's melting point. In DI water, the removed oil was found mostly in solid particles floating on the surface of the washing solution with relatively large particle sizes at 25 °C and much larger liquid droplets at 35 °C. For detergency with surfactant solutions, the removed oil was found to suspend in the washing solution with much smaller particles and without either solid or liquid methyl palmitate particles or droplets floating on the surface.

Mechanistic Insights

Results on this paper shows the relationships between the removal mechanism of solid fat soil below and above the soil melting point. Above the melting point, lower IFT results in better detergency with varying temperature or salinity. Therefore, roll-up of liquid soil is an important mechanism [6–13]. Below the melting point, the detachment of soil as solid particles occurs by surfactant penetration, leading to the soil breaking up and floating away from the fabric surface into solution as small particles [48–50]. Surfactant and salinity improves wetting, dispersion stability, and decreases detached particle size. Unlike particulate soil, electrostatics are not the primary driving force for detergency.

References

1. Bubl JL. Laundering cotton fabric: Part I: effects of detergent type and water temperature on soil removal. Text Res J. 1970;40:637–43.
2. Chi YS, Obendorf SK. Effect of fiber substrates on appearance and removal of aged oily soils. J Surfactants Deterg. 2001;4:35–41.
3. Morris MA, Prato HH. The effect of wash temperature on removal of particulate and oily soil from fabrics of varying fiber content. Text Res J. 1982;52:280–6.
4. Breen NE, Durnam DJ, Obendorf SK. Residual oily soil distribution on polyester/cotton fabric alter laundering with selected detergents at various wash temperatures. Text Res J. 1984;54:198–204.
5. Obendorf SK, Klemash NA. Electron microscopical analysis of oily soil penetration into cotton and polyester/cotton fabrics. Text Res J. 1982;52:434–42.
6. Miller CA, Raney KH. Solubilization–emulsification mechanisms of detergency. Colloids Surf A Physicochem Eng Asp. 1993;74:169–215.
7. Tanthakit P, Chavadej S, Scamehorn JF, Sabatini DA, Tongcumpou C. Microemulsion formation and detergency with oily soil: IV. Effect of rinse cycle design. J Surfactants Deterg. 2008;11:117–28.
8. Tanthakit P, Nakrachata-Amorn A, Scamehorn JF, Sabatini DA, Tongcumpou C, Chavadej S. Microemulsion formation and detergency with oily soil: V. Effects of water hardness and builder. J Surfactants Deterg. 2009;12:173–83.
9. Tanthakit P, Ratchatawetchakul P, Chavadej S, Scamehorn JF, Sabatini DA, Tongcumpou C. Palm oil removal from fabric using microemulsion-based formulations. J Surfactants Deterg. 2013;13:485–95.
10. Tongcumpou C, Acosta EJ, Quencer LB, Joseph AF, Scamehorn JF, Sabatini DA, Chavadej S, Yanumet N. Microemulsion formation and detergency with oily soils: I. Phase behavior and interfacial tension. J Surfactants Deterg. 2003;6:191–203.
11. Tongcumpou C, Acosta EJ, Quencer LB, Joseph AF, Scamehorn JF, Sabatini DA, Chavadej S, Yanumet N. Microemulsion formation and detergency with oily soils: II. Detergency formulation and performance. J Surfactants Deterg. 2003;6:205–14.
12. Tongcumpou C, Acosta EJ, Quencer LB, Joseph AF, Scamehorn JF, Sabatini DA, Yanumet N, Chavadej S. Microemulsion formation and detergency with oily soils: III. Performance and mechanisms. J Surfactants Deterg. 2005;8:147–56.
13. Tongcumpou C, Acosta EJ, Scamehorn JF, Sabatini DA, Yanumet N, Chavadej S. Enhanced triolein removal using microemulsions formulated with mixed surfactants. J Surfactants Deterg. 2006;9:181–9.
14. Rojvoranun S, Chadavipoo C, Pengjun W, Chavadej S, Scamehorn JF, Sabatini DA. Mechanistic studies of particulate soil detergency: I. Hydrophobic soil removal. J Surfactants Deterg. 2012;15:277–89.
15. Rojvoranun S, Chavadej S, Scamehorn JF, Sabatini DA. Mechanistic studies of particulate soil detergency: II: Hydrophilic soil removal. J Surfactants Deterg. 2012;15:663–77.
16. Scheuing DR. Detergency of a nonionic surfactant toward tristearin studied by FT-IR. Langmuir. 1990;6:312–7.
17. Powe WC. Removal of fatty soils from cotton in aqueous detergent systems. J Am Oil Chem Soc. 1963;40:290–4.
18. Kawase T, Yamada K, Fujii T, Minagawa M. Removal of fatty acid by sodium dodecyl sulfate solution removal mechanism by solubilization. J Jpn Oil Chem Soc. 1991;40:126–32.
19. Kawase T, Enishi H, Fujii T, Minagawa M. Removal of fatty acid by solubilization into micelles of nonionic surfactants. J Jpn Oil Chem Soc. 1994;43:124–30.
20. Charoensaeng A, Sabatini DA, Khaodhiar A. Styrene solubilization and adsolubilization on an aluminum oxide surface using linker molecules and extended surfactants. J Surfactants Deterg. 2008;11:61–71.
21. Do LD, Sabatini DA. Aqueous extended-surfactant based method for vegetable oil extraction: proof of concept. J Am Oil Chem Soc. 2010;87:1211–20.
22. Miñana-Perez M, Graciaa A, Lachaise J, Salager JL. Solubilization of polar oils with extended surfactants. Colloid Surface A. 1995;100:217–24.
23. Witthayapanyanon A, Acosta EJ, Harwell JH, Sabatini DA. Formulation of ultralow interfacial tension systems using extended surfactants. J Surfactants Deterg. 2006;9:331–9.
24. Phan TT, Witthayapanyanon A, Harwell JH, Sabatini DA. Microemulsion-based vegetable oil detergency using an extended surfactant. J Surfactants Deterg. 2010;13:313–9.
25. Do LD, Chodchanok A, Scamehorn JF, Sabatini DA. Detergency of vegetable oils and semi-solid fats using microemulsion

mixtures of anionic extended surfactants: the HLD concept and cold water applications. J Surfactants Deterg. 2014;18:373–82.

26. Annual Book of ASTM standards, vol 15.04 Standard guide for evaluating stain removal performance in home laundering, in American Society for test and materials ASTM D 4265–98, West Conshohocken; 2000.

27. Goel S. Measuring detergency of oily soils in the vicinity of phase inversion temperatures of commercial nonionic surfactants using an oil-soluble dye. J Surfactants Deterg. 1998;1:221–6.

28. Scamehorn JF, Sabatini DA, Harwell JH. Surfactants—Part I: Fundamentals. In: Atwood J, Stead J, editors. Encyclopedia of supramolecular chemistry. New York: Marcel Dekker; 2004. p. 1458–69.

29. Moayedi H, Asadi A, Moayedi F, Huat BBK, Kazemian S. Using secondary additives to enhance the physicochemical properties of kaolinite. Int J Phys Sci. 2011;6:2004–15.

30. Schramm LL, Stasiuk EN, Marangoni DG. Surfactants and their applications. Annu Rep Prog Chem Sect C. 2003;99:3–48.

31. Corrin ML, Harkins WD. The effect of salts on the critical concentration for the formation of micelles in colloidal electrolytes. J Am Chem Soc. 1947;19:683–8.

32. Rathman JF, Scamehorn JF. Counterion binding on mixed micelles. J Phys Chem. 1984;88:5807–16.

33. Rathman JF, Scamehorn JF. Counterion binding on mixed micelles: effect of surfactant structure. Langmuir. 1987;3:372–7.

34. Phan TT, Harwell JH, Sabatini DA. Effects of triglyceride molecular structure on optimum formulation of surfactant-oil-water systems. J Surfactants Deterg. 2010;13:189–94.

35. Phan TT, Attaphong C, Sabatini DA. Effect of extended surfactant structure on interfacial tension and microemulsion formation with triglycerides. J Am Oil Chem Soc. 2011;88:1223–8.

36. Illman JC, Finger BM, Shebs WT, Albin TB. Cold water detergency studies using radiolabeled soils. J Am Oil Chem Soc. 1970;47:379–83.

37. Gordon BE, Roddewig J, Shebs WT. A double label radiotracer approach to detergency studies. J Am Oil Chem Soc. 1967;44:289–94.

38. Fort T, Billica HR, Grindstaff TH. Studies of soiling and detergency. J Am Oil Chem Soc. 1968;45:354–61.

39. Velásquez J, Scorzza C, Vejar F, Forgiarini AM, Antón RE, Salager JL. Effect of temperature and other variables on the optimum formulation of anionic extended surfactant–alkane–brine systems. J Surfactants Deterg. 2010;13:69–73.

40. Iwadare Y, Suzawa T. ζ-potentials of natural and synthetic fibers in SDS solutions and the viscosity of SDS solutions above the critical micelle concentration. B Chem Soc Jpn. 1970;43:2326–31.

41. Stachurski J, MichaŁek M. The effect of the ζ potential on the stability of a non-polar oil-in-water emulsion. J Colloid Interf Sci. 1996;184:433–6.

42. Chanwattanakit J. Mechanism and performance of solid non-particulate soil (waxy solid) removal from fabrics. Doctoral Dissertation, The Petroleum and Petrochemical College, Chulalongkorn University, Thailand; 2016.

43. Gu Y, Li D. An electrical suspension method for measuring the electric charge on small silicone oil droplets dispersed in aqueous solutions. J Colloid Interf Sci. 1997;195:343–52.

44. Gu Y, Li D. Electric charge on small silicone oil droplets dispersed in ionic surfactant solutions. Colloid Surface A. 1998;139:213–25.

45. Cosgrove T. Colloid science principles, methods and applications. 2nd ed. West Sussex: Wiley; 2010.

46. Rosen MJ. Surfactants and interfacial phenomena. 3rd ed. New York: Wiley; 2004.

47. Parfitt GD, Wharton DG. The dispersion of rutile powder in aqueous surfactant solution. J Colloid Interf Sci. 1971;38:431–9.

48. Lawrence ASC. The mechanism of detergence. Nature. 1959;183:1491–4.

49. Scott BA. Mechanism of fatty soil removal. J Appl Chem. 1963;13:133–44.

50. Fort T, Billica HR, Grindstaff TH. Studies of soiling and detergency. Part II: detergency experiments with model fatty soils. Text Res J. 1996;36:99–112.

Jarussri Chanwattanakit received her B.S. (2008) degree in industrial chemistry from Faculty of Science, Chiang Mai University. She is currently a Ph.D. candidate in the Petrochemical Technology Program at The Petroleum and Petrochemical College, Chulalongkorn University, Thailand.

John F. Scamehorn is an Emeritus Director of the Institute for Applied Surfactant Research at the University of Oklahoma, where he is an Asahi Glass Chair Emeritus in Chemical Engineering. He received his B.S. and M.S. degrees at the University of Nebraska and his Ph.D. degree at the University of Texas, all in chemical engineering. Dr. Scamehorn has worked for Shell, Conoco, and DuPont, and has been on a number of editorial boards for journals in the area of surfactants and of separation science. He has coedited five books and coauthored over 200 technical papers. His research interests include surfactant properties important in consumer product formulation and thermodynamics of surfactant aggregation processes.

David A. Sabatini is a David Ross Boyd Professor and Sun Oil Company Endowed Chair of Civil Engineering and Environmental Science, Associate Director of the Institute for Applied Surfactant Research, and Director of the WaTER Center at the University of Oklahoma. He received his B.Sc. degree from the University of Illinois (1981), his M.Sc. degree from Memphis State University (1985), and his Ph.D. degree from Iowa State University (1989). His research focuses on surfactant-based environmental technologies, advanced microemulsion systems for vegetable oil extraction, biofuel production and cleaning systems, and sustainable technologies for drinking water treatment in developing countries.

Sumaeth Chavadej is a Professor at The Petroleum and Petrochemical College, Chulalongkorn University. He received his B.Sc. degree in chemical engineering from Chulalongkorn University (1971), his M.Sc. degree in public health engineering from The University of Newcastle upon Tyne (1978), and his Ph.D. degree in chemical engineering from Monash University, Australia (1985). He has published more than 150 articles in international journals. His research focuses on the areas of applied surfactant, plasma for chemical conversion, biohydrogen, and biomethane.

Research article

Escherichia coli expressing endoglucanase gene from Thai higher termite bacteria for enzymatic and microbial hydrolysis of cellulosic materials

CrossMark

Kessara Seneesrisakul [a], Saadet Albayrak Guralp [b], Erdogan Gulari [b], Sumaeth Chavadej [a,c,*]

[a] *The Petroleum and Petrochemical College, Chulalongkorn University, Soi Chula 12, Phyathai Road, Pathumwan, Bangkok 10330, Thailand*
[b] *Department of Chemical Engineering, University of Michigan, Ann Arbor, MI 48109, USA*
[c] *Center of Excellence on Petrochemical and Materials Technology, Chulalongkorn University, Soi Chula 12, Phyathai Road, Pathumwan, Bangkok 10330, Thailand*

ARTICLE INFO

ABSTRACT

Background: Endoglucanase plays a major role in initiating cellulose hydrolysis. Various wild-type strains were searched to produce this enzyme, but mostly low extracellular enzyme activities were obtained. To improve extracellular enzyme production for potential industrial applications, the endoglucanase gene of *Bacillus subtilis* M015, isolated from Thai higher termite, was expressed in a periplasmic-leaky *Escherichia coli*. Then, the crude recombinant endoglucanase (EglS) along with a commercial cellulase (Cel) was used for hydrolyzing celluloses and microbial hydrolysis using whole bacterial cells.
Results: *E. coli* Glu5 expressing endoglucanase at high levels was successfully constructed. It produced EglS (55 kDa) with extracellular activity of 18.56 U/mg total protein at optimal hydrolytic conditions (pH 4.8 and 50°C). EglS was highly stable (over 80% activity retained) at 40–50°C after 100 h. The addition of EglS significantly improved the initial sugar production rates of Cel on the hydrolysis of carboxymethyl cellulose (CMC), microcrystalline cellulose, and corncob about 5.2-, 1.7-, and 4.0-folds, respectively, compared to those with Cel alone. *E. coli* Glu5 could secrete EglS with high activity in the presence of glucose (1% *w/v*) and Tween 80 (5% *w/v*) with low glucose consumption. Microbial hydrolysis of CMC using *E. coli* Glu5 yielded 26 mg reducing sugar/g CMC at pH 7.0 and 37°C after 48 h.
Conclusions: The recombinant endoglucanase activity improved by 17 times compared with that of the native strain and could greatly enhance the enzymatic hydrolysis of all studied celluloses when combined with a commercial cellulase.

1. Introduction

Cellulosic biomass obtained from agricultural residues offers a higher potential than grains and edible feedstocks to serve as a sustainable resource with lower production costs for alternative liquid fuel production in the future [1]. The conversion of cellulose to ethanol is typically accomplished through the enzymatic hydrolysis of cellulosic materials to reducing sugars, followed by fermentation of the produced sugars to ethanol [2]. The enzymatic hydrolysis of cellulose involves synergistic actions of endoglucanases, exoglucanases, and β-glucosidases. Endoglucanases play a major role in initiating cellulose hydrolysis by randomly cleaving internal glucosidic bonds in cellulose fibers and creating free chain ends; exoglucanases release cellobiose either from reducing or non-reducing chain ends; and β-glucosidases finally hydrolyze the cellobiose to glucose [3].

The use of cellulolytic bacteria for the large-scale production of enzymes has increased in recent years because of their short doubling times and ease of cultivation at high cell densities using inexpensive carbon and nitrogen sources [4]. A number of cellulolytic bacteria from termite gut and other sources have been studied and continually developed by genetic engineering techniques to achieve desired properties and high productivity of endoglucanase for industrial applications [5,6,7,8,9,10].

Because of the high cost of enzyme production, biofuel production from cellulose is not feasible at present [11,12]. A consolidated bioprocess, combining cellulase production and conversion of cellulose into desired products as a single step, has been the subject of increased research efforts in recent years [13]. The absence of cellulase whole cell separation step can lower the overall process cost [14]. The term "microbial hydrolysis" referred to cultures of cellulolytic bacteria growing in the presence of cellulose substrate, which is to be

hydrolyzed, without added enzyme [15]. Currently, there is little research available on cellulose hydrolysis using whole cells [14,15]. Hence, a study on this issue is of great interest because it will lead to potential applications for large-scale biofuel production from lignocellulosic materials.

In this study, an endoglucanase gene from *Bacillus subtilis* M015, isolated from Thai higher termites (*Microcerotermes* sp.) [5], was cloned into a periplasmic-leaky *Escherichia coli* strain. The crude recombinant endoglucanase produced by *E. coli* expressing the endoglucanase gene was characterized. A mixture of the recombinant endoglucanase and commercial cellulase was tested for their hydrolytic activity on different cellulosic materials such as soluble cellulose, insoluble microcrystalline cellulose, and corncob compared with the commercial enzyme alone. The recombinant bacteria were also studied for glucose consumption and microbial hydrolysis. Moreover, the effects of Tween 80 on bacterial growth and endoglucanase production were determined.

2. Materials and methods

2.1. Bacterial strains, vectors, and culture conditions

B. subtilis M015 (GenBank accession number **KP192484**), isolated from Thai higher termites (*Microcerotermes* sp.) by our research group [5], was preserved by lyophilization and grown in a 65 modified Deutsche Sammlung von Mikroor Ganismen und Zellkulturen (DSMZ) medium containing 5 g/L of carboxymethyl cellulose (CMC), 4 g/L of yeast extract, and 10 g/L of malt extract at pH 7.0. *E. coli* JE5505 (carrying an *lpp*-deletion), obtained from the Coli Genetic Stock Center (CGSC), Yale University, was maintained in a lysogeny broth (LB; 10 g/L of tryptone, 5 g/L of yeast extract, and 5 g/L of sodium chloride at pH 7.0) for use as an expression host in this study. The expression plasmid, pFLAG-CTS, carrying an OmpA secretion signal for the periplasmic expression of recombinant proteins, and ampicillin sodium salt (100 μg/mL), used as the selection agent, were purchased from Sigma-Aldrich. Isopropyl β-ᴅ-thiogalactopyranoside (IPTG, Invitrogen Life Technologies) at 1 mM concentration was added to the culture to induce protein expression.

2.2. Amplification, cloning, and expression of endoglucanase gene

To obtain the DNA template for gene amplification, *B. subtilis* M015 cells were harvested in the mid-exponential growth phase and separated by centrifugation, and genomic DNA was extracted from the cell pellets using the DNeasy Blood and Tissue Kit (QiaGen, USA). For the amplification of the gene coding for endoglucanase by polymerase chain reaction (PCR), two primers were designed on the basis of the reference sequence of the endoglucanase (*eglS*) gene of *B. subtilis* subsp. *subtilis* 168 (GenBank accession number **BSU18130**); forward primer: 5′-GATCC<u>AAGCTT</u>CTATGAAACGGTCAATCTCTAT-3′, reverse primer: 5′-CTCA<u>CTCGAG</u>TTACTAATTTGGTTCTGTTCCC-3′. Two restriction sites, *Hind*III and *Xho*I, were incorporated to allow directional cloning of the PCR products into the expression vector pFLAG-CTS. The *eglS* gene was amplified using Phusion Hot Start II polymerase (Thermo Scientific, USA) under the following PCR conditions: 2 min of initial denaturation at 98°C, 30 cycles of 30 s denaturation at 98°C, 30 s of annealing at 55°C, and 30 s of extension at 72°C, followed by 5 min of final extension at 72°C.

PCR products were double-digested with *Hind*III and *Xho*I and cloned into the plasmid pFLAG-CTS, which was also digested with the same restriction enzymes. The ligation products (pCTS-*eglS*) were transformed into *E. coli* JE5505 by electroporation. Positive clones were confirmed by recovering plasmid DNA using the QIAprep Spin Miniprep Kit (QiaGen, USA) and running on 0.8% agarose gel. The presence of the endoglucanase gene was confirmed by DNA sequencing. The transformed *E. coli* containing pCTS-*eglS* was named

E. coli Glu5. *E. coli* carrying an empty plasmid was included as a control in the study. All molecular biology studies were performed by following standard techniques [16].

2.3. Preparation of secreted recombinant endoglucanase and size verification

E. coli Glu5 was cultured overnight in 2 mL LB-ampicillin as an inoculum in an orbital shaker at 180 rpm and 37°C under aerobic conditions and then diluted at a ratio of 1:400 into a 250-mL Erlenmeyer flask containing 100 mL of fresh LB-ampicillin medium. The flask was incubated with constant shaking. At the mid-exponential phase of the culture, when the optical density (OD_{600}) reached 0.5, endoglucanase (EglS) expression was induced with 1 mM IPTG. The optimal culturing time of *E. coli* Glu5 for secreted recombinant EglS production was determined during 40 h post-induction by the DNS assay (explained below) and further used for producing enzyme stock. The secreted EglS used as crude form was obtained by centrifuging the cell culture at $11000 \times g$ for 10 min at 4°C and filtered through a 0.22-μm membrane. To verify the molecular size of the secreted mature protein, the secreted EglS was concentrated 10-fold by ultrafiltration (10 kDa MW membrane cut-off, Amicon, Beverly, MA, USA). The protein profile of the concentrated enzyme was determined by SDS-PAGE (12% (*w/v*) acrylamide resolving gel) and native-PAGE (containing 1% (*w/v*) CMC) for zymogram analysis [17]. The cell-free culture supernatant of *E. coli* carrying the empty plasmid was prepared in the same manner and used as a control. The theoretical molecular weight of EglS was calculated using the online tool available at Georgetown University Protein Information Resources Website (http://pir.georgetown.edu/cgi-bin/comp_mw.pl).

2.4. Hydrolytic ability assay

The hydrolytic ability of *E. coli* Glu5 was tested by the Congo red assay [18]. The inoculum (5 μL) was spotted on LB-ampicillin agar plates containing 1% (*w/v*) CMC and 1 mM IPTG. For comparison with the cloned strain (*E. coli* Glu5), *B. subtilis* M015 was assayed on 65 modified DSMZ agar plates at 37°C for 24 h, and then hydrolysis zones were visualized by 1% (*w/v*) Congo red reagent staining for 10 min and destaining with a 1 M sodium chloride solution. The presence of a clear zone around the colonies indicated the hydrolysis of cellulose by the secretion of active endoglucanase. The hydrolysis capacity value was calculated from the clear zone diameter divided by the colony diameter.

2.5. Enzymatic activity and protein determination

Endoglucanase activity was determined from crude enzyme by the standard DNS method using glucose as the standard reference [19]. The assays were conducted in triplicates in 96-well-microplates. Each diluted crude enzyme sample was incubated with 2% (*w/v*) CMC solubilized in 50 mM sodium citrate buffer (pH 4.8) at an equivalent ratio (total volume 60 μL). The mixture was incubated at 50°C for 30 min. The reaction was stopped by adding an equal volume of a DNS solution (1.4% (*w/v*) 3,5-dinitrosalicylic acid, 0.28% phenol, 1.4% sodium hydroxide, 28% sodium potassium tartrate, and 0.07% sodium sulfite) and heating at 95°C for 5 min and, finally, quickly cooled to room temperature. The degree of enzymatic hydrolysis of the soluble cellulose (CMC) was determined spectrophotometrically by measuring the absorbance at 540 nm in a VersaMax Microplate Reader (Molecular Probes, USA). One Unit (U) of endoglucanase activity was defined as the amount of enzyme producing 1 μmol of reducing sugars from CMC per min under the assay conditions. The total protein concentration was determined by the Bradford method (Bio-Rad) using bovine serum albumin standards. The specific activity was

calculated from the number of units of enzyme activity per mg of total proteins.

The hydrolytic mixture of added EglS enzyme at a volume ratio of 1:40 in 50 mM sodium citrate buffer containing 1% (w/v) CMC (9.4 U/g) was incubated at the optimum pH (4.8) and temperature (50°C) for 30 min and then analyzed for sugar products by high-performance liquid chromatography (HPLC) equipped with a refractive index detector (6040 XR, Spectra-Physics, USA) and an Aminex HPX-87H column (Bio-Rad Lab, USA). Sulfuric acid (H_2SO_4) at 5 mM concentration was used as a mobile phase at a flow rate of 0.6 mL/min, and the column temperature was controlled at 60°C. The supernatant of the cultured E. coli carrying the empty plasmid was used as control.

2.6. Characterization of crude endoglucanase

To determine the optimum pH for maximum endoglucanase activity of crude EglS, samples were diluted with citrate and phosphate buffers of various pH (50 mM sodium citrate buffer for pH 3.0–6.0 and 50 mM sodium phosphate buffer for pH 7.0–8.0), with 2% (w/v) CMC at an equivalent volumetric ratio, and incubated at 50°C. The effect of temperature on the endoglucanase activity was determined by incubating the diluted samples with 2% (w/v) CMC in 50 mM sodium citrate buffer (pH 4.8) at an equivalent volumetric ratio under temperatures ranging from 25°C to 80°C. The enzymatic hydrolytic reactions were stopped after 30 min by adding the DNS solution, and the endoglucanase activities were assessed as previously described. Thermal stability was determined by pre-incubating the diluted EglS in the 50 mM sodium citrate buffer (pH 4.8) at different temperatures of 40°C, 50°C, and 60°C. The residual endoglucanase activity of samples was determined as the percentage of the initial activity during an incubation period of 100 h.

The kinetic parameter values of the fresh crude EglS on CMC hydrolysis in terms of Michaelis–Menten constants (K_m) and maximum velocity (V_{max}) were determined using the Lineweaver-Burk plots. The reaction was initiated by adding and mixing the enzyme (0.715 U/mL of reaction mixture) to CMC solutions of various initial CMC concentrations (2.5–47 mg/mL). The initial reaction velocity of the enzyme that produced reducing sugars was determined under the optimal conditions (pH 4.8 and 50°C) within 10 min of reaction time.

2.7. Enzymatic hydrolysis studies with various cellulosic substrates

Crude EglS, commercial cellulase (Cel), and a mixture of the two enzymes were tested for their hydrolytic abilities on various cellulosic substrates including a soluble cellulose (CMC), an insoluble microcrystalline cellulose (Avicel PH-101, Sigma-Aldrich), and a milled corncob (CC) as lignocellulose. The activity of Cel exoglucanase, obtained from Trichoderma reesie ATCC 26921 (Sigma Aldrich), was determined to be 62 FPU/mL by the DNS method. Both CMC and Avicel substrates were used as received without any treatment. A corncob sample, obtained from Kanchanaburi province, Thailand, was dried overnight at 105°C, milled by a hammer mill (Fitzmill Fitzpatrick DAS06 5HP), and sieved to obtain a particle size range of 60–80 mesh. The CC, composed of 44 ± 2% cellulose, 34 ± 1% hemicellulose, 12 ± 1% lignin, and 10 ± 1% extractives on dry weight basis, was used in the experiment without any treatment [20]. The properties of all test cellulosic substrates are summarized in Table 1 [20,21,22,23]. The enzymatic hydrolysis tests were conducted with 100 mL of total reaction volume in Erlenmeyer flasks. The enzyme solutions of EglS (50 U), Cel (50 FPU), and the mixture of EglS and Cel (50 U and 50 FPU, respectively) were loaded into separately into flask containing 0.5 g of each dried substrate in the 50 mM sodium citrate buffer (pH 4.8). Moreover, 0.01% sodium azide reagent was added to prevent microbial contamination. For controls, all the studied substrates were suspended in the buffer solution without any added enzymes. All flasks were incubated at 50°C in a shaking incubator (180 rpm).

Table 1
Properties of cellulosic substrates as crystallinity index (CrI), fraction of β-glucosidic bond accessible to cellulase (F_a), average degree of polymerization (DP_n), degree of substitution (DS), and fraction of reducing ends (F_{Re}) [20,21,22,23].

Substrate	Size (μm)	CrI	F_a (%)	DP_n	DS	F_{Re} (%)
Soluble						
Carboxymethyl cellulose (CMC)	–	–	100	400	0.65–0.9	0.05–1
Insoluble						
Microcrystalline cellulose (Avicel)	50	0.7–0.9	0.6	90–220	–	0.2–0.67
Corncob (CC)	300	0.57	–	–	–	–

The samples were collected every 20 h for 100 h and boiled for 5 min to stop the hydrolytic reaction. Subsequently, the samples were centrifuged and filtered through a 0.22-μm filter for sugar analysis by HPLC. The initial and overall sugar production rates of each hydrolytic reaction were calculated from the total concentration of glucose, cellobiose, and xylose produced in the first 20 h and the entire range of 100 h, respectively.

2.8. Study on the effect of glucose on bacterial growth and endoglucanase production

To determine the effects of glucose on the growth profile and endoglucanase production of E. coli Glu5 compared with B. subtilis M015, glucose (1% w/v) was supplemented in the medium (pH 7.0). E. coli Glu5 was inoculated (1:400) in LB-ampicillin medium (100 mL) with glucose and without glucose as a control. One mM of IPTG was used to induce protein expression at 4 h post inoculation. B. subtilis M015 was diluted at the same ratio (1:400) in LB with and without glucose. CMC (1% w/v) was used as the enzyme-induced substrate. All flasks were incubated at 37°C and 180 rpm for 48 h. The absorbance of samples obtained from the cultures was measured at OD_{600} to determine cell concentration. The endoglucanase activity of cell-free supernatant samples was determined by the DNS assay. The concentration of un-metabolized glucose was determined by HPLC. All experiments were performed in triplicate.

2.9. Microbial hydrolysis experiments of CMC using E. coli Glu5

Microbial hydrolysis of CMC using E. coli Glu5 was investigated by growing E. coli Glu5 in medium containing CMC as substrate to determine whether the secreted EglS from bacterial cells could directly hydrolyze the substrate present in the medium and produce sugar products. Various concentrations of CMC (10–50 g/L) were added to the LB-ampicillin medium (pH 7.0). E. coli Glu5 inoculum was then added into each medium at a volumetric ratio of 1:400, and the entire experiment was performed at 37°C and 180 rpm for 48 h. The reducing sugar amount in the culture solution was determined using the DNS reagent.

2.10. Study of toxicity of Tween 80 on E. coli Glu5 growth and activity of the secreted enzyme

Polyoxyethylenesorbitan monooleate (Tween 80, Sigma-Aldrich), a nonionic surfactant, was added to the LB-ampicillin medium at different concentrations (0.1–10% (w/v)). The OD_{600} of cultures and EglS activities of the supernatants obtained from the stationary phase were measured to determine the toxicity of the added surfactant.

```
EGD-AK10  MKRSISIFITCLLITLLTMGGNLASPASAAGTKTPVAKNGQLSIKGTQLVNRDGKAVQLK 60
168       MKRSISIFITCLLITLLTMGGNIASPASAAGTKTPVAKNGQLSIKGTQLVNRDGKAVQLK 60
M015      MKRSISIFITCLLITLLTMGGNLASPASAAGTKTPVAKNGQLSIKGTQLVNRDGKAVQLK 60
          *********************.*************************::**********

EGD-AK10  GISSHGLQWYGEYVNKDSLKWLRDDWGITVFRAAMYTADGGYIDNPSVKNKVKEAVEAAK 120
168       GISSHGLQWYGEYVNKDSLKWLRDDWGITVFRAAMYTADGGYIDNPSVKNKVKEAVEAAK 120
M015      GISSHGLQWYGEYVNKDSLKWLRDDWGITVFRAAMYTADGGYIDNPSVKNKVKEAVEAAK 120
          ************************************************************

EGD-AK10  ELGIYVIIDWHILNDGNPNQNKEKAKEFFKEMSSLYGNTPNVIYEIANEPNGDVNWKRDI 180
168       ELGIYVIIDWHILNDGNPNQNKEKAKEFFKEMSSLYGNTPNVIYEIANEPNGDVNWKRDI 180
M015      ELGIYVIIDWHILNDGNPNQNKEKAKEFFKEMSSLYGNTPNVIYEIANEPNGDVNWKRDI 180
          ************************************************************

EGD-AK10  KPYAEEVISVIRKNDPDNIIIVGTGTWSQDVNDAADDQLKDANVMYALHFYAGTHGQFLR 240
168       KPYAEEVISVIRKNDPDNIIIVGTGTWSQDVNDAADDQLKDANVMYALHFYAGTHGQFLR 240
M015      KPYAEEVISVIRKNDPDNIIIVGTGTWSQDVNDAADDQLKDANVMYALHFYAGTHGQFLR 240
          ************************************************************

EGD-AK10  DKANYALSKGAPIFVTEWGTSDASGNGGVFLDQSREWLKYLDSKTISWVNWNLSDKQESS 300
168       DKANYALSKGAPIFVTEWGTSDASGNGGVFLDQSREWLKYLDSKTISWVNWNLSDKQESS 300
M015      DKANYALSKGAPIFVTEWGTSDASGNGGVFLDQSREWLKYLNSKTISWVNWNLSDKQESS 300
          *****************************************:*****************

EGD-AK10  SALKSGASKTGGWQLSDLSASGTFVRENILGTKDSTKDIPETPAKDKPTQENGISVQYRA 360
168       SALKPGASKTGGWRLSDLSASGTFVRENILGTKDSTKDIPETPSKDKPTQENGISVQYRA 360
M015      SALKPGASKTGGWQLSDLSASGTFVRENILGTKDSTKDIPETPAKDKPTQENGISVQYRA 360
          ****.*******.*:*****************************:**************

EGD-AK10  GDGSMNSNQIRPQLQIKNNGNTTVDLKDVTARYWYKAKNKGQNFDCDYAQIGCGNVTHKF 420
168       GDGSMNSNQIRPQLQIKNNGNTTVDLKDVTARYWYKAKNKGQNFDCDYAQIGCGNVTHKF 420
M015      GDESMNSNQIRPQLQIKNNGSTTVDLKDVTARYWYKAKNKGQNFDCDYAQIGCGNVTHKF 420
          ** ******************.*************************************

EGD-AK10  VTLHKPKQGADTYLELGFKNGTLAPGASTGNIQLRLHNDDWSNYAQSGDYSFFKSNTFKT 480
168       VTLHKPKQGADTYLELGFKNGTLAPGASTGNIQLRLHNDDWSNYAQSGDYSFFKSNTFKT 480
M015      VTLHKPKQGADTYLELGFKNGTLAPGASTGNIQLRLHNDDWSNYAQSGDYSFFKSNTFKT 480
          *****************:******************************************

EGD-AK10  TKKITLYDQGKLIWGTEPN 499
168       TKKITLYDQGKLIWGTEPN 499
M015      TKKITLYNHGKLIWGTEPN 499
          *******::**********
```

Fig. 1. Sequence alignment of *B. subtilis* M015 endoglucanase (**KP223322**) to that of *B. subtilis* ssp. *subtilis* 168 and EGD-AK10 (**CAB13696**, **WP021479778.1**). The differences between sequences are framed in red. Conserved domains are shown by straight colored bars; yellow bar indicates residues 50 to 296 corresponding to cellulase-encoding sequence (glycosyl hydrolase family 5) and blue bar indicates residues 357 to 436 corresponding to cellulose-binding domain (CBM3) (determined by NCBI Protein Blast).

3. Results and discussion

3.1. Cloning and sequencing results

Amplification of the endoglucanase gene of *Bacillus subtilis* M015 yielded a 1520-bp fragment, which was subsequently cloned into pFLAG-CTS and sequenced. DNA sequencing of the cloned fragment yielded a 1497-bp long open reading frame (ORF) encoding for a 499-amino acid protein with a calculated molecular weight of 55,294 Da. Further investigation of the sequence across GenBank database revealed that the amino acid sequence of *B. subtilis* M015 endoglucanase (accession number **KP223322**) is 99% identical to that of *B. subtilis* EGD-AK10 (**WP021479778.1**) and E1 (**CCU58432.1**), 98% identical to that of *B. subtilis* subsp. *subtilis* 168 (**CAB13696**) and *B.* sp. HY2-3 (**AAV34758.1**), and 93% identical to that of *B.* sp. NK2 (**ADO85705.1**). The alignment of *B. subtilis* M015 endoglucanase with the two reference sequences is shown in Fig. 1. These findings confirm that endoglucanase belongs to glycoside hydrolase (GH) family 5.

3.2. Secretory expression and high activity of recombinant endoglucanase

To verify the expression and secretion of the recombinant endoglucanase (EglS) from periplasmic-leaky *E. coli*, the supernatant samples were visualized on 12% SDS-PAGE gel stained with Coomassie Blue (Biorad) (Fig. 2a). The band corresponding to recombinant endoglucanase was observed at 55 kDa (lane 2). Two additional proteins around 41 and 37 kDa were also observed on the gel, which are most likely the truncated products of EglS due to proteolysis. A barely visible band of approximately 37 kDa was also present in the concentrated supernatant samples of induced *E. coli* carrying empty plasmid (lane 4), which possesses no detectable cellulase activity. The CMC-zymogram of EglS (lane 5) showed two bands consistent with those in lane 2, which confirms that the smaller band does correspond to truncated EglS with some preserved cellulase activity.

The secretion of the recombinant EglS was further verified by the Congo red assay. The presence of a clear zone around *E. coli* Glu5 colony indicated hydrolytic activity on the added CMC by the secreted extracellular enzyme under aerobic incubation, whereas no clear zone was found around the control colonies. The clear zone of *E. coli* Glu5 was significantly larger than that of the native strain *B. subtilis* M015 (Fig. 2b) with hydrolysis capacities of 2.66 ± 0.34 and 1.63 ± 0.02, respectively, corresponding to a 63% increase due to enhanced expression and secretion of the recombinant EglS enzyme by *E. coli*.

From the crude enzyme production profile (Fig. 2c), it was determined that *E. coli* Glu5 secreted crude EglS with a maximum specific endoglucanase activity of 18.56 U/mg total protein (an endoglucanase activity of 3.68 U/mL and a total protein of 0.198 mg/mL) at 16 h post induction. This level is approximately 17 times higher than that of the native strain *B. subtilis* M015 (1.098 U/mg total protein) [5]. This high activity of crude EglS toward CMC, achieved by *E. coli* JE5505-based expression system, also appears to be superior to other crude endoglucanases from *Bacillus velesensis* P3-1 and P4-6 (0.015 U/mL) [10] and other purified recombinant endoglucanases produced by other *E. coli* strains: *E. coli* harboring endoglucanase gene from *Ruminococcus flavefaciens* strain 186 (0.183–0.455 U/mg protein under the studied conditions) [24], *E. coli* BL21 (DE3) harboring cellulase *Cel*DR of *B. subtilis* DR (0.82 U/mL) [18], and *E. coli* harboring the endoglucanase gene of *B. subtilis* UMC7 (0.73 ± 0.002 U/mL) [6]. In 2015, Gao et al. [25] reported an effort to produce extracellular cellulase by using *E. coli* expressing heterologous cellulase with N20 from Cel-CD. Their expression system produced higher amount of extracellular protein (514 mg/L), however, with lower CMCase activity (558.4 U/L), compared to our results. The results revealed that *E. coli* Glu5 has great ability to produce highly active extracellular endoglucanase without a need for downstream purification steps that would be very cost-effective for the cellulosic biofuel production industry.

Fig. 3a shows the sugar end products of the enzymatic hydrolysis of CMC using crude EglS as compared to the control. The broad CMC peak (peak 4) of the control (RT 6.34 min) represents the distribution of CMC degree of polymerization ($DP_n \geq 3$), indicating that it was not hydrolyzed. In contrast, the narrower but much higher CMC peak (peak 4) of the *E. coli* Glu5 system shifted to RT 6.20 min, confirming that CMC was partially hydrolyzed by EglS and still retained the gluco-oligomer portion (peaks 4 and 5). Fig. 3b, the enlarged version of Fig. 3a, shows the presence of three small peaks of glucose (peak 1), cellobiose (peak 3), and remaining gluco-oligomers (peak 5) because endoglucanases randomly cleave the internal bonds of the polymer and not necessarily result in direct soluble sugars [26]. The results suggest that a combination of EglS with exoglucanase and β-glucosidase will be needed to complete the hydrolysis of CMC into glucose. In future, a further attempt will be made to insert both exoglucanase and β-glucosidase genes in *E. coli* Glu5 for complete hydrolysis of cellulosic materials by using a mixed solution of these three enzymes.
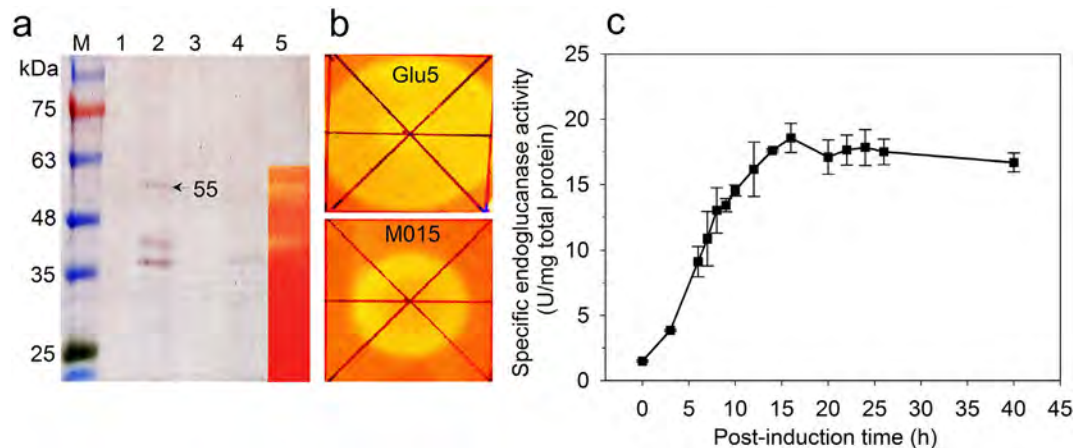
Fig. 2. (a) SDS-PAGE analysis of endoglucanase (EglS) secreted into the culture medium by the recombinant *E. coli*. Lane M: Protein marker, lane 1: uninduced *E. coli* Glu5 (before adding IPTG), lane 2: induced *E. coli* Glu5 (after adding IPTG for 16 h), lane 3: uninduced *E. coli* carrying empty plasmid, lane 4: induced *E. coli* carrying empty plasmid, and lane 5: CMC-zymogram of EglS. (b) Congo red plate assay of *E. coli* Glu5 and native strain *B. subtilis* M015. (c) Crude EglS production rate of *E. coli* Glu5 cultured at 37°C and 180 rpm.
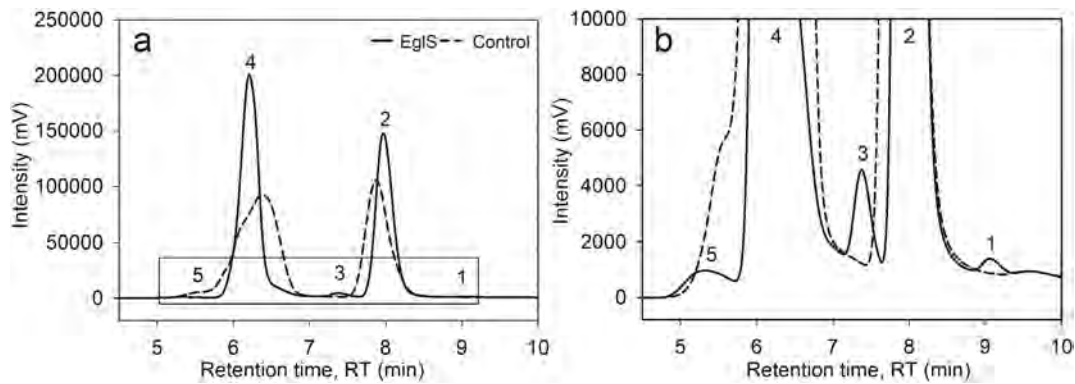
Fig. 3. HPLC chromatograms of sugar end products from the hydrolysis of CMC (1% w/v) by recombinant endoglucanase (EglS) and control in 50 mM sodium citrate buffer (pH 4.8) at 50°C for 30 min, peak 1: glucose, 2: sodium citrate, 3: cellobiose, and 4–5: gluco-oligomers of CMC. The rectangular area in chromatogram (a) is enlarged in (b).

3.3. EglS enzyme characterization results

Crude EglS showed maximum activity at pH 4.8 in the sodium citrate buffer and could retain over 70% of its maximum activity across a broad pH range of 4.0–8.0 in sodium citrate/phosphate buffer (Fig. 4a). Similarly, the EglS activity at pH 5.0 was insignificantly different (only 0.2%) from that at the optimum pH 4.8. The maximum endoglucanase activity at pH 5.0 was also found for other cellulolytic enzymes such as CMCase from *Bacillus* sp. DUSELR13 [8] and cel28a from *E. coli* DH5α expressing *cel28a* with high activity retained in a narrower pH range than crude EglS [7].

As shown in Fig. 4b, maximum endoglucanase activity was observed at 50°C, with 50% of its maximum activity in the temperature range of 30–60°C. This is consistent with other endoglucanases from *B. subtilis*

DR, *E. coli* BL21 (DE3) [18], and *B. velesensis* [10], tested at slightly different pH values (6.5, 6.0, and 7.0, respectively). When the temperature increased to 75°C, the EglS activity approached zero, which is most likely due to denaturation of the enzyme.

The thermal stability of crude EglS sample in the 50 mM sodium citrate buffer (pH 4.8) was determined at different temperatures (40°C, 50°C, and 60°C) for 100 h. The crude enzyme showed high thermal stability at 40°C and 50°C, with residual activities of 98% and 82%, respectively, after 100 h of incubation (Fig. 4c), which is similar to that of non-specific endoglucanase (cel28a) tested at a much shorter incubation time (1 h) [7]. EglS lost almost all of its total enzymatic activity (94%) after 1 h of incubation at 60°C. High stability of EglS during extended incubations of up to 100 h will be beneficial for enzymatic processes that are generally carried out at 50°C for
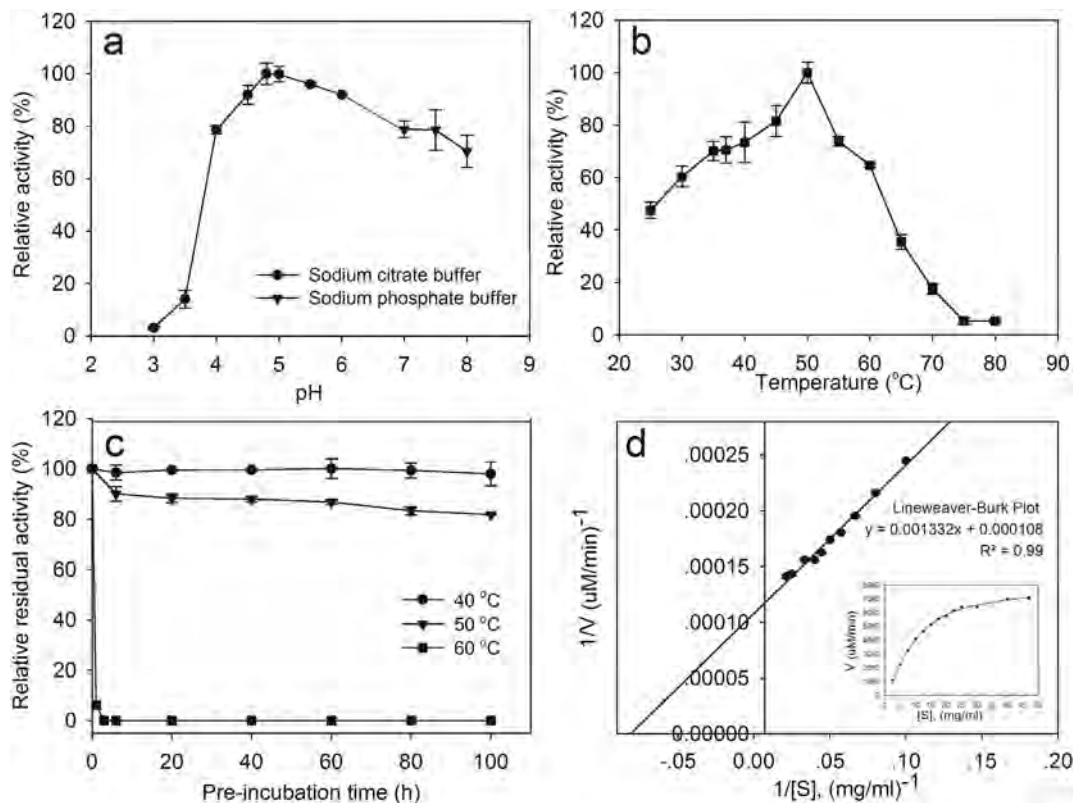
Fig. 4. (a) The effect of pH on endoglucanase activity measured at 50°C for 30 min using buffers at various pH; 50 mM sodium citrate buffer for pH 3.0–6.0; 50 mM sodium phosphate buffer for pH 7.0–8.0. (b) The effect of temperature on endoglucanase activity measured in 50 mM sodium citrate buffer (pH 4.8) for 30 min. (c) Thermal stability of recombinant EglS at different temperatures in 50 mM sodium citrate buffer (pH 4.8) for 100 h measured from residual endoglucanase activity. (d) Kinetic analysis of crude EglS toward various concentrations of CMC using Lineweaver-Burk plot.
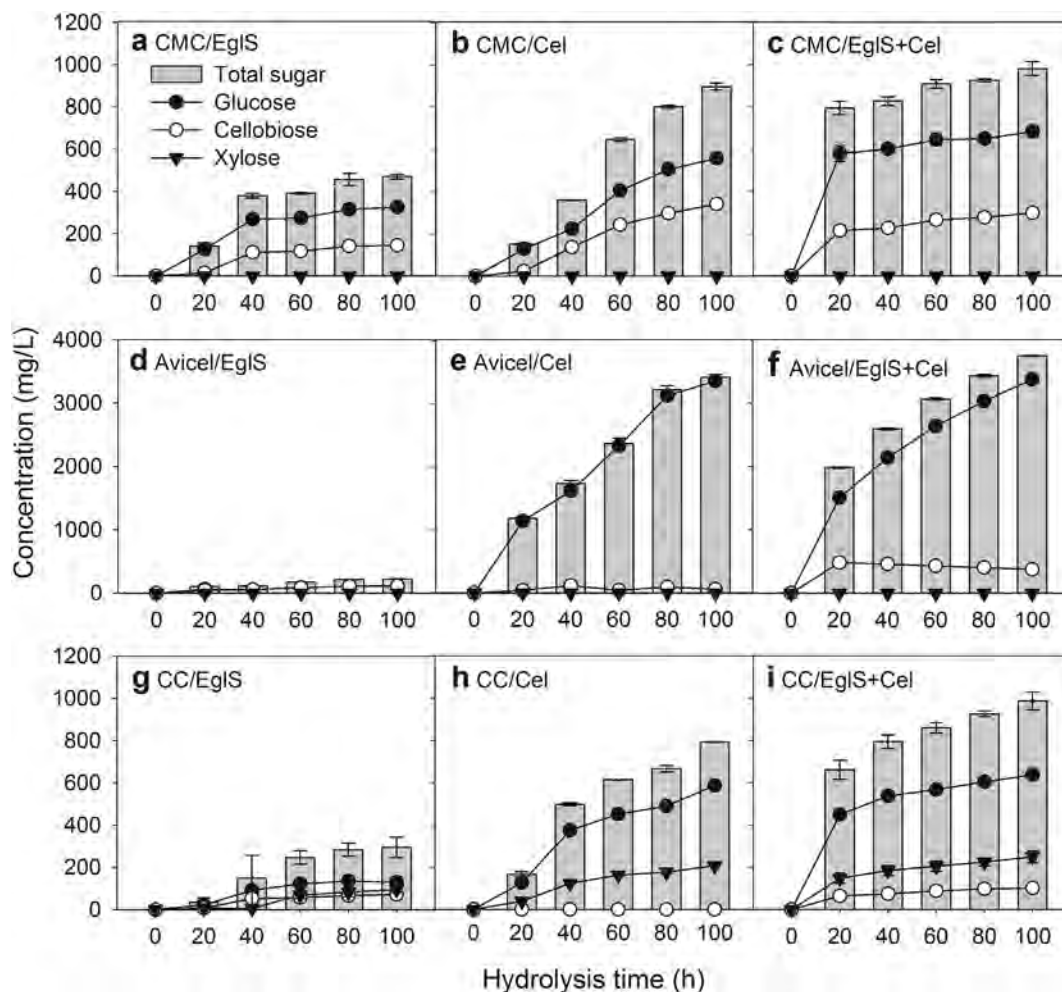
Fig. 5. Sugar products from enzymatic hydrolysis of different cellulosic substrates (5 g/L); (a–c): carboxymethyl cellulose (CMC), (d–f): microcrystalline cellulose (Avicel), and (g–i): corncob (CC) using crude recombinant EglS with 25 U/g substrate, commercial cellulase (Cel) with 25 FPU/g substrate, and enzyme mixture of EglS and Cel with 25 U/g substrate and 25 FPU/g substrate, respectively. The reactions were conducted at 50°C and 180 rpm for 100 h. Bar charts represent total sugar concentration based on glucose, cellobiose, and xylose.

3 days or longer. For industrial applications, material costs can be reduced significantly by using more stable enzymes like EglS [27].

The kinetic parameter values of crude EglS toward CMC were calculated using the Lineweaver–Burk plots (Fig. 4d). The K_m and V_{max} values were 12 mg/mL and 9259 μM/min (0.83 mg/min), respectively. In principle, K_m is independent of the enzyme concentration [28]. Lower K_m values refer to higher affinity between enzyme and substrate, indicating that crude EglS had higher affinity for CMC than purified endoglucanase (Thcel9A) from *E. coli* BL 21(DE) expressing endoglucanase gene from *Thermobifida halotolerans* YIM 90462 (K_m of 37 mg/mL) [9] and purified endoglucanase from *Aspergillus niger* B03 (K_m of 21.01 mg/mL) [29] but lower than the purified cellulase from *Bacillus* sp. MSL2 (K_m of 0.8 mg/mL) [30]. In addition, the K_m value of crude enzyme is normally higher than that of purified enzyme because of the kinetic efficiency of the enzyme, which might be retarded by the complex mixture of crude enzyme in medium and other available proteins [8,31].

3.4. Enzymatic hydrolysis of various cellulosic substrates

Fig. 5 shows all hydrolysis products of three different cellulosic materials over time (soluble cellulose, CMC; insoluble microcrystalline cellulose, Avicel; and 60–80 mesh milled corncob, CC, as a representative of agricultural residue) using crude EglS and the commercial enzyme (Cel) with and without EglS addition. Both EglS and Cel were tested to ensure the enzyme stability after 100 h of

incubation at 50°C, and it was found that they were highly stable with 18% and 4% loss of their initial activity, respectively. The hydrolysis results of the three substrates showed that glucose was the main component of sugar products, followed by cellobiose. A small concentration of xylose was found in CC, which contains hemicellulose, but not in CMC and Avicel. EglS displayed much lower hydrolytic ability with much lower sugar production because EglS has only endoglucanase activity, while Cel has multifunctional cellulolytic ability of endoglucanase, exoglucanase, and β-glucosidase. Interestingly, the use of Cel with added crude EglS showed great

Table 2
The summary of initial and overall sugar production rate from enzymatic hydrolysis at 50°C and pH 4.8.

Substrate	Enzyme	Total sugar production (mg/L)	Sugar production rate (mg/L/h)	
			Initial rate (20 h)	Overall rate (100 h)
CMC	EglS	470 ± 11	7.02 ± 0.80	4.70 ± 0.11
	Cel	897 ± 17	7.59 ± 0.20	8.97 ± 0.17
	EglS + Cel	982 ± 32	39.71 ± 1.58	9.82 ± 0.32
Avicel	EglS	222 ± 03	5.19 ± 0.55	2.22 ± 0.03
	Cel	3424 ± 46	59.20 ± 0.84	34.24 ± 0.46
	EglS + Cel	3743 ± 07	99.10 ± 0.49	37.43 ± 0.07
CC	EglS	294 ± 47	1.75 ± 1.00	2.94 ± 0.48
	Cel	793 ± 01	5.72 ± 0.40	7.93 ± 0.01
	EglS + Cel	987 ± 42	33.02 ± 2.26	9.87 ± 0.42

enhancement on the initial sugar production rate in the first 20 h for any studied substrate (Table 2). The initial sugar production rates from CMC, Avicel, and CC using a mixture of Cel and EglS were higher than those of the Cel alone by 5.23, 1.67, and 5.77 times, respectively. This can be reasonably explained as follows: EglS possessing endoglucanase activity cleaves cellulose at random sites to shorter cellulose chains and increases the number of active sites or reducing ends for subsequent enzymes, specifically exoglucanase to act on [3]. The enzyme mixture could hydrolyze CMC, Avicel, and CC to produce maximum total sugar concentrations of 196, 749, and 197 mg/g substrate, respectively, at 100 h. The sugar level from Avicel hydrolysis was much higher than those from CMC and CC hydrolysis, because of the exoglucanase activity and specificity of Cel toward Avicel. Conversely, CMC, which is a modified cellulose with a degree of substitution of 0.65–0.9, has a very low accessibility (only non-substituted glucose units are accessible for the enzyme) with a high DP_n [21]. CC is a lignocellulosic material that contains not only cellulose but also hemicellulose and lignin as inhibitors for enzymatic hydrolysis. Moreover, the average particle size of corncob was relatively high, and consequently, its available surface area was much lower than that of Avicel.

Comparisons between this work and other previous reports are not straightforward because of differences in the studied conditions such as substrate type, enzyme concentration, reaction volume, pH, temperature, reaction time, and purity of the enzyme used. However, in comparison with other published work performed under relatively similar conditions, the use of enzyme mixture in this study could produce relatively higher reducing sugar content: a purified enzyme mixture (CelZ and CelY) from *Erwinia chrysanthemi* produced 105.12 mg reducing sugar/g CMC [32], and a purified cellulase mixture (EG II, CBH I, CBH II, and β-glucosidase) produced approximately 430 mg glucose/g Avicel [33]. The hydrolysis of Avicel using an enzyme mixture of commercial cellulase and β-glucosidase

(Novozymes) provided a lower carbohydrate conversion of 69.6% at 96 h [34] compared to that of our enzyme mixture (75% conversion at 100 h). Hydrolysis of milled corncob using the purified enzyme mixture of endoglucanase and endoxylanase from *A. niger* B03 resulted in 540 mg/L reducing sugar [29], which is lower than that in the present work (987 mg/L). These results reveal that crude EglS has great potential to be utilized for the enhancement of commercial cellulase, especially for the enzymatic hydrolysis of agricultural residues.

3.5. Effects of glucose on bacterial growth and endoglucanase production

In the microbial hydrolysis of cellulose, bacterial cells play a role in cellulolytic enzyme production for hydrolyzing the cellulose mixed in the liquid medium. Simultaneously, the hydrolysis products, i.e., reducing sugars, mainly glucose, can be further utilized as a carbon source for bacterial growth, leading to a reduction in the sugar yield. A lower sugar level can directly decrease the ethanol production rate during downstream fermentation [35]. Moreover, glucose at high concentrations can inhibit bacterial growth and enzyme activity [36]. Therefore, the effects of glucose concentration in the culture media of *E. coli* Glu5 and *B. subtilis* M015 on bacterial growth and endoglucanase activity were investigated by adding glucose (1% *w/v*) in both systems.

Fig. 6a shows that the addition of 1% glucose can inhibit the growth of *E. coli* Glu5 up to 40% when compared to the growth without added glucose at 48 h. The specific growth rate (μ) obtained from its exponential phase decreased from 0.177 h^{-1} in the absence of glucose to 0.087 h^{-1} in the presence of glucose. The pH of the 48-h culture with added glucose was found to dramatically decrease (from the initial value of 7.0 to 5.0), whereas that of the 48-h culture without added glucose slightly increased (7.5). The results imply that the presence of glucose in the medium causes acid formation, resulting in
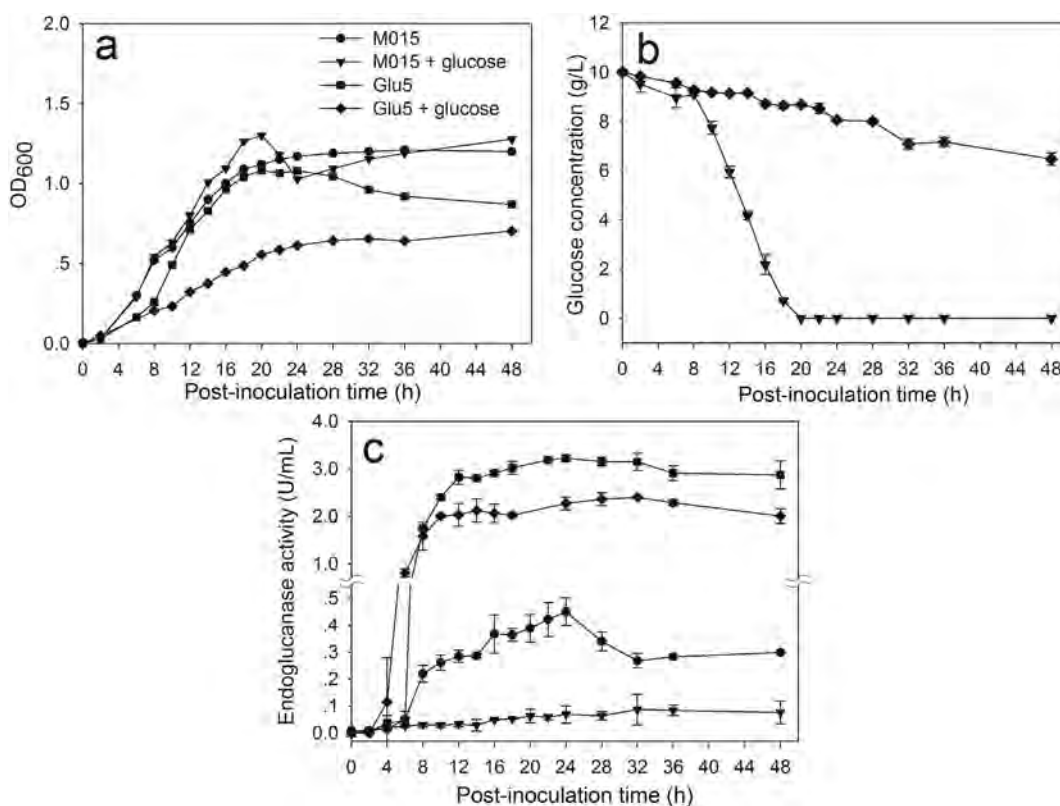
Fig. 6. Effects of glucose (1% *w/v*) on bacterial growth and endoglucanase production. (a) Growth, (b) glucose consumption, and (c) endoglucanase activity of *B. subtilis* M015 in LB with (*triangle*) and without glucose (*circle*) and *E. coli* Glu5 in LB-ampicillin with (*diamond*) and without glucose (*square*). IPTG (1 mM) and CMC (1% (*w/v*)) were used to induce enzyme synthesis in *E. coli* Glu5 and *B. subtilis* M015, respectively, at 37°C and 180 rpm for 48 h.

lower pH, and consequently, both lower cell density and growth rate were observed [36]. For *B. subtilis* M015, glucose supplemented in LB medium with CMC (1% *w/v*) as endoglucanase inducer caused a biphasic growth, resulting from the two carbon sources (glucose and CMC) available in the medium. Glucose was preferentially utilized as a carbon source for *B. subtilis* M015 and rapidly consumed during 8–20 h (Fig. 6b), corresponding to the first exponential phase observed in Fig. 6a. After 20 h of incubation, the growth of *B. subtilis* M015 slightly dropped, with a leveling off of glucose. The new exponential phase started at 24 h, suggesting that *B. subtilis* M015 started to utilize CMC as a carbon source. Interestingly, glucose was found to be slowly consumed by *E. coli* Glu5, with almost 65% of the initial glucose remaining unutilized after 2 days of culturing. This is most likely because LB medium contains abundant catabolizable amino acids as a carbon source for *E. coli* [37].

The presence of glucose in the culture medium resulted in a lower endoglucanase production (activity) in both strains than that in the absence of glucose (Fig. 6c). For *E. coli* Glu5, the lower endoglucanase production (26% relative activity) was consistent with the lower cell density due to acid formation from glucose. This was confirmed by measuring the endoglucanase activities of *E. coli* Glu5 grown at pH 5.0, which was approximately 25% relative activity, compared to that at pH 7.0. In contrast, the lower endoglucanase production in *B. subtilis* M015 might be caused by catabolite repression, preventing the expression of catabolic systems (endoglucanase activity) by preferred carbon sources (glucose) that enable the use of secondary substrates (CMC) [38].

From our findings, it was determined that *E. coli* Glu5 produced endoglucanase with higher activity than that of *B. subtilis* M015 and consumed less glucose. The effect of glucose on lowering endoglucanase production can be reduced by controlling the pH of the culture.

3.6. Microbial hydrolysis activity of CMC by E. coli Glu5

An investigation of microbial hydrolysis using whole cells of *E. coli* Glu5 was conducted at different initial CMC concentrations for 48 h. As shown in Fig. 7, an increase in CMC concentration increases the reducing sugar concentration and decreases the sugar yield slightly. A compromise of the two was found to be at a CMC concentration of 40 g/L, resulting in a reducing sugar concentration of 1060 mg/L or a reducing sugar yield of 27 mg/g CMC. The reducing sugar concentration produced in this study is comparable to that from the hydrolysis of CMC (10 g/L) with an excess of purified endoglucanase Hi Cel5A at room temperature for 48 h (reducing sugar concentration of 5.9 mM or 1062 mg/L); however, the sugar yield in this study was approximately four times lower than that of Hi Cel5A [39]. Zhou et al.
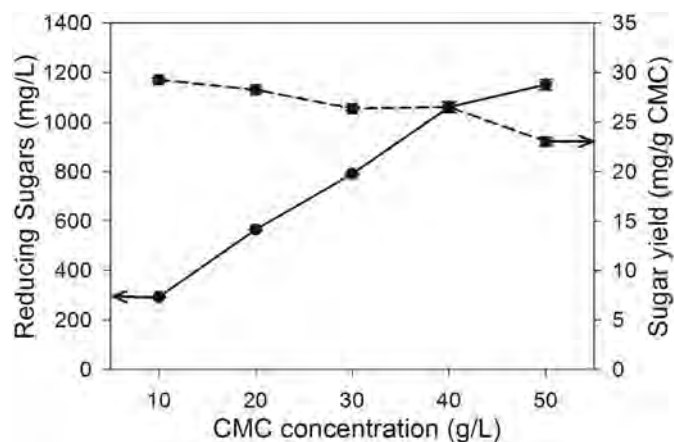
(2000) reported that enzymatic hydrolysis of CMC (20 g/L) with two endoglucanases of CelY and CelZ provided a reducing sugar concentration of 3.83 mM (689 mg/L) and 3.98 mM (716 mg/L), respectively, at 35°C for 4 h [32]. The report showed that the sugar product concentration obtained from purified enzyme (CelY and CelZ) is similar to that obtained from the microbial hydrolysis in the present study but with a shorter time. The use of whole cells of *E. coli* Glu5 for microbial hydrolysis is technically feasible for cellulosic conversion processes. The direct use of *E. coli* Glu5 will reduce the cost of enzyme production resulting from both separation and purification steps. However, reducing sugars produced can be further consumed by bacteria, as mentioned in Section 3.5, resulting in the formation of lesser sugar product. Hence, the use of a two-step process (enzyme production at a lower temperature and enzymatic hydrolysis step at a higher temperature) can improve the sugar concentration [14].

3.7. Toxicity results of Tween 80

Tween 80, a nonionic surfactant, has received great interest to be utilized in the enhancement of enzymatic hydrolysis of lignocellulosic materials because the hydrophobic interaction of the surfactant with lignin can prevent enzyme loss from adsorption onto the lignin surface, leading to higher availability of enzyme [40]. It can also stimulate microbial enzyme production by increasing cell permeability [10]. However, a high concentration of Tween 80 can inhibit bacterial growth [41]. Therefore, the effect of Tween 80 concentration on cell growth rate and activity of the enzyme secreted from *E. coli* Glu5 was investigated. The results indicated that Tween 80 did not affect the cell growth rate in the concentration range of 0.1–0.5% (*w/v*) and enhanced EglS secretion of *E. coli* Glu5 by approximately 10% at 0.2% (*w/v*) (data not shown). Another report showed that CMCase activity of enzyme secreted from *Isopteriola variabilis* sp. IDAH9 was increased approximately 36% with the addition of 0.6% Tween 80 [42]. The effect of Tween 80 on enhancing enzyme secretion of *E. coli* Glu5 was smaller than that on the wild-type strain *I. variabilis* sp. IDAH9, which is most likely due to the fact that the cell wall of *E. coli* strain used in this study was already permeable for recombinant proteins to exit. After 16 h of cultivation, *E. coli* Glu5 could grow in 5% (*w/v*) Tween 80, with 35% reduction in cell density and 18% reduction in enzymatic activity. Compared to another report, *E. coli* (ATCC 11303) growth was inhibited at 4% Tween 80, with only 50% viable cells remaining in nutrient broth [41]. The results reveal that *E. coli* Glu5 has a robust ability to both grow and secrete enzymes under the presence of a high concentration of Tween 80, which will be useful for the microbial hydrolysis process of lignocellulose with Tween 80 treatment.

4. Conclusions

In this study, crude recombinant endoglucanase (EglS) was successfully produced by *E. coli* Glu5 with high activity. The addition of EglS could greatly enhance the initial sugar production rate of commercial cellulase by the hydrolysis of soluble cellulose (CMC), microcrystalline cellulose (Avicel), and corncob (CC). Remarkably, *E. coli* Glu5 had lower glucose consumption than the native strain (*B. subtilis* M015) and retained high enzyme activity at high sugar concentrations, making it a potential candidate for the microbial hydrolysis process. Furthermore, *E. coli* Glu5 also showed a high tolerance to Tween 80. These findings can help in developing an economical biofuel production process in the future.

Fig. 7. Reducing sugar profile from microbial hydrolysis of various concentrations of CMC (10–50 g/L) by *E. coli* Glu5 culturing in LB-ampicillin (pH 7.0) at 37°C and 180 rpm for 48 h.

References

[1] Prasad S, Singh A, Joshi HC. Ethanol as an alternative fuel from agricultural, industrial and urban residues. Resour Conserv Recycl 2007;50:1–39. Doi: http://dx.doi.org/10.1016/j.resconrec.2006.05.007.

[2] Nigam PS, Singh A. Production of liquid biofuels from renewable resources. Prog Energy Combust Sci 2011;37:52–68. Doi: http://dx.doi.org/10.1016/j.pecs.2010.01.003.

[3] Gupta A, Verma JP. Sustainable bio-ethanol production from agro-residues: A review. Renew Sustain Energy Rev 2015;41:550–67. Doi: http://dx.doi.org/10.1016/j.rser.2014.08.032.

[4] Westers L, Westers H, Quax WJ. Bacillus subtilis as cell factory for pharmaceutical proteins: A biotechnological approach to optimize the host organism. Biochim Biophys Acta Mol Cell Res 2004;1694:299–310. Doi: http://dx.doi.org/10.1016/j.bbamcr.2004.02.011.

[5] Taechapoempol K, Sreethawong T, Rangsunvigit P, Namprohm W, Thamprajamchit B, Rengpipat S, et al. Cellulase-producing bacteria from Thai higher termites, Microcerotermes sp.: Enzymatic activities and ionic liquid tolerance. Appl Biochem Biotechnol 2011;164:204–19. Doi: http://dx.doi.org/10.1007/s12010-010-9128-4.

[6] Chuan Wei KS, Teoh TC, Koshy P, Salmah I, Zainudin A. Cloning, expression and characterization of the endoglucanase gene from Bacillus subtilis UMC7 isolated from the gut of the indigenous termite Macrotermes malaccensis in Escherichia coli. Electron J Biotechnol 2015;18:103–9. Doi: http://dx.doi.org/10.1016/j.ejbt.2014.12.007.

[7] Cheng J, Huang S, Jiang H, Zhang Y, Li L, Wang J, et al. Isolation and characterization of a non-specific endoglucanase from a metagenomic library of goat rumen. World J Microbiol Biotechnol 2016;32:1–8. Doi: http://dx.doi.org/10.1007/s11274-015-1957-4.

[8] Rastogi G, Bhalla A, Adhikari A, Bischoff KM, Hughes SR, Christopher LP, et al. Characterization of thermostable cellulases produced by Bacillus and Geobacillus strains. Bioresour Technol 2010;101:8798–806. Doi: http://dx.doi.org/10.1016/j.biortech.2010.06.001.

[9] Zhang F, Chen J-J, Ren W-Z, Nie G-X, Ming H, Tang S-K, et al. Cloning, expression and characterization of an alkaline thermostable GH9 endoglucanase from Thermobifida halotolerans YIM 90462 T. Bioresour Technol 2011;102:10143–6. Doi: http://dx.doi.org/10.1016/j.biortech.2011.08.019.

[10] Akaracharanya A, Taprig T, Sitdhipol J, Tanasupawat S. Characterization of cellulase producing Bacillus and Paenibacillus strains from Thai soils. J Appl Pharm Sci 2014;4:6–11. Doi: http://dx.doi.org/10.7324/JAPS.2014.40502.

[11] Klein-Marcuschamer D, Oleskowicz-Popiel P, Simmons BA, Blanch HW. The challenge of enzyme cost in the production of lignocellulosic biofuels. Biotechnol Bioeng 2012;109:1083–7. Doi: http://dx.doi.org/10.1002/bit.24370.

[12] Maki M, Leung KT, Qin W. The prospects of cellulase-producing bacteria for the bioconversion of lignocellulosic biomass. Int J Biol Sci 2009;5:500–16. Doi: http://dx.doi.org/10.7150/ijbs.5.500.

[13] Olson DG, McBride JE, Joe Shaw A, Lynd LR. Recent progress in consolidated bioprocessing. Curr Opin Biotechnol 2012;23:396–405. Doi: http://dx.doi.org/10.1016/j.copbio.2011.11.026.

[14] Wu J, Liu Z, CHOW HL. A method for enzymatic hydrolysis of cellulose. Google Patents; 2013. Patent no. WO2013122549A1

[15] Lu Y, Zhang Y-HP, Lynd LR. Enzyme–microbe synergy during cellulose hydrolysis by Clostridium thermocellum. Proc Natl Acad Sci U S A 2006;103:16165–9. Doi: http://dx.doi.org/10.1073/pnas.0605381103.

[16] Sambrook J, Russell DW. Molecular cloning: A laboratory manual. New York: Cold Spring Harbor Laboratory Press, Cold Spring Harbour; 2001.

[17] Laemmli UK. Cleavage of structural proteins during the assembly of the head of bacteriophage T4. Nature 1970;227:680–5. Doi: http://dx.doi.org/10.1038/227680a0.

[18] Li W, Zhang W-W, Yang M-M, Chen Y-L. Cloning of the thermostable cellulase gene from newly isolated Bacillus subtilis and its expression in Escherichia coli. Mol Biotechnol 2008;40:195–201. Doi: http://dx.doi.org/10.1007/s12033-008-9079-y.

[19] Miller GL. Use of dinitrosalicylic acid reagent for determination of reducing sugar. Anal Chem 1959;31:426–8. Doi: http://dx.doi.org/10.1021/ac60147a030.

[20] Seneesrisakul K, Gulari E, Chavadej S. Study on microbial pretreatment for enhancing enzymatic hydrolysis of corncob. Int J Biol Food Vet Agril Eng 2014;8:1004–9. [Accessed November 15, 2016, Available from: http://waset.org/publications/9999351].

[21] Percival Zhang YH, Himmel ME, Mielenz JR. Outlook for cellulase improvement: Screening and selection strategies. Biotechnol Adv 2006;24:452–81. http://dx.doi.org/10.1016/j.biotechadv.2006.03.003.

[22] Mittal A, Katahira R, Himmel ME, Johnson DK. Effects of alkaline or liquid-ammonia treatment on crystalline cellulose: Changes in crystalline structure and effects on enzymatic digestibility. Biotechnol Biofuels 2011;4:41. Doi: http://dx.doi.org/10.1186/1754-6834-4-41.

[23] Zhang Z, Zhao ZK. Solid acid and microwave-assisted hydrolysis of cellulose in ionic liquid. Carbohydr Res 2009;344:2069–72. Doi: http://dx.doi.org/10.1016/j.carres.2009.07.011.

[24] Huang C-M, Kelly W, Asmundson R, Yu P-L. Molecular cloning and expression of multiple cellulase genes of Ruminococcus flavefaciens strain 186 in Escherichia coli. Appl Microbiol Biotechnol 1989;31:265–71. Doi: http://dx.doi.org/10.1007/BF00258407.

[25] Gao D, Wang S, Li H, Yu H, Qi Q. Identification of a heterologous cellulase and its N-terminus that can guide recombinant proteins out of Escherichia coli. Microb Cell Fact 2015;14:1–8. Doi: http://dx.doi.org/10.1186/s12934-015-0230-8.

[26] Engel P, Hein L, Spiess AC. Derivatization-free gel permeation chromatography elucidates enzymatic cellulose hydrolysis. Biotechnol Biofuels 2012;5:77. Doi: http://dx.doi.org/10.1186/1754-6834-5-77.

[27] Buchholz K, Kasche V, Bornscheuer UT. Biocatalysts and enzyme technology. John Wiley & Sons; 2012.

[28] Fogler HS. Elements of chemical reaction engineering. 4th ed. New Jersey: Prentice Hall; 2006.

[29] Dobrev GT, Zhekova BY. Biosynthesis, purification and characterization of endoglucanase from a xylanase producing strain Aspergillus niger B03. Braz J Microbiol 2012;43:70–7. Doi: http://dx.doi.org/10.1590/S1517-83822012000100004.

[30] Sriariyanun M, Tantayotai P, Yasurin P, Pornwongthong P, Cheenkachorn K. Production, purification and characterization of an ionic liquid tolerant cellulase from Bacillus sp. isolated from rice paddy field soil. Electron J Biotechnol 2016;19:23–8. Doi: http://dx.doi.org/10.1016/j.ejbt.2015.11.002.

[31] Cavalcante Braga AR, Manera AP, da Costa Ores J, Sala L, Maugeri F, Juliano Kalil S. Kinetics and thermal properties of crude and purified β-galactosidase with potential for the production of galactooligosaccharides. Food Technol Biotechnol 2013;51:45–52.

[32] Zhou S, Ingram LO. Synergistic hydrolysis of carboxymethyl cellulose and acid-swollen cellulose by two endoglucanases (CelZ and CelY) from Erwinia chrysanthemi. J Bacteriol 2000;182:5676–82. Doi: http://dx.doi.org/10.1128/JB.182.20.5676-5682.2000.

[33] Woodward J, Lima M, Lee N. The role of cellulase concentration in determining the degree of synergism in the hydrolysis of microcrystalline cellulose. Biochem J 1988;255:895–9. Doi: http://dx.doi.org/10.1042/bj2550895.

[34] Yu Z, Jameel H, Chang HM, Philips R, Park S. Evaluation of the factors affecting avicel reactivity using multi-stage enzymatic hydrolysis. Biotechnol Bioeng 2012;109:1131–9. Doi: http://dx.doi.org/10.1002/bit.24386.

[35] Sofer SS, Zaborsky OR. Biomass conversion processes for energy and fuels. Springer Science & Business Media; 2012.

[36] Epps HM, Gale EF. The influence of the presence of glucose during growth on the enzymatic activities of Escherichia coli: Comparison of the effect with that produced by fermentation acids. Biochem J 1942;36:619.

[37] Sezonov G, Joseleau-Petit D, D'Ari R. Escherichia coli Physiology in Luria–Bertani broth. J Bacteriol 2007;189:8746–9. Doi: http://dx.doi.org/10.1128/JB.01368-07.

[38] Deutscher J. The mechanisms of carbon catabolite repression in bacteria. Curr Opin Microbiol 2008;11:87–93. http://dx.doi.org/10.1016/j.mib.2008.02.007.

[39] Karlsson J, Momcilovic D, Wittgren B, Schülein M, Tjerneld F, Brinkmalm G. Enzymatic degradation of carboxymethyl cellulose hydrolyzed by the endoglucanases Cel5A, Cel7B, and Cel45A from Humicola insolens and Cel7B, Cel12A and Cel45A core from Trichoderma reesei. Biopolymers 2002;63:32–40. Doi: http://dx.doi.org/10.1002/bip.1060.

[40] Zheng Y, Pan Z, Zhang R, Wang D, Jenkins B. Non-ionic surfactants and non-catalytic protein treatment on enzymatic hydrolysis of pretreated creeping wild ryegrass. Appl Biochem Biotechnol 2008;146:231–48. Doi: http://dx.doi.org/10.1007/s12010-007-8035-9.

[41] Rose MJ, Aron SA, Janicki BW. Effect of various nonionic surfactants on growth of Escherichia coli. J Bacteriol 1966;91:1863–8.

[42] Azizi M, Hemmat J, Seifati SM, Torktaz I, Karimi S. Characterization of a thermostable endoglucanase produced by Isoptericola variabilis sp. IDAH9. Braz J Microbiol 2015;46:1225–34. Doi: http://dx.doi.org/10.1590/S1517-838246420140846.
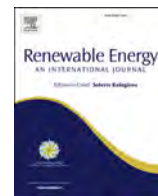
CrossMark

Separate production of hydrogen and methane from biodiesel wastewater with added glycerin by two-stage anaerobic sequencing batch reactors (ASBR)

Pranee Tangkathitipong [a, b], Patcharee Intanoo [d], Janyawan Butpan [c], Sumaeth Chavadej [a, b, *]

[a] The Petroleum and Petrochemical, Chulalongkorn University, Thailand
[b] Center of Excellence on Petrochemical and Materials Technology, Thailand
[c] Bangchak Biofuel Company Limited, Ayuttaya, Thailand
[d] Department of Industrial Chemistry and Textile Technology, Faculty of Science, Maejo University, Chiang Mai 50290, Thailand

ABSTRACT

The objective of this study was to investigate hydrogen and methane production from biodiesel wastewater with added glycerin by using two-stage anaerobic sequencing batch reactors (ASBR) under 37 °C with a recycle ratio of the effluent from the methane ASBR unit-to-the feed flow rate of 1:1. Hydrogen ASBR unit was operated at a constant pH of 5.5 whereas the pH of methane ASBR unit was not controlled. Glycerin was added into biodiesel wastewater having 2330 mg/l COD to obtain a constant feed chemical oxygen demand (COD) of 45,000 m/l. At optimum COD loading rate 11.3 kg/m^{3}d (based on feed COD load and methane ASBR volume), the system provided the highest overall hydrogen and methane production performance (75.15 ml H$_2$/g glycerin removed) which was consistent with the maximum overall COD removal of 76.7% and the highest overall glycerin uptake of 90%. Most of added glycerin was converted to gaseous products with small amounts of organic acids and 1,3 propanediol. The low volumetric ratio of hydrogen ASBR unit-to-methane ASBR unit of 1:6 resulted in low hydrogen yields with high methane yields. Process performance of the two-stage ASBR system was limited by the inhibition of total volatile organic acids produced in both bioreactors.

© 2017 Elsevier Ltd. All rights reserved.

1. Introduction

Biodiesel, one of the most attractive alternative fuels, has gained more and more popularity in many countries around the world and its production has been increasing steadily [1]. In the biodiesel production process, there is 1 volume of glycerol or glycerin generated for 10 volume of biodiesel produced [2]. Hence, an increase in biodiesel production results in a surplus amount of crude glycerin, leading to a decrease in the price of crude glycerin [3]. To overcome this problem, one of the interesting approaches is to convert glycerin to hydrogen and/or methane [4,5]. Hydrogen and methane are very promising as an attractive alternative energy [6] because they are clean and environmentally friendly. Moreover,

they can also reduce the greenhouse gases which cause global warming [6].

There are many available commercial processes to produce hydrogen and methane, including steam reforming of natural gas [7], partial oxidation of natural gas [8], autothermal reforming of natural gas [9], dry reforming of natural gas [10], and supercritical water gasification of biomass [11]. All of these processes require a lot of energy and there is a risk of explosion [12]. A better way commonly used to produce hydrogen and methane is a biological process. Chookaew et al. [13] studied the production of hydrogen from crude glycerin by using a two-stage biological process combining dark fermentation with a microbial fuel cell (MFC) or microbial electrolysis cell (MEC). The maximum hydrogen yield of 0.55 mol H$_2$/mol of glycerin was obtained under a COD loading rate of 0.55 kg/m^{3}dat pH7.0 and 35 °C. Selembo et al. [14] also investigated hydrogen production from biodiesel wastewater which contained 70%glycerin using a single biological process serum glass bottle under a batch mode of operation with an initial feed COD of

1300 mg/l. The maximum hydrogen yield was as high as 0.31 mol-H_2/mol glycerin.

Seifert et al. (2009) [15] studied hydrogen production from pure glycerin with a mixed medium of a single biological process glass reactor (60 ml) under a batch mode of operation at 37 °C and pH6 and they reported the highest hydrogen yield of 0.41 mol H_2/mol glycerin at the lowest concentration of applied inoculums of1.2 g VSS/l. Vlassis et al. [16] studied hydrogen and methane production from pure glycerin using both batch and continuous CSTRs under mesophilic temperature (35 °C). The highest hydrogen and methane yields were 22.14 ml H_2/g COD removed and 300 ml CH_4/g COD removed, respectively at an initial pH of 6.5 and an initial glycerin concentration of 8300 mg COD/l.

Hydrogen and methane are produced via a biological process, which can be operated in both a single anaerobic process [17–21] and a two stage anaerobic process [22–24]. A two-stage anaerobic process is superior to a single anaerobic process because it not only provides additional methane, apart from hydrogen production, but also produces effluents having much lower COD values, leading to lower post treatment costs.

Anaerobic digestion consists of four main sequential steps of hydrolysis, acidogenesis, acetogenesis, and methanogenesis. For hydrolysis, complex organic molecules are enzymatically broken down into water-soluble smaller molecules of simple sugars, amino acids, and fatty acids. The soluble smaller molecules are further converted to organic acids, hydrogen, carbon dioxide, and some alcohols in the acidogenic step by acidogenic bacteria. In the acetogenic step, the higher organic acids produced are further converted to acetic acid, carbon dioxide, and hydrogen by acetogenic bacteria. Finally, the hydrogen produced is combined with carbon dioxide to form methane and water while the acetic acid is converted into methane and carbon dioxide by methanogenic bacteria [25,26]. Using a two-stage anaerobic process can successfully separately produce hydrogen and methane [22,27] whereas all single stage anaerobic processes can produce methane with carbon dioxide without hydrogen.

In this research work, hydrogen and methane were produced separately and spontaneously from biodiesel wastewater with added glycerin at a very high concentration under mesophilic temperature by using a two-stage anaerobic sequencing batch reactor (ASBR) system. The first hydrogen ASBR unit was controlled at pH 5.5 while the pH of methane ASBR unit was not controlled [22]. The two-stage ASBR system was operated at different COD loading rates at a constant temperature of 37 °C. The recycle ratio of the effluent from the methane ASBR unit to feed flow rate was fixed at 1:1 in order to minimize the use of NaOH for pH adjustment in the hydrogen ASBR unit. The uptakes of glycerin, nitrogen and phosphorus were also evaluated to demonstrate a potential use of glycerin for separate production of hydrogen and methane. Moreover, one of the aims of this work was to find out whether the process performance was governed by the concentration of added glycerin or of the produced organic acids in the system.

2. Methods

2.1. Seed sludge preparation

The activated sludge, taken from the biodiesel plant of the Bangchak Biofuel factory at Ayutthaya, was mixed with the anaerobic sludge from a covered lagoon to treat palm oil wastewater from the Suksomboon factory at Chonburi, Thailand. The mixed seed sludge was sieved and screened in order to remove debris and large solid particles before being added to both hydrogen and methane ASBR units to have an initial microbial concentration in terms of mixed liquor volatile suspended solids (MLVSS) of approximately 12,000 mg/l. Only the seed sludge for the hydrogen ASBR unit was boiled for 15 min in order to eliminate methane-producing bacteria (hydrogen-consuming bacteria) and enrich hydrogen-producing bacteria [17–20].

2.2. Feed preparation

Biodiesel wastewater and crude glycerin were obtained from the Bangchak Biofuel factory at Ayutthaya. It was sieved and screened in order to remove debris and large solid particles and kept at 4 °C before use. The biodiesel wastewater used in this experiment had a chemical oxygen demand (COD) of 2330 mg/l. An appropriate quantity of the crude glycerin sample (3.5%w/v) was added into the biodiesel wastewater to obtain a constant COD value of45000 mg/l of the mixed wastewater. The ratio of COD: nitrogen: phosphorous (COD:N:P) was 100:0.44:0.044, indicating that this mixed wastewater had insufficient nutrients for anaerobic digestion (the theoretical ratio of COD:N:P = 100:1:0.2 for anaerobic decomposition) [19]. Ammonium hydrogen carbonate (NH_4HCO_3) and di-potassium hydrogen orthophosphate (K_2HPO_4) were added to meet the theoretical ratio of COD:N:P [20].

2.3. ASBR operation

Both ASBR units used in this study were constructed from opaque PVC pipes and sheets in order to inhibit the activity of photosynthetic bacteria [28]. It had a working volume of 4 and 24 l for the hydrogen and methane ASBR units, respectively. Each ASBR unit was equipped with a magnetic stirrer (450 rpm) to suspend microbial cells during the reaction step. A temperature controller quipped with a heater and a thermocouple and a pH-controller with a dosing pump for a 1 M NaOH solution were used to maintain a constant temperature of 37 °C and a constant pH of 5.5 in the hydrogen ASBR unit, respectively, while the methane ASBR unit had only a temperature controller unit. The two-stage ASBR system was operated at 6 cycles per d and each cycle consisted of a feed step of 15 min, a reaction step of 90 min, a sedimentation step of 120 min and a decant step of 15 min, as reported in our previous work [19].

The two-stage ASBR system was operated at different COD loading rates (33.75, 50.63, 67.50, 84.38 kg/m^{3}d based on feed COD load and hydrogen ASBR volume or 5.63, 8.44, 11.25, 14.06 kg/m^{3}d based on feed COD load and methane ASBR volume). The recycle ratio of the effluent of methane ASBR unit to a feed flow rate was fixed at 1:1 in order to minimize the use of NaOH for pH adjustment in the hydrogen ASBR unit [17,22,23]. The schematic of the two-stage ASBR system is shown in Fig. 1. At any given COD loading rate, the two-stage ASBR system was operated for about 4 weeks to reach a steady state before effluent and produced gas samples of
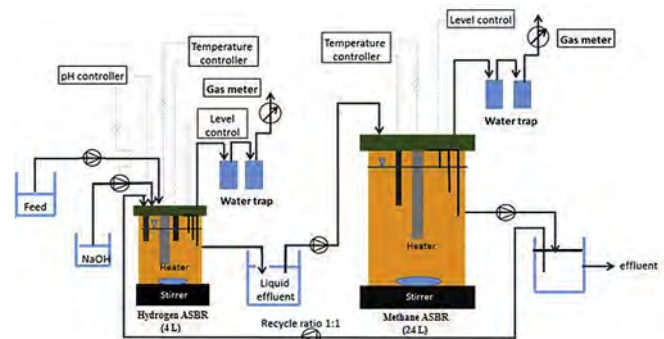

Fig. 1. Schematic of two-stage anaerobic sequencing batch reactor (ASBR)system.

both ASBR units were taken for analysis and measurement. Steady state conditions were attained when effluent COD values and gas production rates of both hydrogen and methane ASBR reactors were invariant with time [22,23].

2.4. Measurements and analytical methods

The volume of produced gas was measured by a wet gas meter (Ritter, TG05/5) at room temperature (25–30 °C). A gas chromatograph (GC, Perkin-Elmer, AutoSystem) equipped with a thermal conductivity detector (TCD) and a stainless-steel $10' \times 1/8' \times 0.085'$HayeSep D 100/120 mesh (Alltech) packed column was used to analyze the composition of produced gas samples [19]. The temperatures of column, injector, and detector were kept at 35, 60, and 150 °C, respectively and argon was used as a carrier gas. A high performance liquid chromatograph (HPLC) (Shimadzu, LC-10AD) equipped with an Aminex HPX-87H column(Bio-Rad Laboratories) and a refractive index (RI) detector at a wavelength of 210 nm with a 4 mM H_2SO_4 mobile phase was used to measure the amount of glycerin, total volatile fatty acids(VFA), and VFA composition [14]. The influent and effluent COD values were analyzed by the dichromate digestion and absorbance measurement by a spectrophotometer (HACH, DR 2700). Nitrogen analysis, in terms of organic nitrogen, was measured by the diazotization and cadmium reduction method and inorganic nitrogens (nitrate-nitrogen, ammonium-nitrogen and nitrite-nitrogen) were analyzed by the salicylate method with TNT persulfate digestion. Total phosphorous content was measured by the molybdovanadate method with acid persulfate digestion (HachCompany).

The mixed liquor volatile suspended solids (MLVSS) to represent the microbial concentration in both ASBR units taken during the reaction step and volatile suspended solids (VSS) to represent microbial washout from each ASBR unit taken during the decanting step were analyzed by the standard methods [29].

3. Results and discussion

3.1. Hydrogen ASBR performances

Fig. 2 shows the process performances of the hydrogen ASBR unit as a function of COD loading rate at 37 °C and pH 5.5with a recycle ratio of 1:1. The actual COD loading rate calculated from the COD values of both feed and recycle effluent was also presented for comparison. The COD removal increased significantly from 20.6 to 36.8% with increasing COD loading rate from 33.8 to 67.5 kg/m^{3}d and then dropped to 35.3% with a further increasing COD loading rate to 84.3 kg/m^{3}d. The gas production rate had a similar trend to the COD removal. The results can be explained by the fact that an increase in COD loading rate simply increased the organic amount available for the microbes to utilize and to convert to hydrogen with a higher gas production rate. However, the COD loading rate increased from 70 to 85 kg/m^{3}d, causing a decrease in both COD removal and gas production rate as a result from the increasing toxicity of VFA accumulation. This will be further discussed later.

Fig. 2b shows the effect of COD loading rate on the composition of produced gas and hydrogen production rate of the hydrogen ASBR unit. The gas produced contained mainly hydrogen and carbon dioxide with a very small amount of methane (less than 0.5%) in the studied range of COD loading rate. Both hydrogen content and hydrogen production rate increased with increasing COD loading rate from 33.8 to 67.5 kg/m^{3}d and then decreased with further increasing COD loading rate from 67.5 to 84.4 kg/m^{3}d. The maximum values of both hydrogen content and hydrogen production rate (33.4% and 1.33 l/d, respectively) were also found at the same COD loading rate of 67.5 kg/m^{3}d. The hydrogen

Fig. 2. Effects of COD loading rate on (a) COD removal and gas production rate. (b) gas composition and hydrogen production rat (c) Specific hydrogen production rate. (d) hydrogen yields (e) alkalinity and system pH when the system was operated at 37 °C, pH 5.5 in the hydrogen ASBR unit and a recycle ratio of 1:1.

production rate increased with increasing COD loading rate, resulting from a higher organic amount available for the microbes to produce more gaseous products. Beyond the COD loading rate of 67.5 kg/m^{3}d, both hydrogen content and hydrogen production rate decreased with the increase in CO_2 content due to the increasing concentration of total VFA in the bioreactor to exceed the toxic level to the microbes [30]. This will be shown later.

A specific hydrogen production rate (SHPR) is a process parameter to indicate the ability of microbes to produce hydrogen from organic compounds per unit volume of bioreactor or per unit dried weight of microbes [20,31]. Both SHPRs increased with increasing COD loading rate from 33.8 to 67.5 kg/m^{3}d and then decreased with further increasing COD loading from 67.5 to 84.4 kg/m^{3}d (Fig. 2c). The maximum SHPRs of 89 ml H_2/g MLVSS d and 333 ml H_2/l d were found at the same COD loading rate of 67.5 kg/m^{3}d for all of the maximum hydrogen production rate, hydrogen content, and COD removal.

Hydrogen yields are another process parameter to indicate the conversion efficiency of organic compounds to hydrogen by microbes expressed in ml H_2/g COD applied and ml H_2/g COD removed [20,31]. As shown in Fig. 2d, both hydrogen yields show a similar trend to the SHPRs, hydrogen production rate and COD removal. The maximum hydrogen yields of 7.8 ml H_2/g COD removed and 4.93 ml H_2/g COD applied were found at the same COD loading rate of 67.5 kg/m^{3}d to provide the highest SHPRs and COD removal. The hydrogen yield from the biodiesel wastewater with added glycerin found in this study is about 68.4% lower than that under the two-stage mesophilic UASB process using cassava wastewater as a substrate [23] because the crude glycerin also contained some other compounds including soap, free fatty acids, methanol, unreacted triglyceride, diglyceride, and monoglycerides [32], which

have lower biodegradability to cause the depletion of the hydrogen production performance [30].

Vlassis et al. [27] reported that pH and the amount of added glycerin in biodiesel wastewater directly affected hydrogen production performance. The suitable pH for hydrogen-producing bacteria to digest biodiesel wastewater containing glycerin was reportedly around 6.5 which was higher than the controlled pH of 5.5 used in this work. Moreover, they also suggested that the COD of glycerin in biodiesel wastewater should not exceed 8300 mg/l which was much lower than that used in the present work. Another reason causing the low hydrogen production activity was more likely from the size of the hydrogen ASBR unit being too small. This will be discussed in more detail latter.

Fig. 2e shows the alkalinity and pH of the hydrogen ASBR unit at different COD loading rates. The alkalinity had a similar trend to the SHPRs, COD removal, gas production rate and hydrogen yields. The maximum alkalinity was also found at the same optimum COD loading rate of 67.5 kg/m³d. The low alkalinity in the hydrogen ASBR unit resulted from the low pH solution of 5.5. The constant pH of 5.5 in the hydrogen ASBR unit could be maintained, resulting from the use of a pH controller and the effluent recycle.

The effects of COD loading rate on total VFA concentration and VFA composition in the hydrogen ASBR unit are shown in Fig. 3a. The total VFA concentration increased steadily with increasing COD

loading rate and reached a maximum value of 16,300 mg/l as acetic acid at the highest COD loading rate of 84.4 kg/m³d. The increase rate in total VFA concentration with increasing COD loading rate was relatively high when the COD loading rate was lower than the optimum COD loading rate of 67.50 kg/m³d, as compared with that at a COD loading rate beyond the optimum COD loading rate. This corresponded well to the reduction of the process performance in terms of hydrogen yields and hydrogen production rate, SHPRs and COD removal with increasing COD loading rate beyond the COD loading rate. The results suggest that the inhibitory level of total VFA to the hydrogen-producing microbes was around 13,000 mg/l as acetic acid which is in good agreement with our previous work [31,33].

As shown in Fig. 3a, the main organic acids produced were in the following concentration order: butyric acid (HBu), valeric acids (Hva), acetic acid (HAc) and propionic acid (HPr). The concentrations of all produced organic acids increased with increasing COD loading rate whereas the concentrations of 1,3 propanediol and ethanol were relatively low and remained almost unchanged. Glycerin ($C_3H_8O_3$), the main organic compound in the feed (94.5% in COD), can be utilized by acidogens as well as acetogenes to produce hydrogen, organic acids, ethanol, butanol and 1,3 propanediol (1,3-PD), as shown in the following equations [32,34].

$$C_3H_8O_3 + H_2O \rightarrow CH_3COOH \text{ (acetic acid)} + CO_2 + 3H_2 \qquad (1)$$

$$C_3H_8O_3 \rightarrow 2C_3H_8O_3C_4H_8O_2 \text{ (butyric acid)} + 2CO_2 + 4H_2 \qquad (2)$$

$$2C_3H_8O_3 \rightarrow C_4H_{10}O \text{ (butanol)} + 2CO_2 + H_2O + 2H_2 \qquad (3)$$

$$C_3H_8O_3 + H_2 \rightarrow C_3H_8O_2 \text{ (1, 3 propanediol)} + H_2O \qquad (4)$$

$$C_3H_8O_3 \rightarrow CH_3CH_2OH \text{ (ethanol)} + CO_2 + H_2 \qquad (5)$$

$$C_3H_8O_3 \rightarrow CH_3CH_2COOH \text{ (propionic acid)} + H_2O \qquad (6)$$

From the COD mass balance (not shown here), glycerin was mostly converted to organic acids, hydrogen and carbon dioxide, as confirmed experimentally, by the glycerin analysis results, which will be discussed later.

3.2. Methane ASBR performances

The effluent from the hydrogen ASBR unit was directly fed to the methane ASBR unit for further methane production and the methane ASBR unit was also operated under mesophilic temperature (37 °C) without pH control. Fig. 4a shows the effects of COD loading rate (based on feed COD load and methane ASBR volume or the actual incoming COD load and methane ASBR volume). The COD removal increased with increasing COD loading rate from 5.6 to 11.3 kg/m³d and it attained a maximum value of 63.2% at a COD loading rate of 11.3kg/m³d (based on feed COD load and methane ASBR volume). Beyond the COD loading rate of 11.3 kg/m³d, the COD removal dramatically decreased with further increasing COD loading rate. The gas production rate showed a similar trend to the COD removal. The increase in COD loading rate simply increased the amount of organic compounds, especially organic acids and glycerin available for the microbes, resulting in both increases in COD removal and gas production rate. Interestingly, the gas production rate of the methane ASBR unit was about four times higher than that of the hydrogen ASBR unit, close to the volumetric ratio of these two bioreactors.

The composition of produced gas from the methane ASBR unit mainly consisted of methane and carbon dioxide with a small

Fig. 3. Total VFA concentration, VFA composition, ethanol concentration and 1,3 propanediol concentration at different COD loading rates (a) in the hydrogen ASBR unit and (b) in the methane ASBR unit when the system was operated at 37 °C, pH 5.5 in the hydrogen ASBR unit and a recycle ratio of 1:1.
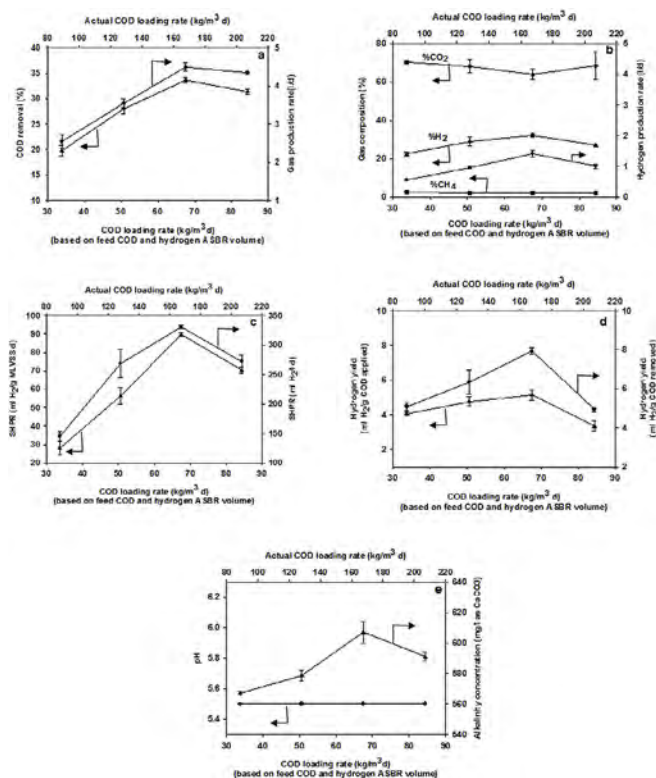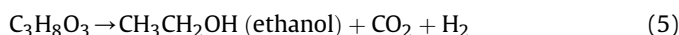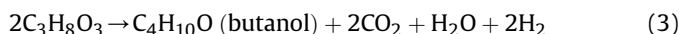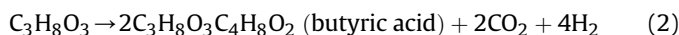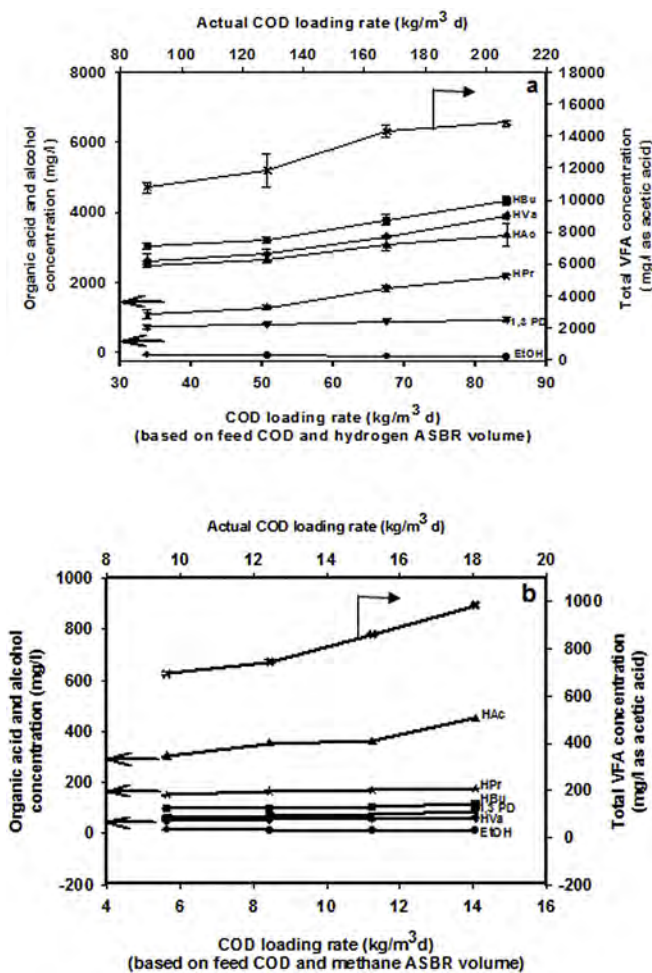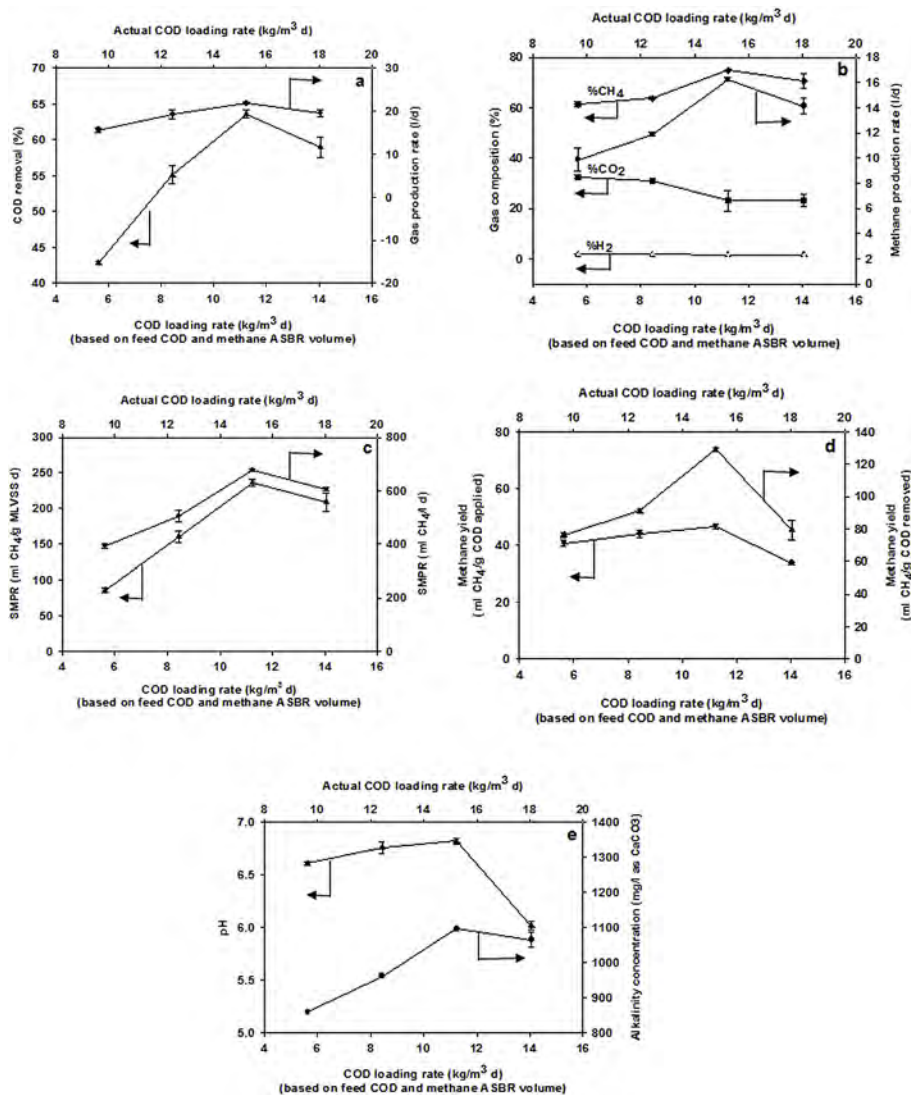
Fig. 4. Effects of COD loading rate on (a) COD removal and gas production rate (b) gas composition and methane production rate (c) specific methane production rate (d) methane yields in the methane ASBR unit when the system was operated at 37 °C, pH 5.5 in the hydrogen ASBR unit, cycle ratio of 1:1 and without controlling pH in methane ASBR unit.

amount of hydrogen (less than 1.9%) (Fig. 4b). Both methane content and methane production rate had a similar trend to the COD removal. This increased with increasing COD loading rate from 5.6 to 11.3 kg/m^{3}d and then decreased with further increasing COD loading rate from 11.3 to 14.1 kg/m^{3}d. In contrast, the carbon dioxide content in the produced gas had an opposite trend to the methane content. The maximum of both methane content and methane production rates were found at a COD loading rate of 11.3 kg/m^{3}d.

Fig. 4c and d shows the specific methane production rates (SMPR) and methane yields as a function of the COD loading rate. Both SMPRs and methane yields increased with increasing COD loading rate from 5.6 to 11.3 kg/m^{3}d and then decreased with further increasing COD loading rate from 11.3 to 14.1 kg/m^{3}d. Both maximum SMPR (232.50 ml CH$_4$/g MLVSS d or 672.84 ml CH$_4$/l d and maximum methane yield (128.4 ml CH$_4$/g COD removed or 47.3 ml CH$_4$/g COD applied) were found at a COD loading rate of 11.3 kg/m^{3}d. Therefore, the COD loading rate of 11.3 kg/m^{3}d based on feed COD load and methane ASBR volume was considered to be an optimum organic loading rate for production of both hydrogen and methane by the two-stage mesophilic ASBR system. The maximum methane yield of 47.3 ml CH$_4$/g COD applied found in

this study was about 39% higher than that from cassava wastewater using a two-stage upflow anaerobic sludge blanket system at ambient temperature [28], suggesting that glycerin is a good substrate for anaerobic digestion to produce methane [30].

Fig. 4e shows the effects of COD loading rate on pH and alkalinity of the methane ASBR unit. They are basically used to indicate the process stability of the methanogenic step. The higher the alkalinity (normally greater than 1000 mg/l as CaCO$_3$), the higher the process stability, and the solution pH in the methane ASBR unit should be in the range of 7—8 but not lower than 6.5 to indicate good process stability. Beyond the optimum COD loading rate, the solution pH drastically dropped lower than 6.5, indicating poor process stability, resulting from the increasing toxicity of VFA accumulation.

The effects of COD loading rate on total VFA concentration and VFA composition of the methane ASBR unit are shown in Fig. 3b. The total VFA concentration steadily increased with increasing COD loading rate and attained a highest value of 980 mg/l as acetic acid at a very high COD loading rate of 14.1 kg/m^{3}d. At this highest COD loading rate of 14.1 kg/m^{3}d, the methane production performances decreased, corresponding to the decrease in COD removal. From the results of total VFA concentration, the toxicity level of VFA to

methane-producing bacteria was around 800 mg/l as acetic acid which is in good agreement with our previous studies [22,23]. The composition of VFA in the methane ASBR unit was found to be much different compared to that in the hydrogen ASBR unit. The acetic acid was the highest and followed by HPr, HBu and HVa. The concentration of acetic acid increased significantly with increasing COD loading rate whereas all other organic acids including ethanol and 1,3 PD were relatively low and remained almost unchanged. The highest concentration of HAc resulted from the sub-sequential degradation of both HPr and HBu, known as acetogenesis, according to Equations (7)–(8) [35]. The formation of methane mainly results from two basic bioconversion reactions, which are the acetotrophic pathway, according to Equation (9) [22,35]and the hydrogenotrophic pathway, according to Equation (10) [35,36]. Furthermore, methane production can directly come from the degradation of the remaining glycerin in the liquid effluent from the hydrogen ASBR unit, described by Equation (11) [30]. The co-digestion of glycerin with biodiesel wastewater was also reported to enhance methane production performance [5].

$$CH_3CH_2CH_2COOH + 2H_2O \rightarrow 2CH_3COOH + 2H_2 \qquad (7)$$

$$CH_3CH_2COOH + 2H_2 \rightarrow CH_3COOH + CO_2 + 3H_2 \qquad (8)$$

$$CH_3COOH \rightarrow CH_4 + CO_2 \qquad (9)$$

$$CO_2 + 4H_2 \rightarrow CH_4 + 2H_2O \qquad (10)$$

$$C_3H_8O_3 \rightarrow 1.75CH_4 + 1.25CO_2 + 0.5H_2O \qquad (11)$$
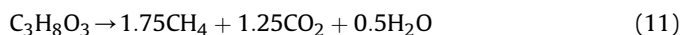
Both SMPRs and methane yields had similar trends to the COD removal. The optimum COD loading rate of 11.3 kg/m^{3}d provided the highest values of SMPRs and methane yields which well corresponded to the maximum values of both alkalinity and system pH. Beyond the optimum COD loading rate of 11.3 kg/m^{3}d, the process performances of the methane ASBR unit in terms methane yields decreased, resulting from the toxicity of VFA accumulation, as described before.

3.3. Microbial concentrations and microbial washout results

Fig. 5 shows the microbial concentrations in terms of mixed liquor volatile suspended solids(MLVSS) in both ASBR units and the microbial washout in terms of effluent volatile suspended solids(VSS) from both ASBR units at different COD loading rates. For both ASBR units, the MLVSS decreased while the effluent VSS increased with increasing COD loading rate.

Under the COD loading rate ranging from 5.6 to 11.3 kg/m^{3}d (based on feed COD load and methane ASBR volume), the increase in hydrogen and methane production performances corresponded to the decreases in the MLVSS. It can be explained by the fact that the increase in COD loading rate directly increased the amount of organic compounds, mainly glycerin available for the microbes to digest, leading to both increases in hydrogen and methane production rates. The results of the decreases in MLVSS with the increases in process performances of both ASBR units and microbial washout indicate that the washout rate of the inactive microbes was lower than the growth rate of active microbes [19]. Beyond the optimum COD loading rate of 67.5 kg/m^{3}d (based on feed COD load and hydrogen ASBR volume) or 11.3 kg/m^{3}d (based on feed COD load and methane ASBR volume), the process performances of both hydrogen and methane ASBR units decreased with further increasing COD loading rate in which both MLVSS and microbial washout remained almost unchanged. The results suggest that the
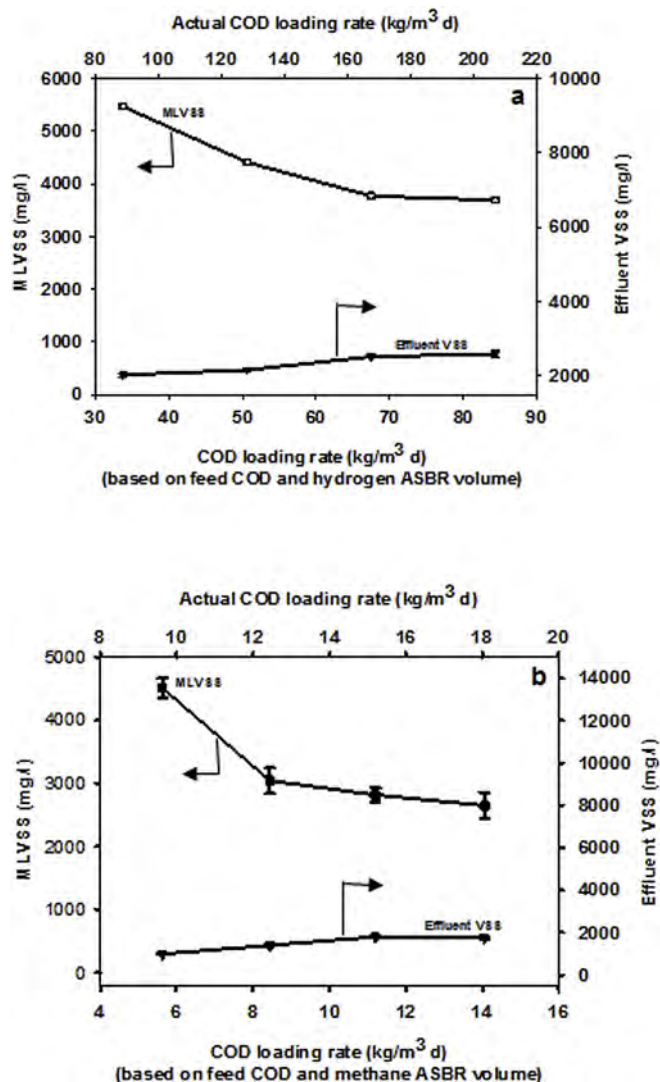
Fig. 5. MLVSS and effluent VSS at different COD loading rates in (a) the hydrogen ASBR. Unit and (b) the methane ASBR unit when the two-stage ASBR system was operated at 37 °C, pH5.5 in the hydrogen ASBR unit, a recycle ratio of 1:1 and without pH control in the methane ASBR unit.

VFA concentrations in both ASBR units already exceeded the toxicity levels of the organic acid concentrations of 13,000 and 800 mg/l as acetic acid to the hydrogen-producing bacteria and methane-producing bacteria, respectively. The inhibition results of the total VFA obtained from the present work are in good agreement with our previous works [17–23].

Sodium is also found insignificant amounts in biodiesel wastewater and it is also one of the necessary elements for the bacterial enzyme cofactors, transport processes and dehydrogenase [21,37–39]. NaOH was also used to control the pH in the hydrogen ASBR unit in this study. Hence, it was necessary to know whether or not the sodium concentration exceeded the inhibitory level of 3500–8000 mg/l [40–42]. The final effluent of the methane ASBR unit was found to have 1600 mg/l of sodium while the sodium concentration in the biodiesel wastewater after 3.5 %w/v glycerin had been added was more or less the same. The sodium concentration in the ASBR system was much lower than the inhibitory level. The result of a very small quantity of NaOH used for the pH control in the hydrogen ASBR unit suggests that recycling the final effluent from the methane ASBR unit was able to raise the pH to

around 5.5 in the hydrogen ASBR unit.

3.4. Nitrogen, phosphorous, and glycerin uptake results

Fig. 6 shows nitrogen, phosphorous, and glycerin uptakes and nitrogen transformation by both hydrogen-producing bacteria and methane-producing bacteria in the hydrogen ASBR unit and methane ASBR unit. The nitrogen, phosphorous, and glycerin uptakes increased with increasing COD loading rate. Under any given COD loading rate, nitrogen, phosphorous, and glycerin uptakes in the hydrogen ASBR unit were higher than those in the methane ASBR unit, which are in good agreement with previous studies [19,22]. The utilization of nitrogen by microbes can come from ammonia-nitrogen, nitrate-nitrogen, nitrite-nitrogen, and organic-nitrogen [43]. The concentrations of ammonium-nitrogen,nitrite-nitrogen and nitrate-nitrogen in both ASBR units slightly decreased with increasing COD loading rate whereas the organic-nitrogen concentration significantly decreased, suggesting that the nitrogen uptakes by both hydrogen-producing bacteria and methane-producing bacteria mostly came from organic-nitrogen [44]. The glycerin uptakes in both ASBR units were high with the overall glycerin removal of 90%, suggesting that glycerin is a good substrate to produce both hydrogen and methane. The results of high glycerine uptakes in both ASBR units also suggest that under the studied conditions, the process performance was affected by the inhibition effect of the VFA accumulation without the toxicity from added glycerin.

3.5. Overall performance

Fig. 7 shows the overall process performance of the two-stage ASBR system as a function of COD loading rate. This two-stage ASBR system operated at the optimum overall COD loading rate of 9.64 kg/m^{3}d (based on total volume of both ASBR units and feed COD load) provided the highest overall hydrogen yield of 26.75 ml

H$_2$/g COD removed or 6.23 ml H$_2$/g COD applied(15.20 ml H$_2$/g glycerin removed or 11.71 ml H$_2$/g glycerin applied), which is lower than that obtained from previous studies [13,17,18]. This is because several toxic compounds are present in the crude glycerin [32]. The process performances in terms of methane yields and SMPRs were found to be comparable to those from other works [45]. The high COD removal of 76.7% and the high glycerin uptake of 90.1% at the optimum COD loading rate suggest that glycerin is a good substrate for production of hydrogen and methane. Under the optimum overall COD loading rate, the two-stage ASBR system gave a relatively low ratio of H$_2$-to-CH$_4$ (1:9.3), as compared with those reported in previous investigations [22,44,46]. The result of the low ratio of H$_2$-to-CH$_4$ suggests that the two steps of hydrogen production by acidogenesis and acidogenesis did not take place completely in the hydrogen ASBR unit and they further continued in the methane ASBR unit. The hydrogen produced in the methane ASBR unit was immediately consumed by the methanogens to yield methane, causing an increase in methane production efficiency with the reduction of hydrogen production efficiency. An attempt to increase the hydrogen production efficiency with the expense of methane production efficiency will be carried out in our future work by increasing the ratio of hydrogen ASBR volume-to-methane ASBR volume. The mixed gases produced from the two-stage ASBR process which contained 6.5%H$_2$, 63.5%CH$_4$ and 30%CO$_2$ at the optimum COD loading rate can provide a higher heating value, as compared with those of single anaerobic processes [18].

4. Conclusions

Under the optimum COD loading rate of 11.25 kg/m^{3}d (based on feed COD load and methane ASBR volume) or 9.64kg/m^{3}d (based on feed COD load and total volume of both ASBR units), the two-stage ASBR system provided the highest process performances of both hydrogen and methane production. The use of final effluent recycle could maintain the pH 5.5 in the hydrogen ASBR unit without NaOH
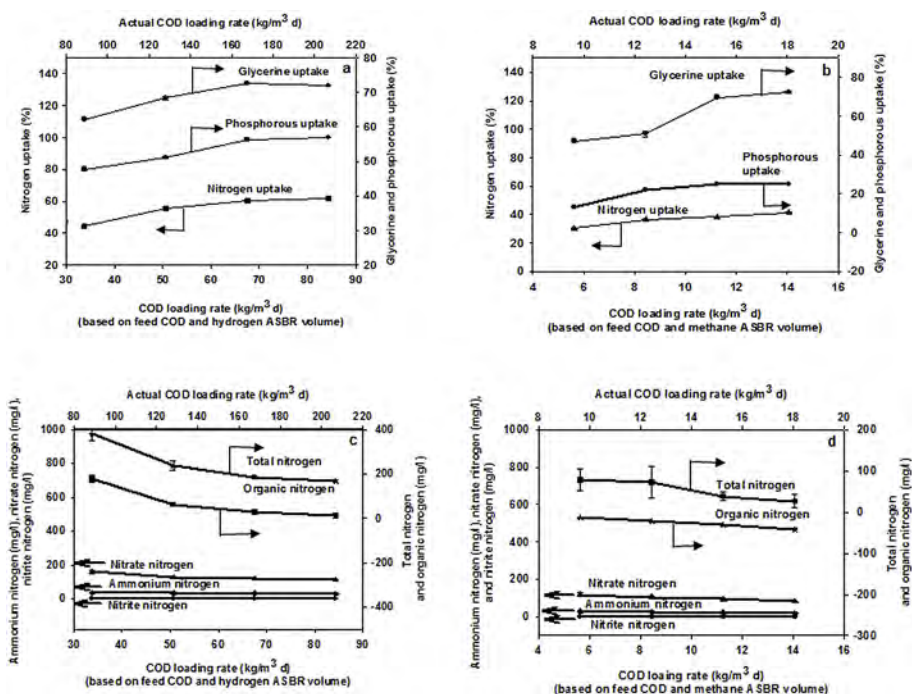
Fig. 6. Effects of COD loading rate on (a) glycerin, nitrogen and phosphorus uptakes in the hydrogen ASBR unit, (b) glycerin, nitrogen and phosphorus uptakes in the methane ASBR unit, (c) concentration profiles of different nitrogen compounds in the hydrogen ASBR unit and (d) concentration profiles of different nitrogen compounds in the methane ASBR unit.
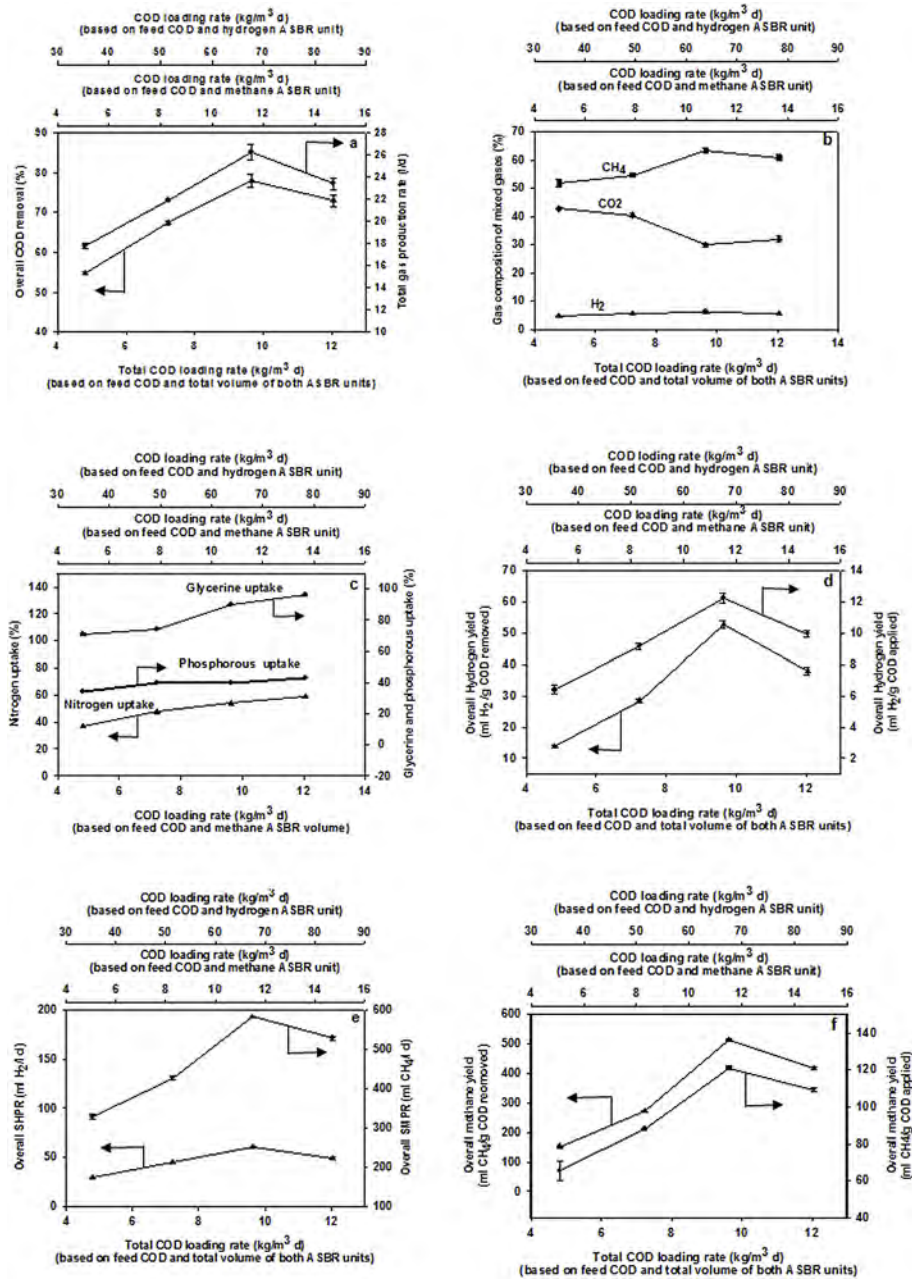
Fig. 7. Effects of COD loading rate on (a) total COD removal and total gas production rate, (b) gas composition of mixed gas, (c) total uptakes of glycerin, nitrogen and phosphorous, (d) overall hydrogen yields, (e) overall SHPRs and SMPRs, and (f) overall methane yields when the system was operated at 37 °C, pH 5.5 in the hydrogen ASBR unit and a recycle ratio of 1:1.

requirement. The results suggest that a use of glycerin as a substrate is feasible technically for separate production of hydrogen and methane by using a two-stage ASBR system. The low volumetric ratio of hydrogen ASBR unit-to-methane ASBR unit (1:6) of the studied two-stage ASBR system favored methane production more than hydrogen production. An increase in the volumetric ratio is hypothesized to increase the hydrogen production efficiency with a reduction of methane production efficiency. The use of mixed gas produced from a two-stage anaerobic system can provide a higher heating value than the biogas generated from any single anaerobic unit. The toxic levels of produced VFA were found to be 13,000 and 800 mg/l as acetic acid to hydrogen-producing bacteria and methane-producing bacteria, respectively.

References

[1] M. Ayoub, A.Z. Abdulah, Critical review on the current scenario and significance of crude glycerol resulting from biodiesel industry towards more sustainable renewable energy industry, Renew. Sust. Energy Rev. 16 (2012) 2671—2686.

[2] M.A. Dasari, P.P. Kiatsimkula, W.R. Sutterlinb, G.J. Suppesa, Low-pressure hydrogenolysis of glycerol to propylene glycol, Appl. Catal. A General 281 (2005) 225—231.

[3] S.S. Yazdani, R. Gonzalez, Anaerobic fermentation of glycerol: a path to economic viability for the biofuels industry, Curr. Opin. Biotechnol. 18 (2007) 213—219.

[4] D.T. Johnson, K.A. Taconi, Paper the glycerin glut: options for the value-added conversion of crude glycerol resulting from biodiesel production, Environ. Prog. 26 (2007) 338—348.

[5] J.A. Sile, M.A. Martín, A.F. Chica, A. Martín, Co-digestion of glycerol and wastewater derived from biodiesel manufacturing, Bioresour. Technol. 101 (2010) 6315—6321.

[6] A. Demirbas, Methane gas hydrate, Green Energy Technol. (2010) 77—111. ISBN: 978-1-84882-871-1.

[7] N.R. Udengaard, Hydrogen production by steam reforming of hydrocarbons, Am. Chem. Soc. Div. 49 (2004) 906—907.

[8] S. Kumar, S. Kumar, J.K. Prajapati, Hydrogen production by partial oxidation of methane: modeling and simulation, Int. J. Hydrogen Energy 34 (2009) 6655—6668.

[9] M.H. Halabi, M.H.J.M. de Croon, J. van der Schaaf, P.D. Cobden, J.C. Schouten, Modeling and analysis of autothermal reforming of methane to hydrogen in a fixed bed reformer, Chem. Eng. J. 137 (2008) 568—578.

[10] M.A. Naeem, A.S. Al-Fatesh, A.H. Fakeeha, A.E. Abasaeed, Hydrogen production from methane dry reforming over nickel-based nanocatalysts using surfactant-assisted or polyol method, Int. J. Hydrogen Energy 39 (2014) 17009—17023.

[11] S.N. Reddy, S. Nanda, A.K. Dalai, J.A. Kozinski, Supercritical water gasification of biomass for hydrogen production, Int. J. Hydrogen Energy 39 (2014) 6912—6926.

[12] A.C.D. Freitas, R. Guirardell, Comparison of several glycerol reforming methods for hydrogen and syngas production using thermodynamic analysis, in: Conference Presentation AlChE, School of Chemical Engineering, University of Campinas, 2013, pp. 13083—13852.

[13] T. Chookaew, P. Prasertsan, Z.J. Ren, Two-stage conversion of crude glycerol to energy using dark fermentation linked with microbial fuel cell or microbial electrolysis cell, New Biotechnol. 31 (2014) 179—184.

[14] P.A. Selembo, M.J. Parez, W.A. Lloyd, B.E. Logan, Enhanced hydrogen and 1,3-propanediol production from glycerol by fermentation using mixed cultures, Biotechnol. Bioeng. 104 (2009) 1099—1106.

[15] K. Seifert, M. Waligorska, M. Wojtowski, M. Laniecki, Hydrogen generation from glycerol in batch fermentation process, Int. J. Hydrogen Energy 34 (2009) 3671—3678.

[16] T. Vlassis, G. Antonopoulou, K. Stamatelatou, G. Lyberatos, Anaerobic treatment of glycerol for methane and hydrogen production, Glob. N. J. 14 (2012) 149—156.

[17] T. Poontaweegeratigarn, S. Chavadej, P. Rangsunvigit, Hydrogen production from alcohol wastewater by upflow anaerobic sludge blanket reactors under mesophilic temperature, Energy Technol. 6 (2012) 396—399.

[18] P. Intanoo, T. Suttikul, M. Leethochawalit, E. Gulari, S. Chavadej, Hydrogen production from alcohol wastewater with added fermentation residue by an anaerobic sequencing batch reactor (ASBR) under thermophilic operation, Int. J. Hydrogen Energy 39 (2014) 9611—9620.

[19] P. Intanoo, P. Rangsunvigit, W. Namprohm, B. Thamprajamchit, J. Chavadej, S. Chavadej, Hydrogen production from alcohol wastewater by an anaerobic sequencing batch reactor under thermophilic operation: nitrogen and phosphorous uptakes and transformation, Int. J. Hydrogen Energy 37 (2012) 11104—11112.

[20] T. Sreethawong, S. Chatsiriwatana, P. Rangsunvigit, S. Chavadej, Hydrogen production from cassava wastewater using an anaerobic sequencing batch reactor: effects of operational parameters, COD: N ratio, and organic acid composition, Int. J. Hydrogen Energy 35 (2010) 4092—4102.

[21] C.Y. Lin, C.H. Lay, A nutrient formulation for fermentative hydrogen production using anaerobic sewage sludge microflora, Int. J. Hydrogen Energy 30 (2004) 285—292.

[22] P. Intanoo, P. Rangsanvigit, P. Malakul, S. Chavadej, Optimization of separate hydrogen and methane production from cassava wastewater using two-stage upflow anaerobic sludge blanket reactor (UASB) system under thermophilic operation, Bioresour. Technol. 173 (2014) 256—265.

[23] P. Intanoo, P. Chaimongkol, S. Chavadej, Hydrogen and methane production from cassava wastewater using two-stage upflow anaerobic sludge blanket reactors (UASB) with an emphasis on maximum hydrogen production, Int. J. Hydrogen Energy 41 (2016) 6107—6114.

[24] E.C. Koutrouli, H. Kalfas, H.N. Gavala, I.V. Skiadas, K. Stamatelatou, G. Lyberatos, Hydrogen and methane production through two-stage mesophilic anaerobic digestion of olive pulp, Bioresour. Technol. 100 (2009) 3718—3723.

[25] Anaerobic Digestion Process, WtERT(Waste-to-Energy Research and Technology Council), 2009. http://www.wtert.eu/ (Accessed 24 January 2014).

[26] Anaerobic digestion, Wikipedia. http://www.en.wikipedia.org/(Accessed on 18 July 2015).

[27] T. Vlassis, G. Antonopoulou, K. Stamatelatou, G. Lyberatos, Anaerobic treatment of glycerol for methane and hydrogen production, Glob. NEST J. 14 (2012) 149—156.

[28] O. Khongsumran, P. Intanoo, P. Rangsunvigit, S. Chavadeja, M. Leethochawalit, Enhancement of anaerobic digestion of cellulosic fraction in cassava production wastewater by microaeration, Chem. Eng. Trans. 39 (2014) 553—558.

[29] A.D. Eaton, L.S. Clesceri, E.W. Rice, A.E. Greenberg, Standard Methods for the Examination of Water and Wastewater, American Public Health Association (APHA), American Water Works Association (AWWA) and Water Environment Federation (WEF), Washington Dc, 2005.

[30] M.S. Fountoulakis, T. Manios, Enhanced methane and hydrogen production from municipal solid waste and agro-industrial by-products co-digested with crude glycerol, Bioresour. Technol. 100 (2009) 3043—3047.

[31] P. Intanoo, J. Chavadej, S. Chavadej, Effect of COD loading rate on hydrogen production from alcohol wastewater, World Acad. Sci. Eng. Technol. 6 (2012) 295—299.

[32] S.J. Sarma, S.K. Brar, E.B. Sydney, Y.L. Bihan, G. Buelna, C.R. Soccol, Microbial hydrogen production by bioconversion of crude glycerol: a review, Int. J. Hydrogen Energy 37 (2012) 6473—6490.

[33] International Conference on Water Resource and Environment, WREP2014, DEStech, 2014 (Accessed 30 April 2016).

[34] B.T. Maru, M. Constanti, A.M. Stchigel, F. Medina, J.E. Sueiras, Biohydrogen production by dark fermentation of glycerol using Enterobacter and Citrobacter Sp, Am. Inst. Chem. Eng. 29 (2012) 31—38.

[35] T. Abbasi, S.M. Tauseef, S.A. Abbasi, Anaerobic digestion for global warming control and energy generation - an overview, Renew. Sust. Energy Rev. 16 (2012) 3228—3242.

[36] B. Demirel, P. Scherer, The roles of acetotrophic and hydrogenotrophic methanogens during anaerobic conversion of biomass to methane: a review, Environ. Sci. Biotechnol. 7 (2008) 173—190.

[37] X. Hao, M. Zhou, H. Yu, Q. Shen, L. Lei, Effect of sodium ion concentration on hydrogen production from sucrose by anaerobic hydrogen-producing granular sludge, Chin. J. Chem. Eng. 14 (2006) 511—517.

[38] W.H. Chen, S.K. Han, S. Sung, Sodium inhibition of thermophilic methanogens, J. Environ. Eng. 129 (2003) 506—512.

[39] A. Rinzema, J.V. Lier, G. Lettinga, Sodium inhibition of acetoclastic methanogens in granular sludge from a UASB reactor, Enzyme Microb. Technol. 10 (1987) 101—109.

[40] G. Parkin, R. Owen, Fundamentals of anaerobic digestion of wastewater sludges, J. Environ. Eng. 112 (1986) 867—920.

[41] Y. Chen, J.J. Cheng, K.S. Creamer, Inhibition of anaerobic digestion process: a review, Bioresour. Technol. 99 (2007) 4044—4064.

[42] P.L. McCarty, Anaerobic Waste Treatment Fundamentals, Stanford University 95, 1964, pp. 107—112.

[43] A.T.W.M. Hendriks, G. Zeeman, Pretreatments to enhance the digestibility of lignocellulosic biomass, Bioresour. Technol. 100 (2009) 10—18.

[44] G. Luo, L. Xie, Z. Zou, W. Wang, Q. Zhou, H. Shim, Anaerobic treatment of cassava stillage for hydrogen and methane production in continuously stirred tank reactor (CSTR) under high organic loading rate (OLR), Int. J. Hydrogen Energy 35 (2010) 11733—11737.

[45] G. Peixoto, J.L.R. Pantoja-Filho, J.A.B. Agnelli, M. Barboza, M. Zaiat, Hydrogen and methane production, energy recovery, and organic matter removal from effluents in a two-stage fermentative process, Biochem. Biotechnol. 16 (2012) 651—671.

[46] N. Pisutpaisal, C. Nathaoa, U. Sirisukpokac, Biological hydrogen and methane production in from food waste in two-stage CSTR, Energy. Procedia 50 (2014) 719—722.

Equilibrium and dynamic surface tension in relation to diffusivity and foaming properties: Effects of surfactant type and structure

CrossMark

Paweena Kanokkarn[a], Takeo Shiina[b], Malee Santikunaporn[c], Sumaeth Chavadej[a,d,*]

[a] *The Petroleum and Petrochemical College, Chulalongkorn University, Bangkok, Thailand*
[b] *Faculty of Horticulture, Graduate School of Horticulture, Chiba University, Chiba, Japan*
[c] *Department of Chemical Engineering, Faculty of Engineering, Thammasat University, Pathumthani, Thailand*
[d] *Center of Excellence on Petrochemical and Materials Technology, Chulalongkorn University, Bangkok, Thailand*

ARTICLE INFO

ABSTRACT

The main objectives of this study were to investigate the effects of molecular structure of surfactant on surface properties and foam characteristics and to correlate surface tension to foam properties. Two series of methyl ester sulfonate with different alkyl chain lengths (MES$_x$, x = 14, 16, and 18) and polyoxyethylated dodecyl alcohol with different head group sizes (C$_{12}$EO$_n$, n = 3, 5, 7, and 9) were measured for equilibrium and dynamic surface tension as well as foamability and foam stability. The equilibrium experimental data were well fitted with the Langmuir adsorption isotherm. The dynamic surface tension data were used to calculate diffusivity values of all studied surfactants by using Word-Tordai equation. The longer the alkyl group of MES$_x$, the lower the diffusivity value. The larger the EO head group size, higher the diffusivity. For both studied surfactant groups, the higher the maximum rate of surface tension reduction, the higher the diffusivity and foaming properties in terms of foamability and foam stability.

1. Introduction

The scarcity of clean fresh water has become a serious issue in relation to urbanization in the last few decades because of the limitations of water resources and increasing pollution. Purification and the treatment of polluted water have become more and more common. Among wastewater technologies available, froth flotation is of great interest for removing oils [1–4], metals [5–7], and solid particles [8–10] from wastewaters at low concentrations because of its simplicity in operation and design and low operational cost [11,12]. To successfully operate froth flotation, both high foamability and high foam stability with dry foam (low water content in generated foam) are crucial to achieve high separation efficiency (high removal with high enrichment ratio) [13]. Therefore, an important point is that the understanding of foam behaviors, which are fundamentally governed by the properties of added surfactants including other soluble components present in water especially type, chemical structure and concentration [14–18]. Under the flotation process, foam is always formed in a very short time and so the equilibrium adsorption does not reach [18,19]. Therefore, the use of equilibrium surface properties cannot apply to froth flotation processes. The relation of dynamic surface tension results of surfactant solutions to the foam behaviors will be, for

the first time of its kind, discussed in this work.

The main objective of this work was to employ a numerical approach to dynamic surface tension data for calculating diffusivity and to correlate dynamic surface tension and diffusivity to foaming properties of different surfactant solutions. The influence of surfactant structures—the alkyl chain length of a series of methyl ester sulfonate (MES$_x$) homologues and the head group size of a series of polyoxyethylated dodecyl alcohol (C$_{12}$EO$_n$) homologues—on the equilibrium and dynamic surface properties, and adsorption behaviors at air/water interface was also investigated systematically. In addition, the effect of an electrolyte (NaCl) on their surface tension (dynamic and equilibrium) and foaming behaviors was also discussed. Both MES$_x$ and C$_{12}$EO$_n$ were selected in this study because they are considered as environmental friendly surfactants and they were hypothesized to be good for froth flotation application.

2. Experimental description

2.1. Materials

Methyl ester sulfonate anionic surfactant homologues with different alkyl chain lengths (MES$_x$, x = 14, 16 and 18) were kindly supplied by

---

* Corresponding author at: The Petroleum and Petrochemical College, Chulalongkorn University, Bangkok, Thailand.
E-mail address: sumaeth.c@chula.ac.th (S. Chavadej).

the Lion Corporation. In this, x stands for average alkyl units having a molecular weight of 372, 400 and 428, respectively with of ≥99% purity in powder form. Sodium dodecyl sulfonate (SDS) having ≥99% purity and a molecular weight of 288.4 in powder form was purchased from Sigma-Aldrich. Commercial polyoxyethylated dodecyl alcohol nonionic surfactant homologues with different head group sizes (a narrow distribution of EO units, $C_{12}EO_n$, n = 3, 5, 7, and 9) were kindly supplied by the Thai Ethoxylate Co., Ltd. In this, n stands for the average number of EO units having molecular weights of 332, 420, 508, and 596, respectively with of ≥99% purity in liquid form. Sodium chloride (NaCl, analytical grade, having 99% purity) was obtained from Labscan Asia Co., Ltd. (Thailand). All chemicals were used as received without further purification and distilled water was used throughout all experiments. A certain amount of each surfactant was dissolved in distilled water to obtain a desired concentration. All surfactant solutions were freshly prepared before used.

2.2. Surface tension measurements

2.2.1. Equilibrium surface tension measurement

Surface tension measurement of various surfactant solutions was carried out by a tensiometer (Krüss, Germany, K100) with a Wilhelmy plate at 25.0 ± 0.1 °C. The plate was cleaned with ethanol and distilled water and flamed before each measurement. Each sample was measured for equilibrium surface tension after at least 10 min to ensure the saturation of surfactant adsorption on the air/water interface.

2.2.2. Dynamic surface tension measurement

The measurement of dynamic surface tension of all surfactant solutions was performed using a bubble pressure tensiometer (Krüss, Germany, BP2) at 25.0 ± 0.1 °C. It involved the measurement of the maximum bubble pressure to blow out a gas bubble through a capillary tube (having a diameter of 0.234 mm), which was submerged in a sample liquid. The measurements of dynamic surface tension were conducted with different surface ages in the range of 5–20,000 ms.

2.3. Foamability and foam stability measurements

Foamability and foam stability measurements were conducted using a glass column having an internal diameter of 5 cm and a column height of 120 cm. A quantity of 200 mL of any aqueous surfactant solutions was added to the column. Compressed air was introduced at the bottom of the column at a constant rate of 0.3 L/min regulated by a mass flow controller (Cole-Parmer, 32457-42) to generate fine air bubbles by passing through a sintered glass disk with pore size diameters in the range of 16–40 μm [2,3]. The time required to reach a maximum height of 120 cm was used to indicate foamability. The time required for the foam height to collapse from 120 to 60 cm without introducing air was used to indicate foam stability [20]. The foam characteristic experiments were carried out at room temperature (25–30 °C).

3. Results and discussion

3.1. Equilibrium surface tension and adsorption isotherm results

Fig. 1a and b illustrates the equilibrium surface tension isotherms of two series of MES$_x$ with different alkyl chain lengths (14, 16 and 18) and $C_{12}EO_n$ with different amounts of EO units (3, 5, 7, and 9) to indicate the effects of the chain length of the hydrophobic portion and the size of the hydrophilic portion, respectively, as compared with that of well-known anionic surfactant, SDS. The surface tension isotherm shifted towards lower surfactant concentrations with increasing either alkyl chain length or the size of the hydrophilic head group but the effect of the increase in alkyl chain length was much more pronounced than that of the increase in the size of the hydrophilic head group.

The Gibbs adsorption isotherm equation (Eq. (1)) [15,19,21,22] was used to calculate the equilibrium surfactant adsorption densities (saturation surface excess concentrations) for the two series of studied surfactants at the air/water interface.

$$\Gamma = -\frac{1}{nRT} \cdot \left(\frac{d\gamma}{dlnC} \right) \tag{1}$$

where γ is the surface tension of surfactant solution (mN/m), C is the bulk concentration of surfactant (μM), R is the gas constant value (8.314 J/mol K), T is the temperature of a solution (K), Γ is the excess surface concentration (μmol/m²), and n is the number of solute species whose concentration at the interface changes with change in the value of C, which is considered to be 1 for a nonionic surfactant system or anionic surfactant with the presence of an excess concentration of electrolyte and 2 for an anionic surfactant system without added electrolyte.

Fig. 2a and b shows the effects of alkyl chain length of MES$_x$ and the size of the hydrophilic head group of $C_{12}EO_n$ on the equilibrium surfactant adsorption density at the air/water interface, respectively, as a function of initial surfactant concentration. The results revealed that the adsorption density of any studied surfactant increased with increasing surfactant concentration and reached a maximum value. The region of constant surfactant adsorption density is known as the Gibbs–close pack monolayer [23]. It also showed that the surfactant with a longer alkyl chain length had a higher adsorption density but the surfactant with a larger hydrophilic head group size had a lower adsorption density. The explanation of the effect of the surfactant structure on the adsorption density will be described later.

The surfactant adsorption density isotherms, as shown in Fig. 2, were found to fit well to the Langmuir adsorption isotherm (Eq. (2)), with two important parameters of the excess surface concentration at saturation or the maximum surfactant adsorption density (Γ_m) and the Langmuir equilibrium adsorption constant (K_L) [24,25].

$$\Gamma = \frac{\Gamma_m K_L C}{1 + K_L C} \tag{2}$$

where Γ_m is the maximum (saturated) excess surface concentration (μmol/m²), and K_L is the Langmuir equilibrium adsorption constant (L/mol).

As shown in Table 1, for the homologous series of MES$_x$, an increase in the alkyl chain length (increasing hydrophobic tail group) increases the steric effect, causing an increase in the aggregation number and the enhancement of micelle formation, leading to a decrease in CMC. For the homologous series of $C_{12}EO_n$, an increase in the number of EO units (increasing hydrophilic head group size) results in a decrease in surfactant adsorption density, causing the reduction of surface activity and an increase in CMC. The present results of CMC, γ_{cmc} and pC_{20} are in excellent agreement with other surfactants, for example SDS, investigated previously [14,16,26–28]. The γ_{cmc} value slightly increased with an increase in alkyl chain length of MES$_x$ series or the number of EO units of $C_{12}EO_n$ series because the longer the alkyl chain length (larger hydrophobic tail group) and the higher the number of EO units (larger hydrophilic head group), the larger the volume of the hydrophobic and hydrophilic portions, respectively, leading to a looser arrangement at the interface of air/water [28].

A higher pC_{20} value was obtained from a longer alkyl chain length or a larger number of EO units, suggesting that both changes in hydrophobic and hydrophilic portions can affect surfactant adsorption efficiency [15,28]. A higher value of pC_{20} generally indicates a higher surfactant adsorption efficiency at the air/water interface and a greater ability for the reduction of surface tension, implying that lower energy is needed to bring the surfactant molecules to the air/water interface [15]. For the homologous series of anionic surfactants, the Γ_m value increased with an increase in alkyl chain length since this simply increases the steric effect, causing a closer pack of surfactant molecules
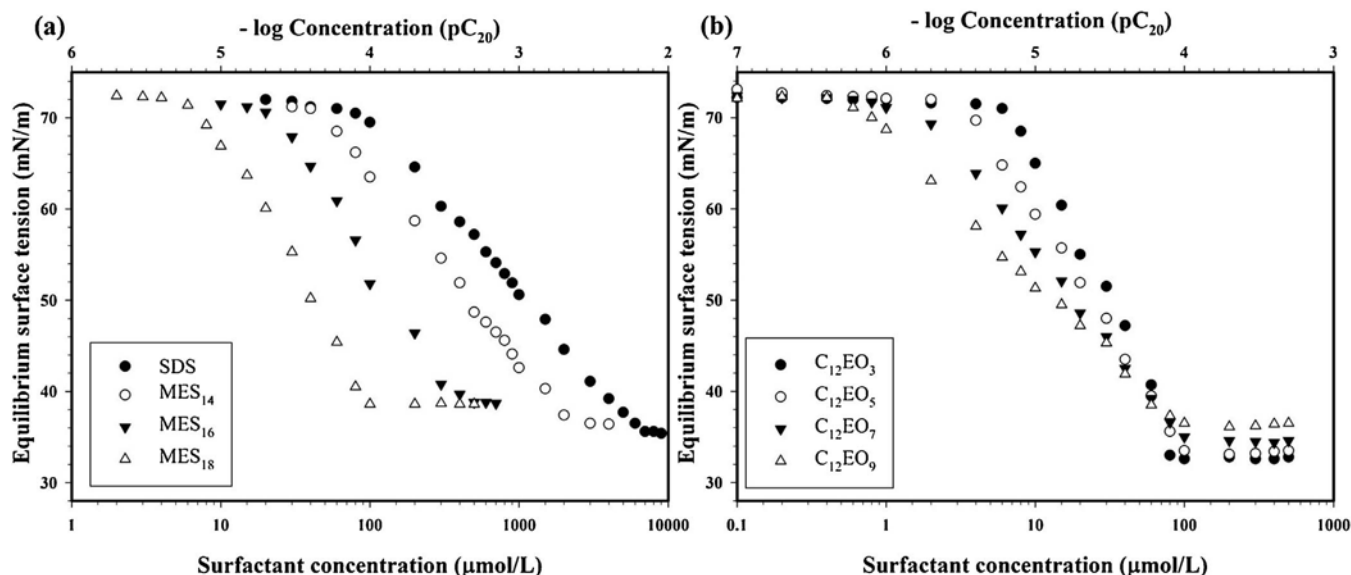
Fig. 1. Surface tension of surfactant solution as a function of concentration (a) MES_x with different alkyl chain length and SDS and (b) $C_{12}EO_n$ with different amounts of EO units.
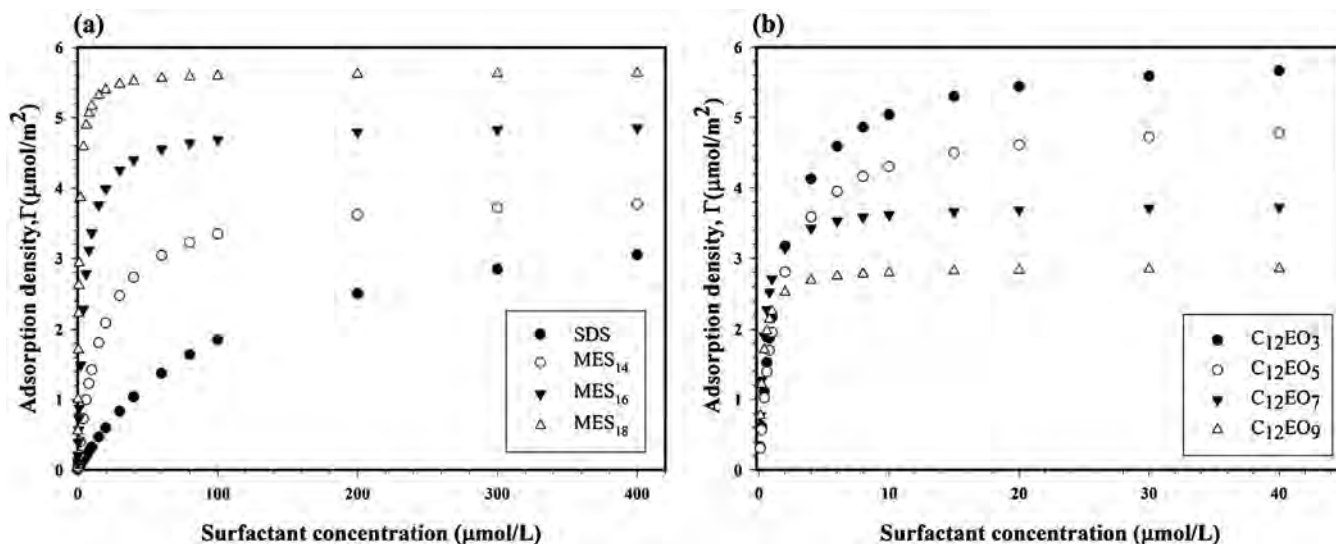
Fig. 2. Adsorption density of surfactant solution as a function of concentration (a) MES_x with different alkyl chain length and SDS and (b) $C_{12}EO_n$ with different amounts of EO units.

Table 1
Calculated values of CMC, γ_{cmc}, pC20, saturated surface concentrations (Γ_m) and Langmuir equilibrium adsorption constant (K_L) of all studied surfactants.

Surfactant	CMC (mol/L)	γ_{CMC} (mN/m)	pC_{20}	Γ_m ($\mu mol/m^2$)	K_L (L/mol)
SDS	7.25×10^{-3}	36.3	3.08	3.89	9.11×10^3
MES_{14}	2.16×10^{-3}	36.7	3.4	3.94	5.66×10^4
MES_{16}	3.26×10^{-4}	38.6	3.93	4.90	2.19×10^5
MES_{18}	1.00×10^{-4}	38.5	4.47	5.64	1.08×10^6
$C_{12}EO_3$	8.00×10^{-5}	32.4	4.53	5.91	5.80×10^5
$C_{12}EO_5$	9.00×10^{-5}	33.4	4.7	4.96	6.51×10^5
$C_{12}EO_7$	1.00×10^{-4}	34.9	4.81	3.76	2.57×10^6
$C_{12}EO_9$	1.00×10^{-4}	36.1	4.97	2.87	3.67×10^6

[29]. It is directly analogous to the corresponding reduction in CMC as explained previously [16,30–32]. For the homologous series of non-ionic surfactants, the Γ_m value decreased with the increasing amount of EO units. It can be explained in that the higher the amount of the EO unit, the larger the head group size of surfactant to lower the surfactant adsorption [26,28,32–34]. The value of free energy ($\Delta G°$) for surfactant adsorption onto the air/water interface directly relates to both pC_{20} and

K_L [15,35–38]. A large K_L caused $\Delta G°$ to become more negative, resulting in higher surfactant adsorption efficiency. The K_L value increased with increasing alkyl chain length or the number of EO units, which corresponded well with the results of pC_{20}. From the results, it can be concluded that the structures of both hydrophobic and hydrophilic portions significantly affect surfactant adsorption at the air/water interface.

3.2. Dynamic surface tension results

Dynamic surface tension measurements were performed using a maximum bubble–pressure technique to investigate the kinetic adsorption at the air/water interface of all studied surfactants. The dynamic surface tension values of two series of studied surfactants (MES_{16} and $C_{12}EO_9$) as a function of bubble age at different concentrations are shown in Fig. 3a and b, respectively. For any given surfactant concentration, an increase in air bubble age provided a higher reduction of surface tension. It was observed that as the surfactant concentration increased, the dynamic surface tension reduction was faster and greater. The profile of the dynamic surface tension isotherm can be divided into four regions: (i) the induction region, (ii) the rapid fall
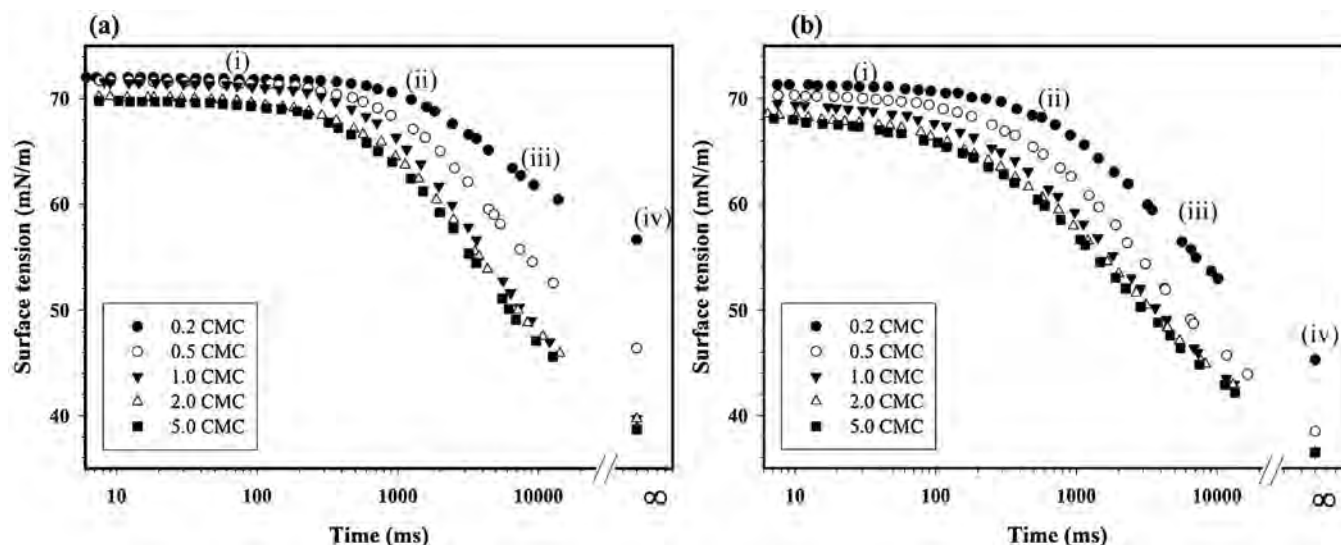
Fig. 3. Dynamic surface tension γ(t) of surfactant solution (a) MES$_{16}$ and (b) C$_{12}$EO$_9$ at air/water interface for five different concentrations.

region, (iii) the meso-equilibrium region, and (iv) the equilibrium region. The first three regions can be described by the following equation [15,16,39–41]:

$$\gamma_t = \gamma_m + \frac{(\gamma_o - \gamma_m)}{[1 + (^t/_{t^*})^n]} \tag{3}$$

where γ_t is the dynamic surface tension at time t, γ_o is the surface tension of pure solvent (water), γ_m is the meso–equilibrium surface tension of surfactant solution, t^* is the time required to attain a half value between γ_o and γ_m, and n is a constant. The values of t^* and n are determined by fitting the above equation with the measured values of dynamic surface tension at different times. The t^* value depends on the diffusion rate of surfactant from the bulk solution to the subsurface. The lower the t^* value, the lower the hindrance of diffusion, or the faster the diffusion rate of added surfactant. The n is a constant, depending on the molecular structure of added surfactant. It indicates the difference between the energies of surfactant adsorption and desorption [15,42]. The higher the n value, the higher the potential barrier of surfactant adsorption or the greater the difficulty for a surfactant to adsorb at the air/water interface [43].

As shown in Table 2, both values of t^* and n decrease with an increase in surfactant concentration of both groups of studied surfactants according to an increase in the driving force from the increase in concentration gradient [15]. For any given surfactant concentration, an increase in the alkyl chain length of MES$_x$ series resulted in the increase in the t^* value, indicating a decrease in the diffusion rate whereas an increase in the head group size (higher EO units) of C$_{12}$EO$_n$ series causes a reduction of the t^* value (an increase in diffusion rate). The results can be explained by the fact that an increase in the hydrophobic portion (alkyl chain length) of the MES$_x$ series caused a larger structure size to delay the transport of surfactant molecules from the bulk liquid to the subsurface or to decrease the surfactant diffusivity [27]. The decrease in the size of the head group (lower EO units) of the C$_{12}$EO$_n$ series can slow down the transport of surfactant molecules from the bulk liquid to the subsurface or cause a decrease in the surfactant diffusivity [28].

Fig. 4a and b illustrates the dynamic surface tension as a function of time for MES$_x$ with different alkyl chain lengths and C$_{12}$EO$_n$ with different amounts of EO units, respectively at very high surfactant concentrations (several times their CMC values). The use of high surfactant concentrations in these experiments was to minimize the lateral surfactant diffusion from the thick surface to the thin surface of a generated air bubble, known as the Gibbs–Marangoni effect [15,23,25], causing the dominance of the vertical surfactant diffusion from the bulk

Table 2
Dynamic surface tension parameters for all studied surfactant solutions.

Surfactant	Conc (times of CMC)	n	t* (ms)	$\left(\frac{\partial \gamma_t}{\partial t}\right)_{max}$
MES$_{14}$	0.2	1.20	5200	1.16
	0.5	1.13	4515	1.84
	1	1.09	3772	2.50
	2	1.06	3472	2.72
	5	1.00	3355	2.65
MES$_{16}$	0.2	1.24	5370	0.89
	0.5	1.16	4739	1.57
	1	1.13	4012	2.27
	2	1.06	3796	2.32
	5	1.03	3680	2.33
MES$_{18}$	0.2	1.28	5446	0.70
	0.5	1.24	5286	1.56
	1	1.18	4815	2.05
	2	1.14	4333	2.20
	5	1.08	4184	2.16

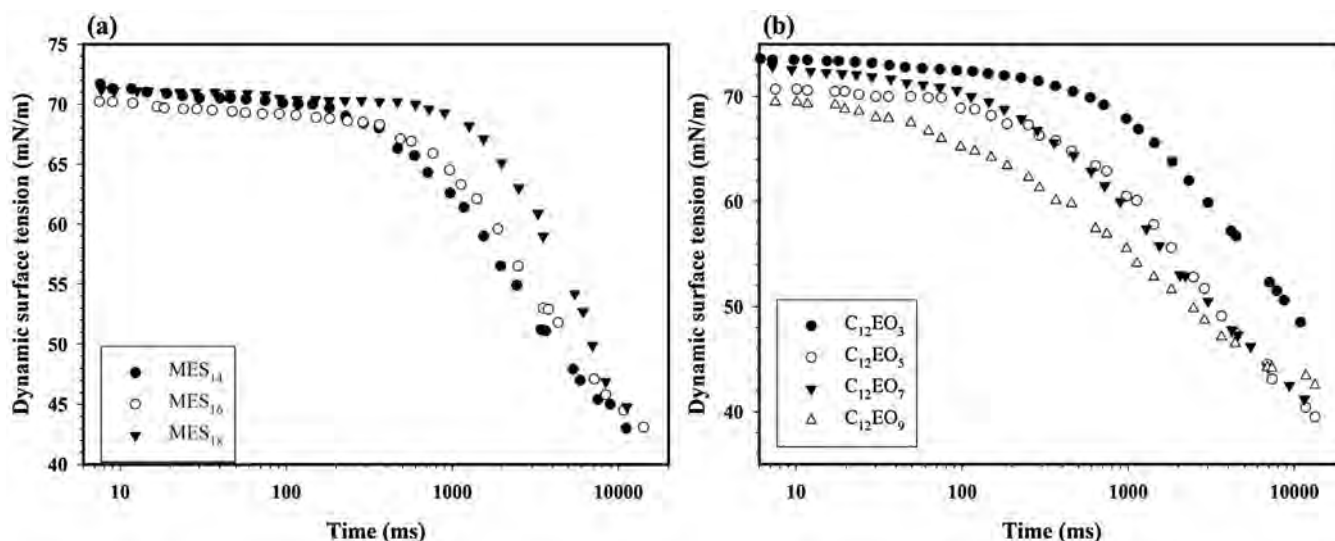| Surfactant	Conc (times of CMC)	n	t* (ms)	$\left(\frac{\partial \gamma_t}{\partial t}\right)_{max}$
C$_{12}$EO$_3$	0.2	1.20	6273	1.28
	0.5	1.08	6094	1.48
	1	0.97	5868	1.47
	2	0.95	5866	1.44
	5	0.90	5710	1.40
C$_{12}$EO$_5$	0.2	1.11	4893	1.36
	0.5	0.98	4578	1.53
	1	0.97	4431	2.11
	2	0.92	4101	2.16
	5	0.85	3991	2.05
C$_{12}$EO$_7$	0.2	1.05	4846	1.59
	0.5	0.98	4409	1.97
	1	0.96	3923	2.27
	2	0.89	3579	2.32
	5	0.81	3344	2.26
C$_{12}$EO$_9$	0.2	0.95	4089	1.56
	0.5	0.93	3042	2.56
	1	0.84	2432	3.05
	2	0.81	2276	3.14
	5	0.73	2090	3.10

Fig. 4. Dynamic surface tension of (a) MES_x with different alkyl chain length at the concentration of 2.0 mM/L (b) $C_{12}EO_n$ with different amounts of EO units at the concentration of 0.2 mM/L.

liquid to the new surface of a generated air bubble.

From Fig. 4, the time required to reach the equilibrium surface tension increased with increasing alkyl chain length for the MES_x series, while it decreased with an increasing number of EO units for the $C_{12}EO_n$ series. The same explanation used for the t^* results can be used to point out the effects of both alkyl chain length and size of the hydrophilic head group on the dynamic surface tension.

3.3. Surfactant diffusivity value results

The surfactant adsorption process consists of two sequential steps of the diffusion of surfactant molecules from the bulk aqueous phase to the subsurface due to the concentration gradient, and the adsorption of surfactant molecules from the subsurface to the air/water interface [16,44,45]. Generally, the diffusion rate is much slower than that of the adsorption rate, thus, the whole process can be reasonably assumed that it is basically controlled by diffusion [44,45]. By using Fick's law to describe the diffusion of surfactant molecules from the bulk liquid to the subsurface and Langmuir adsorption isotherm to describe the surfactant adsorption onto the air/water interface of generated foam, dynamic surfactant adsorption as a function of time can be derived, as shown in Eq. (4) [21,25,27,28,34,44–50]:

$$\Gamma(t) = 2C_o\sqrt{\frac{Dt}{\pi}} - 2\sqrt{\frac{D}{\pi}}\int_0^{\sqrt{t}} C_s d\left(\sqrt{t-\tau}\right) \tag{4}$$

where $\Gamma(t)$ is the surface excess concentration at time t, D is the apparent diffusion coefficient, C_o is the bulk surfactant concentration, and C_s is the surfactant concentration at the subsurface and τ is a dummy time delay variable. The term of $\Gamma(t)$ in Eq. (4) is then replaced by the dynamic surface tension from Eq. (1) and finally the combined equation is simplified for two cases of short time and long time, as shown in Eqs. (5) and (6), respectively [16,19,21,22,27,28,32,40,44,45,47,48]:

Short time $\quad \gamma(t)_{t\to 0} = \gamma_o - 2nRTC_o\sqrt{\frac{Dt}{\pi}} \tag{5}$

Longtime $\quad \gamma(t)_{t\to\infty} = \gamma_{eq} + \frac{nRT\Gamma_{eq}^2}{C_o}\sqrt{\frac{\pi}{4Dt}} \tag{6}$

where R = 8.314 J/molK, T is the absolute temperature (K), C_o is the bulk surfactant concentration (mol/L), γ_0 is the surface tension of pure water (mN/m), $\gamma(t)$ is the dynamic surface tension at time t (mN/m), γ_{eq} is the equilibrium surface tension at infinite time (mN/m), Γ_{eq} is the

equilibrium surface excess concentration (mol/m^2) obtained from the equilibrium surface tension measurement which is equal to Γ_m and n is considered to be 1 for a nonionic surfactant system or anionic surfactant with the presence of an excess concentration of electrolyte and 2 for an anionic surfactant system without added electrolyte.

For any constant bulk surfactant concentration, the plots of γ versus $\sqrt{t}$ based on Eq. (5) and γ versus $1/\sqrt{t}$ based on Eq. (6) should be linear if the adsorption is diffusion–controlled, allowing the evaluation of D value from the slope of each plot. It is worthwhile to point out again that both equations are valid at high surfactant concentrations (many times their CMC values) in order to minimize the lateral surfactant diffusion. As shown in Fig. 5, only the γ–$\sqrt{t}$ plot was found to exhibit linear behavior ($R^2 > 0.99$) for two series of surfactants, suggesting that the adsorption is really controlled by diffusion in the short time range (0.1–3 s). However, there is a deviation from linear behavior once it was plot based on Eq. (6). This is because the surfactant backward diffusion becomes significant at a long time [25,27,28,34]. The diffusion coefficients of all studied surfactants in water could be estimated by simply fitting the initial slope equal to $2nRTC_0\sqrt{D/\pi}$ at short time (< 3 s). The calculated diffusion coefficient values of all studied surfactants are listed in Table 3. The D value decreased with an increase in alkyl chain length but increased with an increasing amount of EO units. The results suggest that the adsorption rate at the air/water interface strongly depends on the molecular structure of the surfactant. The increase in alkyl chain length causes the reduction of mobility, leading to the lowering of the diffusion coefficient. On the other hand, the increase in EO units caused a larger hydrophilic head group increases the mobility of surfactant in water, leading to an increase in diffusion coefficient [51]. Moreover, the calculated D value of SDS and $C_{12}EO_n$ series were found to be of the same order of magnitude of other measurements [51,52], implying that a dynamic surface tension measurement can be pronounced to be a simple technique for the diffusion coefficient determination.

3.4. Foam behaviors results

3.4.1. Foamability results

Foamability is a parameter to indicate how easy or difficult foam can be produced. It is measured by the time required to reach any specific foam height. The shorter the time to reach a specific foam height, the higher the ability to produce foam (higher foamability). An empirical correlation between dynamic surface tension (as shown in Eq. (3)) and foamability has been proved in this present work. To find the
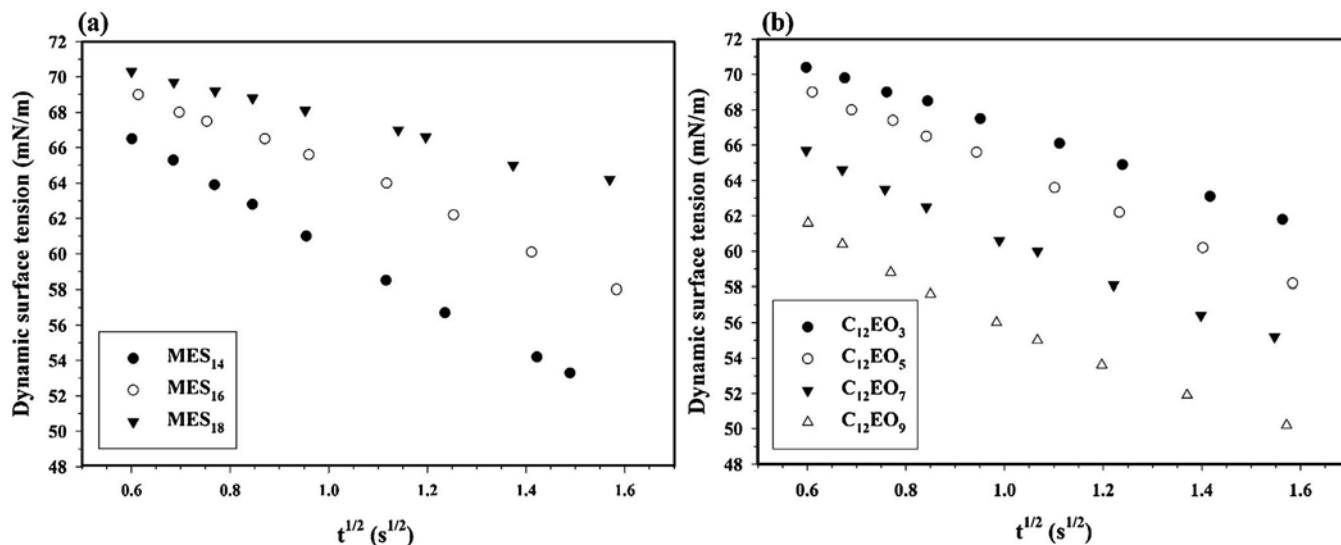
Fig. 5. The linear behavior of $\gamma(t)$–$t^{1/2}$ determined by the short time approximation of (a) MES$_x$ with different alkyl chain lengths were evaluated at the concentration of 2.0 mM/L and (b) C$_{12}$EO$_n$ with different amounts of EO units at the concentration of 0.2 mM/L.

Table 3

Apparent diffusion coefficients of all studied surfactants (at concentration of 2.0 mM for MES$_x$ and 0.2 mM for C$_{12}$EO$_n$).

Surfactant	D (m²/s)
SDS	3.65×10^{-10}
MES$_{14}$	7.21×10^{-12}
MES$_{16}$	4.03×10^{-12}
MES$_{18}$	1.40×10^{-12}
C$_{12}$EO$_3$	2.50×10^{-10}
C$_{12}$EO$_5$	3.92×10^{-10}
C$_{12}$EO$_7$	4.30×10^{-10}
C$_{12}$EO$_9$	5.06×10^{-10}

Table 4

Foam characteristics of all studied surfactants.

Surfactant	Conc (times of CMC)	Foamability (s)	Foam Stability (s)
MES$_{14}$	0.2	1036	35.9
	0.5	791	50.4
	1	676	109
	2	641	111
	5	615	121
MES$_{16}$	0.2	1624	48.0
	0.5	1208	55.5
	1	998	161
	2	994	180
	5	987	191
MES$_{18}$	0.2	2258	20.3
	0.5	1743	4701
	1	1383	72.0
	2	1337	84.2
	5	1351	78.7

Surfactant	Conc (times of CMC)	Foamability (s)	Foam Stability (s)
C$_{12}$EO$_3$	0.2	2890	< 10
	0.5	2539	< 10
	1	2289	25.4
	2	2254	30.1
	5	2233	34.4
C$_{12}$EO$_5$	0.2	2711	< 10
	0.5	2364	< 10
	1	2081	39.0
	2	1983	35.8
	5	1972	37.7
C$_{12}$EO$_7$	0.2	2478	14.2
	0.5	2252	25.5
	1	2013	60.4
	2	1988	70.7
	5	1946	75.2
C$_{12}$EO$_9$	0.2	2344	20.9
	0.5	2031	30.1
	1	1938	80.0
	2	1842	90.3
	5	1853	97.6

time for the maximum change in surface tension $(\frac{\partial \gamma_t}{\partial t})_{max}$, Eq. (3) is differentiated to obtain the following equation [16,41,53]:

$$-\frac{d\gamma}{dt} = \frac{(\gamma_o - \gamma_m)[n(t/t^*)^{n-1}]}{t^*[1 + (t/t^*)^n]^2} \quad (7)$$

The maximum change of dynamic surface tension is at $t = t^*$ and Eq. (7) becomes:

$$\left(\frac{\partial \gamma_t}{\partial t}\right)_{max} = \frac{n(\gamma_o - \gamma_m)}{4t^*} \quad (8)$$

For all studied surfactants, the calculated values of $(\frac{\partial \gamma_t}{\partial t})_{max}$ (Table 2) and foamability (Table 4) were found to have good correlation. Both values of $(\frac{\partial \gamma_t}{\partial t})_{max}$ and foamability increased with an increase in surfactant concentration. Interestingly, both $(\frac{\partial \gamma_t}{\partial t})_{max}$ value and foamability tended to slightly decrease with increasing surfactant concentration beyond the CMC for most studied surfactants. These results suggest that the term $(\frac{\partial \gamma_t}{\partial t})_{max}$ can be used to indicate foaming properties because it reflects the maximum rate of dynamic surface tension reduction [16,53]. The dependence of foamability on the surfactant molecular structure was also investigated. The results show that for the MES$_x$ series, both values of $(\frac{\partial \gamma_t}{\partial t})_{max}$ and foamability decreased with increasing alkyl chain length from 14 to 16. However, MES$_{18}$ showed a very low foamability compared to the others in the homologous because of the very low water solubility of MES$_{18}$ [48]. For the C$_{12}$EO$_n$ series, an increase in EO units (or head group size) increased both value of $(\frac{\partial \gamma_t}{\partial t})_{max}$ and foamability.

3.4.2. Foam stability results

As shown in Table 4, for any given studied surfactant, the foam stability increased greatly with increasing surfactant at a concentration

Table 5
Saturated surface concentrations (Γ_m), diffusivity, foamability and foam stability of MES_{16} at the concentration of 2.0 mM with different NaCl concentrations.

NaCl concentration	wt%	0	0.5	1.0	1.5	2.0
Γ_m	($\mu mol/m^2$)	4.01	4.56	5.15	6.04	6.87
Diffusivity	$(m^2/s) \times 10^{-12}$	3.73	3.51	3.38	3.12	2.89
Foamability	min	11.3 ± 0.8	10.1 ± 0.5	8.6 ± 0.7	7.8 ± 0.7	15.6 ± 1.0
Foam stability	min	2.2 ± 0.2	2.6 ± 0.1	3.0 ± 0.2	3.9 ± 0.2	1.6 ± 0.3

lower than its CMC. The high increment of the foam stability was found with increasing surfactant concentration around its CMC because the Gibbs–Marangoni effect was maximized [16]. The increase in foam stability obviously became insignificant with increasing surfactant concentration beyond its CMC because the Gibbs–Marangoni effect became lower. At a certain surfactant concentration, foam stability increased with an increase in either the alkyl chain length, except MES_{18}, or the number of EO units for MES_x and $C_{12}EO_n$, respectively. Fundamentally, two main factors are responsible for foam destruction. One is the drainage of liquid in the lamellae by gravitational force and another one is the elasticity of the lamellae [15,43,54]. The two factors are directly correlated to the strength of surfactant close packed monolayer [43] and dilatational rheology of the adsorbed foaming agent film [55]. With increasing alkyl chain length of MES_x series, the foam stability increased suggesting that an increase in surface excess concentration can lower liquid drainage and increase film elasticity. The higher the surfactant adsorption density (Γ), the higher the foam stability [56]. Surprisingly, with an increase in the number of EO units of $C_{12}EO_n$ series, even though the surfactant adsorption density (Γ) decreased, foam stability still increased. It can be explained by means of the fact that a large hydrophilic head group (high numbers of EO units) can increase the mobility and diffusivity of surfactant [28,34,51]. The diffusivity of surfactant increases, therefore, the dilational surface elasticity increases accordingly, which can exceed the local depletion of surfactant in the interface. In a comparison between the two groups of studied surfactants, MES_x provided much higher foam stability than that of $C_{12}EO_n$. The negatively charged adsorbed MES_x on the two surfaces of the foam lamellae and the compactness of adsorbed surfactant at the air/water interface are responsible for high foam stability, as compared to that of $C_{12}EO_n$ [15].

3.5. Effect of salt concentration

Table 5 clearly shows that Γ_m increases significantly with an increasing NaCl concentration up to 1.5 wt%, leading to maximum foamability and foam stability. It is because the counterion effect (Na^+) reduces the repulsion force between the negatively charged head group of the surfactant, causing an increase in surfactant adsorption density of both surfaces of foam lamellae. As a result, the increasing repulsion force between two surfaces of foam lamellae from the increasing in surfactant adsorption density leads to both increases in foamability and foam stability. However, in further increases in the NaCl concentration beyond 1.5 wt%, both foamability and foam stability drastically decreased. It is because too much NaCl caused the reduction of the repulsion forces between the two surfaces of foam lamellae, resulting from the neutralization effect by the Na^+ counterion to the negatively charged head group of surfactant adsorbing on the foam lamellae surfaces, causing both reduction of foamability and foam stability. Moreover, the addition of NaCl showed a significantly negative effect on the surfactant diffusivity. It can be explained by the fact that the co-adsorption of Na^+ counterion is responsible for the obstruction of new MES molecules to diffuse and adsorb at the air/water interface.

4. Conclusions

A systematic investigation of the equilibrium and dynamic surface tension as well as foam properties of two series of MES_x with different alkyl chain lengths (14, 16 and 18) $C_{12}EO_n$ with different amounts of EO units (3, 5, 7, and 9) was carried out. The equilibrium surface tension results of all studied surfactants were well fitted with the Langmuir adsorption model. The adsorption process was controlled by the diffusion step of surfactant, which was verified by the linear relation between $\gamma(t)$ and $\sqrt{t}$. The term of $(\frac{\partial \gamma_t}{\partial t})_{max}$ obtained from the dynamic surface tension data can be used to indicate foaming properties in terms of foamability. The anionic surfactant with a moderate alkyl chain length—MES_{14} or MES_{16}—showed higher foamability and foam stability, which is considered to be a promising surfactant for flotation process. In addition, an addition of NaCl provided both a positive and negative effect on the foam properties for the MES anionic surfactant.

Acknowledgements

References

[1] B. Ramaswamy, D. Kar, S. De, A study on recovery of oil from sludge containing oil using froth flotation, J. Environ. Manage. 85 (2007) 150–154.

[2] S. Watcharasing, W. Kongkowit, S. Chavadej, Motor oil removal from water by continuous froth flotation using extended surfactant: effects of air bubble parameters and surfactant concentration, Sep. Purif. Technol. 70 (2009) 179–189.

[3] A. Bunturngpratoomrat, O. Pornsunthorntawee, S. Nitivattananon, J. Chavadej, S. Chavadej, Cutting oil removal by continuous froth flotation with packing media under low interfacial tension conditions, Sep. Purif. Technol. 107 (2013) 118–128.

[4] P. Kanokkarn, T. Shiina, T. Suttikul, S. Chavadej, Removal of motor oil by continuous multistage froth flotation: effect of operational parameters, Sep. Sci. Technol. (2016) 1847–1861.

[5] G. Dermont, M. Bergeron, M. Richer-Laflèche, G. Mercier, Remediation of metal-contaminated urban soil using flotation technique, Sci. Total Environ. 408 (2010) 1199–1211.

[6] I. Ogunniyi, M.K.G. Vermaak, Investigation of froth flotation for beneficiation of printed circuit board comminution fines, Miner. Eng. 22 (2009) 378–385.

[7] A. Vidyadhar, A. Das, Enrichment implication of froth flotation kinetics in the separation and recovery of metal values from printed circuit boards, Sep. Purif. Technol. 118 (2013) 305–312.

[8] F. Maoming, T. Daniel, R. Honaker, L. Zhenfu, Nanobubble generation and its applications in froth flotation (part II): fundamental study and theoretical analysis, Min. Sci. Technol. (China) 20 (2010) 159–177.

[9] P. Chungchamroenkit, S. Chavadej, J.F. Scamehorn, U. Yanatatsaneejit, B. Kitiyanan, Separation of carbon black from silica by froth flotation part 1: Effect of operational parameters, Sep. Sci. Technol. 44 (2009) 203–226.

[10] O. Pornsunthorntawee, S. Chuaybumrung, B. Kitiyanan, S. Chavadej, Purification of single-walled carbon nanotubes (SWNTs) by acid leaching, NaOH dissolution, and froth flotation, Sep. Sci. Technol. 46 (2011) 2056–2065.

[11] C. Wong, M.M. Hossain, C. Davies, Performance of a continuous foam separation column as a function of process variables, Bioprocess Biosyst. Eng. 24 (2001) 73–81.

[12] B. Burghoff, Foam fractionation applications, J. Biotechnol. 161 (2012) 126–137.

[13] R. Lemlich, Adsorptive Bubble Separation Techniques, Elsevier, 2012.

[14] D. Beneventi, B. Carre, A. Gandini, Role of surfactant structure on surface and foaming properties, Coll. Surf. A 189 (2001) 65–73.

[15] M.J. Rosen, Surfactants and Interfacial Phenomena, Wiley, 2004.

[16] T. Tamura, Y. Takeuchi, Y. Kaneko, Influence of surfactant structure on the drainage of nonionic surfactant foam films, J. Colloid Interface Sci. 206 (1998) 112–121.

[17] S.N. Tan, D. Fornasiero, R. Sedev, J. Ralston, The role of surfactant structure on

foam behaviour, Coll. Surf. A 263 (2005) 233–238.

[18] J. Wang, A.V. Nguyen, S. Farrokhpay, A critical review of the growth, drainage and collapse of foams, Adv. Colloid Interface Sci. 228 (2016) 55–70.

[19] X. Gao, Y. Wang, X. Zhao, W. Wei, H. Chang, Equilibrium and dynamic surface tension properties of Gemini quaternary ammonium salt surfactants with ester groups, Coll. Surf. A 509 (2016) 130–139.

[20] S. Boonyasuwat, S. Chavadej, P. Malakul, J.F. Scamehorn, Surfactant recovery from water using a multistage foam fractionator: part I effects of air flow rate, foam height, feed flow rate and number of stages, Sep. Sci. Technol. 40 (2005) 1835–1853.

[21] D.P. Acharya, J.M. Gutiérrez, K. Aramaki, K.-i. Aratani, H. Kunieda, Interfacial properties and foam stability effect of novel gemini-type surfactants in aqueous solutions, J. Colloid Interface Sci. 291 (2005) 236–243.

[22] H. Chang, Y. Wang, Y. Cui, G. Li, B. Zhang, X. Zhao, W. Wei, Equilibrium and dynamic surface tension properties of Gemini quaternary ammonium salt surfactants with hydroxyl, Coll. Surf. A 500 (2016) 230–238.

[23] L.L. Schramm, Surfactants: Fundamentals and Applications in the Petroleum Industry, Cambridge University Press, 2000.

[24] S.I. Karakashev, R. Tsekov, E.D. Manev, A.V. Nguyen, Elasticity of foam bubbles measured by profile analysis tensiometry, Coll. Surf. A 369 (2010) 136–140.

[25] C.M. Phan, T.N. Le, S.-i. Yusa, A new and consistent model for dynamic adsorption of CTAB at air/water interface, Coll. Surf. A 406 (2012) 24–30.

[26] B.W. Barry, D.I.D. Eini, Surface properties and micelle formation of long-chain polyoxyethylene nonionic surfactants, J. Colloid Interface Sci. 54 (1976) 339–347.

[27] Y. Jiang, T. Geng, Q. Li, G. Li, H. Ju, Equilibrium and dynamic surface tension properties of salt-free catanionic surfactants with different hydrocarbon chain lengths, J. Mol. Liq. 204 (2015) 126–131.

[28] X. Liu, Y. Zhao, Q. Li, T. Jiao, J. Niu, Surface and interfacial tension of nonylphenol polyethylene oxides sulfonate, J. Mol. Liq. 216 (2016) 185–191.

[29] K. Karraker, C. Radke, Disjoining pressures, zeta potentials and surface tensions of aqueous non-ionic surfactant/electrolyte solutions: theory and comparison to experiment, Adv. Colloid Interface Sci. 96 (2002) 231–264.

[30] X. Qu, L. Wang, S.I. Karakashev, A.V. Nguyen, Anomalous thickness variation of the foam films stabilized by weak non-ionic surfactants, J. Colloid Interface Sci. 337 (2009) 538–547.

[31] R. Atkin, V.S.J. Craig, E.J. Wanless, S. Biggs, The influence of chain length and electrolyte on the adsorption kinetics of cationic surfactants at the silica-aqueous solution interface, J. Colloid Interface Sci. 266 (2003) 236–244.

[32] J. Eastoe, J.S. Dalton, P.G.A. Rogueda, E.R. Crooks, A.R. Pitt, E.A. Simister, Dynamic surface tensions of nonionic surfactant solutions, J. Colloid Interface Sci. 188 (1997) 423–430.

[33] I. Varga, R. Mészáros, C. Stubenrauch, T. Gilányi, Adsorption of sugar surfactants at the air/water interface, J. Colloid Interface Sci. 379 (2012) 78–83.

[34] A. Casandra, S. Ismadji, B.A. Noskov, L. Liggieri, S.-Y. Lin, A study on the method of short-time approximation-Criteria for applicability, Int. J. Heat Mass Transf. 90 (2015) 752–760.

[35] A. Makievski, D. Grigoriev, Adsorption of alkyl dimethyl phosphine oxides at the solution/air interface, Coll. Surf. A 143 (1998) 233–242.

[36] Y. Liu, Is the free energy change of adsorption correctly calculated? J. Chem. Eng. Data 54 (2009) 1981–1985.

[37] A. Zdziennicka, B. Jańczuk, Behavior of cationic surfactants and short chain alcohols in mixed surface layers at water-air and polymer-water interfaces with

[38] T. Gilányi, I. Varga, C. Stubenrauch, R. Mészáros, Adsorption of alkyl trimethylammonium bromides at the air/water interface, J. Colloid Interface Sci. 317 (2008) 395–401.

[39] J. Eastoe, J.S. Dalton, Dynamic surface tension and adsorption mechanisms of surfactants at the air-water interface, Adv. Colloid Interface Sci. 85 (2000) 103–144.

[40] M.J. Rosen, T. Gao, Dynamic surface tension of aqueous surfactant solutions: 5. Mixtures of different charge type surfactants, J. Colloid Interface Sci. 173 (1995) 42–48.

[41] T. Tamura, Y. Kaneko, M. Ohyama, Dynamic surface tension and foaming properties of aqueous polyoxyethylene n-dodecyl ether solutions, J. Colloid Interface Sci. 173 (1995) 493–499.

[42] X.Y. Hua, M.J. Rosen, Dynamic surface tension of aqueous surfactant solutions: 3. Some effects of molecular structure and environment, J. Colloid Interface Sci. 141 (1991) 180–190.

[43] X.-C. Wang, L. Zhang, Q.-T. Gong, L. Zhang, L. Luo, Z.-Q. Li, S. Zhao, J.-Y. Yu, Study on foaming properties and dynamic surface tension of sodium branched-alkyl benzene sulfonates, J. Dispers. Sci. Technol. 30 (2009) 137–143.

[44] J. Liu, U. Messow, Diffusion-controlled adsorption kinetics at the air/solution interface, Colloid. Polym. Sci. 278 (2000) 124–129.

[45] L. Junji, X. Yun, S. Hongxiu, Diffusion-controlled adsorption kinetics of surfactant at air/solution interface, Chin. J. Chem. Eng. 21 (2013) 953–958.

[46] R.C. Daniel, J.C. Berg, A simplified method for predicting the dynamic surface tension of concentrated surfactant solutions, J. Colloid Interface Sci. 260 (2003) 244–249.

[47] Y.V. Rojas, C.M. Phan, X. Lou, Dynamic surface tension studies on poly (N-vinylcaprolactam/N-vinylpyrrolidone/N, N-dimethylaminoethyl methacrylate) at the air-liquid interface, Coll. Surf. A 355 (2010) 99–103.

[48] S.N. Tan, D. Fornasiero, R. Sedev, J. Ralston, The interfacial conformation of polypropylene glycols and foam behaviour, Coll. Surf. A 250 (2004) 307–315.

[49] M. Eftekhardadkhah, P. Reynders, G. Øye, Dynamic adsorption of water soluble crude oil components at air bubbles, Chem. Eng. Sci. 101 (2013) 359–365.

[50] X. Li, R. Shaw, G.M. Evans, P. Stevenson, A simple numerical solution to the Ward-Tordai equation for the adsorption of non-ionic surfactants, Comp. Chem. Eng. 34 (2010) 146–153.

[51] R. Wang, Effect of Non-Ionic Surfactants and Nano-Particles on the Stability of Foams, (2010).

[52] A.J.M. Valente, H.D. Burrows, M.G. Miguel, V.M.M. Lobo, Diffusion coefficients of sodium dodecyl sulfate in water swollen cross-linked polyacrylamide membranes, Eur. Polym. J. 38 (2002) 2187–2196.

[53] M.J. Rosen, X.Y. Hua, Z.H. Zhu, Dynamic surface tension of aqueous surfactant solutions: IV relationship to foaming, in: K.L. Mittal, D.O. Shah (Eds.), Surfactants in Solution, vol. 11, Springer US, Boston, MA, 1991, pp. 315–327.

[54] V. Carrier, A. Colin, Coalescence in draining foams, Langmuir 19 (2003) 4535–4538.

[55] L. Trujillo-Cayado, P. Ramírez, L. Pérez-Mosqueda, M. Alfaro, J. Muñoz, Surface and foaming properties of polyoxyethylene glycerol ester surfactants, Coll. Surf. A 458 (2014) 195–202.

[56] D. Nguyen, Fundamental surfactant properties of foamers for increasing gas production, Pet. Sci. Technol. 27 (2009) 733–745.

Transformation of Bioderived 1-Decanol to Diesel-like Fuel and Biobased Oil via Dehydration and Oligomerization Reactions

Snunkhaem Echaroj,[†] Malee Santikunaporn,[*,†] and Sumaeth Chavadej[‡]

[†]Department of Chemical Engineering, Faculty of Engineering, Thammasat University, Klongluang, Pathumthani 12120, Thailand
[‡]The Petroleum and Petrochemical College, Chulalongkorn University, Bangkok 10330, Thailand

ABSTRACT: The production of diesel-like fuel and base oil from bioderived fatty alcohol through a two-steps process, dehydration reaction and oligomerization reaction, was studied. The bioderived 1-decanol was converted to olefin mixtures and di-n-decyl ether via the dehydration over commercial γ-alumina catalysts with and without acid modification in a fixed-bed reactor at different temperatures. The catalysts studied were characterized using nitrogen adsorption, temperature-programmed desorption, X-ray diffraction, and thermogravimetric analysis. The dehydration reaction over the unmodified Al_2O_3 was found to be dominant toward the selectivity for 1-decene. The modified Al_2O_3 was shown to promote skeletal internal isomerization and cracking reaction due to strong acid sites. Furthermore, the stability testing results of 1.5 M $(H_2SO_4)/Al_2O_3$ at 573 K demonstrated a rapid deactivation of strong acid sites during the first 10 h of operation. Oligomerization of mixed olefins (1-decanol, 1-decene, and internal olefin) over USY zeolite was found to give the highest conversion of 60%, compared to other zeolites, and the selectivities for dimers, trimers, and heavier hydrocarbons were 72, 24, and 4%, respectively. Evaluation of oligomers properties such as viscosity, viscosity index, simulation distillation, and pour point indicated that dimers and heavier hydrocarbons after hydrogenation can be used as transportation fuel and biobased oil.

1. INTRODUCTION

Due to the limitation in fossil fuels, researchers have been motivated to find sustainable raw materials and new reaction pathways for the synthesis of biofuels for transportation and biobased oils for lubricant manufacture. The first successful attempt for biofuel production was to apply the transesterification reaction to convert the triglyceride content in vegetable oil into biodiesel.[1,2] Apart from its conflict with the food supply, the biodiesel produced also has high viscosity and high density with poor oxidation stability, as compared to diesel oil.[3] In order to overcome these problems, Honeywell UOP trademarked its second generation biofuel under the name of "Green Diesel". The synthesis process involves the deoxygenation of vegetable oil to linear diesel-like hydrocarbons and then isomerization to improve the pour point of the products.[4] Despite the excellent oxidation stability and cold-flow properties, the production of Green diesel is still expensive because it has to be conducted under hydrogen atmosphere over a metal oxide catalyst doped with precious metals. In this work, the synthesis of both diesel-like hydrocarbon and biobased oil from fatty alcohol was investigated using a two-reactions process: dehydration and oligomerization. The feedstock used for this research was 1-decanol, which is considered as a sustainable source because it is a byproduct formed during hydrogenation of fatty acids derived from vegetable oils.[5,6]

Alcohol dehydration generally proceeds through an elimination mechanism on the surface of a solid acid catalyst. Initially, the oxygen atom in an alcohol molecule is chemisorbed onto the Lewis acid sites on the catalyst surface.[7−9] The dissociation of H and OH from alcohol molecules to form α-olefin and H_2O molecules has been detected by using isotope technique.[10] Ether is formed at low temperatures due to the interaction between alcohol adsorbed on Lewis sites and adjacent alcohol molecules adsorbed on Brønsted sites.[11] At a higher reaction temperature, 1-olefin produced from the dehydration reaction can be simultaneously transformed to internal olefins through the internal isomerization reaction on Brønsted sites.[12,13] The general reaction pathways for 1-decanol dehydration and isomerization are shown in Figure 1.

Apart from reaction temperature, the acidity of catalysts also has a significant effect on the transformation of primary alcohols. Catalysts possessing stronger acid sites were found to give a higher conversion of alcohol[14,15] and promote branch isomerization reaction, in which 1-olefin was converted to branched olefins.[16,17] However, it was observed that the amount of acid sites did not correlate with the catalytic activity of the dehydration reaction.[18] Modified catalysts, such as sulfated metal oxides, were reported to be appropriate for the dehydration, isomerization, and cracking reactions due to their strong acidity.[19−21] The metal oxide most commonly used on an industrialized scale is γ-alumina (γ-Al_2O_3), which is obtained by heating boehmite in the temperature range of 723−873 K.[22] It has outstanding thermal stability[23] and abundance in the tetrahedral coordination of aluminum atoms[24,25] and a surface hydroxide group,[26,27] so it provides the Lewis acid sites.

One of the main obstacles in achieving stable dehydration activity over heterogeneous acid catalysts, especially for large molecular weight reactants, is the rapid deactivation rate due to deposition of coke on the catalyst surface.[28] The current method applied to overcome catalytic deactivation problems for light alcohol dehydration included modification of catalyst with Ag[29] and dealumination of zeolite catalyst.[30] However, only a few
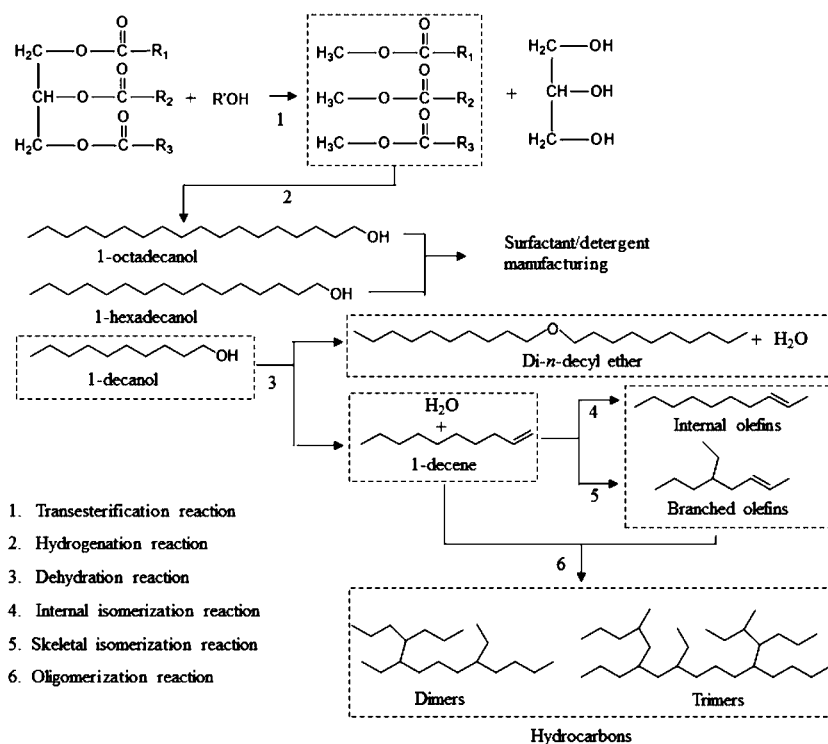
Figure 1. Proposed two-reaction pathways: conversion of primary alcohol to olefins through the dehydration reaction over alumina and the conversion of olefins to hydrocarbon oligomers through the oligomerization reaction over zeolite catalysts.

studies on the dehydration of fatty alcohol with a chain longer than six carbon atoms were reported.[31,32] Nel and de Klerk pointed out that the difficulties in obtaining accurate data for dehydration of 1-decanol resulted from the presence of impurities in the feedstock.[33]

Oligomerization over heterogeneous acid catalysts is a coupling reaction of olefin monomers to form larger molecules through the carbenium-formation mechanism. However, heterogeneous acid catalysts contain a high concentration of Brønsted acid sites, which inevitably causes product loss through the cracking reaction. One way to overcome this problem is to partially block Brønsted sites by impregnating the solid acid catalyst with Ni metals.[34,35] Also, the accessibility of acidic sites is an important factor for the production of heavy hydrocarbon molecules.[36−38] Corma et al. improved internal diffusion by increasing the pore size of H-ZSM through postsynthesis desilication technique.[39] However, both impregnation and desilication techniques were found to give very low conversion. Other types of catalysts used for oligomerization are a chromium silicate catalyst[40,41] and coordination catalysts such as Ziegler−Natta[42,43] and metallocene.[44,45] However, these catalysts require both precious metals and a controlled air-free condition which make the production process highly expensive. Recently, a one-step technique was employed where both dehydration and oligomerization reactions proceeded simultaneously over the same heterogeneous catalyst.[46,47] Despite its lower production cost, this method gave low conversion of the reactant. Therefore, it is of great interest to improve the yield of each reaction, and the dehydration and oligomerization reactions should be studied separately so that each reaction can be controlled in a separate unit.

The present work was a continuation of our previous study on the dehydration reaction of a primary alcohol over precipitated plain Al_2O_3 catalysts to produce olefins.[48] First, the catalytic activity and stability of sulfated-Al_2O_3 catalysts were investigated as a function of reaction temperature and concentration of modifying agents. Three different valuable products can be obtained from 1-decanol, including α-olefin, internal olefins, and di-n-decyl ether. α-Olefins and internal olefins can be used as intermediates for the production of base oil and drilling fluid. Di-n-decyl ether can be used as additive to improve the octane number of gasoline. The main focus of this research was to produce olefins and then to combine these olefins via oligomerization reaction in a separate batch reactor over zeolite catalysts to make transportation fuel and biobased oils.

2. EXPERIMENTAL SECTION

2.1. Chemicals. In this experiment, 1-decanol, with 98% purity, was supplied by Thai Olefin Co. Ltd. The reactant, 1-decanol, is produced as a side product of the conversion of vegetable oil to 1-hexadecanol and 1-octadecanol. Since 1-decanol is derived from vegetable oil, the diesel-like fuel and biobased oil obtained from 1-decanol can be regarded as "green products". The commercial γ-alumina catalyst, γ-Al_2O_3, used in this study was supplied by Sasol (Germany). Concentrated H_2SO_4 (98%) was obtained from Ajax. All reagents were analytical grades and used as received. Nitrogen gas (99.99% purity) for catalyst testings was obtained from Praxair Co. Ltd. USY, mordenite, and beta zeolite catalysts for oligomerization reaction were obtained from Zeolyst International. Before the start of each reaction, beta zeolite was calcined in a muffled reactor at 823 K for 5 h to transform the ammonium form into a proton form. USY and mordenite were dried in an oven at 383 K for 12 h.

2.2. Catalyst Modification Procedure. A 10 g amount of γ-Al_2O_3 was added to 10 mL of a H_2SO_4 solution having various concentrations according to previous work.[49] The mixtures were stirred for 10 min for the acid treatment and then filtered. The filtered solid samples were washed with distilled water five times, then dried overnight at 383 K, and finally calcined at 773 K using a heating rate of 3 K/min for 3 h. The modified catalyst samples were denoted as $x(H_2SO_4)/Al_2O_3$, where x was the concentration of the modifying agent in molarity.

Table 1. Physical and Chemical Characterization of Catalysts Used for Dehydration and Oligomerization Reaction

catalyst	specific surface area (m²/g)	pore vol (mL/g)	pore diam (nm)	weak acid sites (mmol/g)	strong acid sites (mmol/g)	total acid sites (mmol/g)
catalysts for dehydration reaction						
Al_2O_3	210	0.58	10.6	0.311		
1.0 M $(H_2SO_4)/Al_2O_3$	221	0.64	12.9	0.412	0.107	0.311
1.5 M $(H_2SO_4)/Al_2O_3$	224	0.66	12.8	0.541	0.154	0.519
2.5 M $(H_2SO_4)/Al_2O_3$	236	0.71	12.8	0.615	0.181	0.685
catalysts for oligomerization reaction						
mordenite	511	0.16	2.4	0.422	0.133	0.796
USY	746	0.59	3.1	0.551	0.232	0.555
beta	672	0.36	2.0	0.404	0.094	0.784

2.3. Catalyst Characterization Methods. Both adsorption and desorption isotherms of N_2 on 0.1–0.3 g of catalyst samples were obtained by a Quantachrome (Autosorb-1C) instrument at 77 K using liquid nitrogen. Prior to the sorption analysis, each sample was degassed with He gas for at least 6 h at 473 K. The concentration and strength of acid sites on any modified Al_2O_3 sample were determined by ammonia (10% NH_3 in He) temperature-programmed desorption (TPD-NH_3) with a thermal conductivity detector (TCD; SRI Instrument, GC 110). The sample was first treated with He at 773 K for 1 h. After it was cooled to 333 K, the catalyst sample was saturated with NH_3 by a continuous flow of the NH_3 gas mixture for 30 min at 333 K. To remove the excess NH_3, the sample was treated under a flow of He at 373 K for 2 h. Next, the chemisorbed NH_3 was desorbed by a flow of He while by increasing temperature from 373 to 973 K at a heating rate of 10 K/min, and then held at 973 K for 30 min.

All spent catalysts were analyzed for the amount of coke deposition by thermogravimetric analysis (TGA). Approximately 45–60 mg of each spent catalyst sample was heated from room temperature to 973 K at a heating rate of 10 K/min. The flow rate of oxygen was kept at 10 mL/min throughout the analysis.

2.4. Dehydration Reaction Experiments. The dehydration reaction of 1-decanol was performed in a 14 mm diameter stainless steel fixed-bed reactor at atmospheric pressure and various temperatures between 573 and 623 K. Approximately 0.6 g of each catalyst specimen was packed and secured with quartz wool in the heating zone of the reactor. The rest of the reactor was filled with ceramic balls having an average diameter of 2 mm. The catalyst was pretreated in situ for 2 h at 573 K under the presence of N_2 flow (150 mL/min). After that, the 1-decanol liquid was fed through the reactor using a high-pressure pump at a constant residence time of 0.4 h and under a N_2 flow rate of 50 mL/min throughout the catalytic testing period. The residence time used for this experiment was defined in terms of the ratio between catalyst weight and flow rate of reactant (W/F). Liquid effluent samples collected at different times were allowed to separate into two phases. The organic top phase consisted of olefins and di-n-decyl ether products, and the lower layer was the aqueous phase. Material balance revealed that the volumetric ratio between the organic phase and the water phase followed the stoichiometry of the reaction. The conversion of 1-decanol (DA) and selectivities to i (where i are products from dehydration and isomerization reactions and included 1-decene, di-n-decyl ether, internal olefins, and branched olefins) were calculated by using eqs 1 and 2.

$$conversion/\% = \frac{DA(moles\ in) - DA(moles\ out)}{DA(moles\ in)} \times 100 \tag{1}$$

$$(selectivity\ to\ i)/\% = \frac{amount\ of\ i}{\sum(amount\ of\ products\ obtained)} \times 100 \tag{2}$$

2.5. Oligomerization Reaction Experiments. The olefin oligomerization experiments were performed in a three-necked continuously stirred batch reactor (1,000 mL) with different catalysts: 10 wt % USY zeolite (CBV-400, Si/Al = 5.1), beta zeolite (CP814C, Si/Al = 38), and mordenite zeolite (CBV 21A, Si/A = 20) at 474 K, 300 rpm agitation speed, and atmospheric pressure. For this part of the

experiments, three feedstocks with different compositions were used. The feedstocks collected from the dehydration reaction of 1-decanol over 1.5 M $(H_2SO_4)/Al_2O_3$ consisted of 48.4% internal olefins, 33.3% 1-decene, and 18.3% 1-decanol. The second feedstock was also obtained from the dehydration reaction over 1.5 M $(H_2SO_4)/Al_2O_3$, but the contents of 1-decanol and di-n-decyl ether were removed by distillation at 543 K under atmospheric pressure (therefore the ratio of 1-olefin to internal olefins was the same as the first feedstock which was 7:10). The last feedstock was obtained from the dehydration reaction over the unmodified Al_2O_3, and it was also distilled to remove 1-decanol and di-n-decyl ether. The third feedstock consisted of 95% 1-decene, and 5% internal olefins (the ratio of 1-decene to internal olefins = 19:1).

The oligomers obtained by vacuum distillation were further separated for heavy fractions of dimer and trimer by distillation in the temperature range of 523–623 K under vacuum. Both dimer and trimer were then hydrogenated at 503 K, 360 psi, and a W/F of 2.8 h, with a hydrogen flow rate of 200 mL/min over the 0.5% Pt/Al_2O_3. The hydrogenation testing was additionally conducted at a W/F of 0.7 h. These hydrogenated dimers can be used as diesel fuel after blending with smaller molecular weight hydrocarbons, while hydrogenated heavier hydrocarbons can be used as biobased oil.

2.6. Evaluation of Product Compositions and Properties. The compositions of the products obtained from both dehydration and oligomerization reactions were measured by a gas chromatography (GC). The GC system (Hewlett-Packard, HP 6890) used for both reactions was equipped with a FID detector and a capillary column (DB-1, 15 m, 0.530 mm, 0.15 μm) with He gas as the mobile phase. Identification of the peaks in gas chromatography was by gas chromatography–mass spectrometry (GC-MS HP, 7690/5977A MSD) using a fused-silica capillary column, DB-5MS (30 m length, 0.25 mm diameter, and 0.25 μm film thickness).

Oligomer products before and after the hydrogenation reaction were analyzed by Fourier transform infrared (FTIR) technique to investigate the conversion of unsaturated molecules to saturated hydrocarbons. A spectrometer (Parkin Elmer, Spotlight 400) was used to obtain FTIR spectra in the 650–4000 cm^{-1} range. Each analysis was conducted at room temperature using an average of four scans, with a spectral resolution of 4 cm^{-2} and air as the reference spectrum.

Hydrogenated dimers and heavier hydrocarbons were tested for basic properties including viscosity, viscosity index, pour point, heating value, and simulation distillation (SimDist). The viscosity measurements were carried out at 313 and 373 K according to ASTM D455 using a Memmert WNB 14 water bath and Canon–Fenske glass viscometers (sizes 100 and 150). The pour point measurements were determined by obtaining the onset of the cooling peak analyzed by a differential scanning calorimeter (DSC; Mettler Toledo DSC, 1 Module). Approximately, 12 mg of sample was placed inside an aluminum pan which was hermetically sealed before analysis. The temperature of the measurement cell was ramped up at a rate of 5 K/min from room temperature to 323 K and then cooled at the same rate to 203 K. The lower heating values of all samples were obtained using a bomb calorimeter (IKA, C6000).

(a)

(b)

(c)

(d)

(e)

Figure 2. Characterization of modified and unmodified dehydration catalysts including (a) N_2 sorption isotherm, (b) pore diameter distribution curves, (c) XRD patterns, (d) NH_3-TPD patterns, and (e) weight loss profiles of spent catalysts from TGA. Spent catalysts from reaction with the following conditions: T = 583 K; P = 101.3 kPa; N_2 flow, 50 mL/min; W/F = 0.4.

3. RESULTS AND DISCUSSION

3.1. Catalyst Characterization. *3.1.1. Catalysts for Dehydration Reaction.* The N_2 adsorption−desorption data

were obtained for unmodified and modified Al_2O_3 catalysts in order to evaluate the effect of H_2SO_4 concentration on physical characteristics of the catalyst. As shown in Table 1, the surface area of Al_2O_3 slightly increased with increasing H_2SO_4
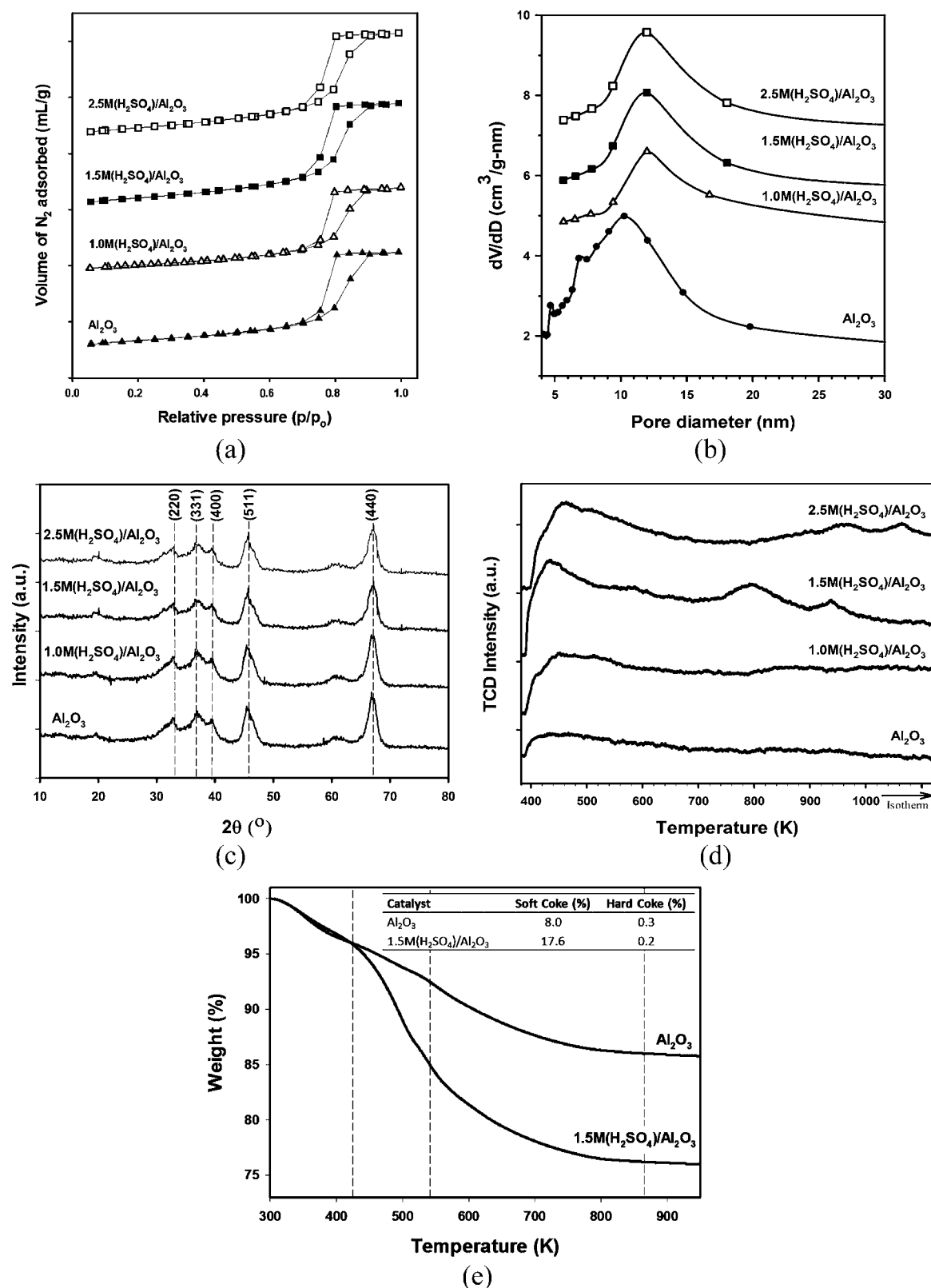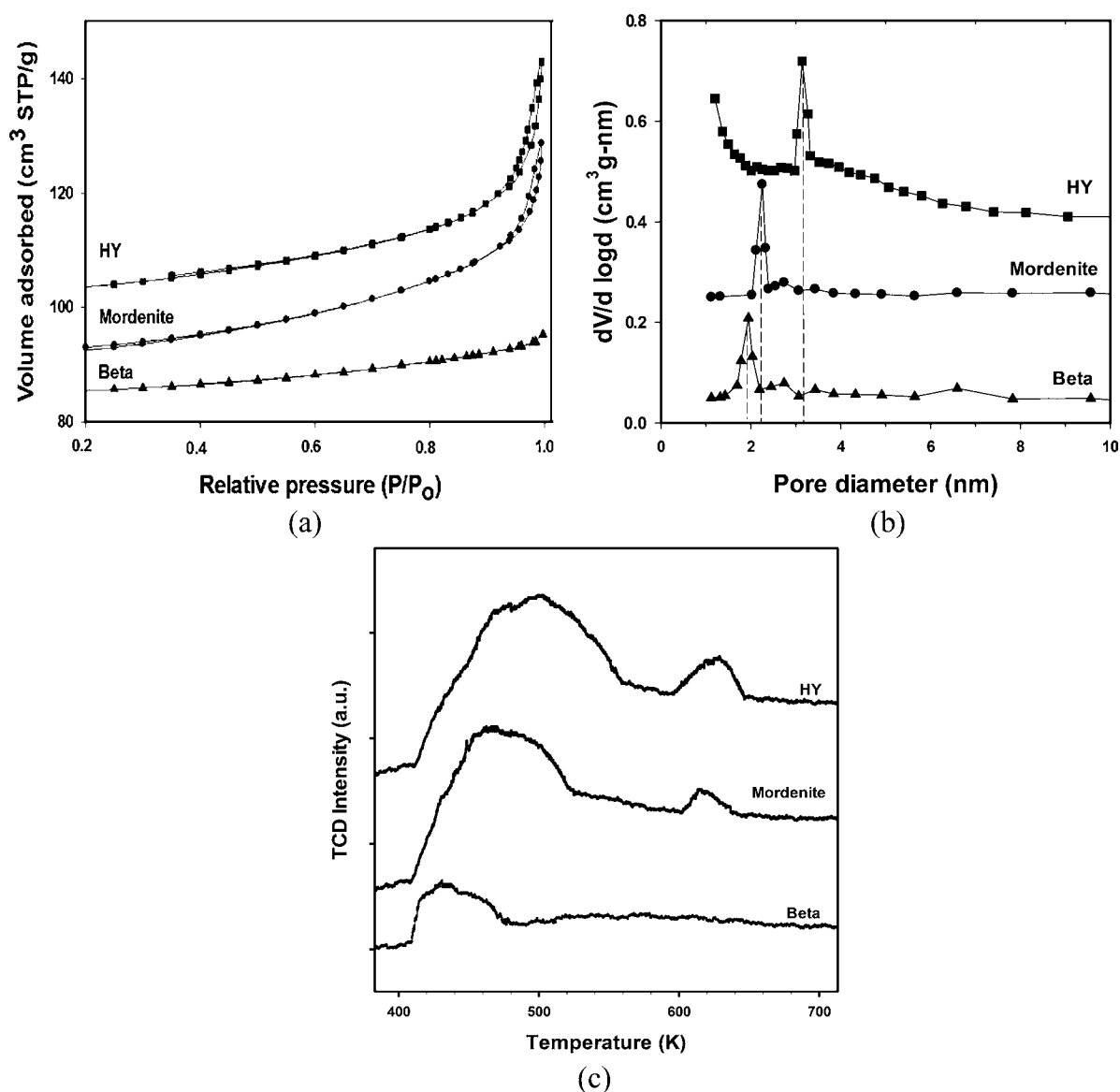
Figure 3. Characterization of oligomerization catalysts including (a) N_2 adsorption isotherms, (b) pore diameter distribution curves, and (c) NH_3-TPD patterns of all three zeolite catalysts.

concentration, in good agreement with other literature.[20,21] The presence of a hysteresis loop in each isotherm, shown in Figure 2a, indicates that all test catalysts had mesoporous structure. The shape of each hysteresis loop showed a clear H1 type, suggesting that the pores of all test catalysts were cylindrical in shape. The average pore size obtained from the adsorption branch of the isotherms slightly increased from 9.5 to 12 nm after the Al_2O_3 was modified by H_2SO_4, as shown in Figure 2b, suggesting that the H_2SO_4 concentration did not significantly affect the average pore sizes of all modified Al_2O_3 catalysts. Wang et al. and Zhao et al. reported similar isotherms with the same type of hysteresis loop for a commercial alumina.[50,51]

The phase structures of all unmodified and modified Al_2O_3 catalysts are shown in Figure 2c. Each catalyst showed typical peaks of γ-Al_2O_3 at about $2\theta = 20°$, $33°$, $38°$, $40°$, $47°$, $62°$, and $67°$ (JCPDS No. 10-0425), corresponding to reflections having crystalline arrangement of 111, 220, 311, 222, 400, 511, and 440, respectively, which agrees well with other work.[50,51] The modification of Al_2O_3 with H_2SO_4 was found to have an insignificant effect on the crystalline structure of the catalysts.

This was because the concentration of H_2SO_4 used as modifying agent for this experiment was lower than 3.6 M. According to Yeh et al., a distinct diffraction peak at $2\theta = 26°$ appeared after the Al_2O_3 was treated by solution with H_2SO_4 concentration of 3.6 M or higher.[49] This peak indicates the formation of crystallized $Al_2(SO_4)_3$ on Al_2O_3 catalyst.

The NH_3 TPD analysis of all modified and unmodified Al_2O_3 catalysts was used to study the impact of H_2SO_4 concentration on the acidity of the treated catalysts. Table 1 summarizes the amount of weak and strong acid sites as a function of H_2SO_4 concentration. Weak acid sites can be identified and quantified by the NH_3 desorption peaks at temperatures lower than 423 K while the desorption peaks at temperatures higher than 523 K indicate strong acid sites.[18,52,53] The desorption temperatures can be observed in the NH_3 TPD profiles, as presented in Figure 2d. All unmodified and modified catalysts contained a dominant peak between 373 and 440 K, indicating the presence of dominant weak acid sites. An increase in H_2SO_4 concentration caused a significant increase in the intensity of weak acid sites due to formation of multilayer sulfate species on the γ-Al_2O_3
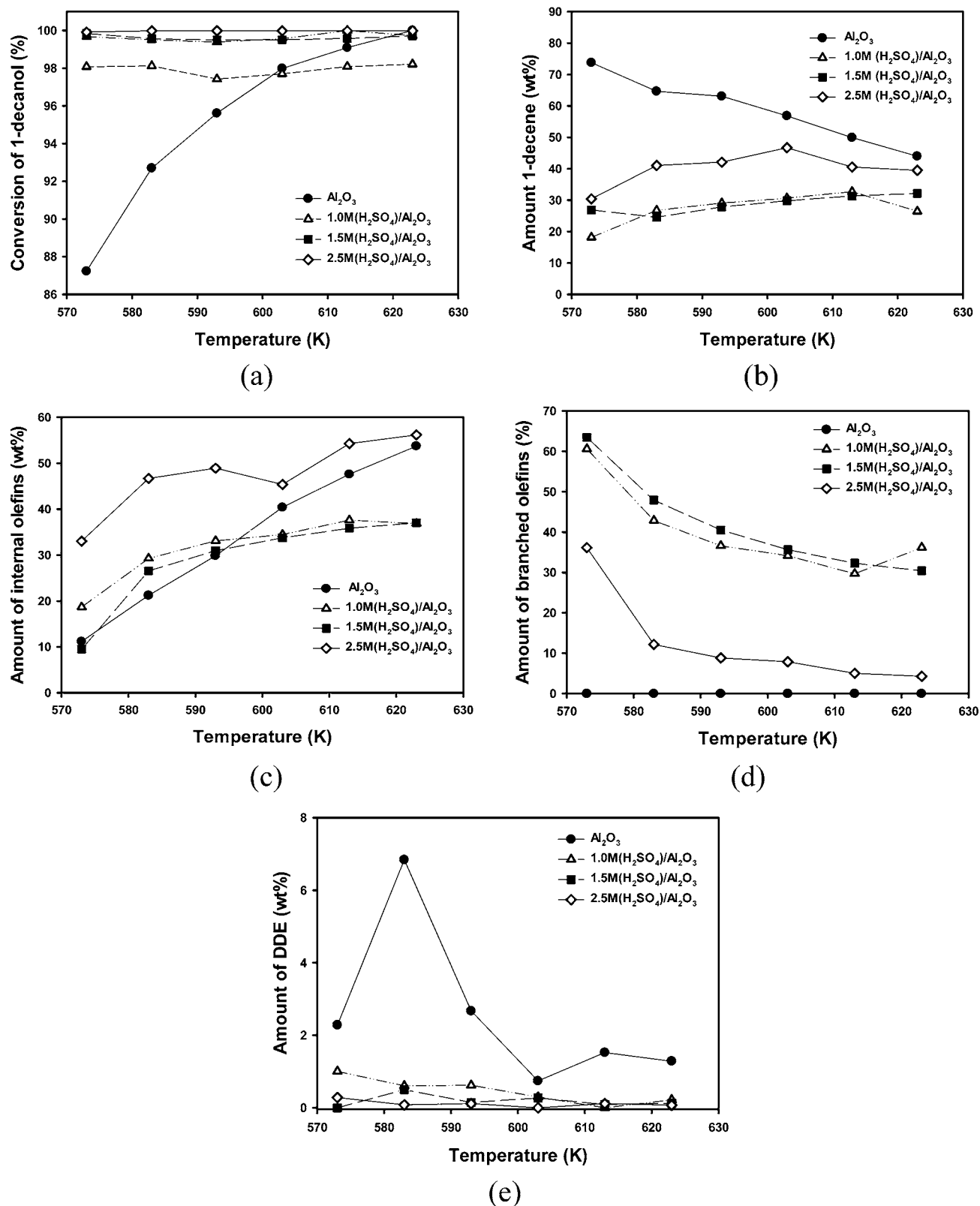
Figure 4. Influence of reaction temperature on (a) conversion of 1-decanol, (b) amount of 1-decene, (c) amounts of internal olefins, (d) amount of branched olefins, and (e) amount of di-*n*-decyl ether over modified Al_2O_3 catalysts at different H_2SO_4 concentrations as compared to the unmodified Al_2O_3 catalyst operated at pressure of 101.3 kPa, a N_2 flow rate of 50 mL/min, and a W/F ratio of 0.4 h.

surface.[49] Additionally, the treatment of Al_2O_3 with H_2SO_4 also created strong acid sites, corresponding to the second and third desorption peaks, as shown in Figure 2d. As the H_2SO_4 concentration increased to 2.5 M, the second and third desorption peaks shifted to higher temperatures, which resulted from an increase in the strength of strong acid sites.

Figure 2e demonstrates the weight loss of the spent catalysts of unmodified and 1.5 M H_2SO_4 treated samples obtained from
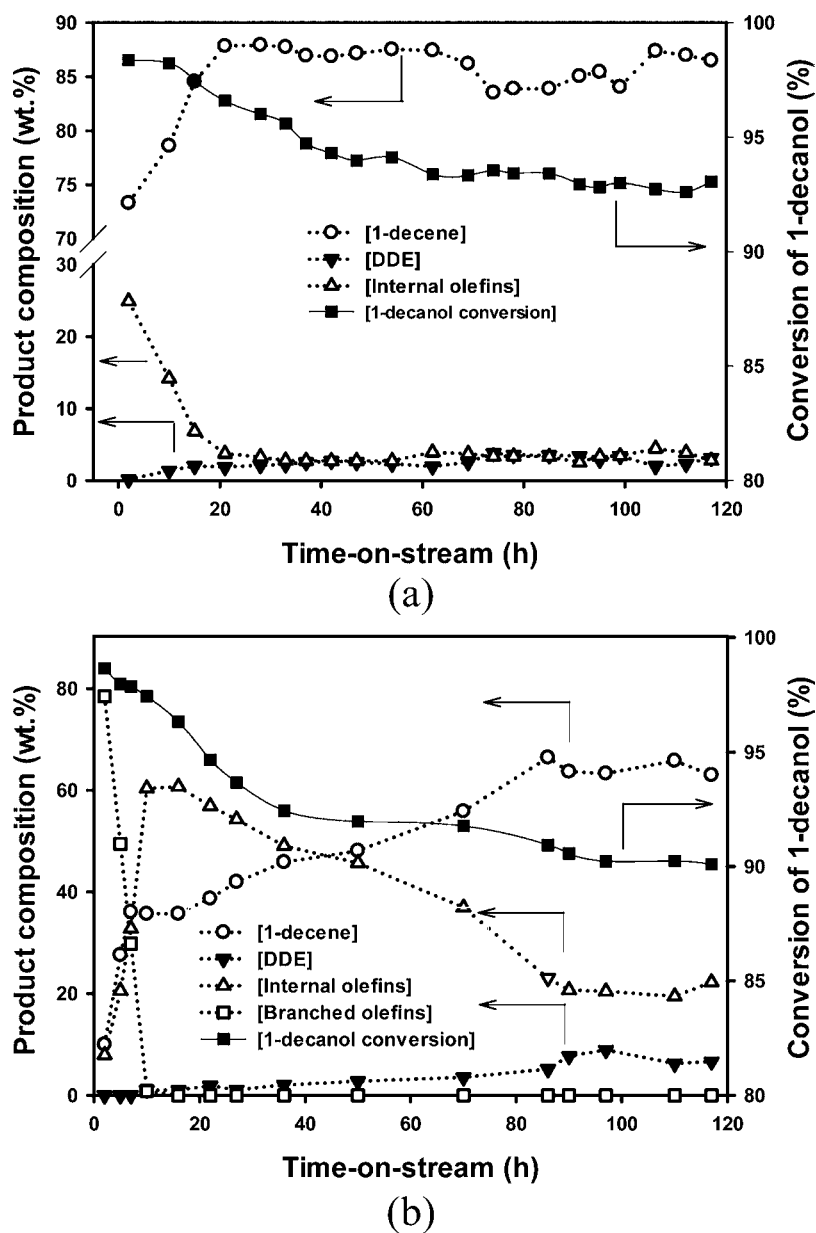
(a)

(b)

Figure 5. Stability testing results of the dehydration of 1-decanol at different times-on-stream over (a) the unmodified Al_2O_3 and (b) 1.5 M (H_2SO_4)/Al_2O operated at a reaction temperature of 583 K, pressure of 101.3 kPa, a N_2 flow rate of 50 mL/min, and a W/F ratio of 0.4 h.

long-run experiments by the thermogravimetric analysis technique. A first decrease in the weight between 303 and 413 K represented the removal of moisture while the second weight loss, in the range of 413−520 K, corresponded to the decomposition of soft coke or aliphatic hydrocarbons. Finally, the third weight loss between 520 and 873 K was due to the decomposition of hard coke or polyaromatics.[54] The results showed that the Al_2O_3 catalysts modified by H_2SO_4 gave higher coke formation. As shown in the inset of Figure 3, the soft coke was the main component of the deposited coke of both spent Al_2O_3 catalysts. Additionally, both test catalysts contained nearly the same small amount of hard coke.

3.1.2. Zeolite Catalysts for Oligomerization Reaction. The results of N_2 physisorption analysis of zeolite catalysts are shown in Table 1. The BET surface area and pore volume values of USY zeolite were significantly higher than those of mordenite and beta zeolite. The N_2 adsorption−desorption isotherms of zeolite catalysts used for the oligomerization reaction are displayed in

Figure 3a. Based on the IUPAC classification, the beta zeolite displayed a typical Type I isotherm, indicating that they possessed microporous structure. In the case of mordenite and USY zeolites, a small hysteresis loop was exhibited in the range above 0.8 P/P_o, indicating the presence of mesopore belonging to Type IV isotherm. This was consistent with the higher average pore sizes of USY and mordenite catalysts, as shown in the pore size distribution graph in Figure 3b. USY zeolite was clearly superior compared to the two other zeolites in terms of accessibility and surface area for reaction to take place.

The weak and strong acid concentrations of all studied zeolite catalysts are shown in Table 1. The desorption profile of beta catalyst, as shown in Figure 3c, demonstrated a dominant desorption peak at 443 K. On the other hand, the desorption profiles of mordenite and USY zeolite catalysts were observed to contain two desorption peaks at higher desorption temperatures relative to beta catalyst. This indicates that both mordenite and USY zeolites have higher concentrations of weak and strong acid

sites while beta zeolite has only weak acid sites with much lower intensity. The amount of both weak and strong acid sites was in the following order: beta < mordenite < USY. USY zeolite was hypothesized to be the best catalyst for the oligomerization reaction due to its high BET surface area, pore volume, pore diameter, weak acid sites, and strong acid sites relative to the other two zeolite catalysts.

3.2. Catalytic Activity on Dehydration Reaction.
3.2.1. Effects of Reaction Temperature and Concentration of H_2SO_4 Modifying Agents. The dehydration reaction of 1-decanol was studied at different reaction temperatures over the Al_2O_3 catalysts modified with different H_2SO_4 concentrations and compared to the unmodified Al_2O_3 catalyst. Figure 4 shows the effects of reaction temperature on the 1-decanol conversion and product composition over all the modified Al_2O_3 catalysts compared to the unmodified Al_2O_3. For the unmodified Al_2O_3 catalyst, the conversion of 1-decanol increased significantly from 87 to 93% with increasing temperature from 573 to 623 K, as shown in Figure 4a. For any H_2SO_4 concentration, the conversion of 1-decanol remained almost constant in the reaction temperature range of 573−623 K. The conversion of 1-decanol could increase marginally with increasing H_2SO_4 concentration from 1 to 2.5 M. The modification of Al_2O_3 with H_2SO_4 resulted in an increase in the conversion, especially at low reaction temperatures. The significant increase in 1-decanol conversion resulted from the increase in the amount of acidic sites (Table 1) which was responsible for the enhancement in 1-decanol adsorption ability especially at low temperatures.[15] As shown in Figure 4b, for the unmodified Al_2O_3 catalyst, the concentration of 1-decene produced decreased significantly with increasing temperature because it was further converted into internal olefins. At any reaction temperature, the modification of Al_2O_3 with H_2SO_4 resulted in a significant decrease in the amount of 1-decene in the product.

The 1-decene produced can undergo either internal or skeletal isomerization to form internal olefins and branched olefins. As shown in Figure 4c, for all studied catalysts the amount of internal olefins increased as the reaction temperature increased. The results are in good agreement with other work.[55−57] The formation of internal olefins was found to depend slightly on the concentration of H_2SO_4 when the range of concentration was varied from 1 to 1.5 M. Interestingly, an increase in H_2SO_4 concentration from 1.5 to 2.5 M caused the composition of internal olefins to significantly increase from 26.2 to almost 48%. The drastic increase in internal olefins resulted from the higher acid concentration of strong acid sites. This is in good agreement with the previous study that an increase in skeletal isomerization of *n*-butene to isobutene was due to the increase in the amount of strong acid sites.[58]

Figure 4d demonstrates the formation of branched olefins. The branched olefins could not be produced over the unmodified Al_2O_3 catalyst throughout the reaction temperature range whereas they were produced over all of the H_2SO_4 modified Al_2O_3 catalysts and decreased with increasing reaction temperature. For any given reaction temperature, the amount of branched olefins tended to increase slightly with increasing H_2SO_4 concentration for catalyst modification from 1.0 to 1.5 M, but it decreased substantially with a further increase in H_2SO_4 concentration from 1.5 to 2.5 M. The results can be explained by the fact that an increase in strong acid sites from the increasing H_2SO_4 concentration for catalyst modification from 1.0 to 1.5 M promotes the formation of branched olefins more than internal olefins. However, a further increase in H_2SO_4 concentration to

2.5 M gave the opposite results because the very high strength of strong acid sites at 2.5 M made the branched olefins produced to be further cracked to smaller gaseous molecules. Lemberton et al. reported the similar tendency of the C_{10} hydrocarbons to be initially converted to multibranch isomers and then undergo the cracking reaction. In this current research, the cracking reaction was confirmed by the gas analysis results and by performing mass balance calculation.[59] For a typical experiment over the 2.5 M $(H_2SO_4)/Al_2O_3$ catalyst for 20 h of operation, 20% product loss was observed. Weng et al. also reported an increase in the cracking activity with an increase in H_2SO_4 concentration.[19] Figure 4e shows the amount of di-*n*-decyl ether (DDE) as a function of reaction temperature over unmodified and modified Al_2O_3 catalysts. The amount of DDE could be reduced by the H_2SO_4 treatment for the Al_2O_3 catalyst. This is because strong acid sites on sulfated alumina promote formation of olefins which can interfere with the diffusion of ether, causing decomposition of ether to olefins.[60]

3.2.2. Catalytic Stability. A set of long-run experiments for catalyst stability testing was performed on the unmodified Al_2O_3 and 1.5 M $(H_2SO_4)/Al_2O_3$ catalysts for 117 h. Figure 5a shows the conversion of 1-decanol and product composition over the unmodified Al_2O_3 catalyst as a function of reaction time. The conversion of 1-decanol remained as high as 93% for at least the first period of 10 h. After 20 h of operation, the composition of 1-decene remained nearly constant at about 85%. On the other hand, the amount of internal olefins decreased sharply with time and remained stable at 4% after 20 h. Beyond 20 h of operation, the main product was 1-decene. From the high conversion of 1-decanol for a long operational time, it can be concluded that the Al_2O_3 catalyst under these operating conditions was relatively stable. Makgoba et al. also reported the good stability of Al_2O_3 in the dehydration reaction of 1-hexanol and 1-octanol with the conversions of 1-hexanol and 1-octanol around 80 to 60%, respectively, which were lower than the results presented here for 1-decanol.[31] This is because the dehydration reaction experiments of the present work were conducted at a higher W/F ratio resulting in a longer reaction time.

Figure 5b shows the stability results of the 1.5 M $(H_2SO_4)/Al_2O_3$ catalyst. It was observed that the product composition changed dramatically during the first 80 h and the deactivation rate was relatively higher than unmodified catalyst. The conversion of 1-decanol decreased from 98 to 90% with increasing operation time to 120 h, whereas the content of 1-decene increased with operational time. The amount of branched olefins started as high as 80%, and decreased to zero after 10 h. The results suggested that branched olefins were formed through the skeletal isomerization, which relies on the carbenium-ion mechanism after 1-decene interacted with the strong acid sites.[61] Therefore, the rapid decrease in branched olefins to zero after 10 h of operation indicates that the deactivation of strong acid sites was responsible for the skeletal isomerization. The deactivation of strong acid sites can occur due to the formation of large molecular weight aliphatics (soft coke) and polyaromatics (hard coke), as the experiment confirmed by the presence of as much as 17.8 wt % total coke on the 1.5 M $(H_2SO_4)/Al_2O_3$ catalyst (Figure 3). The composition of internal olefins increased to reach a maximum level of 60% after 10 h and then decreased rapidly with increasing operational time from 15 to 80 h. However, unlike the formation of branched olefins which approached zero at the time of operation beyond 10 h, the formation of internal olefins still remained at a significant level even after the strong acid sites had been deactivated. The results

suggest that the double bond migration, responsible for the transformation of 1-decene to internal olefins, does not depend solely on the strong acid sites.

3.3. Catalytic Activity on Oligomerization Reaction.

Since an increase in agitation speed beyond 300 rpm did not affect the activity of any test catalyst, the agitation speed of 300 rpm was selected for the oligomerization experiments. Figure 6
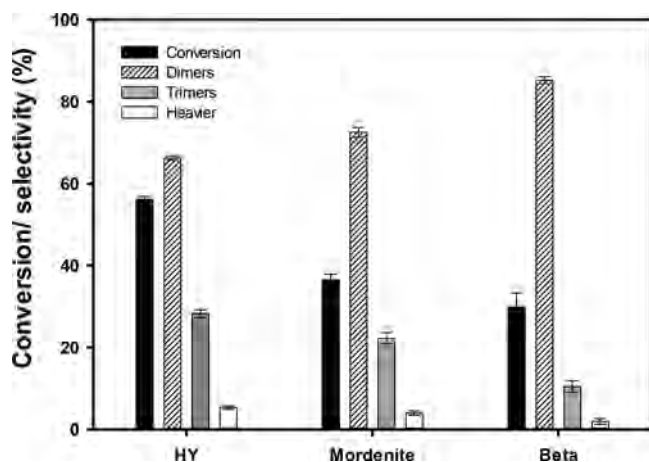

Figure 6. Oligomerization results of the feedstock collected from the dehydration reaction of 1-decanol over 1.5 M $(H_2SO_4)/Al_2O$ catalyst at 583 K and 101.3 kPa with a N_2 flow rate of 50 mL/min and a W/F ratio of 0.4 h. The oligomerization reaction was operated at 473 K, 300 rpm, 10 wt % catalyst, pressure of 101.3 kPa, and a reaction time of 4 h over different catalysts.

shows the results of the oligomerization experiments which were conducted at a reaction temperature of 473 K over different catalysts (USY, beta, and mordenite zeolites). USY catalyst provided the highest olefin conversion of 60% while beta catalyst had the lowest olefin conversion. The selectivities for dimers (C_{20}), trimers (C_{30}), and heavier (C_{30}^+) hydrocarbons over USY were as high as 72, 24, and 4%, respectively. Beta zeolite was found to give the lowest conversion and lowest selectivities for trimers and heavier hydrocarbons. The differences in the activity results of all test zeolites are related to their specific surface areas, pore size, and framework structure. Among the three zeolites, USY contained the largest pore volume, pore diameter, and a cage-like framework, which provided a more effective internal diffusion of reactant and oligomer products, resulting in higher selectivity for trimers and heavier hydrocarbons.[62,63] This was confirmed by our previous work on the oligomerization of 1-decene over sulfated alumina.[64] The spent zeolite catalysts after 4 h of the reaction turned from white to very dark brown color, especially for USY zeolite catalyst, indicating the formation of hard coke in the catalyst pores.[65]

Three feedstocks with different compositions of 1-decene, 1-decanol, and internal olefins were used for the oligomerization reaction to evaluate their effects on catalytic activity and product loss via the cracking reaction. For this part, the oligomerization reaction was conducted using the same batch reactor with USY zeolite catalyst at 473 K and atmospheric pressure. As seen in Table 2, an increase in the content of internal olefins in feedstock was found to reduce the conversion of olefins, the composition of heavier molecules, and product loss. This is because the oligomerization of internal olefins produced highly branched oligomers, which tended to cause blockage and catalytic deactivation due to space restriction of the zeolite pores.[66] Additionally, 1-decanol also had the same effect as internal olefins, because it competed with olefins for adsorption on the active acidic site.[67,68]

3.4. Hydrogenated Dimer and Heavier Oligomer Properties.

The oligomer product samples obtained from the oligomerization reaction and distillation process were hydrogenated to saturate the double bonds in the samples in order to increase the oxidation stability.[69−71] The structural changes of oligomer molecules due to the hydrogenation reaction were observed by FTIR. Figure 7a demonstrates the FTIR spectrum of oligomer before undergoing hydrogenation reaction. The peaks at 1710 and 958 cm^{-1} represent the C=C stretching frequency and the C−H bending frequency of sp^2 in an alkene molecule, respectively. Panels b and c of Figure 7 show the disappearance of both peaks of the dimer and heavier oligomer products after the hydrogenation step. Both final products obtained were colorless and odorless, indicating complete hydrogenation activities.

The basic properties of viscosity, pour point, and a distillation temperature for 90% recovery of the hydrogenated dimers sample compared to those of no. 2 diesel ASTM D975 specifications are shown in Table 3. The hydrogenated dimers sample obtained from this study showed good diesel oil in terms of pour point and distillation temperature for 90% volume recovery except it had a higher viscosity (5.23 mm^2/s) than the range of ASTM D975 no. 2 diesel oil. As expected, the dimers obtained from the oligomerization of 1-decene were mostly hydrocarbons with 20 carbon atoms, whereas commercial diesel oils obtained from refineries mostly contain hydrocarbons with the carbon number range of 15−20.

The basic properties of viscosity, viscosity index, pour point, and distillation temperature for 90% volume recovery of the hydrogenated heavier oligomers sample obtained from this experiment compared to those values of the commercial poly-α-olefins (PAO 5) are shown in Table 3. The viscosities of base oil obtained from this experiment at 313 and 373 K are very close to those of the commercial PAO 5 which is categorized as group 4 synthetic base oil, according to the American Petroleum Institution (API). According to previous studies, base oil produced from the oligomerization reaction over zeolite catalysts

Table 2. Conversion of Olefins, Product Loss, Compositions, and Selectivities (%) from the Oligomerization Experiments Using Feedstocks with Different Compositions[a]

	feed composition (wt %)				catalytic activity (%)		product compositions (%)				selectivity to (%)		
no.	1-decanol	1-decene	internal olefins	1-decene/internal olefin ratio	conversion of olefins	product loss	C_{10}	C_{20}	C_{30}	C_{30}^+	C_{20}	C_{30}	C_{30}^+
1	18.3	33.3	48.4	0.7	72.7	1.0	27.3	52.3	17.4	2.9	72.0	24.0	4.0
2	0.0	40.7	59.2	0.7	76.0	13.0	24.0	52.1	19.9	4.0	68.5	26.2	5.3
3	0.0	95.0	5.0	19.0	80.0	16.0	20.0	52.3	22.8	4.9	65.4	28.5	6.1

[a]Reaction conditions: USY zeolite, at 473 K, 300 rpm, 10 wt % catalyst, pressure of 101.3 kPa, and a reaction time of 4 h.
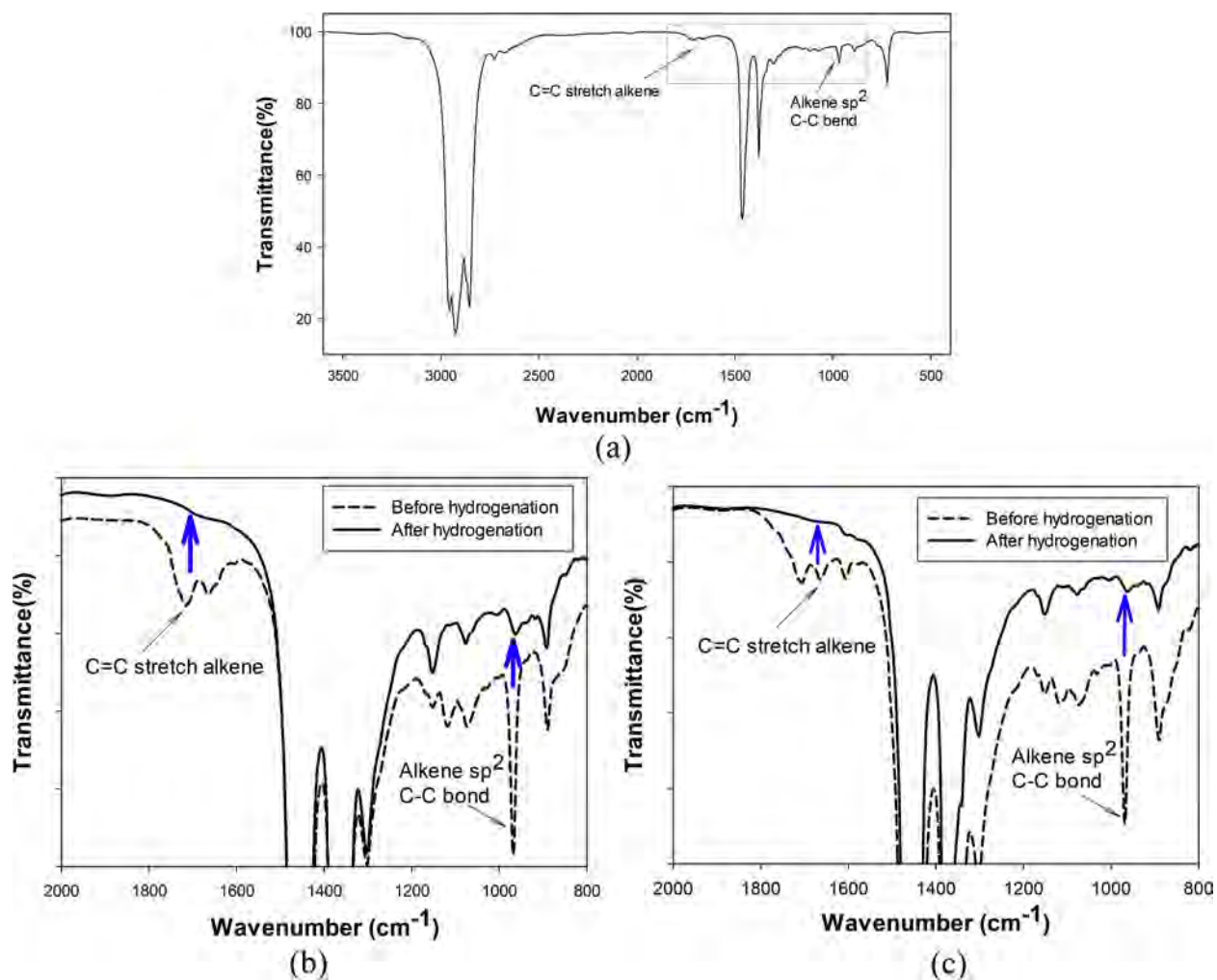
Figure 7. (a) Typical FTIR spectrum of oligomers product before the hydrogenation reaction step, (b) FTIR spectrum of dimer product (diesel oil) before and after hydrogenation step, and (c) FTIR spectrum of heavier product (base oil) before and after the hydrogenation reaction.

had low viscosity index due to high degree of branching in the molecular structure.[61] The high viscosity index of the base oil obtained in this study may be attributed to the linear structure pore of beta zeolite, which promoted the formation of linear hydrocarbons.

One of the cold-flow properties measured was pour point, which indicates the lowest temperature before a liquid sample stops flowing.[72] This characteristic can be accurately estimated from the freezing point or the crystallization onset temperature of the freezing peak obtained during a DSC cooling scan.[73,74] The freezing peak was not detected for both diesel and base oils obtained from this experiment, indicating these liquid samples still behave as fluid even at a temperature as low as 203 K. This outstanding cold-flow property, compared to ASTM standard, was due to the oligomerization reaction through the carbenium-formation mechanism, which yielded oligomers with a high degree of branching.[74]

The lower heating value of hydrogenated dimers synthesized in this research of 46.3 MJ/kg was relatively high in comparison with ASTM standard. Hydrogenation was found to improve the lower heating value of dimers due to the removal of sulfur content (the non-hydrogenated dimers had the lower heating value of 45.4 MJ/kg).

4. CONCLUSIONS

Two different reactions (dehydration and oligomerization) were investigated to produce diesel-like hydrocarbon and biobased oil from 1-decanol over acid modified Al_2O_3 and zeolite catalysts. For the dehydration reaction, acid modification had no effect on the crystalline structure of Al_2O_3 but caused a slight increase in the BET surface area, pore volume, and concentration of strong acid sites. The activity test results reveal that strong acid sites promote branched olefins and internal olefins but suppress the formation of ether. The unmodified Al_2O_3 catalyst exhibited high stability in terms of the amount of 1-decene produced (87.7%). On the other hand, all acid modified catalysts were deactivated rapidly due to coke deposition on strong acid sites, causing branched and internal olefins to diminish after 10 h of operation.

The results of the three zeolite catalysts used for the oligomerization of dehydration products indicate that a cage-like framework and large pores with higher accessibility are needed to have high 1-decene conversion and formation of heavier hydrocarbon. Internal olefins and 1-decanol in the feedstock significantly reduce cracking reaction and product loss at the expense of lower 1-decene conversion. Hydrogenated dimers could be used as an additive for no. 2 diesel oil, whereas the hydrogenated heavier oligomers had characteristics similar to those of the commercial poly-α-olefins (PAO 5) base oil. Also, it

Table 3. Comparison between Standard Properties and Products (Diesel-like Oil and Biobased Oil) Obtained from Oligomerization Reaction[a]

properties	ASTM D975 no. 2 diesel oil	diesel-like oil from this experiment	commercial base oil (PAO 5)	biobased oil from this experiment
viscosity at 313 K (mm²/s)	1.9−4.1	5.23	24.1	25.8
viscosity at 373 K (mm²/s)	–	–	5.1	5.4
viscosity Index	–	–	146	145
pour point (K)	Thailand[b], <283; USA[c], <243; ASTM, 238−263	<203	227	<203
lower heating value (MJ/kg)	43.9[d]	46.3[e]	–	–
Simulation Distillation (K)				
IBP		418		441
volume recovered (%)				
10		561		665
20		586		682
30		591		688
40		595		692
50		597		697
60		600		703
70		603		717
80		606		741
90	573−629	613	–	753
FPB		735		771

[a]Reaction conditions: Beta zeolite, at 473 K, 300 rpm, 10 wt % catalyst, pressure of 101.3 kPa, and a reaction time of 4 h. [b]Thailand standard for diesel. [c]Pacific Northwest region's winter diesel specification. [d]Estimated by ASTM D4809. [e]Lower heating value of hydrogenated dimer. For partially and non-hydrogenated dimer, the lower heating values were 45.8 and 45.4 MJ/kg.

could be blended with additives to make lubricant for engines or other applications.

■ **AUTHOR INFORMATION**

Corresponding Author
*E-mail: smalee@engr.tu.ac.th.

ORCID
Malee Santikunaporn: 0000-0002-6464-2323

Notes
The authors declare no competing financial interest.

■ **REFERENCES**

(1) Xie, W.; Peng, H.; Chen, L. *Appl. Catal., A* **2006**, *300*, 67.
(2) Sani, Y. M.; Daud, W. M. A. W.; Abdul Aziz, A. R. *Appl. Catal., A* **2014**, *470*, 140.
(3) Hermida, L.; Abdullah, A. Z.; Mohamed, A. R. *Renewable Sustainable Energy Rev.* **2015**, *42*, 1223.
(4) Snåre, M.; Kubičková, I.; Mäki-Arvela, P.; Eränen, K.; Murzin, D. Y. *Ind. Eng. Chem. Res.* **2006**, *45*, 5708.
(5) Voeste, T.; Buchold, H. *J. Am. Oil Chem. Soc.* **1984**, *61*, 350.
(6) Godrej, N. B.; Thakur, M. S.; Suri, S. K.; Ruthardt, K. α-Olefins from Oleochemical Raw Materials: The Godrj-Lurgi Process. In *Proceedings of the 3rd World Conference on Detergents: Global Perspectives*; Cahn, A., Ed.; AOCS Press: Champaign, IL, USA, 1994; p 222.
(7) Deo, A. V.; Dalla Lana, I. G. *J. Phys. Chem.* **1969**, *73*, 716.
(8) Deo, A. V.; Chuang, T.-T.; Dalla Lana, I. G. *J. Phys. Chem.* **1971**, *75*, 234.
(9) Clement, G.; Knoezinger, H.; Staehlin, W.; Stuebner, B. *J. Phys. Chem.* **1979**, *83*, 1280.
(10) Shi, B.; Dabbagh, H. A.; Davis, B. H. *J. Mol. Catal. A: Chem.* **1999**, *141*, 257.
(11) Shi, B. C.; Davis, B. H. *J. Catal.* **1995**, *157*, 359.
(12) Katritzky, A. R.; Nichols, D. A.; Siskin, M.; Murugan, R.; Balasubramanian, M. *Chem. Rev.* **2001**, *101*, 837.
(13) de Klerk, A. In *Catalysis*, Vol. 23; Spivey, J. J., Eds.; Royal Society of Chemistry: Cambridge, U.K., 2011; pp 1−49, DOI: 10.1039/9781849732772-00001.
(14) Hong, E.; Sim, H.-I.; Shin, C.-H. *Chem. Eng. J.* **2016**, *292*, 156.
(15) Ciftci, A.; Varisli, D.; Cem Tokay, K.; Asli Sezgi, N.; Dogu, T. *Chem. Eng. J.* **2012**, *207−208*, 85.
(16) Weingarten, R.; Tompsett, G. A.; Conner, W. C.; Huber, G. W. *J. Catal.* **2011**, *279*, 174.
(17) Coleto, I.; Roldán, R.; Jiménez-Sanchidrián, C.; Gómez, J. P.; Romero-Salguero, F. *J. Catal. Today* **2010**, *149*, 275.
(18) Sung, D. M.; Kim, Y. H.; Park, E. D.; Yie, J. E. *Catal. Commun.* **2012**, *20*, 63.
(19) Yang, Y.-C.; Weng, H.-S. *Appl. Catal., A* **2010**, *384*, 94.
(20) Mao, D.; Yang, W.; Xia, J.; Zhang, B.; Lu, G. *J. Mol. Catal. A: Chem.* **2006**, *250*, 138.
(21) Ferreira, M.a.L.; Rueda, E. H. *J. Mol. Catal. A: Chem.* **2002**, *178*, 147.
(22) Xu, B.; Smith, P. *Thermochim. Acta* **2012**, *531*, 46.
(23) Bedia, J.; Barrionuevo, R.; Rodríguez-Mirasol, J.; Cordero, T. *Appl. Catal., B* **2011**, *103*, 302.
(24) Zaki, M. I.; Knözlngem, H. *Spectrochim. Act.* **1987**, *43*, 1455.
(25) Knözinger, H.; Ratnasamy, P. *Catal. Rev.: Sci. Eng.* **1978**, *17*, 31.
(26) Peri, J. B. *J. Phys. Chem.* **1968**, *72*, 2917.
(27) Peri, J.B. A. *J. Phys. Chem.* **1965**, *69*, 220.
(28) Choopun, W.; Jitkarnka, S. *J. Cleaner Prod.* **2016**, *135*, 368.
(29) Sun, D.; Arai, S.; Duan, H.; Yamada, Y.; Sato, S. *Appl. Catal., A* **2017**, *531*, 21.
(30) Müller, J. M.; Mesquita, G. C.; Franco, S. M.; Borges, L. D.; de Macedo, J. L.; Dias, J. A.; Dias, S. C. L. *Microporous Mesoporous Mater.* **2015**, *204*, 50.

(31) Makgoba, N. P.; Sakuneka, T. M.; Koortzen, J. G.; van Schalkwyk, C.; Botha, J. M.; Nicolaides, C. P. *Appl. Catal., A* **2006**, *297*, 145.

(32) Chokkaram, S.; Davis, B. H. *J. Mol. Catal. A: Chem.* **1997**, *118*, 89.

(33) Nel, R. J. J.; de Klerk, A. *Ind. Eng. Chem. Res.* **2009**, *48*, 5230.

(34) Martínez, A.; Arribas, M. A.; Concepción, P.; Moussa, S. *Appl. Catal., A* **2013**, *467*, 509.

(35) Lallemand, M.; Finiels, A.; Fajula, F.; Hulea, V. *Chem. Eng. J.* **2011**, *172*, 1078.

(36) Coelho, A.; Caeiro, G.; Lemos, M.A.N.D.A.; Lemos, F.; Ribeiro, F. R. *Fuel* **2013**, *111*, 449.

(37) de Klerk, A. *Ind. Eng. Chem. Res.* **2005**, *44*, 3887.

(38) Bringué, R.; Cadenas, M.; Fité, C.; Iborra, M.; Cunill, F. *Chem. Eng. J.* **2012**, *207−208*, 226.

(39) Corma, A.; Martínez, C.; Doskocil, E. *J. Catal.* **2013**, *300*, 183.

(40) Fang, Y.; Liu, B.; Terano, M. *Kinet. Catal.* **2006**, *47*, 295.

(41) McDaniel, M. P. Review of Phillips Chromium Catalyst for Ethylene Polymerization. In *Handbook of Transition Metal Polymerization Catalysts*; Hoff, R., Mathers, R. T., Eds.; John Wiley & Sons: Hoboken, NJ, USA, 2010; pp 123−606.

(42) Huang, Q.; Chen, L.; Ma, L.; Fu, Z.; Yang, W. *Eur. Polym. J.* **2005**, *41*, 2909.

(43) Mohammed, A.; Fatee, S.-E.; Ahmed, T. S.; Moustafa, T. M. *Appl. Petrochem. Res.* **2016**, *4*, 287.

(44) Huang, J.; Rempel, G. L. *Appl. Catal. A: Gen.* **1997**, *20*, 153.

(45) Diez de Tuesta, J. L.; Casas, E.; Moreno, J.; Perez Nebreda, P.; Escola, J. M.; Van Grieken, R. *Appl. Catal., A* **2013**, *460-461*, 70.

(46) Chan, X.; Pu, T.; Chen, X.; James, A.; Lee, J.; Parise, J. B.; Kim, D. H.; Kim, T. *Catal. Commun.* **2017**, *97*, 65.

(47) Iwamoto, M. *Molecules* **2011**, *16*, 7844.

(48) Echaroj, S.; Santikunaporn, M.; Chavadej, S. *React. Kinet., Mech. Catal.* **2015**, *114*, 75.

(49) Yang, T.-s.; Chang, T.-h.; Yeh, C.-t. *J. Mol. Catal. A: Chem.* **1997**, *115*, 339.

(50) Wu, Q.; Zhang, F.; Yang, J.; Li, Q.; Tu, B.; Zhao, D. *Microporous Mesoporous Mater.* **2011**, *143*, 406.

(51) Shang, X.; Wang, X.; Nie, W.; Guo, X.; Zou, X.; Ding, W.; Lu, X. *Mater. Lett.* **2012**, *83*, 91.

(52) Katada, N.; Endo, J.-i.; Notsu, K.-i.; Yasunobu, N.; Naito, N.; Niwa, M. *J. Phys. Chem. B* **2000**, *104*, 10321.

(53) Xiu, T.; Wang, J.; Liu, Q. *Microporous Mesoporous Mater.* **2011**, *143*, 362.

(54) Siddiqui, M. R. H.; Holmes, S.; He, H.; Smith, W.; Coker, E. N.; Atkins, M. P.; Kozhevnikov, I. V. *Catal. Lett.* **2000**, *66*, 53.

(55) Gee, J. C.; Prampin, D. S. *Appl. Catal., A* **2009**, *360*, 71.

(56) Jörke, A.; Seidel-Morgenstern, A.; Hamel, C. *Chem. Eng. J.* **2015**, *260*, 513.

(57) An, J.; Bagnell, L.; Cablewski, T.; Strauss, C. R.; Trainor, R. W. *J. Org. Chem.* **1997**, *62*, 2505.

(58) Wichterlová, B.; Žilkova, N.; Uvarova, E.; Čejka, J.; Sarv, P.; Paganini, C.; Lercher, J. A. *Appl. Catal., A* **1999**, *182*, 297.

(59) Soualah, A.; Lemberton, J. L.; Pinard, L.; Chater, M.; Magnoux, P.; Moljord, K. *Appl. Catal., A* **2008**, *336*, 23.

(60) Casas, C.; Bringué, R.; Ramírez, E.; Iborra, M.; Tejero, J. *Appl. Catal., A* **2011**, *396*, 129.

(61) Chen, C. S. H.; Bridger, R. F. *J. Catal.* **1996**, *161*, 687.

(62) Berger, C.; Gläser, R.; Rakoczy, R. A.; Weitkamp, J. *Microporous Mesoporous Mater.* **2005**, *83*, 333.

(63) Ferchiche, S.; Warzywoda, J.; Sacco, A., Jr *Int. J. Inorg. Mater.* **2001**, *3*, 773.

(64) Echaroj, S.; Santikunaporn, M.; Chavadej, S. *React. Kinet., Mech. Catal.* **2017**, *121*, 629.

(65) Van Grieken, R.; Escola, J. M.; Moreno, J.; Rodriguez, R. *Appl. Catal., A* **2008**, *337*, 173.

(66) Ghosh, R.; Bandyopadhyay, A. R.; Jasra, R.; Gagjibhai, M. M. *Ind. Eng. Chem. Res.* **2014**, *53*, 7622.

(67) Cruz, V. J.; Bringué, R.; Cunill, F.; Izquierdo, J. F.; Tejero, J.; Iborra, M.; Fité, C. *J. Catal.* **2006**, *238*, 330.

(68) Cruz, V. J.; Izquierdo, J. F.; Cunill, F.; Tejero, J.; Iborra, M.; Fité, C. *React. Funct. Polym.* **2005**, *65*, 149.

(69) Pinto, F.; Martins, S.; Gonçalves, M.; Gulyurtlu, I.; Costa, P.; Alves, A.; Mendes, B. *Appl. Energy* **2013**, *102*, 272.

(70) Kitayama, Y.; Muraoka, M.; Takahashi, M.; Kodama, T.; Takahashi, E.; Okamura, M. *J. Am. Oil Chem. Soc.* **1997**, *74*, 525.

(71) Shomchoam, B.; Yoosuk, B. *Ind. Crops Prod.* **2014**, *62*, 395.

(72) Sarin, A.; Arora, R.; Singh, N. P.; Sarin, R.; Malhotra, R. K.; Kundu, K. *Energy* **2009**, *34*, 2016.

(73) Dunn, R. O. *J. Am. Oil Chem. Soc.* **1999**, *76*, 109.

(74) Ono, H.; Iki, H.; Koyama, A.; Iguchi, Y. Production of BHD (Bio Hydrofined Diesel) with Improved Cold Flow Properties. *Annual Catalysis in Petroleum Refining and Petrochemicals Symposium Papers*; King Fahd University of Petroleum and Minerals: Dhahran, Saudi Arabia, 2010.